THE DEVELOPMENT OF ALKOXY-BASED SOL-GEL PROCESSING
FOR MAGNETORESISTIVE MANGANITE THIN FILMS

BY

BRENT ALLEN CLOTHIER

B.S., Mechanical Engineering, University of Texas at Austin, 1994
B.A., Plan II Liberal Arts, University of Texas at Austin, 1995

DISSERTATION

Submitted in partial fulfillment of the requirements
for the degree of Doctor of Philosophy in Materials Science and Engineering
in the Graduate College of the
University of Illinois at Urbana-Champaign, 2005

Urbana, Illinois

CERTIFICATE OF COMMITTEE APPROVAL

University of Illinois at Urbana-Champaign
Graduate College

April 20, 2005

We hereby recommend that the thesis by:
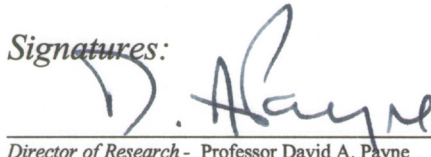
BRENT ALLEN CLOTHIER

Entitled:

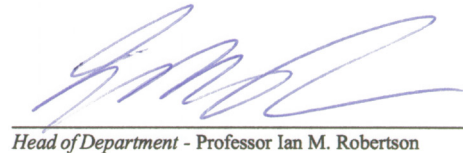**THE DEVELOPMENT OF ALKOXY-BASED SOL-GEL PROCESSING FOR MAGNETORESISTIVE MANGANITE THIN FILMS**

Be accepted in partial fulfillment of the requirements for the degree of:
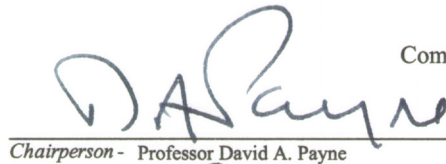
Doctor of Philosophy

Signatures:

_____
Director of Research - Professor David A. Payne

_____
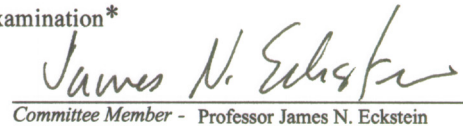*Head of Department -* Professor Ian M. Robertson
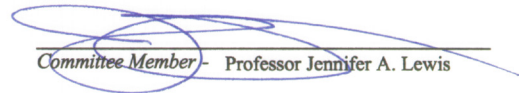
Committee on Final Examination*

_____
Chairperson - Professor David A. Payne

_____
Committee Member - Professor James N. Eckstein

_____
Committee Member - Professor Waltraud M. Kriven

_____
Committee Member - Professor Jennifer A. Lewis

_____
Committee Member -

_____
Committee Member -

* Required for doctoral degree but not for master's degree

ABSTRACT

Doped-lanthanide manganites, $Ln_{1-x}M_x\text{MnO}_3$, represent a class of commercially-attractive perovskite-structured oxides due to room-temperature magnetoresistive behavior when $0.2 < x < 0.4$, Ln = La, and M = Sr, Ba, or Pb. To date, thin-film investigations of these materials have relied mainly on vapor-phase techniques such as pulsed-laser ablation, molecular beam epitaxy, and rf-magnetron sputtering. Deposition conditions almost universally incorporate lattice-matched refractory substrates, typically $\text{LaAlO}_3(100)$ or $\text{SrTiO}_3(100)$, and often require high-temperature post-annealing (i.e., > 900 °C) to establish proper oxygen stoichiometry. Such processes then impart notable challenges for manganite film growth on technologically-relevant silicon substrates due to thermal restrictions and poor epitaxy.

This dissertation presents, for the first time, the successful development of an alkoxy-based, sol-gel process for integrating magnetoresistive doped-lanthanide manganite thin films onto silicon-based substrates. Two candidate compositions (i.e., $\text{La}_{0.67}\text{Ba}_{0.33}\text{MnO}_3$ and $\text{La}_{0.67}\text{Pb}_{0.33}\text{MnO}_3$), choosen for potential room-temperature properties, were deposited on Si(100) and platinized-Si(100). Crystallization of the requisite perovskite phase at temperatures below 650 °C stems from the incorporation of all-alkoxide precursors, and in particular, $\text{Mn}[\text{OC}(\text{CH}_3)_3)]_2$. The steric bulk of the 2-methyl-2-propoxo ligand, when combined with the compact, polyfunctional solvent, 2-methoxyethanol, imparts high solubility and hydrolytic reactivity. This accomplishment represents a significant new contribution because manganese(II) alkoxides derived from low carbon-content ligands (C_6 and below) are well-known to form stable, insoluble coordinate polymers. Such an impediment has, up to this point, forced the adaptation of surrogate manganese precursors, typically acetates. Coatings obtained from such solutions crystallize into the manganite perovskite phase only above 800 °C, even with the aid of lattice-matched templates.

The orange and pinkish-orange all-alkoxide solutions, also synthesized for the first time, were free from any products of aerobic oxidation, and hence, exhibited no discoloration from brown colloids or precipitates. A mild, partial hydrolysis of h = 0.25 induced conversion into a polymeric sol system, conferring both spinnable viscosities and excellent sol longevity. Post-coating hydrolysis via slow spinning under humidified air proved essential to remove

sufficient organic content and thereby prevent excessive carbon dioxide release during pyrolysis. Transparent, dense, and defect-free amorphous thin films were obtained by 1-minute heat treatments at 100, 300, and 450 °C. Conversion into a fine-grain (< 50 nm), polycrystalline microstructure occurred above 600 °C on platinized-Si(100) and above 650 °C on Si(100). This low-temperature densification and crystallization reflects the development of a true sol-gel process with active hydrolysis and condensation mechanisms. The higher temperatures often reported with surrogate precursors are more consistent with simple metallorganic decomposition processes.

Microstructural characterization of the manganite thin films was carried out using X-ray photoelectron spectrometry (XPS), glancing-incidence X-ray scattering (GIXS), scanning electron microscopy (SEM), and atomic force microscopy (AFM). Chemical homogeneity across the substrate was stoichiometric and exhibited no temperature dependence in the 600–750 °C heat-treatment range studied by this investigation. Such an observation is remarkable for $La_{0.67}Pb_{0.33}MnO_3$ given the extensive documentation which reports PbO volatilization from the related $PbZr_xTi_{1-x}O_3$ perovskites. The cubic lattice parameters of the deposited films (e.g., a = 3.900 Å for $La_{0.67}Ba_{0.33}MnO_3$ and a = 3.887 Å for $La_{0.67}Pb_{0.33}MnO_3$ on Si(100) at 650 °C) were in excellent agreement with values published in the literature for bulk, polycrystalline powders. Cross-sectional SEM images indicated film thicknesses of 90–100 nm which corresponded to 30–40 nm of final oxide per spin-coat. Typical grain sizes, as determined by tapping mode AFM, started at 10–15 nm and increased to 20–25 nm by 750 °C. The lead-doped composition on platinized-Si(100), however, was an exception, exhibiting larger initial diameters of 30–35 nm, which by 750 °C, distended to 45–50 nm.

Magnetic and electrical characterization confirmed the development of ferromagnetic and magnetoresistive behavior with the simultaneous emergence of manganite perovskite phase. For films deposited on Si(100), magnetoresistance was observed in specimens heat-treated at 700 °C and 750 °C, and for platinized-Si(100), 650 °C, 700 °C, and 750 °C. These temperatures are in excellent agreement with magnetization onsets (i.e., T_C) measured by SQUID magnetometry. Magnetoresistive response improved with heat-treatment temperature for the more-refractory $La_{0.67}Ba_{0.33}MnO_3$ composition. The lead-doped counterpart, however, offered the best property evolution, with T_C = 320 K and T_{IM} = 254 K by 750 °C on platinized-Si(100). All corresponding transport curves were symmetric, demonstrating clear

metal-insulator transitions (i.e., T_{IM}). High resistivities (i.e., $\sim 10^6$ Ω-cm) were attributed to the fine-grain microstructure. Weak-field cycling between $\pm$ 500 Oe yielded symmetrical loops with appreciable linear regions, a highly-desirable characteristic for magnetic sensing applications.

Dedicated to my parents and sister, without whose prayers and
support, this dissertation would not have been possible.

ACKNOWLEDGEMENTS

sample preparation and mounting techniques necessary to obtain quality measurements with the SQUID MPMS (magnetometry) and PPMS (magnetotransport) systems.

TABLE OF CONTENTS

LIST OF FIGURES

LIST OF TABLES

CHAPTER 1

STATEMENT OF OBJECTIVES

1.1 INTRODUCTION

Magnetoresistance is characterized by the change in electrical resistance of a material due to the presence of an external magnetic field. Exploitation of this phenomenon has tremendous potential for integration into hybrid microelectronics as solid-state sensors and nonvolatile memory elements. Current and proposed devices revolve primarily around one of two magnetoresistive phenomena, both materials-dependent: (1) the anisotropic magnetoresistance of 3d transition-metal alloys or (2) the so-called "giant" magnetoresistance of artificially-engineered superlattices. For example, hard drive manufacturers, led by IBM, have phased out conventional thin-film inductive heads in favor of magnetoresistive elements. As a result, read sensitivity has improved 5 to 10 times enabling dramatic increases in both storage capacity and data transfer rates [1]. Another company, Nonvolatile Electronics, Inc., is now pioneering the application of giant magnetoresistive elements in object position and recognition [2, 3]. Such capabilities are required in the automotive industry where precise engine timing is instrumental in efforts to enhance performance and reduce emissions. Recently, however, much interest has focused on the "colossal" magnetoresistance exhibited by doped-lanthanide manganites. As ceramic oxides, doped-lanthanide manganites bring new deposition and processing challenges. This chapter presents a brief overview of magnetoresistive behavior, correlating magnetotransport with materials implementation. A final discussion highlights the unique opportunities offered by doped-lanthanide manganites and concludes with research objectives for this dissertation.

1.2 ANISOTROPIC MAGNETORESISTANCE

In a ferromagnetic metal, anisotropic magnetoresistance results from differences in resistivity for current traveling parallel to the magnetic moment (longitudinal) versus that traveling perpendicular (transverse). Rotation of the magnetic moment by an external magnetic field, H, therefore changes the resistivity experienced by the current. The performance of

devices based on anisotropic magnetoresistance is characterized by a "figure-of-merit", the anisotropic magnetoresistance ratio (*AMR*), which is defined by convention [4] to be

$$AMR = \frac{\rho_{//} - \rho_{\perp}}{\rho_{Ave}} \times 100\%; \quad \rho_{Ave} = \frac{1}{3}\rho_{//} + \frac{2}{3}\rho_{\perp} \tag{1.1}$$

where $\rho_{//}$ and $\rho_{\perp}$ are, respectively, the longitudinal and transverse resistivities (both generally $\mu\Omega$-cm).   Binary and tertiary alloys of ferromagnetic 3d transition-metals (Co, Ni, Fe, and Mn), extensively studied because of their high anisotropic magnetoresistance, offer the most useful *AMR* values, ranging from 2–6%. Practical devices, however, almost universally rely on $Ni_{0.81}Fe_{0.19}$ permalloy which provides an *AMR* of 2–3% in commercial operating environments; a maximum (saturated) *AMR* of 4% occurs in applied fields of $H_S \cong 2.5$ T at room temperature [5].   This specific composition offers the unusual yet attractive combination of zero cubic magnetocrystalline anisotropy, *K*, and a negligible magnetostrictive coefficient, λ.[1] Lack of magnetocrystalline anisotropy in $Ni_{0.81}Fe_{0.19}$ permalloy results in a low coercive force $(H_C < 1 \text{ Oe})$[2] and high permeability $(\mu > 1000)$ [6].   Negligible magnetostriction is extremely important from a deposition and processing perspective: the formation of residual thin-film stresses with other alloy compositions alters their magnetotransport properties uncontrollably, thereby precluding use in magnetoresistive elements.

1.3 GIANT MAGNETORESISTANCE

The deposition capabilities of modern vapor-phase techniques, particularly molecular beam epitaxy (MBE), have enabled the extension of 3d transition-metal materials into superlattice structures, artificially-engineered to enhance potentially useful properties. In 1988, an investigation of alternating magnetic and nonmagnetic layers revealed magnetoresistance in Fe(001)/Cr(001) bcc superlattices [7].   Upon application of an H = 2.0 T magnetic field, a 30Å-Fe(001)/9Å-Cr(001) thin film superstructure lost approximately 45% of its resistance at T = 4.2 K. The mechanism responsible for magnetoresistance is attributed to spin-dependent scattering of polarized conduction electrons.   Within this superstructure, magnetic Fe(001) layers, separated by nonmagnetic Cr(001) layers, have moments aligned antiparallel

---

[1] Nickel-iron alloys are face-centered cubic (FCC).
[2] 1 Tesla (T) = 10,000 Oersteds (Oe).

to those of Fe(001) neighbors. Application of a magnetic field induces an antiferromagnetic to ferromagnetic transition resulting in parallel alignment of neighboring Fe(001) moments. Coherent transmission of polarized conduction electrons occurs because the antiparallel scattering potentials have been reduced or eliminated.

The thickness of the nonmagnetic Cr(001) layers serves to control the exchange coupling between successive Fe(001) layers, which is quite strong. Coupling between Fe(001) layers can be either ferromagnetic (parallel) or antiferromagnetic (antiparallel), varying in an oscillatory fashion with the nonmagnetic Cr(001) layer thickness. If the thickness of Cr(001) is such that the coupling is ferromagnetic, application of a magnetic field does not induce a transition and magnetoresistance is not observed. This exchange coupling, and associated magnetoresistance, also arises in other 3d transition-metal systems; Co(100)/Cu(100) fcc superlattices, for example, exhibit the effect as well [8]. Because of its greater magnitude with respect to anisotropic phenomenon, the magnetoresistance of magnetic/nonmagnetic multilayers is referred to as "giant" and its ratio (*GMR*) quantified by

$$GMR = \left| \frac{\rho_H - \rho_0}{\rho_0} \right| \times 100\% \qquad (1.2)$$

where ρ_H is the resistivity within a magnetic field of strength *H*; and ρ_0, the resistivity in absence of a magnetic field (both generally $\mu\Omega$-cm). For convenience, *GMR* values are reported in absolute (i.e., "positive") terms, despite the fact that, for 3d transition-metal multilayers, resistivity decreases upon application of a magnetic field.

Because of commercial implications, research emphasis has shifted from anisotropic magnetoresistance to giant magnetoresistance and resulted in novel devices based on "spin-valves" or spin-dependent tunneling.[3] The room temperature *GMR* of spin-valve structures, for example, ranges from 4–20% with saturation fields of 300 Oe, enabling the development of higher-performing magnetic sensors [9]. Figure 1.1 provides an electrical schematic and photomicrograph of a state-of-the-art giant magnetoresistive sensor, the NVE AA002, from Nonvolatile Electronics, Inc. The circuit configuration consists of a Wheatstone bridge containing four lithographically-patterned multilayer elements. Two of these elements (R2 and R3) act as reference resistors, shielded from applied fields by permalloy plated onto the sub-

---

[3] This newly-emerging class of electronics is referred to as "spintronics".
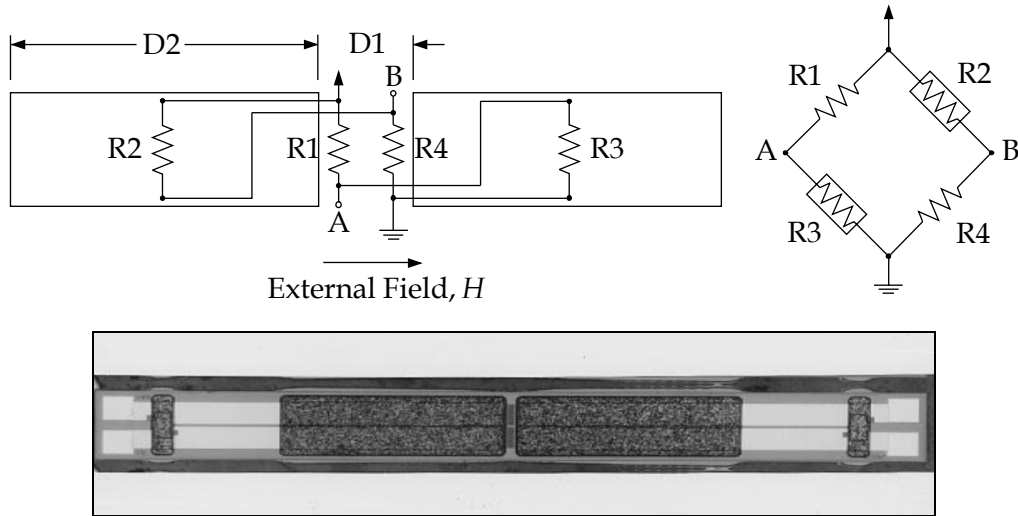
FIGURE 1.1 Electrical schematic and photomicrograph of the NVE AA002 bridge sensor. (Reprinted from [9]. Copyright 1998 MCB University Press.)

strate. The remaining elements (R1 and R4), exposed by a thin gap in the permalloy, sit in a region of magnetic flux concentration. Changing the shield-length to gap-width ratio (D2:D1) allows adjustment of the flux concentration, and by extension, the saturation point and external field sensitivity. As illustrated with the NVE AA002, geometric optimizations can enhance device performance, but new materials offer more efficient routes. For example, the substitution of insulating oxides as nonmagnetic spacer layers results in improved magnetoresistance: structures comprised of $Co_{0.82}Fe_{0.18}/Al_2O_3/Co_{0.82}Fe_{0.18}$ multilayers display a "tunneling" *GMR* of 39–41% at room temperature [10]. Coupled with exceptionally low saturation fields ($H_S \leq 50$ Oe), such spin-dependent tunneling devices are laying the foundation for MRAM, a next-generation nonvolatile memory architecture [11].

1.4 COLOSSAL MAGNETORESISTANCE

In 1994, however, an exceptional *intrinsic* magnetoresistance of 99.9% (negative) was demonstrated in $La_{0.67}Ca_{0.33}MnO_3$ thin films at $T = 77$ K (see Figure 1.2) using an applied magnetic field of $H = 2.0$ T [12]. The display of magnetoresistance in this ceramic oxide extends to a larger class of perovskite-structured materials represented by $Ln_{1-x}M_xMnO_3$, where *Ln* represents a trivalent lanthanide ion (i.e., La, Pr, Nd, or Gd) and *M*, a divalent cat-
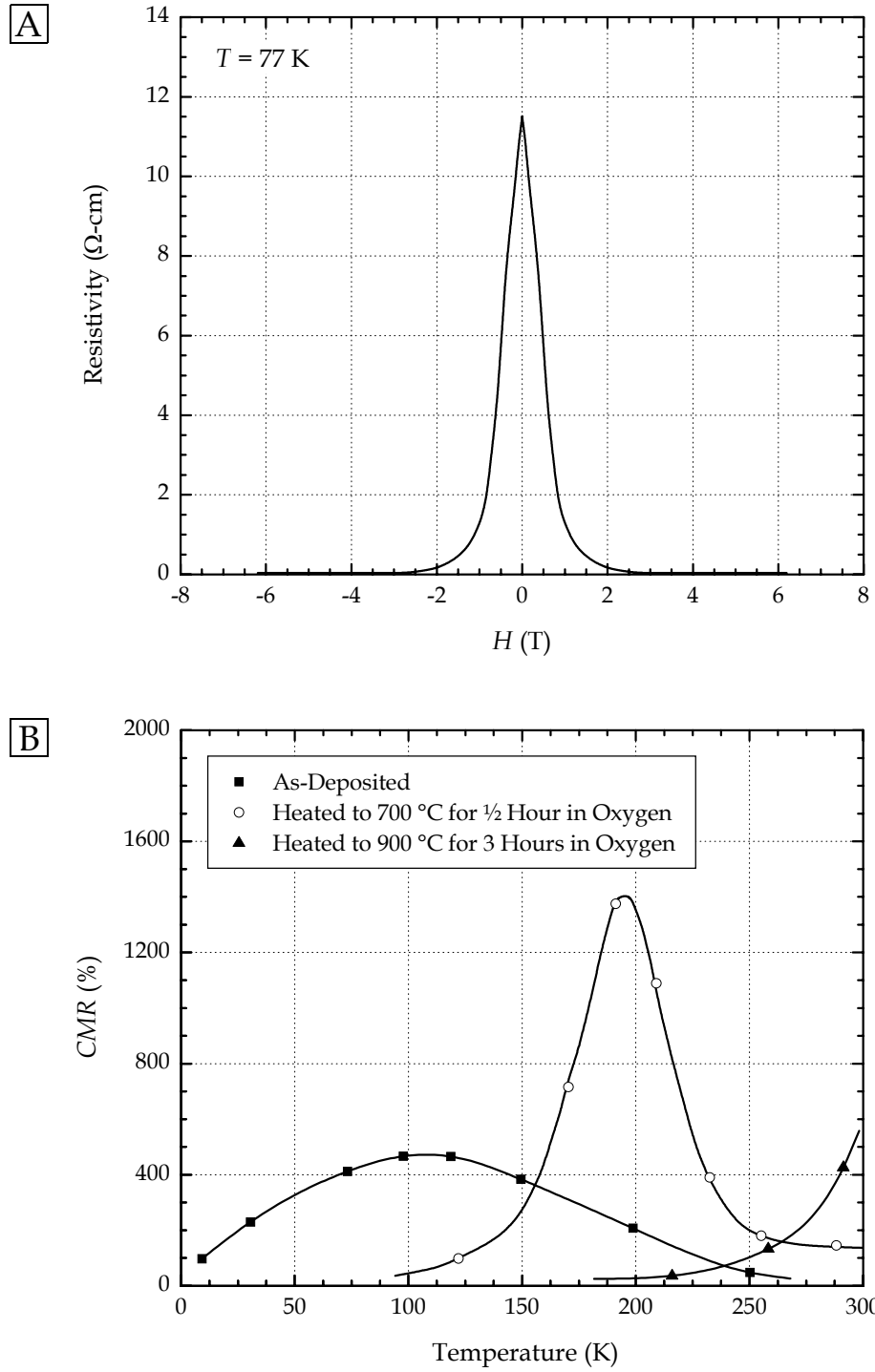
FIGURE 1.2 Magnetoresistance of epitaxial $La_{0.67}Ca_{0.33}MnO_3$ thin films. The data in (A) corresponds to a specimen heated at 900 °C in oxygen for ½ hour. (Adapted from [12]. Copyright 1994 American Association for the Advancement of Science.)

ion (i.e., Ca, Sr, Ba, Cd, or Pb). Progressive substitution of Ln^{3+} by M^{2+} induces a mixed Mn^{3+}/Mn^{4+} state increasing the acceptor (Mn^{4+}) dopant level. Exchange coupling between electron spins of Mn^{3+} and Mn^{4+} critically influences the magnetoresistance of doped-lanthanide manganites. Depending on the composition and processing conditions, the "giant" magnetoresistance ratio (i.e., *GMR*) of these ceramic oxides can be greater than 60% with 90% not being unusual.

Magnetotransport in doped-lanthanide manganites is actually distinguished by the term "colossal"; both the material and conduction mechanism differ fundamentally from 3d transition-metal alloys and their artificially-engineered superlattices. To emphasize this difference, the colossal magnetoresistance ratio (*CMR*) is defined with respect to the "in-field" resistivity, ρ_H, and not the "zero field" resistivity, ρ_0 (both generally mΩ-cm):

$$CMR = \left| \frac{\rho_H - \rho_0}{\rho_H} \right| \times 100\% \tag{1.3}$$

This convention results in *CMR* values often greater than 100% and sometimes spectacularly so.[4] Absolute values are always reported in the literature for the *CMR*, a negative magnetoresistance being assumed. To introduce the behavior of material free from interface effects, Figure 1.3 presents the magnetotransport of bulk single crystal $La_{0.64}Pb_{0.36}MnO_3$ (see inset) grown by PbO-PbF_2 molten flux methods [13].[5] Suppression of the resistive peak, shown in Figure 1.3A, results in a temperature range of maximal magnetoresistance (200–240 K) as depicted in Figure 1.3B. The highest *CMR* for this composition is approximately 230%, occurring slightly below $T = 225$ K at $H = 7.0$ T. For comparison, a corresponding "*GMR*" would be 69%.

In doped-lanthanide manganites, the *CMR* temperature range is affected by chemical composition through: (1) the lanthanide/dopant pair, Ln^{3+}/M^{2+}, (2) the degree of substitution, x, and (3) oxygen nonstoichiometry. For commercial applications, an ideal band of maximal magnetoresistance would straddle room temperature. Manganite compositions capable

---

[4] When comparing *GMR* and *CMR* values, this subtle convention must be remembered. Equation 1.2 is normalized with respect to ρ_0, Equation 1.3 with respect to ρ_H. The $La_{0.67}Ca_{0.33}MnO_3$ thin film from [12], for example, has a "*GMR*" of 99.9% but a *CMR* of 127,000%.

[5] Resistivity measurements are from an as-grown opaque black specimen, cubic in habitat, with a 2.3 mm edge length. {100} crystallographic planes comprise the cube faces. An in-line four-point probe was established across a single crystal face using 0.001" diameter gold wire attached via colloidal silver paste.
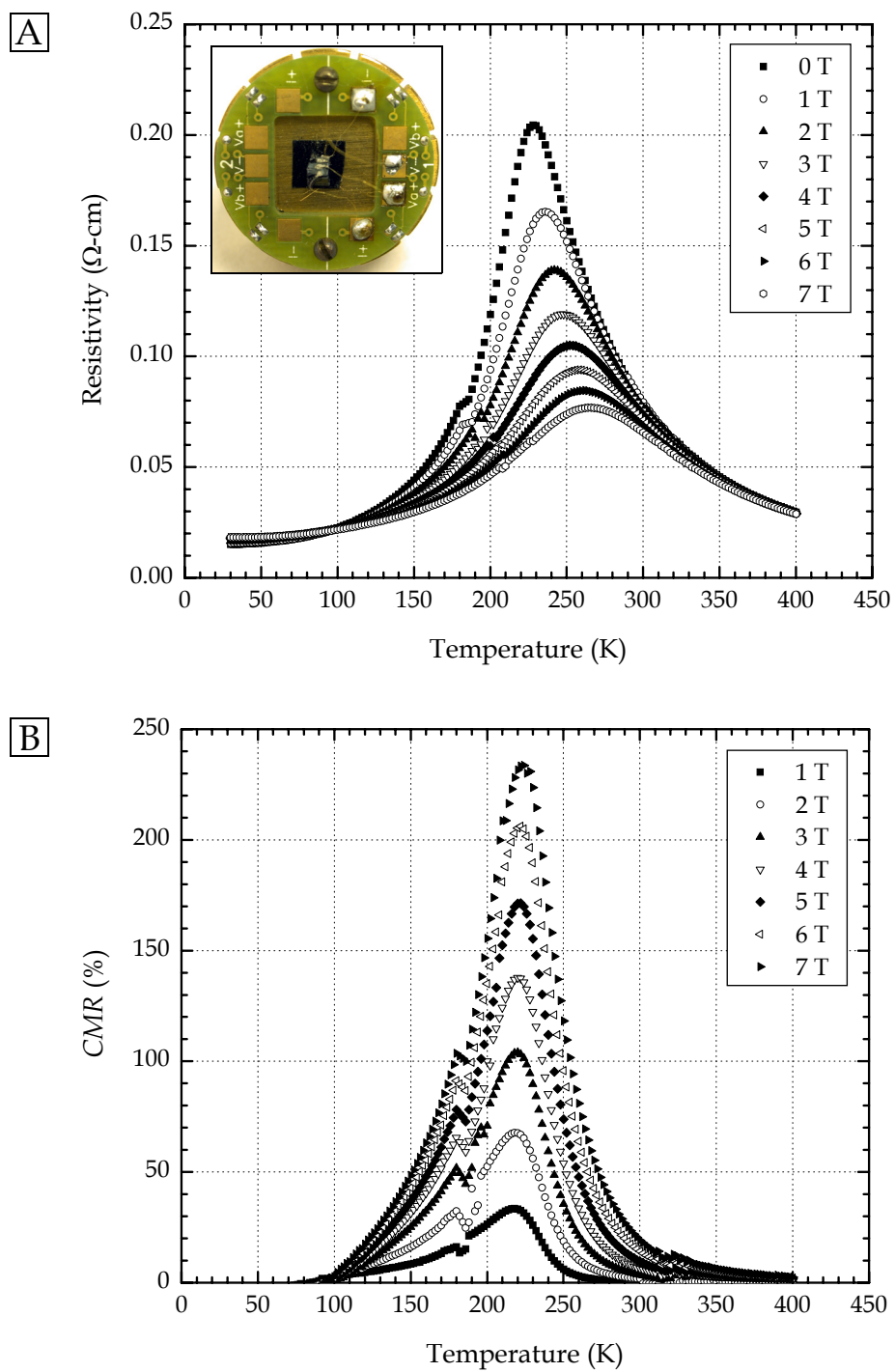
FIGURE 1.3 Magnetotransport behavior of a bulk La$_{0.64}$Pb$_{0.36}$MnO$_3$ single crystal. Resistivity (A) and the *CMR* (B) as a function of temperature and applied field. Inset in (A) shows the specimen attached to a four-point probe.

of meeting this criteria belong to either $La_{1-x}Sr_xMnO_3$, $La_{1-x}Ba_xMnO_3$, or $La_{1-x}Pb_xMnO_3$ where $0.2 < x < 0.4$; all of these systems can demonstrate a peak *CMR* in the vicinity of 300 K with optimal doping levels (i.e., x) [14]. However, one perception often associated with perovskite manganites is poor sensitivity to weak magnetic fields ($H < 1000$ Oe). As mentioned previously, $Co_{0.82}Fe_{0.18}/Al_2O_3/Co_{0.82}Fe_{0.18}$ tunnel junctions saturate their magnetoresistance at 39–41% with only an $H = 50$ Oe applied field. For an equivalent peak "*GMR*" in bulk (i.e., centimeter-sized) $La_{0.64}Pb_{0.36}MnO_3$ single crystals, a dramatically higher field of $H = 3.0$ T would be required. But such comparisons are misleading: absolute changes in magnitude (i.e., $\rho_H - \rho_0$) are obscured by the relative nature of Equations 1.2 and 1.3. Superstructures of 3d transition-metals display resistivities between 10^{-4} and 10^{-6} Ω-cm. In contrast, doped-lanthanide manganites function in the range from 10^{-1} to 10^{-3} Ω-cm. So percentages for giant and colossal magnetoresistance stem from notably different changes in resistivity. To quantify this point, Figure 1.4 presents the weak field ($H = 100$ Oe) magnetotransport behavior of bulk single crystal $La_{0.64}Pb_{0.36}MnO_3$. The resistivity difference ($\rho_H - \rho_0$) reaches its minima of -1.27 x 10^{-3} Ω-cm at $T = 215$ K. The same $H = 100$ Oe field, if applied to a 14Å-Fe(001)/8Å-Cr(001) superstructure, would lower the resistivity in the multilayer by roughly 1 x 10^{-7}
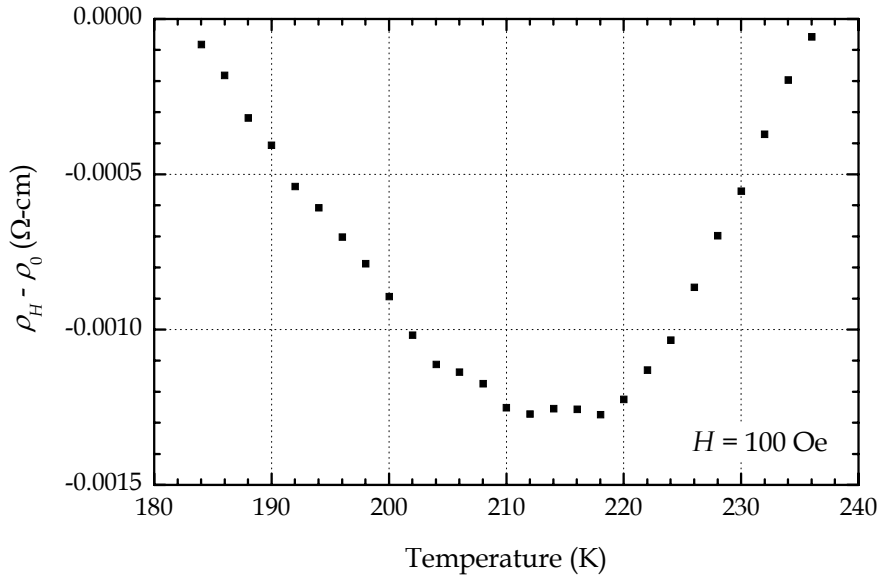
FIGURE 1.4 Weak field magnetotransport behavior of bulk single crystal $La_{0.64}Pb_{0.36}MnO_3$. The ordinate shows the resistivity *difference* as a function of temperature at an applied field of $H = 100$ Oe.

Ω-cm [15]. The corresponding sensitivity for each case, calculated using $(\Delta\rho/\Delta H)_T$, approximates, respectively, to –1 x 10^{-5} Ω-cm/Oe and –1 x 10^{-9} Ω-cm/Oe — *4 orders of magnitude in favor of the doped-lanthanide manganite!* From an "absolute" perspective then, doped-lanthanide manganites clearly offer competitive weak-field sensitivities. In addition, their saturation fields are exceptionally high ($H_S > 7$ T), the actual upper bound not known. This broad dynamic range is unmatched by any other materials system displaying magnetoresistance. Such a unique property combination opens up significant opportunities for doped-lanthanide manganites in magnetic field sensors.

1.5 SUMMARY

The potential for doped-lanthanide manganites to exceed the magnetoresistive performance of newly-introduced *GMR*-based elements remains promising. Already, "proof-of-concept" investigations utilizing bulk, polycrystalline material have resulted in sensors for magnetic fluxgates [16], object proximity and discrimination [17], and angular orientation and velocity [18]. But integration into hybrid microelectronics will require the development of effective thin-film deposition techniques. The elemental complexity of doped-lanthanide manganites creates stringent demands for compositional control, without which, variations in doping would severely degrade the magnetoresistive response. Solution chemical methods, and in particular "sol-gel" processing, provide capabilities well-suited for the growth of homogeneous, stoichiometric thin films of complex ceramic oxides. Yet the literature, while rife with examples from vapor-phase techniques (i.e., pulsed-laser ablation, molecular beam epitaxy, rf-magnetron sputtering, etc.), contains few reports of solution chemical deposition. Accordingly, this dissertation presents the investigation of a new "sol-gel" process for the growth of high-quality magnetoresistive manganite thin films. The following three research objectives were investigated and successfully completed:

(1) *The development of a chemical solution system using all alkoxide precursors*
Prior published research into the chemical-solution processing of doped-lanthanide manganites (and manganese oxides in general) has relied almost exclusively on carboxylate precursors. The principal disadvantage of manganese carboxylates, though, revolves around their insolubility in common

organic solvents and poor reactivity. To circumvent these limitations, the highly-reactive, soluble, non-oxidized manganese(II) alkoxide, 2-methyl-2-propoxo manganese(II), $Mn[OC(CH_3)_3]_2$, was synthesized using the ligand-selective silylamide technique. When combined with the other requisite alkoxides (i.e., lanthanum, barium, and lead), the resulting all-alkoxide solution could be hydrolyzed, forming "sol-gel" system readily adapted to thin-film deposition. Because reports of manganese alkoxides for solution chemical processing remain virtually unkown, this achievement represents an important contribution to the field.

(2) *The demonstration of low-temperature densification and crystallization*

For solution systems utilizing carboxylate precursors, high crystallization temperatures (i.e., greater than 800 °C) are required to fully form the doped-lanthanide manganite phase. Yet for the all alkoxy-based "sol-gel" deposition process, the onset of crystallization begins below 650 °C, enabling compatibility with commercially-desirable silicon substrates. Therefore, the investigation presented herein of thin-film structure and property evolution on Si(100) and platinized-Si(100) remains noteworthy. In contrast, reports from the literature, whether from vapor-phase or chemical solution processing, favor thin films grown at higher temperatures (e.g., 800 °C) on lattice-matched, refractory substrates such as $LaAlO_3$ and $SrTiO_3$.

(3) *The measurement of magnetoresistance in standard and weak-field conditions*

The magnetotransport behavior of epitaxial doped-lanthanide manganite films on oxide substrates has been extensively characterized in the literature. But electrical property measurements for thin films grown on silicon substrates remains sparse, particularly when solution chemical processing is considered. The new alkoxy-based "sol-gel" process successfully integrated magnetoresistive manganite films on both Si(100) and platinized-Si(100). Transport curves under conventional magnetic fields ($H = 0$–$5\,T$) yielded the anticipated insulator-to-metal transition; and weak field ($H = 500\,Oe$) measurements demonstrated an intrinsic sensitivity competitive with that of *GMR* superstructures.

1.6 REFERENCES

[1] Derbyshire, K.; Korczynski, E. Giant Magnetoresistance for Tomorrow's Hard Drives. *Solid State Technology* **1995**, *38* (9), 57–58.

[2] Ajluni, C. Giant Magnetoresistance Technology Paves the Way for Magnetic Field Sensing. *Electronic Design* **1994**, *42* (Nov 21), 48–49.

[3] Smith, C. H.; Schneider, R. W. GMR and SDT Sensors and Arrays for Low-Field Magnetic Applications. Proceedings of Sensors Expo, Anaheim, CA, May 9–11, 2000; Advanstar Publications: Peterborough, NH, 2000; pp 393–402.

[4] McGuire, T. R.; Potter, R. I. Anisoptropic Magnetoresistance in Ferromagnetic 3d Alloys. *IEEE Transactions on Magnetics* **1975**, *MAG-11* (4), 1018–1038.

[5] Bozorth, R. M. Magnetoresistance and Domain Theory of Iron-Nickel Alloys. *Physical Review* **1946**, *70* (11–12), 923–932.

[6] Mallinson, J. C. *Magneto-resistive and Spin Valve Heads: Fundamentals and Applications*, 2nd ed.; Academic Press: San Diego, CA, 2002; p 36.

[7] Baibich, M. N.; Broto, J. M.; Fert, A.; Nguyen Van Dau, F.; Petroff, F.; Eitenne, P.; Creuzet, G.; Friederich, A.; Chazelas, J. Giant Magnetoresistance of (001)Fe/(001)Cr Magnetic Superlattices. *Physical Review Letters* **1988**, *61* (21), 2472–2475.

[8] Parkin, S. S. P.; Bhadra, R.; Roche, K. P. Oscillatory Magnetic Exchange Coupling through Thin Copper Layers. *Physical Review Letters* **1991**, *66* (16), 2152–2155.

[9] Smith, C. H.; Schneider, R. W. Magnetic Field Sensing Utilizing GMR Materials. *Sensor Review* **1998**, *18* (4), 230–236.

[10] Cardoso, S.; Gehanno, V.; Ferreira, R.; Freitas, P. P. Ion Beam Deposition and Oxidation of Spin-Dependent Tunnel Junctions. *IEEE Transactions on Magnetics* **1999**, *35* (5), 2952–2954.

[11] Cowburn, R. P. The Future of Universal Memory. *Materials Today* **2003**, *6* (7–8), 32–38.

[12] Jin, S.; Tiefel, T. H.; McCormick, M.; Fastnach, R. A.; Ramesh, R.; Chen, L. H. Thousand-fold Change in Resistivity in Magnetoresistive La-Ca-Mn-O Films. *Science* **1994**, *264* (5157), 413–415.

[13] Yang, J.; Hu, S.; Uher, C.; Han, P. D.; Payne, D. A. Magnetic and Electronic Transport Properties of Single Crystal $La_{0.64}Pb_{0.36}MnO_3$. In *Science and Technology of Magnetic Oxides*, Materials Research Society Symposia Proceedings, Vol. 494, Boston, MA, Dec 1–4, 1997; Hundley, M. F., Nickel, J. H., Ramesh, R., Tokura, Y., Eds.; Materials Research Society: Warrendale, PA, 1998; pp 317–322.

[14] Rao, C. N. R.; Cheetham, A. K.; Mahesh, R. Giant Magnetoresistance and Related Properties of Rare-Earth Manganates and Other Oxide Systems. *Chemistry of Materials* **1996**, *8* (10), 2421–2432.

[15] Fullerton, E. E.; Conover, M. J.; Mattson, J. E.; Sowers, C. H.; Bader, S. D. 150% Magnetoresistance in Sputtered Fe/Cr(100) Superlattices. *Applied Physics Letters* **1993**, *63* (12), 1699–1701.

[16] Nossov, A.; Rinkevich, A.; Rigmant, M.; Vassiliev, V. Combined Lanthanum Manganite Magnetoresistive-Fluxgate Magnetic Sensor. *Sensors and Actuators A: Physical* **2001**, *94* (3), 157–160.

[17] Balcells, L. I.; Enrich, R.; Mora, J.; Calleja, A.; Fontcuberta, J; Obradors, X. Manganese Perovskites: Thick-Film Based Position Sensors Fabrication. *Applied Physics Letters* **1996**, *69* (10), 1486–1488.

[18] Xu, Y.; Memmert, U.; Hartmann, U. Magnetic Field Sensors from Polycrystalline Manganites. *Sensors and Actuators A: Physical* **2001**, *91* (1–2), 26–29.

CHAPTER 2

BACKGROUND AND LITERATURE REVIEW

2.1 INTRODUCTION

The adaptation of alkoxy-based sol-gel techniques for perovskite-structured oxides remains perhaps best-established for titanates and zirconates, prized for their commercially-attractive dielectric, ferroelectric, piezoelectric, and pyroelectric properties. Pioneering contributions to this development included the investigations of BUDD, DEY, and PAYNE [1, 2] into the sol-gel processing of $PbTiO_3$ and $PbZr_xTi_{1-x}O_3$ during the mid-1980s. A critical factor enabling the materials chemistry of these systems stems from the general availability of Group IVB (i.e., titanium, zirconium, and hafnium) alkoxides; various moieties of either element can be readily obtained in both quantity and high-purity. In stark contrast to this situation stands that of the manganites. The needed manganese(II) alkoxides suffer from two immediate drawbacks: poor chemical characterization and a paucity of industrial sources. So their utilization in alkoxy-based sol-gel methods has been virtually unknown.

Yet the new, resurgent interest in manganese perovskites, driven by potential applications for magnetoresistance, offers a seminal research opportunity similar to that of titanates and zirconates nearly two decades ago. This chapter provides an overview of doped-lanthanide manganites, describing relationships between structure, magnetic ordering, and transport phenomena. The chemistry and mechanisms of alkoxy-based sol-gel processing are illustrated through an examination of Group IVB alkoxides, their oxo-polymerization, the corresponding oxide end-products, and the physics of film deposition. Design of an all-alkoxide $La_{1-x}M_xMnO_3$ sol-gel method (where M = Ca, Sr, Ba, or Pb) concludes the literature review. Synthetic routes to Mn, La, Pb, and Group II alkoxides are discussed with an emphasis on the ability of the silylamido ligand to assist in the design of alkoxide precursors.

2.2 DOPED-LANTHANIDE MANGANITES

Magnetoresistive properties in doped-lanthanide manganites were first reported in 1954 by VOLGER [3] using polycrystalline specimens of $La_{0.7}Sr_{0.3}MnO_3$. Subsequent investigations

by Searle and Wang [4] in 1970 demonstrated similar magnetoresistive behavior in bulk single crystals of $La_{1-x}Pb_xMnO_3$ grown by Morrish, et al. [5]. Doped-lanthanide manganites represent a class of correlated electron systems wherein spin, valence, and orbital degrees of freedom interact simultaneously; magnetoresistance then emerges from a cooperative interplay between magnetic, charge, and orbital ordering, which in turn, produces a competition between metallic and semiconducting ground states. After nearly fifty years, the nature of such interactions is only partially understood and remains the focus of active research in solid-state chemistry and physics. This section seeks to present only the salient features of doped-lanthanide manganites as developed from empirical structure-property observations. For a more exhaustive treatment of the subject, the reader is referred to the excellent review by Salamon and Jaime [6].

2.2.1 Structural Chemistry

Doped-lanthanide manganites crystallize in a distorted perovskite structure, so-called after the mineral perovskite, $CaTiO_3$.[1] A general stoichiometry for perovskites, $^{XII}A^{VI}BO_3$, can be developed from considerations of ionic neutrality and coordination. First, the cummulative cation valence must equal six (i.e., $A^{1+}B^{5+}$, $A^{2+}B^{4+}$, $A^{3+}B^{3+}$, etc.) otherwise the charge of oxygen (i.e., O_3^{2-}) remains uncompensated. Substitutional variations on the basic $^{XII}A^{VI}BO_3$ formula unit, expressed as $^{XII}(A_{y_1}^1 A_{y_2}^2 \ldots)^{VI}(B_{z_1}^1 B_{z_2}^2 \ldots)O_3$, then result in complex oxides often containing mixed valence states, the deliberate manipulation of which, can induce useful properties.[2] Second, perovskite oxides represent only one of many structural subclasses displaying ABO_3 stoichiometry. The perovskite lattice itself derives from the cubic close-packing of oxygen planes wherein one quarter of the oxygen atoms have been replaced with large A cations [8]. Oxygen octahedra enclose the smaller B cations. As shown in Figure 2.1, an ideal, undistorted perovskite unit cell contains three easily-distinguished features: (1) a single 6-fold-coordinated B cation at the body center (i.e., ^{VI}B), (2) eight 12-fold-coordinated A cations situated at the corners (i.e., ^{XII}A), and (3) six face-centered oxygen atoms forming an octahedral "cage". The stability of the perovskite structure can be approx-

---

[1] An extensive catalog of known perovskite compounds has been complied by Galasso [7], covering prepatory methods, lattice parameters, and physical properties.
[2] Overall charge neutrality must still be preserved so $y_1 + y_2 + \ldots = 1$ and $z_1 + z_2 + \ldots = 1$.
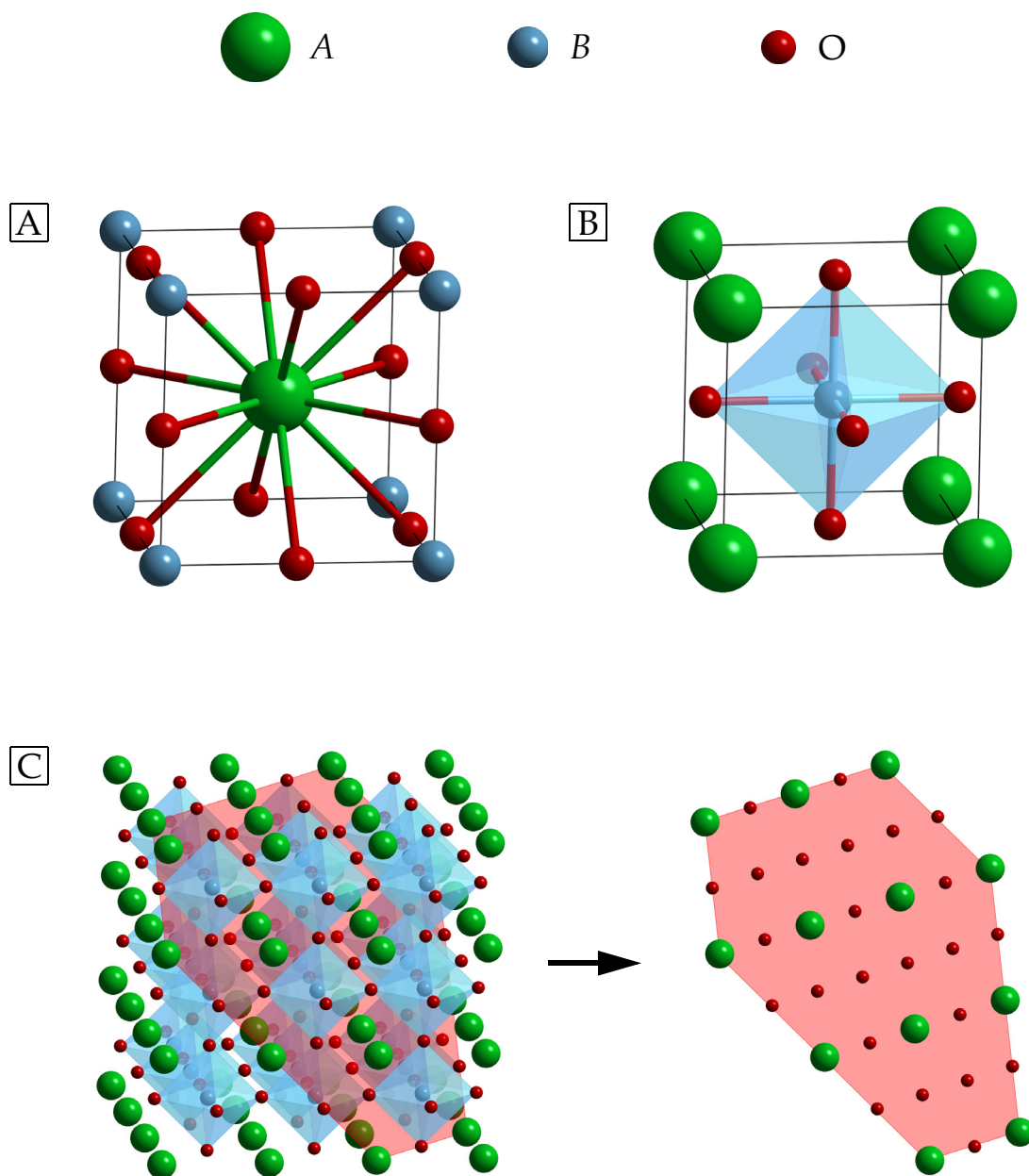
FIGURE 2.1 The ideal $^{XII}A^{VI}BO_3$ perovskite unit cell. Specific site perspectives can be emphasized by drawing the unit cell with either an A-site center (A) or a B-site center (B). The conventional representation highlights the sixfold symmetry of the BO_6 octahedra. Cubic close-packed planes of oxygen have one quarter of their lattice sites occupied by A-site cations (C). Note that for clarity, the oxygen anions are drawn smaller than normal (see Table 2.1 for effective radii).

15

imated by the Goldschmidt tolerance factor (t), which when equal to unity, implies a purely cubic Bravais lattice. This metric, introduced by GOLDSCHMIDT, et al. [9] in 1926, has proven highly useful despite its simple geometric assumptions (i.e., purely spherical atoms):

$$t = \frac{r_A + r_O}{\sqrt{2}(r_B + r_O)} \tag{2.1}$$

Here, r_A, r_B, and r_O denote, respectively, the radii of the A, B, and O ions. Modern adaptations of the tolerance factor, however, presume effective ionic radii that are corrected for coordination and spin state (when applicable). Accordingly, Table 2.1 provides an excerpt of values relevant to manganites from the comprehensive tables of SHANNON and PREWITT [10, 11]. Extensive studies of ABO_3 compositions by ROTH, et al. [12–15] reveal that when $0.8 < t < 1.0$, the corresponding oxide crystallizes in the perovskite structure. Tolerance factors outside these bounds, though, indicate a transition in coordination away from $^{XII}A^{VI}BO_3$. For example, $^{VI}A^{VI}BO_3$ structures, such as ilmenite, bixbyite, or corundum, predominate when $t < 0.8$ [16]. Above unity, $^{VI}A^{IV}BO_3$ polymorphs form, typically enstatite or pseudowollastonite [12].

In doped-lanthanide manganites, the A-site incorporates both trivalent lanthanides and divalent dopants. The presence of multiple A-site species therefore requires the use of a weighted average when calculating t (i.e., $\langle r_A \rangle = y_1 r_{A1} + y_2 r_{A2} + \dots$). Although manganese occupies the B-site exclusively, the mixed Mn^{3+}/Mn^{4+} valence state compels a similar approach: $\langle r_B \rangle = z_1 r_{Mn^{3+}} + z_2 r_{Mn^{4+}}$. Investigations by JONKER and VAN SANTEN [17] established an upper critical limit of $t_C \leq 0.97$ for manganite perovskites, beyond which, non-perovskite impurity phases appear.[3] The smallest value, $t = 0.88$, occurred in the undoped manganite, $GdMnO_3$, but a lower limit was not determined. Full substitutional ranges for various dopants, though, were shown to meet the stability criteria given above. For example, the $La_{1-x}Ca_xMnO_3$ perovskite series (i.e., $0 \leq x \leq 1$) corresponds to $t = 0.90$–0.95.

The conventional formula for doped-lanthanide manganites, $Ln_{1-x}M_xMnO_3$, can be interpreted as a solid solution of $LnMnO_3$ and $MMnO_3$ whose A-site substitutions yield compatible values for t (i.e., $\langle r_A \rangle$ and $\langle r_B \rangle$). Accordingly, the end-members themselves need not be

---

[3] The actual value reported by JONKER and VAN SANTEN [17], $t_C \leq 0.96$, relies on uncorrected Goldschmidt radii. For consistency with Table 2.1, all tolerance factors in this dissertation have been recalculated using radii from the revised tables of SHANNON [11].

Cation or Anion	Electronic Configuration	Coordination	Radius (Å)
Lanthanide, Ln^{3+}			
La^{3+}	[Xe]	9[a]	1.216
Pr^{3+}	$[Xe]4f^2$	9[a]	1.179
Nd^{3+}	$[Xe]4f^3$	9[a]	1.163
Sm^{3+}	$[Xe]4f^5$	9[a]	1.107
Gd^{3+}	$[Xe]4f^7$	9[a]	1.132
Divalent Dopant, M^{2+}			
Ca^{2+}	[Ar]	9[a]	1.18
Sr^{2+}	[Kr]	9[a]	1.31
Ba^{2+}	[Xe]	9[a]	1.47
Cd^{2+}	$[Kr]4d^{10}$	9[a]	1.16[b]
Pb^{2+}	$[Xe]4f^{14}5d^{10}6s^2$	9[a]	1.35
Manganese			
Mn^{3+}	$[Ar]3d^4$	6	0.645[c]
Mn^{4+}	$[Ar]3d^3$	6	0.530
Oxygen			
O^{2-}	[Ne]	6	1.40

[a] Any distortion of the perovskite structure lowers *A*-site symmetry from its ideal 12-fold coordination. The mineral itself, for example, exhibits 10-fold coordination [8]. A 9-fold coordination agrees well with Goldschmidt tolerance factors currently reported in the literature for doped-lanthanide manganites.

[b] Fitted from values of 4-, 5-, 6-, 7-, 8-, and 12-fold coordination.

[c] Corresponds to the high-spin configuration.

TABLE 2.1 The effective ionic radii of elements relevant to doped-lanthanide manganites [11].

perovskites even though the resulting composition often is: $YMnO_3$ and $SrMnO_3$, which crystallize in a hexagonal "perovskite-like" lattice, form a compound, $Y_{0.40}Sr_{0.60}MnO_3$, with a perovskite structure [18, 19].[4] This observation highlights the influential role played by the ionic radii of A-site cations in stabilizing crystal structure. Undoped lanthanide manganites, LnMnO$_3$, generally form orthorhombic Bravais lattices, transitioning to rhombohedral (pseudocubic) cells with progressive substitution of MMnO$_3$. At some value of x, a fully cubic perovskite structure occurs, depending specifically on the chemical nature of the A-site species.[5]   For example, the composition $La_{1-x}Ca_xMnO_3$ starts with a rhombohedral (pseudocubic) lattice at $x = 0.1$ but by $x = 0.2$ becomes cubic [20]. $La_{1-x}Sr_xMnO_3$, on the other hand, requires $x \geq 0.4$ for a cubic unit cell [20, 21]. Substitution on the A-site serves to create an internal "pressure", distorting, tilting, and/or rotating the MnO_6 octahedra, which in turn, effects lattice geometry.[6] From a survey of $Ln_{1-x}M_xMnO_3$ systems, experimental evidence suggests that optimal magnetoresistive behavior occurs for cubic perovskites with $\langle r_A \rangle = 1.23 \pm 0.01$ Å and $[Mn^{4+}] = 30 \pm 4\%$ (i.e., $t = 0.93$) [24].

Closely interrelated with A-site doping is the presence of a mixed Mn^{3+}/Mn^{4+} valence state, the product of both M^{2+} substitution *and* cation defect states in the crystal structure. A more descriptive formula unit, derived from considerations of composition and charge neutrality, would then be $(Ln^1_{y_{Ln1}}Ln^2_{y_{Ln2}}...)^{3+}_{1-x}(M^1_{y_{M1}}M^2_{y_{M2}}...)^{2+}_x Mn^{3+}_{1-x}Mn^{4+}_xO^{2-}_3$, where for simplicity, the representation of defect chemistry has been temporarily omitted (see Section 2.2.4 for further discussion). Clearly, substitution of M^{2+} for Ln^{3+} on the A-site induces Mn^{3+} to ionize into Mn^{4+} on the B-site. Larger M^{2+} sizes then lead to structural transitions that approach the cubic unit cell. But increasing the concentration of Mn^{4+} via cation vacancies alone can stabilize a cubic structure (i.e., varying $\langle r_B \rangle$ independently of $\langle r_A \rangle$). This outcome is achieved by annealing in strong oxidizing atmospheres. For instance, $La_{1-\varepsilon}Mn_{1-\varepsilon}O_3$ exhibits three polymorphs including orthorhombic, rhombohedral, and cubic, which correspond to $[Mn^{4+}] =$

---

[4] The difference between the cubic and hexagonal structure lies in the cubic stacking of AO_3 layers; the former contains an fcc stacking sequence (*abc*) while the latter has an hcp sequence (*ab* or *abac*). Notable MnO_6 distortion occurs in the hexagonal lattice, which for $YMnO_3$, results in a change of manganese coordination from sixfold (i.e., octahedral) to fivefold (i.e., trigonal dipyramid). Larger tolerance factors (i.e., $t > 1$) suggest crystallization in the hexagonal "perovskite-like" structure, although $YMnO_3$ with its small non-lanthanide Y^{3+} cation remains an exception with $t = 0.86$.

[5] The chemistry of the A-site also restricts the ability of $[Mn^{4+}]$ to deviate from x (i.e., cation defects). See discussion in Section 2.2.4 for further details.

[6] GLAZER [22, 23] originally classified octahedral tilt mechanisms in perovskites, relating structural displacements to Bravais lattice geometries.

12%, 24%, and 33% (ε = 0.020, 0.038, and 0.052) [25].[7] Yet the composition incorporates no divalent dopants, indicating a structural effect for vacancy mechanisms similar to that of A-site internal pressure. Because [Mn^{4+}] is common to both M^{2+} and cation defect compositions, the correlation of [Mn^{3+}]/[Mn^{4+}] with equilibrium lattice geometry then suggests an influence of electronic state on manganese site symmetry.

General relationships between electronic configuration and point group symmetry were first explored in a pair of seminal papers by JAHN and TELLER [26, 27] resulting in the subsequent classification of octahedral Mn^{3+} as a "Jahn-Teller ion". For octahedral point groups, transition metal 3d orbitals form two distinct symmetry-adapted sets: a t_{2g} set from the three d_{xy}, d_{xz}, and d_{yz} orbitals and an e_g set from the two $d_{x^2-y^2}$ and d_{z^2} orbitals. The electronic state for octahedral manganese then reduces to either $t_{2g}^3 e_g^1$ (i.e., Mn^{3+}) or t_{2g}^3 (i.e., Mn^{4+}) depending on the cation. But the e_g set contains a double degeneracy, which if split, allows the single e_g^1 electron of Mn^{3+} to occupy the lower of the two levels, thereby decreasing its energy. The manganite crystal achieves this splitting by deforming the $Mn^{3+}O_6$ octahedra, diminishing the site symmetry and creating a so-called static Jahn-Teller distortion. Splitting the three (degenerate) t_{2g} orbitals, however, provides no energetic benefit as all three levels remain singly occupied.[8]

As exemplified by $LaMnO_3$, a competitive interaction between $Mn^{3+}O_6$ and $Mn^{4+}O_6$ octahedra determines the equilibrium phase. WOLD, et al. [28, 29] pointed out that the large orthorhombic distortion from cubic symmetry stems from cooperative Jahn-Teller deformations of $Mn^{3+}O_6$ octahedra throughout the lattice. But the presence of Mn^{4+} cations progressively relieves the non-cubic distortion as [Mn^{4+}] increases, eventually destroying the structural $Mn^{3+}O_6$ ordering. Careful measurements of the lattice parameters by BOGUSH, et al. [30] showed three distinct Mn−O bond distances of 2.20 Å, 1.96 Å, and 1.89 Å in the orthorhombic phase; a rapid convergence to 1.96 Å occurred at [Mn^{4+}] = 14%, with the rhombohedral (pseudocubic) unit cell emerging at [Mn^{4+}] = 22%.[9] The inclusion of M^{2+} and/or

---

[7] A subtle O′- to O-orthorhombic transition occurs at [Mn^{4+}] = 14% due to mismatch of the La^{3+} radius and volume available to its cubo-octohedral site. Overall morphology, however, remains dominated by [Mn^{4+}].

[8] Orbital splitting, by itself, preserves energy between initial and final configurations. But the *occupancy*, based on the availability of electrons to populate levels, can still lower the energy of the crystal. See the discussion in Appendix B for further details.

[9] The reported rhombohedral lattice parameters were a = 5.576 Å and α = 60.65°, or in terms of a pseudocubic basis, a = 3.879 Å and α = 90.40°.

cation vacancies on the *A*-site therefore results in similar phase transitions as related through [Mn^{4+}], and by extension, manganese octahedral site symmetry.

The interrelationship between *A*-site chemistry and [Mn^{4+}] in manganese perovskites was directly explored by MAHENDRIAN, et al. [31]. Their detailed survey of the $La_{1-\varepsilon}Mn_{1-\varepsilon}O_3$, $La_{1-x}Ca_xMnO_3$, and $La_{1-x}Sr_xMnO_3$ systems demonstrated magnetoresistive behavior in all compositions but only for those structures with rhombohedral (i.e., pseudocubic) or cubic symmetry. The presence of magnetotransport was always accompanied by [Mn^{4+}] greater than 20%, with an ideal concentration ranging between 25–35%. Equally important, the display of magnetoresistive behavior in undoped $La_{1-\varepsilon}Mn_{1-\varepsilon}O_3$, first reported by MANOHARAN, et al. [32], emphasizes the crucial role of [Mn^{4+}] via $Mn^{3+}-Mn^{4+}$ interactions in manganite transport phenomena. *A*-site chemistry modifies this interaction by distorting the MnO_6 octahedra, influencing both the $Mn-O-Mn$ bond lengths and angles. Considerations of structural chemistry then offer parameters such as $\langle r_A \rangle$, [Mn^{4+}], and lattice geometry (i.e., reflected in part through *t*) that provide guidelines for optimizing magnetoresistive behavior. Hence, smaller lanthanides (i.e., Pr^{3+}, Nd^{3+}, or Gd^{3+}) and M^{2+} species (i.e., Ca^{2+} or Cd^{2+}) should be avoided, doping should fall in between $0.2 < x < 0.4$, the structure of crystallization should preferentially be cubic, and so forth. Indeed, the best candidate compositions have been identified empirically as cubic $La_{1-x}M_xMnO_3$ where $0.2 < x < 0.4$ and *M* = Sr, Ba, and Pb, all of which, display magnetoresistance at or near room temperature.

2.2.2 MAGNETIC ORDERING AND TRANSPORT BEHAVIOR

In their pioneering investigations of doped-lanthanide manganites, specifically, the system $La_{1-x}M_xMnO_3$ where *M* = Ca, Sr, Ba, and Pb, JONKER and VAN SANTEN [17, 33, 34] observed the development of ferromagnetic ordering with increasing [Mn^{4+}], a result which they attributed to positive $Mn^{3+}-Mn^{4+}$ exchange interactions. The exclusion of 4f lanthanide electrons from the magnetization was rationalized by the following: saturation values, M_S, when extrapolated to 0 K for the ferromagnetic range of $0.2 < x < 0.4$, corresponded to the spin-only character of unpaired manganese 3d electrons. The emergence of ferromagnetism with the Mn^{3+}/Mn^{4+} mixed valence stands in contrast to that of the end members, *Ln*MnO_3 and *M*MnO_3. Both of these undoped binary oxides order antiferromagnetically, the former containing only $Mn^{3+}-Mn^{3+}$ exchange interactions and the latter, $Mn^{4+}-Mn^{4+}$.

Specifically, LnMnO$_3$ compositions like LaMnO$_3$, PrMnO$_3$, and NdMnO$_3$ transform into A-type spin structures below $T_N \approx 150 \text{ K}$ with adjacent ferromagnetic planes being antiferromagnetically coupled.[10] Compositions of MMnO$_3$, such as CaMnO$_3$, form G-type lattices at $T_N \approx 130 \text{ K}$ wherein every manganese cation coordinates to six nearest-neighbors of opposite spin [35].[11] Both types of magnetic ordering are illustrated in Figure 2.2. A solid solution of the two, however, exhibits ferromagnetism even when MMnO$_3$ represents as little as ten percent of the content (i.e., $x = 0.10$).

Jonker and Van Santen noted that different compositions with the same lattice parameter displayed varying Curie points (T_C). This behavior suggested that the manganese bond angle played a more crucial role in affecting $Mn^{3+} - Mn^{4+}$ exchange interactions than the bond distance. Interestingly, such a conclusion also arises from considerations of the Goldschmidt tolerance factor. Since t for manganese perovskites represents the ratio of $A - O$ and $Mn - O$ distances, its deviation from unity measures bond mismatch, thereby scaling with the $Mn - O - Mn$ angle. So t decreases as the space group symmetry lowers, corresponding to angles less than 180°. For example, cubic La$_{0.7}$Ca$_{0.3}$MnO$_3$, and La$_{0.6}$Sr$_{0.4}$MnO$_3$ all have experimental $Mn - O - Mn$ bond angles of 180°. But their non-cubic counterparts, rhombohedral La$_{0.9}$Ca$_{0.1}$MnO$_3$ and rhombohedral La$_{0.9}$Sr$_{0.1}$MnO$_3$ exhibit lower angles of 164° [31]. Accordingly, the Curie points of compositions with linear $Mn - O - Mn$ angles are higher than those without: 260 K and 315 K versus 245 K and 260 K, respectively.

Magnetic ordering and the resulting exchange interactions within manganese perovskites were examined by GOODENOUGH [37], yielding a detailed but qualitative "theory of semicovalent exchange". The predictions provided therein summarized structural, magnetic, and transport properties as a function of $[Mn^{4+}]$, represented (ideally) through x. Three conclusions in particular remain noteworthy: (1) the saturation magnetization, M_S, should attain its largest magnitude in the range $0.2 < x < 0.4$, (2) the Curie temperature, T_C, should reach a maximum when $x = 0.31$ and (3) a resistivity minima should occur for $x = 0.31$, increasing as x departs on either side. Indeed, all of these predictions correlate exceptionally well with the empirical observations of Jonker and Van Santen. But the simultaneous onset

---

[10]Magnetic ordering occurs below a critical temperature, which if antiferromagnetic, is given by the Néel point (T_N), and if ferromagnetic, the Curie point (T_C).

[11]A discussion of the various antiferromagnetic arrangements in perovskite structures for manganese ions (i.e., Type A, B, C, C-E, D, D-E, D-F, E, F, and G) is given by WOLLAN and KOEHLER [36] based on neutron diffraction studies of La$_{1-x}$Ca$_x$MnO$_3$.
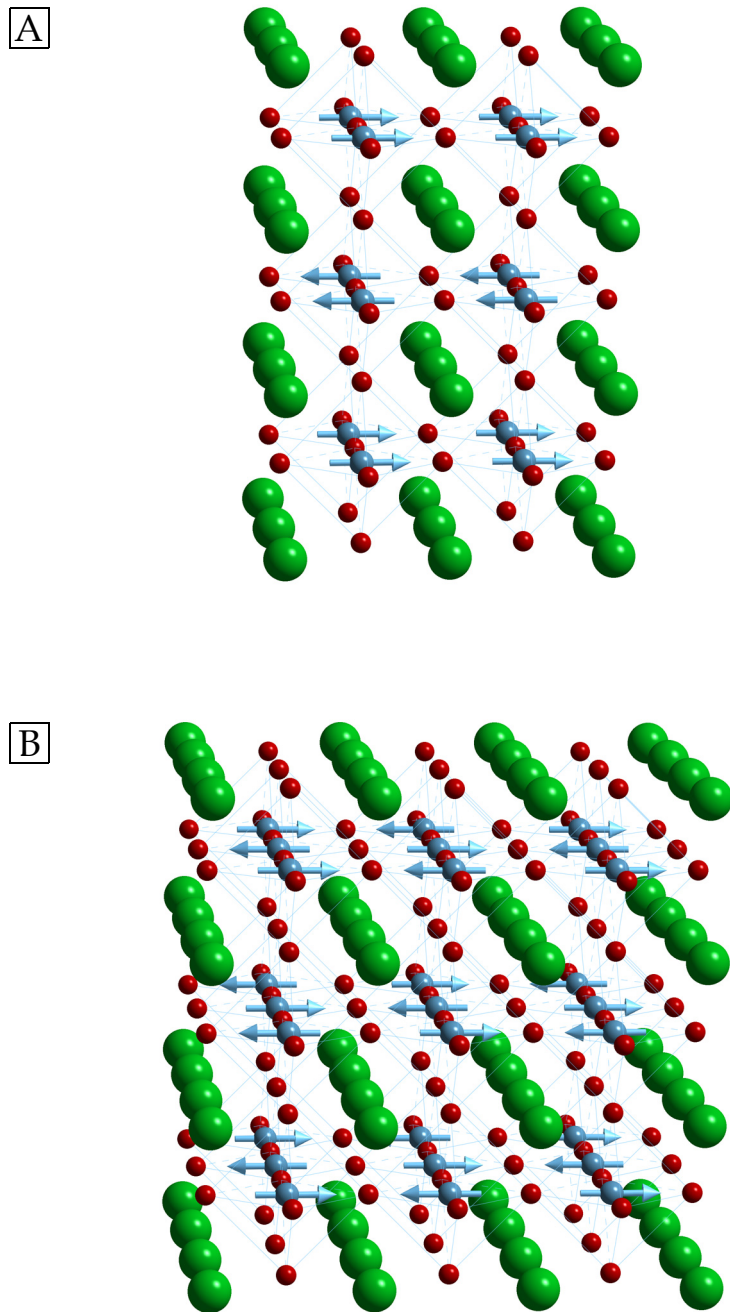
FIGURE 2.2 Examples of magnetic ordering in LnMnO$_3$ and MMnO$_3$ compositions. LaMnO$_3$ displays A-type ordering (A) whereas CaMnO$_3$ exhibits G-type ordering (B). A classification of magnetic structures for doped-lanthanide manganites can be found in WOLLAN and KOEHLER [36].

of ferromagnetism with metallic-like conductivity had never been observed previously in oxides.[12] Doped-lanthanide manganites therefore exhibited novel behavior with positive, but indirect (i.e., through the oxygen anion) exchange interactions occurring concomitantly with transport. Subsequent measurements [33] reported an anomalous peak in the resistivity near T_C which, as discovered in collaboration with VOLGER [3], could be suppressed when subjected to magnetic fields.

To illustrate these physical properties, Figure 2.3 presents the ferromagnetic ordering of a bulk $Pr_{0.63}(Ca,Pb)_{0.37}MnO_3$ single crystal specimen grown by the author for this dissertation [39]. The Curie point in Figure 2.3A (i.e., $T_C = 175\,K$) marks the transition from a paramagnetic to ferromagnetic state as confirmed by Figure 2.3B; for $T \gg T_C$, the M-H curve displays linear, paramagnetic behavior but when $T \ll T_C$, the field-induced magnetization increases rapidly, reaching a saturation plateau beginning at $H \approx 1\,T$. This composition crystallizes in an orthorhombic cell having lattice parameters of $a = 5.487$ Å, $b = 5.494$ Å, and $c = 7.746$ Å.[13] In comparison, single crystals of the related manganite, $La_{0.65}(Ca,Pb)_{0.35}MnO_3$, were reported as cubic ($a = 7.791$ Å), displaying a much higher transition of $T_C = 300\,K$ [40]. Clearly, incorporation of the smaller Pr^{3+} cation in place of La^{3+} stabilizes a lower-symmetry lattice, distorting the $Mn-O-Mn$ bond angle and lowering the Curie point. Extrapolation of the saturated magnetization to 0 K (i.e., the ferromagnetic state) for $Pr_{0.63}(Ca,Pb)_{0.37}MnO_3$ gives $M_S = 84.5\,emu/g$ — very close to the theoretical spin-only value ($M_S = 85.1\,emu/g$) calculated from an ideal consideration of the stoichiometry (see Appendix A for further details).

Closely correlated with magnetic ordering is electronic transport; Figure 2.4 shows a notable and sharp peak in the resistivity, centered at $T = 146\,K$ for the zero-field curve but increasing to $T = 186\,K$ when $H = 5\,T$. This cusp delineates a transition between semiconducting (i.e., $\partial\rho/\partial T$ negative) and metallic (i.e., $\partial\rho/\partial T$ positive) states. For manganites, the semiconducting state is considered p-type when $x < 0.5$ (i.e., doping generates Mn^{4+} acceptors in a host Mn^{3+} lattice) and n-type when $(1 - x) < 0.5$ (i.e., doping generates Mn^{3+} donors in a host Mn^{4+} lattice). The composition $Pr_{0.63}(Ca,Pb)_{0.37}MnO_3$ therefore exhibits p-type resistivity when in the semiconducting regime. Conventions in the literature, however, dictate

---

[12]Semiconductivity, however, had been observed in *ferri*magnetic oxides [38]. But these materials contain distinct magnetic sublattices, unlike the doped-lanthanide manganites, whose *ferro*magnetic state derives solely from randomly-distributed manganese cations within $0.2 < x < 0.4$ [37].

[13]However, a pseudocubic basis (i.e., $a_P \cong \sqrt{2}a \cong \sqrt{2}b \cong c$) would give $a_P \cong 7.758$ Å and $\alpha, \beta, \gamma \cong 89.97°$.
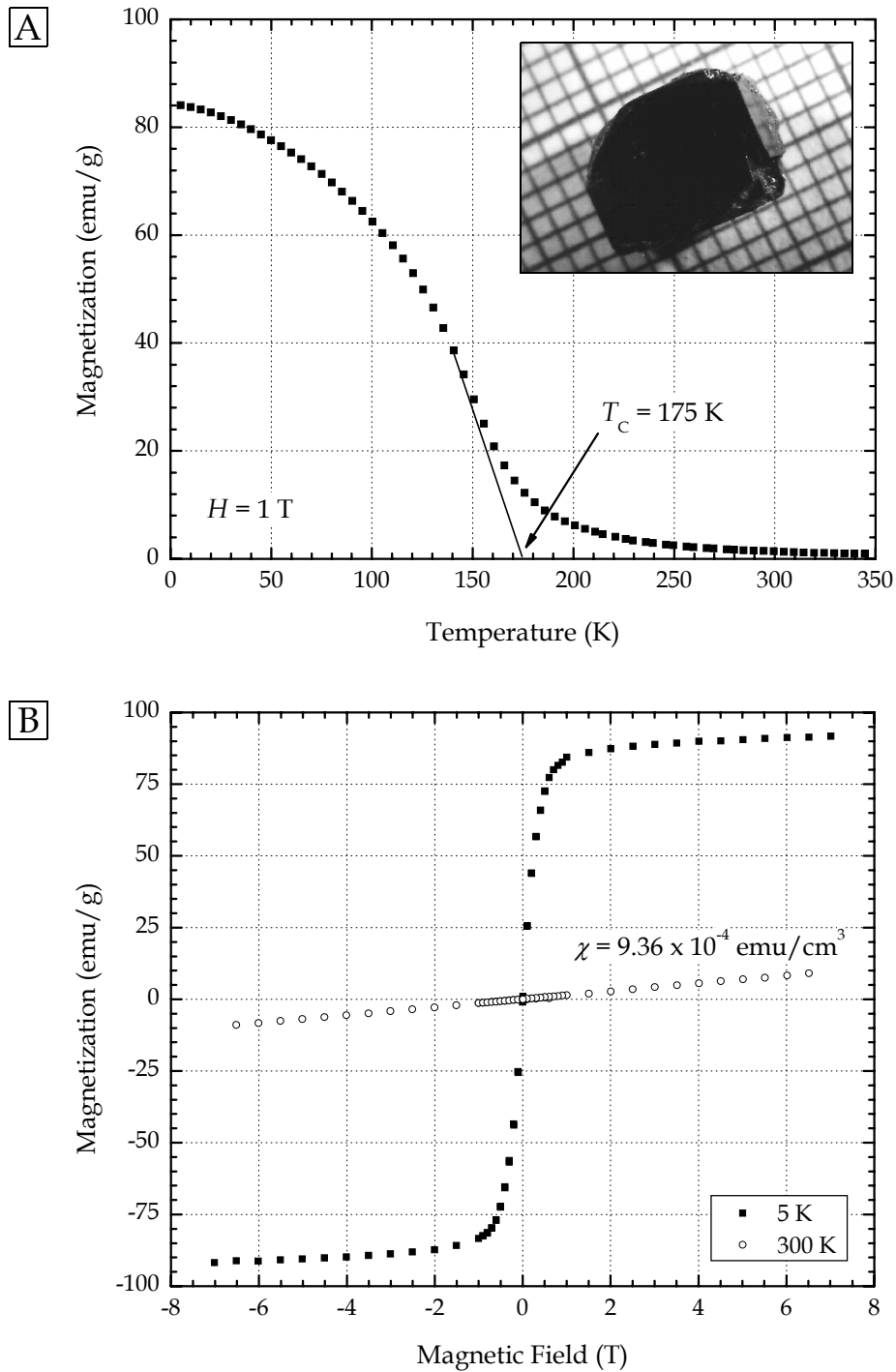
FIGURE 2.3 Ferromagnetic ordering for a bulk $Pr_{0.63}(Ca,Pb)_{0.37}MnO_3$ single crystal. The onset of a magnetic moment at 175 K (A) marks the transition between paramagnetic and ferromagnetic states (B). The inset in (A) shows a large, as-grown single crystal on a mm^2 background grid. (Adapted from [39]. Copyright 1999 Kluwer Academic Publishers.)
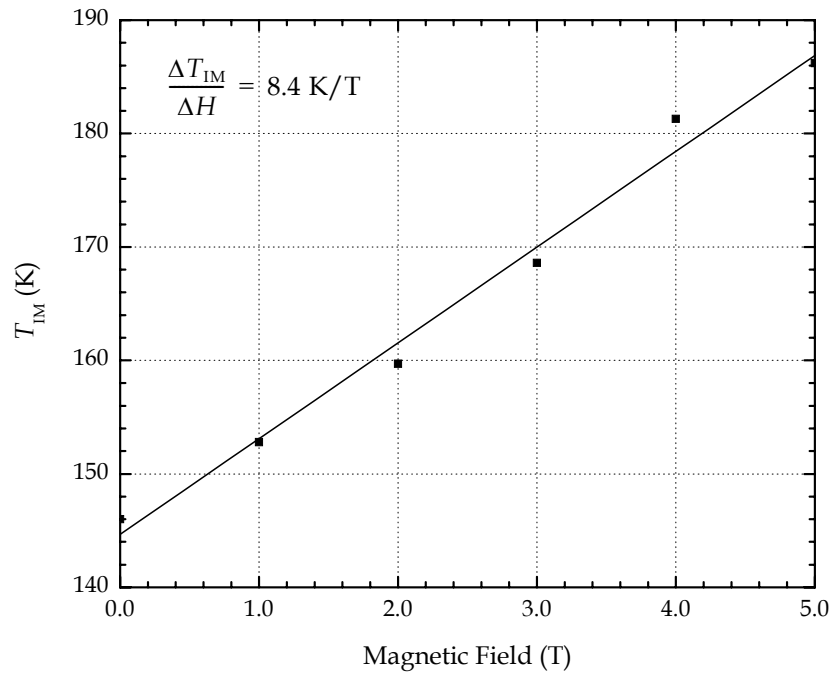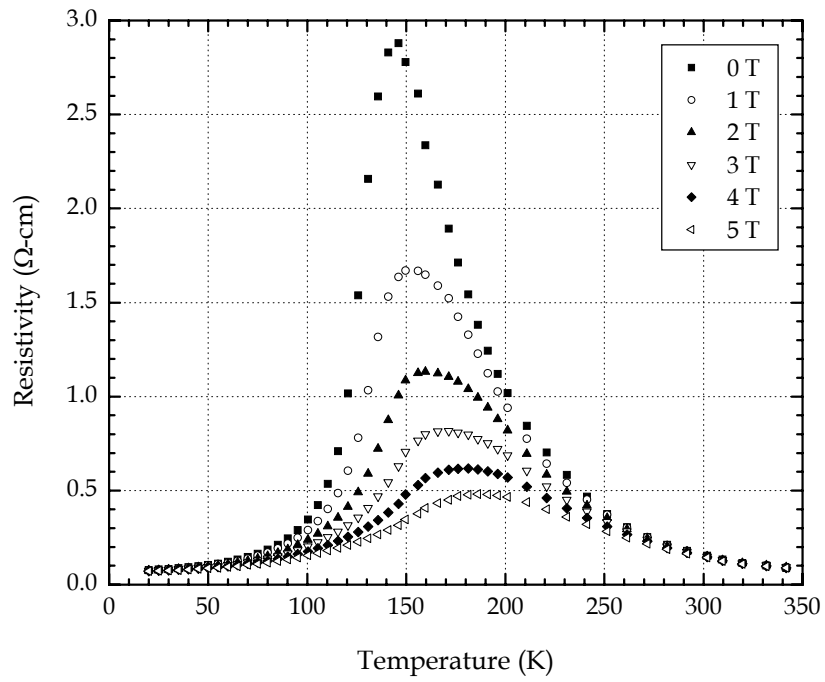
FIGURE 2.4 Magnetotransport behavior of a bulk $Pr_{0.63}(Ca,Pb)_{0.37}MnO_3$ single crystal. Lower figure shows the linear variation of T_{IM} with applied magnetic field. (Adapted from [39]. Copyright 1999 Kluwer Academic Publishers.)

that the semiconducting state, in fact, be designated as "insulating" — an unusual nomenclature. Typical insulating oxides such as $BaTiO_3$ or Al_2O_3 exhibit resistivities of 10^{13}–10^{14} Ω-cm. In contrast, metallic behavior, as exemplified by copper or aluminum, falls in the range of 10^{-5}–10^{-6} Ω-cm. Relative placement of doped-lanthanide manganites, whose resistivity generally lies between 10^{-1}–10^{-3} Ω-cm, therefore compares better with that of a "dirty" metal, not an insulator. But instead, convention characterizes a so-called "insulator"-to-metal transition at the resistivity peak (i.e., T_{IM} and ρ_{IM}). A comparison of T_C with the zero-field T_{IM} for doped-lanthanide manganites shows that both transition points coexist in relative close proximity. For for the $Pr_{0.63}(Ca,Pb)_{0.37}MnO_3$ composition, the corresponding 29 K difference disappears as the applied field, when increased, displaces T_{IM} past T_C. So the sensitivity of ρ_{IM} and T_{IM} to magnetic fields implies the onset of a spin-mediated transport strongly dependent on ferromagnetic ordering.

The interplay between magnetic and electronic states in doped-lanthanide manganites results in rich phase diagrams. Figure 2.5 displays the characterization of the $La_{1-x}Ca_xMnO_3$ system by SCHIFFER, et al. [41]. Although not indicated directly, an $Mn^{3+}-Mn^{3+}$ antiferro-
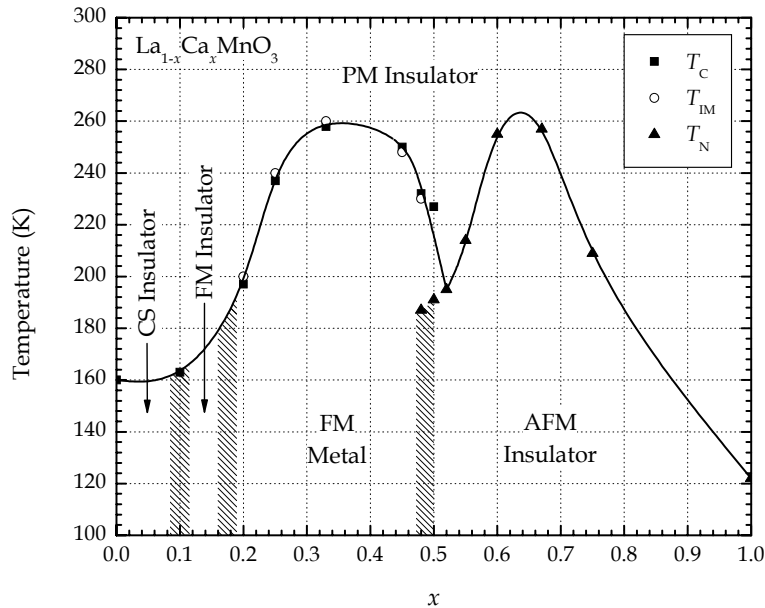
FIGURE 2.5 Magnetic and electronic phase diagram of the $La_{1-x}Ca_xMnO_3$ system. Paramagnetic (PM), ferromagnetic (FM), antiferromagnetic (AFM), and canted-spin (CS) states are given as a function of temperature and composition. (Adapted from [41]. Copyright 1995 The American Physical Society.)

magnetic interaction (i.e., from the parent LaMnO$_3$) maintains a presence up until $x \approx 0.3$, diminishing with increasing [Mn^{4+}]. The influence of this negative exchange remains significant enough below $x \approx 0.1$ to maintain a canted (antiferromagnetic) order but with a weak ferromagnetic moment overall. Suppression of the resistivity peak (as indicated by T_{IM}) remains confined to $0.2 < x < 0.45$, outside of which, only poorly-defined insulator-to-metal transitions occur, if at all. The switch from paramagnetic, insulating (PI) to ferromagnetic, metallic (FM) states produces sharp cusps, a prerequisite for large *CMR* values. The association of optimal magnetoresistive properties with $0.2 < x < 0.4$ stems specifically from the PI to FM transition. This characteristic, highlighted by the La$_{1-x}$Ca$_x$MnO$_3$ phase diagram, extends to other $Ln_{1-x}M_x$MnO$_3$ systems as well.

But the actual complexity of interactions in manganese perovskites cannot be illustrated by magnetic-electronic phase diagrams alone. Neutron diffraction studies of La$_{1-x}$Ca$_x$MnO$_3$ by WOLLAN and KOEHLER [36] and a subsequent theoretical interpretation by GOODENOUGH [37] suggested another state: charge-ordering, the product of cooperative orbital and spin alignments. Nominal compositions of $x > 0.5$, and in particular, smaller average *A*-site radii, $\langle r_A \rangle$, favor the advent of charge ordering due to increased orthorhombic distortion and buckling of the Mn-O-Mn bond angle.[14] But only the capabilities of modern analytical techniques have allowed such states to be visualized directly. For example, CHEN, et al. [42] in 1997 used high resolution transmission electron microscopy (HRTEM) to image alternating Mn^{3+}O$_6$ and Mn^{4+}O$_6$ stripes in La$_{0.33}$Ca$_{0.67}$MnO$_3$ thin films.[15] The emergence of charge-ordering in systems with smaller $\langle r_A \rangle$ such as Pr$_{1-x}$Ca$_x$MnO$_3$, Pr$_{1-x}$Sr$_x$MnO$_3$, and Nd$_{1-x}$Sr$_x$MnO$_3$ have been extensively studied by KUWAHARA, et al. [46] and TOKURA, et al. [47]. Zero-field transport shows a discontinuous (i.e., first-order) jump in resistivity at the onset of charge-ordering (T_{CO}). Applied magnetic fields, though, can induce a "melting" of the orbital and spin alignments, causing this transition to disappear. The interaction of structural, magnetic, and charge states, however, remains a complicated phenomenon and cannot

---

[14]This structural shift away from cubic symmetry decreases the overlap of the manganese e$_g$ orbitals with the oxygen 2p orbitals, reducing the one-electron bandwidth of the e$_g$-state carriers. As a result, charge ordering (i.e., carrier localization) can more effectively compete against double exchange, becoming dominant at certain temperatures and doping levels (see Appendix B for further details).

[15]Current HRTEM investigations by ZUO and TAO [43–45] have added significant detail to the La$_{1-x}$Ca$_x$MnO$_3$ phase diagram of Figure 2.5, revealing new charge-ordered states for $0.5 < x < 0.8$. The updated phase diagram was not included here due to the "on-going" nature of this research. Current progress, however, is summarized in [45].

be adequately presented here. Further discussion of orbital and spin degrees of freedom in doped-lanthanide manganites can be found in a review by TOKURA and NAGAOSA [48].

2.2.3 COLOSSAL MAGNETORESISTANCE

For doped manganese perovskites, transport in the semiconducting state arises from an activated hopping mechanism. Thermal ionization converts some of the Mn^{3+} cations into Mn^{4+} according to the process: $Mn^{3+} \rightarrow Mn^{4+} + e^-$. The disassociated electrons occupy hydrogenic-like orbits, a state easily absorbed by neighboring Mn^{4+} cations. Any corresponding reduction to Mn^{3+} then activates ionic migration since Mn^{3+} and Mn^{4+} effectively switch places. Depending on the doping level, either n- or p-type conductivity emerges as the carriers, Mn^{3+} or Mn^{4+}, respectively, "hop" through the lattice. In doped-lanthanide manganites, the range $0.2 < x < 0.4$ coincides with a minimum resistivity (p-type) but maximum *CMR*, both occurring during the PI to FM transition. This empirical observation suggests the influence of a positive, spin-dependent exchange between Mn^{3+} and Mn^{4+} cations below T_C. Such an interaction, however, must be indirect (i.e., mediated through the oxygen anion) because the distance separating manganese sites in the perovskite structure inhibits direct orbital overlap. Furthermore, measurements of M_S indicate a spin alignment of *unpaired* manganese 3d electrons in the metallic state.

The relationship between itinerant electron behavior and ferromagnetic ordering in doped-lanthanide manganites was first discussed by ZENER [49], who developed the so-called theory of double exchange. This model presumes the hybridization of *vacant* 3d, 4s, and 4p orbitals, which for Mn^{3+}, results in a square-planar dsp^2 configuration (i.e., $d_{x^2-y^2}$, s, p_x, and p_y), and for Mn^{4+}, an octahedral d^2sp^3 configuration (i.e., $d_{x^2-y^2}$, d_{z^2}, s, p_x, p_y, and p_z).[16] Spatial extension of the e_g set via hybridization allows orbital overlap with the adjoining O^{2-} 2p manifolds, bringing covalent character to otherwise ionic bonds. Below the Curie point, the emergence of a magnetic moment induces exchange interactions with the shared oxygen 2p electrons: both Mn^{3+} and Mn^{4+} have e_g orbitals less than half-filled, a characteristic which, in accordance with Hund's rule, favors parallel spin alignment during covalent

---

[16]GOODENOUGH [37] pointed out that, due to perturbations caused by neighboring atoms, the manganese 4s and 4p manifolds comprise lattice orbitals and not atomic orbitals. Accordingly, their energy levels are nearly degenerate with that of the 3d lattice orbitals (i.e., the e_g and t_{2g} sets).

bonding. For example, in a single e_g-2p interaction, one of the two oxygen electrons orients parallel to the cation moment; the remaining electron, by Pauli's exclusion principal, must be antiparallel to the first (see Figure 2.6A).[17] Concomitant with magnetic ordering is covalent bond ordering, the slight shift of oxygen 2p charge density towards Mn^{4+} [37]. Overlap between the Mn^{4+} and O^{2-} orbitals is therefore strengthened at the expense of the $Mn^{3+} - O^{2-}$ bond. An empty e_g orbital from Mn^{3+}, however, remains coordinated to the oxygen anion (see Figure 2.6A). Thus, coupling between the net moments of O^{2-} and Mn^{3+} proceeds via direct exchange (i.e., an antiferromagnetic interaction), producing a ferromagnetic manganese sublattice.

The conceptual basis for Zener's double exchange derives from the degeneracy of the possible $Mn^{4+} - O^{2-} - Mn^{3+}$ and $Mn^{3+} - O^{2-} - Mn^{4+}$ states. As depicted in Figure 2.6 using grey arrows, the $Mn^{4+}:e_g - O^{2-}:2p$ bond is spin-polarized (i.e., semicovalent) and delocalized. Yet because of energetic equivalence, neither state can predominate, so the oxygen 2p orbital serves as a conduit for electron transport: transfer of an e_g electron from Mn^{3+} to O^{2-} occurs simultaneously with transfer of a 2p electron from O^{2-} to Mn^{4+} (see Figure 2.6B). This cooperative displacement provides the basis for the expression "double exchange". More importantly, e_g electron mobility mediates the ferromagnetic coupling of t_{2g}^3 core spins (and vice versa). The periodic ferromagnetic potential then gives rise to a metallic-like conduction which corresponds to low resistivities (i.e., 10^{-1}–10^{-3} Ω-cm) below T_C.

Colossal magnetoresistance in doped-lanthanide manganites (i.e., $0.2 < x < 0.4$) can be related to a competition between thermally-activated and double-exchange transport mechanisms near T_C. An external magnetic field enhances the ordering of manganese spins, and hence, increases the mobility of the e_g electrons. This intuitive understanding, however, belies the actual complexity of concurrent interactions between spin, valence, orbital, and structural degrees of freedom. For example, double exchange fails to consider the coupling of electrons to lattice vibrations, and hence, the influence of polarons. Because the conversion of $Mn^{3+}O_6$ into $Mn^{4+}O_6$ removes the Jahn-Teller distortion associated with octahedrally-coordinated Mn^{3+}, polaronic effects should be present during FM-state transport. Accordingly, Appendix B presents a more thorough discussion of double exchange, given from the

---

[17]The emergence of an unpaired, spin-polarized covalent bond below T_C is referred to as semicovalency. Concepts of covalence and semicovalence were originally introduced by GOODENOUGH and LOEB [50] during their theoretical investigation of spinel-structured magnetic oxides.
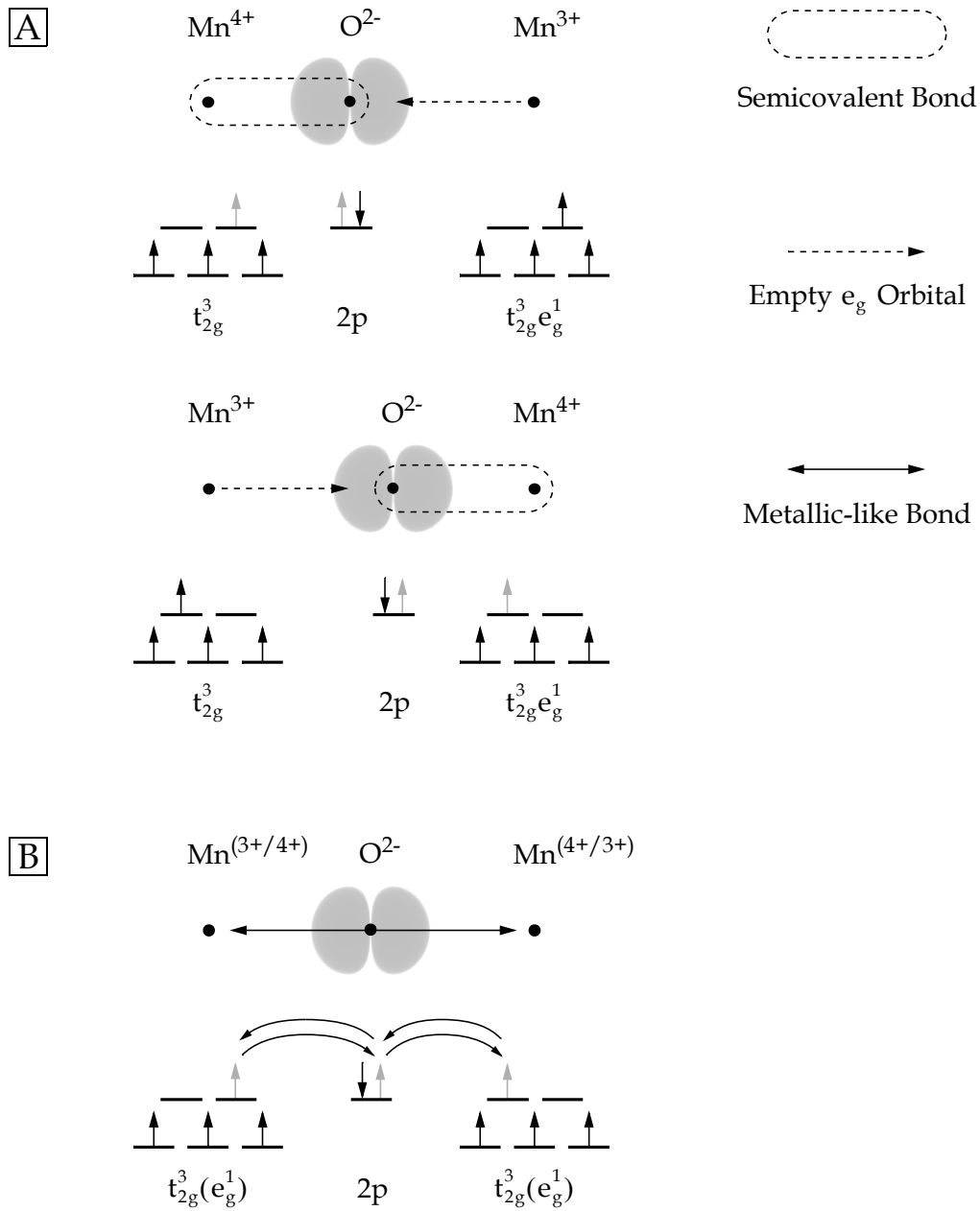
FIGURE 2.6 Double exchange in perovskite manganites. The dengeneracy of the mixed Mn^{3+}/Mn^{4+} valence state (A) results in a metallic-like conduction of the e_g electrons within a periodic t_{2g}^3 ferromagnetic potential (B). Grey arrows indicate a single, shared electron in a semicovalent bond.

perspective of manganese octahedral site symmetry (i.e., point group theory). A discussion of current issues in the transport and structure of manganite oxides, however, can be found in the comprehensive review by SALAMON and JAIME [6].

As a final comment, Zener's double exchange mechanism should not be confused with superexchange interactions which also occur in doped-lanthanide manganites.[18] Superexchange presumes $Mn^{n_1+} - O^{2-} - Mn^{n_2+}$ configurations that exhibit either double semicovalent (i.e., n_1, $n_2 = 3$ or 4) or semicovalent-ionic (i.e., $n_1 = 3$ or 4; $n_2 = 3$) bonding [37].[19] The former orders antiferromagnetically, and the latter, ferromagnetically. Both arrangements, however, leave participating electrons in highly-localized bonds, and hence, yield semiconducting or insulating states (i.e., not the metallic state concomitant with double exchange).

2.2.4 NON-STOICHIOMETRY AND DEFECT STRUCTURE

As presented in Section 2.2.1, control over the mixed Mn^{3+}/Mn^{4+} valence state, and hence the extent of $Mn^{3+}O_6$ and $Mn^{4+}O_6$ interactions, can be exercised through manipulation of A-site chemistry. But a review of manganite compositions, summarized in Table 2.2, highlights an important characteristic: $[Mn^{4+}]$ should not necessarily be presumed equivalent to $[M^{2+}]$. The influence of defect states on $[Mn^{4+}]$ occurs in addition to that of M^{2+}, often raising $[Mn^{4+}]$ beyond the nominal doping value, x. The practical upper bound for $[Mn^{4+}]$ in oxidized, unsubstituted $LaMnO_3$ (i.e., $La_{1-\varepsilon}Mn_{1-\varepsilon}O_3$) is almost 35% ($\varepsilon \leq 0.06$), beyond which, decomposition begins. This threshold therefore suggests a limit for purely defect-induced acceptor doping. But the substitution of divalent cations for the trivalent lanthanide (i.e., $0.2 < x < 0.4$) can stabilize higher ranges (i.e., 30% < $[Mn^{4+}]$ < 45%), attractive because both T_C and T_{IM} shift toward useful operating temperatures. Of the manganese perovskites, the defect chemistry of $LaMnO_3$ has been most extensively studied, followed by the doped derivatives $La_{1-x}M_xMnO_3$ where M = Ca, Sr, and Ba. Investigations by TOFIELD and SCOTT [54] explored three potential defect mechanisms resulting from oxidation: (1) interstitial oxygen atoms, whether at the midpoint of unit cell edges or inside the smaller LaO_3 tetrahedral sites,

---

[18]Superexchange coupling, also an indirect interaction, was originally proposed by KRAMERS [51] in 1934 and subsequently refined by ANDERSON [52], GOODENOUGH, et al. [37, 50], and KANAMORI [53].
[19]Ionic bonding occurs when the square-planar dsp^2 hybrid on Mn^{3+} is orthogonal to (i.e., does not point towards) the oxygen 2p manifold. In contrast, the d^2sp^3 hybrid of Mn^{4+}, due to its octahedral geometry, overlaps with all 2p orbitals from its oxygen neighbors.

COMPOSITION ($Ln_{1-x}M_xMnO_3$)	LATTICE[a]	PARAMETERS (Å OR °)			[Mn^{4+}] (%)	T_C (K)	T_{IM} (K)	GMR[b] (%)	REFERENCE
The $La_{1-\varepsilon}Mn_{1-\varepsilon}O_3$ System									
$La_{0.98}Mn_{0.98}O_3$	O	a = 5.543	b = 5.594	c = 7.805	12	240	c	12	[31]
$La_{0.96}Mn_{0.96}O_3$	R	a = 5.478	α = 60.55		24	230	180	53	[31]
$La_{0.955}Mn_{0.955}O_3$	C	a = 7.788			33	240	200	68	[31]
The $La_{1-x}Ca_xMnO_3$ System									
$La_{0.9}Ca_{0.1}MnO_3$	R	a = 5.480	α = 60.40		19	245	225	72	[31]
$La_{0.8}Ca_{0.2}MnO_3$	C	a = 7.744			25	260	242	52	[31]
$La_{0.7}Ca_{0.3}MnO_3$	C	a = 7.699			33	260	260	55	[31]
$La_{0.6}Ca_{0.4}MnO_3$	C	a = 7.677			39	240	235	42	[31]
$La_{0.5}Ca_{0.5}MnO_3$	C	a = 7.668			44	240	100	90	[31]
The $La_{1-x}Sr_xMnO_3$ System									
$La_{0.9}Sr_{0.1}MnO_3$	R	a = 5.523	α = 60.60		27	260	260	44	[31]
$La_{0.8}Sr_{0.2}MnO_3$	R	a = 5.482	α = 60.40		34	320	270	46	[31]
$La_{0.7}Sr_{0.3}MnO_3$	R	a = 5.454	α = 60.14		37	360	330	45	[31]
$La_{0.6}Sr_{0.4}MnO_3$	C	a = 7.721			41	315	290	44	[31]
$La_{0.5}Sr_{0.5}MnO_3$	C	a = 7.714			47	300	c	34	[31]

TABLE 2.2 Physical characteristics of selected $Ln_{1-x}M_xMnO_3$ compositions (*continued on page 33*).

COMPOSITION $(Ln_{1-x}M_xMnO_3)$	LATTICE[a]	PARAMETERS (Å OR °)			$[Mn^{4+}]$ (%)	T_C (K)	T_{IM} (K)	GMR^b (%)	REFERENCE
The $La_{1-x}Ba_xMnO_3$ System									
$La_{0.7}Ba_{0.3}MnO_3$	C	$a = 7.798$			31	315	235	50	[24]
$La_{0.67}Ba_{0.33}MnO_3$	C	$a = 3.897$			31	340	340	33[d]	[66]
$La_{0.5}Ba_{0.5}MnO_3$	C	$a = 7.781$			45	300	200	48	[24]
The $La_{1-x}Pb_xMnO_3$ System									
$La_{0.9}Pb_{0.1}MnO_3$	R	$a = 5.498$	$\alpha = 60.48$		e	315	310	85	[67]
$La_{0.7}Pb_{0.3}MnO_3$	R	$a = 5.494$	$\alpha = 60.36$		e	330	330	64	[67]
$La_{0.5}Pb_{0.5}MnO_3$	C	$a = 7.790$			e	355	340	30	[67]
Other Systems									
$Pr_{0.63}(Ca,Pb)_{0.37}MnO_3$	O	$a = 5.487$	$b = 5.494$	$c = 7.746$	37	175	146	90[d]	[39]
$Nd_{0.7}Sr_{0.3}MnO_3$	C	$a = 7.738$			28	195	185	54	[24]
$Nd_{0.7}Ba_{0.3}MnO_3$	C	$a = 7.751$			26	140	105	96	[24]
$Nd_{0.5}Ba_{0.5}MnO_3$	C	$a = 7.743$			43	120	95	92	[24]
$Gd_{0.7}Ba_{0.3}MnO_3^f$	C	$a = 7.725$			25	-	c	28	[24]

[a] C = Cubic, R = Rhombohedral, O = Orthorhombic.
[b] Unless otherwise specified, GMR values correspond to applied fields of $H = 6$ T.
[c] No observed peak in resistivity.
[d] Measured in an applied field of $H = 5$ T.
[e] Not given.

TABLE 2.2 Physical characteristics of selected $Ln_{1-x}M_xMnO_3$ compositions *(continued from page 32)*.

(2) La and Mn site vacancies, or (3) oxygen nonstoichiometry compensated by La migration onto Mn sites. The corresponding chemical formula units are $LaMnO_{3+\delta}$, $La_{3/(3+\delta)}Mn_{3/(3+\delta)}O_3$, and $La_{(3-\delta)/(3+\delta)}(La_{\delta/(3+\delta)}Mn_{3/(3+\delta)})O_3$, respectively.[20] Neutron diffraction of polycrystalline $LaMnO_{3.12}$ revealed an actual stoichiometry of $La_{0.94}Mn_{0.98}O_3$, implicating La and Mn site vacancies as the preferential defect mechanism. The absence of secondary phases eliminated the possibility of a decomposition reaction. For example, depleting the La or Mn sublattices through the formation of La_2O_3 or Mn_2O_3, respectively, can also create vacancies:

$$LaMnO_3 + \frac{\delta}{2}O_2 \rightarrow LaMnO_{3+\delta} \rightarrow La_{1-2\delta/3}MnO_3 + \frac{\delta}{3}La_2O_3 \qquad (2.2)$$

$$LaMnO_3 + \frac{\delta}{2}O_2 \rightarrow LaMnO_{3+\delta} \rightarrow LaMn_{1-2\delta/3}O_3 + \frac{\delta}{3}Mn_2O_3 \qquad (2.3)$$
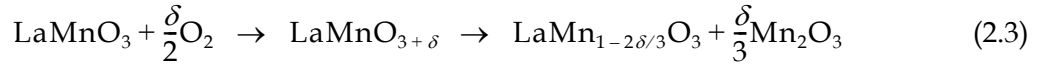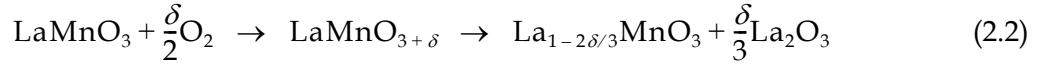
But the characterization of $La_{0.94}Mn_{0.98}O_3$ demonstrates that manganese perovskites do not incorporate excess oxygen into their structure (i.e., no interstitial mechanism). Instead, the uptake of atmospheric oxygen expands the crystalline sublattice, increasing the number of cation sites available for occupancy. The La and Mn cations, in turn, must redistribute to preserve both structural continuity and charge neutrality. This rearrangement generates vacancies because, unlike oxygen, the La and Mn atoms cannot increase their number. So the formula unit $LaMnO_{3+\delta}$, sometimes cited in the literature, is erroneous; its usage implies an interstitial mechanism, $LaMnO_3(O_i^{''})_\delta$. The correct reference should be $La_{1-\varepsilon}Mn_{1-\varepsilon}O_3$. Conversion to the proper nomenclature is easily obtained by first normalizing $LaMnO_{3+\delta}$ to generate $La_{3/3+\delta}Mn_{3/3+\delta}O_3$ and then comparing with $La_{1-\varepsilon}Mn_{1-\varepsilon}O_3$ to yield $\varepsilon = \delta/(3+\delta)$.

Subsequent studies into the defect chemistry of $La_{1-\varepsilon}Mn_{1-\varepsilon}O_3$ by VAN ROOSMALEN and CORDFUNKE [55–58] verified the cation vacancy mechanism of TOFIELD and SCOTT [54]. Their meticulous and detailed examinations conclusively proved that La and Mn vacancies populate the structure randomly but in equal amounts [55].[21] Additional investigations using electron diffraction and HRTEM indicated no defect clustering or crystallographic shear (i.e., from inclusion of fine La_2O_3 or Mn_2O_3 impurities within the lattice). So in an oxidizing envi-

---

[20]For the third case, La vacancies form due to La_{Mn} cation anti-site point defects.

[21]VAN ROOSMALEN and CORDFUNKE [55] pointed out that the lattice parameter associated with the sample of TOFIELD and SCOTT [54] strongly suggested a starting (i.e., prepatory) La:Mn ratio less than unity, hence the unequal $La_{0.94}Mn_{0.98}O_3$ stoichiometry.

ronment at annealing temperatures (i.e., > 700 °C), a complete description of the defect chemistry of $La_{1-\varepsilon}Mn_{1-\varepsilon}O_3$ using the standardized Kröger-Vink notation [59, 60] is written as:

$$LaMnO_3 + \frac{\delta}{2}O_2 \rightarrow La_{1-\varepsilon}(V_{La}''')_\varepsilon Mn_{1-\varepsilon}(V_{Mn}''')_\varepsilon O_3 \tag{2.4}$$

$$\rightarrow \frac{3+\delta}{3}[La_{3/(3+\delta)}(V_{La}''')_{\delta/(3+\delta)}Mn_{3/(3+\delta)}(V_{Mn}''')_{\delta/(3+\delta)}O_3]$$
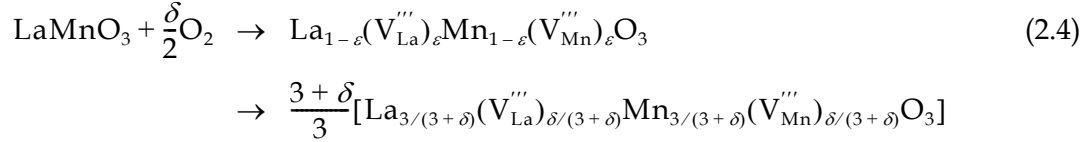
Growth of the oxygen sublattice, however, occurs via oxidation of manganese cations. So the mixed Mn^{3+}/Mn^{4+} valence state is introduced by noting that formation of a single O^{2-} anion converts two Mn^{3+} cations into Mn^{4+}

$$LaMnO_3 + \frac{\delta}{2}O_2 \rightarrow \frac{3+\delta}{3}[La_{3/(3+\delta)}(V_{La}''')_{\delta/(3+\delta)}Mn_{(1-2\delta)\cdot 3/(3+\delta)}^{x} \tag{2.5}$$

$$Mn_{(2\delta)\cdot 3/(3+\delta)}^{\bullet}(V_{Mn}''')_{\delta/(3+\delta)}O_3]$$

where, in terms of the reaction species alone:

$$2\delta Mn_{Mn}^{x} + \frac{\delta}{2}O_2 \rightarrow 2\delta Mn_{Mn}^{\bullet} + \delta O_O^{x} + \frac{\delta}{3}V_{La}''' + \frac{\delta}{3}V_{Mn}''' \tag{2.6}$$
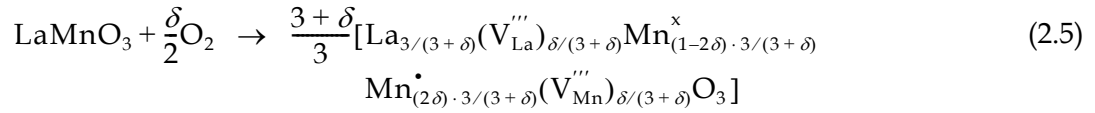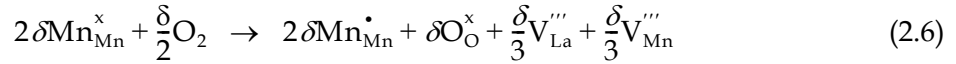
In Kröger-Vink notation, the positive (i.e., $\bullet$) and negative (i.e., $'$) charge states reference a standard state (i.e., x) derived from the perfect crystal, $LaMnO_3$. For example, V_{La}''' carries a triply negative valence relative to the La_{La}^{x} species it replaces. But in absolute terms, the La cation remains positively charged (i.e., 3+) and its corresponding vacancy, charge neutral (i.e., 0). So growth of the oxygen sublattice, indicated by δO_O^{x}, occurs via charged O^{2-} anions which generate neutral vacancies, not V_{La}^{3-} and V_{Mn}^{3-}.

But adaptation of Equation 2.6 to doped-lanthanum manganites, $La_{1-x}M_xMnO_3$, encounters a minor challenge: the premises of this defect model would, by logical extension, require $[Mn^{4+}]$ to be calculated using $x + 2\delta$. Yet determination of $[Mn^{4+}]$ in $La_{1-x}Sr_xMnO_3$ reveals that, for the tested range $0 < x < 0.4$, $[Mn^{4+}]$ stays more or less constant at 40% [61]. Such a value matches the 40% bound in $La_{1-\varepsilon}Mn_{1-\varepsilon}O_3$ (i.e., $\varepsilon \cong 0.062$) for purely defect-induced $[Mn^{4+}]$.[22] So the inclusion of a divalent dopant, M^{2+}, suggests that δ decreases as a function

[22]The best reported value for $[Mn^{4+}]$ is 40% [57]. But a preponderance of the literature suggests that oxidizing conditions, even when strong, rarely produce $[Mn^{4+}]$ greater than 35%.

of x, reaching zero at $x = 0.4$. To account for this behavior, VAN ROOSMALEN and CORDFUNKE [57] proposed a charge disproportionation mechanism wherein Mn^{3+} ionizes into Mn^{2+} and Mn^{4+} at elevated temperatures. Charge disproportionation has been reported for Fe^{4+} in the perovskite ferrite $La_{1-x}Ca_xFeO_{3-y}$, evidenced via Mössbauer spectroscopy by a lattice distribution of Fe^{3+} and Fe^{5+} [62]. Interestingly, Mn^{3+} and Fe^{4+} both occur in the $t_{2g}^3 e_g^1$ octahedral Jahn-Teller state which, as already discussed, is quite susceptible to electronic activity. Starting from the perfect crystal then:

$$LaMnO_3 \quad \rightarrow \quad LaMn'_\xi Mn^x_{1-2\xi} Mn^{\bullet}_\xi O_3 \tag{2.7}$$
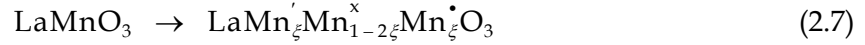
In charge disproportionation, Mn^{2+} cations are preferentially oxidized over Mn^{3+}. So the full mechanism expands to:

$$LaMn'_\xi Mn^x_{1-2\xi} Mn^{\bullet}_\xi O_3 + \frac{\delta}{2}O_2 \quad \rightarrow \quad \frac{3+\delta}{3}[La_{3/(3+\delta)}(V'''_{La})_{\delta/(3+\delta)}Mn'_{(\xi-2\delta)\cdot 3/(3+\delta)} \tag{2.8}$$
$$Mn^x_{(1-2\xi+2\delta)\cdot 3/(3+\delta)}Mn^{\bullet}_{(\xi)\cdot 3/(3+\delta)}(V'''_{Mn})_{\delta/(3+\delta)}O_3]$$

where, in terms of the reaction species alone:

$$2\delta Mn'_{Mn} + \frac{\delta}{2}O_2 \quad \rightarrow \quad 2\delta Mn^x_{Mn} + \delta O^x_O + \frac{\delta}{3}V'''_{La} + \frac{\delta}{3}V'''_{Mn} \tag{2.9}$$
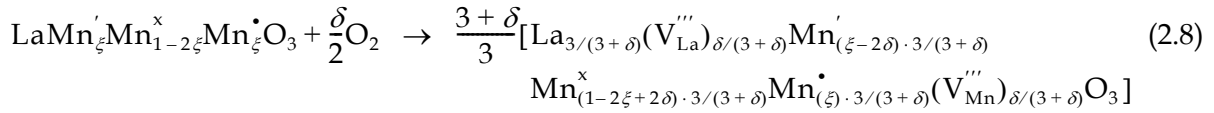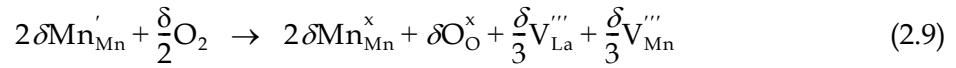
To substantiate the charge disproportionation mechanism, Van Roosmalen and Cordfunke analyzed an $La_{1-\varepsilon}Mn_{1-\varepsilon}O_3$ sample thermogravimetrically from 737 to 1017 °C. The resulting p_{O_2} versus δ data curves fit the model of Equation 2.8 exceptionally well, but the vacancy-only counterpart, represented by Equation 2.5, exhibited a poor fit. To extend charge disproportionation to doped compositions then, M'_{La} is presumed to act as a substitutional impurity for the La^x_{La} species remaining after vacancy creation:

$$La_{1-x}(M'_{La})_x Mn'_\xi Mn^x_{1-2\xi} Mn^{\bullet}_\xi O_3 + \frac{\delta}{2}O_2 \quad \rightarrow \quad \frac{3+\delta}{3}[La_{(1-x)\cdot 3/(3+\delta)}(M'_{La})_{x\cdot 3/(3+\delta)} \tag{2.10}$$
$$(V'''_{La})_{\delta/(3+\delta)}Mn'_{(\xi-2\delta)\cdot 3/(3+\delta)}$$
$$Mn^x_{(1-x+2\xi+2\delta)\cdot 3/(3+\delta)}Mn^{\bullet}_{(x+\xi)\cdot 3/(3+\delta)}$$
$$(V'''_{Mn})_{\delta/(3+\delta)}O_3]$$
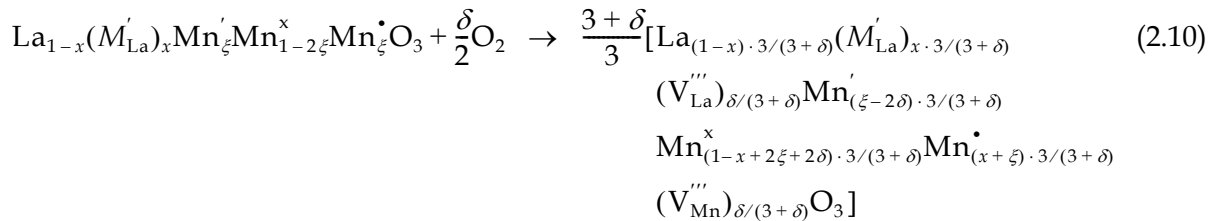
A careful examination of Equation 2.10 shows that the species-only reaction will stay unchanged from that given by Equation 2.9. In similar fashion to $La_{1-\varepsilon}Mn_{1-\varepsilon}O_3$, thermogravimetric analysis showed that the nominal composition $La_{0.85}Sr_{0.15}MnO_3$ also followed a charge disproportionation model. The primary difference between the charge disproportionation and vacancy-only models emerges through a determination of $[Mn^{4+}]$. For the former, $[Mn^{4+}] = x + \xi$, while for the latter, $[Mn^{4+}] = x + 2\delta$. By shifting the product of oxidation from Mn^{4+} to Mn^{3+}, charge disproportionation presumes that the divalent dopant, M^{2+}, influences $[Mn^{4+}]$ in a manner reminiscent of Le Châtelier's principle. For example, by raising the doping level, and hence x, the corresponding increase in $[Mn^{4+}]$ progressively suppresses the ability of Mn^{3+} to ionize into Mn^{2+} and Mn^{4+} at elevated temperatures. So ξ should decrease with increasing x. This prediction is confirmed empirically: in $LaMnO_3$ (i.e., $x = 0$), ξ reaches 0.38, yet for $La_{0.85}Sr_{0.15}MnO_3$, ξ drops to 0.24 [58]. In both cases, $[Mn^{4+}]$ comes close to the 40% upper bound discussed earlier.

The measurements of Van Roosmalen and Cordfunke depended on *in situ* characterization at elevated temperatures. However, the presence of Mn^{2+} required by charge disproportionation is not observed at ambient temperatures or below; magnetization curves from 4.2 to 400 K contain no signatures from either a manganese d^5 high spin (i.e., $t_{2g}^3e_g^2$, $S = 5/2$) or low spin (i.e., $t_{2g}^5e_g^0$, $S = 1/2$) state. So the disproportionation mechanism must remain confined to higher temperatures. But the influence of disproportionation on $[Mn^{4+}]$ does decrease with increasing $[M^{2+}]$ during oxidizing processes. Furthermore, vacancy concentrations decrease as the doping level rises. VAN ROOSMALEN and CORDFUNKE [56] determined that for $La_{1-x}M_xMnO_3$ compositions fired in air, δ becomes less than 0.025 (i.e., $\varepsilon < 0.009$) by the time x exceeds 0.30 — regardless of whether of M is Ca, Sr, or Ba. Clearly then, the inclusion of divalent dopants serves to stabilize the ideal chemical stoichiometry of doped-lanthanide manganites. *This observation carries important ramifications for the thin film specimens presented by Chapter 4: any deviations from ideal stoichiometry for the x = 0.33 compositions (i.e., $La_{0.67}Ba_{0.33}MnO_3$ and $La_{0.67}Pb_{0.33}MnO_3$) should be minimal, if at all.*

Two other defect mechanisms have also been explored in perovskite manganites: (1) the creation of oxygen vacancies through reducing atmospheres (i.e., $LaMnO_{3-\delta}$ and $La_{1-x}M_xMnO_{3-\delta}$) [63, 64] and (2) deliberate A-site nonstoichiometry via reduction of lanthanum content (i.e., $La_{1-x}MnO_3$) [65]. These models will not be discussed here as neither carries any

particular relevance to the thin film process presented in this dissertation. Specifically, all firing processes transpire in air (i.e., an oxidizing environment) and formulation of the *A*-site is for a net occupancy of unity.

2.3 SOL-GEL PROCESSING

Conventional techniques for preparing perovskite manganites rely on a generic mixed-oxide method wherein: (1) homometallic oxides or carbonates are ground in a mortar and pestle, and (2) the resulting mixture is fired at high temperature to enable both reaction and solid-state diffusion. Regrinding and refiring of the intermediate product is often required to ensure a complete transformation to the desired crystalline phase. For example, during the conventional synthesis of $La_{1-x}Ba_xMnO_3$ and $La_{1-x}Pb_xMnO_3$ powders, a multi-stage "grind and fire" employs temperatures of 1500 °C and 950 °C, respectively [66, 67]. A modification to the starting procedure can sometimes lower processing temperatures: simple dissolution of metal salts in aqueous media creates a uniform, atomically-mixed solution. Subsequent evaporation then leaves a precipitate whose intimate association reduces the necessary diffusion lengths during heating. But $La_{1-x}Ba_xMnO_3$ and $La_{1-x}Pb_xMnO_3$ powders prepared with this modification still require temperatures in excess of 950 °C for phase-pure material.[23] Such high formation temperatures, even after atomic mixing, reflect the refractory nature of perovskite manganites and therefore present a notable challenge for integration onto commercially-desirable silicon substrates.

By comparison, the sol-gel process developed in Chapter 3 for manganites produces crystalline $La_{0.67}Ba_{0.33}MnO_3$ and $La_{0.67}Pb_{0.33}MnO_3$ perovskite phases below 650 °C, a dramatic improvement over conventional methods. The ability of sol-gel processing to lower the thermal barrier to phase formation stems from a polymerized metal-oxygen framework formed in solutia (i.e., $M-O-M-O-M-O-$, etc. where M = metal). In essence, chemical reactions between intimately-mixed metal precursors initiate metal-oxygen bonding, reducing the thermal energy needed to complete the transformation to final oxide. Besides lower temperatures of formation, however, sol-gel processing also offers excellent compositional uni-

---

[23]The author has prepared $La_{0.67}Ba_{0.33}MnO_3$ and $La_{0.67}Pb_{0.33}MnO_3$ by dissolving the appropriate acetate salts in deionized water. Intermediate "grind and fire" steps followed heating at 350 °C and 500 °C in air. A final step at 1100 °C and 950 °C in air, respectively, ensured perovskite-only X-ray diffraction patterns.

formity and microstructural control, resulting in homogeneous end-products with tailored grain and pore morphologies. When applied as a coating technology (i.e., for thin-film deposition), this solution-based approach produces uniform, conformal coverage on non-planar substrates and readily adapts to large surface areas without compositional gradients. Conventional thin-film methods, dependent on vapor phase deposition in vacuum, do not offer such flexibility. In addition, the capital-intensive requirements of vacuum-based deposition make sol-gel processing an economically-attractive alternative for multi-element, complex oxides such as the doped-lanthanide manganites. Accordingly, this section presents a description of sol-gel processing and terminology, focusing on the effects of alkoxide chemistry upon the underlying hydrolysis and condensation mechanisms. A discussion of polymerization behavior and structural evolution during heating details the transition to the final ceramic product. Adaptation of sol-gel processing to thin film deposition, specifically spin-coating, concludes the section. For an in-depth examination of sol-gel processing, the reader is referred to the seminal reference text by BRINKER and SCHERER [68].

2.3.1 PREPATORY ROUTES TO CERAMICS

In ceramic preparation, sol-gel processing can be broken down into three stages: (1) dissolution and reaction of metallorganic precursors in solutia to form the "sol", (2) continued reaction via hydrolysis and condensation to create the "gel", and (3) removal of solvent thereby leaving a porous, self-supporting body. The principal feature distinguishing a sol from standard solutions is that the reaction of dissolved precursors produces regions of solid phase within the solvent. The term "sol" therefore refers to a diphasic system wherein the solvent serves as a suspending medium. Depending on the nature of the solid phase, sols can be differentiated as either colloidal or polymeric. Colloidal sols contain a dispersion of small (i.e., 1–100 nm) particles or aggregates whereas polymeric sols support randomly-branched molecular networks. Unfortunately, the term "colloid" originally referred to macromolecules unable to pass through porous membranes [69]. Such a definition would then imply that virtually all sol systems are, in fact, colloids. So to avoid the confusion produced by pre-existing convention, FLORY [70] and RABINOVICH [71] have recommended the revised terminology, "particulate sol". In addition, certain aqueous-based sols can produce dense "particles" with an average diameter approaching 1 nm — a dimension also characteristic of

the oligomeric species found in polymeric sols.[24] But at this length scale, the molecular distinction between "crystalline" (i.e., particulate) or randomly-branched (i.e., polymeric) can be nebulous. So BRINKER and SCHERER [68] have suggested a further refinement: particulate sols represent systems exhibiting dense particles larger than 1 nm; polymeric sols contain randomly-branched molecules where any "crystalline" component is less than 1 nm.

In order to transition into a gel, the constituents dispersed in the sol, whether particulate or polymeric, must form a continuous solid skeleton with an interspersed, but connected liquid phase. Growth of this network reaches the so-called gel point when a single giant spanning cluster achieves the boundaries of its container. As a result, a sharp rise in viscosity occurs and the viscoelastic behavior of a gel replaces the fluidity of a sol. The gelation process itself, however, depends on the nature of the system. For particulate sols, modification of surface charges, steric interactions, and Van der Waals forces induces flocculation, typically through changes in concentration, pH, temperature, and/or the addition of a gelation agent [72, 73]. But in polymeric sols, the reaction of monomeric and oligomeric functional units creates macromolecules which continue to crosslink to form randomly-branched, three-dimensional structures. So gel formation in polymeric sols stems from chemical bonding whereas an aggregation mechanism dominates particulate sols. In general though, both systems drive the growth of small individual clusters which eventually impinge on one another to form a spanning cluster. The gel point, however, does not correspond to the end of the sol-to-gel transition. Fluid entrapped within the solid network still contains particle aggregates or polymer fragments capable of attaching to the spanning cluster. During the subsequent period of aging then, continued reinforcement of the skeletal structure causes the stiffness of the gel to increase with some gels undergoing spontaneous shrinkage.[25]

The complete evaporation of solvent from a gel leaves a solid, amorphous preform ready for heat treatment and conversion to the desired ceramic. But control over the evaporative process aids in the selection of the gel morphology, and hence, the end-product. For example, drying under standard atmospheric conditions generates capillary pressures within the

---

[24]An oligomer is a molecule of intermediate relative mass comprised of a small number of monomeric functional units of lower relative mass. For example, many metallic or metalloid alkoxides are sufficiently reactive to form oligomers in solutia by themselves.

[25]Spontaneous shrinkage results from syneresis, a process wherein continued bond formation or attraction between particles contracts the solid network. As a result, pore volume decreases, expelling entrapped fluid from the gel.
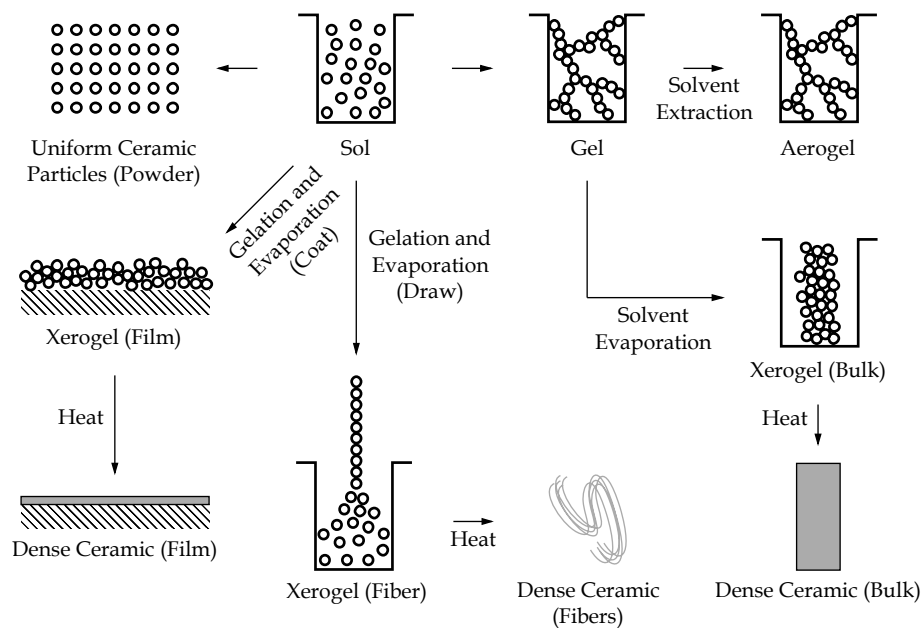
FIGURE 2.7 Prepatory routes to various ceramic end-products using sol-gel processing. (Adapted from [68]. Copyright 1989 Academic Press)

gel, compressing the solid framework and creating a porous xerogel (the prefix "xero" means dry).[26] The resulting shrinkage is notable, with a volume reduction of ~ 90% (or more) not being unusual. If instead, the gel is supercritically dried (i.e., by means of an autoclave at the appropriate temperature and pressure), no liquid-vapor interface exists and capillary pressures never develop. Drying therefore occurs with virtually no shrinkage, leaving an exceptionally porous and open structure. This structure, referred to as an aerogel, contains a low volume fraction of solid, which with deliberate process control, can approach values less than 1%. Figure 2.7 summarizes the various preparative stages leading to different preforms and their associated end-products. During the production of xerogels (bulk) and aerogels, evaporation occurs principally after gelation. But for certain routes, as shown in Figure 2.7, evaporation itself helps to induce the sol-to-gel transition: a progressive increase in concentration via solvent removal can further drive hydrolysis and condensation, eventually yielding a dried gel. Exploitation of this mechanism plays an important role during drawing or coating, wherein respectively, fibrous or substrate-supported xerogels result. For example, the sol-gel route for manganite thin films detailed in Section 3.4 employs a spin-coating pro-

---

[26]Dried gels whose smallest preform dimensions exceed a couple millimeters are commonly called monoliths. Monoliths are typically cast to shape and carefully dried to avoid cracking.

cess to deposit a dried, amorphous xerogel layer on Si(100) and platinized-Si(100). Because this method relies on the polymerization of alkoxides, further discussion of sol-gel processing will focus on the utility of these versatile precursors, emphasizing dissolution and reaction in organic solvent systems.

2.3.2 CHARACTERISTICS OF ALKOXIDE PRECURSORS

Metal alkoxides, represented stoichiometrically by $[M(OR)_z]_n$, comprise a class of compounds wherein an oxygen atom bridges a central metal atom to a carbon atom thereby forming the characteristic alkoxy bond (i.e., $M-O-C$). Here, R refers to any saturated hydrocarbon ligand (i.e., CH_3, CH_2CH_3, etc.); z corresponds to the valence of the metal and n, the degree of molecular association. The functional ligand of these compounds (i.e., OR) is derived from the parent alcohol (i.e., HOR), hence the designation "alkoxy". EBELMAN [74, 75] synthesized the first alkoxide compounds, based on boron and silicon, by direct reaction of their anhydrous chlorides with alcohol. Since then, the systematic investigation of alkoxy chemistry has extended to virtually all elements of the periodic table and is exhaustively covered in the texts by BRADLEY, MEHROTRA, and co-workers [76, 77] and TUROVA, et al. [78]. Of the transition metal elements, however, the properties of Group IVB (i.e., Ti, Zr, and Hf) remain the best-known, with Group VIIB (i.e., Mn, Tc, and Re) representing least-known [79]. Accordingly, an examination of the Group IVB alkoxides forms the basis (here) for discussing the chemistry of transition metal alkoxides, particularly as related to sol-gel processing.

From the perspective of polymerization, metal alkoxides can be viewed in terms of their functionality, f, which corresponds to the number of bonds available for reaction. For example, the compound $Ti[OC(CH_3)_3]_4$ contains labile (i.e., reactive) sites at each $Ti-O$ bond so $f = 4$. When $f = 2$, polymerization yields chain and ring structures, but if $f > 2$, additional crosslinking will generate three dimensional structures. The chemical lability of transition metal alkoxides stems from two principal factors: (1) polarization of the metal-oxygen bond resulting in high metal oxidation states and (2) the possibility of greater metal coordinations unsatisfied by the simple molecular unit. Both properties result from the electronegativity of the alkoxy ligand. Electron distribution along the alkoxy bond exhibits an ionic character (i.e., $M^{\delta+}-O^{\delta-}-C^{\delta+}$) due to individual electronegativity differences of the constituent atoms. On the Pauling scale, the electronegativity of oxygen is 3.5, and along either bond direction

this value decreases, whether towards carbon (i.e., 2.5) or the transition metal (i.e., 1.3–1.5).[27] So the oxygen atom acquires a distinct negative partial charge; the greater electric moment along $M^{\delta+}-O^{\delta-}$ therefore produces a polar covalent metal-oxygen bond. Yet the solubility of transition metal alkoxides in common organic solvents and their volatility indicate a greater covalent character than suggested by considerations of electronegativity alone. This heightened covalency has been postulated to arise from three mechanisms [77]. First, a +I inductive effect (i.e., electron release), enhanced when R corresponds to branched alkyl groups, further shifts electron density from carbon to oxygen.[28] Polarization of the metal-oxygen bond relaxes in response. Second, hybridization of transition metal 3d orbitals with 2p orbitals on oxygen can delocalize the electron density, particularly for early transition metals. And lastly, the electron-rich oxygen of the alkoxy ligand can coordinate with another metal atom (i.e., bridging), creating oligomeric species via dipolar bonding:[29]

$$
\begin{array}{c}
R \\
O \\
\diagup \diagdown \\
--M \qquad M-- \\
\diagdown \diagup \\
O \\
R
\end{array}
$$
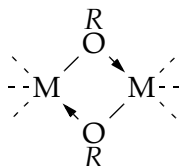
So the parameter n in $[M(OR)_z]_n$ presented earlier reflects the degree of oligomerization resulting from molecular association. But the tendency of a metal to expand its coordination sphere stems from the high configurational energy of its monomeric structure. By withdrawing electrons from the transition metal, the electronegative alkoxy ligands leave an electropositive center susceptible to nucleophilic attack (i.e., reaction via electron donation). Oligomerization then corresponds to a polymerization process wherein alkoxy ligands comprise surrogate nucleophiles; dipolar bonding to neighboring metal centers lowers the configurational energy through structural aggregation.

A qualitative theory on the molecular association of metal alkoxides, developed by BRA-DLEY [80] in 1958, predicts the equilibrium structure to be one wherein all metal centers achieve their preferred coordination, but with a minimum degree of oligomerization. Empirical observations agree reasonably well with theory although predictions can occasionally be

---

[27]Specifically, the Group IVB series gives 1.5, 1.4, and 1.3 for Ti, Zr, and Hf, respectively. By comparison, Group VIIB electronegativities for Mn, Tc, and Re are, respectively, 1.5, 1.9, and 1.9.

[28]Removal of a hydrogen atom from its alkane (i.e., a saturated hydrocarbon like CH_4, CH_3CH_3, etc.) creates an alkyl ligand (i.e., CH_3, CH_2CH_3, etc.). An example of a branched alkyl is $C(CH_3)_3$.

[29]Dipolar bonding refers to the coordination of two neutral molecules, the combination of which, results in charge-separated structures.

incorrect. So for example, according to Bradley, a quadrivalent metal alkoxide, $M(OR)_4$, with octahedral coordination should exhibit a trimeric association, $[M(OR)_4]_3$. X-ray diffraction patterns by IBERS [81] on single crystals of titanium ethoxide instead indicate the tetramer, $Ti_4(OCH_2CH_3)_{16}$; subsequent collaboration with MARTIN and WINTER [82], though, did yield the expected trimer when dissolved in benzene (i.e., an inert non-polar solvent). In the solid state, the preference of one oligomeric structure over another depends on: (1) the monomeric formula unit, $M(OR)_z$, (2) the size and formal oxidation state of the metal center, (3) the steric encumbrance of the alkyl ligand, R, and (4) the d orbital filling of the transition metal [83].

Comparative investigations of silicon and Group IVB alkoxides by BRADLEY, et al. [84–87] established three trends regarding molecular association. First, the tendency towards alkoxy bridging increases with the electron deficiency of the metal. Silicon ethoxides, for instance, are monomeric (i.e., $n = 1.0$) in non-polar solvents while the titanium, zirconium, and hafnium moieties exhibit molecular associations of $n = 2.4, 3.6$, and 3.6, respectively. Such behavior can be anticipated from comparisons of electronegativity: 1.74, 1.32, 1.22, and 1.23, respectively. Second, the larger the metal center, the higher the structural aggregation. Accordingly, the aforementioned molecular associations correlate well with their metal atomic radii of 1.11, 1.32, 1.45, and 1.44 Å, respectively. And finally, enlarging the steric bulk of the alkoxy ligand inhibits oligomerization since the electropositive metal center becomes increasingly shielded. Titanium alkoxides, representative of the Group IVB series, become monomeric as the alkyl functional unit expands: changing R from CH_2CH_3, $CH(CH_3)_2$, to $C(CH_3)_3$ produces in turn, $n = 2.4$, $n = 1.4$, and $n = 1.0$. Of these three trends though, steric demands influence molecular complexity greater than the electronic nature of OR or M. Investigations into titanium and zirconium alkoxides by BRADLEY, et al. [86] demonstrated that symmetrical secondary alkoxides (i.e., $R = CHR'_2$) reduce association more rapidly as R' lengthens than their unsymmetrical analogues (i.e., $R = CHCH_3R'$).[30] The former emphasizes the rapid growth of steric bulk whereas the latter allows more progressive control. Yet the unsymmetrical group still followed the shielding behavior of the symmetrical one. Therefore, the magnitude of any $+I$ inductive effects were minimal relative to steric influences. This behavior remained the same regardless of the Group IVB metal.

---

[30]In alkoxides, the principal carbon (i.e., oxygen-bearing) can be characterized by its degree of bonding to other carbon atoms. So in a primary alkoxide (i.e., 1°), the principal carbon is bonded to only one other carbon atom. In a secondary alkoxide (i.e., 2°), the principal carbon is bonded to two, and so forth.

Variations in steric bulk cause n to transition throughout a broad dynamic range (i.e., $1 \leq n \leq \infty$). For example, virtually all transition metal methoxides, $M(OCH_3)_z$, form infinite polymers, $[M(OCH_3)_z]_\infty$, which if replaced with some bulkier alkoxy ligand, convert to discrete oligomers (or monomers). From the perspective of sol-gel processing, infinite polymers are highly undesirable because $n \rightarrow \infty$ implies the emergence of a lattice energy, thereby stabilizing an insoluble, nonvolatile, and often unreactive precursor. But discrete oligomers contain dipolar metal-oxygen bridges with no associated lattice energy. For instance, BRADLEY, et al. [87] discovered that the latent heats and entropies of vaporization in zirconium alkoxides correspond to a depolymerization process, $[Zr(OR)_4]_n$ (liquid) $\leftrightarrow nZr(OR)_4$ (vapor), verified by density determinations in both phases. This disassociation reflects the decoupling of weak, charge-separated metal-oxygen bonds of approximately 9 kcal. So the steric bulk of the alkoxy ligand plays a crucial role in stabilizing reactive precursors with small oligomeric bond energies and labile $M^{\delta+}-O^{\delta-}-C^{\delta+}$ sites. *Exploitation of this phenomenon enabled the author to design and synthesize a highly-soluble manganese(II) alkoxide suitable for sol-gel processing (see Section 2.5) − a new and significant contribution to the field!*

Clearly, the preparation of alkoxide precursors for sol-gel processing begins with dissolution in a solvent medium. But oligomerization depends strongly on both solute concentration and the nature of the solvent. In general, dilution reduces the molecular association of metal alkoxides. MARTIN and WINTER [82] observed that titanium ethoxide, when dissolved in benzene, exhibited small complexities (i.e., $n < 1.9$) for molalities below 10 m; a rapid convergence to the expected trimer, however, occurred as the concentration increased. Coordination expansion of the metal, however, alters notably when protic, polar solvents comprise the dissolution medium. For example, titanium ethoxide dissolves in its parent alcohol (i.e., ethanol) forming the solvate species, $[Ti(OCH_2CH_3)_4]_2 \cdot 2CH_2CH_3OH$. Comparison with the trimer, $[Ti(OCH_2CH_3)_4]_3$, reveals the loss of alkoxy bridging to solvate coordination [88]. This change highlights the susceptibility of the electrophilic titanium center, stabilized by electronegative OCH_2CH_3 ligands, to attack by external nucleophiles such as CH_3CH_2OH. In essence, stronger Lewis bases (i.e., electron donors) can displace the weak dative bonds associated with alkoxy bridging (i.e., the alkoxy ligand is a weaker Lewis base). Protic, polar solvents therefore follow a nucleophilic addition mechanism (A_N) wherein the alkoxide serves as a Lewis acid (i.e., an electron acceptor) and the solvent, a Lewis base.

The significance of this chemical activity becomes apparent if small, highly-polar molecules of water are present in the alcoholic solvent: the electrophilic metal center is preferentially attacked by H_2O, cleaving the $M^{\delta+}-O^{\delta-}R$ alkoxy bond and leaving an $M^{\delta+}-O^{\delta-}H$ hydroxyl bond in its place. With respect to alkoxides then, water acts as a stronger Lewis base than its organic analog, the alcohol (i.e., HOH versus ROH). So a nucleophilic substitution mechanism (S_N) emerges in place of the addition mechanism thereby allowing the removal of the entire alkoxy ligand. The ability of alkoxides to participate in such a reaction pathway enables the construction of polymerized metal-oxygen frameworks (i.e., $M-O-M-O-M-O-$). The high reactivity of alkoxides to water therefore plays a crucial role in sol-gel processing, underscoring their utility as precursors.

2.3.3 ALKOXY-BASED HYDROLYSIS AND CONDENSATION

Two fundamental classes of reactions drive the formation of polymeric networks in alkoxy-based sol-gel processing: hydrolysis and condensation reactions. As illustrated in Figure 2.8, a single reaction sequence comprises the hydrolysis pathway but condensation can proceed via any of three unique sequences (i.e., alcoxolation, oxolation, or olation). For clarity, only the participating ligands have been drawn in Figure 2.8; the possibility of alternate facile sites, however, should not be excluded (i.e., $f > 1$). From the perspective of the metal center, basic distinctions between the two classes can be revealed by examining their constituent pathways. For example, an inspection of the reactants indicates that hydrolysis always presumes the availability of an alkoxy ligand, whereas, condensation requires at least one hydroxyl ligand. In similar fashion, a review of the products shows that hydrolysis always generates a terminal hydroxyl ligand. Condensation, on the other hand, creates a bridging ligand, whether oxo or hydroxyl. So initiation of hydrolysis then serves as an enabling mechanism for subsequent condensation reactions. But condensation forms the basis for crosslinking the metal centers, and hence, constructing the metal-oxygen framework. When interpeting Figure 2.8 though, one naive conclusion must be avoided. Condensation should not be construed to proceed via a simple sequential step after hydrolysis. In reality, both reaction classes occur simultaneously in solutia, particularly for polyfunctional alkoxides; the reaction rates of all four pathways exhibit complex interdependencies understood incompletely even for single precursor systems.

Hydrolysis

$H-OH + M-OR \rightarrow$ [intermediate] $\rightarrow HO-M \cdots O \rightarrow M-OH + ROH$
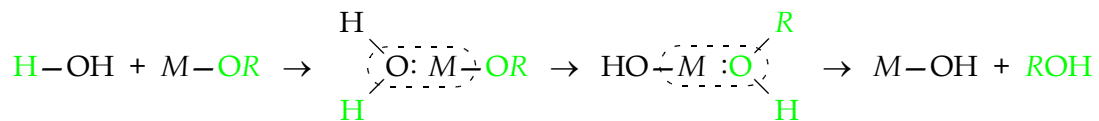
Condensation (Alcoxolation)

$M-OH + M-OR \rightarrow$ [intermediate] $\rightarrow M-O-M \cdots O \rightarrow M-O-M + ROH$
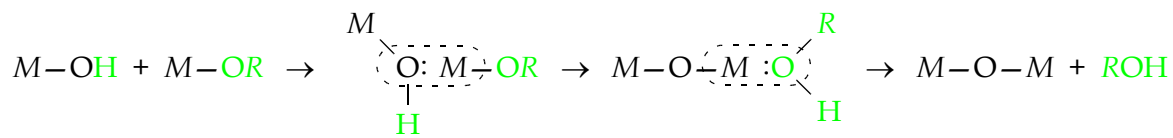
Condensation (Oxolation)

$M-OH + M-OH \rightarrow$ [intermediate] $\rightarrow M-O-M \cdots O \rightarrow M-O-M + H_2O$

Condensation (Olation)

$M-OH + [M \cdots O] \rightarrow M-\overset{H}{O}-M + ROH$

$M-OH + [M \cdots O] \rightarrow M-\overset{H}{O}-M + H_2O$
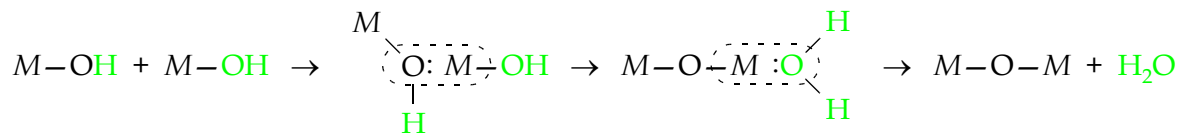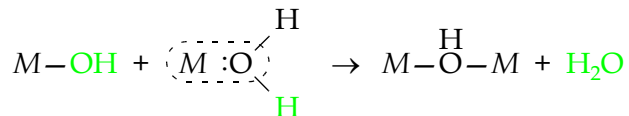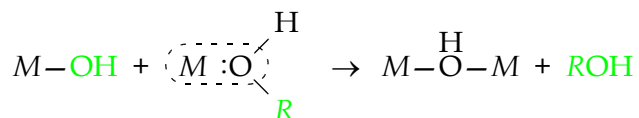
FIGURE 2.8 The reaction pathways of hydrolysis and condensaion in sol-gel processing. Dashed boundaries indicate oxygen coordination to the metal via lone pair electrons. Green color highlights atoms of the leaving group.

During hydrolysis though (see Figure 2.8), a water molecule coordinates to the positively-charged alkoxide metal center through a lone electron pair available on the oxygen atom. This nucleophilic addition yields in an alkoxo-aqua intermediate, $M(OR)_z(OH_2)$, with an expanded metal coordination sphere (i.e., increased by unity). The Lewis basicity of water, stronger than alcohol, induces a proton transfer to the alkoxy ligand, which in turn, produces a coordinated alcohol molecule. The subsequent release of this new molecule, referred to generically as a leaving group, signifies the completion of a nucleophilic substitution. The resulting alkoxo-hydroxo complex, $M(OR)_{z-1}(OH)$, remains available for further reaction. For example, the general alkoxo-hydroxo formula, $M(OR)_{z-y}(OH)_y$ where $y \leq z$, would represent the effects of progressive hydrolysis; the end members, $y = 0$ or $z = 0$, are the initial alkoxide, $M(OR)_z$, or the completed hydroxide, $M(OH)_y$, respectively.

In condensation, the alkoxo-hydroxo species, $M(OR)_{z-y}(OH)_y$, undergo three possible nucleophilic substitutions, reacting with either alkoxy ligands (i.e., alcoxolation), hydroxyl ligands (i.e., oxolation), or coordinated metal centers (i.e., olation).[31] The alcoxolation sequence proceeds in a manner similar to hydrolysis except that M replaces H in the entering group (see Figure 2.8). The final species, $(RO)_{z-y}(OH)_{y-1}M{-}O{-}M(OR)_{z-y-1}(OH)_y$, contains an oxygen bridge with still-labile alkoxy and/or hydroxyl ligands. Oxolation follows the same pathway as alcoxolation but a proton substitutes for R in the both the reactant and leaving group (see Figure 2.8). The reaction between two hydroxyl ligands, however, ensures the production of a water molecule instead of an alcohol molecule. This difference provides one reason for rate interdependencies between hydrolysis and condensation pathways. Water molecules produced during oxolation can catalyze further hydrolysis reactions; alcoxolation, on the other hand, liberates only (relatively) inert alcohol groups. As discussed previously, if the metal center of a dissolved species contains an unsaturated coordination sphere, nucleophilic addition can lead to either an alcoholate or hydrate, depending on the water concentration in the solvent. Such chemical configurations are vulnerable to olation, wherein the hydroxyl ligand of the alkoxo-hydroxo species bridges both metals, releasing the coordinated alcohol or water molecule (see Figure 2.8); in essence, the metal center trades a weak dative bond for a stronger polar-covalent bond, stabilizing the higher coordination. Unlike

[31]For descriptive simplicity, oxygen-bridged reactants have been temporarily omitted. Alkoxo-hydroxo species with single or multiple oxo or hydroxyl bridges may participate in condensation reactions. A terminal hydroxyl ligand, however, must be present.

alcoxolation or oxolation, though, olation requires no protron transfer so its reaction kinetics proceed faster. The repetitive occurrence of these three condensation sequences enables the construction of oxygen-bridged metal polymers.

The susceptibility of a metal center to the various hydrolysis and condensation pathways, however, depends considerably on the ligands populating the coordination sphere. Otherwise, the strong Lewis basicity of water would ensure the constant dominance of hydrolysis, causing the metal alkoxides (i.e., $y = 0$) to convert directly into their full hydroxides (i.e., $z = 0$); little, if any, crosslinking from condensation would occur. In order to discern the different chemical reactivities of metal oligomers during hydrolysis and condensation, LIVAGE, et al. [89, 90] extended the theory of partial-charges to cover the sol-gel chemistry of transition metal oxides. The resulting thermodynamic model, whose roots derive from the equalization of chemical potential, accounts for electron density shifts during reaction and describes the equilibrium charge distribution of the participating species and ligands. One limitation, however, stems from the inability to properly incorporate chemical structure and coordination changes into the theory; resonance effects and π-orbital overlapping are also neglected. Nevertheless, predictions correlate well with empirical observations in sol-gel systems. Table 2.3 lists the charge distribution for titanium 2-propoxide (i.e., $z = 4$), a known monomer, and its hydolyzed moeities (i.e., $y > 0$).

In general, considerations of the partial charge model dictate that, for hydrolysis, the metal center carry a positive charge (i.e., $\delta_{M} \gg 0$) and water, a negative charge (i.e., $\delta_{H_{2}O} \ll 0$). This arrangement enables the coordination of a water molecule to the metal center. Proton transfer can then occur, provided that $\delta_{OR} < 0$. The resulting alcohol molecule de-coordinates from the metal when $\delta_{ROH} \gg 0$. A review of the titanium complexes in Table 2.3 clearly shows that $\delta_{OR} > 0$ when $y > 2$, indicating a barrier to protonation. Hydrolysis then is favorable primarily for Ti[OCH(CH$_3$)$_2$]$_4$ and Ti[OCH(CH$_3$)$_2$]$_3$(OH) but poorly so, if at all, for either Ti[OCH(CH$_3$)$_2$]$_2$(OH)$_2$ or Ti[OCH(CH$_3$)$_2$](OH)$_3$. In essence, the progressive substitution of hydroxyl ligands is self-limiting, retarding hydrolysis after $y = 1$. So the emergence of full hydroxides remains exceedingly unprobable due to protonation barriers. Furthermore, with the presence of hydroxyl ligands, condensation becomes thermodynamically favorable, especially for species with multiple substitutions. Polymerization reactions then would significantly hinder any isolated, fully-hydroxylated species from forming (see below).

COMPLEX	δ_{Ti}	δ_{OR}[a]	δ_{OH}	δ_{ROH}[a]	δ_{H_2O}
$Ti[OCH(CH_3)_2]_4$	-	−0.15	-	-	-
$Ti[OCH(CH_3)_2]_3(OH)$	+0.62	−0.08	−0.38	+0.02	−0.28
$Ti[OCH(CH_3)_2]_2(OH)_2$	+0.64	+0.04	−0.36	+0.15	−0.25
$Ti[OCH(CH_3)_2](OH)_3$	+0.67	+0.28	−0.32	+0.41	−0.18
$Ti(OH)_4$	-	-	−0.19	-	+0.01

[a] $R = CH(CH_3)_2$

TABLE 2.3 Charge distribution for titanium 2-propoxide and its hydrolyzed derivatives [90].

The reaction mechanisms of condensation may be analyzed in similar fashion. In alcoxolation, for example, the hydroxyl ligand of the $M^{\delta+}-O^{\delta}H$ bond must exhibit a negative charge in order to coordinate with a metal center containing an $M^{\delta+}-O^{\delta}R$ bond. All complexes in Table 2.3 satisfy this requirement, and therefore, may serve as entering groups. But proton transfer is favorable only for complexes displaying $\delta_{OR} < 0$. Of the alkoxo-hydroxo species, only $Ti[OCH(CH_3)_2]_4$ and $Ti[OCH(CH_3)_2]_3(OH)$ meet this criteria. So for alcoxolation, one of the reacting complexes must always have $y \leq 1$ or the reaction encounters an activation barrier. Oxolation, on the other hand, remains an unfavorable sequence entirely because unlike alcoxolation, the leaving group (i.e., water) retains a strong negative partial charge (i.e., $\delta_{H_2O} < 0$).[32] In olation though, this property, combined with the unsaturated metal sphere of titanium, enables water molecules to readily coordinate, regardless of the alkoxo-hydroxo species. So any hydrolyzed moiety, including a full hydroxide, can provide the hydroxyl bridge during olation because $\delta_{OH} < 0$. The assistance of alcohol adducts during olation, however, is highly improbable because $\delta_{ROH} > 0$ for all complexes. A comparison of the active condensation mechanisms (i.e., alcoxolation and olation) reveals that both these sequences are limited by the availability of $y = 1$ complexes. Because both hydrolysis and condensation operate in the regime $y \leq 1$ for the titanium 2-propoxide system, alcoxo-

---

[32]The ability of a molecule to de-coordinate is referred to as its nucleofugal character (i.e., literally "fleeing the nucleus"). In contrast to water, $\delta_{ROH} > 0$ for all complexes in Table 2.3 so repulsion from the positive metal center gives 2-propanol a strong nucleofugal character.

hydroxo species generated by hydrolysis become rapidly incorporated into polymer structures, not isolated hydroxides.

Analysis of alkoxide sol systems using partial charge theory also highlights the effect of competitive hydrolysis and condensation interactions on polymer growth. For example, in the titanium 2-propoxide system linear polymers would be expected since the removal of tertiary or quartenary alkoxy ligands is thermodynamically unfavored. Figure 2.9 presents a hypothetical oxo-polymer comprised of four unique units labeled A–D. The partial charge on the alkoxy ligand, δ_{OR}, varies with its coordination environment, which corresponds to –0.01, +0.22, +0.04, –0.08, respectively [90]. The ease of protonation then follows the relation, $D \gg A > C \gg B$. Clearly, the most functional (i.e., reactive) units of the oxo-polymer are at its ends, suggesting a predominantly linear growth mechanism.

As mentioned previously though, one deficiency of the partial charge theory remains its inability to account for structural changes during hydrolysis and condensation. BRADLEY, et al. [88] investigated the structural aspects of hydrolytically-derived titanium oxoalkoxides. The resulting three models predicted the formation of discrete or infinite oxo-polymers comprised of linked titanium octahedra: $Ti_3O_6(ROH)_6$, $[Ti_3O_4(OR)_4]_\infty$, and $[Ti_2O_3(OR)_2(ROH)]_\infty$. Discrete oxoalkoxide oligomers from initial reactions can often be crystallized from solution if hydrolysis can be successfully quenched. WATENPAUGH and CAUGHLEN [91], for instance, dissolved titanium ethoxide in ethanol and after passing partially-dried air through the solution, produced $Ti_7O_6(OCH_2CH_3)_{19}$ as the initial reaction product. Another Group IVB alkoxide, zirconium methoxide, formed $Zr_{13}O_8(OCH_3)_{36}$ when exposed to sodium hydroxide in
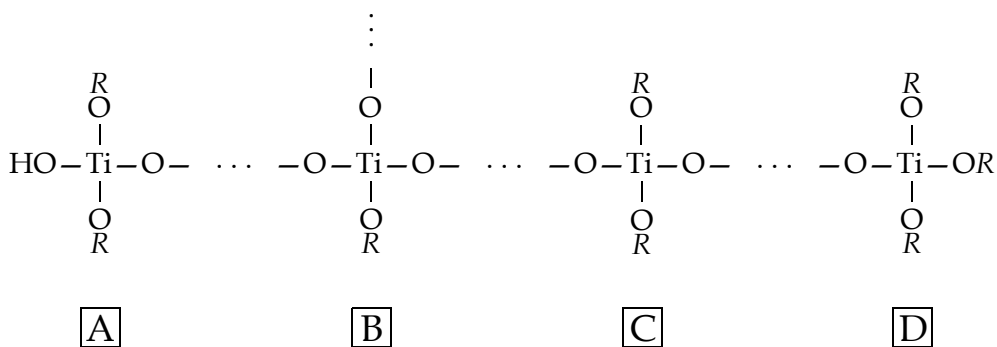
FIGURE 2.9 A hypothetical linear oxo-polymer constructed from titanium 2-propoxide. Four unique units (i.e., A–D) are present. Here, $R = CH(CH_3)_2$. (Adapted from [90]. Copyright 1989 Permagon Press.)

methanol [92]. Crystal structures of both compounds revealed metal centers packed exclusively in oxygen "cages"; oxo ligands comprised the core of the framework whereas alkoxy ligands extended outward from the periphery (see Figure 2.10).

Both theory and experiment point towards a mechanism of coordinate expansion during hydrolysis and condensation. The difference between N, the maximum coordination number of a metal in its oxide, and z, its oxidation state in the starting alkoxide, provides a driving force for oxo-polymeric construction. In the case of titanium ethoxide, $Ti_4(OCH_2CH_3)_{16}$, $N = 6$ and $z = 4$ so $N - z = 2$ (i.e., coordinate expansion should result from hydrolysis and condensation). Accordingly, the oxoalkoxide intermediate, $Ti_7O_6(OCH_2CH_3)_{19}$, contains titanium atoms in an exclusively octahedral coordination as shown in Figure 2.10A [91]. This development, not predicted by the partial charge model, carries significant practical importance for sol-gel processing: the oxoalkoxide structures of titanium and zirconium exhibit metal coordination environments characteristic of the full oxide. So oxoalkoxides represent an intermediate, derivative product whose further polymerization enables the assembly of long-range metal oxide networks via functionalized sub-groups on the periphery:

$$[M(OR)_z]_n \quad \rightarrow \quad [MO_x(OR)_{z-2x}]_{n_p} \quad \rightarrow \quad [M_2O_z]_\infty$$
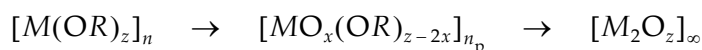
Here, x refers to the degree of hydrolysis (see page 56). Oxoalkoxide structure therefore forms a basis for *the chemical assembly* of ceramic oxide materials. Such a molecular "building block" approach was first pioneered by KLEMPERER, et al. [93–95] in the design of polysilicic acid esters (i.e., silicon oxoalkoxides) for silicates. An extension of this technique (i.e., the deliberate engineering of molecular structures) to multi-component ceramics remains the focus of current research, as discussed in a recent review by KESSLER [96].

Because though, both alkoxy bridging (see Section 2.3.2) and oxoalkoxide formation result from an underlying tendency to expand the metal coordination sphere, factors influencing molecular association (i.e., oligomerization) also affect hydrolysis and condensation. Indeed, the alkyl ligand (i.e., R) strongly impacts the reaction pathway through its chain length, steric hindrance, $\pm I$ inductive effect, and possibly $\pm E$ mesomeric effect [90].[33] For example, hydrolysis rates decrease with increasing R because longer aliphatic groups reduce

---

[33]In general, the inductive effect refers to electron transfer in a chemical bond induced by an adjacent, polarized bond. The mesomeric effect (i.e., resonance effect) occurs when orbitals of a chemical subgroup overlap with orbitals of the remaining molecule, introducing or extending electron delocalization.
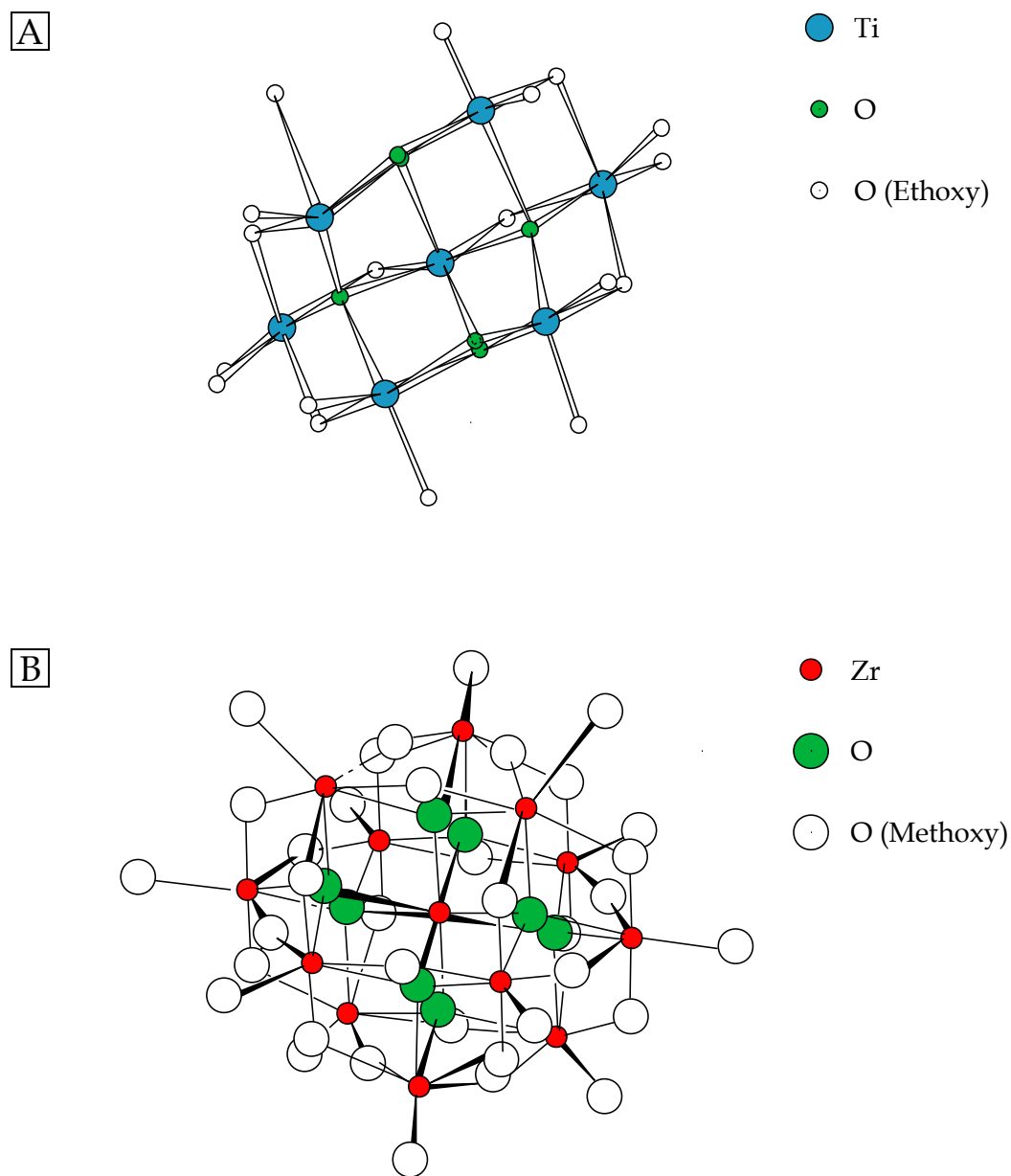
FIGURE 2.10 Crystal structures of titanium and zirconium oxoalkoxides. The top half (A) shows $Ti_7O_{24}(OCH_2CH_3)_{19}$ and the bottom half (B), $Zr_{13}O_8(OCH_3)_{36}$. For clarity, the alkoxy ligands on the periphery are represented by their oxygen atoms only. (Adapted from [91] and [92], respectively. Copyright 1967 London: The Chemical Society and 1977 The International Union of Crystallography.)

the positive charge on the metal center. Furthermore, bulky groups hinder the initial hydrolysis reaction due to shielding of the electrophilic metal; cleavage of subsequent alkoxy bonds, however, is progressively faster. So the alkyl ligand provides a means to adjust the competition between hydrolysis and condensation, and hence, the resulting oxo-polymer morphology. This synthetic structure, in turn, strongly influences the equilibrium phase emerging in the oxide end-product. For instance, the ratio of anatase and rutile phases in TiO_2 and the monoclinic-tetragonal transformation temperature of ZrO_2 both vary with the molecular weight of the alkoxide precursor [97, 98]. In addition to alkoxide composition, solute-solvent interactions prove equally important. Section 2.3.2 noted the change in coordination mechanism upon switching from an inert, nonpolar to a protic, polar media. The former exhibited alkoxy bridging but the latter relied on alcoholate adducts. This difference alters reaction pathways because alkoxy bridges produce molecular structures (i.e., via oligomerization) more resistant to hydrolysis than solvate bonds. For example, zirconium 1-propoxide precipitates from solutia when hydrolyzed in 1-propanol but yields polymeric gels in cyclohexane [99].[34] So deliberate selection of the solvent may be a necessary requisite to ensure a stable sol system.

The exceptional utility of alkoxide precursors and the significance of verifiable hydrolysis and condensation pathways (i.e., alkoxy-based sol-gel processing) can best be appreciated when considering the following: film preparation via sol-gel techniques comprises a subset of so-called "soft chemistry" approaches generically referred to as chemical solution deposition (CSD). For example, HASENKOX, et al. [101, 102] have developed an aqueous-based CSD method for $La_{1-x}(Ca, Sr)_x MnO_3$ films that enabled spin-coating of carboxylate precursors (i.e., exclusively acetate salts) dissolved in carboxylic acid (i.e., propionic acid).[35] Despite lattice-matched templating onto $LaAlO_3(100)$ substrates, temperatures greater than 800 °C are still required for the complete crystallization of manganite perovskite phase. This behavior sug-

---

[34]Adducted alkoxides often form in the presence of alcohol. For example, $Zr_2[OCH(CH_3)_2]_8 \cdot 2HOCH(CH_3)_2$ was crystallized and characterized by X-ray diffraction after exposure to excess 2-propanol [100].

[35]The carboxyl ligand, RCOO, contains two oxygen atoms bonded to a central carbon atom (as opposed to a single oxygen in the alkoxy ligand). Hybridization of p orbitals along the OCO group creates a delocalized electron cloud (i.e., negatively charged) that gives the ligand strong ionic character. Bonding to hydrogen yields an acid; coordination to a metal forms an organic salt. The presence of two oxygen atoms enables chelation, the coordination of both oxygens to the metal. This behavior more effectively saturates the metal coordination sphere, stablizing the complex against nucleophilic attack. An acetate occurs when R = CH_3 and a propionate when R = CH_2CH_3. A comprehensive review of carboxylate chemistry can be found in the reference text by MEHROTRA and BOHRA [103].

gests a basic metal-organic decomposition (MOD). In contrast, the alkoxy-based sol-gel process developed in Chapter 3 for $La_{0.67}Ba_{0.33}MnO_3$ and $La_{0.67}Pb_{0.33}MnO_3$ films indicates crystallization below 650 °C. *So intimate mixing and complexing via dissolution and reflux should not be construed as equivalent to hydrolysis and condensation.* The formation of oxoalkoxide building blocks and their subsequent polymerization remains a unique advantage of alkoxy-based sol-gel processes. This feature enables the low-temperature preparation of oxide ceramics, an achievement not easily obtained through other CSD approaches prior to this dissertation.

2.3.4 SOL SYSTEMS FOR COATING PROCESSES

For the development of sols suitable for film deposition, hydrolysis and condensation reactions must be controlled in order to ensure a polymeric or particulate system, but not precipitation or gelation prior to coating. For this reason, water of hydrolysis is first diluted in pure solvent and only then subsequently added to the unhydrolyzed alkoxide solution; a direct addition, by comparison, would generate a massive local excess of water, catalyzing either metal oxide precipitation or a gel front at the boundary of initial contact. Polymeric sols are generally preferred over their particulate counterparts because, as will be discussed in Section 2.3.5, the latter sometimes follow a diffusive (as opposed to a viscous) sintering mechanism. Considerations of alkoxide concentration, functionality (i.e., *f*), and condensation rates have led LIVAGE, et al. [90] to propose a "rule of thumb" for products obtained by hydrolyzed sols (see Table 2.4). Clearly for coating processes, slow hydrolysis and condensa-

HYDROLYSIS RATE[a]	CONDENSATION RATE[a]	RESULT
Slow(er)	Slow(er)	Metastable Sol[b]
Fast(er)	Slow(er)	Polymeric Gel
Fast(er)	Fast(er)	Particulate Gel or Gelatinous Precipitate
Slow(er)	Fast(er)	Controlled Precipitation

[a] Relative to each other.
[b] Polymeric or particulate.

TABLE 2.4 Effect of relative rates of hydrolysis and condensation on a hydrolyzed sol [90].

tion rates are preferable; complete gelation should only be induced through evaporation (i.e., via concentration) after deposition. The most direct route for selecting the desired reaction rates stems from the control of water concentration as measured by h, the hydrolysis ratio:

$$h = \frac{\text{mol of } H_2O}{\text{mol of } [M(OR)_z]_n} \tag{2.11}$$

When less than z, h can be presumed equivalent to the average degree of hydrolysis, $\langle x \rangle$, that characterizes oxoalkoxide intermediates in solutia. Through h, BRADLEY, et al. [104–108] established a correlation between $\langle x \rangle$ and $\langle n_p \rangle$, the number-average degree of polymerization, via an empirical examination of oxo-polymers, $[MO_x(OR)_{z-2x}]_{n_p}$, derived from Group IVB and VB metals. Ebulliometric measurements on the molecular weights of hydrolyzed alkoxides resulted in the so-called pq model, which offers a straight-forward relationship between $\langle x \rangle$ and $\langle n_p \rangle$ [108]:

$$\frac{1}{\langle n_p \rangle} = \frac{1}{p} - \frac{1}{q} \cdot \langle x \rangle \tag{2.12}$$

Bradley's pq nomenclature corresponds to the $MpOq$ substructure of the oxo-polymeric product [109]. Here, p refers to the extent of oligomerization of the unhydrolyzed alkoxide (i.e., n in Section 2.3.2) and q tabulates the number of $M-O-M$ links between adjacent $MpOq$ units. For example, the designation p_3q_4 characterizes an oxo-polymer based on an alkoxide trimer (i.e., $p = 3$) whose trimeric substructures share four $M-O-M$ bonds (i.e., $q = 4$). The compositions $Ti_6O_4(OCH_2CH_3)_{16}$ and $[Ti_3O_4(OCH_2CH_3)_4]_\infty$ belong to the p_3q_4 oxo-polymeric class as illustrated in Figure 2.11. But the dependence of $\langle n_p \rangle$ on $\langle x \rangle$ indicates that polymerization is strongly influenced by hydrolysis. So h in Equation 2.11 therefore provides a method to control oxo-polymer growth, and hence, gelation. Note though, that subsequent investigations into oxo-polymer chemistry have shown the structure and bonding of other transition metals to be far more complex than the Group IVB and VB constituents discussed here. For further details, the reader is directed towards the recent comprehensive review of high-valent early transition metal compounds by GOLOBOY, et al. [110].

In practice, Equation 2.11 can be partitioned into three qualitative regimes for alkoxy-based solutions: (1) $h < 1$, (2) $1 \leq h \leq z$, and (3) $h > z$ [90]. When less than unity, the hydroly-
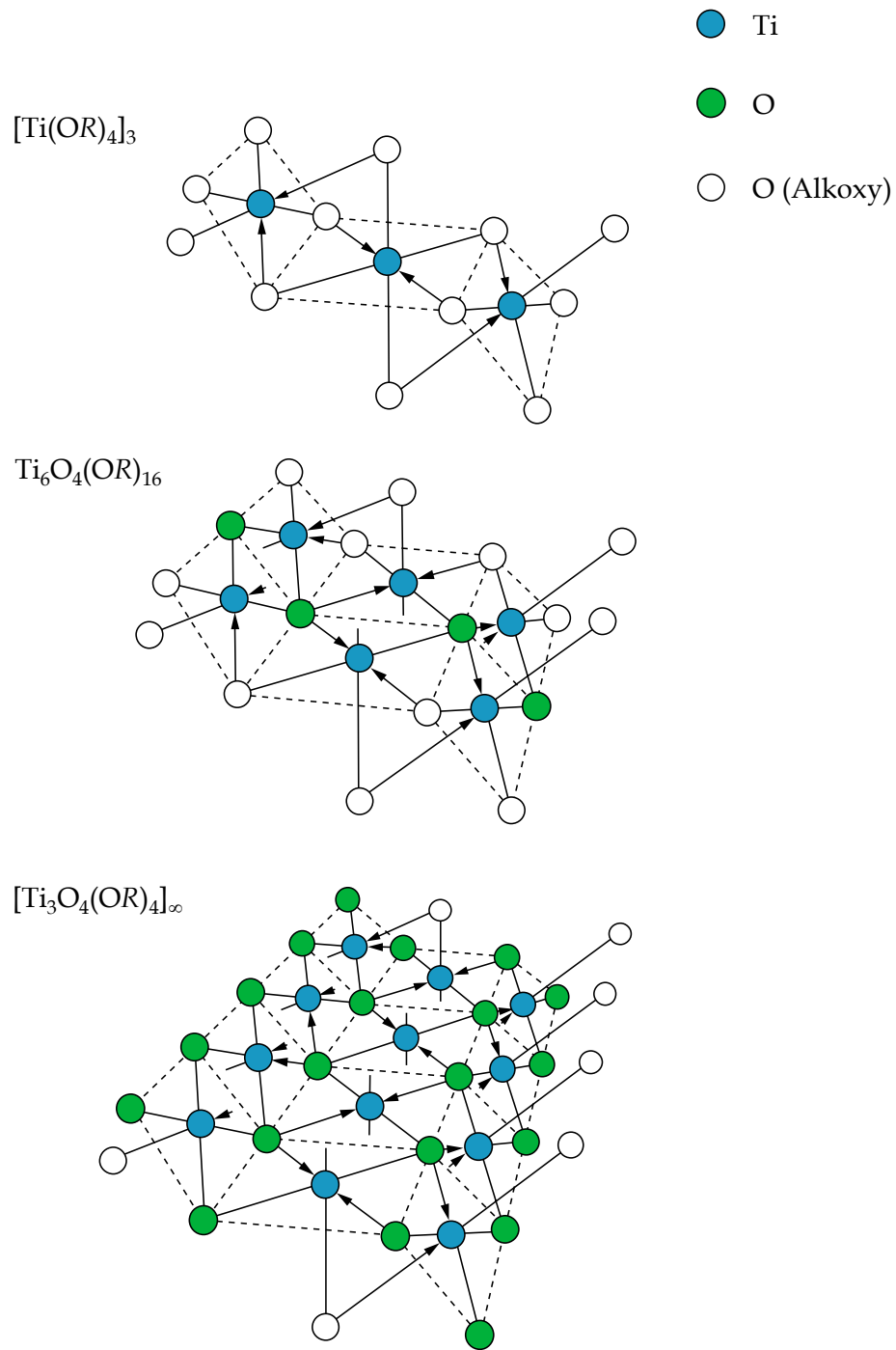
FIGURE 2.11 Progressive hydrolysis of the p_3q_4 class of titanium alkoxide oxo-polymers. Alkoxy ligands are are represented by their oxygen atoms only, and for clarity, some have been omitted entirely. (Adapted from [104]. Copyright 1961 National Research Council.)

sis ratio ensures the dominance of alcoxolation and alcolation.[36] But with regard to alcoxolation, the functionality cannot exceed one because multiple hydroxyl substitutions (i.e., $y > 1$) remain thermodynamically unfavorable; partial charge calculations show that unhydrolyzed alkoxides have a greater susceptibility to nucleophilic attack by water than those already hydrolyzed. Accordingly, the lack of excess (localized) water severely retards the growth of long-range structures and prevents the emergence of a spanning cluster (i.e., the gel point). Instead, the combination of alcoxolation and alcolation leads to the synthesis of discrete oxoalkoxides, which as mentioned in Section 2.3.3, can often be isolated from solutia via crystallization. For the intermediate domain, $1 \leq h \leq z$, the availability of multiply-hydrolyzed species enables the development of polymer networks, principally through alcoxolation and oxolation. But enhanced precursor functionality beyond $f > 2$ (i.e., $y > 2$) may only occur if the partial charge chemistry of a system permits (see, for example, Table 2.3).[37] So hydrolysis may not go to completion even if $h = z$. Polymer growth in this regime proceeds primarily through linear or branched construction and the formation of dense oxide particles is unfavorable. However, if the hydrolysis ratio surpasses z (i.e., $h > z$), heavily-crosslinked polymers, particulate gels, or precipitates can result due to the presence of substantial quantities of localized water. This latter regime has been exploited to allow the controlled precipitation of mono-dispersed TiO_2 and ZrO_2 powders from titanium ethoxide and zirconium 1-propoxide, respectively [111, 112].

For coating, however, consideration of the three regimes suggests an optimal (partial) hydrolysis of $h < 2$. This range enables polymeric growth but minimizes the risk of precipitation or premature gelation. Clearly though, the actual value must be matched to the specific solution. Partial hydrolysis plays a crucial role in developing soluble oxo-polymers suitable for film deposition. During the initial hydrolysis and condensation reactions, $\langle n_p \rangle$ increases quickly due to the copious presence of labile alkoxy bonds. Nucleophilic attack at these sites, however, progressively reduces their availability, redistributing electron charge and diminishing reactivity.[38] Because of partial hydrolysis, a sol eventually enters a metastable state where $\langle n_p \rangle$ changes slowly with time, establishing a (relatively) steady viscosity for

---

[36]Alcolation refers to a reaction where the alkoxy ligand of one metal forms a bridge to another via nucleophilic addition (i.e., an "alcol" bridge). By comparison, olation uses the hydroxyl ligand (i.e., an "ol bridge).
[37]When referring to Table 2.3, assume $y \approx h$.
[38]Refer to discussion concerning Figure 2.9 on page 51.

coating. Failure to hydrolyze before coating, however, leaves a solution vulnerable to the adventitious behavior of atmospheric moisture.[39] At the air-liquid interface, reaction layers can form, creating a "skin". This condition alters the rheology of the sol during deposition and interferes with substrate wetting and gel adhesion [113]. SAKKA, et al. [114] investigated the film formation of hydrolyzed, alkoxy-derived sols for SiO_2. Examination of the relationship with time between intrinsic viscosity, $[\eta]$, and the number-average molecular weight, M_n, highlighted three transitional regions characterized by: (1) an initial short and rapid jump in $[\eta]$ resulting from polymerization, (2) an optimal intermediate range for $[\eta]$ with linear polymers of $M_n \sim$ 950–1900, and (3) a final spike in $[\eta]$ denoting the approach of the gel point. Interestingly, only sols with $h \leq 2$ were considered "spinnable" by Sakka, et al.[40] Sols with higher hydrolysis ratios developed polymer morphologies unsuitable for dipping or spinning. So the emergence and growth of oxo-polymers *before coating* (i.e., partial hydrolysis) is critical for rheologies that produce uniform, defect-free films.

Dilute concentrations of water in solvent enable controlled hydrolysis and condensation, producing oxo-polymers with exceptional chemical homogeneity. By hydrolyzing in solutia, the solvent serves as a separation medium for the reactants, tempering the reaction kinetics by controlling diffusion [115]. Hydrolysis is slightly favored over condensation due to a lower dependency on the reduced mobility of large oxo-polymer macromolecules. In multi-elemental solutions, however, strong concentrations of water can accentuate hydrolysis rate differences between alkoxide species. For example, during the sol-gel preparation of mullite powder (i.e., $3Al_2O_3 \cdot 2SiO_2$), a slow, restricted hydrolysis produces chemically uniform oxo-polymers that, as measured by differential thermal analysis (DTA), decompose with a sharp crystallization peak at 980 °C [116]. In contrast, rapid hydrolysis of the same solution (i.e., via "excess water") induces the synthesis of silicon-rich oxo-polymer segments; a higher crystallization temperature results, suggesting that refractory SiO_2 forms before conversion to the final mullite phase.

Preferential hydrolysis creates notable challenges for the deposition of multi-elemental sols. Coating processes accelerate hydrolysis and condensation reactions through solvent

---

[39]Because of sensitivity to moisture, alkoxides and their solutions are handled exclusively under inert atmosphere (see Chapter 3). For convenience though, coating processes are generally conducted in air.

[40]Hydrolysis rates for silicon alkoxides are orders of magnitude slower than transition metal alkoxides [90]. So a greater tolerance to water, and hence higher limits for *h,* would be expected.

evaporation and exposure to moisture. But without partial hydrolysis (and subsequent aging), the most sensitive alkoxide species will be selectively attacked by water vapor. The resulting oligomers can phase segregate upon concentration, bringing inconsistent wetting and adhesion, compositional inhomogeneities, and nonuniform film morphology. YOLDAS [115] explored the order of mixing in the hydrolysis of aluminum-borosilicate sols by partially hydrolyzing either alkoxysilanol or trimethylborate solutions, and afterwards, adding the needed, unhydrolyzed alkoxide constituents. The oxo-polymer products depended critically on h and the mixing order. Often, irreversible phase segregation occurred within the solvent, rendering the sol unusable.

For descriptive clarity, the hydrolysis and condensation mechanisms of sol-gel processing have, so far, been presented with the presumption of homometallic reactants. Yet the preceding discussion clearly highlights empirical observations differentiating the chemical activity of multi-element containing solutions from that of uni-element ones. Because many ceramic materials, particularly the oxide perovskites, gain technological value specifically through compositional variation, further elaboration on the lability of heterometallic alkoxides remains in order. The complexity of multi-elemental solutions during hydrolysis stems from oligomerization reactions that occur before exposure to water. For example, the dissolution of two homometallic alkoxides in solutia results in a Lewis acid-base interaction, creating a heterometallic product:

$$a_1 M^1(OR^1)_{z_1} + a_2 M^2(OR^2)_{z_2} \quad \rightarrow \quad M^1_{a_1} M^2_{a_2}(OR^1)_{a_1 z_1}(OR^2)_{a_2 z_2} \tag{2.13}$$
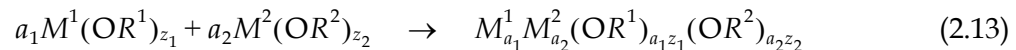
In essence, one alkoxide species represents a better donor of electron density and the other a stronger acceptor. MEERWEIN and BERSIN [117] first exploited this behavior in 1929 during attempts via titration to prove (unsuccessfully) the existence of so-called protic ansolvoacids such as H[Al(OR)$_4$]. Like alkoxy-bridging (i.e., $M^1 = M^2$), oligomerization reactions raise the metal coordination and lower configurational energy. But because $M^1 \neq M^2$, any dative bonding will activate partial charge transfer between the differing metal centers, establishing a stable bridge. So unlike the depolymerization exemplified by Group IVB alkoxides, many heterometallic alkoxides volatilize unchanged upon heating with no separation into their homometallic parents; further heating only brings decomposition, not disassociation. Inter-

estingly, Equation 2.13 offers a subtle yet useful means to incorporate otherwise insoluble metal alkoxides into solutia: a reactive alkoxide can often overcome the lattice energy of an infinite polymer by cleaving alkoxy bridges and forming a soluble, heterometallic complex. For example, in the all alkoxy-based sol-gel processing of $PbTiO_3$, titanium 2-propoxide can depolymerize $\{Pb[OCH(CH_3)_2]_2\}_\infty$ in refluxing toluene [118].

With regard to sol-gel processing, an ideal heterometallic alkoxide would exhibit a metal ratio that precisely matches that of its final oxide product. CAMPION, et al. [120] synthesized an intimate, "single source" precursor, $BaTi(OCH_2CH_2OCH_3)_6$, for the sol-gel preparation of $BaTiO_3$ by direct dissolution of equimolar $Ba(OCH_2CH_2OCH_3)_2$ and $Ti(OCH_2CH_2OCH_3)_4$ in 2-methoxyethanol. Such an achievement remains noteworthy: the metal ratios of heterometallic products in solutia rarely correspond to the starting proportions of their homometallic reactants.[41] Characterization of alkoxy-based solutions for the titanate perovskites, $CaTiO_3$, $SrTiO_3$, and $BaTiO_3$, demonstrates that an equilibrium distribution of multiple, off-stoichiometric species occurs instead. TUREVSKAYA, et al. [121] reported that the addition of calcium and titanium ethoxides in ethanol or benzene produces the complex, $Ca[Ti_2(OCH_2CH_3)_9]_2$, with unreacted $Ca(OCH_2CH_3)_2$ remaining. After dissolving strontium and titanium 2-propoxides in 2-propanol, RIMAN [122] measured alkoxides with strontium-titanium ratios ranging from 2:1 to 1:2. Similarly, the reaction of $Ba(OR)_2$ with $Ti(OR)_4$ by TUREVSKAYA, et al. [123] in the parent alcohol or benzene yielded $BaTi_4(OR)_{18}$ with excess $Ba(OR)_2$ regardless of whether $R = CH_2CH_3$, $CH(CH_3)_2$, or $CH_2CH_2CH_3$.

The presence of multiple, off-stoichiometric species in solutia requires a modification to Equation 2.11. Otherwise, the exact complex referenced in the denominator becomes ambiguous. The most logical revision incorporates the homometallic reactants only:

$$h = \frac{[\text{mol of } H_2O]}{\sum_i [\text{mol of } [M(OR)_z]_n]_i} \tag{2.14}$$

This amended ratio defines h with respect to a controllable system quantity: the cation(s) content. Here, the summation in the denominator occurs over the starting metal alkoxides as indicated by the subscript i. The necessity of Equation 2.14 can be better appreciated in light

---

[41]Overall solution stoichiometry, however, is preserved.

of an additional pathway to the Lewis acid-base interaction of Equation 2.13. In multi-element solutions, condensation reactions can emerge despite the absence of hydrolytic water. During this process, two alkoxy groups are replaced with a single oxo ligand, generating a heterometallic oxoalkoxide and an ether molecule:

$$a_1 M^1 (OR^1)_{z_1} + a_2 M^2 (OR^2)_{z_2} \quad \rightarrow \quad M^1_{a_1} M^2_{a_2} (O)(OR^1)_{a_1 z_1 - 1}(OR^2)_{a_2 z_2 - 1} + R^1 OR^2 \quad (2.15)$$
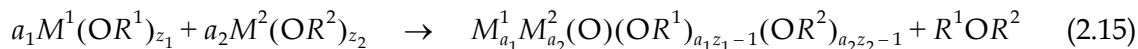
For example, when titanium 2-propoxide depolymerizes $\{Pb[OCH(CH_3)_2]_2\}_\infty$ during reflux, the presence of 2-propanol is reported to catalyze the formation of $Pb_4 Ti_4 O_3[OCH(CH_3)_2]_{18}$ [118]. Clearly then, oligomerization reactions of homometallic alkoxides in solutia can produce both heterometallic and heteroleptic products.[42] Accordingly, all values of h cited in this dissertation (i.e., for tertiary La-Ba-Mn and La-Pb-Mn alkoxy-based sols) utilize Equation 2.14. Further discussion concerning the synthesis, molecular structure, and reactivity of heterometallic alkoxides, however, will not be presented here but can be found in a comprehensive review by CAULTON and HUBERT-PFALZGRAF [119].

The susceptibility of multi-elemental systems to preferential hydrolysis stems from their tendency to distribute several alkoxide and (possibly) oxoalkoxide species in solutia. Each complex exhibits a different sensitivity to water that depends on the constituent metals and their associated coordination environments. By partially hydrolyzing in a solvent though, these differences subside because diffusion paths play a mitigating role in the reaction kinetics. A more equitable participation in condensation results and the growing oxo-polymers reflect overall solution stoichiometry.

But during coating, a sol experiences a disproportionately large air-liquid interface that provides unrestricted access to moisture. If deposited without prior hydrolysis, solvent evaporation quickly reduces the diffusion lengths between dissolved species, accentuating differences in hydrolytic sensitivity; water vapor preferentially attacks the most susceptible alkoxide complex. The emergence, in excess, of one hydrolyzed species over others virtually guarantees oxo-polymers of off-stoichiometry. As already discussed, Yoldas demonstrated that such conditions are highly-undesirable for the sol-gel preparation of oxide ceramics.

---

[42]In transition metal chemistry, a complex is termed heteroleptic if the ligands occupying its coordination sphere differ from each other. Equation 2.13 includes the possibility of heteroleptic coordination (i.e., $R^1 \neq R^2$) but Equation 2.15 requires it (i.e., both oxo and alkoxy ligands).

The order and magnitude of hydrolysis plays a crucial role in developing usable sols. So for multi-elemental solutions, partial hydrolysis *under dilute conditions in solutia* enables the growth of chemically uniform oxo-polymers. In turn, the detrimental influence of atmospheric moisture during coating is alleviated because the resulting oxo-polymers exhibit a diminished lability towards water.

To prepare sols for film deposition, therefore, a partial hydrolysis ratio should be selected that provides slow relative rates of hydrolysis and condensation (i.e., $h < 2$). But low hydrolysis rates, unfortunately, often produce oxo-polymers with high percentages of alkoxy groups, and hence, lower oxo-bridging (i.e., oxide yields). This characteristic can create a number of undesirable side-effects during the drying of gels and their subsequent pyrolysis into ceramic end-products.

First, atmospheric carbon dioxide readily adsorbs on the surfaces of a porous, drying gel which coordinates to the constituent metal centers via insertion or nucleophilic substitution. This interloping ligand produces high-temperature amorphous carbonate or hydroxycarbonate phases. Such behavior is well-established in soda-silicate gels prepared for the nominal glass compositions, $(Na_2O)_x(SiO_2)_{1-x}$ [124]. But the phenomenon also applies to transition metal perovskites, particularly compositions containing Group IIA elements. KIRBY [125], for example, demonstrated that the drying of alkoxy-derived gels for $BaTiO_3$ powders avoided carbonate formation when performed under argon. When conducted in air, however, atmospheric carbon dioxide successfully competed with water for labile barium centers, excluding a measurable fraction from hydrolysis: carbonate stretching modes could be observed in the xerogel by infrared spectroscopy. Subsequent investigation by FREY [126] indicated the availability of free barium species in the (wet) gel, which upon complete hydrolysis, formed carbonate according to: $Ba(OH)_2 + CO_2 \rightarrow BaCO_3 + H_2O$.

Second, the decomposition of hydrocarbon fragments during pyrolysis generates rapid, localized pressures of water vapor and carbon dioxide. In a xerogel film, excessive organic content then risks the emergence of pin holes and surface defects. Such a morphology degrades insulating properties and prevents reliable patterning of device structures.

Lastly, high organic contents left by insufficient hydrolysis can increase the partial pressures of carbon dioxide experienced by the pores of a decomposing xerogel. This environment alters local reaction equilibria, suppressing the organic decomposition pathways.

TEMPLETON and PASK [127] investigated the preparation of $BaTiO_3$ from $BaCO_3$ and TiO_2 powders using conventional "grind and fire" methods; the barium metal center retained carbonate at temperatures as high as 1300 °C under flowing carbon dioxide. In contrast, carbonate removal for the same preparation in air started at 900 °C, being complete after isothermal treatment for four hours. Accordingly, MOD techniques for $BaTiO_3$ report a final reaction of

$$Ba_2Ti_2O_5CO_3 \;\leftrightarrow\; 2BaTiO_3 \;+\; CO_2\uparrow \tag{2.16}$$
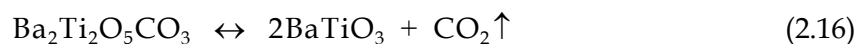
suggesting that $BaTiO_3$ formation can be hindered by increased partial pressures of carbon dioxide [126, 128, 129].

So low partial hydrolysis ratios, while suitable for coating, may prove inadequate for crucial organic removal. On the other hand, higher hydrolysis ratios enhance oxide yield, but by accelerating oxo-polymer growth, often produce unusable rheologies, accentuate hydrolytic differences in multi-elemental solutions, and/or induce gelation. Therefore, the development of a sol system for coating processes, particularly from multi-elemental solutions, introduces unique challenges. *The ability to prepare sol-gel derived powders does not imply a straight-forward adaptation to film deposition − a capability often inappropriately presumed in the literature.* As will be discussed in Section 3.4.2, alkoxy-based sol systems for manganite perovskites require low partial hydrolysis ratios (i.e., $h < 0.75$) for stable, spinnable sols. Further hydrolysis in a stream of humidified air, post-coating, comprises a necessary final step to produce defect-free, chemically homogeneous $La_{0.67}Ba_{0.33}MnO_3$ and $La_{0.67}Pb_{0.33}MnO_3$ films.

2.3.5 DRYING, PYROLYSIS, AND SINTERING

The conversion of a gel into its corresponding dense ceramic relies on drying (i.e., xerogel formation), pyrolysis, and sintering. Pyrolysis, conducted at intermediate temperatures, causes the molecular components of a xerogel to fragment and decompose, restructuring atomic bonds and releasing volatile by-products such as water vapor and carbon dioxide. The resulting oxidized framework, generally still amorphous, retains the open porous structure of its parent gel. Sintering at elevated temperatures then collapses the pore cavities of the preform and densifies the amorphous oxide structure. This naive description, however, belies the underlying complexity of a seemingly simple process, begging the question: How

does a gel densify into a ceramic body? Despite intense research, particularly during the 1980s, definitive answers remain elusive. The following discussion presents *proposed* mechanisms as constructed from a traditional understanding of densification and sintering.

An examination of alkoxy-derived borosilicate bulk gels led BRINKER, et al. [130–132] to conclude that four principal mechanisms influence the densification of polymeric gels: (1) capillary contraction, (2) condensation polymerization, (3) structural relaxation, and (4) viscous sintering. Capillary contraction arises during solvent removal when the receding liquid creates surface tensions that compress the viscoelastic framework. Oxo-polymer fragments impinge on one another, enabling unreacted hydroxy and alkoxy groups to further crosslink (i.e., condensation polymerization). When the skeleton is sufficiently stiff to resist continued compaction, the remaining open volume forms a residual porosity. Sols containing weakly-crosslinked oxo-polymers (i.e., linear or marginally-branched) leave highly-compacted xerogels with fine pores and low porosities (i.e., 35–40%) [130]. Heavily-crosslinked oxo-polymers, on the other hand, desiccate to produce globular clusters whose low-compliance approximates particulate behavior; porosity approaches values of 60–70%.[43]

The thermodynamic driving force to densify a dried gel stems from its considerable free energy relative to that of the corresponding melted glass (see Figure 2.12). Large surface areas contribute the most to a xerogel's free energy but other factors include: (1) a low crosslink density and (2) a high free volume, both with respect to the glass [130].[44] Heating an alkoxy-derived xerogel then causes an exothermic conversion that enhances crosslinking, reduces free volume (i.e., structural relaxation), and diminishes surface area (i.e., viscous sintering). But as depicted in Figure 2.12, particulate xerogels exhibit lower free energies than their polymeric counterparts. This difference results from the dense oxide cores comprising the skeleton of the former: hydroxy and alkoxy groups, primarily on the surface, are unable to produce meaningful crosslinking and the framework itself contains little free volume. So unlike polymeric xerogels, particulate systems exhibit little skeletal transformation upon heating; densification occurs mostly through surface area reductions.

---

[43]Particulate gels contain extended networks of rigid oxide microgranules. Solvent removal compacts this structure, but only moderately. So high porosities (i.e., 70–80%) are common [130].

[44]Non-periodic bonding in amorphous materials creates spacing in excess of ordered, crystalline structures. This openness is referred to as free volume. In polymeric xerogels, a low crosslink density arises from large numbers of nonbridging oxygen atoms (i.e., terminal hydroxy and alkoxy ligands). Skeletal density is thereby reduced, producing "extra" free volume within the framework.
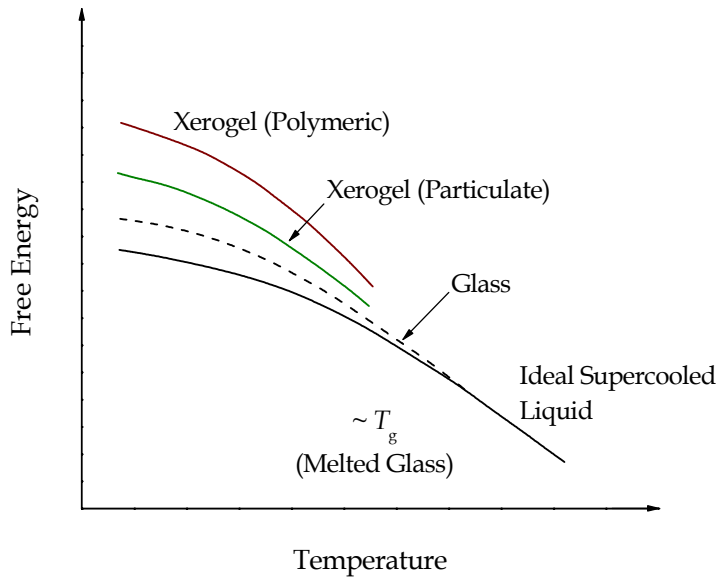
FIGURE 2.12 Free energy versus temperature of a xerogel, glass, and ideal supercooled liquid. All curves reflect the same oxide composition. (Adapted from [130]. Copyright 1985 Elsevier Science Publishers B. V.)
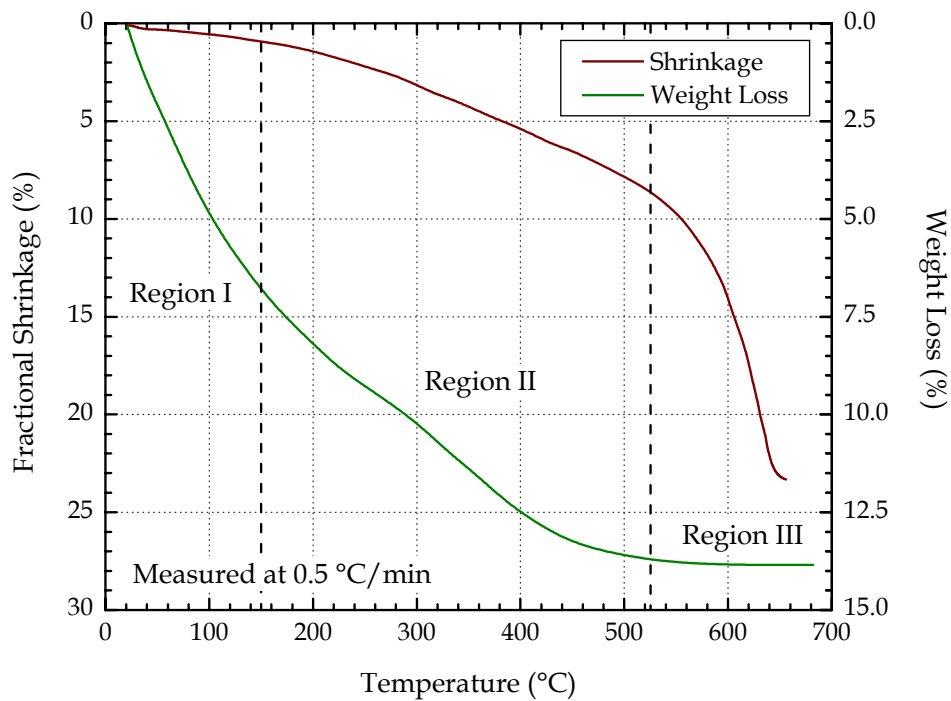
FIGURE 2.13 Linear shrinkage and weight loss of multicomponent silicate bulk gels. (Adapted from [131]. Copyright 1985 Elsevier Science Publishers B. V.)

Measurements of linear shrinkage and weight loss in alkoxy-derived borosilicate gels during thermal processing (see Figure 2.13) highlight three qualitative trends applicable to bulk polymeric xerogels: (1) weight loss without shrinkage (i.e., $T = 25$–150 °C), (2) shrinkage proportional to weight loss (i.e., $T = 150$–525 °C), and (3) shrinkage without weight loss (i.e., $T > 525$ °C) [131]. In Region I, physisorbed water and alcohol detaches from the xerogel, decreasing its weight. As a result, the surface energy increases, inducing a capillary pressure that shrinks the xerogel slightly (i.e., capillary contraction). Further heating into Region II, however, activates condensation and pyrolysis. Water vapor and carbon dioxide volatilize from the skeletal structure as crosslinking generates leaving groups (i.e., condensation polymerization) and hydrocarbon fragments decompose. As expected, the weight of the xerogel continues to decline.

Shrinkage in Region II proceeds via skeletal densification but with negligible rearrangement of oxo-polymer packing. Such behavior is attributed to the mobility of oxo-polymers which diffuse to relax the skeleton and decrease its free volume. For example, observations on silica xerogels demonstrate that polymeric systems exhibit substantial intermediate-temperature shrinkage; the contraction of (comparable) particulate systems, however, is negligible [131]. This latter characteristic stems from the density of anhydrous oxide particles which varies only slightly from that of the melted glass. Any driving force for skeletal densification is therefore very small.[45] Thus, shrinkage in Region II arises predominantly from condensation polymerization and structural relaxation. Attempts to quantify their relative contributions, however, have proven inconclusive so far.

The onset of rapid shrinkage, accompanied by a stabilization in weight, marks the transition into Region III. Here, surface tension emerges within the oxide framework, activating viscous flow (i.e., viscous sintering). Densification proceeds to completion as the amorphous preform decreases its solid-vapor interfacial area; the free energy of the densifying body approaches that of an ideal supercooled liquid (refer to Figure 2.12). The mechanism of viscous flow, however, remains exclusive to Region III [131]. If extended into Region II, only pores with diameters less than ~ 4 Å would be susceptible to surface tension, a feature length indistinguishable from the free volume within the structural skeleton. By comparison, con-

---

[45]The lack of skeletal densification in particulate xerogels requires all shrinkage to result from increases in packing efficiency (i.e., particle rearrangement). But because empirical observations show virtually no intermediate temperature contraction, the packing efficiency must remain unchanged.

densation polymerization and structural relaxation still play a role within Region III, albeit ancillary to viscous flow.

Caution, however, must be exercised when adapting the observations of bulk gel densification to coated preforms. In films, sub-micron thicknesses and exceptionally high (planar) surface areas combine to significantly reduce the diffusive length of escape paths for volatile species. Furthermore, the low values of h conducive to coatable, alkoxy-based sols correspond to systems containing weakly-crosslinked oxo-polymers (i.e., linear or marginally-branched morphologies). Deposition then leaves a compacted preform of minimal porosity, particularly for spin-coating (see Section 2.3.6). These characteristics tend to shift the onset of Region III to lower temperatures, compressing (or even eliminating) Regions I and II. For example, Figure 2.14 presents the shrinkage and weight loss of a densifying, polymeric gel coating on Si(100) [133]. Comparison with Figure 2.13 highlights the virtual absence of behavior associated with either Region I or II. This difference suggests the early activation, with respect to bulk gels, of condensation polymerization, structural relaxation, and most
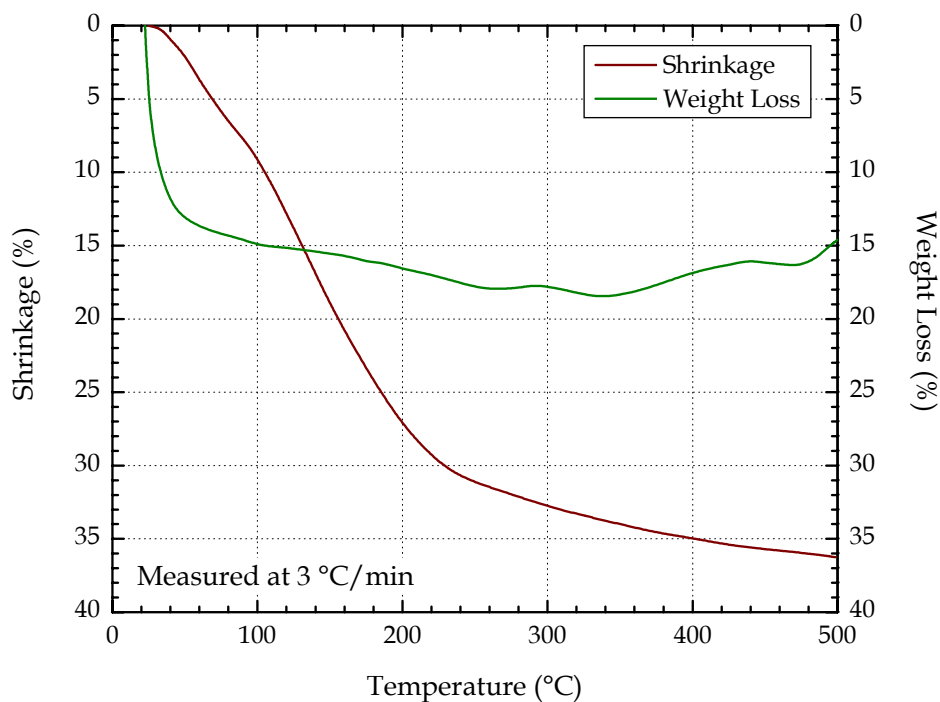
FIGURE 2.14 Shrinkage and weight loss of a gel coating on Si(100). The initial 131 nm thickness densified and crystallized into a 82 nm PbTiO$_3$ thin film. (Adapted from [133]. Copyright 1996 Samit S. Sengupta)

notably, viscous sintering. Unfortunately, the relative contributions of these three mechanisms cannot be determined without further investigation.

The desirability of viscous sintering during the densification of xerogels becomes clearer when contrasted with diffusive sintering. The ensuing discussion, developed from conventional sintering theory, offers a qualitative framework that supports the preferential deployment of polymeric systems in sol-gel processing. But the analysis provided here represents an approximation and cannot adequately model the phenomenon of gel densification. As stated previously, the complexity of gel behavior during heat treatment continues to defy complete characterization and remains an area of active research.

The first theoretical model for viscous sintering, derived from considerations of viscous flow, was proposed in 1945 by FRENKEL [134] who developed a time-dependent relationship describing the fusion of two juxtaposed spheres via neck growth. Subsequent experiments by KUCZYNSKI [135] with pairs of alkali-silicate glass spheres confirmed the validity of Frenkel's model for amorphous materials.[46] The definition of viscous flow, $\sigma = \eta \dot{\varepsilon}$, presumes the availability of an acting stress (σ) which creates a strain (ε), enabling bulk motion as quantified by viscosity (η). In amorphous materials, the emergence of surface tension during heating provides this stress. Accordingly, the linear shrinkage (i.e., $\Delta l / l_0$) of an amorphous body comprised of spheres with initial radii a is given by

$$\frac{\Delta l}{l_0} \cong \frac{3}{8}\left(\frac{\gamma_{SV}}{\eta a}\right) \cdot t \tag{2.17}$$

where γ_{SV} is the surface energy of the solid-vapor interface; and η, the viscosity [136]. In contrast, KINGERY and BERG [137] determined that lattice diffusion for an identical system of spheres produces linear shrinkage following

$$\frac{\Delta l}{l_0} \cong \frac{5}{4}\left(\frac{\gamma_{SV} D_L \delta^3}{kTa^3}\right) \cdot t^{2/5} \tag{2.18}$$

where γ_{SV} is the surface energy of the solid-vapor interface; D_L, the lattice diffusion coefficient; δ, the molecular radius; k, the Boltzmann constant; and T, the sintering temperature.[47]

---

[46]Kuczynski also corrected an erroneous factor of π in Frenkel's original derivation.

[47]For comparison with Equation 2.17, the results of Kingery and Berg (i.e., Equation 2.18) were reformulated using the procedure adapted by [136] for Frenkel's derivation.

A simple comparison of the exponents (i.e., t versus $t^{2/5}$) suggests that, at a given temperature, linear shrinkage occurs faster with viscous flow. The strong temperature dependence of η in amorphous materials lends further credence to this conclusion: small increases in temperature (i.e., 25–50 °C) often decrease viscosity by orders of magnitude [138]. Thus at sintering temperatures, the scaling term in Equation 2.17 is greater than Equation 2.18.

Both Equations 2.17 and 2.18 refer to the initial stage of sintering but their predictions extend qualitatively to subsequent stages.[48] SEIGLE [140] demonstrated that neck growth and void closure in amorphous materials is dominated by viscous flow during all stages of sintering. Furthermore, pore elimination proceeds more rapidly with viscous flow than lattice diffusion. This latter observation carries notable implications for the densification of xerogel preforms if the end-product is crystalline. Unlike the borosilicate composition investigated by Brinker, et al., many technologically-relevant ceramic oxides do not incorporate glass network formers (i.e., B, P, Si, Ge, etc.). So contrary to Figure 2.12, an equilibrium crystalline phase emerges as the high-temperature reference state instead of an ideal supercooled liquid.

For example, FREY and PAYNE [141] reported that alkoxy-based monoliths, after copious hydrolysis and thorough drying, could form nascent perovskite $BaTiO_3$ crystallites at $T = 125$ °C — an astonishing result! Subsequent growth of such regions during heating can transition a xerogel from viscous to diffusive sintering. The rate of densification drops accordingly and undesirably high processing temperatures may be required to fully eliminate entrapped voids.[49] *So for the thermally-efficient processing of xerogel preforms, nucleation of crystallites should be suppressed until viscous flow accomplishes complete densification.* For this reason, polymeric gels are preferable to their particulate counterparts. Skeletal structures of the former contain lower desiccated porosities and densify at reduced temperatures. Anhydrous oxide cores of the latter, on the other hand, exhibit little free volume, a characteristic which delays densification and increases the susceptibility to crystallization.

The preservation of viscous sintering is particularly important for the thermal processing of coatings. Constraints associated with an underlying substrate may prohibit tempera-

---

[48]Sintering progresses through three sequential steps classified as initial, intermediate, and final. Qualitative divisions are based on the relative density (ρ_{rel}): $\rho_{rel} < 0.65$ (initial), $0.65 < \rho_{rel} < 0.90$ (intermediate), and $\rho_{rel} > 0.90$ (final). For further details, see the reference text by RAHAMAN [139].

[49]In crystalline materials, any decrease in pore volume requires grain growth, and hence, increases in grain boundary area. But gains in surface energy from pore reduction are partially offset by larger grain boundaries which have crystallographically-mismatched interfaces.

tures necessary for sintering crystalline oxide particles into pore-free films. For example, this dissertation employs Si(100) and platinized-Si(100) wafers which limit thermal processing to $T < 800\ °C$; exceeding this threshold initiates unwanted film-substrate interactions. Equally important, pre-patterned structures and devices on a substrate often require further consideration beyond the substrate itself. Thus, for compatibility with silicon-based microelectronics, processing temperatures below 700 °C are highly-preferable.[50] But with electroceramic oxides, such as the doped-lanthanide manganites, residual porosity must be avoided to prevent the degradation of desirable transport properties. *So sol-gel processes for film deposition should offer both low-temperature densification (i.e., viscous sintering) and crystallization, the former completing before onset of the latter.* Alkoxide precursors are optimally-suited to satisfy this stringent criteria because their hydrolysis can be readily controlled to ensure polymeric sols. As will be discussed in Section 3.4.3, the La-Ba-Mn and La-Pb-Mn polymeric gels (i.e., 2:1:3) deposited onto Si(100) and platinized-Si(100) substrates easily produced dense, pore-free amorphous coatings at $T = 450\ °C$; subsequent heating to 600–650 °C then activated nucleation of the perovskite phase. Details on the crystallization of amorphous oxides, however, will not be presented here. Instead, the reader is referred to standard texts on the processing and physical properties of inorganic glasses (e.g., see VARSHNEYA [138]).

2.3.6 SPIN-COATING OF THIN FILMS

Sol-gel processes for thin-film deposition have typically involved spinning, dipping, or spraying [68]. However, the extreme sensitivity of manganese(II) alkoxides to atmosphere (see introduction in Section 2.4) precludes the convenient adaptation of dipping or spraying to manganite perovskite coatings. Both of these latter techniques, if conducted in air, allow excessive exposure of the sol to water vapor and oxygen, enabling the development of fine, insoluble, brown (i.e., oxidized) precipitates within the solvent media.[51] The need for inert environments, though, can be mitigated by spinning, a relatively quick method that induces gelation before any appreciable products of oxidation emerge. In addition, spin-coating is an

---

[50]Above 700 °C, dopant diffusion in silicon becomes significant, dissolving source and drain channels into the crystal and contaminating the gate oxides [142].
[51]Dipping or spraying under inert atmosphere, although feasible, requires the utilization of glove box techniques or specialized equipment. As demonstrated in Section 3.4.3, the spin-coating of partially-hydrolyzed sols was routinely achieved without contamination from oxidized particles.

accepted method in the microelectronics industry, employed universally for the deposition of ultrathin photoresist films. Accordingly, this dissertation utilizes spin-coating to integrate $La_{0.67}Ba_{0.33}MnO_3$ and $La_{0.67}Pb_{0.33}MnO_3$ thin films onto silicon-based substrates. Further elaboration on dipping and spraying will, therefore, not be discussed here but can be found, with references, in BRINKER and SCHERER [68].

To model the physics of film formation by spinning, BORNSIDE, et al. [143] and SCRIVEN [144] divided the process into four qualitative stages: (1) deposition, (2) spin-up, (3) spin-off, and (4) evaporation. As depicted in Figure 2.15, spin-coating is a batch process wherein the first three stages proceed sequentially. The last two, however, sometimes occur concomitantly although all stages can overlap to some extent. During deposition, fluid from the sol inundates the substrate, displacing gas at the solid-vapor interface thereby wetting the surface. Rotation of the substrate imparts angular velocity to the fluid via viscous drag, leading to spin-up. But viscous drag forces remain insufficient to establish a circumferential-only velocity. So a wave front propagates radially outward, carrying excess fluid off the edge of the substrate. The sol left in its wake forms a liquid coating of nearly even height — provided that Newtonian behavior dominates (i.e., η is not shear-dependent). Droplets continue to spin off the side, causing further thinning which enhances film uniformity. During this period, mass loss also occurs from the volatilization of solvent at the liquid-vapor interface. A rapid, progressive increase in concentration (i.e., ~ 20–30 fold) reduces the diffusion length of solvated oxo-polymers (or particulates), and hence, improves the kinetics for hydrolysis and condensation. Polymerization and aggregation then raise the viscosity, which in turn, decreases the mobility of the film. Eventually, mass loss through the surface exceeds that leaving the edge, marking the transition to a final, evaporative stage. During evaporation, convective currents quickly transport volatile solvent molecules away from the body and induce gelation. The resulting immobile layer, however, still contains solvent entrapped within its pores and therefore cannot yet be considered a xerogel. At this point, dessication becomes limited by the rate of molecular diffusion through the porous network. Thus, in the short timeframe allotted to spinning, the deposited gel may be unable fully convert into a solvent-free body.

The effectiveness of spin-coating as a process stems from its ability to ensure that a rotating liquid film ultimately approaches a uniform height. This behavior was first modeled by
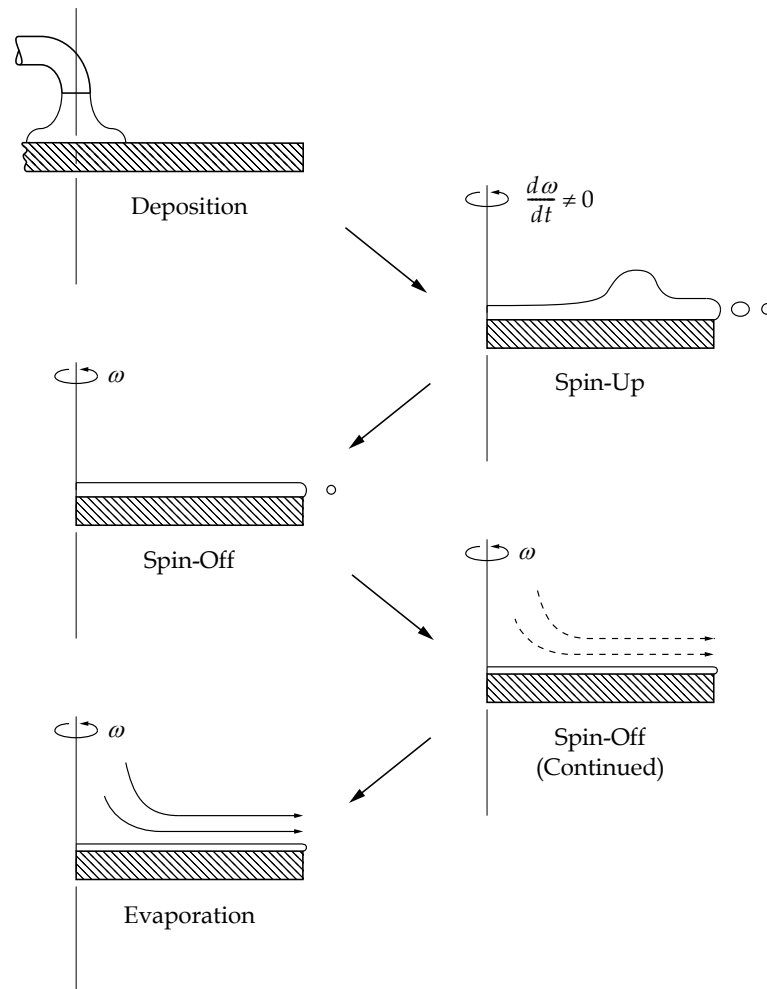
FIGURE 2.15 Stages of the spin-coating batch process. Although portrayed distinctly, the stages overlap to some extent. (Adapted from [143]. Copyright 1987 The Society for Imaging Science and Technology.)

EMSLIE, et al. [145], who derived the time-dependent height, $h(t)$, of a liquid coating during spin-off, assuming negligible evaporation:

$$h(t) = \frac{h_0}{\sqrt{1 + (4\rho\omega^2 h_0^2 t)/(3\eta)}} \tag{2.19}$$

Here, h_0 is the initial height at spin-off; ρ, the fluid density; ω, the angular velocity; t, the time; and η, the fluid viscosity. According to Equation 2.19, deviations in film thickness should monotonically converge with time to zero (i.e., a uniform height); this prediction is confirmed empirically for Newtonian viscosities [143, 144]. But the presence of η in the denominator also underscores the importance of relatively stable rheologies during spin-coating. As pointed out in Section 2.3.4, polymeric sols used immediately after hydrolysis or close to the gel point offer poor coating performance. In either state, small increases in concentration (i.e., from evaporation) can raise the viscosity notably and therefore impart non-Newtonian flow to the thinning liquid film.

The effects of evaporation are challenging to incorporate into any model because ambiguity surrounds the transition points at which: (1) solvent loss through the surface dominates mass loss at the edge and (2) forced convection yields to diffusive transport [143, 144]. Fortunately, the planar geometry of a substrate-supported rotating film allows the mass transfer coefficient, k, to be presumed constant over the entire liquid-vapor interface. This simplification enabled MEYERHOFER [146], who also separated the spin-off and evaporation stages, to determine h_{f}, the final film thickness, and t_{f}, the total elapsed time:

$$h_{\mathrm{f}} = \sqrt[3]{\frac{3\eta e}{2\rho_{\mathrm{A}}^0 \omega^2}} \left(1 - \frac{\rho_{\mathrm{A}}^0}{\rho_{\mathrm{A}}}\right) \tag{2.20}$$

$$t_{\mathrm{f}} = t_0 + h_0 \left(\frac{\rho_{\mathrm{A}}^0}{e\rho_{\mathrm{A}}}\right) \tag{2.21}$$

Evaporative effects are accounted for through e, the evaporation rate, which depends on the aforementioned mass transfer coefficient, k. The variable ρ_{A} refers to the mass of volatile solvent per unit volume. The null sub- and superscripts correspond, in all cases, to the initial values at the onset of spin-off. All other variables are as before (i.e., Equation 2.19). In Meyerhofer's model, evaporation commences only after the film-thinning rate during spin-off

74

reaches $e\rho_A / \rho_A^0$. Then, the coating is assumed instantly immobilized and further attenuation proceeds exclusively through solvent volatilization (i.e., e). This theory encompasses sol systems because gelation (crudely) matches Meyerhofer's boundary conditions, i.e., the sharp rise in viscosity (i.e., $\eta \to \infty$) quickly arrests lateral flow and subsequent mass transport occurs via evaporation. Equations 2.20 and 2.21, for example, have been successfully correlated to actual, physical film thicknesses obtained from nonvolatile polymers in solutia [143].

One difficulty, however, in applying Equation 2.20 to the spin-coating of polymeric sols arises from competing mechanisms which emerge during evaporation: capillary stresses and crosslinking are both induced by solvent loss. The former compacts the growing skeletal structure, shrinking the overall body, but the latter stiffens it, enhancing its ability to withstand deformation. These counterbalancing effects make predictions of final film thicknesses particularly challenging. The effectiveness of either mechanism depends on the relative rates of evaporation and condensation, the result of which, influences oxo-polymer morphology [150].[52] If solvent removal proceeds faster than crosslinking, considerable skeletal collapse occurs before condensation reactions can strengthen the framework. The gel structure is then comprised of stacked, interpenetrating linear or marginally-branched oxo-polymers. This characteristic produces a dense preform of low porosity. Conversely, when polymerization dominates, the compliance of the skeleton is sufficient to resist the onset of capillary pressures. That is, heavily-crosslinked clusters or globules aggregate and form connected, but weakly-interpenetrating species, that entrap higher open volumes. A comparison of coated and bulk xerogels (see Section 2.3.5) then reveals a similar dependence of porosity on oxo-polymer morphology.

Such an observation is notable because evaporation during spinning rapidly increases the concentration. In contrast, sols for monolithic bodies approach the gel point under conditions of invariant concentration. But coated xerogels exhibit lower porosities than their bulk counterparts. This distinction stems from the ballistic nature of film-thinning: evaporation causes the planar liquid-vapor interface to impinge on the substrate (i.e., along a direction normal to the surface). The resulting compression of solvated, but still reacting, oxo-polymers therefore establishes a more compact gel structure. Interpenetration and packing effi-

---

[52]The following description presumes an initial sol of dilute, weakly-interacting oxo-polymers (i.e., partially hydrolyzed according to the criteria developed in Section 2.3.4). Structural evolution during spin-coating then begins with linear or marginally-branched oligomers.

ciency are enhanced relative to bulk gels. So for equivalent oxo-polymer morphologies, a pathway of intense concentration will generate preforms of higher density. Thus, to deposit a xerogel film of minimal porosity, evaporation should be strongly accentuated. Factors which affect evaporation include the spinning rate (i.e., ω), ambient atmosphere, solvent chemistry, solvent vapor pressure, and temperature.[53]

In addition to compression, radial shear and in-plane tensile stresses also play a prominent role, respectively, during the spin-off and evaporation stages. For example, BRINKER, et al. [150] reported the shear-induced radial alignment of linear polysilicate structures upon spinning. The ability of viscous drag forces to influence the radial motion of oxo-polymers decreases with increasing molecular weight. So species of higher mass may separate from those of lower mass as spin-off progresses. For multi-elemental sols, this potential behavior raises a note of caution: oxo-polymer products should be chemically uniform (i.e., no preferential hydrolysis) otherwise phase separation can produce compositional gradients.

Arrival at the gel point, however, shifts the stress mode from radial shear to in-plane tension. As already discussed, evaporation activates film shrinkage (i.e., negative strain) via capillary pressure. But because of adhesion to the substrate, strain development in a desiccating gel is actively opposed. The resulting in-plane tension sometimes induces the development of striations, spoke-like ridges of thicker film extending out from a substrate's center. Recent investigations into this phenomenon by BIRNIE, et al. [147–148] underscore the importance of controlling solvent volatility to ensure stable and uniform surface tensions: by eliminating differential evaporation, the formation of such defects can be avoided.

A simple consideration of equilibrium mechanics shows that in-plane tensile stresses can be approximated by the capillary pressure [68]. In bulk preforms, stresses of this magnitude (e.g., $\sigma_{\mathrm{Max}} \approx 100\,\mathrm{MPa}$) would crack or shatter a xerogel body.[54] Yet films thinner than ~ 0.5 μm never fracture regardless of the drying rate — a remarkable characteristic! Above ~ 1 μm, though, crack-free coatings are virtually unattainable. The origin of both these metrics remains poorly understood. But the upper bound has led to a practical guideline commonly referred to as the "micron rule". To achieve crack-free thicknesses greater than ~ 1 μm then,

---

[53]The ambient atmosphere surrounding a liquid film can be deliberately pre-saturated with solvent vapor to suppress the evaporation rate.

[54]Evaporation from a desiccating gel establishes a stress gradient that deforms the exterior surface greater than the interior body. The corresponding differential strain often induces fracture.

multiple depositions (i.e., spin, dry, and pyrolyze) are clearly required.[55] Further discussion of crack formation and propagation in sol-gel coatings, however, lies beyond the scope of this dissertation. Instead, the reader is directed towards the excellent review (and subsequent investigation) of such phenomena by MIKALSEN [149].

2.4 ALKOXIDE PRECURSOR SYNTHESIS

The utility of alkoxide precursors in sol-gel processing stems from their ability to: (1) produce a diverse range of condensed, synthetic structures and (2) confer control over these morphologies through selection of the alkyl group and hydrolysis ratio. Such advantages are largely absent from aqueous systems because the constituent inorganic salts react almost universally to form dense hydrous oxide precipitates or particulate gels [68, 89].[56] In contrast, the weak hydrolysis of alkoxide precursors in organic solvents commonly forms metastable, polymeric sols. As emphasized in Section 2.3.5, xerogels derived from the latter exhibit finer porosities and densify at reduced temperatures than those based on the former. *Thus, polymeric systems play a crucial role in the low-temperature integration of complex oxide films onto non-refractory substrates.* This section, therefore, details the synthetic approach needed to produce homometallic, homoleptic alkoxides for the polymeric sol-gel processing of manganite perovskites.

An opening discussion highlights the limitations of conventional surrogate precursors, and in particular, carboxylates and β-diketonates. Publications in the literature and private attempts by the author will conclusively demonstrate the unsuitability of such surrogates for low-temperature CSD methods. After establishing the basis for an all-alkoxide approach, the (known) physical characteristics of manganese(II) alkoxides are presented with an emphasis on overcoming the challenges affiliated with: (1) their extreme air sensitivity and (2) their tendency to form stable, infinite polymers. Accordingly, the molecular engineering of soluble, reactive alkoxide structures is then described from the perspective of the silylamido

---

[55]Pyrolysis should be conducted between coating iterations to minimize the risk of fracture. Thicker xerogel films generate larger quantities of gaseous decomposition products and contain longer diffusion paths. Together, these characteristics may combine to congest exit pathways, and therefore, produce regions of high, localized pressure. If substantial, the resulting stress concentration will dissipate by forming and propagating cracks. Thinner xerogel films are less susceptible to this behavior.

[56]In aqueous systems, dissolution, in and of itself, implies the coordination of a metal center by aqua ligands. Hydrolysis (i.e., the generation of hydroxo or oxo ligands via proton loss) then proceeds quite fast. Table 2.4 on page 55 lists typical end-products.

ligand, an exceedingly flexible and potent synthon. Adaptation of the corresponding synthetic procedures to each relevant element (i.e., Mn, La, Pb, and Group IIA) concludes the section.

2.4.1 SURROGATE PRECURSORS

For doped-lanthanide manganites, the general unavailability of Group VIIB alkoxides has, up to this point, forced the adaptation of manganese salts (i.e., nitrates, carboxylates, and β-diketonates) as surrogate precursors. The precedence for such an approach was established by BUDD, DEY, and PAYNE [1, 2] who employed lead(II) acetate during the sol-gel processing of $PbTiO_3$ and $PbZr_xTi_{1-x}O_3$ thin films. Their procedure exploited the polyfunctional nature of 2-methoxyethanol (i.e., ethereal and alcoholic groups) to react with and dissolve otherwise insoluble carboxylates: $Pb(OOCCH_3)_2 \cdot 3H_2O$ was converted into the alkoxo-acylate, $Pb(OCH_2CH_2OCH_3)(OOCCH_3)$, upon reflux and distillation [151]. Further investigations have yielded many similar alkoxy-based heteroleptic intermediates containing carboxyl or β-diketone ligands [152, 153]. The incorporation of nitrates in sol-gel processes, however, is eschewed because the NO_3^- anion during reflux tends to displace the hydroxyl group from an alcohol (i.e., the solvent) forming unstable $RC-ONO_2$ bonds. This functional structure comprises the explosive basis for nitroglycerin [154]. For example, preliminary attempts by the author to prepare 2-methoxyethanol-based sols using manganese(II) nitrate hydrate garnered the following observation: after spin-coating, pyrolysis at 300 °C generated faint plumes of smoke above the substrate. Not surprisingly, chemical analysis of the surface by XPS revealed none of the "deposited" metals.

The first CSD method for manganite perovskite thin films was developed by BAE and WANG [155] who reported the formation of $La_{0.67}Ca_{0.33}MnO_3$ on lattice-matched, refractory $LaAlO_3(100)$ and $MgO(100)$ substrates. By processing at 80 °C for 24 hours, lanthanum, calcium, and manganese acetate were dissolved, with an unspecified ratio of water, in 2-methoxyethanol. But the inclusion of water prior to heating suggests an effort to improve solubility; all three acetates are normally insoluble in 2-methoxyethanol (i.e., under ambient conditions), but their dissolution occurs readily in water. In addition, the opportunity for templated epitaxial growth proved inadequate to overcome high processing temperatures (i.e., 950 °C) and special atmospheres (i.e., flowing oxygen). These observations are reminis-

cent of characteristics exhibited by the acetate-based, aqueous process of HASENKOX, et al. [101, 102]. Without further (clarifying) investigations, they suggest a synthetic pathway of simple complexation followed by metal-organic decomposition; the lack of demonstrated hydrolysis and condensation products therefore raises questions about the "successful sol-gel growth" claimed by Bae and Wang.

A proper refinement of the approach pioneered by Budd, et al. was undertaken in a collaborative endeavor by the author [156, 157]. Three principles governed the transfer of this technique from titanate to manganite perovskites: (1) alkoxides were preferentially selected over carboxylates when available, (2) each precursor was dissolved separately in 2-methoxy-ethanol, forming individual homometallic solutions, and (3) stoichiometric mixing and reflux *preceded* hydrolysis. Accordingly, two compositions, $La_{0.67}Ca_{0.33}MnO_3$ and $La_{0.67}Pb_{0.33}MnO_3$, were derived from lanthanum 2-methoxyethoxide, calcium 2-methoxyethoxide, lead(II) acetate, and manganese(II) acetate. Figure 2.16 shows scanning electron micrographs of the corresponding microstructures formed on $LaAlO_3(100)$. The faceted, columnar islands clearly reflect the influence of substrate lattice-matching. But despite the benefit of templated growth, firing temperatures in excess of 800 °C were still required. So the progressive reduction of carboxylate content (i.e., to manganese(II) acetate at minimum) failed to confer a processing regime compatible with silicon-based microelectronics. Comparison with the CSD method of Bae and Wang does, however, indicate a lowering of crystallization temperature. This trend favors the increased utilization of alkoxide precursors, and in particular, an all-alkoxide approach.

Similar behavior was also demonstrated by BECK, et al. [158] during a comparative investigation into the sol-gel processing of $BaTiO_3$. The replacement of barium 2-propoxide by its corresponding acetate salt resulted in substantial carbonate contamination upon pyrolysis, requiring higher temperatures (i.e., $T > 1200$ °C) for phase-pure material.[57] In contrast, mass spectrometry detected no organic evolution above 700 °C for xerogels derived solely from alkoxides; crystallization of $BaTiO_3$ was reported to occur between 500–600 °C with all foreign phases absent by 1000 °C. Beck, et al. reported that carbonate formation involved the segregation of $BaCO_3$, leaving Ti-rich regions in the previously homogenous system. Higher

---

[57]In all cases, titanium 2-propoxide served as the Ti source. Reactions were carried out in either 2-propanol (alkoxide-only) or glacial acetic acid and 2-propanol (acetate-alkoxide). Glacial acetic acid is required to dissolve the otherwise insoluble barium acetate.

Cross Section   Surface View

La$_{0.67}$Ca$_{0.33}$MnO$_3$

1.0 μm

3.8 μm

La$_{0.67}$Pb$_{0.33}$MnO$_3$

3.0 μm

3.0 μm
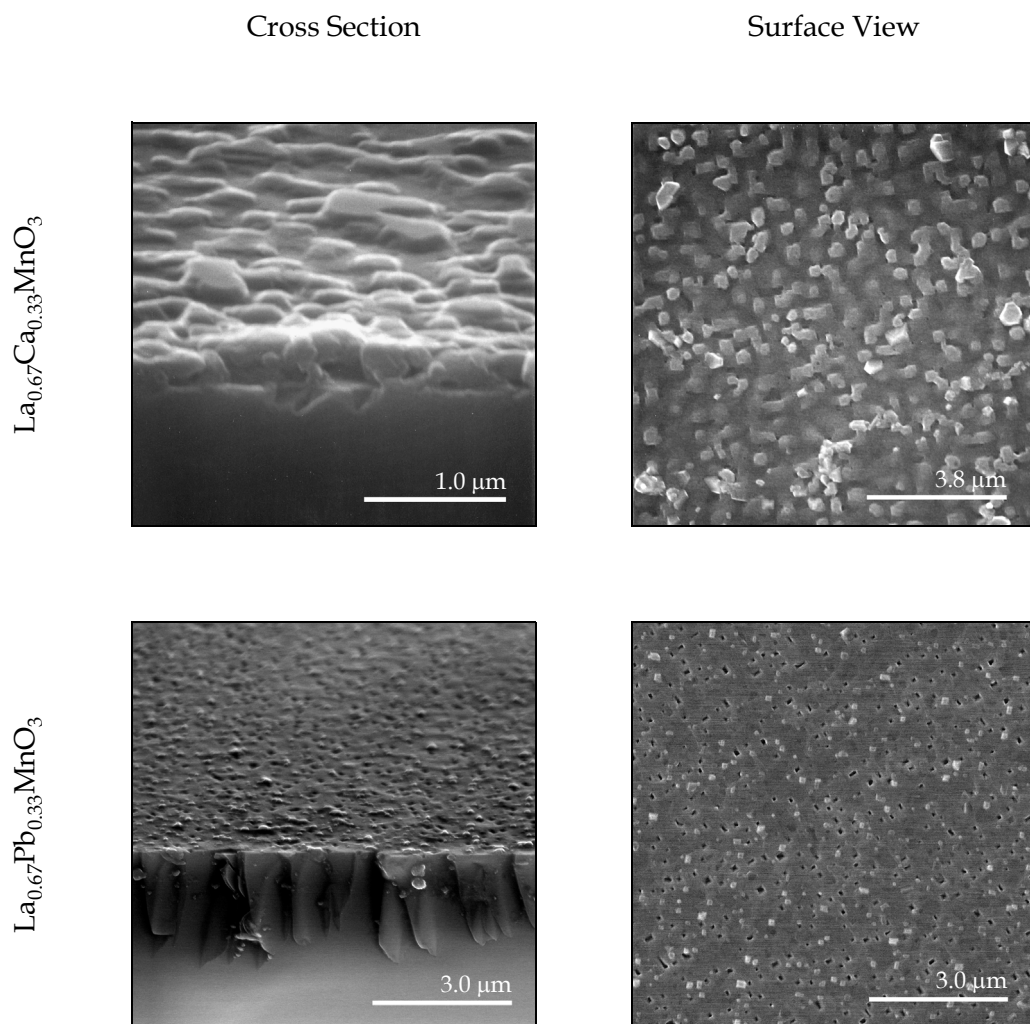
FIGURE 2.16 Manganite perovskite thin films grown on lattice-matched LaAlO$_3$(100). The xerogel coatings were fired in air at 850 °C for one hour [156].

temperatures were therefore required to decompose the refractory carbonate and re-integrate, via reaction, the oxidized product back into the host matrix. This observation has significant implications for the sol-gel processing of doped-lanthanide manganites: *the thermal decomposition of carboxylates and β-diketonates proceeds almost exclusively through oxycarbonate or carbonate intermediates* [103, 159]. For example, $La(OOCCH_3)_3$ converts, upon heating, to $La_2O_2CO_3$, achieving the full oxide only above 910 °C [160]; similarly, $Ca(OOCCH_3)_2$ transforms into $CaCO_3$ with CaO first appearing after the temperature exceeds 800 °C [161].[58]

The tendency of carboxyl and β-diketone ligands to decompose into thermally-stable oxycarbonate and carbonate species stems from the bidentate nature of their underlying functional groups: unlike alkoxy ligands, carboxyl or β-diketone groups bond through two oxygen atoms, and thus, more effectively saturate the coordination sphere of an electrophilic metal.[59] This activity matches the coordination mode of the corresponding anionic decomposition product, CO_3^{2-}. Equally important, by imparting higher coordination numbers (i.e., N), the configurational energy of a metal decreases, enhancing its resistance to nucleophilic attack (i.e., hydrolysis). Such behavior has been exploited in heteroleptic acetate and pentane-2,4-dionate derivatives of titanium 2-proproxide and titanium 1-butoxide to avoid precipitation [163, 164]. Partial charge considerations indicate that carboxylate-alkoxides or β-diketonate-alkoxides experience preferential hydrolysis of their more labile unidentate alkoxy bonds [165]. The growth of oxo-polymer or particulate morphologies then progresses with carboxyl or β-diketone ligands maintaining an exterior presence on the condensing structure [166]. Therefore, the survival of these bidentate ligands, even under aggressive hydrolytic conditions, brings the undesirable prospect of carbonate formation during decomposition, and hence, the potential for high processing temperatures.

This possibility becomes particularly acute in heterometallic species where carboxyl or β-diketone ligands can join differing metal centers through a bridging mechanism. Such

---

[58]Carbonates of other relevant Group IIA metals (i.e., Sr and Ba), exhibit even higher thermal stabilities due to larger cation radii. For example, the decomposition temperatures of *phase-pure* $CaCO_3$, $SrCO_3$ and $BaCO_3$ are, respectively, 840 °C, 1100 °C, and 1300 °C [162].

[59]The functional unit of the β-diketone ligand stems from its open $OC-C-CO$ ring. Alkyl groups, R^1 and R^3, bond (respectively) to the outer carbon atoms but the central carbon exhibits both R^2 and H. The generic formula is given by $R^1COCHR^2COR^3$. Pentane-2,4-dione (i.e., acetylacetone), the most common moiety, occurs when $R^1 = R^3 = CH_3$ and $R^2 = H$. In a fashion similar to carboxylates, the hybridization of p orbitals along the $OC-C-CO$ ring creates a delocalized electron cloud that imparts ionic character to the ligand. An organic salt is formed upon coordination with a metal. A comprehensive review of β-diketonate chemistry can be found in the reference text by MEHROTRA, et al. [159].

coordination often replaces bidentate chelation in mixed-metal systems: HUBERT-PFALZGRAF [167] examined various heterometallic alkoxide-acetate crystal structures and found only bridging modes; infrared measurements on xerogel end-products (i.e., powders) confirmed the retention of heterometallic, bridging coordination after hydrolysis. This observation, in light of the results of Beck, et al. with $BaTiO_3$, offers a *plausible* explanation for the high formation temperatures (i.e., $T > 800\ °C$) encountered so far in the sol-gel processing of $La_{1-x}M_xMnO_3$ materials: the utilization of surrogate, acetate precursors activates a bridging mechanism between metals of low-temperature (i.e., Pb or Mn) and those of refractory (i.e., La or Group IIA) oxycarbonate or carbonate phases.[60] Thermal energy during pyrolysis then is quite sufficient to enable the decomposition product, CO_3^{2-}, to transfer full coordination into the more stable bond (i.e., La or Group IIA). So preliminary results using metal acetates suggest that, due to similar functionality with CO_3^{2-}, carboxylate or β-diketonate precursors are poorly suited for the sol-gel processing of doped-lanthanide manganites. *Thus, the need for lower temperatures (i.e., $T < 800\ °C$) clearly justifies the development of an all-alkoxide precursor system (i.e., unidentate), the principal objective of this dissertation.*

2.4.2 CHALLENGES OF MANGANESE(II) ALKOXIDES

As mentioned previously in Section 2.3.2, Group VIIB alkoxides represent the least-characterized members of the transition metal series. With regard to sol-gel processing, their utilization remains virtually unknown. An extensive survey of the literature, performed by the author according to guidelines outlined in MAIZELL [169], yielded only 11 articles containing information on manganese(II) alkoxides (e.g., see references [170–180]). Unfortunately, the poor understanding reflected by this paucity of data extends directly into the publications themselves: many articles unwittingly report on the products of oxidation and not the actual alkoxides, rendering any conclusions (therein) highly suspect [170–172, 175, 180]. Such articles are easily identified by their descriptions of "brown", "dark brown", or "black" material (i.e., crystals, powders, or solutions). Yet manganese(II) alkoxides, when isolated in pure form, exhibit either colorless, pink, lavender, or yellow hues [176]. The observed darkening of color, caused by exposure to molecular oxygen, indicates a transition in valence from

---

[60]$Pb(OOCCH_3)_2$ and $Mn(OOCCH_3)_2$ convert, respectively, to PbO and MnO at $\sim 360\ °C$ and $\sim 350\ °C$ [160, 168].

Mn^{2+} to Mn^{3+}. A brown, dark-brown, or black appearance is unusual for d^5 high-spin systems (i.e., Mn^{2+}) but characteristic for Mn^{3+}. Accordingly, the only manganese(III) alkoxides reported to date, the 2,2′-biphenoxides, were synthesized directly in solution (i.e., not by aerobic oxidation), crystallizing as "dark brown" or "black" solids [181].

The reaction of manganese(II) alkoxides with oxygen occurs via an insertion mechanism, establishing a coordinately-saturated manganese(III) oxoalkoxide, $[MnO_{x/2}(OR)_2]_n$.[61] For example, derivatives of secondary alcohols undergo oxidation through unstable, green-colored intermediates, suggesting the brief emergence of a seminal $[Mn(OR)_2]_n \cdot yO_2$ complex [176]. Susceptibility to ligation by O_2, however, is not alleviated by heterometallic oligomerization (i.e., Equation 2.13): MEHROTRA, et al. [180] synthesized various mixed-metal (i.e., $M^1 = Mn^{2+}$, $M^2 = Al, Zr,$ and Nb) alkoxides, which due to improper precautions, oxidized *in situ* immediately following metathesis (see Section 2.4.3). Manganese(III) oxoalkoxides and their heterometallic counterparts are unsuitable for sol-gel processing because Mn^{3+}, when coordinated by oxo and/or oxygen-functionalized ligands, displays exceptional resistance to hydrolysis. In addition, continued aerobic exposure of initially-oxidized products allows the growth of inert, dense particulates.[62] This latter complication is difficult to control due to the extreme oxygen sensitivity of alkoxy-coordinated Mn^{2+}. Even minor contamination can induce precipitation from solution. Fortunately, manipulation under purified argon gas enables the routine synthesis and handling of manganese(II) alkoxides — provided all solvents are *scrupulously degassed* beforehand. Such procedures (and affiliated equipment) comprise the subject matter of Chapter 3.

ADAMS, et al. [173, 174] achieved the first successful isolation of a manganese(II) alkoxide, reporting the magnetic moment and diffuse reflectance spectrum of the pale pink methoxide, $[Mn(OCH_3)_2]_\infty$. But a meticulous investigation into manganese(II) alkoxide chemistry was not conducted until 1979 when HORVATH, et al. [176], in pioneering research, systematically synthesized and characterized 22 homoleptic moieties. Their examination revealed that

---

[61]Preliminary results with aliphatic manganese(II) alkoxides indicate tentative range of $x = 0.5$–0.75 [176].

[62]These particulates can only be dissolved in *concentrated* mineral acids (i.e., aqueous HCl, HNO_3, H_2SO_4, etc.). Their negligible reactivity stems from the conversion $[MnO_{x/2}(OR)_2]_n$ into $[MnO(OR)]_n$ when excess oxygen is present [176]. For example, commercial $Mn(OCH_3)_2$ purchased by the author arrived inadequately packaged, and hence, as an insoluble brown powder. Elemental analysis indicated half of the required hydrocarbon content. A comparison of the measured values with their theoretical weight percents (i.e., Mn, C, and H, respectively) gave 44.08, 10.38, and 3.21 versus 46.95, 20.53, and 5.17, respectively.

$[Mn(OR)_2]_n$ species demonstrate solubility only if R contains appreciable steric bulk, and in particular, tertiary branching.[63] Large aliphatic chains or modified phenyl groups (i.e., R) were needed to inhibit molecular association, and hence, polymerization. The oligomerization of lower carbon derivatives (i.e., $R = C_5$ and below) was shown to proceed via long-range cooperative bridging, yielding bonds of notable strength. For example, decomposition of these high molecular-weight compounds (under argon) required temperatures in excess of 300 °C; melting or sublimation was not observed [176]. Clearly though, insolubility and poor reactivity render such polymers unsuitable for sol-gel processing. Thus, current research into $[Mn(OR)_2]_n$ chemistry has emphasized the utilization of "designer" ligands with high steric bulk to stabilize monomeric or discrete oligomeric structures [177–179].

An intuitive explanation for the oxygen sensitivity and polymerization of manganese(II) alkoxides can be developed by considering two interrelated aspects of manganese oxide chemistry [182]. First, Mn^{2+} represents the lowest oxidation state for manganese in a purely oxo-ligand environment: the complete binary oxide series, MnO, Mn_2O_3, MnO_2, and Mn_2O_7, corresponds to a progressive increase in valence, respectively, from Mn^{2+} to Mn^{3+}, Mn^{4+}, and Mn^{7+}. Second, MnO crystallizes in the rock-salt structure (i.e., NaCl) which contains MnO_6 site symmetry (i.e., O_h). Thus, the driving force for coordinate expansion in manganese(II) alkoxides is exceptionally large because $N - z = 4$. By comparison, the Group IVB alkoxides exemplified in Sections 2.3.2 and 2.3.3 exhibit only $N - z = 2$. So low-coordination $[Mn(OR)_2]_n$ structures remain highly susceptible to nucleophilic attack by oxygen-functionalized ligands. Indeed, ADAMS, et al. [173, 174] and HORVATH, et al. [176] confirmed that polymeric manganese(II) alkoxides, $[Mn(OR)_2]_\infty$, manifest O_h stereochemistry, matching the oxo-coordination of MnO via alkoxy bridging. Unfortunately, no stereochemical information exists for manganese(III) oxoalkoxides. Any discussion then beyond simple considerations of oxidation in $[MnO_{x/2}(OR)_2]_n$ would therefore be speculative.

As a final comment, the special handling requirements of manganese(II) alkoxides might be construed as inconvenient enough, relative to other surrogate precursors, to inhibit their general adaptation within sol-gel processing (i.e., powders, fibers, aerogels, monoliths, etc.). Such a conclusion, however, would be premature. To illustrate this point, anhydrous man-

---

[63]Pentane, benzene, tetrahydrofuran, pyridine, and acetonitrile were investigated as representative organic solvents (i.e., alkanes, arenes, ethers, aromatic heterocycles, and nitriles, respectively).

ganese(II) acetate was refluxed in 2-methoxyethanol at 135 °C (under argon) for 12–16 hours.[64] Dissolution proceeded slowly but eventually yielded a pink, transparent solution (see Figure 2.17). Any exposure to oxygen, however, induced the immediate precipitation of brown material (not shown). This behavior strongly suggests the synthesis of an unidentified alkoxo-acylate, perhaps $Mn(OCH_2CH_2OCH_3)(OOCCH_3)$.[65] Oxidation was also noted in the acetate-based, multi-elemental sols developed for $La_{0.67}Ca_{0.33}MnO_3$ and $La_{0.67}Pb_{0.33}MnO_3$ (i.e., the collaborative endeavor of [156, 157]). Both systems darkened after one week, producing brown sediment shortly thereafter.[66] So clearly, conversion of manganese(II) surrogates (i.e., carboxylates and β-diketonate) into soluble derivatives concomitantly confers oxygen sensitivity. *Thus, the handling precautions remain the same, regardless of whether the initial precursor is an alkoxide or its surrogate!*

2.4.3 THE SILYLAMIDE SYNTHESIS ROUTE

The syntheses of late transition metal or lanthanide alkoxides rely almost entirely on metathetic reactions (i.e., ligand exchange) [76–78]. Traditionally, anhydrous halide salts and Group IA alkoxides are employed, the latter selected according to the desired O*R* group:

$$MX_n + yM^{IA}OR \xrightarrow{ROH} M(OR)_yX_{n-y} + yM^{IA}X \qquad (2.22)$$
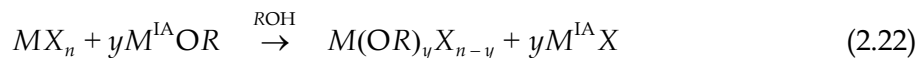
Here, M refers to the transition metal or lanthanide; M^{IA}, the alkali metal (usually Na); and X, the halide (commonly Cl). The parent alcohol (i.e., *R*OH) provides the reaction medium

---

[64]The anhydrous precursor was prepared from Aldrich 22,977-6, manganese(II) acetate tetrahydrate, 99.99%, by heating the corresponding pink crystals in a flask under vacuum. A four-step procedure was utilized to prevent the rapid release of water vapor which otherwise would condense on the flask interior and dissolve the dehydrating solid: (1) heat at 50 °C for 12 hours, (2) heat at 100 °C for 12 hours, (3) grind under argon, and (4) reheat at 100 °C for 12 hours. Elemental analysis confirmed the still-pink, extremely-brittle powder to be completely devoid of water. This process is essential to destabilize the octahedral coordination of manganese in the tetrahydrate [183]. Progressive removal of aqua ligands causes the crystal structure to collapse, leaving an incomplete coordination sphere susceptible to solvation (i.e., coordination of the metal by solvent molecules).

[65]In manganese(II) acetate, anionic carboxyl ligands coordinate Mn^{2+} centers exclusively through bridging modes [183]. Highly-polar, protic solvents such as water can easily disrupt this long-range coordination via repeated hydrolysis (i.e., nucleophilic attack, proton transfer, and liberation of acetic acid). Weaker protic solvents (i.e., 2-methoxyethanol), however, require the heat of reflux to activate proton transfer. Formation of an alkoxy bond, terminal in nature, then disjoins the Mn^{2+} centers. Continued reaction breaks up the solid.

[66]The glassware pictured in Figure 2.17 was not available during the author's collaboration with Dr. Duk-Young Jung. At the time, less reliable Subaseal stoppers were employed, which after prolonged contact with 2-methoxyethanol vapors, cracked and allowed contamination by oxygen.
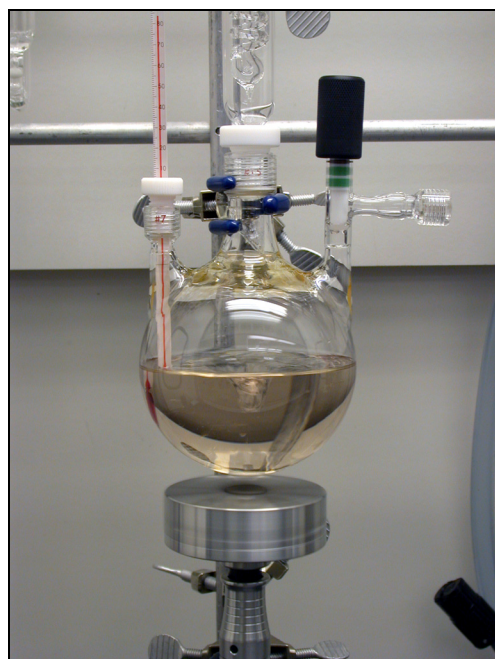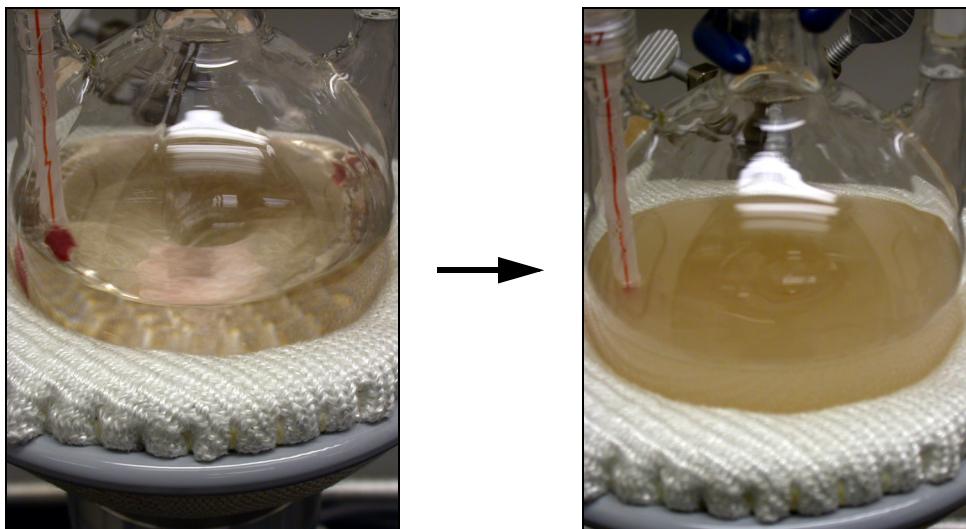
FIGURE 2.17 Dissolution of Mn(OOCCH$_3$)$_2$ in 2-methoxyethanol. A pink, transparent solution results after extended reflux under inert gas. Oxidation occurs immediately upon exposure to air, darkening the solution and precipitating brown sediment.

but mixtures with arene (i.e., benzene, toluene, etc.) or ethereal solvents (i.e., tetrahydrofuran) are often utilized to improve yield and purity. Before metathesis, however, the anhydrous halide salt must first be refluxed to form a coordinated adduct, typically $MX_n \cdot xR\text{OH}$ [184–186]. This solvation procedure comprises a critical enabling step for subsequent ligand exchange. Unfortunately, the synthetic intermediates of Equation 2.22 are prone to side-reactions which incorporate halide and M^{IA} impurities into the final product. For example, a 1:3 stoichiometric reaction of YCl_3 with $NaOC(CH_3)_3$ in tetrahydrofuran does not generate $Y[OC(CH_3)_3]_3$, but rather, the solvent-adducted $Y_3[OC(CH_3)_3]_8Cl$ [187]. Both halide and M^{IA} contamination results from the high Lewis acidity of $M(OR)_n$, a characteristic which enables chemical interactions with more basic $M(OR)_y X_{n-y}$ or $M^{IA}OR$ species [119]. Increasing the steric bulk of OR improves the chances for such reactions as partially-substituted intermediates gain enhanced screening of their smaller halide ligands.

Heteroleptic and/or heterometallic impurities present acute challenges for the synthesis of metal alkoxides because soluble derivatives usually arise only with higher alkyl homologues.[67] Fortunately, modern research into the chemistry of metal alkoxides has provided a potent modification of the simple metathetic pathway offered by Equation 2.22 [77, 78]:

$$MX_n + yM^{IA}N[Si(CH_3)_3]_2 \overset{\text{THF}}{\rightarrow} M\{N[Si(CH_3)_3]_2\}_n X_{n-y} + yM^{IA}X \qquad (2.23)$$

$$M\{N[Si(CH_3)_3]_2\}_n + nR\text{OH} \overset{\text{Toluene}}{\rightarrow} M(OR)_n + nHN[Si(CH_3)_3]_2 \qquad (2.24)$$

By integrating the novel silylamido ligand, $N[Si(CH_3)_3]_2$, this elegant solution bifurcates the previous synthetic pathway into two distinct steps (i.e., Equations 2.23 and 2.24). Metathesis now occurs via an amido (as opposed to an alkoxy) ligand and nucleophilic substitution with

---

[67]Manganese(II) alkoxides provide an excellent case in point. The preparation of polymeric $[Mn(OCH_3)_2]_\infty$ by ADAMS, et al. [173, 174] used $MnCl_2$ and $LiOCH_3$, exploiting the partial solubility of LiCl in methanol. Repeated washings with pure solvent then removed the entrapped salt. Lithium chloride, however, is not soluble in other, less-polar alcohols. Furthermore, to avoid heterometallic contamination, lithium alkoxides are usually eschewed in favor of sodium or potassium analogues. The larger cationic size of these latter Group IA atoms enhances coordination by chlorine and inhibits incorporation into the otherwise homometallic alkoxide product. Unfortunately, separation becomes virtually impossible if the manganese(II) alkoxide is polymeric (i.e., insoluble). Attempts by the author to synthesize the 2-propoxide derivative, $\{Mn[OCH(CH_3)_2]_2\}_\infty$, from $MnCl_2$ and $NaOCH(CH_3)_2$ in 2-propanol yielded a fine, white powder (i.e., NaCl) interspersed within the expected pink, amorphous product. Extraction efforts proved futile. HORVATH, et al. [176] reported that the adaptation of Equation 2.22 to the synthesis of *soluble* manganese(II) alkoxides (i.e., with large hydrocarbon groups) significantly diminished yields and often included contaminating side-products.

$$Ln-N[Si(CH_3)_3]_2 \quad + \quad HL \longrightarrow \quad \boxed{\begin{array}{l} Ln-C\equiv CR \\ Ln-Cp \\ Ln-SnR_3 \\ Ln-NR_2 \\ Ln-PR_2 \\ Ln-OR \\ Ln-SR \\ Ln-SeR \\ Ln-TeR \\ Ln-Cl \end{array}} \quad + \quad HN[Si(CH_3)_3]_2$$
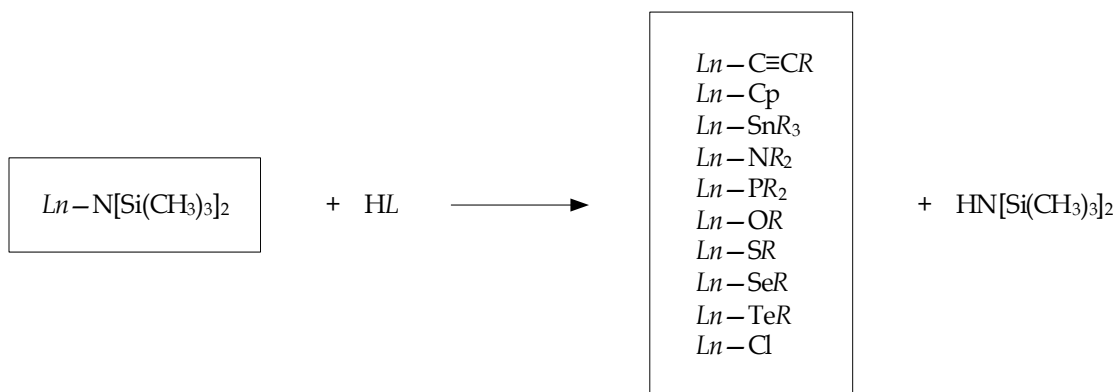
FIGURE 2.18 Silylamido metathesis as represented through lanthanide chemistry. The abbreviation, Cp, refers to η^5-cyclopentadienyl . (Adapted from [188]. Copyright 1999 Springer-Verlag.)

a pre-selected alcohol generates the desired metal alkoxide. The sheer efficacy of the silylamide route in engineering new inorganic precursors is summarized by Figure 2.18 which highlights a specific adaptation to lanthanide chemistry [188]. As in alkoxy-based metathesis, solvation of the halide prior to reaction plays a crucial role in enabling high yields. The silylamido metal-nitrogen bond, however, contains an obvious sensitivity to cleavage by proton transfer. So non-protic coordinating solvents, commonly ethers, provide the dissolution medium.

In general, ethereal solvents can be viewed as organic analogues of water where carbon-based groups replace protons in the molecule (i.e., R^1OR^2 versus HOH). But the absence of polar $O^{\delta-}-H^{\delta+}$ bonds significantly reduces the dipole moment of ethers relative to alcohols (i.e., R^1 or R^2 = H) or water (i.e., R^1 and R^2 = H). To circumvent this deficiency, any selection of ethereal solvent must emphasize high $C^{\delta+}-O^{\delta-}-C^{\delta+}$ polar covalencies and minimize steric bulk. Both criteria are readily satisfied by tetrahydrofuran (THF), the nearly universal choice for silylamide syntheses. Organic groups in its molecular structure form a compact heterocyclic ring (i.e., R^1 and R^2 = CH_2CH_2), enhancing exposure of its electron-rich oxygen donor. This configuration imparts aggressive coordinating ability, enabling THF to solvate anhydrous MX_n salts and assist in ligand exchange.

The susceptibility of metal silylamides to nucleophilic substitution arises from: (1) low metal coordinations, (2) π-bonding interactions at the $Si-N$ bond, and (3) the weak Lewis

basicity of the leaving group, $HN[Si(CH_3)_3]_2$. In a manner analogous to alkoxides, silyla-mides display polarization of their $M^{\delta+} - N^{\delta}$ bonds, the result of high nitrogen electronega-tivity [191]. Accordingly, intermolecular back-donation of lone-pair electrons from nitrogen can induce oligomerization (i.e., discrete or infinite), a common observation for metal amides based on small alkyl groups (i.e., $[M(NR^1R^2)_z]_n$). But steric considerations of the bis(trime-thylsilyl)amine parent (i.e., 1,1,1,3,3,3-hexamethyldisilazane) clearly underscore a derivative ligand with significant bulk, as shown in Figure 2.19. This feature, when incorporated into an amide structure, forces the metal into an unusually low coordination. A dramatic exam-ple of this phenomenon was uncovered by BRADLEY, et al. [190] in the crystal structure of $Mn\{N[Si(CH_3)_3]_2\}_2$ (see Figure 2.20). Note that a 3-fold coordination for manganese is rare! Such open, unsaturated environments render silylamide metal centers highly susceptible to nucleophilic attack, even by protic reagents with significant steric bulk. Furthermore, numerous methyl groups confer excellent solubility in common organic solvents, most nota-
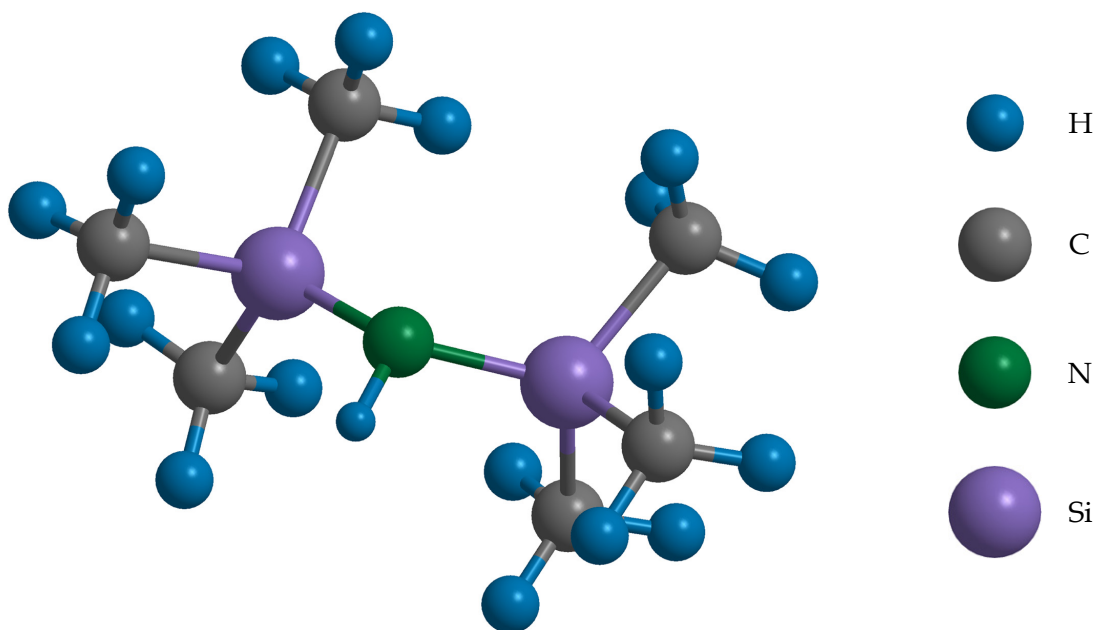
FIGURE 2.19 The molecular structure of 1,1,1,3,3,3-hexamethyldisila-zane. Cleavage of the amine bond (i.e. N−H) yields the silylamido ligand. Bond lengths and angles have been adapted from the electron diffraction results of [189].
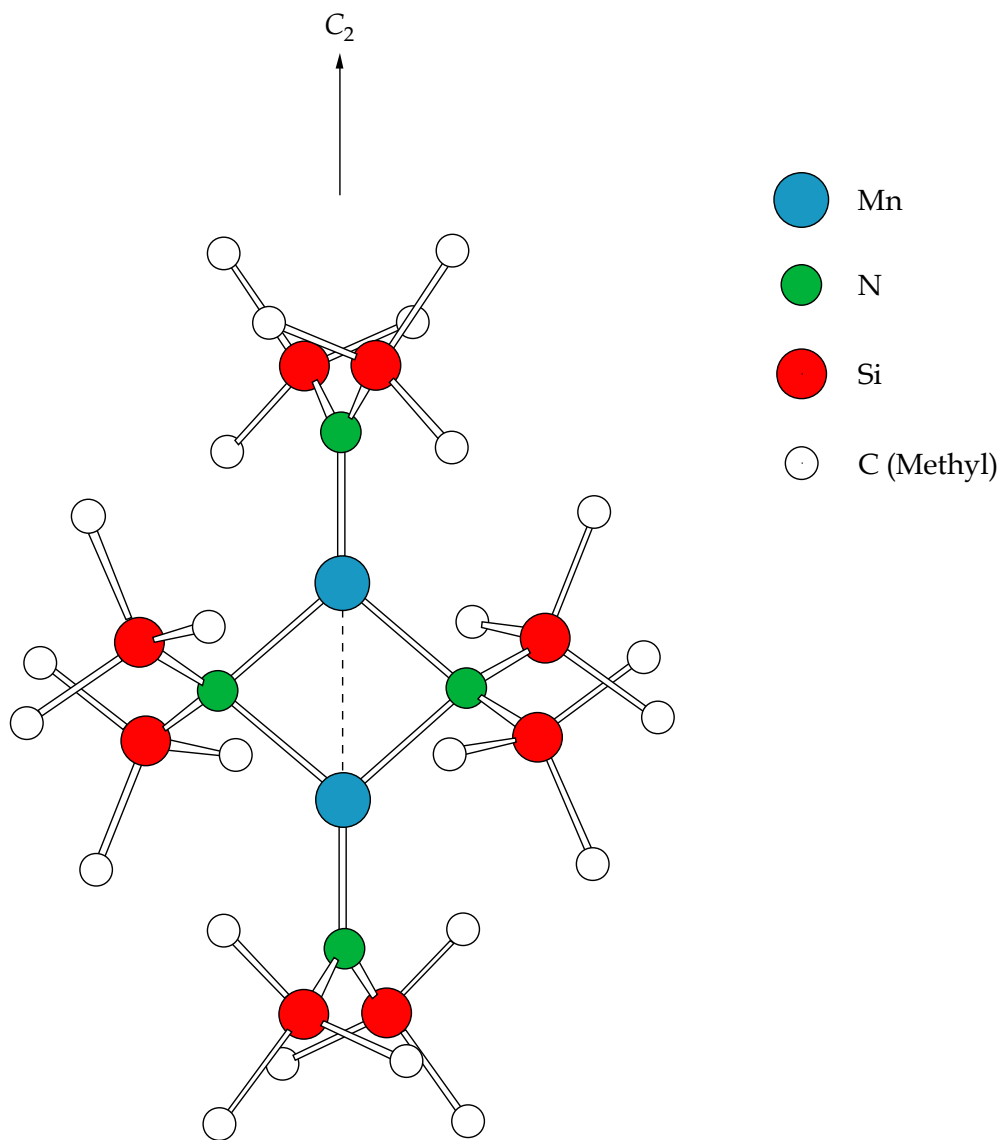
FIGURE 2.20 The crystal structure of Mn{N[Si(CH$_3$)$_3$]$_2$}$_2$. For clarity, the methyl groups are depicted by carbon atoms only. (Adapted from [190]. Copyright 1978 Verlag Chemie.)

bly alkanes. As a result, silylamides can be easily and conveniently separated from $M^{IA}X$ by-products. For example, metal halide salts are solvated by ethers but remain inert to hydrocarbon media. Thus, the replacement of THF with an alkane solvent (i.e., pentane, cyclohexane, etc.) affords a rapid, salt-free extraction. Equally important, the low nuclearity of silylamides imparts melting and/or volatility *without decomposition* at readily-accessible temperatures (i.e., $T < 150\ °C$). Subsequent reduced-pressure distillation or sublimation then produces $M\{N[Si(CH_3)_3]_2\}_z$ material of excellent purity, often 99+% after a single iteration, higher if repeated.

The potency of the silylamido ligand arises from the exceptional strength of its $Si-N$ bonds, the greatest of the Group IVA elements (i.e., C < Si > Ge > Sn > Pb) [191]. The silylamine parent (i.e., $HN[Si(CH_3)_3]_2$), for example, is inert to water and aqueous alkali metals, even during boiling; acid catalysts are required activate hydrolysis [192, 193]. This reduction in lability arises from the orbital overlap of full nitrogen 2p and vacant silicon 3d manifolds: a p→d π-interaction via the nitrogen lone pair electrons enables back-donation to silicon. The resulting delocalization contracts the bond length and stabilizes a planar geometry (i.e., maximizes steric bulk) [189]. So nucleophilic substitution (i.e., Equation 2.24) occurs at the desired $M-N$ site and not its $Si-N$ counterpart.

In contrast, purely organic moieties (i.e., NR^1R^2) exhibit pyramidal configurations that approximate sp^3 hybridization. The lack of p→d interactions leaves exposed electron density on the nitrogen which allows oligomerization or decomposition by β-hydrogen elimination (i.e., conversion to $R^1N{=}CH_2$).[68] For example, $Pb\{N[Si(CH_3)_3]_2\}_2$ was first reported in 1977 but an organonitrogen complement has never been isolated [191]. The $Si-N$ π-bonding interaction within this silylamide is believed to: (1) impart steric hindrance and (2) stabilize the weak Pb−N bond (i.e., ~ 20–30 kcal/mol). The former shields the labile Pb−N site, impeding decomposition kinetics, and the latter inhibits charge redistribution.

In addition, the p→d π-interaction, by trapping electron density within the $Si-N$ bond, confer weak Lewis basicity. Thus, the silylamido ligand, in combination with its high steric bulk, serves as an effective leaving group: $HN[Si(CH_3)_3]_2$ is not observed to form adducts. Furthermore, $HN[Si(CH_3)_3]_2$ exists as a liquid under ambient conditions. So the nucleo-

---

[68]Large, sterically-bulky alkyl groups, however, can force planar restructuring although π-bonding remains absent. For a discussion of β-hydrogen elimination, see page 469 of [191].

philic substitution represented by Equation 2.24 is particularly convenient: a simple "solvent strip" (i.e., reduced-pressure with no heating) suffices to leave the virgin metal alkoxide. No subsequent separation is required. *So the ultimate purity of the title product rests solely on that of the starting reactants and not the reaction process.* For this reason, the silylamide synthesis route carries a significant advantage over its alkoxy counterpart.[69] Further elaboration on metal silylamide chemistry, however, will not be presented here. Instead, the reader is directed to the review by LAPPERT and HARRIS [194], and in particular, the comprehensive reference text by LAPPERT, et al. [191].

2.4.4 MANGANESE(II) ALKOXIDES

The first synthesis of bis[bis(trimethylsilyl)]amido manganese(II) was reported in 1964 by BÜRGER and WANNAGAT [195] during their pioneering research into the silylamido chemistry of late transition metals. Subsequent refinement by HORVATH, et al. [196], however, has provided the accepted literature preparation and assumes reaction under inert gas:

$$MnCl_2 + 2LiN[Si(CH_3)_3]_2 \xrightarrow{\text{Reflux in THF}} Mn\{N[Si(CH_3)_3]_2\}_2 + 2LiCl \qquad (2.25)$$
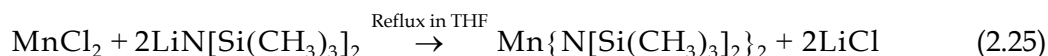
Horvath, et al. determined that yields for $Mn\{N[Si(CH_3)_3]_2\}_2$ depend critically on the solvation of $MnCl_2$. For example, the anhydrous chloride forms $MnCl_2 \cdot 2THF$ upon reflux in THF but the same procedure in weaker-coordinating diethyl ether (DEE) gives the lesser adduct, $MnCl_2 \cdot 0.5DEE$. This simple difference corresponds to a reduction in yield from 85–93% to 15–20%, respectively. Proper preparation of $MnCl_2 \cdot 2THF$, however, starts with the dehydration of $MnCl_2 \cdot 4H_2O$, conducted in vacuo by heating.[70] Alternative approaches produce lower solvates (i.e., $MnCl_2 \cdot xTHF$ where $x = 0.5, 1.0,$ and 1.5), and hence, diminish yields (see references in [196]).

To initiate reaction, $LiN[Si(CH_3)_3]_2$ is first dissolved in THF and then cannulated into the chloride suspension. Reflux of the combined system for 5–6 hours generates a transpar-

---

[69]Late transition metal or lanthanide alkoxides, if synthesized via alkoxy metathesis, depend on recrystallization for purification. Recrystallization, however, is slow and tedious (i.e., days or weeks) compared to distillation or sublimation (i.e., hours).

[70]Depopulation of aqua ligands from the metal center desaturates the coordination sphere. Because the temperatures employed (i.e., 55 °C, 135 °C, and 210 °C) do not allow for the effective reorganization of the perturbed lattice, the altered $MnCl_2$ material exhibits an enhanced reactivity towards solvent coordination.

ent orange solution from which LiCl precipitates. This extended reflux ensures that metathesis reaches completion. For instance, Horvath, et al. successfully isolated the partially-substituted intermediate, $MnCl\{N[Si(CH_3)_3]_2\}$, and verified that disproportionation occurs above 50 °C according to:[71]

$$2MnCl\{N[Si(CH_3)_3]_2\} \xrightarrow{\text{Reflux in THF}} Mn\{N[Si(CH_3)_3]_2\}_2 + MnCl_2 \qquad (2.26)$$
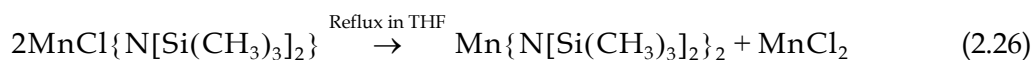
This process plays an indispensable role in preventing the incorporation of $LiN[Si(CH_3)_3]_2$ into its manganese derivative: a slight excess of $MnCl_2$ reagent guarantees the consumption of all initial $LiN[Si(CH_3)_3]_2$.

Separation of $Mn\{N[Si(CH_3)_3]_2\}_2$ from LiCl (and leftover $MnCl_2$) begins by replacing THF with cyclohexane. The extract is filtered through a very-fine, sintered-glass frit. Horvath, et al. reported that the resulting orange-red crude, distilled at 75–95 °C under vacuum (i.e., 10^{-3} torr), generated an initial yellow forerun (i.e., ~ 3–5% by weight) followed by a rose-colored fraction. The former was shown to be $Mn\{N[Si(CH_3)_3]_2\}_2 \cdot 2THF$, and the latter, $Mn\{N[Si(CH_3)_3]_2\}_2 \cdot THF$. Their ratio, however, could not be controlled. Elimination of all THF content could be accomplished by melting the purified product at 120 °C under a flow of argon for approximately one hour (i.e., thermolysis).

The oxygen sensitivity of $Mn\{N[Si(CH_3)_3]_2\}_2$ is quite extraordinary and cannot be overstated: while manganese(II) alkoxide, upon aerobic exposure, darkens over the course of a few seconds, the silylamide analogue turns black *instantly*. Long-term storage, even in a glove box, must be in sealed, leak-proof containers. The ability of manganese silylamide to scavenge residual oxygen and moisture from the surrounding atmosphere easily exceeds the performance of virtually all glove-box purifiers.

Once synthesized, however, manganese silylamide reacts spontaneously with alcohol in an inert organic solvent thereby generating the title product:

$$Mn\{N[Si(CH_3)_3]_2\}_2 + 2ROH \xrightarrow{\text{Reflux in Pentane}} Mn(OR)_2 + 2HN[Si(CH_3)_3]_2 \qquad (2.27)$$

---

[71]The boiling point of THF under ambient conditions is 66 °C.

Equation 2.27 presumes a slight excess (i.e., 1–3% by weight) of starting alcohol and produces virtually quantitative yields. The precedence for this method was established by Horvath, et al. [176] during their investigations of manganese(II) alkoxide chemistry. Depending on the alkoxy ligand, though, different recovery methods are required to ensure an adduct-free, stoichiometric material. The procedure adapted for this dissertation (i.e., for a precipitate) required the drying of isolated solid under vacuum at temperatures between 60–80 °C for approximately 1–3 hours. Methods for other compositions (i.e., different morphologies) can be found in [176].

2.4.5 Lanthanum Alkoxides

The generic silylamide route for the lanthanides was pioneered by Bradley, et al. [197, 198] during the early 1970s and provided a synthetic foundation for many other lanthanide metallorganic compounds (see Anwander [199, 200]). The original preparation (see below)

$$Ln\text{Cl}_3 + 3\text{LiN}[\text{Si}(\text{CH}_3)_3]_2 \xrightarrow{\text{THF}} Ln\{\text{N}[\text{Si}(\text{CH}_3)_3]_2\}_3 + 3\text{LiCl} \qquad (2.28)$$

resulted in moderate yields (~ 60–70%), which upon refinement, yielded a more efficient process [199, 201, 202].[72] Three modifications in particular are noteworthy. First, reflux should be conducted after addition of the alkali-metal silylamide. This step was ignored by Bradley, et al., who instead, relied on room-temperature reaction kinetics. Second, $\text{NaN}[\text{Si}(\text{CH}_3)_3]_2$ or $\text{KN}[\text{Si}(\text{CH}_3)_3]_2$ *must* be substituted for the lithium analogue. Failure to observe this requirement guarantees notable $\text{LiN}[\text{Si}(\text{CH}_3)_3]_2$ contamination. For example, Bradley, et al. reported an intermediate purification step where the extract was "recrystallized three times from pentane". Lastly, the solid residue left after solvent removal, *but before extraction*, must be thermolyzed at 150 °C under flowing argon. This last precaution liberates any remaining, coordinated THF and activates a disproportionation mechanism similar to Equation 2.26. Accordingly, the slight excess of anhydrous chloride salt ensures the complete consumption of alkali-metal silylamide. When observed together, these three refinements raise the yield

---

[72]Equation 2.28 presumes reaction under inert atmosphere.

above 90% for all elements within the lanthanide series. Sublimation at 70–100 °C in vacuo (i.e., 10^{-3} torr) then comprises a final purification step.[73]

Conversion to the alkoxide follows a procedure similar to that of manganese. Substitution kinetics, however, encounter greater steric hinderance in the (early) lanthanides because of trivalency. For this reason, the reaction pathway is assisted by replacing the alkane solvent with an electron-accessible, but non-coordinating arene such as toluene:

$$Ln\{N[Si(CH_3)_3]_2\}_3 + 3ROH \quad \overset{\text{Reflux in Toluene}}{\rightarrow} \quad Ln(OR)_3 + 3HN[Si(CH_3)_3]_2 \qquad (2.29)$$
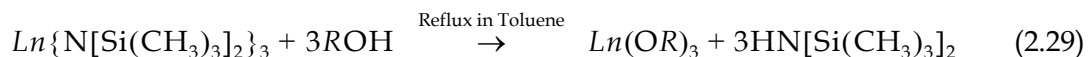
After reflux, the solvent is removed and the residue dried at 60–80 °C under vacuum. With a slight excess of starting alcohol (i.e., 1–3% by weight), the yields are quantitative.

2.4.6 LEAD(II) ALKOXIDES

LAPPERT, et al. [204–207] originally investigated the synthesis and physical properties of the Group IVB silylamides (i.e., the later Ge, Sn, and Pb members). The specific procedure for lead very much follows that established for manganese:[74]

$$PbCl_2 + 2LiN[Si(CH_3)_3]_2 \quad \overset{\text{THF}}{\rightarrow} \quad Pb\{N[Si(CH_3)_3]_2\}_2 + 2LiCl \qquad (2.30)$$

$$Pb\{N[Si(CH_3)_3]_2\}_2 + 2ROH \quad \overset{\text{Pentane}}{\rightarrow} \quad Pb(OR)_2 + 2HN[Si(CH_3)_3]_2 \qquad (2.31)$$
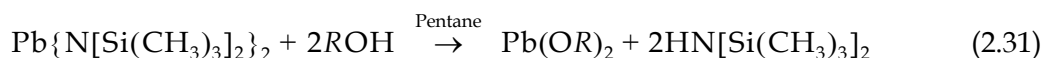
Three differences, however, make this reaction notably more convenient. First, reflux of the anhydrous chloride salt has little effect, if any, on yield. Second, the addition of lithium silylamide to the chloride suspension must be conducted at room temperature (or below). Due to the weak Pb—N bond, $Pb\{N[Si(CH_3)_3]_2\}_2$ rapidly decomposes when heated under conditions of atmospheric pressure, producing very-fine, dark-grey particles (i.e., metallic lead). So the work-up represented by Equation 2.30 avoids any heating procedure until reduced-

---

[73]For the individual lanthanides, see [198] for exact temperatures. Lanthanum silylamide, for example, sublimes under vacuum between ~ 100–102 °C. Note that the melting point of lithium silylamide (i.e., 71–72 °C at 10^{-2} torr) prevents sublimation from being used as a separation technique [203].

[74]The procedure provided here was developed by the author from descriptions of $Sn\{N[Si(CH_3)_3]_2\}_2$ syntheses. Original literature preparation(s) utilized DEE as the solvent and a 0 °C reaction temperature. But no deletarious effects were observed by relying on THF and 20–25 °C (i.e., room temperature).

pressure distillation. Finally, the distillation step must be conducted below ~ 30 torr and utilize a *heated* glass column [208]. This latter adaptation minimizes the thermal energy required to drive distillate out of the main flask. Such a precaution is essential to avoid the undesirable decomposition of $Pb\{N[Si(CH_3)_3]_2\}_2$. Unlike the preparation of manganese silylamide, however, reduced-pressure distillation of the Group IVB members, however, leaves pure, adduct-free material (i.e., thermolysis not needed). The title product, lead(II) silylamide, is a bright-yellow, opaque solid at room temperature. But grinding (i.e., heat from compression and shear) or the presence of solvent *vapors* can readily liquify the compound.

Conversion to the alkoxide follows the same method as described in Section 2.4.4. Yields are quantitative. Interestingly, only the silylamide synthesis route has been demonstrated to produce a homoleptic alkoxide precursor [209]. For example, attempts to prepare either the 2-propoxide or 2-methyl-2-propoxide (i.e., *tert*-butoxide) via electrolysis or alkoxy-based metathesis creates, instead, oxoalkoxide intermediates [210, 211].

2.4.7 GROUP IIA ALKOXIDES

Traditional methods for preparing Group IIA alkoxides rely on the direct reaction of a requisite alkali earth and its corresponding alcohol:

$$M^{IIA} + 2ROH \overset{\text{Toluene}}{\rightarrow} M^{IIA}(OR)_2 + H_2\uparrow \qquad (2.32)$$
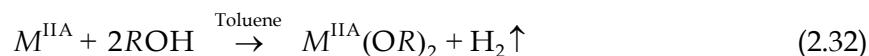
To prevent the formation of oxoalkoxide derivatives though, the solvent media should either be an alkane or arene but not the parent alcohol. Large excesses of the latter are believed to catalyze side-reactions similar in nature to Equation 2.15 [212]. The pathway of Equation 2.32 is usually vigorous and exothermic owing to the highly electropositive nature of M^{IIA}. Thus, the addition of alcohol should be slow. Reaction kinetics, however, decrease with higher atomic mass (i.e., of the Group IIA members) and/or steric bulk (i.e., of the alcohol). So reflux may be required to increase the reaction rate to a practical level.

Oxo-formation can be avoided by utilizing a modified silylamide route. This method also enables the synthesis of bulky derivatives not accessible to Equation 2.32. A transmetalation scheme, devised originally by BRADLEY, et al. [213] using mercuric silylamide, employs an alkali earth and the less-toxic tin(II) silylamide [214–216]:

96

$$M^{\mathrm{IIA}} + \mathrm{Sn}\{\mathrm{N[Si(CH_3)_3]_2}\}_2 \overset{\mathrm{Toluene}}{\rightarrow} M^{\mathrm{IIA}}\{\mathrm{N[Si(CH_3)_3]_2}\}_2 + 2\mathrm{Sn} \qquad (2.33)$$

$$M^{\mathrm{IIA}}\{\mathrm{N[Si(CH_3)_3]_2}\}_2 + 2R\mathrm{OH} \overset{\mathrm{Pentane}}{\rightarrow} M^{\mathrm{IIA}}(OR)_2 + 2\mathrm{HN[Si(CH_3)_3]_2} \qquad (2.34)$$
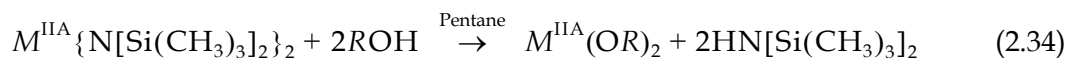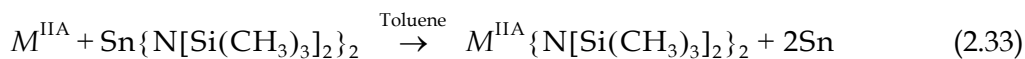
The basis for this reaction stems from the inherently weak $M^{\mathrm{IVB}} - \mathrm{N}$ bond, which for Equation 2.33 corresponds to $M^{\mathrm{IVB}} = \mathrm{Sn}^{2+}$ (see Section 2.4.3). But to obtain an adduct-free product, the (conventional) ether must be replaced by a non-coordinating arene, typically toluene. Attempts to liberate complexing molecules via thermolysis activate a decomposition process in addition to adduct volatization [215].

Again, all reactions (i.e., Equations 2.32, 2.33, and 2.34) presume handling under an inert gas. Note that this environment, the solvent media, and alcohol must be rigorously purified of molecular oxygen to prevent conversion into oxoalkoxide intermediates. For this dissertation, however, the modified silylamide route was not used; the reaction of Equation 2.32 proved sufficient to provide a soluble, homoleptic Group IIA alkoxide precursor. Hence, the brief discussion provided here (i.e., of the modified silylamide route) is mainly for consistency and completeness. Further details can be found in the aforementioned literature (see specifically [191, 213–216]).

2.5 SUMMARY AND RESEARCH OBJECTIVES

From the perspective of materials chemistry, doped-lanthanide manganites offer fertile research opportunities due to: (1) the lack of adequate CSD techniques, particularly with regard to the sol-gel processing of thin films and (2) the poor chemical characterization and availability of manganese(II) alkoxides. The principal challenge confronted by this dissertation then revolves around the development of a suitable alkoxy-based, solvent-precursor system, and in particular, the synthesis of a soluble, highly-reactive manganese(II) alkoxide. Characteristics desired from such a system must include low-temperature densification and crystallization, both prerequisites for compatibility with silicon-based microelectronics. Current investigations into the alkoxy-based, sol-gel processing of $\mathrm{La_{1-x}}M_x\mathrm{MnO_3}$ (i.e., M = Ca and Sr) by POHL, et al. [217, 218] have started to explore this nascent area but have emphasized xerogel powders. Equally important, the underlying manganese(II) precursor was an oxoalkoxide, the decomposition by-product of an attempted, homoleptic alkoxide [219].[75] *So*

an alkoxy-based sol system incorporating true alkoxide precursors and designed specifically for thin-film deposition would represent a new and important contribution to the solution processing of manganite perovskites.

When selecting alkoxide precursors, however, compounds with minimal carbon content are highly preferable. As highlighted in Section 2.4.2, manganese(II) alkoxides exhibit solubility only if their alkoxy ligands contain bulky, branched alkyls (i.e., $R = C_{18}$ and above).[76] But HORVATH, et al. [176] reported that "alkoxides of tert-butylalcohol and phenol appear to have an aggregation state between the polymeric and crystalline species" — an observation duly noted by the author. This intermediate state emerges from a transitional morphology where steric interference from alkoxy ligands just begins to perturb the long-range coordinate polymerization. A small polyfunctional molecule then, such as 2-methoxyethanol, can coordinate via insertion, possibly disrupting the aggregation (i.e., solvate the metal center). Indeed, as will be shown in Section 3.5.1, the 2-methyl-2-propoxo derivative (i.e., *tert*-butoxide) is highly soluble in 2-methoxyethanol! The author wishes to point out that conclusions from HORVATH, et al. [176] would suggest *quite the contrary*: 2-methyl-2-propoxo manganese(II) was insoluble in virtually all solvents tested (i.e., alkanes, arenes, ethers, and nitriles) although weak solubility was detected in pyridine. Note that the 2-methyl-2-propoxo ligand incorporates low-carbon content (i.e., $R = C_4$), a property conducive to reduced carbon dioxide emissions during pyrolysis.

Therefore, to develop an alkoxy-based sol-gel process for manganite perovskites, this dissertation utilizes two representative stoichiometries, both chosen from compositional series with room-temperature magnetoresistance (i.e., M = Sr, Ba, and Pb): $La_{0.67}Ba_{0.33}MnO_3$ and $La_{0.67}Pb_{0.33}MnO_3$. The divalent dopants in each correspond to distinct periodic groups with unique chemical properties. But the barium analogue is the most refractory element in the Group IIA column. Thus, because of similar chemical activity, a low-temperature sol-gel method developed for barium would readily extend to other, less-refractory members (i.e., Ca or Sr). A review of alkoxide literature indicates that the 2-methyl-2-propoxo ligand also

---

[75]The research presented in this dissertation focuses exclusively on thin films and represents an independent contribution. For example, the synthesis procedure employed by Pohl, et al. follows an alkoxy and not a silyla-mido metathesis. The resulting manganese(II) alkoxide was reported to be unstable, decomposing rapidly into an oxoalkoxide [219]. Such behavior is absent in the precursor-solvent system developed by the author (see Section 4.2).

[76]See also the theoretical considerations presented in Section 2.3.2.

confers solubility to the La, Group IIA, and Pb derivatives [209, 220–222]. Accordingly, a homoleptic system based on 2-methyl-2-propoxide precursors in 2-methoxyethanol comprises the prepatory goal for this research. Like their manganese(II) counterparts, these alkoxide precursors also exhibit oxygen sensitivity, although to a much lesser extent [210, 211, 220, 223]. To handle the demands of ultra-high purity inert-gas processing and the diverse range of aggressive chemical environments (i.e., during synthesis), the author designed a greaseless Schlenkware system (see Appendices C and D). But the actual air-sensitive manipulations (and affiliated observations) form the subject matter of Chapter 3.

2.6 REFERENCES

[1] Budd, K. D.; Dey, S. K.; Payne, D. A. Sol-Gel Processing of $PbTiO_3$, $PbZrO_3$, PZT, and PLZT Thin Films. In *Electrical Ceramics*, British Ceramics Proceedings, Vol. 36, London, Dec 17–18, 1984, Steele, B. C. H., Ed.; Institute of Ceramics: Shelton, Stoke-on-Trent, Staffs., U. K., 1985; pp 107–121.

[2] Dey, S. K., Budd, K. D.; Payne, D. A. Structure of Polymeric $PbTiO_3$ Gels. *Journal of the American Ceramic Society* **1987**, *70* (10), C295–C296.

[3] Volger, J. Further Experimental Investigations on Some Ferromagnetic Oxidic Compounds of Manganese with Perovskite Structure. *Physica* **1954**, *20* (1), 49–66.

[4] Searle, C. W.; Wang, S. T. Studies of the Ionic Ferromagnet $(LaPb)MnO_3$. V. Electric Transport and Ferromagnetic Properties. *Canadian Journal of Physics* **1970**, *48* (17), 2023–2031.

[5] Morrish, A. H.; Evans, B. J.; Eaton, J. A.; Leung, L. K. Studies of the Ionic Ferromagnet $(LaPb)MnO_3$. I. Growth and Characteristics of Single Crystals. *Canadian Journal of Physics* **1969**, *47* (23), 2691–2696.

[6] Salamon, M. B.; Jaime, M. The Physics of Manganites: Structure and Transport. *Reviews of Modern Physics* **2001**, *73* (3), 583–628; see also references therein.

[7] Galasso, F. S. *Perovskites and High T_C Superconductors*; Gordon and Breach Science Publishers: New York, 1990.

[8] Kline, C.; Hurlbut, E. *Manual of Mineralogy*, 21st ed.; John Wiley and Sons: New York, 1993; p 212.

[9] Goldschmidt, V. M.; Barth, T.; Lunde, G.; Zachariasen, W. Geochemische Verteilungsgesetze der Elemente. VII. Die Getsetze der Krystallochemie. *Skrifter utgitt av Det Norske Videnskaps-Akademi i Oslo. I. Matematisk-Naturvidenskapelig Klasse* **1926**, (2), 1–117.

[10] Shannon, R. D.; Prewitt, C. T. Effective Ionic Radii in Oxides and Fluorides. *Acta Crystallographica, Section B* **1969**, *25* (5), 925–946.

[11] Shannon, R. D. Revised Effective Ionic Radii and Systematic Studies of Interatomic Distances in Halides and Chalcogenides. *Acta Crystallographica, Section A* **1976**, *32* (5), 751–767.

[12] Roth, R. S. Classification of Perovskite and Other ABO_3-Type Compounds. *Journal of Research of the National Bureau of Standards* **1957**, *58* (2), 75–88.

[13] Roth, R. S.; Schneider, S. J. Phase Equilibria in Systems Involving the Rare-Earth Oxides. Part I. Polymorphism of the Oxides of the Trivalent Rare-Earth Ions. *Journal of Research of the National Bureau of Standards — A. Physics and Chemistry* **1960**, *64* (4), 309–316.

[14] Schneider, S. J.; Roth, R. S. Phase Equilibria in Systems Involving the Rare-Earth Oxides. Part II. Solid State Reactions in Trivalent Rare-Earth Oxide Systems. *Journal of Research of the National Bureau of Standards — A. Physics and Chemistry* **1960**, *64* (4), 317–332.

[15] Schneider, S. J.; Roth, R. S.; Waring, J. L. Solid State Reactions Involving Oxides of Trivalent Cations. *Journal of Research of the National Bureau of Standards — A. Physics and Chemistry* **1961**, *65* (4), 345–374.

[16] Giaquinta, D. M.; zur Loye, H.-C. Structural Predictions in the ABO_3 Phase Diagram. *Chemistry of Materials* **1994**, *6* (4), 365–372.

[17] Jonker, G. H.; Van Santen, J. H. Ferromagnetic Compounds of Manganese with Perovskite Structure. *Physica* **1950**, *16* (3), 337–349.

[18] Yakel, H. L.; Koehler, W. C.; Bertaut, E. F.; Forrat, E. F. On the Crystal Structure of the Manganese (III) Trioxides of the Heavy Lanthanides and Yttrium. *Acta Crystallographica* **1963**, *16* (10), 957–962.

[19] Syono, Y.; Akimoto, S.; Kohn, K. Structure Relations of Hexagonal Perovskite-Like Compounds ABX_3 at High Pressure. *Journal of the Physical Society of Japan* **1969**, *26* (4), 993–999.

[20] Mahesh, R.; Mahendiran, R.; Raychaudhuri, A. K.; Rao, C. N. R. Giant Magnetoresistance in Bulk Samples of $La_{1-x}A_xMnO_3$ (A = Sr or Ca). *Journal of Solid State Chemistry* **1995**, *114* (1), 297–299.

[21] Harwood, M. G. The Crystal Structure of Lanthanum-Strontium Manganites. *Proceedings of the Physical Society, Section B* **1955**, *68* (9), 586–592.

[22] Glazer, A. M. The Classification of Tilted Octahedra in Perovskites. *Acta Crystallographica, Section B* **1972**, *28* (11), 3384–3392.

[23] Glazer, A. M. Simple Ways of Determining Perovskite Structures. *Acta Crystallographica, Section A* **1975**, *31* (6), 756–762.

[24] Mahesh, R.; Mahendiran, R.; Raychaudhuri, A. K.; Rao, C. N. R. Effect of the Internal Pressure Due to the A-site Cations on the Giant Magnetoresistance and Related Properties of Doped Rare Earth Manganates, $Ln_{1-x}A_xMnO_3$ (Ln = La, Nd, Gd, Y; A = Ca, Sr, Ba, Pb). *Journal of Solid State Chemistry* **1995**, *120* (1), 204–207.

[25] Hervieu, M.; Mahesh, R.; Rangavittal, N.; Rao, C. N. R. Defect Structure of $LaMnO_3$. *European Journal of Solid State Inorganic Chemistry* **1995**, *32* (2), 79–94.

[26] Jahn, H. A.; Teller E. Stability of Polyatomic Molecules in Degenerate Electronic States. I—Orbital Degeneracy. *Proceedings of the Royal Society of London, Series A — Mathematical and Physical Sciences* **1937**, *161* (905), 220–235.

[27] Jahn, H. A. Stability of Polyatomic Molecules in Degenerate Electronic States. II—Spin Degeneracy. *Proceedings of the Royal Society of London, Series A — Mathematical and Physical Sciences* **1938**, *164* (916), 117–131.

[28] Wold, A.; Arnott, R. J.; Goodenough, J. B. Some Magnetic and Crystallographic Properties of the System $LaMn_{1-x}Ni_xO_{3+\lambda}$. *Journal of Applied Physics* **1958**, *29* (3), 387–389.

[29] Wold, A.; Arnott, R. J. Preparation and Crystallographic Properties of the Systems $LaMn_{1-x}Mn_xO_{3+\lambda}$ and $LaMn_{1-x}Ni_xO_{3+\lambda}$. *Journal of Physics and Chemistry of Solids* **1959**, *9* (2), 176–190.

[30] Bogush, A. K.; Pavlov, V. I.; Balyko, L. V. Structural Phase Transitions in the $LaMnO_{3+\lambda}$ System. *Crystal Research and Technology* **1983**, *18* (5), 589–598.

[31] Mahendiran, R.; Tiwary, S. K.; Raychaudhuri, A. K.; Ramakrishnan, T. V.; Mahesh, R.; Rangavittal, N.; Rao, C. N. R. Structure, Electron-Transport Properties, and Giant Magnetoresistance of Hole-Doped $LaMnO_3$ Systems. *Physical Review B* **1996**, *53* (6), 3348–3358.

[32] Manoharan, S. S.; Kumar, D.; Hegde, M. S.; Satyalakshmi, K. M.; Prasad, V.; Subramanyam, S. V. Giant Magnetoresistance in Self-Doped $La_{1-x}MnO_{3-\delta}$ Thin Films. *Journal of Solid State Chemistry* **1995**, *117* (2), 420–423.

[33] Van Santen, J. H.; Jonker, G. H. Electrical Conductivity of Ferromagnetic Compounds of Manganese with Perovskite Structure. *Physica* **1950**, *16* (7–8), 599–600.

[34] Jonker, G. H. Magnetic Compounds with Perovskite Structure IV Conducting and Non-Conducting Compounds. *Physica* **1956**, *22* (8), 707–722.

[35] Goodenough, J. B.; Longo J. M. In *Crystallographic and Magnetic Properties of Perovskite and Perovskite-Related Compounds*; Hellwege, K.-H., Hellwege A. M., Eds.; Landolt-Börnstein Group III, Vol. 4, Part a; Springer-Verlag: Berlin, 1970, pp 126–314.

[36] Wollan, E. O.; Koehler, W. C. Neutron Diffraction Study of the Magnetic Properties of the Series of Perovskite-Type Compounds [(1-x)La, xCa]MnO$_3$. *Physical Review* **1955**, *100* (2), 545–563.

[37] Goodenough, J. B. Theory of the Role of Covalence in the Perovskite-Type Manganites [La,M(II)]MnO$_3$. *Physical Review* **1955**, *100* (2), 564–573.

[38] Standley, K. J. *Oxide Magnetic Materials*, 2nd ed.; Bawn, C. E. H., Hirsch, P. B., Frohlich, H., Mott, N. F., Eds.; Monographs on the Physics and Chemistry of Materials; Clarendon Press: Oxford, U. K., 1972.

[39] Clothier, B. A.; Jung, D. Y.; Han, P. D.; Xu, Z. K.; Payne, D. A. Magnetic Field and Pressure Effects on the Electrical Resistivity of Single Crystal Pr$_{2/3}$(Ca,Pb)$_{1/3}$MnO$_3$. *Journal of Electroceramics* **1999**, *3* (3), 225–232.

[40] Liu, J. Z.; Chang, I. C.; Irons, S.; Klavins, P.; Shelton, R. N.; Song, K.; Wasserman, S. R. Giant Magnetoresistance at 300K in Single Crystals of La$_{0.65}$(PbCa)$_{0.35}$MnO$_3$. *Applied Physics Letters* **1995**, *66* (23), 3218–3220.

[41] Schiffer, P.; Ramirez, A. P.; Bao, W.; Cheong, S.-W. Low Temperature Magnetoresistance and the Magnetic Phase Diagram of La$_{1-x}$Ca$_x$MnO$_3$. *Physical Review Letters* **1995**, *75* (18), 3336–3339.

[42] Chen, C. H.; Cheong, S.-W.; Hwang, H. Y. Charge-Ordered Stripes in La$_{1-x}$Ca$_x$MnO$_3$ with x > 0.5. *Journal of Applied Physics* **1997**, *81* (8), 4326–4330.

[43] Tao, J.; Zuo, J. M. Nanometer-Sized Regions of Charge Ordering and Charge Melting in La$_{2/3}$Ca$_{1/3}$MnO$_3$ Revealed by Electron Diffraction. *Physical Review B* **2001**, *63* (6), R060407-1–R060407-4.

[44] Tao, J.; Zuo, J. M. Nanoscale Phase Competition during Charge Ordering in Intrinsically Strained La$_{0.33}$Ca$_{0.67}$MnO$_3$. *Physical Review B* **2004**, *69* (18), R180404-1–R180404-4.

[45] Tao, J. Phase Transformations in La$_{1-x}$Ca$_x$MnO$_3$: Charge Ordering and Phase Competition. Ph. D. Thesis, University of Illinois, Urbana, IL, Feb 2005.

[46] Kuwahara, H.; Tomioka, Y.; Asamitsu, A.; Morimoto, Y.; Tokura, Y. A First-Order Phase Transition Induced by a Magnetic Field. *Science* **1995**, *270* (5238), 961–963.

[47] Tokura, Y.; Tomioka, Y.; Kuwahara, H.; Asamitsu, A.; Morimoto, Y.; Kasai, M. Origins of Colossal Magnetoresistance in Perovskite-Type Manganese Oxides. *Journal of Applied Physics* **1996**, *79* (8), 5288–5291.

[48] Tokura, Y.; Nagaosa, N. Orbital Physics in Transition-Metal Oxides. *Science* **2000**, *288* (5465), 462–468.

[49] Zener, C. Interaction Between the d-Shells in the Transition Metals. II. Ferromagnetic Compounds of Manganese with Perovskite Structure. *Physical Review* **1951**, *82* (3), 403–405.

[50] Goodenough, J. B.; Loeb, A. L. Theory of Ionic Ordering, Crystal Distortion, and Magnetic Exchange Due to Covalent Forces in Spinels. *Physical Review* **1955**, *98* (2), 391–408.

[51] Kramers, H. A. L'Interaction Entre Les Atomes Magnétogènes Dans Un Cristal Paramagnétique. *Physica* **1934**, *1*, 182–192.

[52] Anderson, P. W. Antiferromagnetism. Theory of Superexchange Interaction. *Physical Review* **1950**, *79* (2), 350–356.

[53] Kanamori, J. Superexchange Interaction and Symmetry Properties of Electron Orbitals. *Journal of Physics and Chemistry of Solids* **1959**, *10* (2–3), 87–98.

[54] Tofield, B. C.; Scott, W. R. Oxidative Nonstoichiometry in Perovskites, an Experimental Survey; the Defect Structure of an Oxidized Lanthanum Manganite by Powder Neutron Diffraction. *Journal of Solid State Chemistry* **1974**, *10* (3), 183–194.

[55] Van Roosmalen, J. A. M.; Cordfunke, E. H. P. The Defect Chemistry of $LaMnO_{3\pm\delta}$ 2. Structural Aspects of $LaMnO_{3+\delta}$. *Journal of Solid State Chemistry* **1994**, *110* (1), 100–105.

[56] Van Roosmalen, J. A. M.; Cordfunke, E. H. P. The Defect Chemistry of $LaMnO_{3\pm\delta}$ 3. The Density of $(La,A)MnO_{3+\delta}$ (A = Ca, Sr, Ba). *Journal of Solid State Chemistry* **1994**, *110* (1), 106–108.

[57] Van Roosmalen, J. A. M.; Cordfunke, E. H. P. The Defect Chemistry of $LaMnO_{3\pm\delta}$ 4. Defect Model for $LaMnO_{3+\delta}$. *Journal of Solid State Chemistry* **1994**, *110* (1), 109–112.

[58] Van Roosmalen, J. A. M.; Cordfunke, E. H. P. The Defect Chemistry of $LaMnO_{3\pm\delta}$ 5. Thermodynamics. *Journal of Solid State Chemistry* **1994**, *110* (1), 113–117.

[59] Kröger, F. A.; Vink, H. J. Relations between the Concentrations of Imperfections in Crystalline Solids. In *Solid State Physics: Advances in Research and Applications*; Seitz, F., Turnbull, D., Eds.; Academic Press: New York, 1956; Vol. 3, pp 307–435.

[60] Kröger, F. A. *The Chemistry of Imperfect Crystals*, 2nd ed.; North Holland Publishing: Amsterdam, 1974.

[61] Mizusaki, J.; Tagawa, H.; Naraya, K.; Sasamoto, T. Nonstoichiometry and Thermochemical Stability of the Perovskite-Type $La_{1-x}Sr_xMnO_{3-\delta}$. *Solid State Ionics* **1991**, *49* (Dec), 111–118.

[62] Komornicki, S.; Fournès, L.; Grenier, J.-C.; Ménil, F.; Pouchard, M.; Hagenmuller, P. Investigation of Mixed Valency Ferrites $La_{1-x}Ca_xFeO_{3-y}$ ($0 \le x \le 0.5$) with the Perovskite Structure. *Materials Research Bulletin* **1981**, *16* (8), 967–973.

[63] Van Roosmalen, J. A. M.; Cordfunke, E. H. P. A New Defect Model to Describe the Oxygen Deficiency in Perovskite-Type Oxides. *Journal of Solid State Chemistry* **1991**, *93* (1), 212–219.

[64] Kuo, J. H.; Anderson, H. U.; Sparlin, D. M. Oxidation-Reduction Behavior of Undoped and Sr-Doped LaMnO$_3$ Nonstoichiometry and Defect Structure. *Journal of Solid State Chemistry* **1989**, *83* (1), 52–60.

[65] Nakamura, K. The Defect Chemistry of La$_{1-\Delta}$MnO$_{3+\delta}$. *Journal of Solid State Chemistry* **2003**, *173* (2), 299–308.

[66] Ju, H. L.; Gopalakrishnan, J.; Peng, J. L.; Li, Qi; Xiong, G. C.; Venkatesan, T.; Greene, R. L. Dependence of Giant Magnetoresistance on Oxygen Stoichiometry and Magnetization in Polycrystalline La$_{0.67}$Ba$_{0.33}$MnO$_z$. *Physical Review B* **1995**, *51* (9), 6143–6146.

[67] Mahendiran, R.; Mahesh, R.; Raychaudhuri, A. K.; Rao, C. N. R. Room Temperature Giant Magnetoresistance in La$_{1-x}$Pb$_x$MnO$_3$. *Journal of Physics D: Applied Physics* **1995**, *28* (8), 1743–1745.

[68] Brinker, C. J.; Scherer, G. W. *Sol-Gel Science: The Physics and Chemistry of Sol-Gel Processing*; Academic Press: San Diego, CA, 1989.

[69] Flory, P. J. *Principles of Polymer Chemistry*; Cornell University Press: Ithaca, NY, 1953.

[70] Flory, P. J. Introductory Lecture. *Faraday Discussions of the Chemical Society* **1974**, *57*, 7–18.

[71] Rabinovich, E. M. Particulate Silica Gels and Glasses from the Sol-Gel Process. In *Sol-Gel Technology for Thin Films, Fibers, Preforms, Electronics, and Specialty Shapes*; Klein, L. C., Ed.; Noyes Publications: Park Ridge, NJ, 1988; pp 260–294.

[72] Overbeek, J. Th. G. Recent Developments in the Understanding of Colloidal Stability. *Journal of Colloid and Interface Science* **1977**, *58* (2), 408–422.

[73] Matijević, E. Monodispersed Metal (Hydrous) Oxides—A Fascinating Field of Colloid Science. *Accounts of Chemical Research* **1981**, *14* (1), 22–29.

[74] Ebelmen, J. J. Untersuchungen über die Verbindungen der Borsäure und Kieselsäure mit Aether. *Annalen der Chemie und Pharmacie* **1846**, *57* (3), 319–355.

[75] Ebelmen, J. J.; Bouquet M. Sur de Nouvelles Combinaisons de l'Acide Borique avec les Éthers, et sur l'Éther Sulfureux. *Annales de Chimie et de Physique* **1846**, *17*, 54–73.

[76] Bradley, D. C.; Mehrotra, R. C.; Gaur, D. P. *Metal Alkoxides*; Academic Press: London, 1978.

[77] Bradley, D. C.; Mehrotra, R. C.; Rothwell, I. P.; Singh, A. *Alkoxo and Aryloxo Derivatives of Metals*; Academic Press: San Diego, CA, 2001.

[78] Turova, N. Y.; Turevskaya, E. P.; Kessler, V. G.; Yanovskaya, M. I. *The Chemistry of Metal Alkoxides*; Kluwer Academic Publishers: Boston, MA, 2002.

[79] Mehrotra, R. C. Synthesis and Reactions of Metal Alkoxides. *Journal of Non-Crystalline Solids* **1988**, *100* (1), 1–15.

[80] Bradley, D. C. A Structural Theory for Metal Alkoxide Polymers. *Nature* **1958**, *182* (4644), 1211–1214.

[81] Ibers, J. A. Crystal and Molecular Structure of Titanium (IV) Ethoxide. *Nature* **1963**, *197* (4868), 686–687.

[82] Martin, R. L.; Winter, G. Association of Titanium (IV) Alkoxides in Benzene. *Nature* **1963**, *197* (4868), 687.

[83] Chisholm, M. H.; Rothwell, I. P. Alkoxides and Aryloxides. In *Comprehensive Coordination Chemistry: The Synthesis, Reactions, Properties, and Applications of Coordination Compounds*; Wilkinson, G., Gillard, R. D., McCleverty, J. A., Eds.; Pergamon Press: Oxford, U. K., 1987; pp 335–364.

[84] Bradley, D. C.; Mehrotra, R. C.; Wardlaw, W. Structural Chemistry of the Alkoxides. Part I. Amyloxides of Silicon, Titanium, and Zirconium. *Journal of the Chemical Society* **1952**, (2), 2027–2032.

[85] Bradley, D. C.; Mehrotra, R. C.; Wardlaw, W. Structural Chemistry of the Alkoxides. Part II. Tertiary Alkoxides of Silicon, Titanium, Zirconium, and Hafnium. *Journal of the Chemical Society* **1952**, (4), 4204–4209.

[86] Bradley, D. C.; Mehrotra, R. C.; Wardlaw, W. Structural Chemistry of the Alkoxides. Part III. Secondary Alkoxides of Silicon, Titanium, and Zirconium. *Journal of the Chemical Society* **1952**, (4), 5020–5023.

[87] Bradley, D. C.; Mehrotra, R. C.; Swanwick, J. D.; Wardlaw, W. Structural Chemistry of the Alkoxides. Part IV. Normal Alkoxides of Silicon, Titanium, and Zirconium. *Journal of the Chemical Society* **1953**, (2), 2025–2030.

[88] Bradley, D. C.; Gaze, R.; and Wardlaw, W. Structural Aspects of the Hydrolysis of Titanium Alkoxides. *Journal of the Chemical Society* **1957**, (1), 469–478.

[89] Livage, J.; Henry, M. A Predictive Model for Inorganic Polymerization Reactions. In *Ultrastructure Processing of Advanced Ceramics*, Proceedings of the Third International Conference on Ultrastructure Processing of Ceramics, Glasses, and Composites, San Diego, CA, Feb 23–27, 1987; Mackenzie, J. D., Ulrich, D. R., Eds.; John Wiley and Sons: New York, 1988; pp 183–195.

[90] Livage, J.; Henry, M.; Sanchez, C. Sol-Gel Chemistry of Transition Metal Oxides. *Progress in Solid State Chemistry* **1988**, *18* (4), 259–341.

[91] Watenpaugh, K.; Caughlan, C. The Crystal and Molecular Structure of the First Hydrolysis Product Product ($Ti_7O_{24}Et_{19}$) of Titanium Tetraethoxide. *Chemical Communications* **1967**, (2), 76–77.

[92] Morosin, B. Molecular Configuration of a Tridecazirconium Oxide-Methoxide Complex. *Acta Crystallographica, Section B* **1977**, *33* (1), 303–305.

[93] Day, V. W.; Klemperer, W. G.; Mainz, V. V.; Millar, D. M. Molecular Building Blocks for the Synthesis of Ceramic Materials: $[Si_8O_{12}](OCH_3)_8$. *Journal of the American Chemical Society* **1985**, *107* (26), 8262–8264.

[94] Klemperer, W. G.; Mainz, V. V.; Millar, D. M. A Solid State Multinuclear Magnetic Resonance Study of the Sol-Gel Process using Polysilicate Precursors. In *Better Ceramics Through Chemistry II*, Materials Research Society Symposia Proceedings, Vol. 73, Palto Alto, CA, Apr 15–19, 1986; Brinker, C. J., Clark, D. E., Ulrich, D. R., Eds.; Materials Research Society: Pittsburgh, PA, 1986; pp 15–25.

[95] Cagle, P. C.; Klemperer, W. G.; Simmons, C. A. Molecular Architecture and its Role in Silica Sol-Gel Polymerization. In *Better Ceramics Through Chemistry IV*, Materials Research Society Symposia Proceedings, Vol. 180, San Francisco, CA, Apr 16–20, 1990; Zelinski, B. J. J., Brinker, C. J., Clark, D. E., Ulrich, D. R., Eds.; Materials Research Society: Pittsburgh, PA, 1990; pp 29–37.

[96] Kessler, V. G. Molecular Structure Design and Synthetic Approaches to the Heterometallic Alkoxide Complexes (Soft Chemistry Approach to Inorganic Materials by the Eyes of a Crystallographer). *Chemical Communications* **2003**, (11), 1213–1222.

[97] Springer, L.; Yan, M. F. Sintering of TiO_2 from Organometallic Precursors. In *Ultrastructure Processing of Ceramics, Glasses, and Composites*, Proceedings of the International Conference, Gainsville, FL, Feb 13–17, 1983; Hench, L. L., Ulrich, D. R., Eds.; John Wiley and Sons: New York, 1984; pp 464–475.

[98] Yoldas, B. E. Zirconium Oxides Formed by Hydrolytic Condensation of Alkoxides and Parameters that Affect their Morphology. *Journal of Materials Science* **1986**, *21* (3), 1080–1086.

[99] Kundu, D.; Ganguli, D. Monolithic Zirconia Gels from Metal-Organic Solutions. *Journal of Materials Science Letters* **1986**, *5* (3), 293–295.

[100] Vaartstra, B. A.; Huffman, J. C.; Gradeff, P. S.; Hubert-Pfalzgraf, L. G.; Daran, J.-C.; Parraud, S.; Yunlu, K.; Caulton, K. G. Alcohol adducts of Alkoxides: Intermolecular Hydrogen Bonding as a General Structural Feature. *Inorganic Chemistry* **1990**, *29* (17), 3126–3131.

[101] Hasenkox, U.; Mitze, C.; Waser, R. Metal Propionate Synthesis of Magnetoresistive $La_{1-x}(Ca,Sr)_xMnO_3$ Thin Films. *Journal of the American Ceramic Society* **1997**, *80* (10), 2709–2713.

[102] Hasenkox, U.; Mitze, C.; Waser, R. Chemical Solution Deposition of Epitaxial $La_{1-x}(Ca, Sr)_xMnO_3$ Thin Films. *Journal of Electroceramics* **1999**, *3* (3), 255–260.

[103] Mehrotra, R. C.; Bohra, R. *Metal Carboxylates*; Academic Press: London, 1983.

[104] Bradley, D. C.; Carter, D. G. Metal Oxide Alkoxide Polymers Part I. The Hydrolysis of Some Primary Alkoxides of Zirconium. *Canadian Journal of Chemistry* **1961**, *39* (7), 1434–1443.

[105] Bradley, D. C.; Holloway, H. Metal Oxide Alkoxide Polymers Part II. The Hydrolysis of Tantalum Pentaethoxide. *Canadian Journal of Chemistry* **1961**, *39* (9), 1818–1826.

[106] Bradley, D. C.; Carter, D. G. Metal Oxide Alkoxide Polymers Part III. The Hydrolysis of Secondary and Tertiary Alkoxides of Zirconium. *Canadian Journal of Chemistry* **1962**, *40* (1), 15–21.

[107] Bradley, D. C.; Holloway, H. Metal Oxide Alkoxide Polymers Part IV. The Hydrolysis of Some Tantalum Alkoxides. *Canadian Journal of Chemistry* **1962**, *40* (1), 62–72.

[108] Bradley, D. C.; Holloway, H. Metal Oxide Alkoxide Polymers Part V. The Hydrolysis of Some Alkoxides of Tin (IV), Cerium (IV), and Uranium (V). *Canadian Journal of Chemistry* **1962**, *40* (6), 1176–1182.

[109] Bradley, D. C. Metal Oxide Alkoxide (Trialkylsilyloxide) Polymers. *Coordination Chemistry Reviews* **1967**, *2* (3), 299–318.

[110] Goloboy, J. C.; Klemperer, W. G.; Marquart, T. A.; Westwood, G.; Yaghi, O. M. Complex Oxides as Molecular Materials: Structure and Bonding in High-Valent Early Transition Metal Compounds. In *Polyoxometalate Molecular Science*; Borrás-Almenar, J. J.; Coronado, E.; Müller, A.; Pope, M. T., Eds.; Kluver Academic Publishers: Dordrecht, The Netherlands, 2003; pp 79–174.

[111] Barringer, E. A.; Bowen, H. K. High-Purity, Monodisperse TiO_2 Powders by Hydrolysis of Titanium Tetraethoxide. 1. Synthesis and Physical Properties. *Langmuir* **1985**, *1* (4), 414–420.

[112] Fegley, B.; White, P.; Bowen, H. K. Preparation of Zirconia-Alumina Powders by Zirconium Alkoxide Hydrolysis. *Journal of the American Ceramic Society* **1985**, *68* (2), C60–C62.

[113] Birnie, D. P., III. Surface Skin Development and Rupture During Sol-Gel Spin-Coating. *Journal of Sol-Gel Science and Technology* **2004**, *31* (1–3), 225–228.

[114] Sakka, S.; Kamiya, K.; Makita, K.; Yamamoto, Y. Formation of Sheets and Coating Films from Alkoxide Solutions. *Journal of Non-Crystalline Solids* **1984**, *63* (1–2), 223–235.

[115] Yoldas, B. E. Modification of Polymer-Gel Structures. *Journal of Non-Crystalline Solids* **1984**, *63* (1–2), 145–154.

[116] Yoldas, B. E. Molecular and Microstructural Effects of Condensation Reactions in Alkoxide-Based Alumina Systems. In *Ultrastructure Processing of Advanced Ceramics*, Proceedings of the Third International Conference on Ultrastructure Processing of Ceramics, Glasses, and Composites, San Diego, CA, Feb 23–27, 1987; Mackenzie, J. D., Ulrich, D. R., Eds.; John Wiley and Sons: New York, 1988; pp 333–345.

[117] Meerwein, H.; Bersin, T. Untersuchungen über Metallalkoholate und Orthosäureester. I. Über Alkoxosäuren und Ihre Salze. *Annalen der Chemie* **1929**, *476* (3) 113–150.

[118] Papiernik, R.; Hubert-Pfalzgraf, L. G.; Chaput, F. Molecular Routes to Ternary Metal Oxides: Pb:Ti Heterometallic Oxoisopropoxide as a Precursor to PbTiO$_3$. *Journal of Non-Crystalline Solids* **1992**, *147–148*, 36–40.

[119] Caulton, K. G.; Hubert-Pfalzgraf, L. G. Synthesis, Structural Principles, and Reactivity of Heterometallic Alkoxides. *Chemical Reviews* **1990**, *90* (6), 969–995.

[120] Campion, J.-F.; Payne, D. A.; Chae, H. K.; Maurin, J. K.; Wilson, S. R. Synthesis of Bimetallic Barium Titanium Alkoxides as Precursors for Electrical Ceramics. Molecular Structure of the New Barium Titanium Oxide Alkoxide Ba$_4$Ti$_{13}$(μ_3-O)$_{12}$(μ_5-O)$_6$(μ_1-η^1-OCH$_2$CH$_2$OCH$_3$)$_{12}$(μ_1,μ_3-η^2-OCH$_2$CH$_2$OCH$_3$)$_{12}$. *Inorganic Chemistry* **1991**, *30* (17), 3244–3245.

[121] Turevskaya, E. P.; Turova, N. Y.; Novoselova, A. V. Interaction of Calcium and Titanium Ethoxides. *Russian Journal of Inorganic Chemistry* **1978**, *23* (3), 355–358.

[122] Riman, R. E. The Role of the Chemical Processing Variables for the Synthesis of Ideal Alkoxy-Derived SrTiO$_3$ Powder. Ph. D. Thesis, Massachusetts Institute of Technology, Cambridge, MA, Feb 1987.

[123] Turevskaya, E. P.; Yanovskaya, M. I.; Lymar, V. K.; Turova, N. Y. Bimetallic Barium-Titanium Alcoholates and Their Reactions of Decomposition with the Formation of Oxocomplexes. *Russian Journal of Inorganic Chemistry* **1993**, *38* (4), 609–617.

[124] Prassas, M.; Hench, L. L. Physical Chemical Factors in Sol-Gel Processing. In *Ultrastructure Processing of Ceramics, Glasses, and Composites*, Proceedings of the International Conference, Gainsville, FL, Feb 13–17, 1983; Hench, L. L., Ulrich, D. R., Eds.; John Wiley and Sons: New York, 1984; pp 100–125.

[125] Kirby, K. W. Alkoxide Synthesis Techniques for BaTiO$_3$. *Materials Research Bulletin* **1988**, *23* (6), 881–890.

[126] Frey, M. H. Grain Size Effect on Structure and Properties for Chemically Prepared Barium Titanate. Ph. D. Thesis, University of Illinois, Urbana, IL, May 1996.

[127] Templeton, L. K.; Pask, J. A. Formation of BaTiO$_3$ from BaCO$_3$ and TiO$_2$ in Air and CO$_2$. *Journal of the American Ceramic Society* **1959**, *42* (5), 212–216.

[128] Gopalakrishnamurthy, H. S.; Rao, M. S.; Kutty, T. R. N. Thermal Decomposition of Titanyl Oxalates—I Barium Titanyl Oxalate. *Journal of Inorganic and Nuclear Chemistry* **1975**, *37* (4), 891–898.

[129] Kumar, S.; Messing, G. L.; White, W. B. Metal Organic Resin Derived Barium Titanate: I, Formation of Barium Titanium Oxycarbonate Intermediate. *Journal of the American Ceramic Society* **1993**, *76* (3), 617–624.

[130] Brinker, C. J.; Scherer G. W. Sol → Gel → Glass: I. Gelation and Gel Structure. *Journal of Non-Crystalline Solids* **1985**, *70* (3), 301–322.

[131] Brinker, C. J.; Scherer G. W. Sol → Gel → Glass: II. Physical and Structural Evolution During Constant Heating Rate Experiments. *Journal of Non-Crystalline Solids* **1985**, *72* (2–3), 345–368.

[132] Brinker, C. J.; Scherer G. W. Sol → Gel → Glass: III. Viscous Sintering. *Journal of Non-Crystalline Solids* **1985**, *72* (2–3), 369–389.

[133] Sengupta, S. S. Evolution of Local Structure and Stress Development During Thermal Treatment of Sol-Gel Derived PZT-Based Thin Layers. Ph. D. Thesis, University of Illinois, Urbana, IL, Aug 1996.

[134] Frenkel, J. Viscous Flow of Crystalline Bodies under the Action of Surface Tension. *Journal of Physics (Moscow)* **1945**, *9* (5), 385–391.

[135] Kuczynski, G. C. Study of the Sintering of Glass. Journal of Applied Physics **1949**, *20* (11), 1160–1163.

[136] Exner, H. E.; Petzow, G. Shrinkage and Rearrangement during Sintering of Glass Spheres. In *Sintering and Catalysis*, Proceedings of the Fourth International Conference on Sintering and Related Phenomena, Notre Dame, IN, May 26–28, 1975; Kuczynski, G. C., Ed.; Plenum Press: New York, 1975; pp 279–293.

[137] Kingery, W. D.; Berg, M. Study of the Initial Stages of Sintering Solids by Viscous Flow, Evaporation-Condensation, and Self-Diffusion. *Journal of Applied Physics* **1955**, *26* (10), 1205–1212.

[138] Varshneya, A. K. *Fundamentals of Inorganic Glasses*; Academic Press: Boston, 1994.

[139] Rahaman, M. N. *Ceramic Processing and Sintering*; Marcel Dekker: New York, 1995.

[140] Seigle, L. L. Powder Metallurgy Fundamentals Lecture: Atom Movements during Solid State Sintering. In *Progress in Powder Metallurgy*, Proceedings of the Twentieth Annual Powder Metallurgical Technical Conference and Magnetic Inductance Core Conference, Vol. 20, Chicago, IL, Apr 27–29, 1964; Metal Powder Industries Federation: New York, 1964; pp 221–238.

[141] Frey, M. H.; Payne, D. A. Synthesis and Processing of Barium Titanate Ceramics from Alkoxide Solutions and Monolithic Gels. *Chemistry of Materials* **1995**, *7* (1), 123–129.

[142] Mayer, J. W.; Lau, S. S. *Electronic Materials Science: For Integrated Circuits in Si and GaAs*; Macmillan Publishing, Co.: New York, 1990; Chapter 7.

[143] Bornside, D. E.; Macosko, C. W.; Scriven, L. E. On the Modeling of Spin Coating. *Journal of Imaging Technology* **1987**, *13* (4), 122–130.

[144] Scriven, L. E. Physics and Applications of Dip Coating and Spin Coating. In *Better Ceramics Through Chemistry III*, Materials Research Society Symposia Proceedings, Vol. 121, Reno, NV, Apr 5–8, 1988; Brinker, C. J., Clark, D. E., Ulrich, D. R., Eds.; Materials Research Society: Pittsburgh, PA, 1988; pp 717–729.

[145] Emslie, A. G.; Bonner, F. T.; Peck, L. G. Flow of a Viscous Liquid on a Rotating Disk. *Journal of Applied Physics* **1958**, *29* (5), 858–862.

[146] Meyerhofer, D. Characteristics of Resist Films Produced by Spinning. *Journal of Applied Physics* **1978**, *49* (7), 3993–3997.

[147] Birnie, D. P., III. Rational Solvent Selection Strategies to Combat Striation Formation During Spin Coating of Thin Films. *Journal of Materials Research* **2001**, *16* (4), 1145–1154.

[148] Haas, D. E.; Birnie, D. P., III. Nondestructive Measurement of Striation Defect Spacing Using Laser Diffraction. *Journal of Materials Research* **2001**, *16* (12), 3355–3360.

[149] Mikalsen, E. A. Mediated Patterning of Sol-Gel Thin Layers: Shrinkage, De-Cohesion, and Lift-Off. Ph. D. Thesis, University of Illinois, Urbana, IL, May 2003.

[150] Brinker, C. J.; Hurd, A. J.; Ward, K. J. Fundamentals of Sol-Gel Thin-Film Formations. In *Ultrastructure Processing of Advanced Ceramics*, Proceedings of the Third International Conference on Ultrastructure Processing of Ceramics, Glasses, and Composites, San Diego, CA, Feb 23–27, 1987; Mackenzie, J. D., Ulrich, D. R., Eds.; John Wiley and Sons: New York, 1988; pp 223–240.

[151] Ramamurthi, S. D.; Payne, D. A. Structural Investigations of Prehydrolyzed Precursors Used in the Sol-Gel Processing of Lead Titanate. *Journal of the American Ceramic Society* **1990**, *73* (8), 2547–2551.

[152] Hubert-Pfalzgraf, L. G. Heterometallic Alkoxides and Oxoalkoxides as Intermediates in Chemical Routes to Mixed Metal Oxides. *Polyhedron* **1994**, *13* (8), 1181–1195.

[153] Hubert-Pfalzgraf, L. G. Metal Alkoxides and β-Diketonates as Precursors for Oxide and Non-Oxide Thin Films. *Applied Organometallic Chemistry* **1992**, *6* (8), 627–643.

[154] McMurry, J. *Organic Chemistry*, 4th ed.; Brooks/Cole Publishing: Pacific Grove, CA, 1996; pp 171–172.

[155] Bae, S.-Y.; Wang, S. X. Sol-Gel Epitaxial Growth of $La_{1-x}Ca_xMnO_3$ with Colossal Magnetoresistance Effect. *Applied Physics Letters* **1996**, *69* (1), 121–123.

[156] Clothier, B. A.; Jung, D.-Y. University of Illinois, Urbana, IL. Unpublished work, 1998.

[157] Jung, D.-Y.; Payne, D. A. Patterning of Rare-Earth Manganate Thin Layer Using Self-Assembled Organic Thin-Film Templates. *Bulletin of the Korean Chemical Society* **1999**, *20* (7), 824–826.

[158] Beck, H. P.; Eiser, W.; Haberkorn, R. Pitfalls in the Synthesis of Nanoscaled Perovskite Compounds. Part I: Influence of Different Sol-Gel Preparation Methods and Characterization of Nanoscaled BaTiO$_3$. *Journal of the European Ceramic Society* **2001**, *21* (6), 687–693.

[159] Mehrotra, R. C.; Bohra, R.; Gaur, D. P. *Metal β-Diketonates and Allied Derivatives*; Academic Press: London, 1978.

[160] Patil, K. C.; Chandrashekhar, G. V.; George, M. V.; Rao, C. N. R. Infrared Spectra and Thermal Decompositions of Metal Acetates and Dicarboxylates. *Canadian Journal of Chemistry* **1968**, *46* (2), 257–265.

[161] Judd, M. D.; Plunkett, B. A.; Pope, M. I. The Thermal Decomposition of Calcium, Sodium, Silver, and Copper(II) Acetates. *Journal of Thermal Analysis* **1974**, *6* (5), 555–563.

[162] Shriver, D. F.; Atkins, P.; Langford, C. H. *Inorganic Chemistry*, 2nd ed.; W. H. Freeman and Company: New York, 1994; pp 174–176.

[163] Sanchez, C.; Babonneau, F.; Doeuff, S.; Leaustic, A. Chemical Modifications of Titanium Precursors. In *Ultrastructure Processing of Advanced Ceramics*, Proceedings of the Third International Conference on Ultrastructure Processing of Ceramics, Glasses, and Composites, San Diego, CA, Feb 23–27, 1987; Mackenzie, J. D., Ulrich, D. R., Eds.; John Wiley and Sons: New York, 1988; pp 77–87.

[164] Livage, J.; Sanchez, C.; Henry, M.; Doeuff, S. The Chemistry of the Sol-Gel Process. *Solid State Ionics* **1989**, *32–33* (2), 633–638.

[165] Sanchez, C.; Livage, J.; Henry, M.; Babonneau, F. Chemical Modification of Alkoxide Precursors. *Journal of Non-Crystalline Solids* **1988**, *100* (1–3), 65–76.

[166] Babonneau, F.; Leaustic, A.; Livage, J. Structural Investigation of the Hydrolysis-Condensation Process of a Modified Titanium Alkoxide. In *Better Ceramics Through Chemistry III*, Materials Research Society Symposia Proceedings, Vol. 121, Reno, NV, Apr 5–8, 1988; Brinker, C. J., Clark, D. E., Ulrich, D. R., Eds.; Materials Research Society: Pittsburgh, PA, 1988; pp 317–322.

[167] Hubert-Pfalzgraf, L. G. Heterometallic Aggregates as Intermediates on the Molecular Routes to Multicomponent Oxides. In *Better Ceramics Through Chemistry V*, Materials Research Society Symposia Proceedings, Vol. 271, San Francisco, CA, Apr 27–May 1, 1992; Hampden-Smith, M. J., Klemperer, W. G., Brinker, C. J., Eds.; Materials Research Society: Pittsburgh, PA, 1992; pp 15–25.

[168] Edwards, D. A.; Hayward, R. N. Transition Metal Acetates. *Canadian Journal of Chemistry* **1968**, *46* (22), 3443–3446.

[169] Maizell, R. E. *How to Find Chemical Information: A Guide for Practicing Chemists, Educators, and Students*; John Wiley and Sons: New York, 1998.

[170] Kandelaki, B. S. Hydrolysis and Gelation of Ethylates (in Russian). *Kolloidnyi Zhurnal* **1937**, *3* (6), 483–499; *Chemical Abstracts* **1938**, *32*, 6227[1].

[171] Druce, J. G. F. Ethoxides and isoPropoxides of Manganese and Rhenium. *Journal of the Chemical Society* **1937**, (2), 1407–1408.

[172] Prasad, S.; Kacker, K. P. Phenoxides of Manganese. *Journal of the Indian Chemical Society* **1958**, *35* (12), 890–892.

[173] Adams, R. W.; Bishop, E.; Martin, R. L.; Winter, G. Magnetism, Electronic Spectra, and Structure of Transition Metal Alkoxides. *Australian Journal of Chemistry* **1966**, *19* (2), 207–210.

[174] Adams, R. W.; Martin, R. L.; Winter, G. Possible Ligand Field Effects in Metal-Oxygen Vibrations of Some First-Row Transition Metal Alkoxides. *Australian Journal of Chemistry* **1967**, *20* (4), 773–774.

[175] Radoslovich, E. W.; Raupach, M.; Slade, P. G.; Taylor, R. M. Crystalline Cobalt, Zinc, Manganese, and Iron Alkoxides of Glycerol. *Australian Journal of Chemistry* **1970**, *23* (10), 1963–1971.

[176] Horvath, B.; Möseler, R.; Horvath, E. G. Manganese(II) Alkoxides. *Zeitschrift für Anorganische und Allgemeine Chemie* **1979**, *449*, 41–51.

[177] Bochmann, M.; Wilkinson, G.; Young, G. B.; Hursthouse, M. B.; Abdul Malik, K. M. Synthesis and Properties of Bis(t-butyl)methoxides of Chromium(III,IV), Manganese(II), Iron(III), Cobalt(II), and Copper(I). The Crystal and Molecular Structures of Lithium Tetrakis[bis(t-butyl)methoxo]chromate-(III)–Tetrahydrofuran (1/1), Tetrakis[bis(t-butyl)methoxo]chromate-(IV), and Lithium Tetrakis[bis(t-butyl)methoxo]ferrate(III)–Bis(t-butyl)-methanol (1/1). *Journal of the Chemical Society, Dalton Transactions* **1980**, (10), 1863–1870.

[178] Murray, B. D.; Power, P. P. Monomeric Manganese(II) Alkoxides: Synthesis and X-ray Crystal Structures of Novel Three- and Four-Coordinate Manganese Complexes of the Tri-tert-butylmethoxide Ligand. *Journal of the American Chemical Society* **1984**, *106* (23), 7011–7015.

[179] Murray, B. D.; Hope, H.; Power, P. P. An Unusual C—C Bond Cleavage in a Bulky Metal Alkoxide: Syntheses and X-ray Crystal Structures of Three-Coordinate Mn(II) and Cr(II) Complexes Containing the Di-tert-butylmethoxide Ligand. *Journal of the American Chemical Society* **1985**, *107* (1), 169–173.

[180] Dubey, R. K.; Singh, A.; Mehrotra, R. C. Synthesis and Characterization of Novel Homo- and Hetero-leptic Alkoxometallates of Manganese(II). *Indian Journal of Chemistry* **1992**, *31A* (7–12), 156–159.

[181] Schake, A. R.; Schmitt, E. A.; Conti, A. J.; Streib, W. E.; Huffmann, J. C.; Hendrickson, D. N.; Christou, G. Preparation and Properties of Mononuclear and Ferromagnetically Coupled Dinuclear Manganese Complexes with 2,2'-Biphenoxide. *Inorganic Chemistry* **1991**, *30* (16), 3192–3199.

[182] Greenwood, N. N.; Earnshaw, A. *Chemistry of the Elements*, 2nd ed.; Butterworth-Heinemann: Oxford, U. K., 1997; pp 1044–1049.

[183] Bertaut, E. F.; Duc, T. Q.; Burlet, P.; Burlet, P.; Thomas, M.; Moreau, J. M. Crystal Structure of Manganese Acetate Tetrahydrate. *Acta Crystallographica, Section B* **1974**, *30* (9), 2234–2236.

[184] Mehrotra, R. C.; Mahendra, K. N.; Aggrawal, M. Alcoholate Derivatives of 3*d* Transition Metal Chlorides. *Proceedings of the Indian Academy of Sciences (Chemical Sciences)* **1984**, *93* (4), 719–727.

[185] Misra, S. N.; Misra, T. N.; Mehrotra, R. C. Organic Compounds of Lanthanide Elements—III Alcoholates of Lanthanum and Cerium (III) Chlorides. *Journal of Inorganic and Nuclear Chemistry* **1965**, *27* (1), 105–113.

[186] Mehrotra, R. C.; Misra, T. N.; Misra, S. N. Organic Compounds of Lanthanide Elements. Part IV. Alcoholates of Praseodymium and Neodymium Chlorides. *Journal of the Indian Chemical Society* **1965**, *42* (6), 351–358.

[187] Evans, W. J.; Sollberger, M. S.; Hanusa, T. P. Synthesis and Structure of the Polymetallic Yttrium Alkoxide Complex $Y_3(\mu_3\text{-OCMe}_3)(\mu_3\text{-Cl})(\mu\text{-OCMe}_3)(\text{OCMe}_3)_4(\text{THF})_2$ and Related Complexes: $Ln_3(\mu_3\text{-OR})(\mu_3\text{-X})(\mu\text{-OR})_3$ Building Blocks in Yttrium and Lanthanide Alkoxide Chemistry. *Journal of the American Chemical Society* **1988**, *110* (6), 1841–1850.

[188] Anwander, R. Principles in Organolanthanide Chemistry. In *Lanthanides: Chemistry and Use in Organic Synthesis*; Kobayashi, S., Ed.; Topics in Organometallic Chemistry; Springer-Verlag: Berlin, 1999; Vol. 2, pp 1–61.

[189] Robiette, A. G.; Sheldrick, G. M.; Sheldrick, W. S.; Beagley, B.; Cruickshank, D. W. J.; Monaghan, J. J.; Aylett, B. J.; Ellis, I. A. The Conformation of Three Disilazanes. *Chemical Communications* **1968**, (15), 909–910.

[190] Bradley, D. C.; Hursthouse, M. B.; Abdul Malik, K. M.; Möseler, R. The Crystal Molecular Structure of "Bis(hexamethyldisilylamido) Manganese". *Transition Metal Chemistry* **1978**, *3* (4), 254–255.

[191] Lappert, M. F.; Power, P. P.; Sanger, A. R.; Srivastava, R. C. *Metal and Metalloid Amides: Syntheses, Structures, and Physical and Chemical Properties*; Ellis Horwood Series in Chemical Science; Ellis Horwood: Chichester, U. K., 1980.

[192] Sauer, R. O. Derivatives of the Methylchlorosilanes. I. Trimethylsilanol and its Simple Ethers. *Journal of the American Chemical Society* **1944**, *66* (10), 1707–1710.

[193] Sauer, R. O.; Hasek, R. H. Derivatives of the Methylchlorosilanes. IV. Amines. *Journal of the American Chemical Society* **1946**, *68* (2), 241–244.

[194] Lappert, M. F.; Harris, D. H. Metal and Metalloid Dialkylamides Containing the Bis(trimethylsilyl)amido or *t*-Butyl(trimethylsilyl)amido Ligand. In *Organometallic Chemistry Reviews: Organosilicon Reviews*; Seyferth, D., Davies, A. G., Fischer, E. O., Normant, J. F., Reutov, O. A., Eds.; Journal of Organometallic Chemistry Library; Elsevier Scientific Publishing: Amsterdam, 1976; Vol. 2, pp 13–102.

[195] Bürger, H.; Wannagat, U. Silylamido- Verbindungen von Chrom, Mangan, Nickel und Kupfer. *Monatshefte für Chemie* **1964**, *95* (4–5), 1099–1102.

[196] Horvath, B.; Möseler, R.; Horvath, E. G. Manganese(II) Silylamides. *Zeitschrift für Anorganische und Allgemeine Chemie* **1979**, *450*, 165–177.

[197] Bradley, D. C.; Ghotra, J. S.; Hart, F. A. Three-co-ordination in Lanthanide Chemistry: Tris[bis(trimethlysilyl)amido]lanthanide(III) Compounds. *Journal of the Chemical Society, Chemical Communications* **1972**, (6), 349–350.

[198] Bradley, D. C.; Ghotra, J. S.; Hart, F. A. Low Co-ordination Numbers in Lanthanide and Actinide Compounds. Part I. The Preparation and Characterization of Tris{bis(trimethylsilyl)-amido}lanthanides. *Journal of the Chemical Society, Dalton Transactions* **1973**, (10), 1021–1023.

[199] Anwander, R. Lanthanide Amides. *Topics in Current Chemistry* **1996**, *179*, 33–112.

[200] Anwander, R. Routes to Monomeric Lanthanide Alkoxides. *Topics in Current Chemistry* **1996**, *179*, 151–245.

[201] Herrmann, W. A.; Anwander, R.; Kleine, M.; Scherer, W. Solvensfreie Alkoxid-Komplexe des Neodyms und Dysprosiums. Kristall- und Molekülstrukur von *trans*-Bis(acetonitril)tris(tri-*tert*-butylmethoxy)neodym. *Chemische Berichte, Part A* **1992**, *125* (9), 1971–1979.

[202] LaDuca, R. L.; Wolczanski, P. T. Preparation of Lanthanide Nitrides via Ammonolysis of Molten {(Me$_3$Si)$_2$N}$_3$Ln: Onset of Crystallization Catalyzed by LiNH$_2$ and LiCl. *Inorganic Chemistry* **1992**, *31* (8), 1311–1313.

[203] Amonoo-Neizer, E. H.; Shaw, R. A.; Skovlin, D. O.; Smith, B. C. In *Lithium Bis(trimethylsilyl)amide and Tris(trimethylsilyl)amine*; Holtzclaw, H. F., Jr.; Brimm, E. O.; Cady, G. H.; Dwyer, F. P.; Jolly, W. L.; Katz, J. J.; Muetterties, E. L.; Netherton, L. E.; Nielsen, M. L.; Parry, R. W.; Scott, J. D.; Tyree, S. Y., Jr.; Wilkinson, G., Eds.; Inorganic Syntheses, Vol. VIII; McGraw-Hill: New York, 1966; pp 19–22.

[204] Davidson, P. J.; Harris, D. H.; Lappert, M. F. Subvalent Group 4B Metal Alkyls and Amides. Part I. The Synthesis and Physical Properties of Kinetically Stable Bis[bis(trimethylsilyl)]-germanium(II), -tin(II), and -lead(II). *Journal of the Chemical Society, Dalton Transactions* **1976**, (21), 2268–2274.

[205] Cotton, J. D.; Davidson, P. J.; Lappert, M. F. Subvalent Group 4B Metal Alkyls and Amides. Part II. The Chemistry and Properties of Bis[bis(trimethylsilyl)]tin (II) and Its Lead Analogue. *Journal of the Chemical Society, Dalton Transactions* **1976**, (21), 2275–2286.

[206] Cotton, J. D.; Davidson, P. J.; Lappert, M. F.; Donaldson, J. D.; Silver, J. Subvalent Group 4B Metal Alkyls and Amides. Part III. Mössbauer Spectroscopy Studies of Bis[bis(trimethylsilyl)]tin (II) and Its Derivatives. *Journal of the Chemical Society, Dalton Transactions* **1976**, (21), 2286–2290.

[207] Gynane, M. J. S.; Harris, D. H.; Lappert, M. F.; Power, P. P.; Rivière, P.; Rivière-Baudet, M. Subvalent Group 4B Metal Alkyls and Amides. Part 5. The Synthesis and Physical Properties of Thermally Stable Amides of Germanium(II), Tin(II), and Lead(II). *Journal of the Chemical Society, Dalton Transactions* **1977**, (20), 2004–2009.

[208] Schaeffer, C. D., Jr.; Myers, L. K.; Coley, S. M.; Otter, J. C.; Yoder, C. H. Preparation, Analysis, and Reactivity of Bis[*N*,*N*-bis(trimethylsilyl)amino]tin(II). An Advanced Undergraduate Laboratory Project in Organometallic Synthesis. *Journal of Chemical Education* **1990**, *67* (4), 347–349.

[209] Goel, S. C.; Chiang, M. Y.; Buhro, W. E. Preparation of Six Lead(II) Dialkoxides, X-ray Crystal Structures of $[Pb(\mu,\eta^1\text{-OCH}_2\text{CH}_2\text{OMe})_2]_\infty$ and $[Pb_3(\mu\text{-O-}t\text{-Bu})_6]$, and Hydrolysis Studies. *Inorganic Chemistry* **1990**, *29* (23), 4640–4646.

[210] Yanovskii, A. I.; Turova, N. Y.; Turevskaya, E. P.; Struchkov, Y. T. Structure of the First Hydrolysis Product of Lead(II) Isopropoxide. *Russian Journal of Coordination Chemistry* **1982**, *8* (2), 153–158.

[211] Papiernik, R.; Hubert-Pfalzgraf, L. G.; Massiani, M.-C. Heavy Main Group Molecular Precursors of Oxides: Volatile and Soluble Lead(II) Alkoxides and Oxoalkoxides. *Inorganica Chimica Acta* **1989**, *165* (1), 1–2.

[212] Turova, N. Y.; Turevskaya, E. P.; Yanovskaya, M. I.; Kotova, N. M.; Shifrina, R. R. Barium Alkoxides. *Russian Journal of Inorganic Chemistry* **1993**, *38* (7), 1137–1142.

[213] Bradley, D. C.; Hursthouse, M. B.; Ibrahim, A. A.; Abdul Malik, K. M.; Motevalli, M.; Möseler, R.; Powell, H.; Runnacles, J. D.; Sullivan, A. C. Synthesis and Chemistry of the Bis(trimethylsilyl)amido Bistetrafuranates of the Group 2 Metals Magnesium, Calcium, Strontium, and Barium. X-ray Crystal Structures of $Mg[N(SiMe_3)_2]_2 \cdot 2THF$ and Related $Mn[N(SiMe_3)_2]_2 \cdot 2THF$. *Polyhedron* **1990**, *9* (24), 2959–2964.

[214] Herrmann, W. A.; Huber, N. W.; Priermeier, T. Solvent-Free Volatile Alkoxides of the Alkaline-Earth Elements. *Angewandte Chemie International Edition in English* **1994**, *33* (1), 105–107.

[215] Westerhausen, M. Synthesis and Spectroscopic Properties of Bis(trimethylsilyl)amides of the Alkaline-Earth Metals Magnesium, Calcium, Strontium, and Barium. *Inorganic Chemistry* **1991**, *30* (1), 96–101.

[216] Vaarstra, B. A.; Huffman, J. C.; Streib, W. E.; Caulton, K. G. Syntheses and Structures of a Series of Very Low Coordinate Barium Compounds: $Ba[N(SiMe_3)_2]_2(THF)_2$, $\{Ba[N(SiMe_3)_2]_2(THF)\}_2$, and $Ba[N(SiMe_3)_2]_2$. *Inorganic Chemistry* **1991**, *30* (1), 121–125.

[217] Pohl, A.; Westin, G.; Jansson, K. Preparation of $La_{0.67}Ca_{0.33}MnO_3$ Nanophase Powders and Films from Alkoxide Precursors. *Chemistry of Materials* **2002**, *14* (5), 1981-1988.

[218] Pohl, A.; Westin, G.; Jansson, K. Preparation of $La_{0.75}Sr_{0.25}MnO_3$ Nano-Phase Powders and Films from Alkoxide Precursors. *Journal of Sol-Gel Science and Technology* **2003**, *26* (1–3), 257–260.

[219] Pohl, I. A. M.; Westin, L. G.; Kritikos, M. Preparation, Structure, and Properties of a New Giant Manganese Oxo-Alkoxide Wheel, $[Mn_{19}O_{12}(OC_2H_4OCH_3)_{14}(HOC_2H_4OCH_3)_{10}] \cdot HOC_2H_4OCH_3$. *Chemistry − A European Journal* **2001**, *7* (16), 3438–3445.

[220] Hubert-Pfalzgraf, L. G. Toward Molecular Design of Homo- and Heterometallic Precursors for Lanthanide-Based Oxide Materials. *New Journal of Chemistry* **1995**, *19* (5–6), 727–750.

[221] Bradley, D. C.; Chudzynska, H.; Hursthouse, M. B.; Motevalli, M. Volatile Tris-Tertiary-Alkoxides of Yttrium and Lanthanum. The X-ray Crystal Structure of $[La_3(OBu^t)_9(Bu^tOH)_2]$. *Polyhedron* **1991**, *10* (10), 1049–1059.

[222] Borup, B.; Samuels, J. A.; Streib, W. E.; Caulton, K. G. A Soluble Alkoxide of Barium with a Cubane Structure. *Inorganic Chemistry* **1994**, *33* (5), 994–996.

[223] Turova, N. Y.; Turevskaya, E. P.; Kessler, V. G.; Yanovsky, A. I.; Struchkov, Y. T. Synthesis, Crystal and Molecular Structure of Calcium Oxo Ethoxide, $[Ca_6(\mu_4\text{-}O)_2(\mu_3\text{-}OEt)_4(OEt)_4] \cdot 14EtOH$. *Journal of the Chemical Society, Chemical Communications* **1993**, (1), 21–23.

Chapter 3

Experimental Methodology

3.1 Overview

Because of their exceptional reactivity with moisture and oxygen, the syntheses of alkoxides and their solutions are achieved under inert atmosphere using air-sensitive techniques. Furthermore, all requisite solvents must be scrupulously purified, anhydrous, and sparged of any atmospheric gases. This chapter describes the specific procedures followed for such syntheses, presents the optimizations developed for spin-coating, and discusses the characterization techniques used to investigate thin-film properties (i.e., microstructure and transport behavior). Familiarity with the fundamentals of synthetic chemical methodology, however, is presumed and will not be elaborated on here. For additional details, the reader is directed to the standard texts (e.g., Harwood, et al. [1]), and in particular, the classic reference by Shriver and Drezdzon [2]; information on general laboratory care and maintenance can be found in the excellent practical guide by Coyne [3].

But due to the diverse aggressive environments produced during chemical processing, conventional greased ground-glass connectors were eschewed in favor of *grease-free*, fluoroelastomeric compression seals.[1] Accordingly, all glassware used in this dissertation incorporated the Ace-Thred® connector system developed by Ace-Glass, Inc.[2] The operating principle for this design is simple but effective (see Figure 3.1): at the base of every Ace-Thred® plug or bushing is a circumferential groove, in which, sits an O-ring. When screwed against the mating glass socket, force from the groove compresses the O-ring onto a beveled side-wall, creating a seal. Thus, by selecting an appropriate threaded PTFE plug or bushing, leak-proof joints between a variety of components can be achieved.

Individual component lists, pictures, and schematics for all reaction apparatus (including the Schlenk manifold system designed by the author) are given in Appendices C and D.

---

[1] Prolonged reflux in strong coordinating solvents undermines grease integrity, and hence, the joint seal. Substitution of inert, fluoroelastomeric O-rings between the mating surfaces eliminates this problem.

[2] The Ace-Thred® glass connector system was determined to be incompatible with comparable systems from other manufacturers.
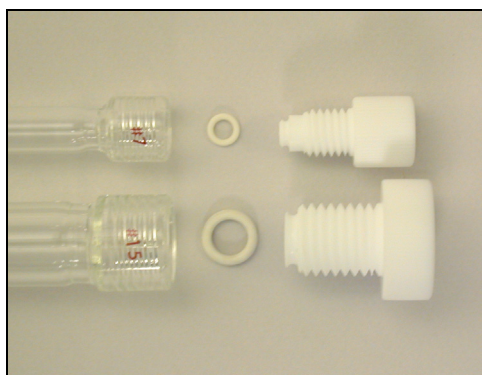
Ace-Thred® Plug   Ace-Thred® Bushing
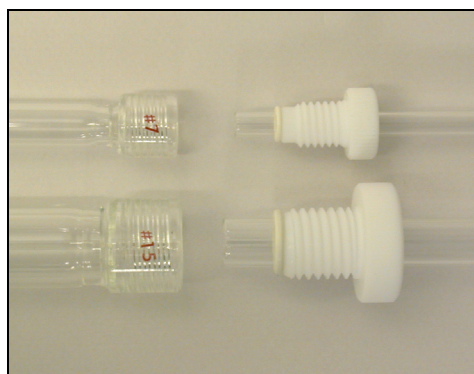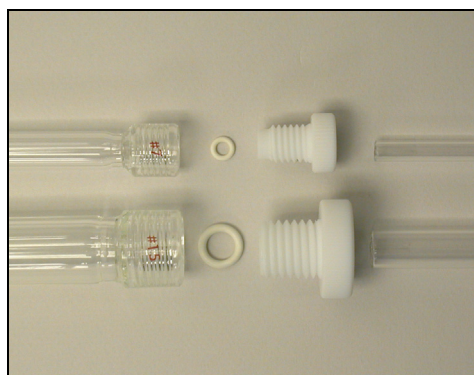
FIGURE 3.1 The Ace-Thred® universal glass joint system. Leak-proof seals
are formed by compressing fluoroelastomeric O-rings against beveled glass
seats via PTFE plugs or bushings.

In addition, the chemical syntheses illustrated in this chapter rely on complex, modular assemblies. For brevity, the corresponding subcomponents are not listed here. Instead, all functional reaction assemblies have been cataloged into comprehensive tables provided in Appendix E.

3.2 PREPARATIONS FOR SYNTHESIS

Before use, all glassware, PTFE components (i.e., bushings, plugs, stir bars, etc.), and O-rings (i.e., FETFE® or Aegis®), were soaked in a sulfuric acid bath which was augmented by a proprietary, non-toxic oxidizing agent (i.e., NoChromix® from GODAX Laboratories). After two days, the items were removed, rinsed with deionized water (i.e., $\rho \cong 18 \ M\Omega\text{-cm}$), and transferred to a deionized water bath for an additional two-day soak. Copious rinsing with fresh deionized water followed removal from this second bath. For drying, the items were stored in an autoclave operating at 130 °C. Complete dessication of all surfaces was ensured by allowing a residence of no shorter than 6 hours. The items, *still hot*, were then moved directly from the oven into the transfer chamber of a glove box and *immediately placed under vacuum*.[3] After cooling *in vacuo*, the reaction appartus could be assembled inside the inert environment of the glove box. Reaction apparatus prepared in this manner were free from deletarious moisture and oxgyen (i.e., physisorbed on the surface).

Solvents were purchased from commercial sources pre-purified (i.e., 99+%), anhydrous, and packaged under inert atmosphere. Unfortunately, these conditions proved inadequate to ensure liquid free of dissolved molecular oxygen. *Thus, all solvents, including the water used for hydrolysis, required de-oxygenation.* Removal of trace quantities of oxygen was accomplished by passing a stream of fine argon bubbles (i.e., sparging) through the refluxing solvent for a minimum of 12 hours (see Figure 3.2). Upon completion, the flask was fully-stoppered and stored in the glove box until needed. The specific solvents used for this disseration were: (1) Aldrich 40,175-7, tetrahydrofuran, 99.9%, anhydrous, inhibitor free, (2) Aldrich 23,670-5, pentane, 99+%, anhydrous, (3) Aldrich 24,451-1, toluene, 99.8%, anhydrous, (4) Alfa Aesar 41857, *tert*-butyl alcohol, anhydrous, 99.9%, and (5) Aldrich 28,446-7, 2-methoxyethanol, anhydrous, 99.8%. Deionized water was prepared using a Barnstead NAN-

---

[3] To ensure no trapped pockets of air reached the glove box, all items were maintained in a fully-disassembled state. Items essential to a synthesis, but not required for assembly, were left inside the autoclave until needed.
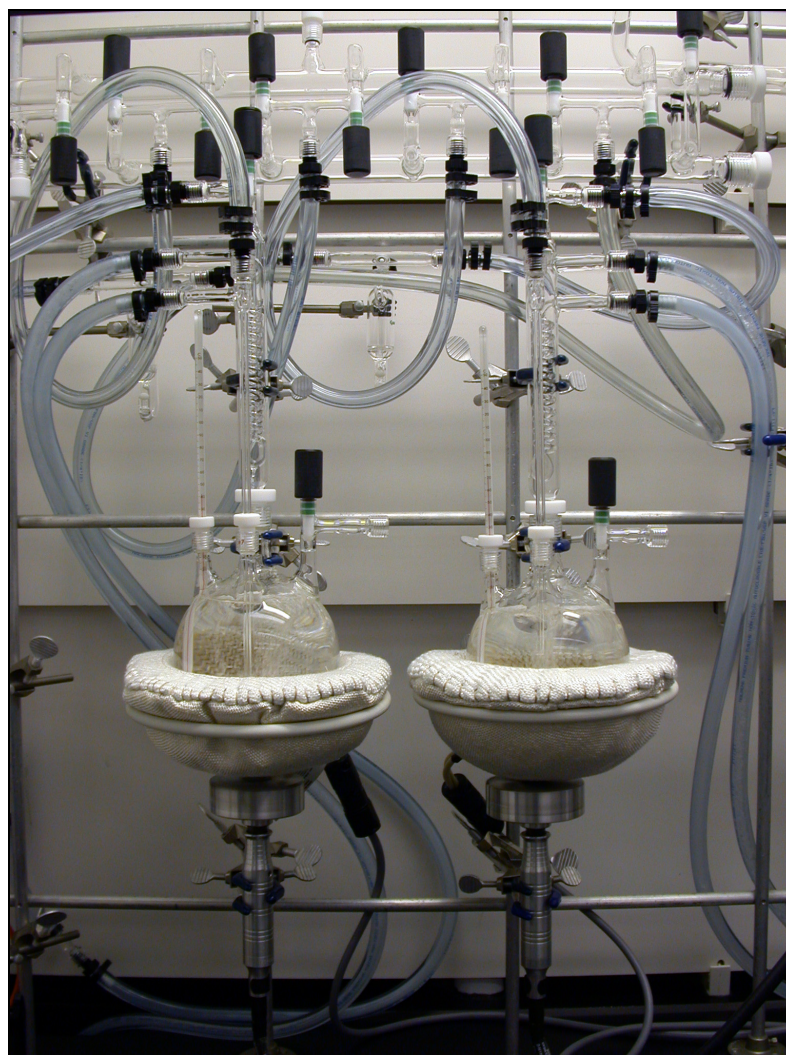
FIGURE 3.2 De-oxygenation by sparging with argon gas. A dispersion tube delivers fine bubbles of argon to a solvent under reflux. Pentane (left) and tetrahydrofuran (right) are shown in this picture.

Opure water system and utilized only when $\rho = 18.0\pm0.1$ MΩ-cm. All solvents henceforth will be cited by their generic names, the sources/descriptions here being presumed.

As indicated by Sections 2.4.4 and 2.4.6, the synthesis of manganese(II) and lead(II) silylamide depends on a common, starting reactant: $LiN[Si(CH_3)_3]_2$. Thus, a substantial quantity of lithium silylamide is required for the preparation of these derivatives in sufficient amounts. This reagent was synthesized in large batches (i.e., in advance) according to the accepted literature procedures [4]. Due to the routine nature of this synthesis, further elaboration will not be given.[4] The preparation of $LiN[Si(CH_3)_3]_2$, however, requires the handling of n-butyl lithium, a precursor notorious for pyrophoric behavior upon exposure to air. Guidelines for the safe manipulation of n-butyl lithium can be found in the classic reference by WAKEFIELD [5].

3.3 ALKOXIDE SYNTHESES

This section presents the syntheses of precursors required for the alkoxy-based sol-gel processing of doped-lanthanum manganites. For a discussion of the general approach (i.e., the silylamide synthesis route), refer back to Section 2.4.3. All compounds were stored as solid powders in an argon glove box in sealed, leak-proof containers. Figure 3.3 depicts samples of the individual precursors as packed under ultra-high purity argon. Before use, all compositions were verified by chemical analysis in the Microanalytical Laboratory of the School of Chemical Sciences. Carbon, hydrogen, and nitrogen contents were measured using combustion analysis and the metal content via inductively coupled plasma (ICP) spectrometry. Elemental weight percentages, purity, and yields are summarized in Table 3.1. For completeness, the results of lithium silylamide have been included. *In the desciptions which follow, the handling and reaction of chemical reagents are presumed to be conducted under argon, either in a glove box (i.e., weighing, grinding, etc.) or within Schlenkware (i.e., reflux, filtration, etc.).*

3.3.1 2-METHYL-2-PROPOXO MANGANESE(II)

This subsection details the specific procedure for synthesizing 2-methyl-2-propoxo manganese(II); familiarity with Sections 2.4.2 through 2.4.4 is presumed. To a flat-bottom 500-

---

[4] But an equipment list is provided in Table E.2.

Mn{N[Si(CH$_3$)$_3$]$_2$}$_2$

Mn[OC(CH$_3$)$_3$]$_2$

Pb{N[Si(CH$_3$)$_3$]$_2$}$_2$

Pb[OC(CH$_3$)$_3$]$_2$

Ba[OC(CH$_3$)$_3$]$_2$

FIGURE 3.3 Powders of silylamide and alkoxide precursors. Arrows correlate the silylamide with its alkoxide derivative.

PRECURSOR	METAL, M[a] (%)	N[a,b] (%)	Si[a] (%)	C[a] (%)	H[a] (%)	PURITY[c,d] (%)	YIELD (%)
Lithium (M = Li)							
LiN[Si(CH$_3$)$_3$]$_2$	4.14 (4.15)	7.54 (8.37)	e (33.57)	41.50 (43.07)	11.08 (10.84)	99+	92.2
Manganese (M = Mn)							
Mn{N[Si(CH$_3$)$_3$]$_2$}$_2$	14.54 (14.62)	6.40 (7.46)	e (29.90)	38.21 (38.36)	9.41 (9.66)	99+	98.2
Mn[OC(CH$_3$)$_3$)]$_2$	27.29 (27.31)	-	-	48.19 (47.77)	9.03 (9.02)	99+	99+
Lead (M = Pb)							
Pb{N[Si(CH$_3$)$_3$]$_2$}$_2$	39.21 (39.24)	5.29 (5.31)	e (21.28)	26.90 (27.30)	7.24 (6.87)	99+	86.7
Pb[OC(CH$_3$)$_3$)]$_2$	57.94 (58.62)	-	-	26.78 (27.19)	4.96 (5.13)	99+	99+
Barium (M = Ba)							
Ba[OC(CH$_3$)$_3$)]$_2$	48.00 (48.43)	-	-	31.32 (33.89)	6.40 (6.29)	99+	99+

[a] Left value is the determined weight percent. Right value (i.e., parentheses) is the theoretical weight percent.
[b] Slightly low nitrogen values are often reported in the literature for silylamides. One explanation stems from possible metal nitride formation during combustion analysis. Any thermally-stable nitride residue lowers the amount of liberated gaseous nitrogen available for detection.
[c] Calculated using the metal, M, as the reference basis.
[d] All silylamides were subsequently tested (not shown) to confirm chlorine-free material. In addition, the manganese and lead moeities were checked to verify no contamination from lithium (i.e., trace amounts of the corresponding chloride or silylamide).
[e] The acidic dissolution required for metals analysis yields fugative silicon-based species. Process of elimination using other elements, however, indicates actual silicon values are at (or near) theoretical expectations.

TABLE 3.1 Chemical analyses of synthesized metal silylamides and alkoxides.

mL, 3-neck flask was added 43.613 g of (0.2606 mol) of lithium silylamide. Dissolution was induced by adding 179.45 g (202 mL) of THF, generating a golden-yellow solution. Separately, 16.414 g (0.1304 mol) of Alfa Aesar 42844, manganese(II) chloride, ultra dry, 99.99% (metals basis) was added to a glass reflux assembly containing a 1000-mL, 3-neck, round-bottom flask. Addition of 186.27 g (210 mL) of THF caused the opaque, pink powder to whiten. Reflux for 3 hours at 70 °C left a white suspension of notably higher viscosity which exhibited a faint, pink hue. This process is depicted in Figure 3.4. Combining the silylamide solution with the chloride suspension (see Figure 3.5) caused the immediate dissolution of the fine, suspended particles, creating a transparent orange solution. Lithium chloride was not observed to precipitate, even after the reflux (i.e., conducted overnight for ~ 12 hours). Stripping the THF via reduced pressure, however, induced LiCl precipitation via concentration (see Figure 3.6).[5] Complete removal of THF was followed by the addition of 125.13 g (200 mL) pentane. A mild boil (~ 40 °C) and aggressive stirring enhanced the extraction. Upon cooling, a reddish-orange crude was observed to segregate, forming an immiscible layer. Gentle warming, though, restored homogeneity. Thus, filtration (i.e., through a 4–8 μm porosity frit) was carried out *with a warm solution* to ensure the smooth transfer of *homogeneous* liquid.

After filtration, the pentane was stripped and the flask attached to a distillation apparatus with a heated column (see Figure 3.7). A glass wool plug was inserted into the glass stem of the exit valve. This procedure was necessary to protect the vacuum manifold from silylamide vapors. The apparatus was placed *under vacuum first* and then *slowly heated* to 110 °C.[6] Residual organic volatiles (i.e., THF and pentane) were driven out during ramp-up, after which, the vacuum stabilized (i.e., ~ 2 x 10^{-2} torr). At the moment silylamide liquid appeared on the *lowest* glass fingers of the distillation column, the receiving flask was submerged in liquid nitrogen. Reduced-pressure distillation was allowed to proceed until a 3–5 mL pool of rose-colored liquid remained in the main flask.

Next, the collected distillate was thermolyzed. Again, a glass wool plug was placed into the glass stem of the exit valve. Argon flow was increased so that the rate of bubbles through the in-line bubbler just barely maintained a distinct, separated spherical geometry. Heating

---

[5] A stainless-steel, gas-flow metering valve was placed after the exit valve to control the internal vacuum.
[6] A ~ 100 °C surface temperature was maintained on the sidewalls of the distillation column, as monitored by an exterior thermocouple.
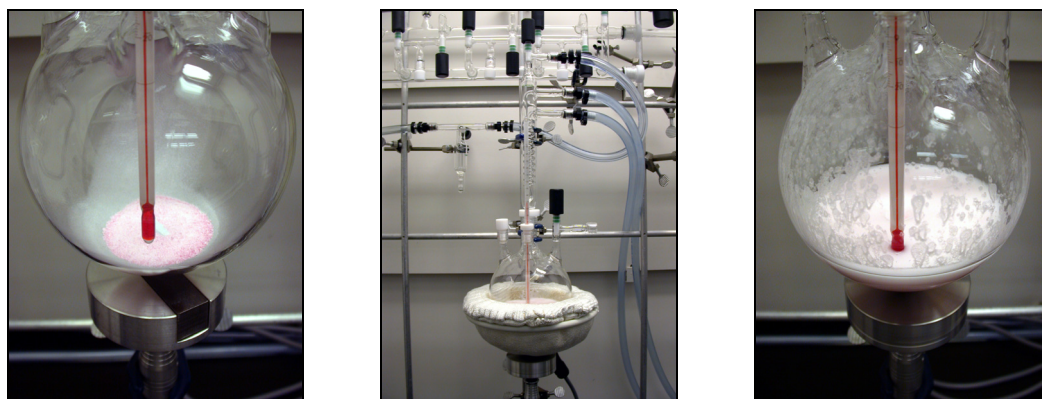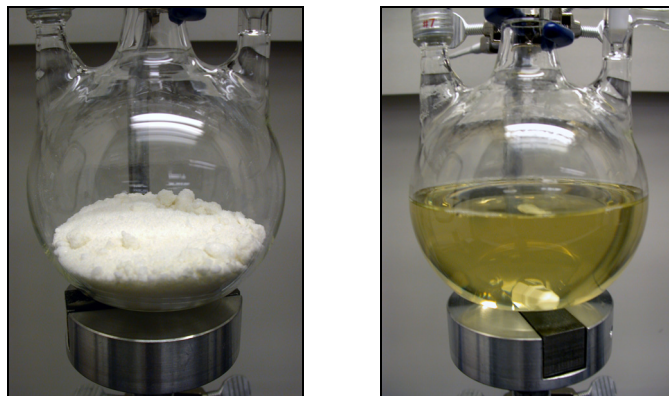
FIGURE 3.4 Preparation of lithium silylamide and anhydrous manganese(II) chloride. The top row corresponds to a simple dissolution, the bottom row, a solvent reflux.
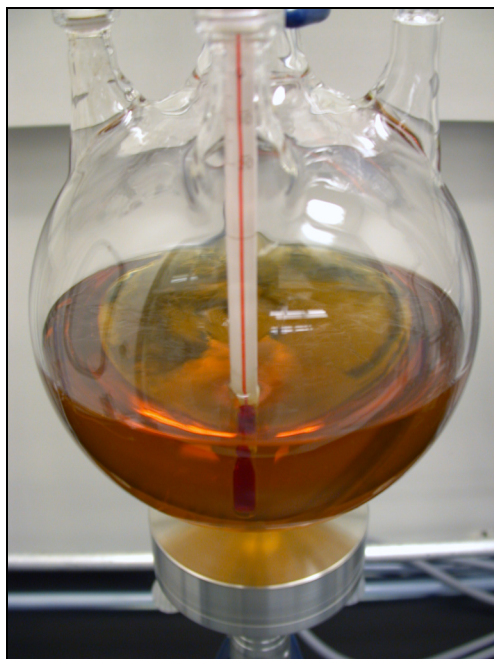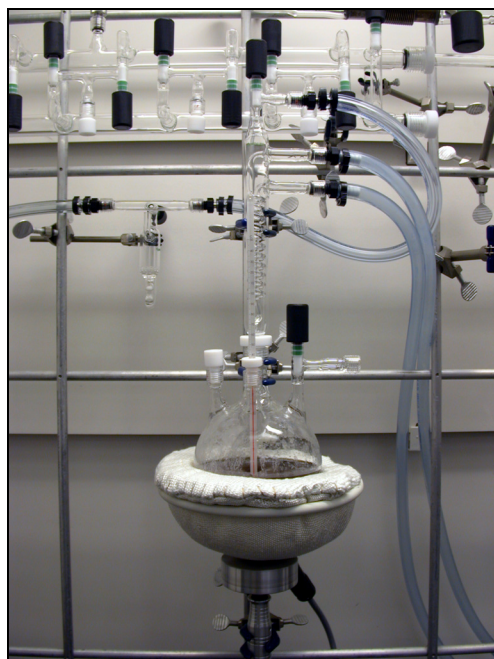
FIGURE 3.5 The reaction of manganese(II) chloride with lithium silylamide in THF. After mixing and reflux, a transparent orange solution remains.
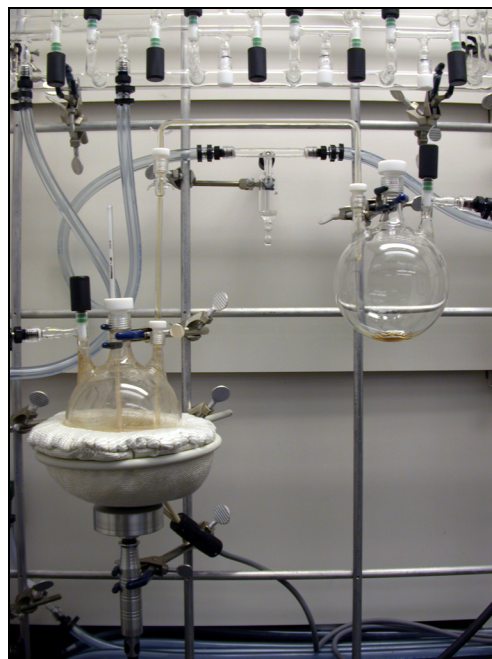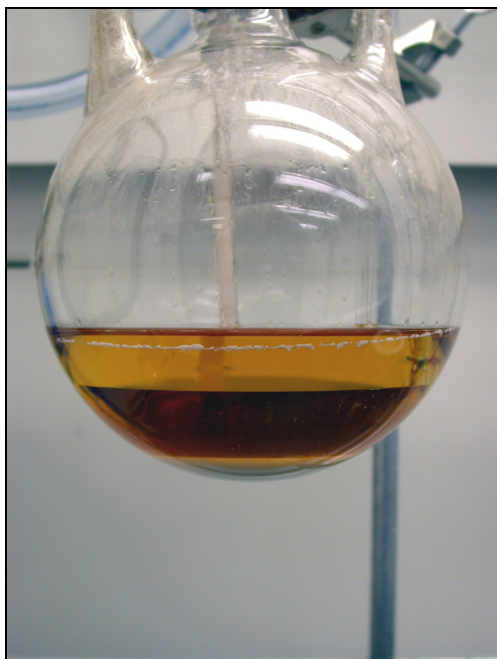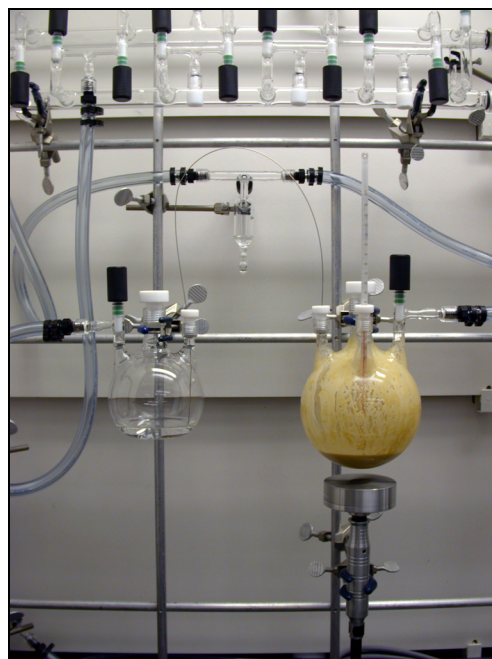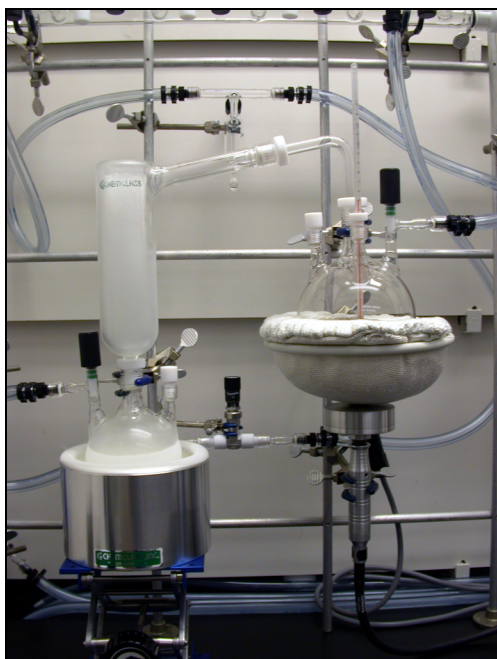
FIGURE 3.6 Separation of the manganese(II) silylamide crude from lithium chloride. THF is removed (top right) and replaced with pentane (top left). To prevent immiscibility (bottom left), the main flask is gently warmed during filtration, producing a uniform solution.
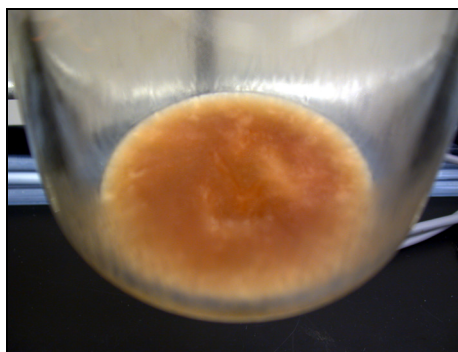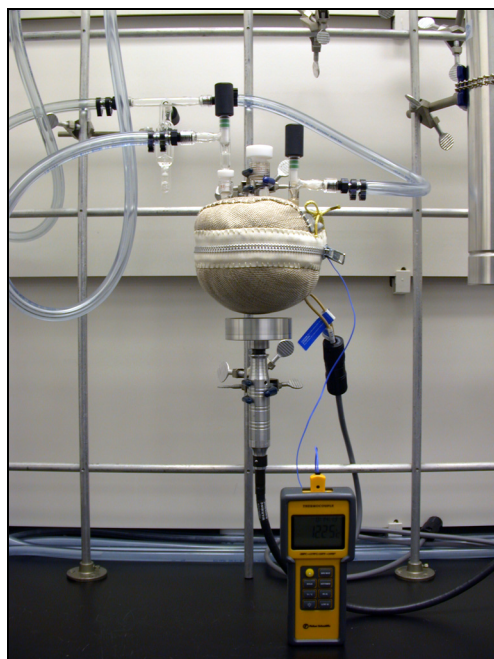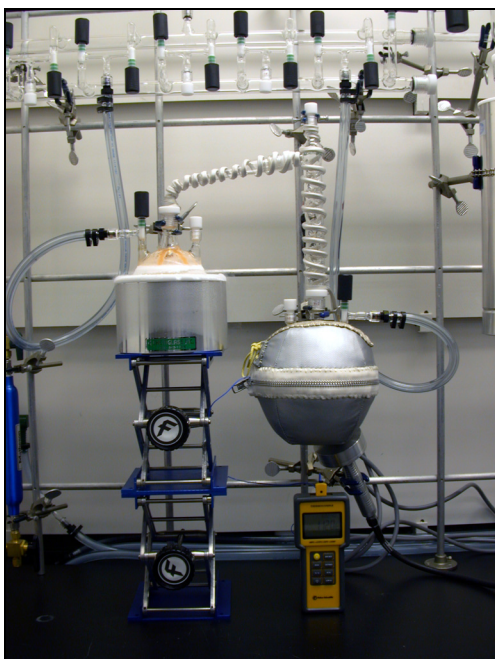
FIGURE 3.7 Thermolysis of purified manganese(II) silylamide. After elimination of residual THF, dissolution in pentane allows transfer to a container suitable for solids removal. A solvent strip then leaves the crystalline, flesh-colored product.

the flask to 125 °C under aggressive stirring caused clear droplets to condense on the glass wool (i.e., THF). A pinkish vapor clouded the interior of the flask, depositing dark-brown residue at the exit valve. *But the interior manganese(II) silylamide remained unoxidized.* To facilitate solids removal, transfer to a large reaction kettle was required. So after cooling and solidification, 68.44 g (109 mL) of pentane was cannulated into the flask, dissolving the purified manganese(II) silylamide. This solution was transferred into the cylindrical flask and the pentane stripped. A gentle heating (i.e., ~ 40 °C) under vacuum ensured the complete removal of pentane. Then, the reaction kettle was moved into the glove box where the solid was ground in a mortar and pestle, placed in a leak-proof jar, and stored until needed.

To synthesize 2-methyl-2-propoxide manganese(II), 63.871 g (0.1700 mol) of manganese(II) silylamide was weighed into a reaction kettle containing a large stir bar with a raised, octagonal ring (see Figure 3.8).[7] To this solid, 177.80 g (284 mL) of pentane was added, producing a flesh-colored, transparent solution. The addition of 26.45 g (0.3568 mol) of 2-methyl-2-propanol caused the immediate precipitation of lavender-white "streamers", which upon agitation, broke up and left a very-thick, pink suspension. The solvent, along with any remaining 2-methyl-2-propanol, was stripped via reduced-pressure and strong stirring. To prevent excessive gurgling and splashing, the system was exposed to vacuum very gently. Once the majority of liquid was removed, the reaction flask was heated (~ 60 °C) until the vacuum level stabilized. The container was then quickly back-flushed with argon gas.[8] The resulting pinkish material was especially brittle and easily ground in a mortar and pestle. Precautions had to be taken to prevent the generation of fine dust in the glove box. Again, storage occurred in leak-proof containers.

3.3.2 2-PROPOXO LANTHANUM

Attempts to synthesize lanthanum silylamide resulted in exceptional frustration for the author. The modern method presented in Section 2.4.5 represents recent advances and is not referenced by the standard (i.e., older) literature. Furthermore, the synthetic difficulties experienced by the author were ultimately traced to an incompatible source of anhydrous

---

[7] The precipitation of 2-methyl-2-propoxo manganese(II) creates a suspension with high viscosity. A large stir bar is required to maintain agitation throughout the mixture.

[8] Vacuum enhances the diffusion of trace amounts of oxygen past the dry, compression seals.
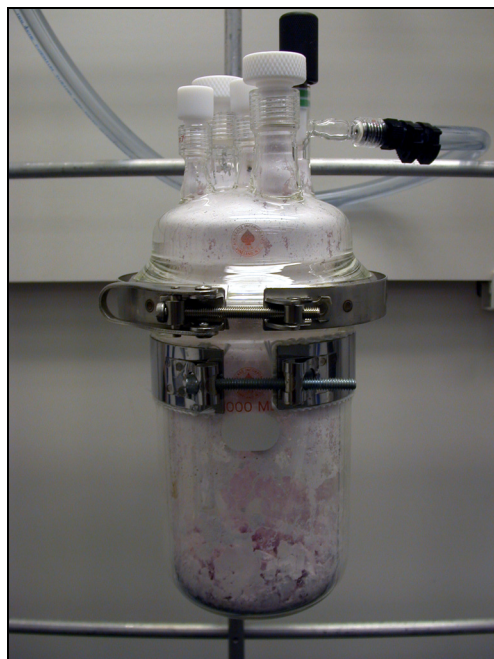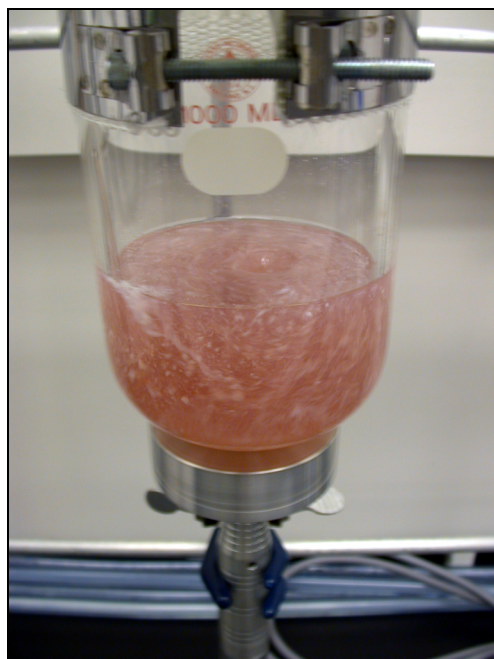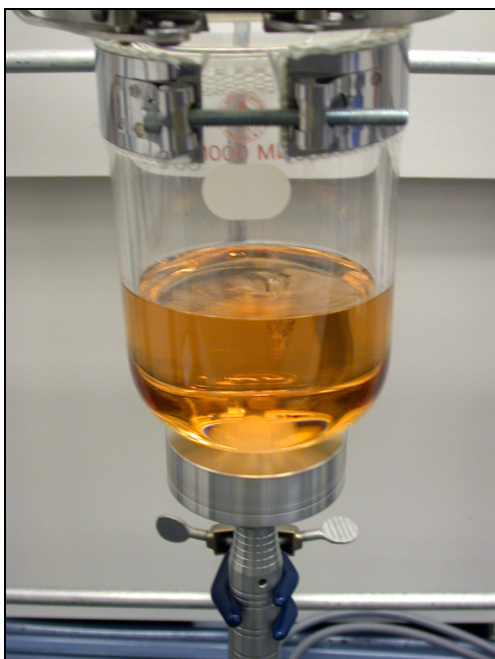
FIGURE 3.8 Conversion to 2-methyl-2-propoxo manganese(II). The addition of 2-methyl-2-propanol induces the spontaneous precipitation of lavender-white solid. Solvent removal followed by gentle heating under vacuum leaves the adduct-free, title product (heating mantle not shown).

lanthanum chloride, as documented in Appendix F. Unfortunately, much time was lost during this discovery process. So the author purchased Alfa Aesar 14616, lanthanum(III) isoproxide, La 40% from a commercial source. As anticipated, unacceptable levels of chlorine contamination were confirmed by the Microanalytical Laboratory (i.e., 1.213% by weight). Interestingly, dissolution of this product in 2-methoxyethanol yielded a small quantity of fine white precipitate, presumably $LaCl_3$. By filtering the supernatant (i.e., a transparent, pale-yellow solution) and removing the 2-methoxyethanol, an off-white powder was isolated. Upon analysis, no chlorine was found.

Structural investigations have shown the synthesis of 2-propoxo lanthanum to actually produce the adducted oxoalkoxide, $La_5O[OCH(CH_3)_2]_{13} \cdot nHOCH(CH_3)_2$ [7]. For the off-white solid, measurements of metal content (i.e., La) yielded 40.91% and 40.05% by weight using, respectively, ICP and thermal analysis.[9] The corresponding carbon and hydrogen values were 32.39% and 6.31%, respectively. Together, these three weight percents are in good agreement with the oxoalkoxide adduct, $La_5O[OCH(CH_3)_2]_{13} \cdot 3.5HOCH_2CH_2OCH_3$ (i.e., theoretical weight percents of 39.80%, 34.07%, 6.87%, respectively). The 40.91% value was adopted as a reference standard for lanthanum content.

3.3.3 2-METHYL-2-PROPOXO LEAD(II)

This subsection details the specific procedure for synthesizing 2-methyl-2-propoxo lead(II); familiarity with Sections 2.4.3 and 2.4.6 is presumed. To a round-bottom 500-mL, 3-neck flask was added 31.690 g (0.1894 mol) of lithium silylamide. Dissolution was induced by adding 137.13 g (154 mL) of THF, generating a golden-yellow solution. Separately, 26.343 g (0.09472 mol) of Alfa Aesar 42841, lead(II) chloride, ultra dry, anhydrous, 99.999% (metals basis) was added to another 500-mL, 3-neck, round-bottom flask. Subsequent exposure to 135.24 g (152 mL) of THF (i.e., a suspension), however, caused no discernable change unlike with anhydrous $MnCl_2$. Cannulation of the silylamide solution into the chloride suspension produced an immediate reaction, yielding a solution which changed hue from bright yellow to brownish-yellow as the addition proceded (see Figure 3.9). *At no point during this process was either system refluxed (i.e., separate or combined).* Instead, the solution was allowed to stir at

---

[9] Thermogravimetric analysis measured the mass loss upon conversion to anhydrous La_2O_3. This measurement was conducted separately by the author. For the procedure, see discussion in Section 3.5.2.
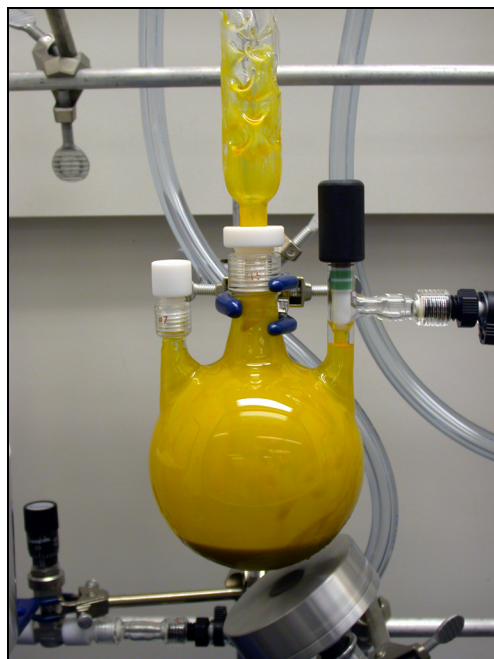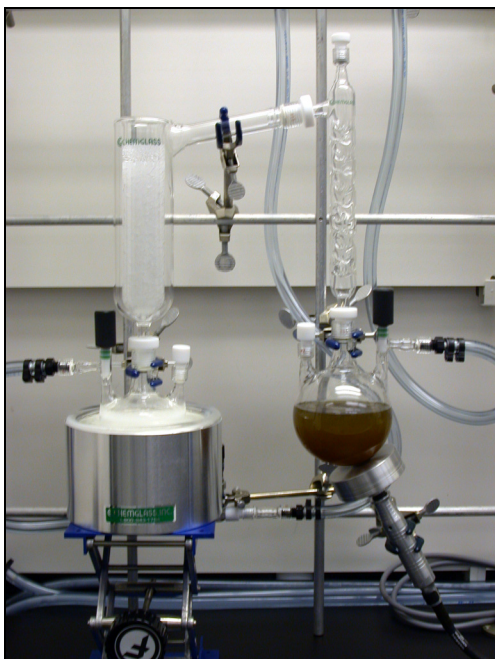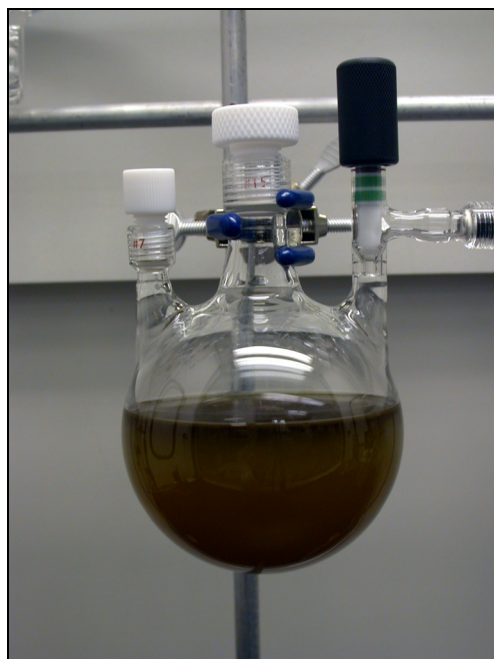
FIGURE 3.9 The reaction of lead(II) chloride with lithium silylamide in THF. The solution progresses in color from brilliant yellow to yellow-brown (top). Caution, however, must be exercised during the solvent strip because lead(II) silylamide is volatile in the presence of solvent vapors.

room temperature for approximately 4 hours. No lithium chloride was observed to precipitate, presumably due to a sufficient quantity of THF in the flask. Because of the volatility of lead(II) silylamide, all solvent strips were conducted *very slowly*, particularly with coordinating agents such as THF. Accordingly, the distillation apparatus included a Vigreux column in addition to the (expected) stainless-steel, gas-flow metering valve. The internal fingers of the column provide a condensing surface for the lower vapor-pressure silylamide, a characteristic which prevents excessive loss of the compound to the receiving flask. Trace amounts of lead(II) silylamide, however, were observed to reach the interior sidewall of the cold finger. No discernable reduction in yield, though, was measured.

The removal of THF (i.e., *without any heat*) was followed by a pentane "wash" which proceeded via cannulation from the top of the Vigreux column, along the interior sides, and finally down into the main flask (see Figure 3.10). The flask was then removed from the distillation apparatus and the supernatant liquid filtered through a gas frit (i.e., 4–8 μm porosity). The resulting transparent orange solution was observed by the author to deposit an extremely faint grey film on the interior flask wall when stored.[10] So room temperature, in combination with the weak argon over-pressure (i.e., 3–5 psig for standard Schlenk procedures), was sufficient to activate decomposition (i.e., formation of metallic lead).[11] The pentane was subsequently stripped, leaving a dark orange crude.

Next, the attached cold-finger was swapped for a reaction kettle with an extension adapter (i.e., the Vigreux column remained).[12] Distillation proceeded in a manner analogous to that of manganese(II) counterpart but with the following exception. Because of the volatility of lead(II) silylamide, the receiving flask was submerged in liquid nitrogen immediately after the initial pressure spike (i.e., due to escaping organic volatiles). The temperature of the main flask and column side walls were held at ~ 90 °C. The thermochromic nature of lead(II) silylamide is obvious in Figure 3.10. As a heated liquid, this compound is orange, but as a crystalline solid, bright yellow. When only a 3–5 mL pool remained in the main flask, the distillation was halted. The reaction kettle was transferred to the glove box where the solid was ground in a mortar and pestle. Storage occurred in a leak-proof jar.

---

[10]The flask was fully-stopped (i.e., completely sealed) and moved into the glove box.
[11]This process does not occur with the isolated solid.
[12]Clean glassware, however, was used for each solvent strip. So the apparatus used to remove THF (at first) was not saved for the pentane strip despite being comprised of the same components.
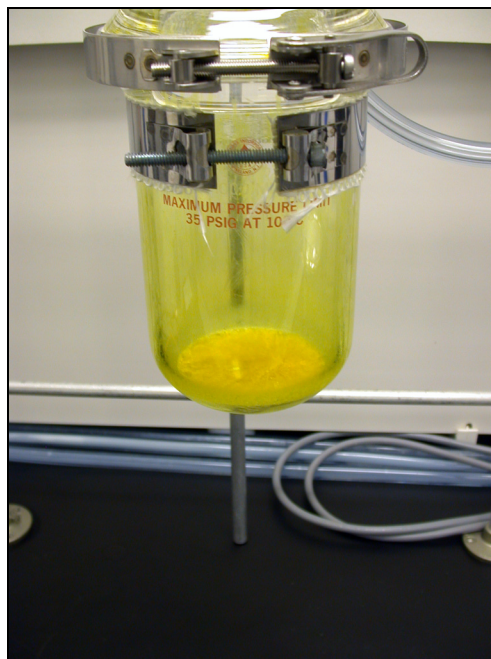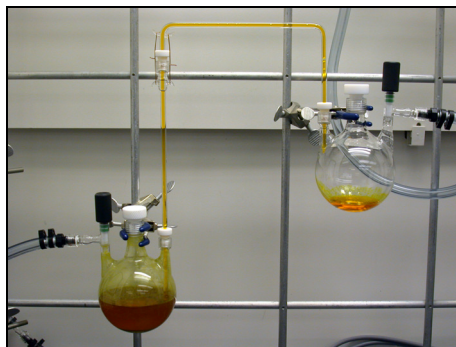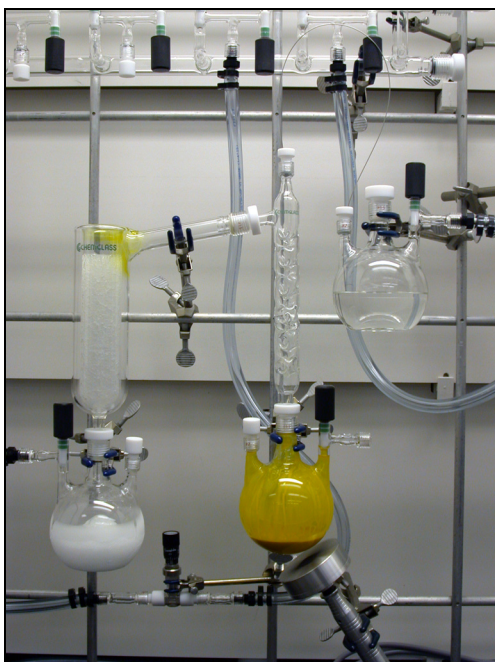
FIGURE 3.10 The separation and purification of lead(II) silylamide. Pentane is added from the top to wash volatilized product on the Vigreux column back into the main flask. Filtration (top right), solvent removal (not shown), and reduced-pressure distillation (bottom left) leave the purified material.

To synthesize 2-methyl-2-propoxo lead(II), 13.202 g (0.02501 mol) of lead(II) silylamide was weighted and placed into a reaction kettle. Dissolution was induced by adding 116.71 g (186 mL) of pentane (see Figure 3.11). To initiate the reaction, 4.65 g (0.06273 mol) of 2-methyl-2-propanol was cannulated into the cylindrical flask. The reaction proceeded spontaneously, with the color changing from tangerine-orange to faint-yellow within 3 minutes. The solution was left stirring at room temperature for approximately 1 hour. Removal of the pentane left a slightly off-white solid. The reaction kettle was then moved to the glove box where the material was ground in a mortar and pestle, and stored in a leak-proof jar.

3.3.4 2-METHYL-2-PROPOXO BARIUM

This subsection details the specific procedure for synthesizing 2-methyl-2-propoxo barium; familiarity with Section 2.4.7 is presumed. To a reaction kettle was added 11.55 g (0.08411 mol) of Aldrich 44,188-0, barium, distilled, dendritic pieces, 99.9%. Cannulation of 96.55 g (112 mL) of toluene into the cylindrical flask was followed by the addition of 50.09 g (0.6758 mol) of 2-methyl-2-propanol (see Figure 3.12).[13] The evolution of hydrogen gas required an incubation period of approximately 5 minutes, and afterwards, proceeded very slowly. A white hazy precipitate formed around the granules which dissolved upon dispersal by stirring. The system was heated to 50–60 °C to increase the reaction rate, consuming all the barium in approximately 3 hours.[14] The toluene was then stripped from the resulting yellow, transparent solution. An off-white solid was obtained, which upon further exposure to vacuum (i.e., at room temperature), left the adduct-free title product.

3.4 SOLUTION AND SOL SYNTHESIS

This section details the synthesis of La-Ba-Mn (2:1:3) or La-Pb-Mn (2:1:3) "stock" solutions and their partial hydrolysis into "spinnable" sols. Figure 3.13 offers a concise flow diagram of the corresponding procedure developed by the author. Dissolution of the requisite alkoxides in 2-methoxyethanol was carried out at room temperature with stirring only (i.e.,

---

[13]A 2 molar equivalent excess of 2-methyl-2-propanol was used to ensure the formation of the highly-soluble adduct (i.e., $Ba[OC(CH_3)_3]_2 \cdot 2HOC(CH_3)_3$) [6].

[14]The temperature was maintained below the boiling point of 2-methyl-2-propanol (i.e., 83 °C) to prevent its volatilization out of the toluene.
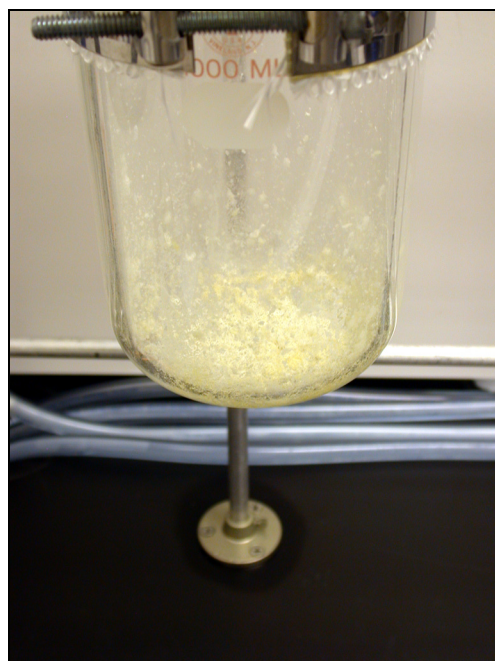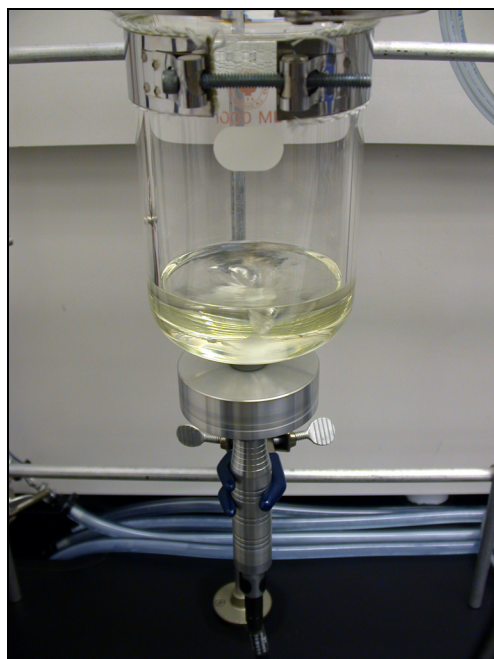
FIGURE 3.11 Conversion to 2-methyl-2-propoxo lead(II). The addition of 2-methyl-2-propanol produces a transparent, faint-yellow solution. Solvent removal followed by gentle heating under vacuum leaves the adduct-free, title product (heating mantle not shown).
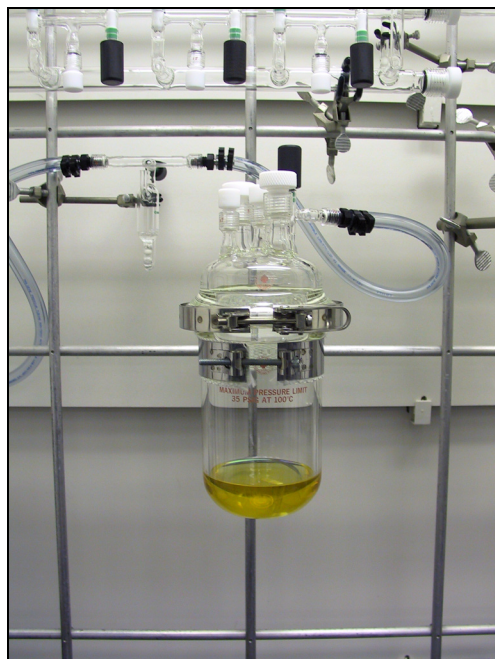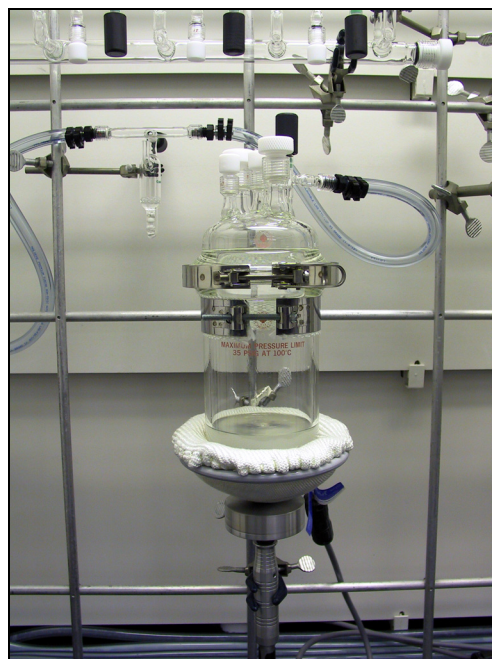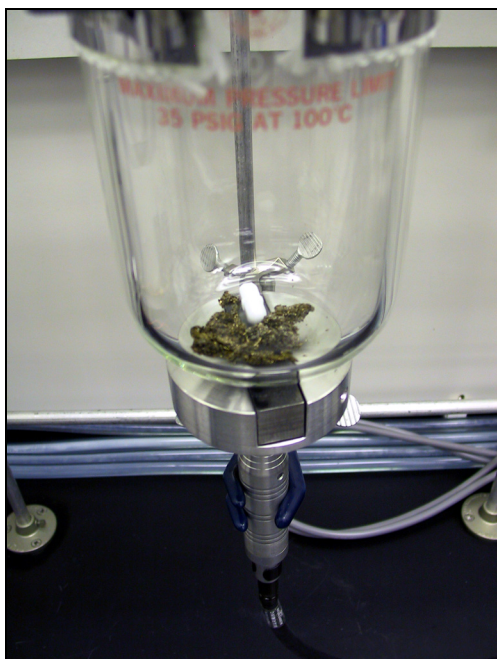
FIGURE 3.12 Synthesis of 2-methyl-2-propoxo barium. The addition of 2-methyl-2-propanol induces the slow evolution of hydrogen gas. To increase the reaction to practical rate, gentle heating is applied. A transparent, yellow solution remains.

50.00 mmol of Mn[OC(CH₃)]₂

6.667 mmol of La₅O[OCH(CH₃)₂]₁₃ · 3.5 HO(CH₂)₂OCH₃

16.67 mmol of Ba[OC(CH₃)]₂

(Or)

16.67 mmol of Pb[OC(CH₃)]₂

Flat-bottom 500 mL 3-neck flask

Stir for 20 – 30 minutes. Age for 2 days.

193.0 g (200 mL) of 2-methoxyethanol

0.25 M "stock" solution

Remove small aliquots as needed.

Stir for 20 – 30 minutes.* Age for 7 days.

Mixture containing 9.334 mg of H₂O per 1.000 g of 2-methoxyethanol

0.20 M Sol (h = 0.25)

* Add 0.2223 g of mixture per 1.000 g of 0.25 M La-Ba-Mn "stock" solution.
  Add 0.2211 g of mixture per 1.000 g of 0.25 M La-Pb-Mn "stock" solution.

FIGURE 3.13 Synthesis of alkoxy-based solutions and sols. Note the slightly different masses extracted from the hydrolytic mixture for the La-Ba-Mn (2:1:3) and La- Pb-Mn (2:1:3) "stock" solutions. Molarities are referenced to [Mn].

no reflux). Transparent, orange solutions resulted within 20–30 minutes (see Figure 3.14). *The 2-methyl-2-propoxo manganese(II) precursor, however, solvated in under 2 minutes (see further discussion in Section 3.5.1)! The absence of dark-brown hue from either sol system indicates proper synthetic technique.* Three principal investigations comprise the focus of this section: (1) bulk powder preparation, (2) gelation behavior, and (3) hydrolytic optimization for spin-coating. Bulk xerogels were decomposed into oxide powders to verify compositional stoichiometry and perovskite phase formation. The hydrolysis ratio was varied according to h = 0.25, 0.75, 1.25 in order to observe subsequent effects on gelation, if induced. A specific procedure for spin-coating and pyrolysis was designed for dense, defect-free coatings (see Figure 3.19). This process relied on post-coating hydrolysis via humidified air to ensure sufficient organic removal prior to heat treatment.

3.4.1 BULK POWDER PREPARATION

In the glove box, approximately 3 mL was withdrawn (separately) from the La-Ba-Mn (2:1:3) and La-Pb-Mn (2:1:3) "stock" solutions and placed into individual 15-mL platinum crucibles. The solvent was removed by heating at 100 °C for 1 hour in air, after which, a brownish-black residue remained. Both materials were (separately) removed from the crucibles, ground and pressed into small pellets, placed in clean crucibles, and heated at 10 °C/minute in a horizontal tube furnance to 500 °C. This temperature was held for 12 hours; cooling occurred at 10 °C/minute (i.e., to room temperature).

For the barium analogue, a greyish-black hue emerged as a result of the initial heat treatment. The pellet was ground, re-pressed, and returned to the 15-mL platinum crucible. The La-Ba-Mn composition was fired at 1100 °C and again at 1350 °C (i.e., for 12 hours, with a 10 °C/minute ramp rate, etc.); grinding and re-pelletization occurred in between. The final appearance was also greyish-black.

Firing at 500 °C left the lead-bearing pellet with a black hue. Due to the volatility of lead oxide, however, special precautions were observed during subsequent, higher-temperature heat treatments: the La-Pb-Mn composition, after being ground and re-pressed, was placed under 2 cm of loose, sacrificial $La_{0.67}Pb_{0.33}MnO_3$ powder (i.e., in the 15-mL platinum crucible). The material was then fired at 800 °C and again at 950 °C (i.e., for 12 hours, with a 10 °C/minute ramp rate, etc.); grinding and re-pelletization occurred in between. Fresh sacrifi-

La-Ba-Mn (2:1:3)   La-Pb-Mn (2:1:3)

0.25 M "Stock" Solution

0.2 M Sol ($h = 0.25$)
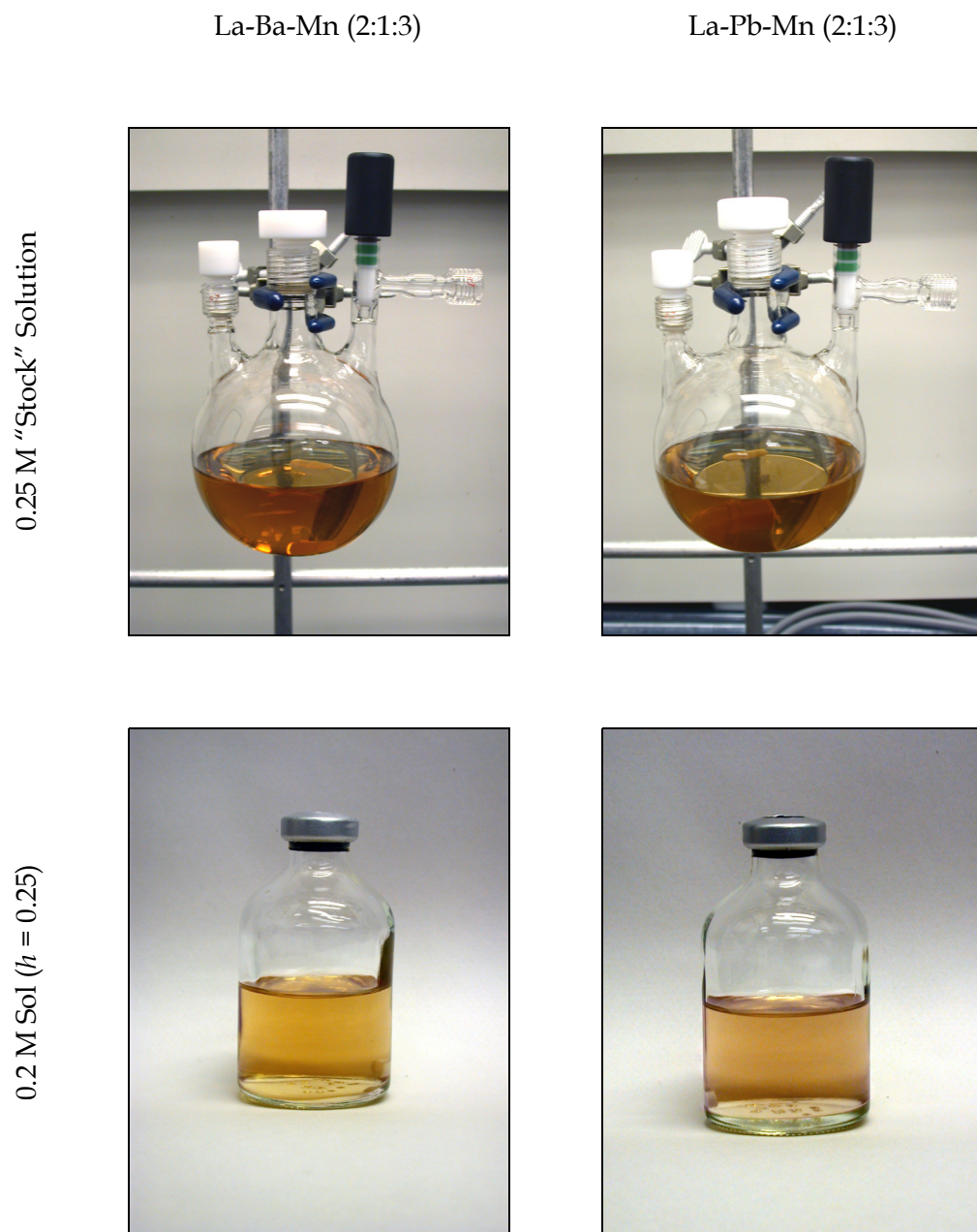
FIGURE 3.14 La-Ba-Mn (2:1:3) and La-Pb-Mn (2:1:3) solutions and sols. Note the transparent, orange color of the stock solutions. The absence of any dark-brown hue indicates the preservation of the manganese(II) (i.e., no oxidation).

cial powder was used for each heat treatment and gently compacted using a stainless-steel spatula. The final appearance was also black.

Both powders were characterized by X-ray diffraction and SQUID magnetometry (see Figures 3.15 and 3.16). Note the sharp diffraction peaks and the absence of secondary phases. Such an observation could not be made for powders prepared (equivalently) using aqueous solutions of acetate salts. Further "grind and fire" steps were required to remove small contaminating peaks corresponding to oxycarbonate phases. So as discussed in Section 2.3.3, the synthesis of heterometallic oxo-polymers (i.e., the activation of hydrolysis and condensation) is superior to simple dissolution and complexation.

The (cubic) perovskite lattice constants of a = 3.904 Å and 3.890 Å for, respectively, $La_{0.67}Ba_{0.33}MnO_3$ and $La_{0.67}Pb_{0.33}MnO_3$ are in good agreement with those published in the literature.[15] So for example, JU, et al. [8] reported that bulk, polycrystalline $La_{0.67}Ba_{0.33}MnO_3$ exhibited a cubic lattice parameter of a = 3.897 Å. The orthorhombic lattice constants measured by YANG, et al. [9] for single-crystal $La_{0.64}Pb_{0.36}MnO_3$ (i.e., a = 5.474 Å, b = 5.510 Å, and c = 7.763 Å) correspond to a pseudocubic value of $a_P \cong 3.88$ Å. Furthermore, the ferromagnetic Curie points (i.e., T_C = 340 K and 350 K, respectively) correlate well with those reported for the M = Ba and Pb compositions near x = 0.33 (refer back to Table 2.2). *Combined, both observations confirm that the "stock" solutions are of correct stoichiometry, and when processed using conventional mixed-oxide temperatures, provide phase-pure, perovskite material.*

3.4.2 GELATION BEHAVIOR

To determine a suitable hydrolysis ratio, 30-mL aliquots were extracted from the "stock" solutions, to which were added appropriate quantities of water pre-dissolved in 2-methoxy-ethanol.[16] The resulting 0.20 M sols corresponded to h = 0.25, 0.75, 1.25.[17] Note that subsequent aging occurred within sealed 50-mL Wheaton serum bottles, and hence, reflected a *closed system* (i.e., no concentration by evaporation). Precipitation or sedimentation into phase-segregated layers was never observed. All systems retained a uniform, transparent hue until densification of the gel mass within solution.

---

[15]Both diffraction patterns were checked against the "ideal" (i.e., cubic) perovksite, $SrTiO_3$, with a lattice constant of a = 3.905 Å (see JCPDS PDF 35-0734 from the International Centre for Diffraction Data).
[16]To ensure precision, all measurements were taken via mass.
[17]Specific masses for h = 0.25 are given in Figure 3.13.

A

a = 3.904 Å (Cubic)

(100) (110) (111) (200) (210) (211) (220) (300) (310) (311) (222)

Intensity (Counts)

2-Theta (Degrees)

B

H = 25 Oe

T_C = 340 K

Magnetization (emu/g)

Temperature (K)
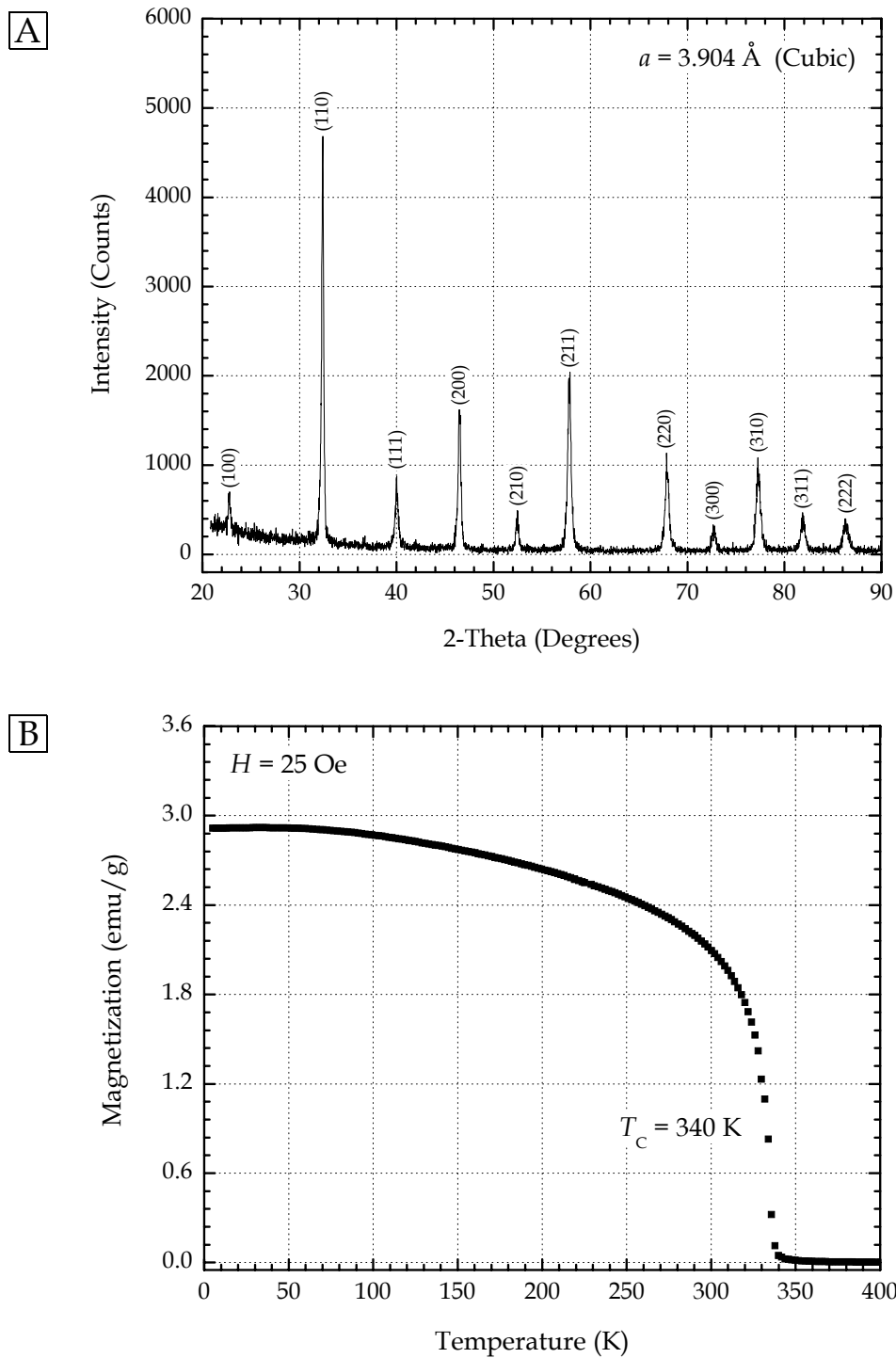
FIGURE 3.15 Characterization of alkoxy-derived $La_{0.67}Ba_{0.33}MnO_3$ powder. Both X-ray diffraction (A) and magnetization (B) data confirm phase-pure manganite perovskite material.
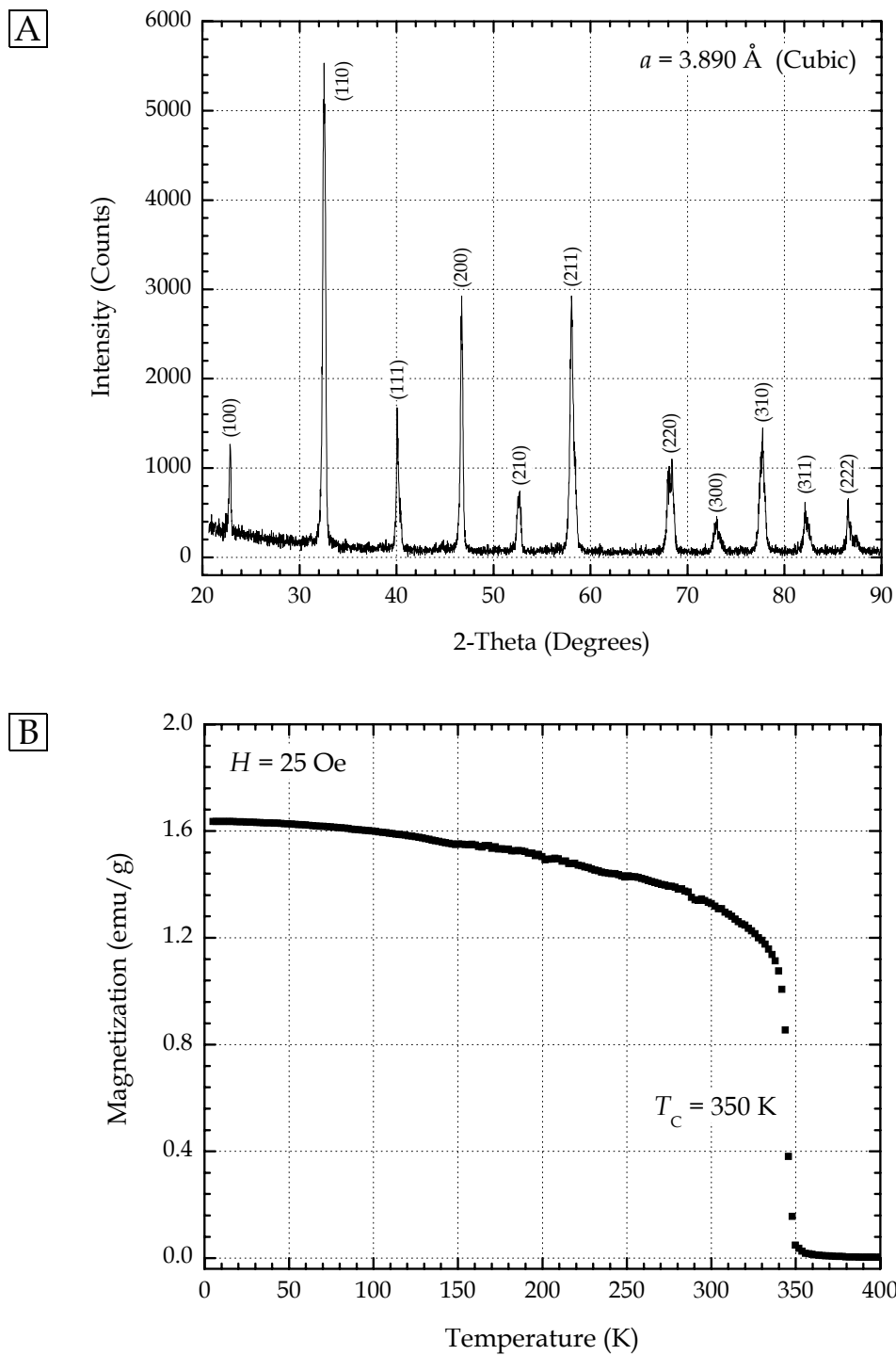
FIGURE 3.16 Characterization of alkoxy-derived $La_{0.67}Pb_{0.33}MnO_3$ powder. Both X-ray diffraction (A) and magnetization (B) data confirm phase-pure manganite perovskite material.

For the La-Ba-Mn (2:1:3) sol with $h = 1.25$, partial hydrolysis induced turbidity within two weeks, producing a viscous fluid after one month; gelation occurred at an undetermined point one year after synthesis. In contrast, the La-Pb-Mn (2:1:3) sol (i.e., $h = 1.25$) became viscous after only 2 weeks, reaching the gel point within a month. This latter system eventually formed an opaque white "plug" (i.e., gel mass). The expulsion of clear liquid, presumably pure 2-methoxyethanol, formed an immiscible top layer (i.e., syneresis). A comparison of the two compositions suggests the lead-bearing system is the more hydrolytically-sensistive of the two (but see discussion on next page). The rapid onset of gelation affliated with $h = 1.25$, however, makes this hydrolysis ratio unsuitable for spin-coating.

The next lowest ratio (i.e., $h = 0.75$) was observed to delay gelation and provide a suitable "spinning" viscosity for approximately 1–2 months. A transparent orange (i.e., La-Ba-Mn) or pinkish-orange (i.e., La-Pb-Mn) color persisted throughout this period. But afterwards, the viscosity of these sols became unstable to spinning, preventing proper wetting of the substrate during coating: V-shaped, radial "wakes" left bare regions on the substrate surface.[18] Longer aging periods generated turbid fluids. Gelation, however, was not observed within 1 year although the sols became extremely viscous. Similar to the $h = 1.25$ sols, the La-Pb-Mn (2:1:3) system aged faster than its barium counterpart.

In order to improve the "shelf life" of synthesized sols, a partial hydrolysis of $h = 0.25$ was selected. Accordingly, both compositions exhibited no deleterious changes in viscosity for 4–5 months, retaining the fluidity of the host solvent. Spinnability during this time was excellent. *For this reason, all sols used in this dissertation rely on a partial hydrolysis of $h = 0.25$, and based on the aforementioned observations, a compatability limit of $h < 1$ was established for spin-coating.* This guideline is in good agreement with the empirical regimes discussed in Section 2.3.4 for coating processes.

The influence of hydrolysis on oxygen sensitivity was also investigated. Figure 3.17 presents gels prepared with three different environments. The first row (A) corresponds to "stock" solutions (i.e., $h = 0$) allowed to hydrolyze directly in air. Aliquots were extracted under argon in the glove box, which upon exposure to atmosphere, resulted in the immediate precipitation of fine, brown material at the air-liquid interface. These particles darkened

---

[18]During spinning, solvent evaporation induces gelation at arbitrary points on the surface. Fluid motion is arrested, impeding radial flow. Sols with high viscosities often correspond to systems close to the gel point. This state, if unstable, is unsuitable for spin-coating (see Section 2.3.4).

La-Ba-Mn (2:1:3) Gel

La-Pb-Mn (2:1:3) Gel
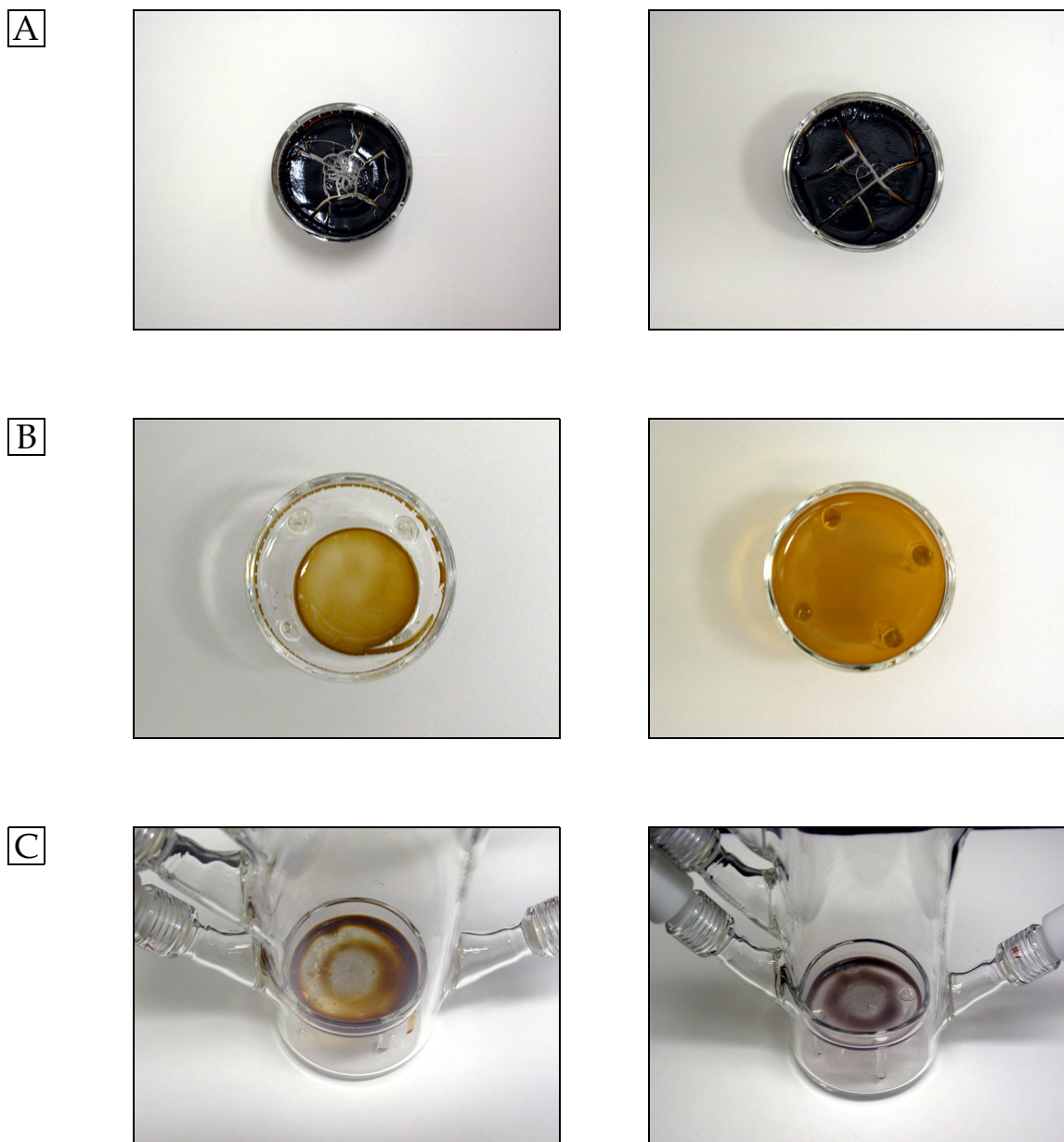
FIGURE 3.17 The gelation of 0.2 M La-Ba-Mn (2:1:3) and La-Pb-Mn (2:1:3) sols. The environments included air (A), fully-humidified argon (B), and a current of flowing argon (C). Note that the pictures of (A) and (B) correspond to atmosphere while (C) was sealed under argon (stagnant).

with time, coarsening and slowly sinking into the solution. Within 2–3 minutes, the entire system transformed from a transclucent orange (i.e., La-Ba-Mn) or pinkish-orange (i.e., La-Pb-Mn) liquid into an opaque, brownish-black suspension. Hydrolysis occurred concomitantly (albeit slower), congealing the solution so that within 10–15 minutes, the body exhibited a gel-like appearance. Within 1 hour, shrinkage began and cracks emerged.

The second row (B) reflects hydrolysis conducted in a moisture-saturated argon environment. Aliquots of 0.20 M sol (i.e., $h = 0.25$) were extracted in the glove box, placed into dishes with stilts, and sealed in a gelation chamber (see Figure D.29). Deionized water was added to the chamber, forming a pool, above which, sat the exposed dish (i.e., on stilts). The systems were left overnight to gel (~ 12 hours). The La-Pb-Mn (2:1:3) sol formed a clear, orange body whereas the La-Ba-Mn (2:1:3) counterpart shrank into a smaller, semi-translucent disk (i.e., syneresis).[19] This observation is the opposite of that found in the closed systems where h remained fixed. The author wishes to point out that, when this experiment was repeated using the unhydrolyzed "stock" solutions, white fractal "blooms" grew at the gas-liquid interface. This behavior corresponds to preferential hydrolysis and phase segregation. *Thus, partial hydrolysis in solutia (i.e., $h = 0.25$) remains crucial for the development of homgeneous gels, a conclusion underscored by Section 2.3.4.*

But this fractal geometry provides prima facie evidence for a polymeric, and not a particulate, sol system. As stated in Section 2.3.5, such morphology plays a critical role in low-temperature densification, an important goal of this dissertation. Equally important, the picture depicted by Figure 3.17 was taken in air, yet the translucent orange color remains![20] *Thus, the activation of hydrolysis (and condensation) before exposure to air confers resistance to oxidation.* With a rapid concentration process such as spin-coating, gelation for partially-hydrolyzed sols may be induced before oxidized precipitation, by-passing the growth of brown, insoluble particles. As will be shown in Section 3.4.3, this conjecture was proven.

The last row (C) depicts the gelation products of solvent evaporation. Aliquots of 0.20 M sol (i.e., $h = 0.25$) were extracted in the glove box, placed into dishes with stilts, and sealed in a gelation chamber. The chamber was then connected to the inert-gas manifold and a strong current of ultra-high purity argon flowed overhead. Over a 2 day period, the transparent

---

[19]The La-Ba-Mn (2:1:3) sol, however, did start as a transparent, orange *gelled* mass like La-Pb-Mn (2:1:3).

[20]After 15–20 minutes in air, however, a slight darkening was noticed.

sols congealed via concentration into semi-translucent, orange-brown (i.e., La-Ba-Mn) and lavender (i.e., La-Pb-Mn) gels. The resulting sticky mass was immediately collected *in the glove box* for thermal analysis. This latter experiment was carried out to crudely approximate the rapid evaporation which occurs during spin-coating (see Section 2.3.6). As will be demonstrated in Section 4.3, the thermal decomposition of this material was notably different from xerogels prepared in air and moisture-saturated argon.

3.4.3 SPIN-COATING AND HEAT TREAMENT

For spin-coating, aliquots of 0.20 M, h = 0.25 sol were drawn in a glove box from serum bottles via 3-mL, pre-sterilized, latex-free Becton-Dickinson syringes with Luer-lock tips. To avoid excessive coring of the serum bottle septa, 20-gauge, 1½" disposable needles (i.e., Precision Glide™ from Becton-Dickinson) were employed. Between the syringe and needle resided a Whatman 0.45 µm PTFE filter body (see Figure 3.18). This latter component ensured the delivery of fluid free from particulate contaminates. To protect the sol from aerobic reaction, a #7 vacuum cap, a 11 mm silicone septa, and a #7 bushing were assembled into a "sheath" inside the glove box (see Appendix D). The syringe needle was then inserted into the sheath and transported outside the glove box. During application, fluid was ejected from the syringe *at a uniform rate*. The first three drops of any deposition *were always discarded* with the fourth and subsequent drops *placed immediately* (i.e., no pause) onto the substrate. The syringe was then returned to its sheath. This practice enabled the delivery of fresh, unoxidized sol to the substrate.

Before spin-coating, substrates underwent a cleaning procedure which consisted of: (1) ultrasonication in methanol for 10 minutes, (2) ultrasonication in acetone for 10 minutes, and (3) ultrasonication in water for 10 minutes.[21] Between each iteration, substrates were blown dry with filtered, compressed air. The substrates were then moved to a 300 °C hot plate and baked for 5 minutes to volatilize any residual organics. When first mounted into the spin-coater, a substrate was covered by the host solvent (i.e., 2-methoxyethanol) and spun at 3000 rpm for 30 seconds. This procedure was repeated twice, after which, began the deposition. La-Ba-Mn (2:1:3) and La-Pb-Mn (2:1:3) sols, when delivered to the substrate surface, nucle-

---

[21]These organic solvents were purchased anhydrous and with 99.9% purity.
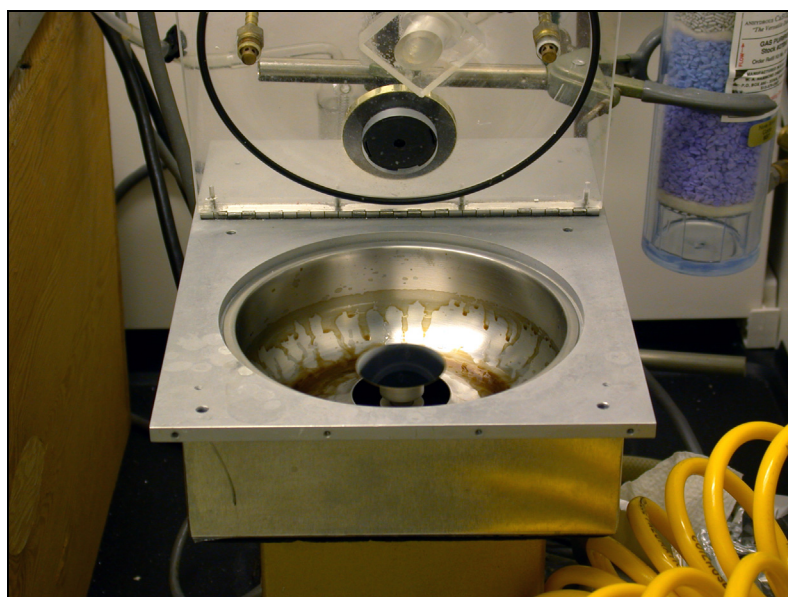
FIGURE 3.18 Spin-coating of 0.2 M La-Ba-Mn (2:1:3) and La-Pb-Mn (2:1:3) sols with $h = 0.25$. A filtered syringe (A), sheathed betweened uses, deposited fluid onto the substrate. Spin-coating (B) occurred in air at 3000 rpm for 30 seconds.

ated fine, brown particles at the air-liquid interface (i.e., within 2–3 seconds after exposure to air). But angular acceleration, if initiated immediately, swept this surface layer off the substrate leaving a gel coating. *Inspection under an optical microscope indicated a clear, defect-free film with no inclusions of particulate matter.* Thus, the radial ejection of fluid and subsequent (rapid) solvent evaporation induced gelation before the onset of precipitation.[22]

Two silicon substrates were used in this dissertation: (1) p-type, boron-doped Si(100) from Komatsu Electronics, Ltd. and (2) thermally-oxidized (i.e., 5000 Å), p-type, boron-doped Si(100) from Silicon Quest, Intl. The surface of the latter was sputtered with a 300 Å titanium buffer layer followed immediately by a 1700 Å platinum layer.[23] The as-deposited platinized film exhibited an out-of-plane (111)-orientation but contained no preferred in-plane orientation (i.e., "fiber" texture). Spin-coating was carried out on either: (1) circular wafers, provided the diameter was not greater than 3" or (2) 1 cm x 1 cm squares. Film thicknesses were not dependent on substrate type. The square substrates were prepared by scoring centimeter-spaced, orthogonal lines onto the backside of a circular wafer with a diamond scribe. The wafer was then fractured, individual pieces cleaned, and the polished side inspected for defects.[24]

A flow chart for the sol-gel processing of manganite thin-films is given in Figure 3.19. Spin-coating was initiated by flooding the substrate with sol. For the 1 cm x 1 cm squares, the entire surface was wetted. Whole wafers, however, required a more efficient approach. These larger substrates were rotated at a constant ~ 200 rpm. Fluid delivery from the syringe started at the center, moving radially outward to the edge. The angular velocity was then immediately increased to 3000 rpm.

The first hot-plate treatment of 100 °C was necessary to enhance the diffusion of 2-methoxyethanol out of the compacted (but porous) gel. Higher temperatures were observed to generate pin-holes and surface defects in the coating.[25] The second hot-plate treatment at 300 °C initiated organic pyrolysis, densifying the xerogel. A final stage at 450 °C was used to complete the pyrolytic transformation and ensure a defect-free film before proceeding to

---

[22]The film, however, does oxidize but only after the establishment of a gelled (i.e., condensed) morphology. Thus, precipitation of oxidized particles is avoided. As stated in Section 3.4.2, partial hydrolysis aids this transformation by conferring resistance to oxidation.

[23]The author wishes to acknowledge Dr. Ryan Ong's selfless preparation of these substrates.

[24]To facilitate analysis, coated circular wafers were also diced into 1 cm x 1 cm squares after heat treatment.

[25]The boiling point of 2-methoxyethanol is 124–125 °C.
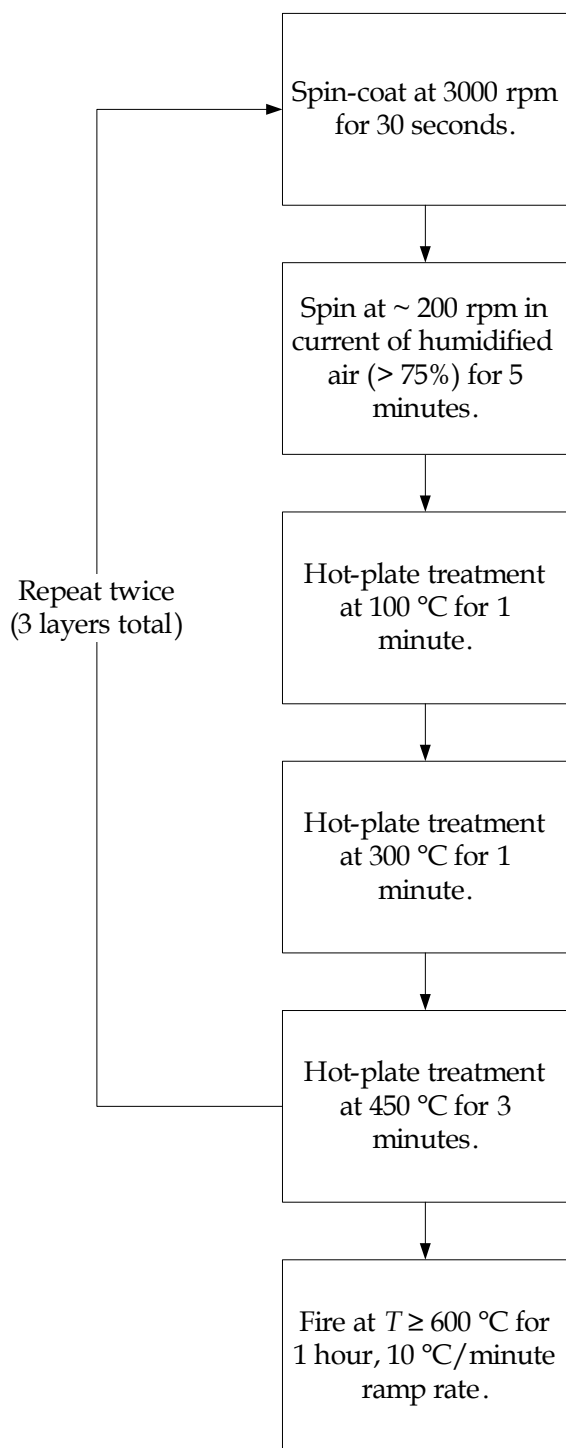
FIGURE 3.19 Flow chart for the thin-film deposition process. Spinning in a current of humidified air served as a critical step to form defect-free manganite films. The final 1-hour heat treatment is for crystallization.

crystallization. Notable color changes, however, accompanied each thermal stage and provided a visual observation of the densification process (see Table 3.2). Interestingly, the film color remained unchanged if further processing occurred between 550–600 °C (i.e., before crystallization). This behavior suggests that the amorphous films produced by the 450 °C heat treatment contained no porosity and were mostly-free of organic content.

One step in particular played a critical role in the formation of dense, defect-free films: the slow spinning (i.e., ~ 200 rpm) of a coated substrate under a stream of humidified air (i.e., > 75%).[26] Forced convention then hastened the evaporation of solvent entrapped within the gel pores, enabling penetration of aerobic moisture into the oxopolymer network. The resulting hydrolysis (and condensation) induced substantial organic removal, increasing the oxide content of the gel. In essence, this procedure counterbalanced the low partial hydrolysis (i.e., $h = 0.25$) used to delay gelation and preserve spinnable viscosities (see Section 2.3.6). The effects on film microstructure were quite dramatic as pictured in Figure 3.20. Specimens without this post-coating hydrolysis exhibited extensive porosity and phase separation (see Figure 3.20A), appearing hazy to the naked eye. In contrast, the exposure to humidified air always produced transparent, dense, defect-free coatings upon pyrolysis (see Figure 3.20B). The 450 °C hot-plate treatment then served as a useful checkpoint: films clear to the naked eye after this stage represented defect-free, amorphous coatings ready for crystallization. *Thus, because of the limitations imposed by spinnability (i.e., h < 1), post-coating hydrolysis comprises an essential step for the alkoxy-based, sol-gel processing of manganite thin films.*

To underscore this conclusion further, consider the adaptation by FORS, et al. [10] of the sol-gel process developed by POHL, et al. [11, 12] for bulk xerogels (see Section 2.5). The latter's *lack of partial hydrolysis (i.e., h = 0)* was duplicated in the coating method: hydrolysis occurred *solely* from the reaction of atmospheric moisture with the deposited gel. Fors, et al. reported that the "porous, percolation-like structure of the sol-gel film", formed after processing at 800 °C on LaAlO$_3$, could "be explained by the removal of carbonate groups". *In other words, by failing to properly exploit the hydrolysis and condensation mechanisms crucial to sol-gel processing, excessive organic content remained in the coated xerogel, producing defects upon pyrolysis.*[27] As will be shown Sections 4.8 and 4.9, the dense, amorphous coatings prepared

---

[26]The lid on the spin-coater was closed to ensured that the flow of humidified air passed directly over the coated surface.

ITERATION	As-Spun	100 °C	300 °C	450 °C
Si(100)				
1st layer	greyish-purple	redish-yellow	orangish-yellow	orange
2nd layer	bluish-yellow	sky blue	blue	blue
3rd layer	orangish-yellow	yellow	bluish-yellow	bluish-yellow
Platinized-Si(100)				
1st layer	redish-purple	brownish-yellow	brownish yellow	brownish-yellow
2nd layer	blue	blue	deep blue	deep blue
3rd layer	yellowish-green	sky blue	sky blue	sky blue

TABLE 3.2 Progression of transparent film color during deposition and heat treatment. These observations are from substrates coated with 0.20 M La–Ba–Mn (2:1:3) and La–Pb–Mn (2:1:3) sols where $h = 0.25$.
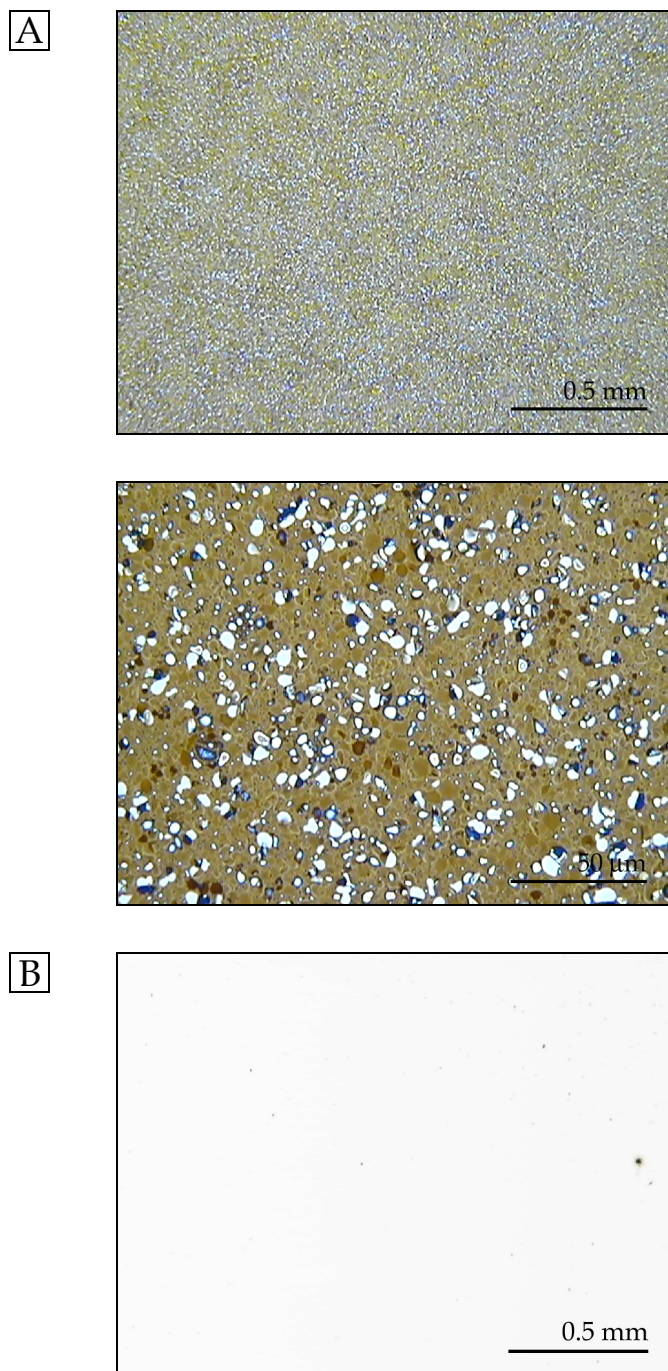
FIGURE 3.20 Representative optical micrographs of a pyrolyzed sol coating. This particular film corresponds to La-Ba-Mn (2:1:3) on Si(100) fired at 450 °C (i.e., amorphous). When inadequately hydrolyzed, a hazy appearance results, the product of extensive defects and phase separation (A). Proper hydrolysis, however, generates dense, transparent, and defect-free films.

according to the procedures of Figure 3.19 all crystallized into defect-free manganite perovskite thin-films.

3.5 CHARACTERIZATION

This section presents the characterization methods used to investigate alkoxide solution chemistry, bulk-gel decomposition, and thin-film properties. Individual thin-film specimens remained exclusive to one of three groups of instrumental analyses: Group (1) consisted of X-ray diffraction (XRD), X-ray photoelectron spectroscopy (XPS), optical microscopy, and atomic force microscopy (AFM); Group (2), SQUID magnetometry and scanning electron microscopy (SEM); and Group (3), magnetotransport.[28] In addition, 16 reference specimens were prepared according to the spin-coating process developed in Section 3.4.3. These specimens correspond to two doped-lanthanum manganite compositions (i.e., $La_{0.67}Ba_{0.33}MnO_3$ or $La_{0.67}Pb_{0.33}MnO_3$), four firing temperatures (i.e., 600, 650, 700, or 750 °C), and two substrate surfaces, (i.e., Si(100) or platinized-Si(100)). Thus, with regard to the three groups of instrumental analyses, 48 reference specimens were required in all.

3.5.1 FOURIER TRANSFORM INFRARED SPECTROSCOPY

Infrared spectroscopy was employed to investigate the interaction of 2-methoxyethanol with 2-methyl-2-propoxo manganese(II). In an argon glove box, 4.024 g of $Mn[OC(CH_3)_3]_2$ was transferred into a flat-bottom 500-mL, 3-neck flask. Cannulation was then used to deliver 96.25 g of 2-methoxyethanol into the flask. The dissolution of 2-methyl-2-propoxo manganese(II) was *extremely rapid*, finishing within 1–2 minutes and before the majority of 2-methoxyethanol had been added. *This observation validates the approach proposed by the author in Section 2.5, fulfilling a principal goal of this dissertation, namely, to design a reactive and highly-soluble manganese-based precursor (see Figure 3.21).* In contrast, 4.216 g of $La[OCH(CH_3)_2]_2$ required 10–15 minutes to dissolve in 96.01 g of 2-methoxyethanol *and only after* the full ali-

---

[27]Fors, et al. eliminated these defects by post-annealing at 1000 °C in air. Such corrective measures are entirely incompatible with silicon-based substrates and could only be accomplished because the underlying $LaAlO_3$ is *lattice-matched* and *refractory*.

[28]These divisions reflect the destructiveness of their constituent characterization techniques. For example, preparation for magnetotransport requires substrate breakage, electrode deposition, attachment of electrical leads, and so forth. Such modified specimens are unusable with other analytical methods.

FIGURE 3.21 A 0.20 M solution of 2-methyl-2-propoxo manganese(II) in 2-methoxyethanol. Dissolution occurred on contact at room temperature. The pinkish color corresponds to a manganese(II) oxidation state (i.e., not brown).

quot had been transferred. This latter alkoxide is an accepted, conventional precursor for the sol-gel processing of lanthanum-containing ceramic oxides [7].

Infrared adsorption spectra of the alkoxide solutions were obtained via a Nicolet Magna-IR 550 with: (1) a DTGS detector and (2) a continuous dry, high-purity nitrogen purge (i.e., of the sample chamber). A response from 4000–400 cm^{-1} was measured using 512 scans, a resolution of 4 cm^{-1}, a gain of 2.0, a mirror velocity of 0.6329 cm/s, Happ-Genzel apodization, and Mertz phase correction. To eliminate background interference, a scan of each sample cell was taken when empty (i.e., argon-filled). This reference was subtracted from actual spectra *in situ* by the Nicolet OMNIC control software (Version 5.2).

To prepare a sample, one or two drops of the requisite solution was placed between two 25 x 4 mm KBr disks, which in turn, were separated by a 0.015 mm PTFE spacer. These components were carefully positioned within an Spectra-Tech Presslok demountable cell holder. Due to aerobic sensitivity, both sample placement and cell holder assembly occurred within an argon glove box. The fully-assembled fixture was then placed into a leak-proof, screw-top jar for removal from the glove box and subsequent transport to the interferometer. After mounting the cell holder within the Nicolet Magna-IR 550, 10–15 minutes were allowed to elapse, ensuring adequate purging of CO_2 gas and moisture from around the sample cell. Measurements taken within 30 minutes of aerobic exposure indicated no contamination of the contained liquid (i.e., as otherwise would be indicated by brown discoloration of oxidized $Mn[OC(CH_3)_3]_2$).

3.5.2 THERMAL ANALYSIS

Thermogravimetric (TGA) and differential thermal (DTA) analysis was used to characterize the decomposition of La-Ba-Mn (2:1:3) and La-Pb-Mn (2:1:3) gels into manganite perovkiste powders from 25–1000 °C. Accordingly, two instruments recorded data from this conversion process: (1) a TA Instruments Hi-Res TGA 2950 and (2) a TA Instruments DTA 1600. All samples were heat-treated at 10 °C/minute in air with a flow rate of 20 scfm. Alumina powder (i.e., Al_2O_3) was used as the inert reference material inside the TA Instruments DTA 1600.

The gel samples hydrolyzed in air and moisture-saturated argon, however, were first placed in a drying oven at 110 °C for 2 hours to produce a xerogel. Shrinkage was quite dra-

matic, leaving very-small, hard, and brittle pieces (i.e., *at least* 1/20 their original volume). Equally important, the dessication process was observed to rapidly accelerate oxidization of gels synthesized in the moisture-saturated argon environment. The semi-translucent (i.e., La-Ba-Mn) or translucent (i.e., La-Pb-Mn) orange bodies transformed into opaque, black shards upon heating. On the other hand, gels created through solvent evaporation were handled in the glove box and transferred to the appropriate instrument only when needed. The initial gel weight was measured (under argon) using either platinum foil (TGA) or an alumina cup (DTA). After sealing in a screw-top, glass vial, the specimen was transported outside the glove box and immediately loaded into the sample chamber. The residence time in air before the start of analysis was less than 1 minute.

3.5.3 X-RAY PHOTOELECTRON SPECTROSCOPY

A Kratos AXIS ULTRA was used to investigate the chemical homogeneity of thin-film specimens.[29] This instrument contained an aluminum X-ray source which was filtered by a monochromator to produce a characteristic Kα energy of 14.866 keV and a resolution better than 3 eV. A 0.7 mm x 0.3 mm rectangular area was selected for the beam profile. The penetration depth was approximately 1 μm although scattering within the sample reduced the actual analyzed depth to 10–20 nm. Analysis was carried out on a 1 cm x 1 cm specimen using two orthogonal axes which partitioned the film into quadrants; their origin lay directly at the specimen center. A photoelectron spectrum was taken at this origin and also along 1 mm axial increments (i.e., ± 1, ± 2, and ± 3 mm). The outermost border (i.e., ± 4 mm) was ignored due to the possibility of spin-coating edge defects.

Refinement and interpetation of the corresponding data required the processing of 512 individual spectra. Elemental peaks in the film spectra were compared against the published standards of MOULDER, et al. [13]. Labeled, representative spectra are given by Figures 3.22 and 3.23.[30] Software provided with the Kratos AXIS ULTRA enabled the determination of atomic concentration percents as corrected for elemental variations in cross-section. Thus, the ratios of calculated mass concentrations indicated the relative La:Ba:Mn or La:Pb:Mn sto-

---

[29]The author wishes to acknowledge the assistance of Dr. Rick Haasch who operated the instrument and carried out the actual measurements (i.e., on behalf of the author).
[30]The very small carbon peak at ~ 280 eV in Figures 3.22 and 3.23 is from volatile organics in chamber of the Kratox AXIS ULTRA and not the film specimens themselves.
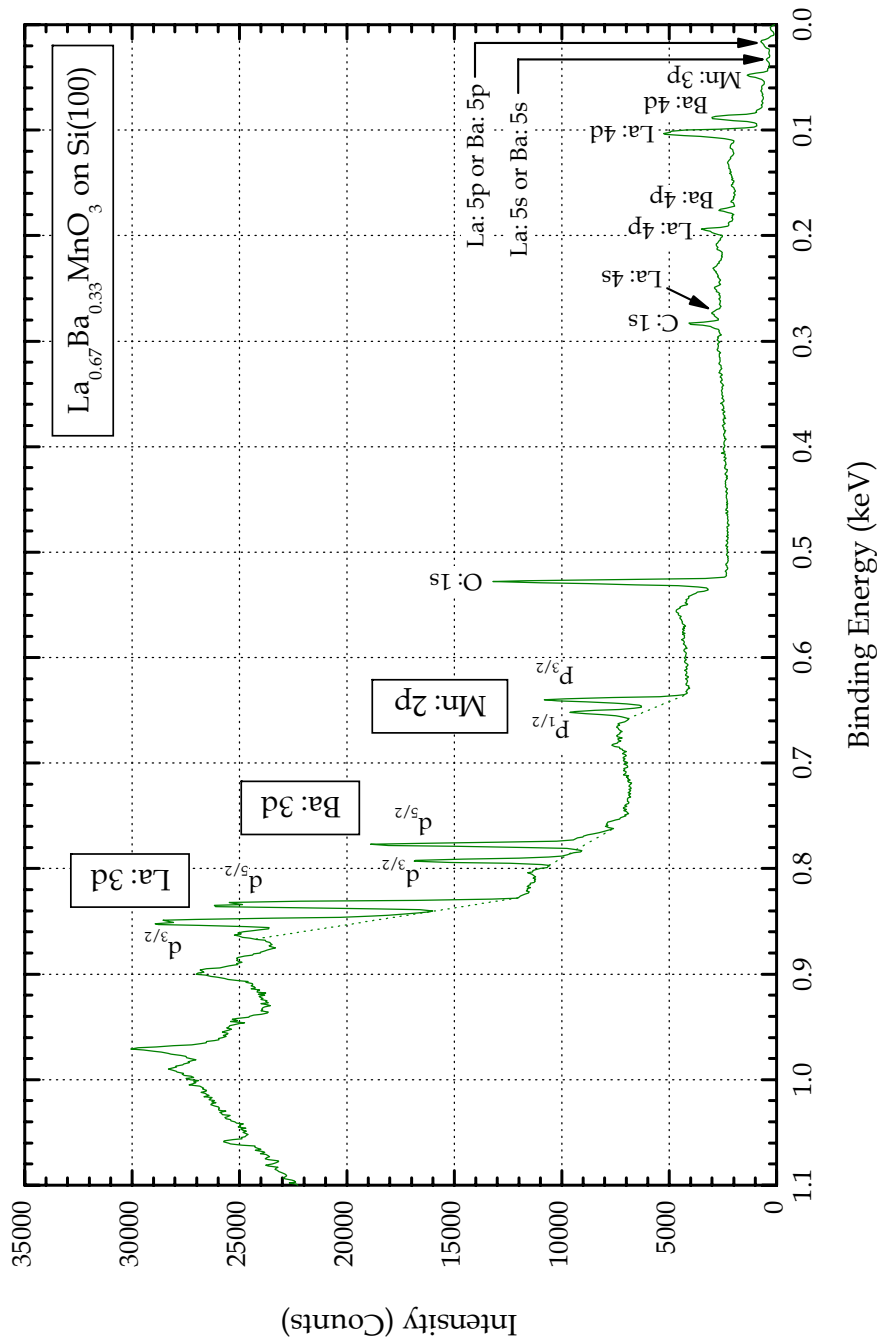
FIGURE 3.22 XPS spectrum for an $La_{0.67}Ba_{0.33}MnO_3$ film on Si(100). Standardized peaks for compositional analysis (with corresponding baselines) are indicated by shadowed boxes. The presence of carbon stems from trace contamination within the instrument chamber and should be ignored.
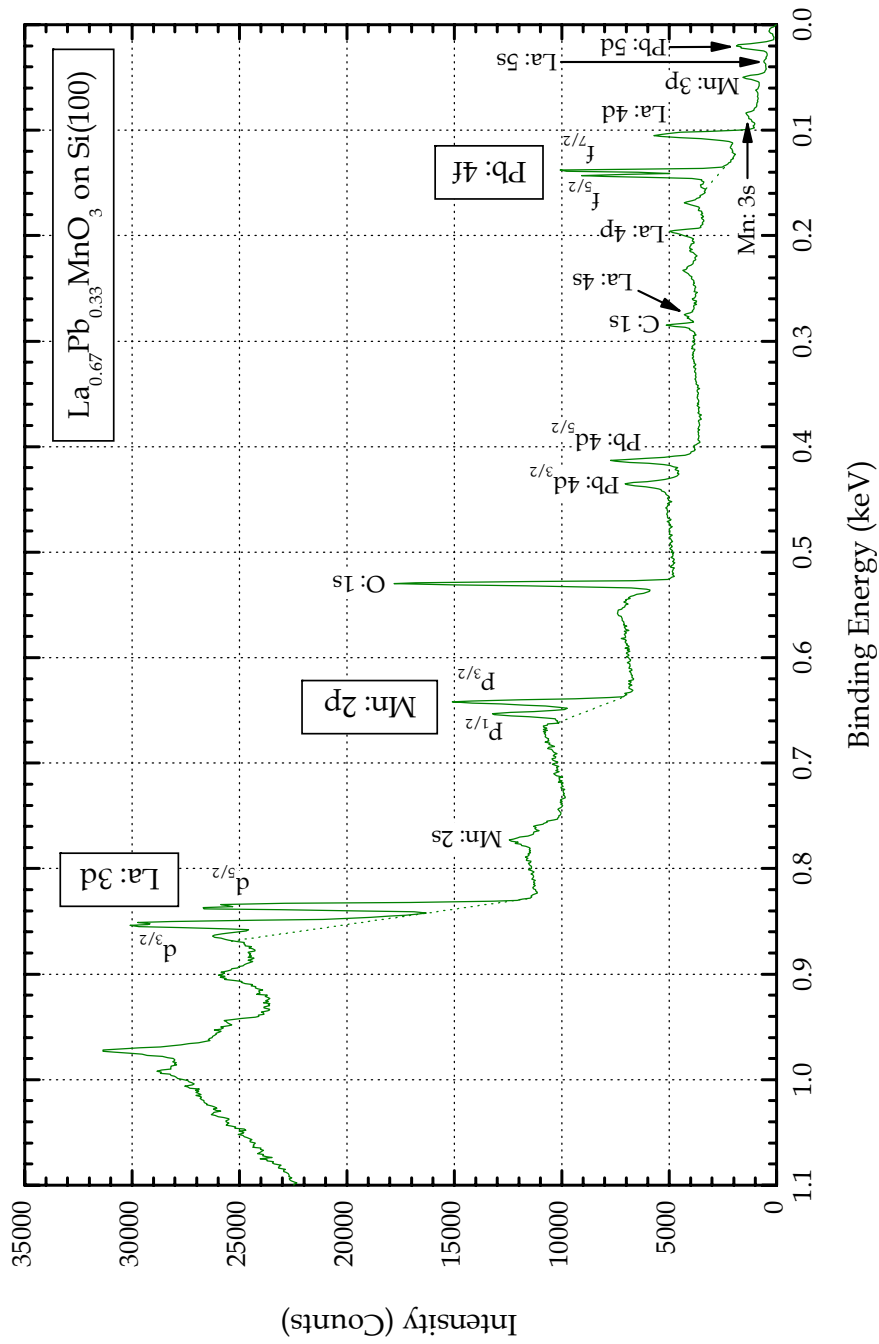
FIGURE 3.23 XPS spectrum for an La$_{0.67}$Pb$_{0.33}$MnO$_3$ film on Si(100). Standardized peaks for compositional analysis (with corresponding baselines) are indicated by shadowed boxes. The presence of carbon stems from trace contamination within the instrument chamber and should be ignored.

ichiometries. Further attempts, however, to authenticate [Mn^{4+}] proved futile. Peak widths of the manganese $2p_{3/2}$ binding-energy lines were sharp and contained no shoulders (i.e., no separation into discernable Mn^{3+} and Mn^{4+} sub-peaks).[31]

3.5.4 OPTICAL MICROSCOPY

To verify that the films, after crystallization, were dense, uniform, and defect-free, optical images were taken in reflectance mode by a Panasonic GP-KR222 digital camera connected to an Olympus BH-2 microscope. All images were from representative specimens, and hence, do not reflect "best-case" results. Analysis with cross-polarized filters, however, yielded no new discernable features, whether before or after crystallization.

3.5.5 SQUID MAGNETOMETRY

The onset of ferromagnetism was measured using a Quantum Design Magnetic Property Measurement System (MPMS). Small, rectangular samples were cut from the larger 1 cm x 1 cm specimens and their edge lengths measured via a micrometer (i.e., ± 10–15%). These samples were placed (separately) into gelatin capsules along with an appropriate quantity of cotton (i.e., to prevent sample motion). An individual capsule was then centrally-mounted into a (common) straw and held snug with plastic plugs above and below. The straw was subsequently inserted into the MPMS and calibrated to precisely locate the sample position.

To initiate measurement, the samples were first heated to 400 K (i.e., above the Curie point) to ensure a paramagnetic state. A 25 Oe field was then applied and the temperature decreased at 10 °C/minute to 5 K. Absolute magnetization (i.e., in units of emu) was recorded at intervals of 2 °C in high-resolution (i.e., oscillating) mode. The diamagnetic component of the bare Si(100) and platinized-Si(100) substrates was also measured in order to verify the integrity of the ferromagnetic data. Ferromagnetic signals (i.e., from the films) were found to be 7–8 orders of magnitude higher than their diamagnetic counterparts (i.e., from the underlying substrate). Thus, the diamagnetic component of the substrate was ignored (i.e., not subtracted from the paramagnetic or ferromagnetic signal).

---

[31]Also, the reference binding energies of Mn^{3+} in Mn_2O_3 (i.e., 641.2–641.7 eV) and Mn^{4+} in MnO_2 (i.e., 641.2–642.4 eV) overlap almost completely [13].

Magnetization data was converted to emu/cm^3 using film thickness values obtained via the scanning electron microscope (see Section 3.5.7). *The author wishes to stress that, because of possible errors in the measured film dimensions (i.e., ± 10–15% per edge length), the graphs presented in Section 4.6 should be used for relative comparisons only.* The Curie points, however, are not dependent on sample dimensions and are therefore accurate. Furthermore, due to the weak-field condition (i.e., H = 25 Oe), extrapolation of the magnetization to 0 K does not provide the saturated value (i.e., M_S). Proper determination of this metric requires very strong fields (i.e., $H > 1$ T) to ensure alignment of all manganese 3d electron spins. A strong-field measurement was not attempted because errors in the sample dimensions would produce unreliable M_S values.

3.5.6 X-RAY DIFFRACTION

Powder X-ray diffraction patterns were obtained on a Rigaku D-Max, Cu X-ray source at 45 kV and 20 mA (i.e., Kα_1 = 1.5406 Å and Kα_2 = 1.5444 Å), for 2θ values ranging from 20–90°. Soller slits filtered the beam at the X-ray source and in combination with a curved graphite monochromator at the detector. Ten individual scans were summed in "2-Theta/Theta-Reflection" mode to form a single pattern. The following three instrument settings were used: (1) a 10°/minute scan speed, (2) a 0.020° step interval, and (3) a "counts/second" detection state. To prepare samples, small portions (i.e., ~ 0.5–1.0 g) of oxide powder were placed onto a glass slide. A couple of drops of Aldrich 22,747-1, amyl acetate, 99% were added to the powder, enabling a uniform dispersion of the material on the slide (i.e., agitated with a clean, stainless-steel razor blade). Rapid volatilization of the amyl acetate left a solid mass, randomly-oriented, adhering to the glass slide. The slide was then mounted onto an aluminum plate with a central, rectangular hole (i.e., dimensions appropriate for the Rigaku D-Max sample chamber).

Because of possible (small) alignment errors, the *exact same powder* was transferred onto a Si(100) single crystal substrate (i.e., same preparative procedure described above). This substrate was then mounted onto the sample holder of a Philips X'pert 2 diffractometer (see next paragraph) and precisely aligned (i.e., 2θ, ψ, and ω) using the (400) peak of silicon as a reference (i.e., 2θ = 69.1290°). The largest diffraction peak of the manganite perovskite powder (i.e., corresponding to the {110} planes) was located and the 2θ value of its centroid recorded.

This value corrected the first (full) pattern taken on the Rigaku D-Max. Analysis of the powder patterns was carried out using JADE software (Version 6.5.23 from Materials Data, Inc.), which during processing, corrected peak broadening caused by extraneous $K\alpha_2$ radiation. Results obtained in this way were in excellent agreement with values reported in the literature.

X-ray diffraction patterns for thin film specimens were obtained on a Philips X'pert 2, Cu X-ray source at 45 KV and 40 mA (i.e., $K\alpha_1$ = 1.5406 Å and $K\alpha_2$ = 1.5444 Å), for 2θ values ranging from 20–90°. The instrument was programmed to run in glancing-incidence mode with ω fixed at 1.5°.[32] The cross-slit collimator of the X-ray source was adjusted to a 1 mm horizontal and 4 mm vertical gap. A nickel plate, parallel plate collimator, and flat graphite monochromator filtered the diffracted beam before reaching the detector. The x, y, and z coordinates of a central spot on each individual thin-film specimen was precisely determined before measurement. In addition, each specimen was also aligned (i.e., 2θ, ψ, and ω) using the (400) reference peak (i.e., 2θ = 69.1290°) of the underlying Si(100) substrate. Absolute intensities (i.e., counts) were collected in continuous scan mode using these settings: (1) a point-parallel plate configuration, (2) a 0.0400° step size, and (3) a 0.0200°/second scan speed. As with the powder diffraction patterns, analysis of thin film data was carried out using JADE software. But if a pattern contained less than three perovskite-phase reflections, no calculation of the lattice parameter was attempted.

3.5.7 SCANNING ELECTRON MICROSCOPY

Electron photomicrographs of film cross-sections were obtained using a Hitachi S-4700 scanning electron microscope (SEM). Samples were prepared by scoring the backside of the substrate with a diamond scribe and breaking. For platinized-Si(100), the substrate was submerged for 2–3 minutes in liquid nitrogen (i.e., after scoring) to ensure brittle fracture. Otherwise, the 1700 Å platinum and 300 Å titanium layers would deform plastically, making any determination of film thickness virtually impossible. To prevent surface charging, a conductive Au:Pd layer was sputtered onto the film before insertion into the sample chamber. A Sloan Dektak[3] stylus surface profilometer was used to confirm thicknesses measured by the

---

[32]This value corresponds to a penetration depth of ~ 300 nm.

SEM. Comparable values were obtained within experimental uncertainties (i.e., less than ± 5 nm) for a representative sample. Thus, all film thicknesses reported in this dissertation were obtained from cross-sectional SEM photomicrographs.

3.5.8 ATOMIC FORCE MICROSCOPY

The surface topography of thin-film specimens was measured using a Digital Instruments Dimension 3100 AFM in tapping mode. A tapping mode etched silicon probe (TESP) was mounted and calibrated according to procedures specified by the manufacturer [14]. Scans were taken within a 1 μm x 1 μm area, at a 1.969 Hz rate, and with 512 samples per line. To remove artifacts from the resulting images, Nanoscope III software (Version 5.12r2) from Digital Instruments was used to apply zeroth- and first-order polynomial filters to the topographical data. Root-mean-square (rms) surface roughness was calculated using WSxM software (Version 3.0) from Nanotec, Electrónica, S. L.

3.5.9 MAGNETOTRANSPORT

Magnetotransport properties were investigated using a Quantum Design Physical Property Measurement System (PPMS) with a DC resistivity puck (i.e., electrical bridge). Before measurement, however, all specimens were checked with a multimeter. Two probes of the multimeter were spaced ~ 1 mm apart, gently touched to the film, and the resistance measured. If an insulating phase predominated (i.e., little or no crystallization of manganite perovskite), the resistance could not be determined (i.e., greater than 50 MΩ). Such films were outside the measurement capability of the PPMS, and thus, not analyzed.

For attachment to the electrical bridge, specimens were sectioned into three identically-sized, rectangular pieces (i.e., via "score and fracture"). The central portion was selected for analysis. Four equally-spaced leads were mounted onto the film surface using Ted Pella 16032, colloidal silver paste.

Specifically, the following procedure was used: a fine, rounded, stainless-steel tip was dipped into the colloidal paste and then carefully touched to the film surface. This process left a ~ 1 mm diameter, hemispherical meniscus which dried into a circular pad. After curing (i.e., ~ 30 minutes), the end of a 0.001" diameter gold wire was placed onto the pad and a

small drop of paste applied to the top. This process was repeated three times to form individual leads spaced in-line and ~ 1 mm apart (i.e., four total). The remaining gold-wire ends were then soldered directly to corresponding pads on the DC resistivity puck.

To initiate measurement, the bridge was inserted into the PPMS and the integrity of the electrical connections confirmed. DC resistivity was obtained via a four-point geometry and 50 μA of current. The system was heated in zero-field to 400 K and cooled at 4 K/minute to 30 K. The resistivity was determined at 4 K intervals but only after the temperature equilibrated. After a full 400 K to 30 K cycle, the specimen was re-heated to 400 K, a magnetic field of H = 1 T applied, and the temperature cooled. In this way, magnetotransport was measured via 1 T increments from 0–5 T. Weak field measurements utilized the same 50.000 μA current but the temperature was fixed at T_{IM} (i.e., as determined from the zero-field magnetotransport curve). The magnetic field was then cycled in a loop according to: (1) 0 Oe to +500 Oe, (2) +500 Oe to –500 Oe, and (3) –500 Oe to 0 Oe.[33]

Much to the chagrin of the author, magnetotransport signals from films deposited on platinized-Si(100) corresponded to the temperature-dependent resistivity of platinum alone: small oxide film thicknesses (i.e., 90–100 nm) enabled substantial leakage to the higher-conducting platinum metal (i.e., the "path of least resistance").[34] To alleviate this problem, thicker films were prepared (i.e., 9 coatings). But even with this modification, magnetoresistive behavior could only be measured by *switching from in-plane (i.e., longitudinal), four-point to through-plane (i.e., transverse), two-point geometry*. This latter configuration exploited the platinum layer as a bottom electrode. Despite extensive efforts, weak-field measurements proved inconsistent, and hence, were not pursued. Further discussion is deferred to Section 4.10.

To prepare specimens for two-point analysis, a central 5 mm x 5 mm square was left on the substrate by etching off the film borders with dilute hydrochloric acid.[35] Scotch Magic™ Tape 810 from 3M was found to serve as an excellent patterning mask, producing sharp step-edges with no damage from lift-off. To remove undesired material, a cotton swab was *moistened* with the dilute acid solution and *gently* rubbed on the film surface. After etching, the substrate was rinsed with deionized water and cleaned according to procedures detailed in

---

[33]Stablizing a persient current in the superconducting coils requires 3–5 minutes. Thus, the rate of increase (or decrease) of the magnetic field is discontinuous and slow.

[34]Note that doped-lanthanide manganites exhibit resistivities typical of "dirty" metals (see Section 2.2.2).

[35]One part Fisher Scientific A144-212, Hydrochloric acid was dissolved into four parts deionized water.

Section 3.4.3. Inspection using an optical microscope ensured no residual adhesive remained on the specimen. A thin top electrode of silver paste was applied with the masking aid of the Scotch Magic™ Tape. The corresponding dimensions were *just less* than the 5 mm x 5 mm oxide film geometry. This precaution prevented contact with the platinum layer, and hence, shorting. Two leads were then attached as described for the four-point measurement.

3.6 CONCLUSION

From the experimental data presented here, three critical milestones were achieved that enable the alkoxy-based, sol-gel processing of manganite thin films. First, the isolation of 2-methyl-2-propoxo manganese(II), 2-methyl-2-propoxo lead(II), and 2-methyl-2-propoxo barium, *all as true alkoxides and not oxoalkoxide derivatives*, provides the basis for an all-alkoxide approach. Second, the synthesis of orange and pinkish-orange solutions demonstrates the preparation of unoxidized systems free from brown colloidal or particulate inclusions. And lastly, the development of proper hydrolytic procedures ensures the decomposition of xerogel coatings into transparent, dense, and defect-free films *before crystallization*. This latter accomplishment stems from the deliberately-designed (i.e., $h = 0.25$) *polymeric nature* of the 0.2 M La-Ba-Mn and La-Pb-Mn sols (see Section 2.3.5). The resulting amorphous films then readily crystallize into manganite perovskite between 600–650 °C, the subsequent investigation of which, comprises the subject matter of Chapter 4.

3.7 REFERENCES

[1] Harwood, L. M.; Moody, C. J.; Percy, J. M. *Experimental Organic Chemistry: Standard and Microscale*, 2nd, ed.; Blackwell Science: Malden, MA, 1999.

[2] Shriver, D. F.; Drezdzon, M. A. *The Manipulation of Air-Sensitive Compounds*, 2nd ed.; John Wiley and Sons: New York, 1986.

[3] Coyne, G. S. *The Laboratory Companion: A Practical Guide to Materials, Equipment, and Technique;* John Wiley and Sons: New York, 1997.

[4] Amonoo-Neizer, E. H.; Shaw, R. A.; Skovlin, D. O.; Smith, B. C. In *Lithium Bis(trimethylsilyl)amide and Tris(trimethylsilyl)amine*; Holtzclaw, H. F., Jr.; Brimm, E. O.; Cady, G. H.; Dwyer, F. P.; Jolly, W. L.; Katz, J. J.; Muetterties, E. L.; Netherton, L. E.; Nielsen, M. L.; Parry, R. W.; Scott, J. D.; Tyree, S. Y., Jr.; Wilkinson, G., Eds.; Inorganic Syntheses, Vol. VIII; McGraw-Hill: New York, 1966; pp 19–22.

[5] Wakefield, B. J. *Organolithium Methods*; Katritzky, A. R., Meth-Cohn, O., Rees, C. W., Eds.; Best Synthetic Methods; Academic Press: London, 1988.

[6] Borup, B.; Samuels, J. A.; Streib, W. E.; Caulton, K. G. A Soluble Alkoxide of Barium with a Cubane Structure. *Inorganic Chemistry* **1994**, *33* (5), 994–996.

[7] Hubert-Pfalzgraf, L. G. Toward Molecular Design of Homo- and Heterometallic Precursors for Lanthanide-Based Oxide Materials. *New Journal of Chemistry* **1995**, *19* (5–6), 727–750.

[8] Ju, H. L.; Gopalakrishnan, J.; Peng, J. L.; Li, Qi; Xiong, G. C.; Venkatesan, T.; Greene, R. L. Dependence of Giant Magnetoresistance on Oxygen Stoichiometry and Magnetization in Polycrystalline $La_{0.67}Ba_{0.33}MnO_z$. *Physical Review B* **1995**, *51* (9), 6143–6146.

[9] Yang, J.; Hu, S.; Uher, C.; Han, P. D.; Payne, D. A. Magnetic and Electronic Transport Properties of Single Crystal $La_{0.64}Pb_{0.36}MnO_3$. In *Science and Technology of Magnetic Oxides*, Materials Research Society Symposia Proceedings, Vol. 494, Boston, MA, Dec 1–4, 1997; Hundley, M. F., Nickel, J. H., Ramesh, R., Tokura, Y., Eds.; Materials Research Society: Warrendale, PA, 1998; pp 317–322.

[10] Fors, R.; Khartsev, S.; Grishin, A.; Pohl, A.; Westin, G. Sol-Gel Derived Versus Pulsed Laser Deposited Epitaxial $La_{0.67}Ca_{0.33}MnO_3$ Films: Structure, Transport, and Effect of Post-Annealing. *Thin Solid Films* **2004**, *467* (1–2), 112–116.

[11] Pohl, A.; Westin, G.; Jansson, K. Preparation of $La_{0.67}Ca_{0.33}MnO_3$ Nanophase Powders and Films from Alkoxide Precursors. *Chemistry of Materials* **2002**, *14* (5), 1981-1988.

[12] Pohl, A.; Westin, G.; Jansson, K. Preparation of $La_{0.75}Sr_{0.25}MnO_3$ Nano-Phase Powders and Films from Alkoxide Precursors. *Journal of Sol-Gel Science and Technology* **2003**, *26* (1–3), 257–260.

[13] Moulder, J. F.; Stickle, W. F.; Sobol, P. E.; Bomben, K. D. *Handbook of X-ray Photoelectron Spectroscopy. A Reference Book of Standard Spectra for Identification and Interpetation of XPS Data*; Chastain, J., King, R. C., Jr., Eds.; Physical Electronics: Eden Prairie, MN, 1995.

[14] *Basic SPM Training Course*, Revision B; Digital Instruments, Veeco Metrology Group, LLC: Santa Barbara, CA, 2000; revised Feb 2003.

CHAPTER 4

RESULTS AND DISCUSSION

4.1 OVERVIEW

In order to develop an alkoxy based, sol-gel processing method for manganite-perovskite thin films, the completion of three objectives was required: (1) the development of a chemical-solution system using all alkoxide precursors, and in particular, the synthesis of a highly soluble and reactive manganese(II) alkoxide, (2) the demonstration of low-temperature densification and crystallization behavior, and (3) the measurement of characteristic magnetoresistive properties under standard (i.e., $H = 0$–5 T) and weak-field (i.e., $H < 500$ Oe) conditions. This chapter presents conclusive evidence for the successful accomplishment of all these objectives. Solution chemistry, xerogel decomposition, and thin-film microstructure are investigated with an emphasis on correlating the resultant magnetic and electrical properties with perovskite phase evolution.

4.2 ALKOXIDE SOLVATION

As stated in Section 2.5, HORVATH, et al. [1] reported that 2-methyl-2-propoxo manganese(II) failed to dissolve in alkane, ethereal, alcoholic, and nitrile media — a sizable collection of fundamental organic solvents! Yet in Section 3.5.1, the author clearly demonstrates the solubility of this alkoxide in 2-methoxyethanol. Accordingly, fourier transform infrared (FTIR) spectroscopy was used to determine the solute-solvent interactions which lead to solvation. First, an infrared absorbance spectra of the pure solvent was obtained (see Figure 4.1) and all functional groups identified (see Table 4.1) [2]. This reference pattern was then compared against the requisite alkoxide solutions and the differences noted.

Of particular importance are perturbations in the bending modes of the highly-polar $O^{\delta-}$ $-H^{\delta+}$ group. Solvate coordination to the electrophilic metal center of alkoxides proceeds via nucleophilic addition, leaving an adduct upon crystallization (see Section 2.3.2). In solutia, such interactions remain due to weak $M^{\delta+}-O^{\delta-}$ interactions analogous to hydrogen bonding in water. To illustrate this point, Figure 4.2 provides the infrared spectra of 2-propoxo lan-
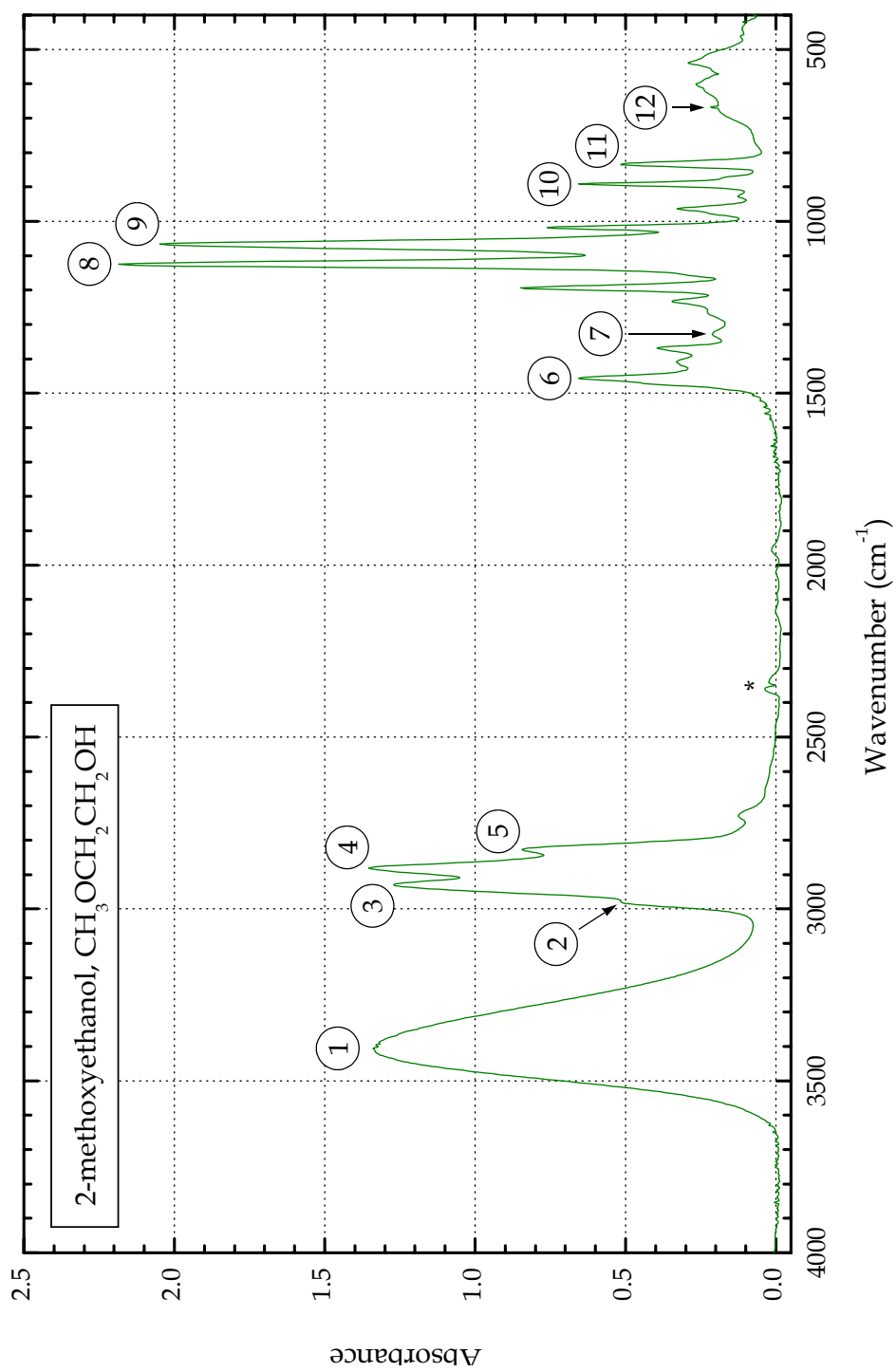
FIGURE 4.1 Infrared absorbance spectrum of 2-methoxyethanol. The asterisk marks the signature of adventitious CO_2 molecules in the inert nitrogen atmosphere surrounding the sample cell.

Structural Group[a]	Vibration Mode	Typical Wavenumber[b] (cm⁻¹)	Observed Wavenumber (cm⁻¹)	Label in Figure 4.1
General Alcohol (ROH)				
O–H	Bend, Scissors	3350 ± 50	3397	1
	Bend, In-Plane	1350 ± 50	1329	7
	Bend, Out-of-Plane	650 ± 50	667	12
C–C–O	Stretch, Asymmetric	1040 ± 40	1066	9
	Stretch, Symmetric	850 ± 50	891	10
General Ether (ROR)				
C–O–C	Stretch, Asymmetric	1105 ± 35	1124	8
	Stretch, Symmetric	850 ± 50	835	11
Methyl-Oxy ($-OCH_3$)				
C–H	Stretch, Asymmetric	2945 ± 25	2979[c]	2
	Stretch, Symmetric	2830 ± 10	2827	5
	Bend, Symmetric	1455 ± 15	1456	6
Methylene-Oxy ($-OCH_2-$)				
C–H	Stretch, Asymmetric	2940 ± 20	2929	3
	Stretch, Symmetric	2855 ± 20	2881	4

[a] R corresponds to a saturated alkyl ligand.
[b] Reference values obtained from [2].
[c] Partially embedded inside another peak. Value taken from shoulder maximum.

TABLE 4.1 Infrared frequencies of active structural groups in 2-methoxyethanol. Position assignments and labels refer to the spectrum given by Figure 4.1.

169
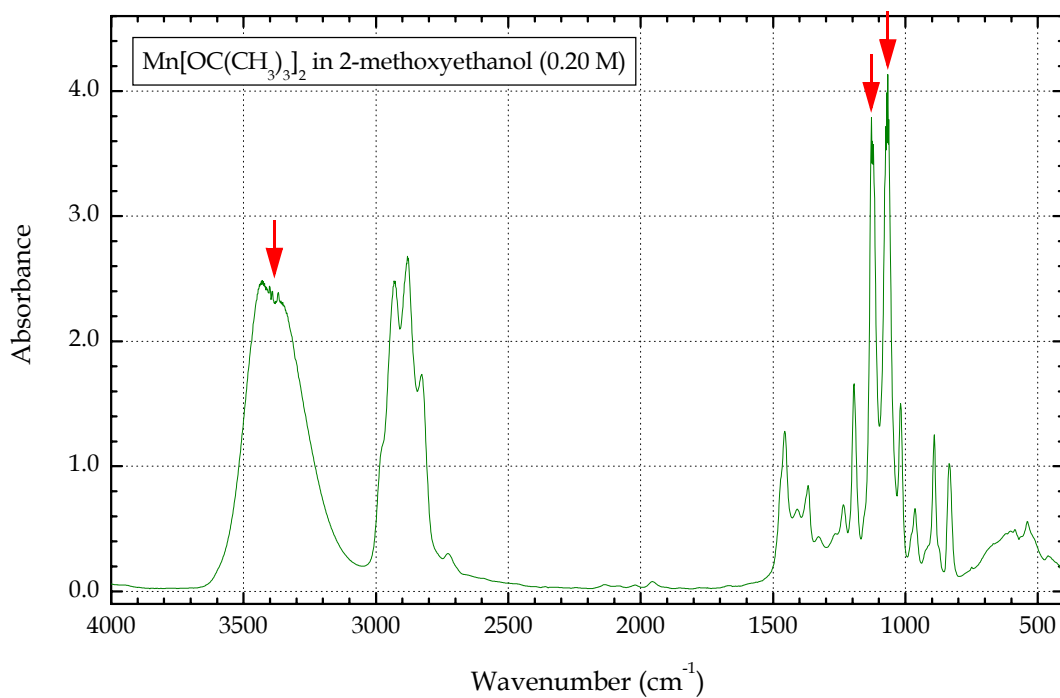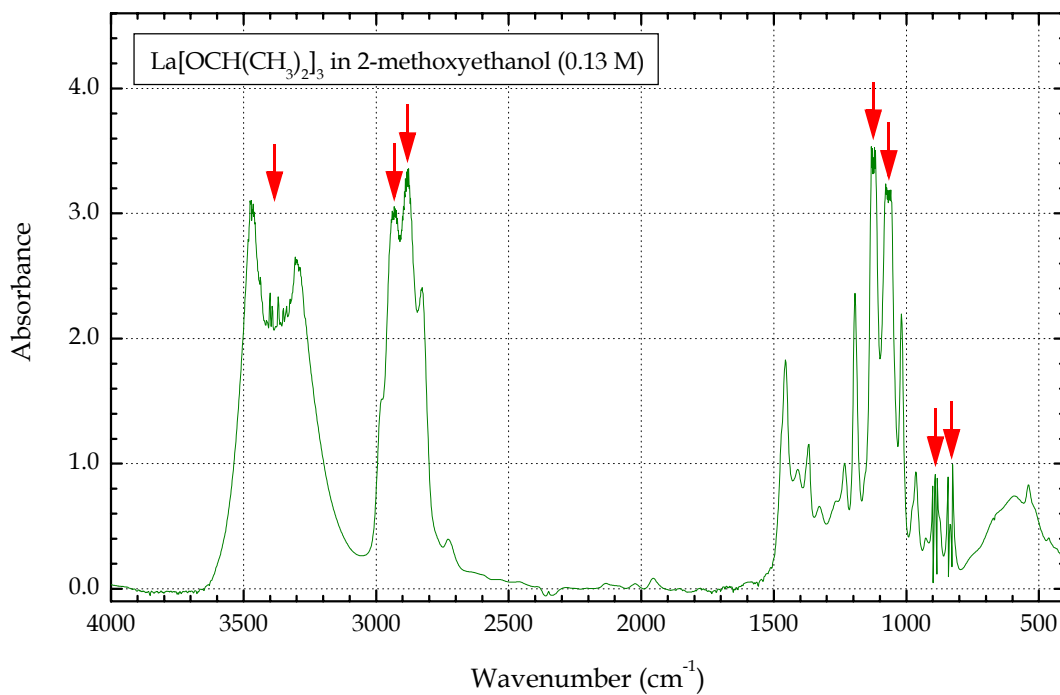
FIGURE 4.2 Infrared absorbance spectra of homometallic alkoxide solutions. Arrows highlight perturbations in the native solvent stretching modes.

thanum and 2-methyl-2-propoxo manganese(II) in 2-methoxyethanol.[1] In the former, splitting of the broad 3400–2900 cm^{-1} absorbance band (i.e., the $O^{\delta-}-H^{\delta+}$ scissors bending mode), is reminiscent of the $La_5O[OCH(CH_3)_2]_{13} \cdot 3.5HOCH_2CH_2OCH_3$ species characterized by chemical analysis in Section 3.3.2. Not surprisingly, the $C-C-O$ symmetric stretch mode at 891 cm^{-1} is also heavily split. The ether group (i.e., $C-O-C$) both experiences a splitting of its symmetric (i.e., 835 cm^{-1}) and asymmetric (i.e., 1124 cm^{-1}) stretching modes. But the larger perturbation of the $O^{\delta-}-H^{\delta+}$ vibration mode implicates an $M^{\delta+} \leftarrow O^{\delta-}-H^{\delta+}$ interaction as the principal dissolution mechanism.

In similar fashion, inspection of the spectrum corresponding to solvated 2-methyl-2-propoxo manganese(II) reveals a clear perturbation of the $O^{\delta-}-H^{\delta+}$ scissors bending mode. But the magnitude of this splitting is diminished compared to 2-propoxo lanthanum. Very weak splitting is also found in the peaks attributed to $C-C-O$ and $C-O-C$ symmetric stretching modes. Together, these observations indicate a predominance of alcoholic over ethereal interactions. Furthermore, the absence of both a $C-C-C$ stretch mode (i.e., 914 cm^{-1}) and a split CH_3 umbrella mode (i.e., 1379 cm^{-1} and 1366 cm^{-1} in 1:2 relative intensity) eliminates the possibility of free 2-methyl-2-propanol in solution [2]. *Thus, the dissolution of 2-methyl-2-propoxo manganese(II) is thought to occur via coordination (i.e., nucleophilic addition) and not through reaction (i.e., nucleophilic substitution).* Attempts to crystallize a solid-state adduct (i.e., with subsquent characterization), however, were not undertakened by the author. Instead, such an investigation is recommended as future research (see Chapter 6). The weak $O^{\delta-}-H^{\delta+}$ perturbation, however, suggests a smaller alcoholate composition (i.e., less than $n = 3.5$ value found with $La_5O[OCH(CH_3)_2]_{13} \cdot 3.5HOCH_2CH_2OCH_3$).

As discussed in Section 2.3.4, the presence of multiple alkoxides in solution often enables Lewis acid-base reactions, forming new, heterometallic species. Indeed, the infrared absorbance spectra of the 0.25 M La-Ba-Mn (2:1:3) and La-Pb-Mn (2:1:3) "stock" solutions reveals no perturbations of either the alcoholic or ethereal vibration modes (see Figure 4.3). Hence, the lack of detectable solvent interactions implies the creation of highly-soluble, heterometallic alkoxides with saturated coordination spheres. In the region below 800 cm^{-1}, small peaks emerge which are consistent with $M-O$ stretching modes. For example, ADAMS, et al. [3]

---

[1] As discussed in Section 3.3.2, 2-propoxo lanthanum is, in fact, an oxoalkoxide compound. For convenience though, the "2-propoxo" designation will be continued throughout this section.
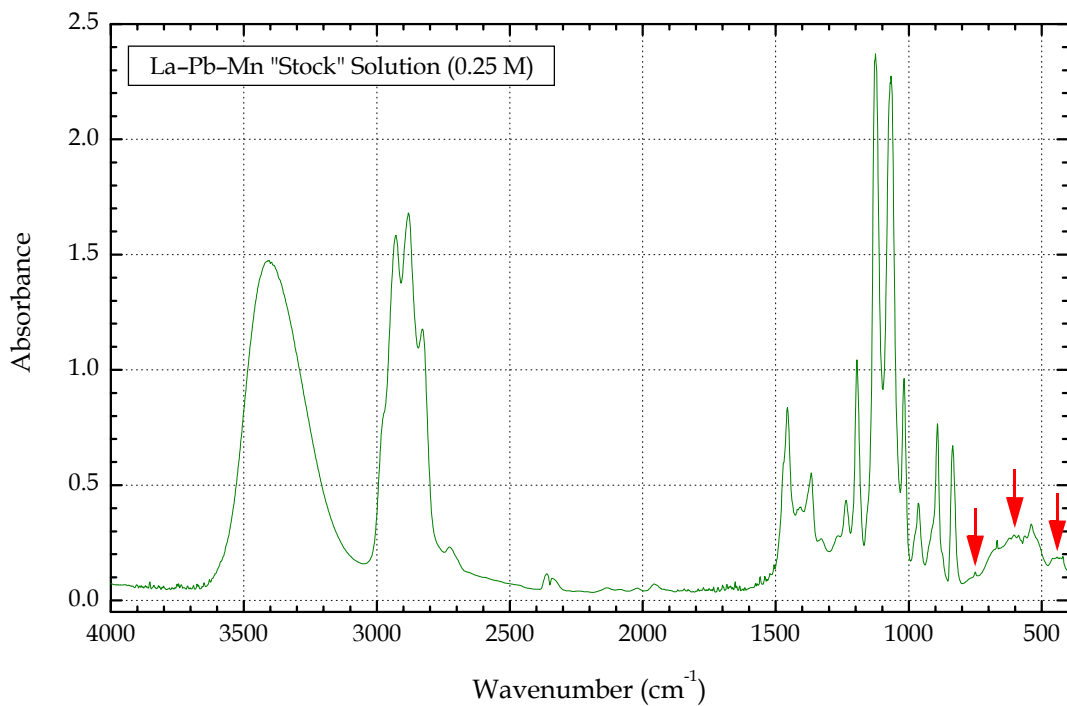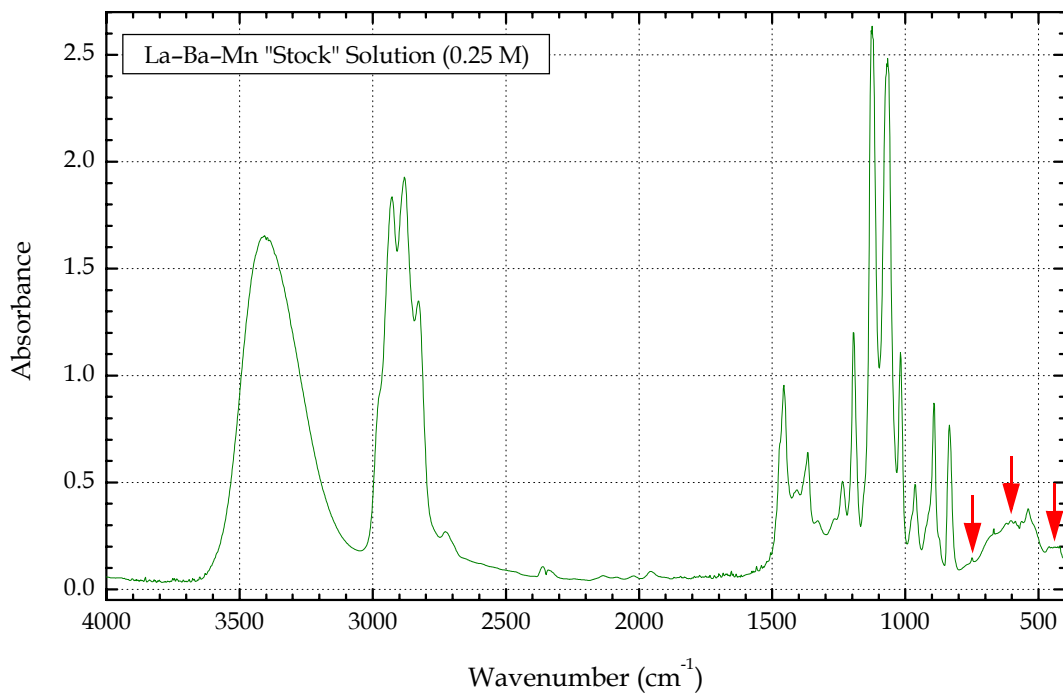
FIGURE 4.3 Infrared absorbance spectra of La-Ba-Mn and La-Pb-Mn "stock" solutions. Arrows indicate potential $M-O-C$ stretching modes.

172

reported that transition-metal (i.e., Cr, Mn, Fe, Co, Ni, and Cu) methoxides exhibited infrared $M-O$ asymmetric and symmetric stretching modes between 600–300 cm^{-1}. Unfortunately, due to the complexity of multi-component solutions, elemental identification of these modes was not possible.

4.3 THERMAL ANALYSIS

In order to develop the heat treatment process described by Section 3.4.3, investigation of La-Ba-Mn (2:1:3) and La-Pb-Mn (2:1:3) xerogel decomposition was conducted using thermogravimetric (TGA) and differential thermal (DTA) analyses (see Figures 4.4 and 4.5). But because the samples prepared by solvent evaporation (i.e., a dry, argon current) were not fully-desiccated, a discussion of their decompositional behavior will be presented last. These latter samples start as *gels*, and hence, are distinguished as such.

For all xerogels, the 25–200 °C range corresponds to a region of thermally-driven hydrolysis and condensation; mass loss stems from liberated water, 2-methoxyethanol, 2-methyl-2-propanol, and volatilized organics (i.e., solvent molecules, leaving groups, and decompositional by-products). But at 180–230 °C, a shoulder develops in the TGA curves which marks the onset of pyrolysis. Accordingly, a very sharp exotherm emerges within this temperature range (see DTA plots). *A comparison of the hydrolysis environments clearly shows that gelation under moisture-rich atmospheres shifts the onset of decomposition to lower temperatures.* For example, the exothermic peak of the La-Ba-Mn (2:1:3) xerogels decreases from 238 °C to 214 °C to 200 °C for samples hydrolyzed, respectively, in lower-humidity air, higher-humidity air, and moisture-saturated argon.[2] Equivalent temperatures for La-Pb-Mn (2:1:3) are 222 °C, 194 °C, and 191 °C, respectively.

The 240–550 °C temperature range involves the decomposition of carbonate, oxycarbonate, and/or hydroxycarbonate compositions which slowly generate CO_2 gas and H_2O vapor. For La-Ba-Mn (2:1:3), mass loss approaches a plateau at ~ 460 °C (i.e., lower-humidity air) and ~ 540 °C (i.e., higher-humidity air), indicating the formation of a thermally-stable oxycarbonate phase (see Section 2.3.5). Similar profiles develop in the La-Pb-Mn (2:1:3) system.

---

[2] "Lower humidity" corresponds to less than 30%; "higher humidity", greater than 65%. As discussed above, this difference affects decomposition behavior, underscoring the need for partial (i.e., controlled) hydrolysis. An alkoxy-based, sol-gel process would otherwise be susceptible to fluctuations in aerobic moisture.
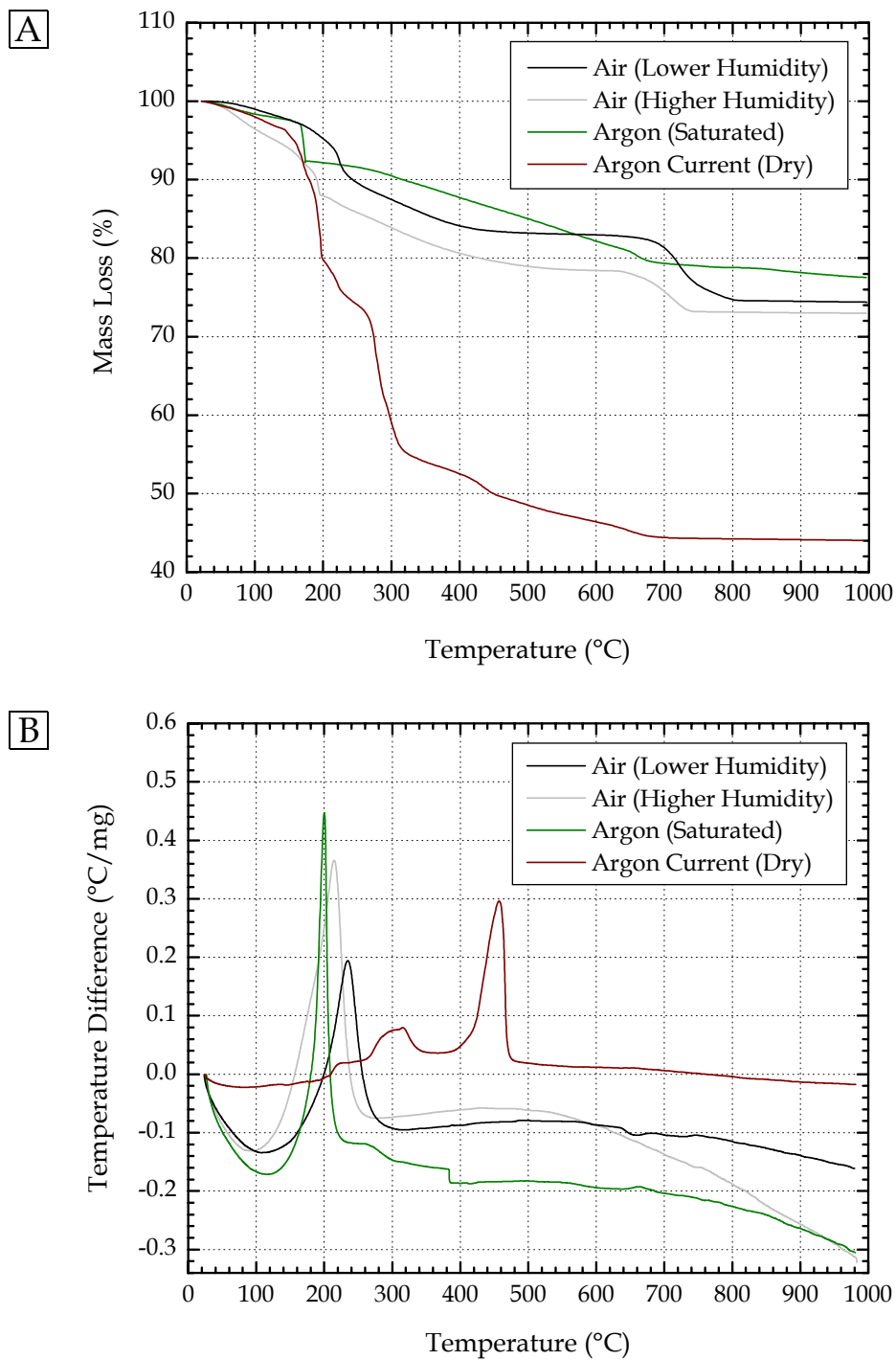
FIGURE 4.4 Decomposition behavior of La-Ba-Mn polymeric gels during pyrolysis. Thermogravimetric (A) and differential thermal (B) plots are shown. The elemental ratio of the metals is, respectively, 2:1:3.

174
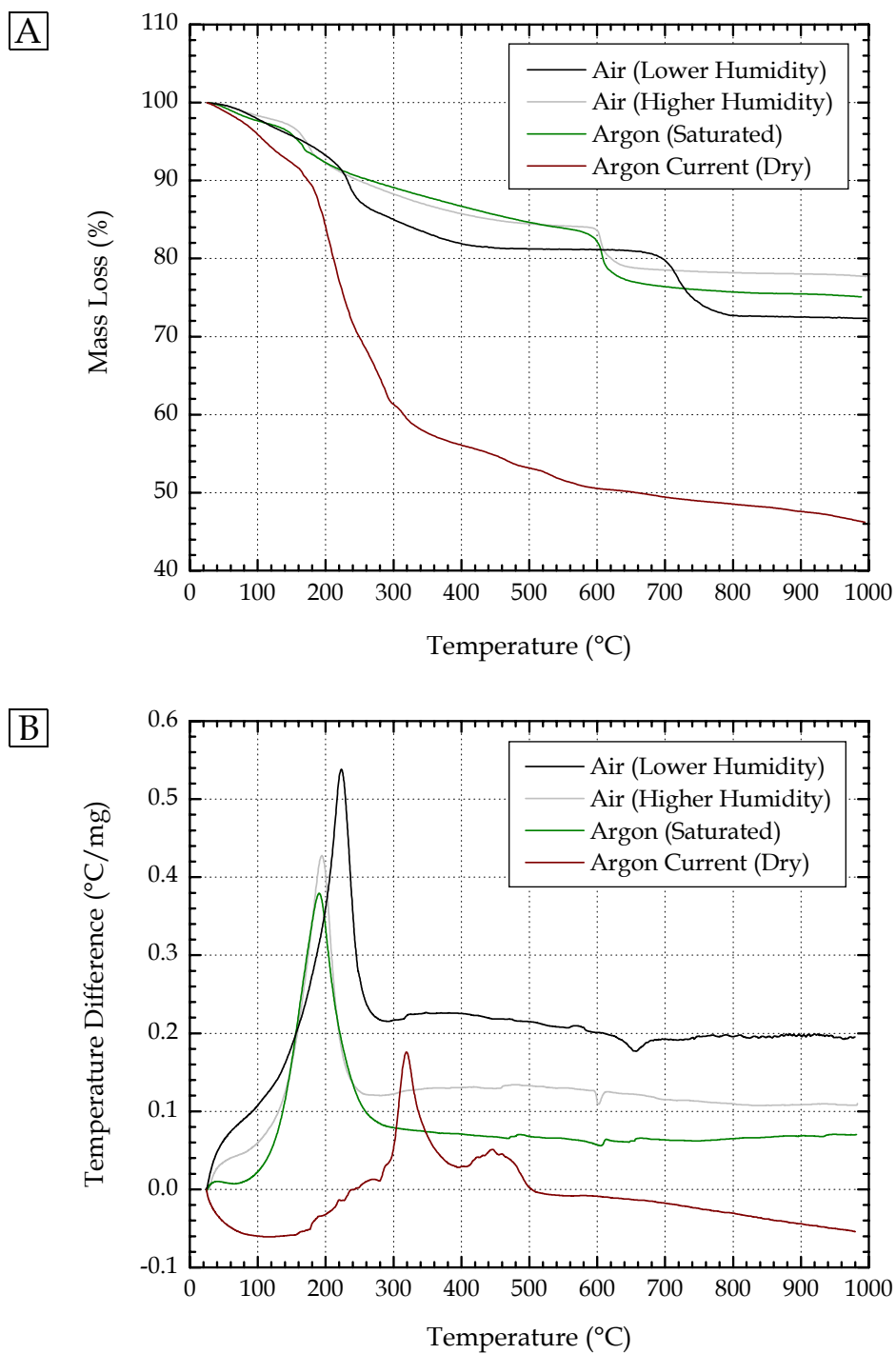
FIGURE 4.5 Decomposition behavior of La-Pb-Mn polymeric gels during pyrolysis. Thermogravimetric (A) and differential thermal (B) plots are shown. The elemental ratio of the metals is, respectively, 2:1:3.

Such thermal behavior compares well with that of alkoxy-derived La-Ca-Mn (2:1:3) and La-Sr-Mn (3:1:4) sol-gel powders synthesized by POHL, et al. [4, 5]. In contrast, xerogels prepared in moisture-saturated argon, however, lose mass continuously until ~ 650 °C (i.e., La-Ba-Mn) and ~ 600 °C (i.e., La-Pb-Mn) at which a small shoulder appears.

In each system, the shoulders which appear above ~ 550 °C correlate directly to small endothermic peaks (see DTA plots). These characteristics reflect the elimination of remaining carbonate groups and the emergence of manganite-perovksite phase.[3] Thermal analysis would then suggest a "best-case" crystallization temperature of ~ 650 °C and ~ 600 °C for, respectively, La-Ba-Mn (2:1:3) and La-Pb-Mn (2:1:3). Such values are in good agreement with the ferromagnetic onset and X-ray diffraction patterns of thin films crystallized on platinized-Si(100) (see Table 4.2).[4] Furthermore, xerogels prepared using moisture-saturated argon exhibit earlier carbonate decomposition and sharper decomposition shoulders. *Thus, the results of thermal analysis support the utilization of post-coating hydrolysis (see Section 3.4.3) for manganite films: improved hydrolysis, by increasing oxide content, lowers the perovskite crystallization temperature, a critical goal of this dissertation.*

Thermal analysis of the *partially-dessicated* gels (i.e., concentrated under a dry, current of argon) reveals a large initial drop in mass below 300 °C (i.e., 40–45%). Clearly, the removal of pore-entrapped solvent accounts for much of the loss below ~ 200 °C but further by-products of hydrolysis and condensation are also liberated. Unfortunately, the author lacked access to a mass spectrometer (i.e., a combined TGA-MS system). Species identification, therefore, was not possible and is recommended as future research (see Chapter 6). The DTA curves indicate two large, distinct exotherms at ~ 300 °C and ~ 450 °C. Such decompositional behavior is notably different from that exhibited by the xerogels. *Hence, caution must be excercised when adapting the results of bulk xerogels to spin-coated films.* Final carbonate removal and crystallization, however, does proceed at similar temperatures.

4.4 CHEMICAL HOMOGENEITY

Although the bulk, polycrystalline pellets, characterized in Section 3.4.1, confirmed a proper *solution* stoichiometry, the chemical homogeneity of coated specimens was analyzed

---

[3] POHL, et al. [4, 5] reported the decomposition of $La_{1-x}M_xMnO_3(CO_3)_y$ compounds above 600 °C where $y < 1$.
[4] For thermogravimetric analysis, both xerogel and gel samples were loaded into pans lined with platinum foil.

via XPS to ensure a uniform elemental distribution within the *films* (i.e., La-Ba-Mn and La-Pb-Mn of 2:1:3). *Figures 4.6 through 4.9 indicate that, within experimental uncertainty (i.e., ± 0.025), all films exhibit the 2:1:3 stoichiometry regardless of substrate-type, heat-treatment temperature, or composition.* Furthermore, the XPS spectra indicate no contamination from elements corresponding to the underlying substrate or residual carbonate groups (refer to Figures 3.22 and 3.23).[5] *Thus, firing at 600 °C (or higher) forms a dense amorphous oxide film that readily crystallizes upon further heat treatment (see Section 4.7).*

Interestingly, in the $La_{0.67}Pb_{0.33}MnO_3$ coatings, the lead content was not observed to decrease as the firing temperature increased from 600 °C to 750 °C; the Pb:Mn ratio stayed constant at 0.33 ± 0.025 with no temperature-dependent skew. This finding is unusual given the well-known volatilization of PbO from titanate and zirconate perovskites at similar temperatures. For example, TANI and PAYNE [6] pioneered the use of a lead oxide cover-coat to inhibit lead loss during the heat treatment of sol-gel $PbTiO_3$, $PbZr_xTi_{1-x}O_3$, and lanthanum-modified $PbZr_xTi_{1-x}O_3$ films. No cover-coat, however, was incorporated for the sol-gel processing of $La_{0.67}Pb_{0.33}MnO_3$ films presented in this dissertation. Subsequent investigation of surface topology (see Section 4.9), however, suggests the activation of thermal etching via PbO volatilization from the surface of the grain.

4.5 OPTICAL MICROSCOPY

To provide a quick, straight-forward verification of film quality, optical micrographs were taken of the specimens in reflectance mode. *Figures 4.10 and 4.11 indicate transparent, smooth, dense, and crack-free films.* Thus, partial hydrolysis, in combination with exposure to humidified air (i.e., post-spinning), successfully diminished organic content within the coated xerogel so that upon pyrolysis, no porosity or phase separation developed (i.e., refer back to Figure 3.20). Within each temperature sequence, however, a slight change in hue occurred, which to the naked eye, corresponded to the emergence of blue coloring. The onset temperatures are given as follows: (1) 700 °C for La-Ba-Mn on Si(100), (2) 650 °C for La-Ba-Mn on platinized-Si(100), (3) 650 °C for La-Pb-Mn on Si(100), and (4) 650 °C for La-Pb-Mn on platinized-Si(100). These observations are in good agreement with the onset of crystalliza-

---

[5] A film-substrate reaction layer, however, was present for all films deposited on Si(100) (see discussion in Section 4.7).
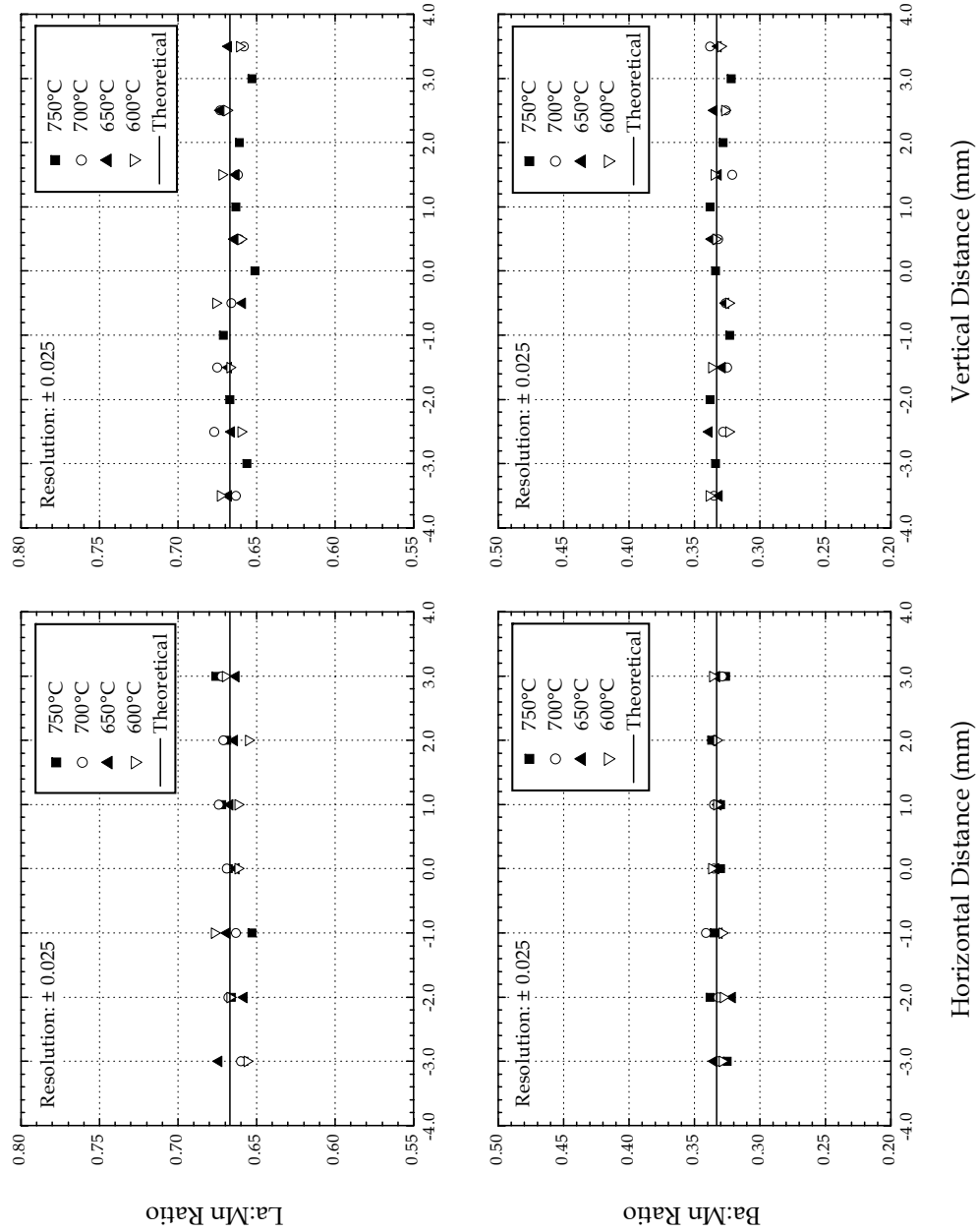
FIGURE 4.6 XPS analysis of $La_{0.67}Ba_{0.33}MnO_3$ film surfaces on Si(100). Horizontal and vertical distances correspond to lengths, from the center, along axes bisecting a 1 cm^2 substrate into four equal quadrants.
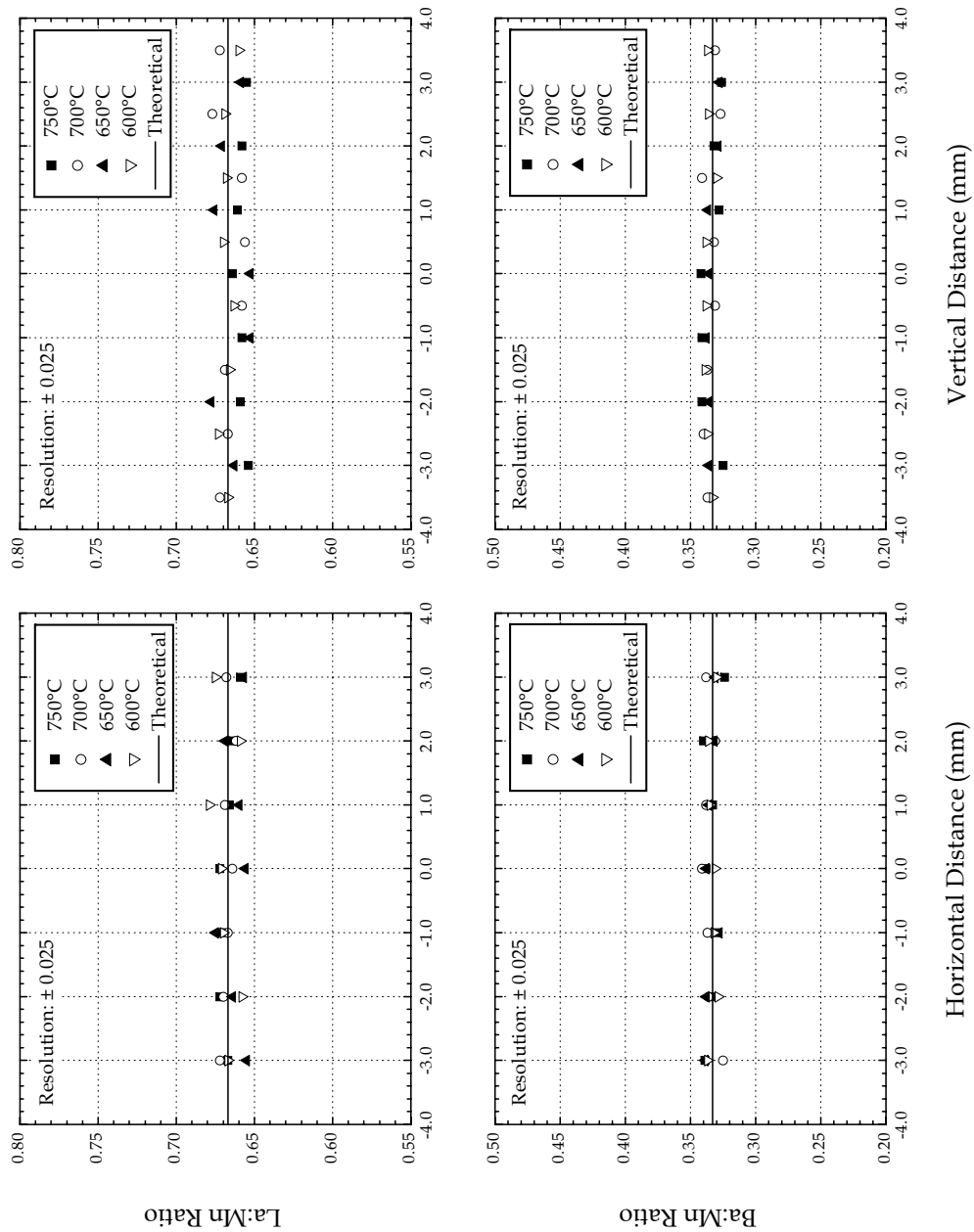
FIGURE 4.7 XPS analysis of $La_{0.67}Ba_{0.33}MnO_3$ film surfaces on platinized-Si(100). Horizontal and vertical distances correspond to lengths, from the center, along axes bisecting a 1 cm² substrate into four equal quadrants.

179
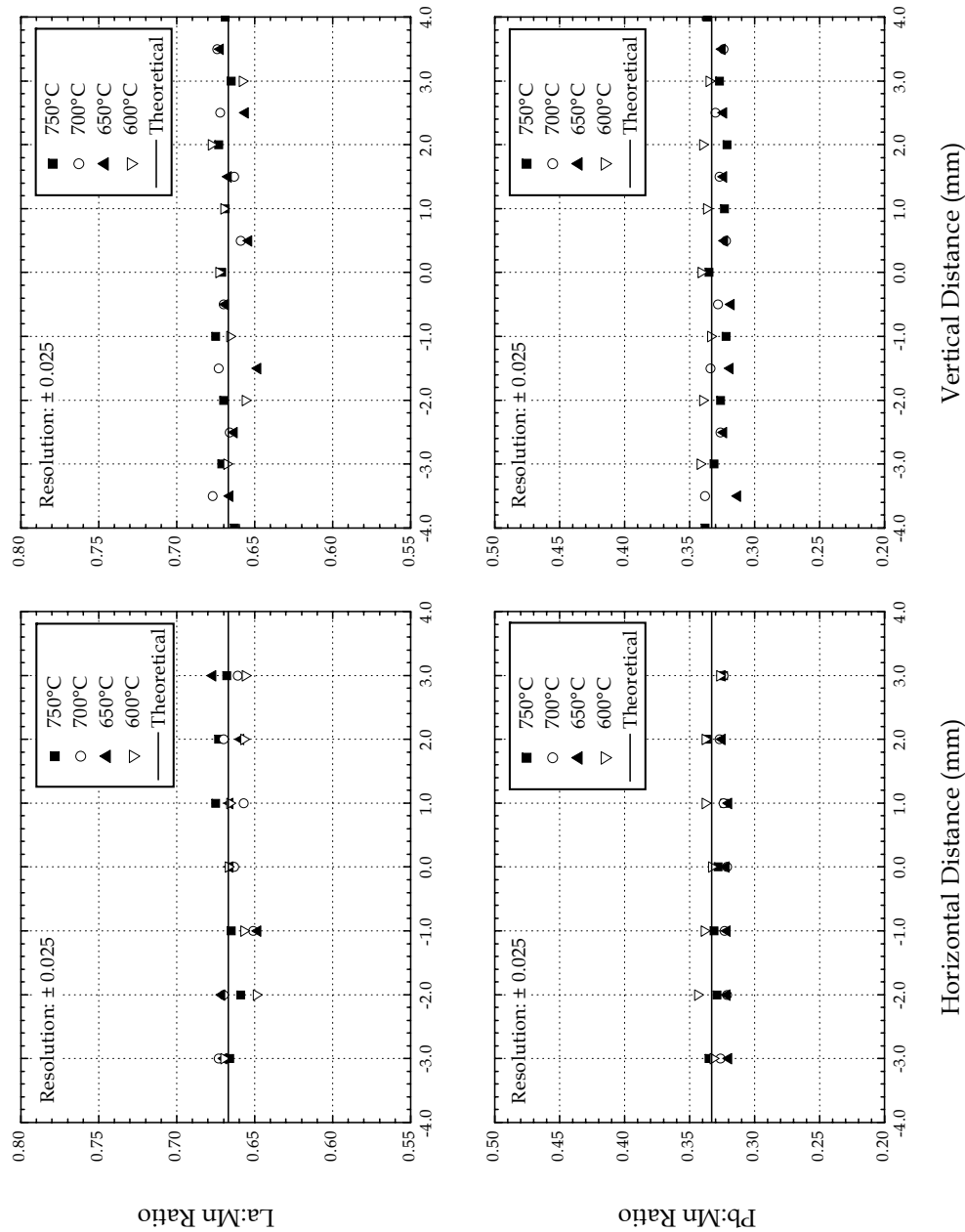
FIGURE 4.8 XPS analysis of $La_{0.67}Pb_{0.33}MnO_3$ film surfaces on Si(100). Horizontal and vertical distances correspond to lengths, from the center, along axes bisecting a 1 cm² substrate into four equal quadrants.
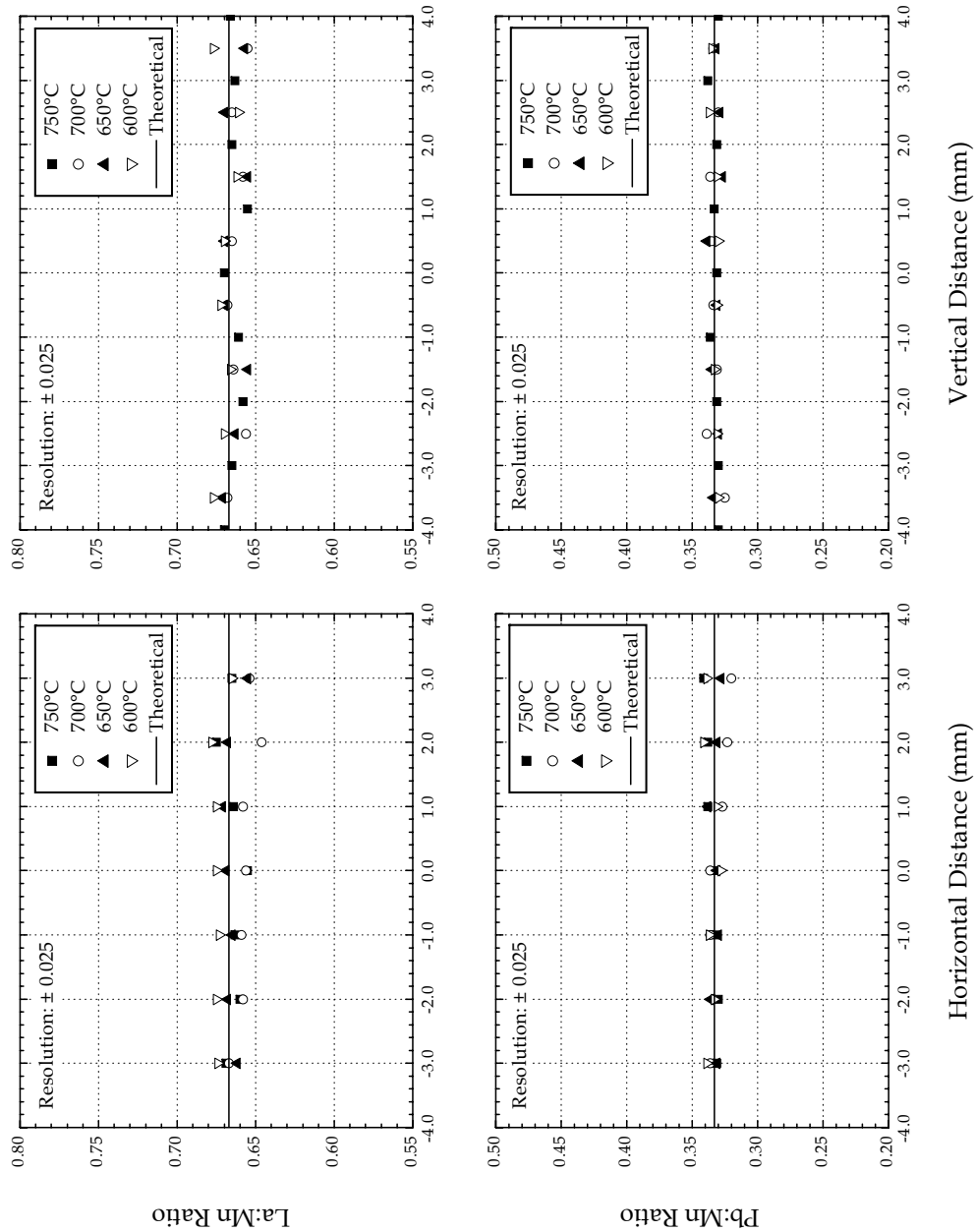
FIGURE 4.9 XPS analysis of $La_{0.67}Pb_{0.33}MnO_3$ film surfaces on platinized-Si(100). Horizontal and vertical distances correspond to lengths, from the center, along axes bisecting a 1 cm^2 substrate into four equal quadrants.

Si(100) Pt(111) ⁄ Ti ⁄ SiO$_2$ ⁄⁄ Si(100)

600 °C

650 °C

700 °C

750 °C
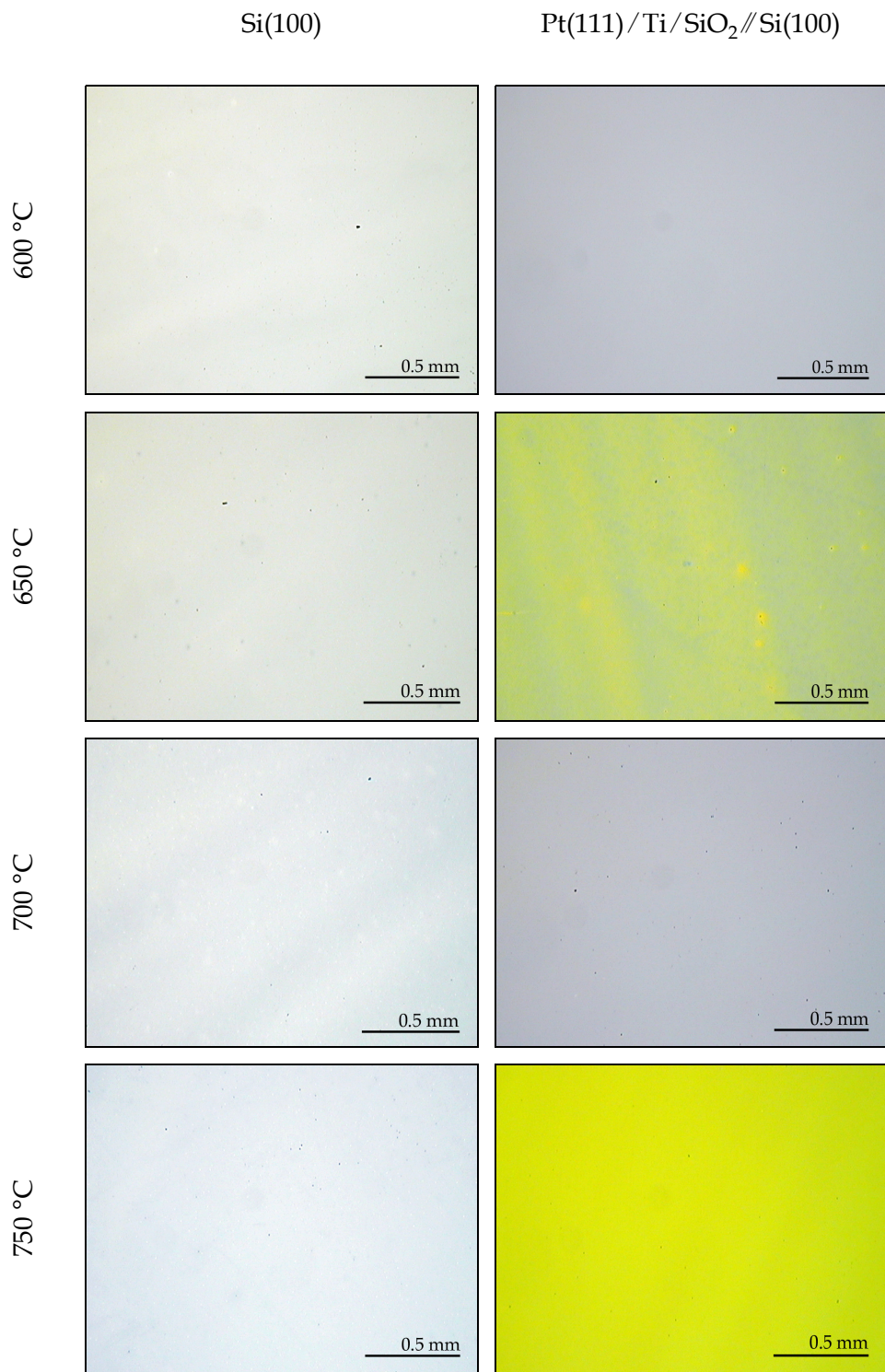
FIGURE 4.10 Optical micrographs of crystallized La$_{0.67}$Ba$_{0.33}$MnO$_3$ films.

Si(100)   Pt(111)/Ti/SiO$_2$//Si(100)

600 °C

0.5 mm   0.5 mm

650 °C

0.5 mm   0.5 mm

700 °C

0.5 mm   0.5 mm

750 °C

0.5 mm   0.5 mm
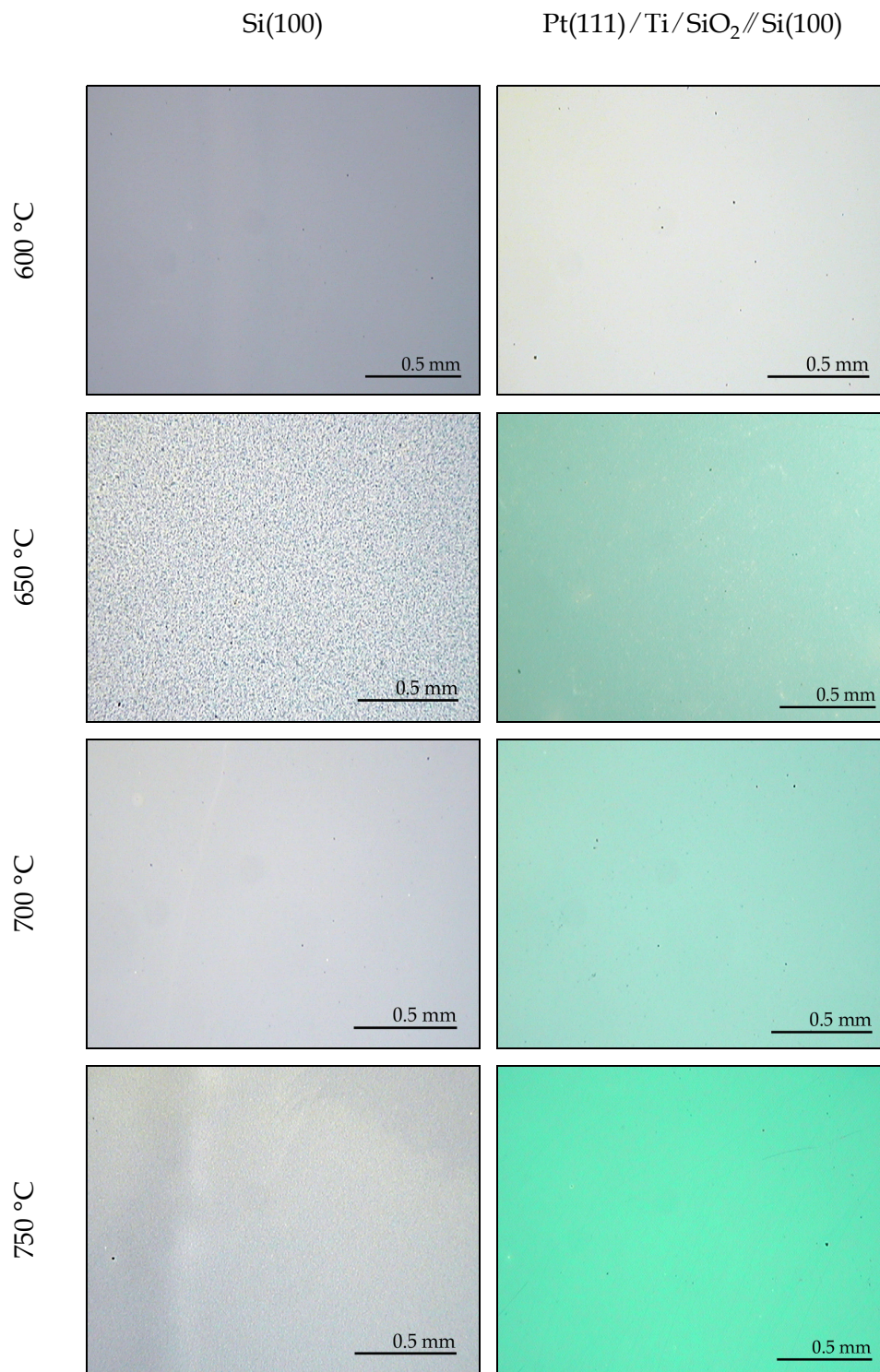
FIGURE 4.11   Optical micrographs of crystallized La$_{0.67}$Pb$_{0.33}$MnO$_3$ films.

tion determined from magnetization behavior and X-ray diffraction patterns (see Table 4.2). For example, the speckled appearance of the 650 °C La-Pb-Mn specimen on Si(100) in Figure 4.11 stems from the nucleation of perovskite-structured oxide (i.e., blue) within the amorphous matrix (i.e., grey). Hence, the change in hue correlates to a decrease in film thickness that results from crystallization of the perovskite phase (see Section 4.9).

4.6 MAGNETIZATION

A more appropriate technique, however, for determining the presence of perovskite phase is SQUID magnetometry. Both $La_{0.67}Ba_{0.33}MnO_3$ and $La_{0.67}Pb_{0.33}MnO_3$ are ferromagnets, and as such, display Curie points upon cooling from the paramagnetic state. The exceptional sensitivity of the SQUID superconducting coil to changes in magnetic field strength (i.e., as small as 10^{-15} T) then allows for the detection of manganite perovskite, even if isolated within the amorphous oxide matrix. Furthermore, as discussed in Sections 2.2.2 and 2.2.3, the paramagnetic-to-ferromagnetic transition is essential for a corresponding insulator-to-metal transition. Thus, characterization of ferromagnetic behavior provides an indirect confirmation of magnetoresistance.

Evidence for ferromagnetism is conclusively provided by Figures 4.12 through 4.14. In general, films on Si(100) substrates exhibit slightly higher Curie temperatures whereas those on platinized-Si(100) produce stronger magnetic moments. Both compositions, however, exhibit Curie points only when heat-treated at temperatures of 650 °C or higher, regardless of substrate.[6] Processing at 600 °C remains insufficient to induce crystallization. But further comparision reveals that films containing $La_{0.67}Pb_{0.33}MnO_3$ offer both notably stronger magnetic moments and higher Curie temperatures than their $La_{0.67}Ba_{0.33}MnO_3$ counterparts. In addition, the ferromagnetic onset is sharper and better resembles that of the bulk, polycrystalline pellet (refer back to Figure 3.16). For example, the highest T_C for $La_{0.67}Ba_{0.33}MnO_3$ is 254 K, but for $La_{0.67}Pb_{0.33}MnO_3$, 326 K; bulk, polycrystalline values are, respectively, 340 K and 350 K (see Figures 3.15 and 3.16).

Such observations are consistent with the refractory nature of barium-containing oxides: as stated in Section 2.3, 1500 °C is necessary for the preparation of $La_{0.67}Ba_{0.33}MnO_3$ by con-

---

[6] Note the weak signal of the $La_{0.67}Ba_{0.33}MnO_3$ film on Si(100) (i.e., fired at 650 °C) in Figure 4.13.
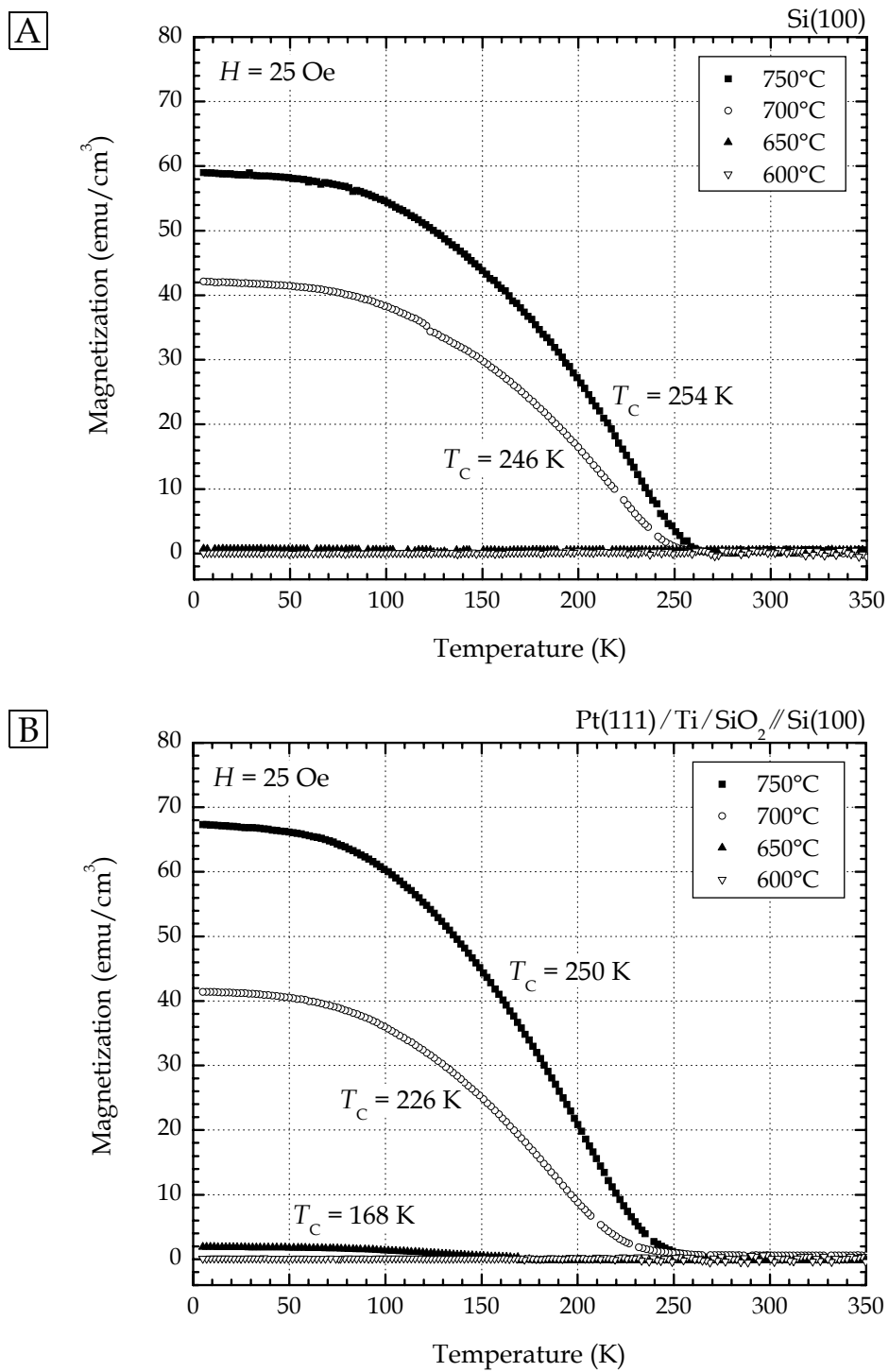
FIGURE 4.12 Magnetic behavior of $La_{0.67}Ba_{0.33}MnO_3$ films. The surfaces of Si(100) substrates (A) exhibit slightly higher Curie temperatures (i.e., T_C) but the platinized-Si(100) substrates (B) produce stronger magnetic moments.
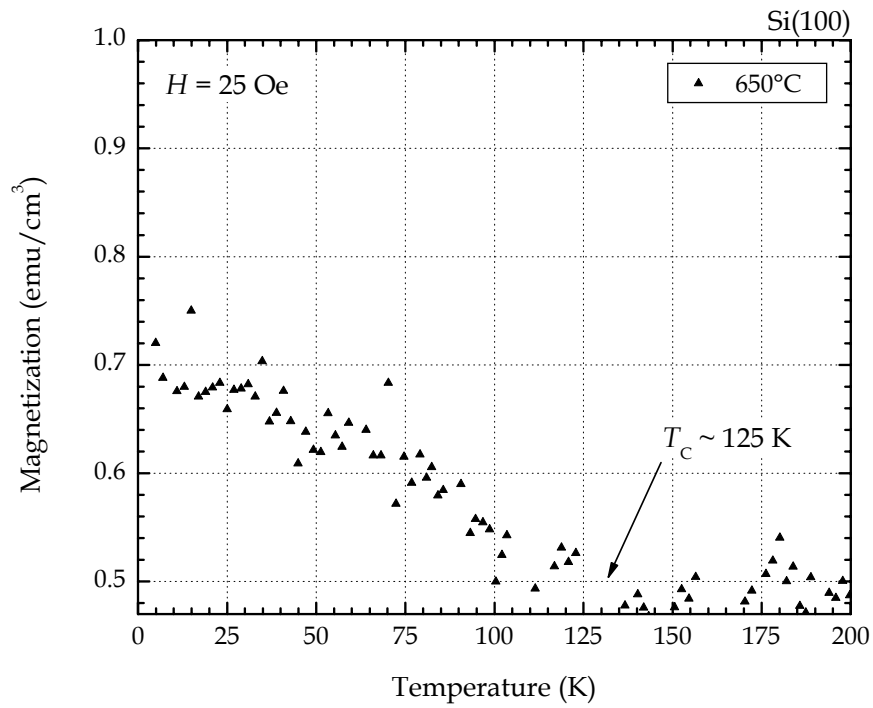
FIGURE 4.13 Magnetic behavior of $La_{0.67}Ba_{0.33}MnO_3$ film fired at 650 °C on Si(100). This graph is an enlargement of the corresponding region in Figure 4.12A.
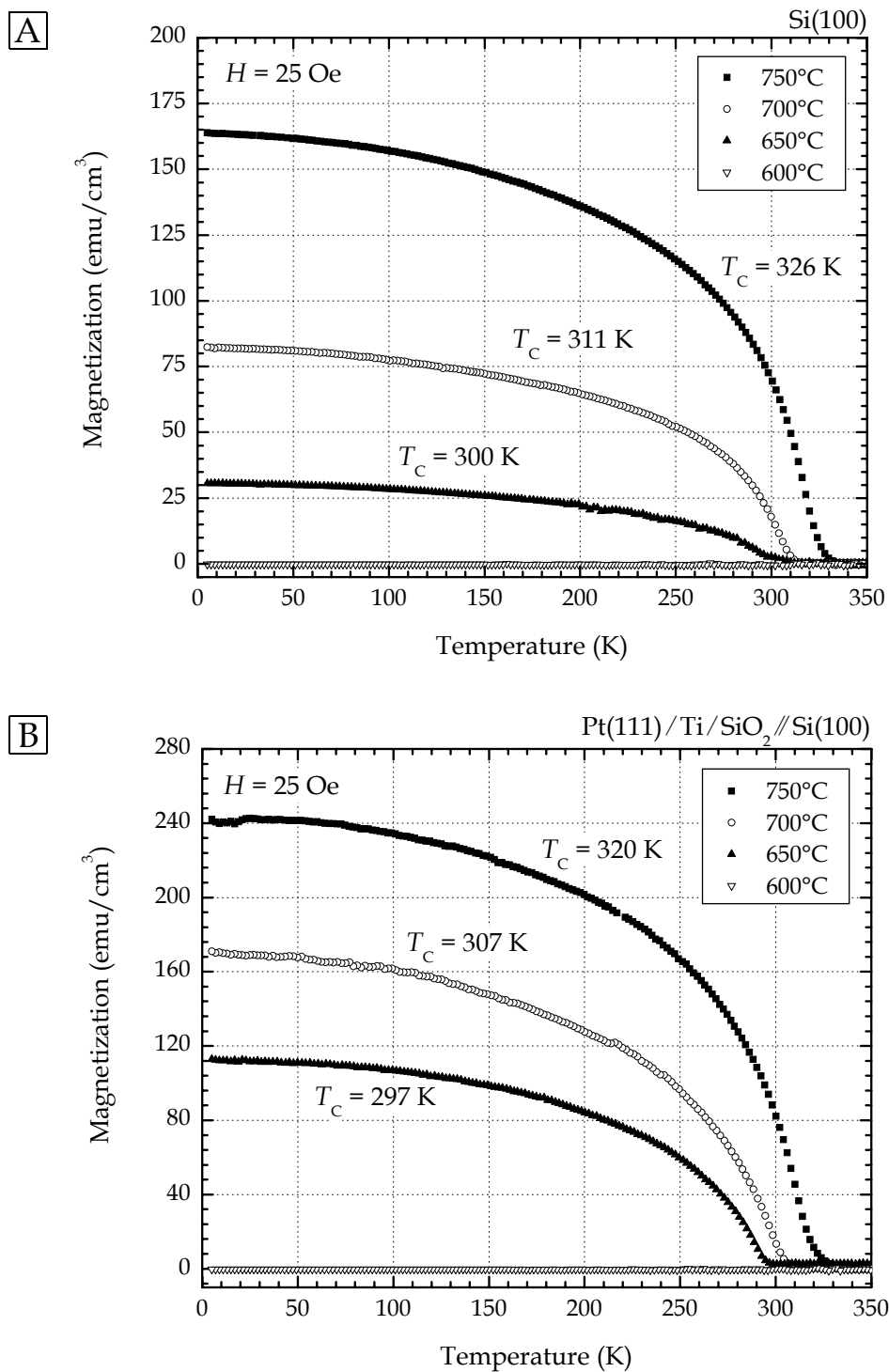
FIGURE 4.14 Magnetic behavior in $La_{0.67}Pb_{0.33}MnO_3$ films. The surfaces of Si(100) substrates (A) exhibit slightly higher Curie temperatures (i.e., T_C) but the platinized-Si(100) substrates (B) produce stronger magnetic moments.

vential mixed-oxide methods but only 950 °C is required for $La_{0.67}Pb_{0.33}MnO_3$. *Yet the emergence of ferromagnetism clearly reflects the development of perovskite structure within the amorphous oxide matrix at 650 °C!* Subsequent improvements in the magnitude of the magnetic moment (i.e., with heat-treatment temperature) result from the optimization of $[Mn^{3+}]/[Mn^{4+}]$ induced by stronger oxidation (see Section 2.2.4). To stay within the thermal compatibility range for silicon, however, investigation beyond 750 °C was not attempted; typical heat treatments for refractory substrates such as $LaAlO_3$ or $SrTiO_3$ *start* at 800 °C.

4.7 X-ray Diffraction

The direct measurement of thin-film crystallinity was obtained using glancing-incidence X-ray scattering (i.e., $\omega = 1.5°$). The corresponding patterns are given in Figures 4.15 through 4.18. Three general comments must be made before discussing the results. First, all films deposited on Si(100) exhibited unidentified peaks at $2\theta = \sim 54°$ and $\sim 56°$, the former sharp and the latter broad. These peaks are attributed to a reaction layer between the doped-lanthanum manganite and silicon; no equivalent peak could be found for films deposited on platinized-Si(100). Second, an additional anamolous peak sometimes appeared at $2\theta = \sim 26.2°$. A review of the published crystallographic data indicated that polycrystalline β-SiO_2 exhibits its highest-intensity diffraction peak at $2\theta = 26.243°$.[7] No other compositions corresponding to permutations of La, Ba, Pb, Mn, Si, and O provided a reasonable match. Thus, β-SiO_2 is offered as a logical *but suggested* phase, perhaps crystallizing to reduce interfacial strain. Direct confirmation, however, was not attempted, but instead, is offered as a recommendation for future work (see Chapter 6). Lastly, the platinized-Si(100) specimens often fail to demonstrate the expected Pt(111) peak (i.e., $2\theta = 39.763°$).[8] This characteristic, if absent, most likely stems from the shallow X-ray incidence angle combined with: (1) a (111)-perovskite diffraction condition at $2\theta = \sim 39.9°$ and (2) the strong scattering cross-sections of La, Ba, and Pb.[9]

Data presented by Figures 4.15 through 4.18 are in good agreement (see Table 4.2) with the reference patterns obtained from the bulk, polycrystalline pellets (see Figures 3.15 and

---

[7] See JCPDS PDF 47-1144 from the International Centre for Diffraction Data.
[8] See JCPDS PDF 04-0802 from the International Centre for Diffraction Data.
[9] Standard θ-2θ (i.e., $\omega = \theta$) scans from the same film specimens, however, *do* show the dominant Pt(111) peak. Unfortunately, the signal is so strong that the (111) peak from the perovskite film becomes obscured.
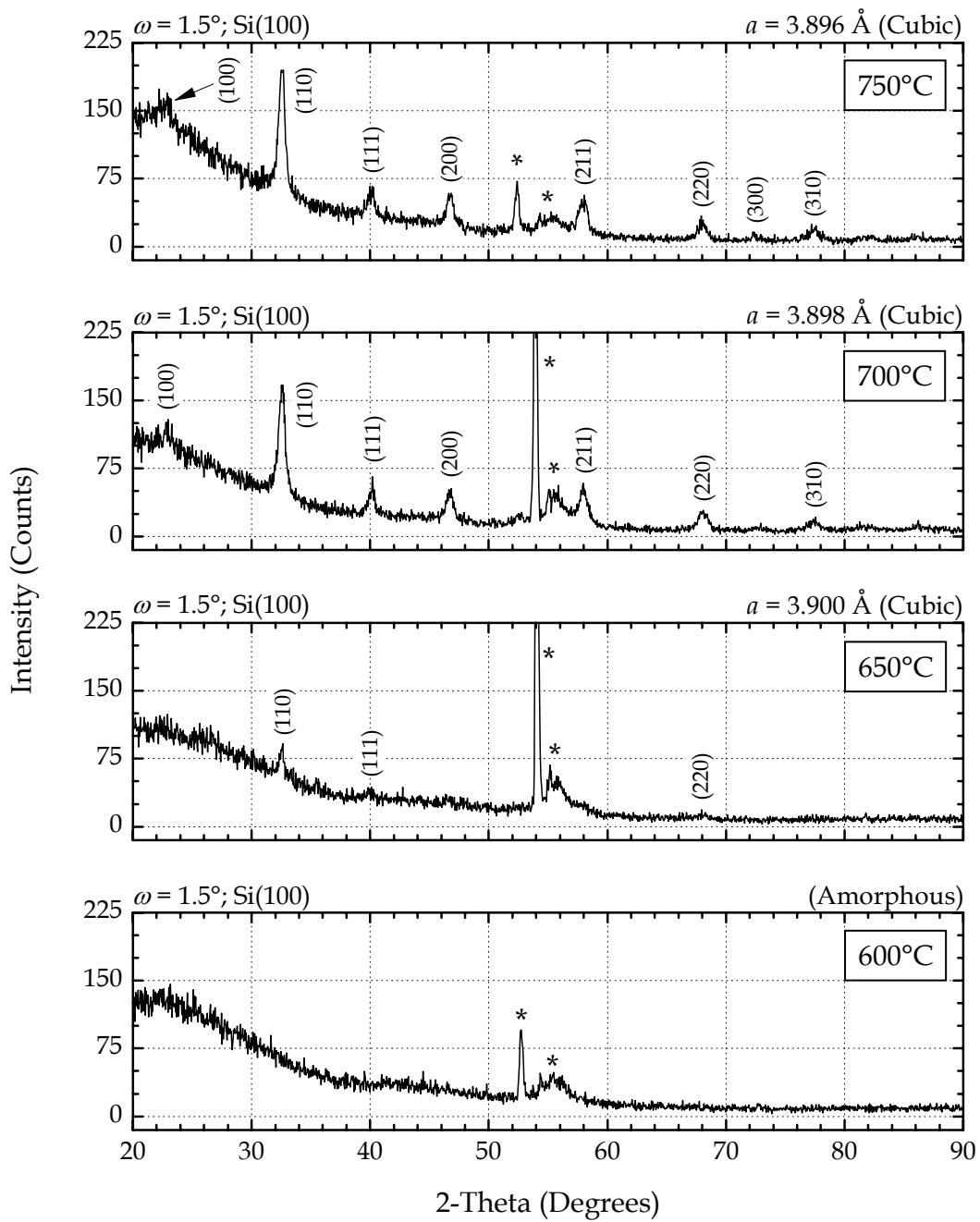
FIGURE 4.15 X-ray diffraction patterns of $La_{0.67}Ba_{0.33}MnO_3$ films grown on Si(100). Asterisks mark peaks from unidentifiable phases.
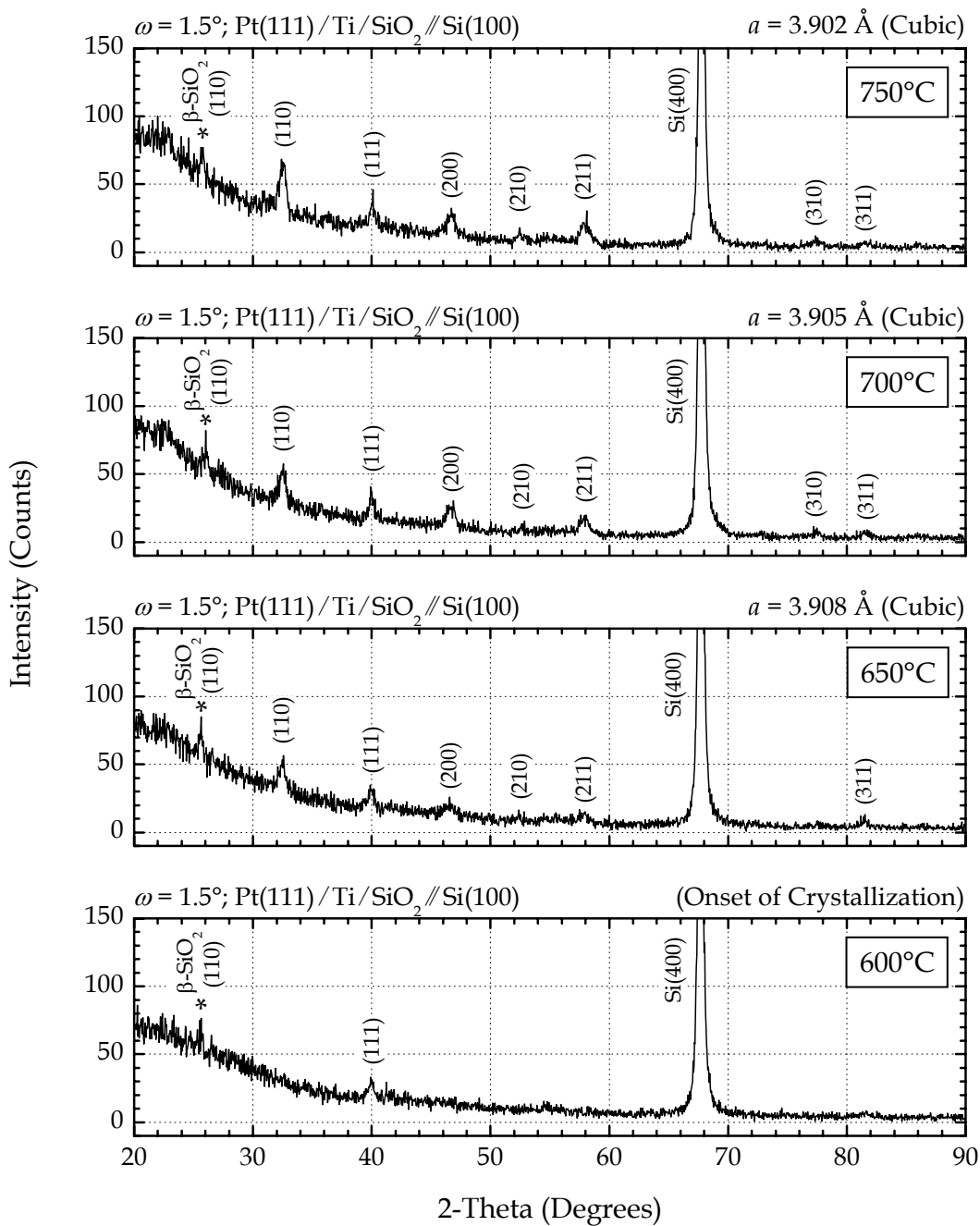
FIGURE 4.16 X-ray diffraction patterns of $La_{0.67}Ba_{0.33}MnO_3$ films grown on platinized-Si(100). Note the (111) peak at 600 °C marking the onset of crystallization. Asterisks mark peaks from unidentifiable phases.
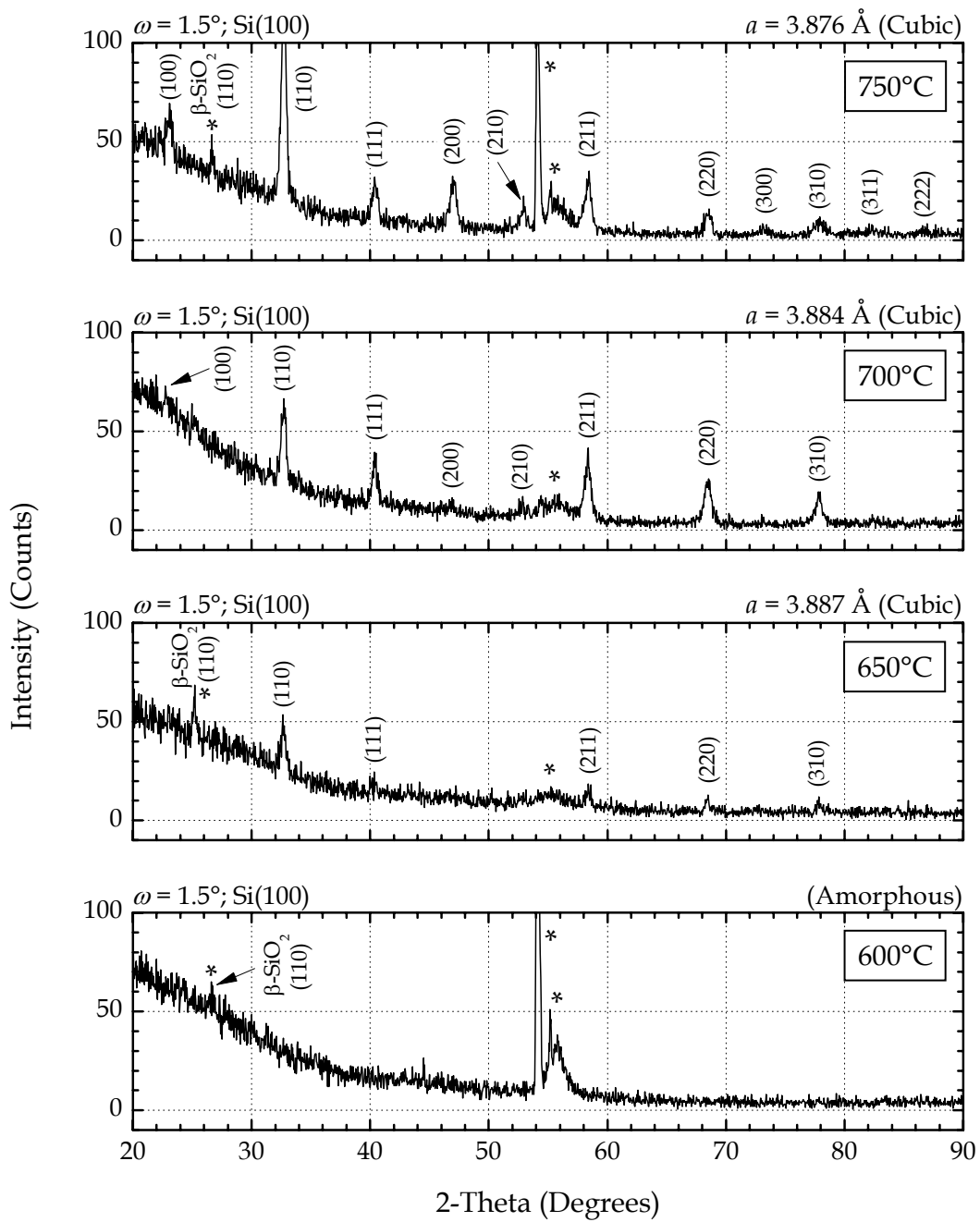
FIGURE 4.17 X-ray diffraction patterns of $La_{0.67}Pb_{0.33}MnO_3$ films grown on Si(100). Asterisks mark peaks from unidentifiable phases.
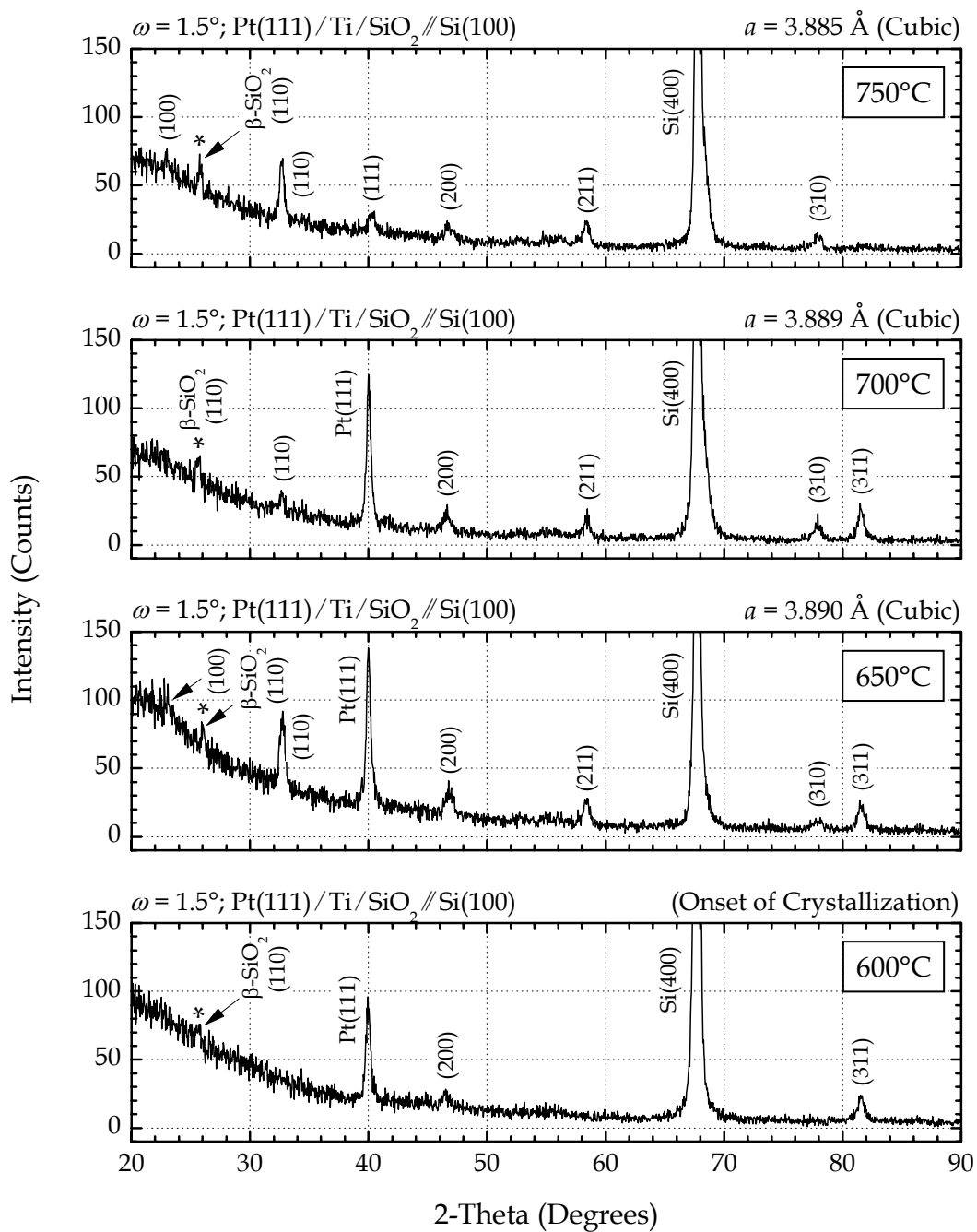
FIGURE 4.18 X-ray diffraction patterns of $La_{0.67}Pb_{0.33}MnO_3$ films grown on platinized-Si(100). Note the (200) and (311) peaks at 600 °C marking the onset of crystallization. Asterisks mark peaks from unidentifiable phases.

THIN-FILM SPECIMEN	SUBSTRATE TYPE	LATTICE PARAMETER[a] (Å)	T_C (K)	T_{IM} (K)
$La_{0.67}Ba_{0.33}MnO_3$				
600 °C	Si(100)	–[b]	–	–
650 °C	Si(100)	3.900	125	–
700 °C	Si(100)	3.898	246	115
750 °C	Si(100)	3.876	254	144
600 °C	Pt(111)/Ti/SiO$_2$//Si(100)	–	–	–
650 °C	Pt(111)/Ti/SiO$_2$//Si(100)	3.908	168	–
700 °C	Pt(111)/Ti/SiO$_2$//Si(100)	3.905	226	120
750 °C	Pt(111)/Ti/SiO$_2$//Si(100)	3.902	250	264
$La_{0.67}Pb_{0.33}MnO_3$				
600 °C	Si(100)	–[b]	–	–
650 °C	Si(100)	3.887	300	–
700 °C	Si(100)	3.884	311	236
750 °C	Si(100)	3.876	326	228
600 °C	Pt(111)/Ti/SiO$_2$//Si(100)	–	–	–
650 °C	Pt(111)/Ti/SiO$_2$//Si(100)	3.890	297	262
700 °C	Pt(111)/Ti/SiO$_2$//Si(100)	3.889	307	252
750 °C	Pt(111)/Ti/SiO$_2$//Si(100)	3.885	320	254

[a] For the cubic unit cell. Reference values from bulk, polycrystalline pellets are, respectively, 3.904 Å and 3.890 Å for $La_{0.67}Ba_{0.33}MnO_3$ and $La_{0.67}Pb_{0.33}MnO_3$.

[b] The onset of crystallization was observed but less than three diffraction peaks were available.

TABLE 4.2 Comparison of lattice parameters, T_C, and T_{IM} for manganite thin films. Note the excellent correlation between the onset of crystallization and magnetization.

3.16). Virtually all diffraction peaks are present by 750 °C, and with the exception of the Si(100) reaction layer, no intermediate (crystalline) phases occur during the transformation from amorphous oxide to doped-lanthanum manganite. *As evidenced by the films crystallized on platinized-Si(100), the alkoxy-based sol-gel process developed in this dissertation is capable of a direct pathway to the requisite perovskite phase. Furthermore, the onset of crystallization occurs below 650 °C on Si(100) and near 600 °C on platinized-Si(100) − a remarkable improvement over temperatures from competing CSD methods (i.e., > 800 °C) using lattice-matched substrates (see Section 2.4.1)!* Equally important, the lead-doped composition crystallizes earlier than its barium counterpart, as evident by slightly-stronger and more numerous diffraction peaks at lower firing temperatures.

In addition, the cubic lattice parameters of films crystallized at 650 °C are virtually identical to the values obtained from the bulk, polycrystalline reference pellets (see Table 4.2). *Thus, specimens prepared via the alkoxy-based, sol-gel process of Chapter 3 exhibit stoichiometric oxygen content without the need for further heat treatment.* Such a feature is not typical for comparable films grown via pulsed-laser deposition (PLD), even when using lattice-matched substrates. This vacuum-based process typically produces *oxygen-deficient* films which require *high-temperature post-annealing* (i.e., > 900 °C) [7, 8]. A slight decrease in the lattice parameter, however, occurs in the sol-gel films with increasing heat-treatment temperature. The small magnitude of this change, concomitant with notable improvements in the ferromagnetic moment (see Figures 4.12 through 4.14), suggests the continued oxidation of Mn^{3+} into Mn^{4+} according to $[Mn^{3+}]/[Mn^{4+}] \rightarrow 0.33$ (see Section 2.2.4).[10] Changes in film stress (i.e., from the underlying substrate) also effect the lattice parameters and therefore cannot not be eliminated from consideration, particularly for films deposited on Si(100).

4.8 FILM THICKNESSES

Film thicknesses were obtained from cross-sectional images using a scanning electron microscope (SEM). An inspection of Figures 4.19 through 4.22 clearly indicates the amorphous nature of the coatings fired at 600 °C. *No cracking or porosity, however, is exhibited by any specimen regardless of heat-treatment temperature, composition, or substrate-type.* This observation

---

[10]As discussed in Section 2.2.1, increases in $[Mn^{4+}]$ relieve the non-cubic distortion caused by Mn^{3+}, a Jahn-Teller ion, and therefore enable the unit cell parameters to decrease.

600 °C t = 103 nm   650 °C t = 88 nm

500 nm   500 nm

700 °C t = 85 nm   750 °C t = 94 nm

500 nm   500 nm
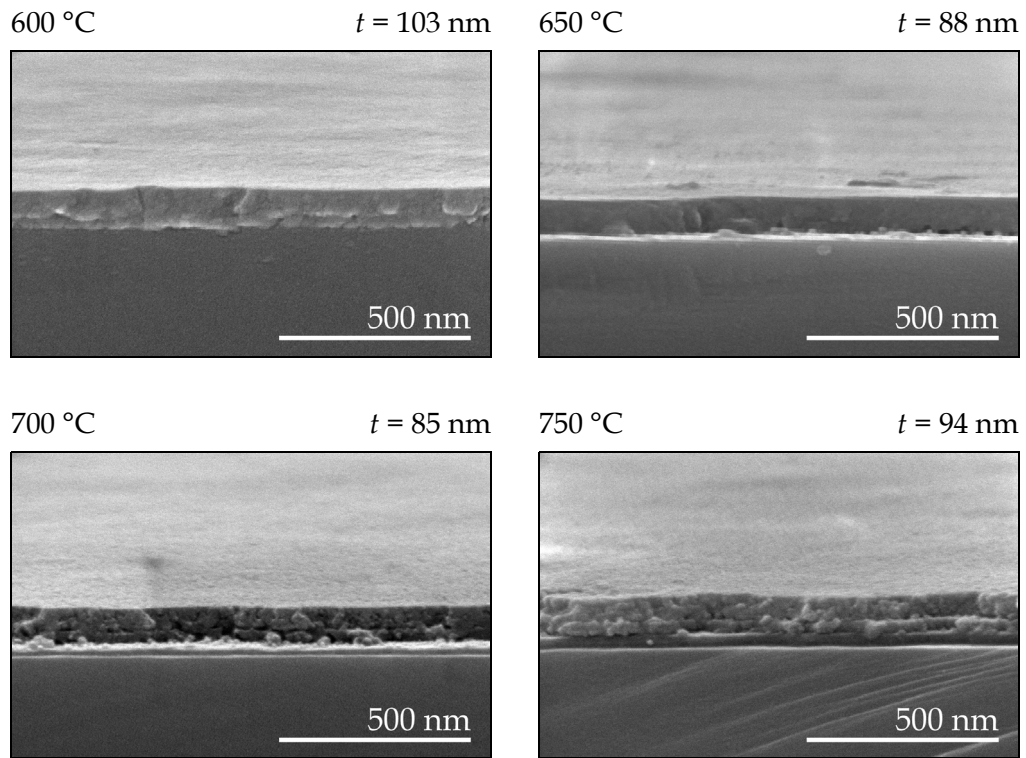
FIGURE 4.19 Cross-sectional images of $La_{0.67}Ba_{0.33}MnO_3$ films deposited on Si(100). Film thicknesses are given above the upper right of each image.

600 °C t = 140 nm   650 °C t = 130 nm

500 nm   500 nm

700 °C t = 120 nm   750 °C t = 103 nm

500 nm   500 nm
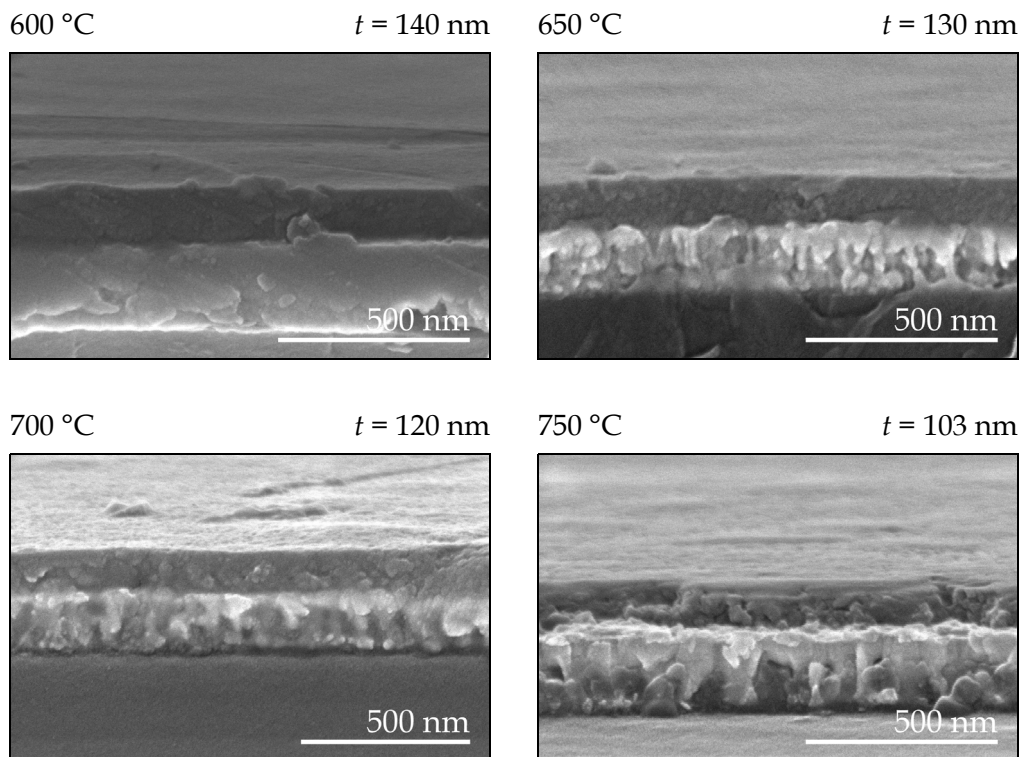
FIGURE 4.20 Cross-sectional images of $La_{0.67}Ba_{0.33}MnO_3$ films deposited on platinized-Si(100). Film thicknesses are given above the upper right of each image.

600 °C $t = 105$ nm

650 °C $t = 102$ nm

500 nm

500 nm

700 °C $t = 113$ nm

750 °C $t = 75$ nm

500 nm

500 nm
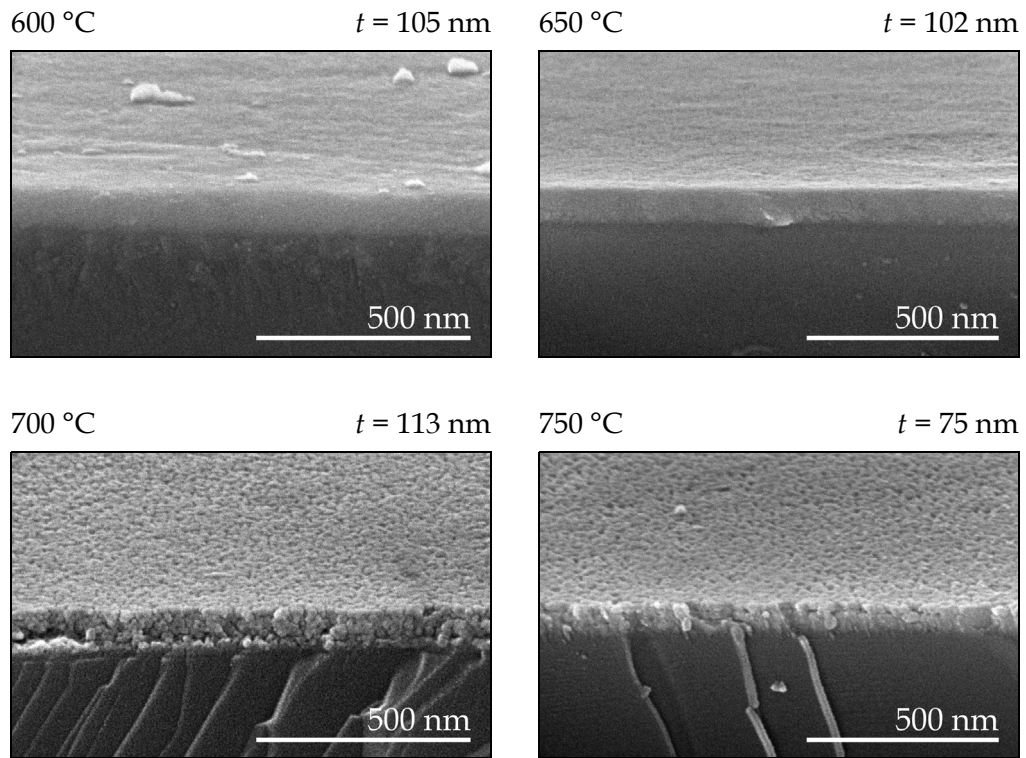
FIGURE 4.21 Cross-sectional images of $La_{0.67}Pb_{0.33}MnO_3$ films deposited on Si(100). Film thicknesses are given above the upper right of each image.

600 °C t = 88 nm   650 °C t = 75 nm

500 nm   500 nm

700 °C t = 90 nm   750 °C t = 80 nm

500 nm   500 nm
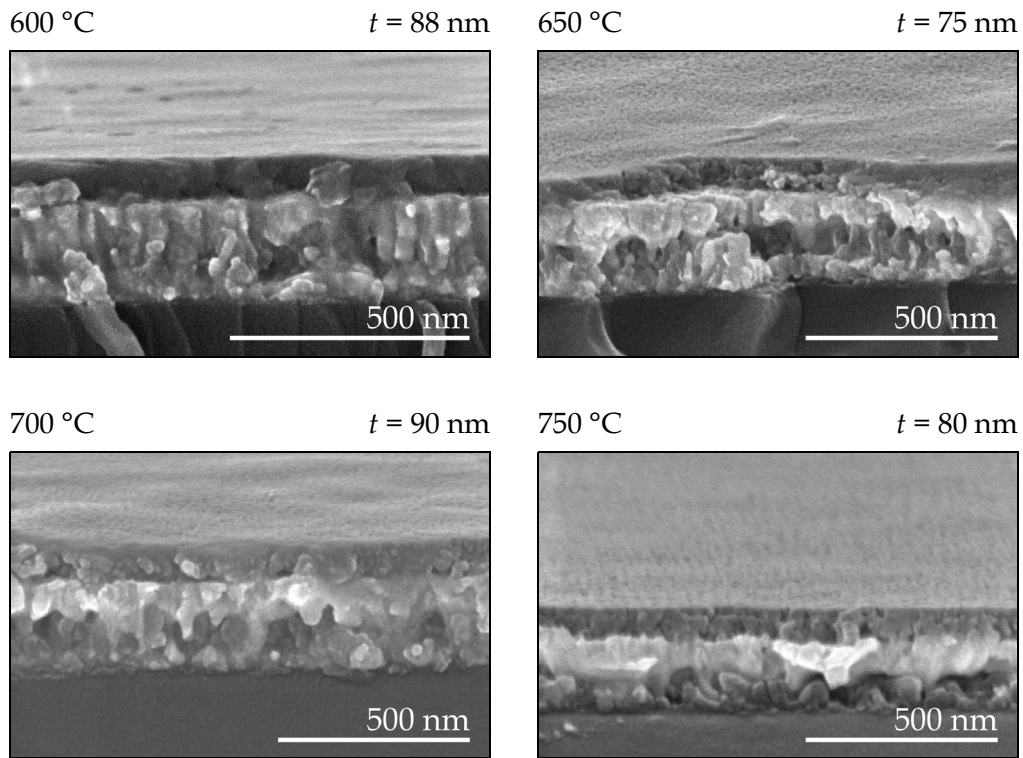
FIGURE 4.22   Cross-sectional images of $La_{0.67}Pb_{0.33}MnO_3$ films deposited on platinized-Si(100). Film thicknesses are given above the upper right of each image.

is in excellent agreement with the optical micrographs presented in Section 4.5. For either composition, crystalline features first appear at 700 °C for films deposited on Si(100) and 650 °C on platinized-Si(100). The most detailed example of grain structure, though, can be seen in the $La_{0.67}Pb_{0.33}MnO_3$ films prepared at 700 °C and 750 °C on Si(100). Consideration of the three spin-coating iterations (refer to Figure 3.19) implies that each deposited layer from the 0.20 M La-Ba-Mn or La-Pb-Mn sols corresponds to ~ 30–40 nm of final oxide film thickness.

In general, film thicknesses decrease upon crystallization from amorphous oxide into doped-lanthanum manganite. The continued growth of silicon oxide and/or the reaction layer for films crystallized on Si(100), however, precludes further elaboration for this substrate type. Thicknesses measured for $La_{0.67}Ba_{0.33}MnO_3$ on platinized-Si(100), though, do indicate a gradual decrease from 600 °C to 750 °C. A similar trend was not observed for $La_{0.67}Pb_{0.33}MnO_3$, but instead, thicknesses seemed to fluctuate around ~ 85 nm. The less-refractory nature of $La_{0.67}Pb_{0.33}MnO_3$ may allow for a more dense amorphous phase by 600 °C (i.e., lower free volume); oxo-coordinated lead is a well-known glass network former in noncrystalline solids [9]. So any corresponding changes in specific volume upon crystallization may be small and not easily captured by cross-sectional images.

4.9 SURFACE TOPOLOGY

The surface topology of the manganite films is illustrated in Figures 4.23 through 4.26, providing direct visualization of surface roughness and grain size. Typical roughness values (i.e., root-mean-sqaure) fall in the range from 1.2–2.3 nm. For $La_{0.67}Pb_{0.33}MnO_3$ crystallized on platinized-Si(100), however, heat-treatment above 700 °C increases this metric to ~ 7.3 nm. Grain diameters for $La_{0.67}Ba_{0.33}MnO_3$ start at 15–20 nm for a heat-treatment temperature of 650 °C, increasing to 20–25 nm by 750 °C. Similar values are obtained for $La_{0.67}Pb_{0.33}MnO_3$ on Si(100). Grain sizes for lead-doped films on platinized-Si(100), though, begin larger at 30–35 nm for 650 °C and increase to 45–50 nm by 750 °C.

A progressive comparison of $La_{0.67}Pb_{0.33}MnO_3$ specimens fired at 650 °C, 700 °C, and 750 °C on platinized-Si(100) indicates an obvious roughening of microstructure with a slightly-diminished connectivity by 750 °C. Such behavior is reminiscent of thermal etching due to PbO volatilization at the grain surface (and subsequent mobility within the boundaries). Referencing back to the cross-sectional SEM images (see Figures 4.21 and 4.21), however, con-
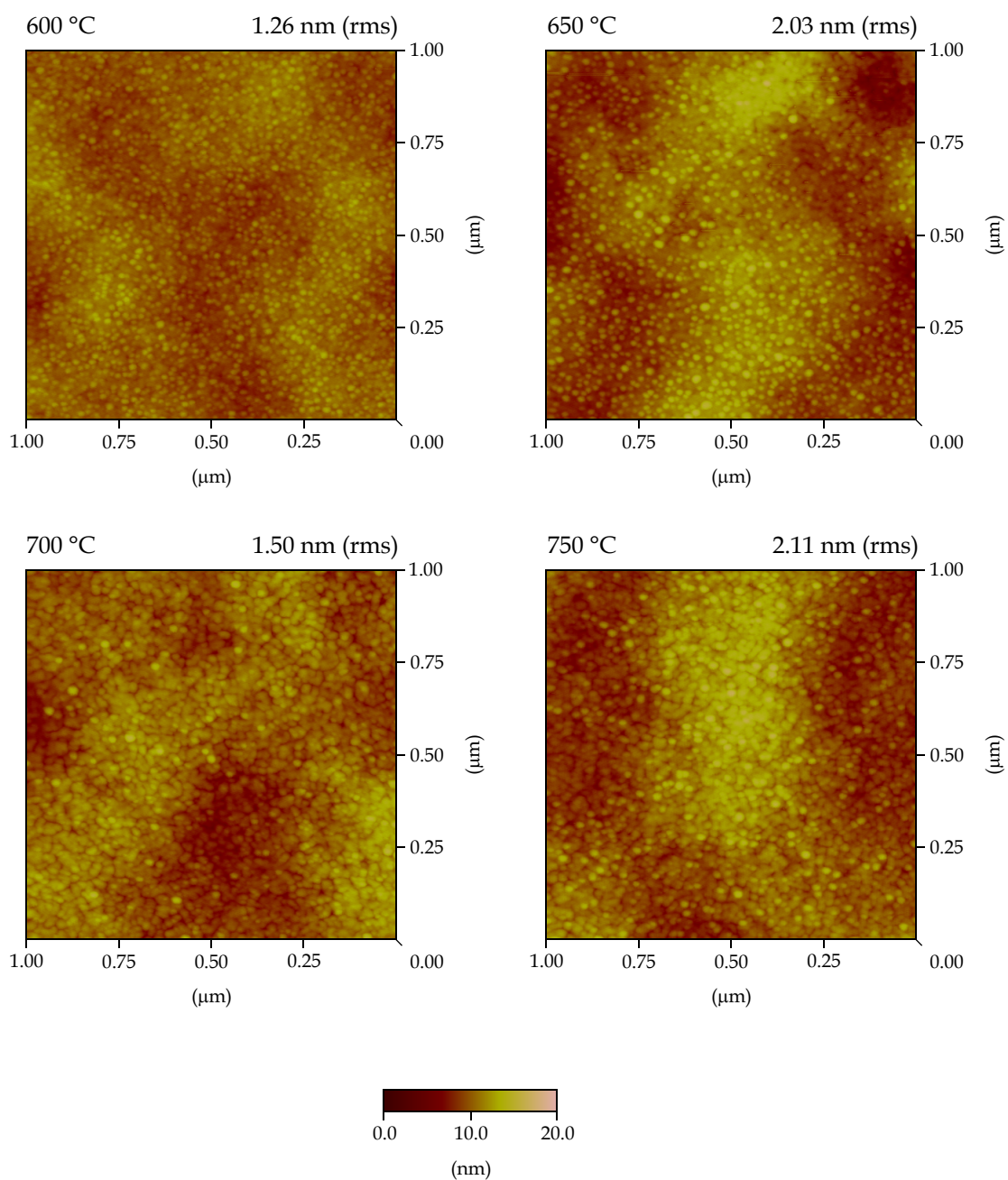
FIGURE 4.23 Surface profile of $La_{0.67}Ba_{0.33}MnO_3$ films fired on Si(100). The scale length is constant for each image. Surface roughness values are given in the upper-right corner of each profile.

200
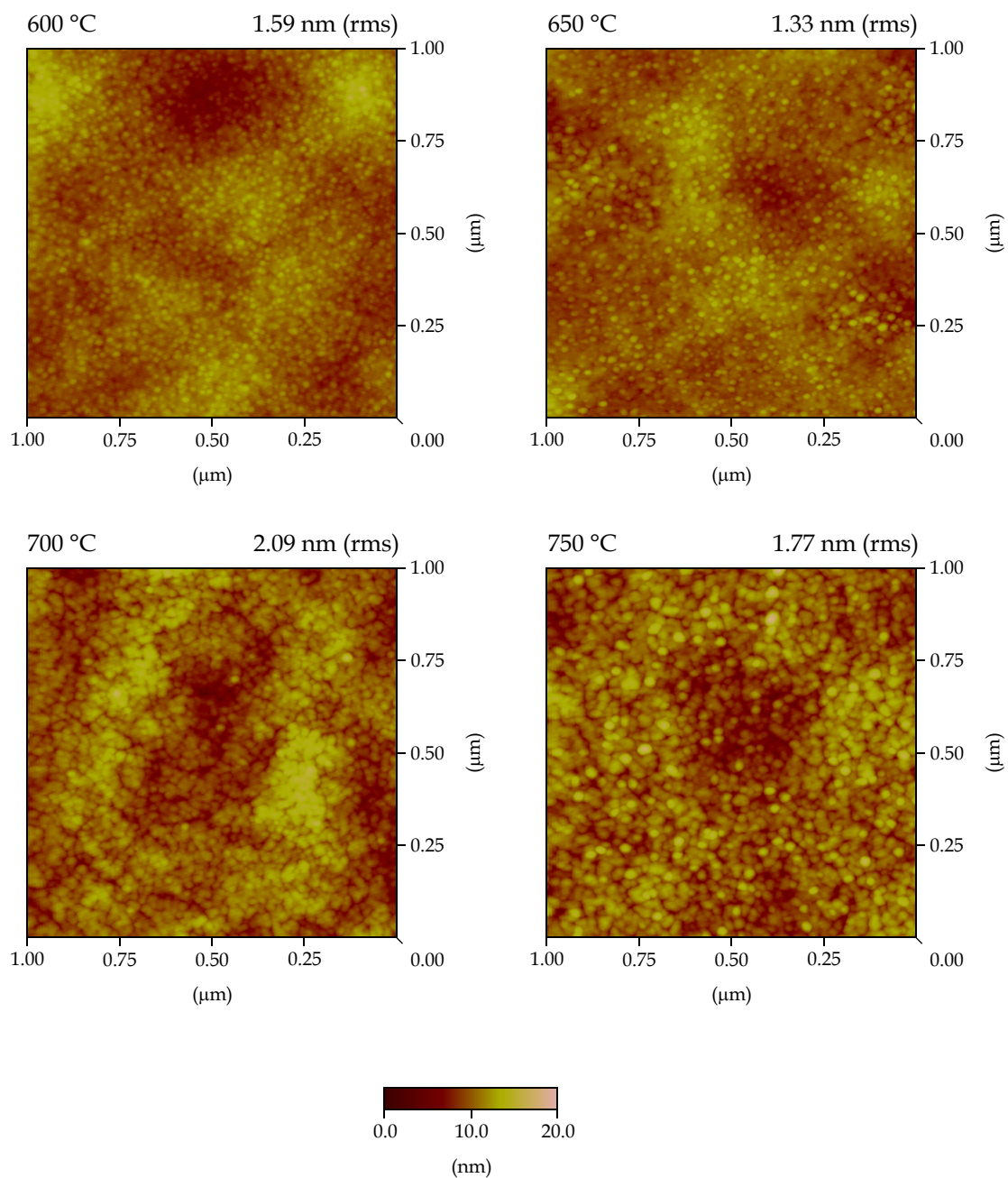
FIGURE 4.24 Surface profile of $La_{0.67}Ba_{0.33}MnO_3$ films fired on platinized-Si(100). The scale length is constant for each image. Surface roughness values are given in the upper-right corner of each profile.
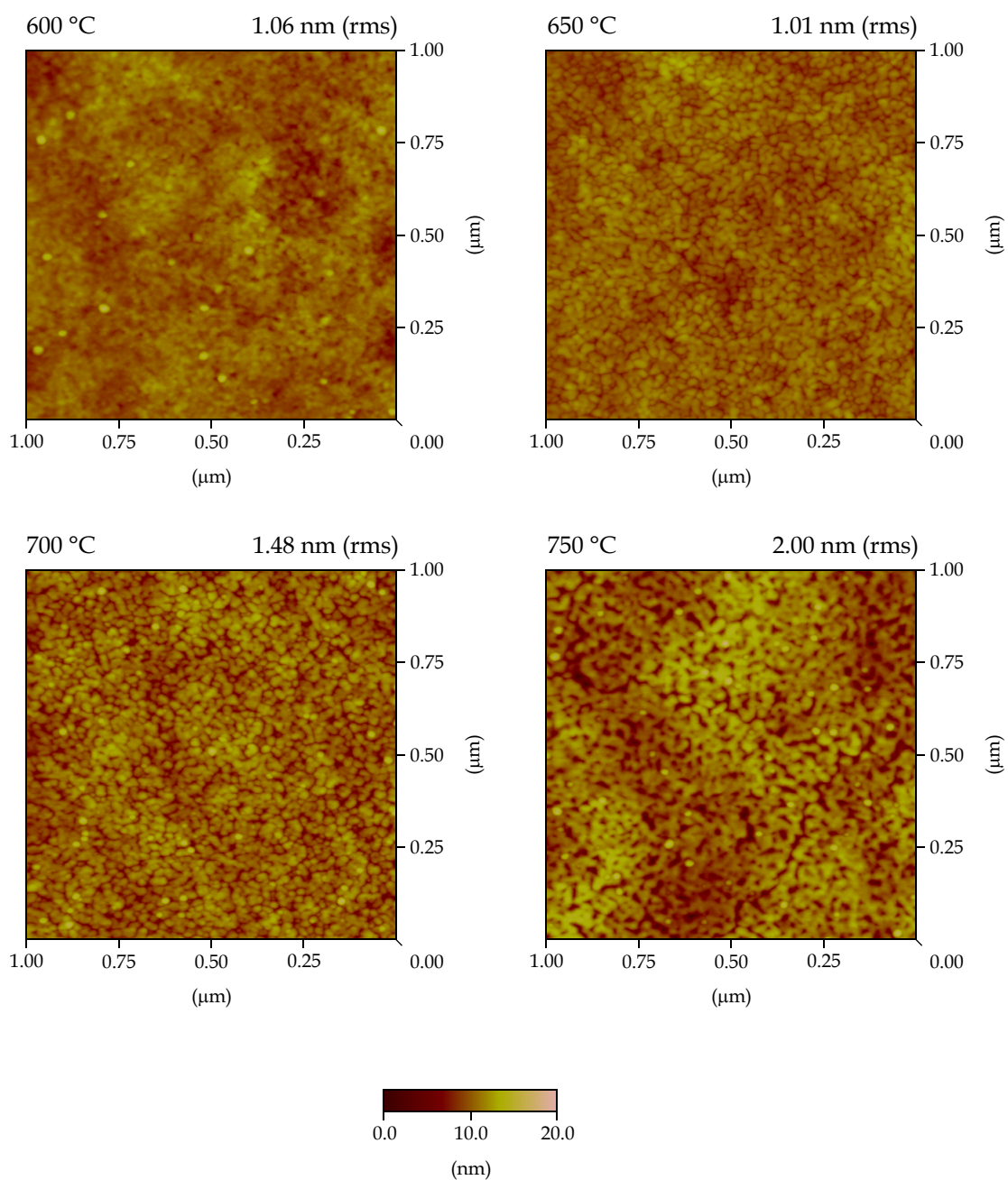
FIGURE 4.25 Surface profile of $La_{0.67}Pb_{0.33}MnO_3$ films fired on Si(100). The scale length is constant for each image. Surface roughness values are given in the upper-right corner of each profile.
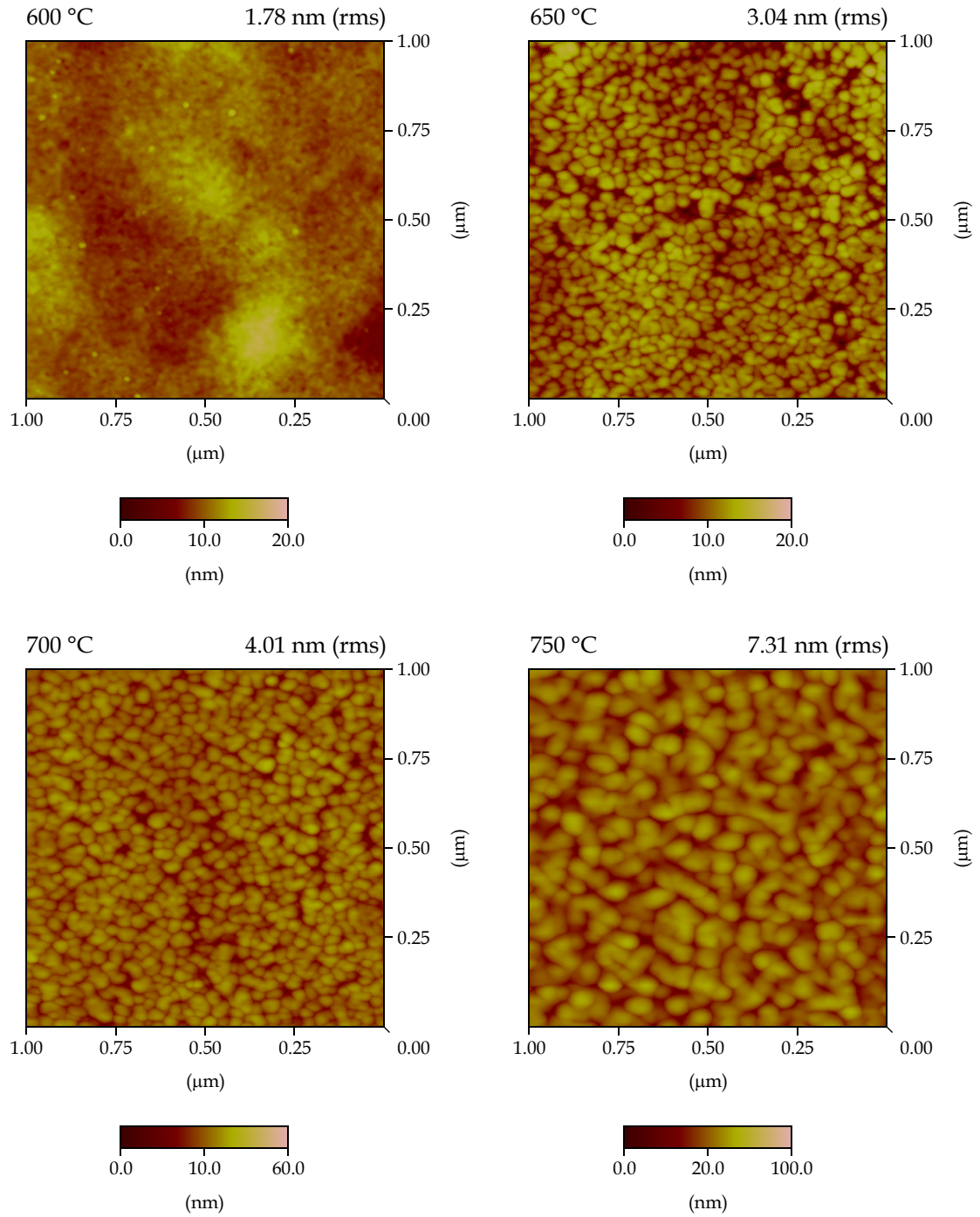
FIGURE 4.26 Surface profile of $La_{0.67}Pb_{0.33}MnO_3$ films fired on platinized-Si(100). Note the increased scale length for the 700 °C and 750 °C samples. Surface roughness values are given in the upper right corner of each profile.

firms the dense, non-porous nature of the films. Closer inspection of the $La_{0.67}Pb_{0.33}MnO_3$ cross-sections, and in particular, a relative comparison of films crystallized on Si(100) and platinized-Si(100), reveals the following: the microstructure on the former appears more spherical and grainy whereas the latter seems to emerge from the underlying Pt(111) layer. Thus, the roughening trend observed for $La_{0.67}Pb_{0.33}MnO_3$ on platinized-Si(100) may also include thermally-activated substrate-templating.[11] Such a conclusion would be consistent with the low crystallization onset (i.e., 600 °C from Figure 4.18) and excellent T_C evolution (see Table 4.2). Note also the reduction of granular definition for $La_{0.67}Pb_{0.33}MnO_3$ grown on Si(100) at 750 °C (see Figure 4.25). This behavior suggests the onset of intergrain necking, perhaps activated due to poor registry with the substrate after crystallization.

A fine grain size (i.e., < 50 nm) persists for virtually all specimens with the best grain definition corresponding to heat treatments at 700 °C and 750 °C. *This characteristic suggests the rapid nucleation of perovskite phase from the amorphous oxide matrix with little grain growth.* As will be shown in Section 4.10, such an extensive grain boundary network dramatically influences the resistivity exhibited by the films. One possible explanation for this microstructure is the contribution of strain energy to the free energy change during nucleation.[12] For example, SENGUPTA [10] examined the stress evolution of $PbTiO_3$ thin films (i.e., ~ 90 nm) deposited on platinized-Si(100) via sol-gel processing. Thermal expansion mismatch (i.e., strain) produced substantial tensile stresses of ~ 150 MPa upon heating the xerogel coating to 500 °C; only near the onset of crystallization did the magnitude diminish significantly. Such stresses can shift nucleation to lower temperatures, or alternatively, raise the nucleation rate at given temperature. Investigation of interfacial strain effects, however, was not possible in the time frame allotted for this dissertation. Due to possible influences on microstructural development and electrical properties, the examination of stress evolution is therefore recommended as future research (see Chapter 6).

4.10 MAGNETOTRANSPORT

The magnetotransport behavior of doped-lanthanide manganite films was investigated

---

[11]Note that the cubic lattice parameter of the platinum layer is 3.923 Å, close to the 3.890 Å value measured for the bulk (i.e., unclamped), polycrystalline $La_{0.67}Pb_{0.33}MnO_3$ pellet.

[12]Further discussion on the kinetics of nucleation and growth for amorphous materials can be found in the reference text by VARSHNEYA [9].

using two different magnetic-field conditions: (1) a standard 0–5 T range with 1 T increments and (2) a single weak-field cycle between ± 500 Oe. In agreement *with both* the magnetization (see Section 4.6) and X-ray diffraction data (see Section 4.7), only films prepared at 700 °C and 750 °C on Si(100) and 650 °C, 700 °C, and 750 °C on platinized-Si(100) demonstrated magnetoresistive behavior; a ferromagnetic moment *and* crystallinity (i.e., at least five major diffraction peaks) were required for magnetoresistance. Thus, the *conclusive presence* of manganite-perovskite phase was essential to ensure magnetotransport in the thin-film specimens.

Electrical measurements for films crystallized on platinized-Si(100), however, proved to be quite challenging. In-plane leakage through the underlying platinum layer was notable, completely obscuring the signal of the manganite film.[13] To mitigate this problem, new specimens were prepared with an increased final oxide thickness of 270–280 nm (i.e., 9 spin-coating iterations). Furthermore, the contact geometry was changed from a four-point in-plane to a two-point through-plane configuration. This modification represented a compromise but allowed for the observation of magnetoresistive behavior under standard 0–5 T conditions.[14] Unfortunately, weak-field measurements were erratic and unreliable. Further investigation was therefore not undertaken.

Regardless of composition or substrate-type, all films exhibited resistivities significantly higher than the intrinsic, single-crystal values (i.e., 10^6–10^8 Ω-cm versus 10^{-3}–10^{-1} Ω-cm). Furthermore, a comparison of T_{IM} values given in this section with Curie temperatures obtained from Section 4.6 (see Table 4.2) shows that $T_{IM} < T_C$. These two characteristics are associated with the extremely fine-grain structure comprising the manganite-perovskite films. The crystallographic mismatch of grain boundaries is expected to weaken the ferromagnetic interaction within an otherwise continuous perovskite structure. So by increasing the concentration of such impediments, metallic conduction becomes hindered, lowering the temperature needed for the insulator-to-metal transition. The Curie point, however, remains mostly unaffected. Such behavior was also reported by MAHENDIRAN, et al. [11] in bulk, polycrystalline $La_{0.7}Sr_{0.3}MnO_3$: a reduction in grain size from 3.5 µm to 250 nm corresponded to an increase in resistivity from 3.6 mΩ-cm to 0.48 kΩ-cm and a drop in T_{IM} from 375 K to 170

---

[13]Note that the resistivity of platinum is 1.06 x 10^{-5} Ω-cm, a couple orders of magnitude lower than the best values for doped-lanthanide manganites.

[14]A 4-point geometry is superior to its 2-point counterpart because the former avoids the influence of contact resistance. Not surprisingly, concomitant with 2-point geometry were unexplainable artifacts in the magnetotransport curves of $La_{0.67}Pb_{0.33}MnO_3$.

K; T_C decreased slightly from 395 K to 388 K. Similar trends have been observed in polycrystalline $La_{0.5}Pb_{0.5}MnO_3$ [12]. Due to the thin nature of the films prepared for this dissertation, however, the possibility of residual stress and the influence of reaction layers (if present) cannot be excluded.

The magnetotransport curves presented in this section are organized as follows: (1) the 0–5 T high-field behavior is given in Figures 4.27 through 4.32 and (2) the ± 500 Oe weak-field response in Figures 4.33 and 4.34. Within each of these two groups, the barium-doped composition is provided first. So Figures 4.27–4.30 and 4.33 correspond to $La_{0.67}Pb_{0.33}MnO_3$ and Figures 4.30–4.32 and 4.34 to $La_{0.67}Pb_{0.33}MnO_3$. Accordingly, the high-field magnetotransport of $La_{0.67}Ba_{0.33}MnO_3$ will now be discussed.

A comparison of $La_{0.67}Ba_{0.33}MnO_3$ films crystallized on Si(100) shows that increasing the heat-treatment temperature from 700 °C and 750 °C generates the following three results: (1) metallic conductivity below T_{IM} improves (i.e., the curve develops symmetry), (2) resistivity decreases by an order of magnitude, and (3) T_{IM} increases from 115 K to 144 K. These observations are consistent with enhanced grain size (i.e., see Figure 4.23) and an increased ferromagnetic moment (i.e., Figure 4.12). The development of insulator-metal behavior, however, is more obvious for platinized-Si(100) specimens than for Si(100). For example, the specimen heat-treated at 650 °C (see Figure 4.29) exhibits only insulator properties, behavior in agreement with a weak ferromagnetic moment and broad onset (see Figure 4.12B). By 700 °C though, an insulator-metal transition clearly emerges, which by 750 °C, becomes fully symmetric. Similar to films crystallized on Si(100), higher heat-treatment temperatures lower the magnitude of resistivity and increase T_{IM} (i.e., from 120 K to 264 K). The T_{IM} value for 750 °C, however, is much greater for platinized-Si(100), suggesting enhanced [Mn^{4+}] content.

In contrast, for $La_{0.67}Pb_{0.33}MnO_3$ films on Si(100), the magnetotransport curves are highly symmetrical, but unlike the barium analogue, increasing the heat-treatment temperature: (1) raises the resistivity by an order of magnitude and (2) decreases T_{IM} slightly from 236 K from 228 K. This behavior may stem from a reduction in grain connectivity from 700 °C to 750 °C caused by roughening (see Figure 4.25). Increases in resistivity may also result from the intergrain accumulation of fine amounts of volatilized PbO. So despite a high ferromagnetic onset (i.e., T_C = 311 K and 326 K, respectively), microstructural changes may counteract concomitant improvements in magnetoresistive response. A similar trend can be found in the

206
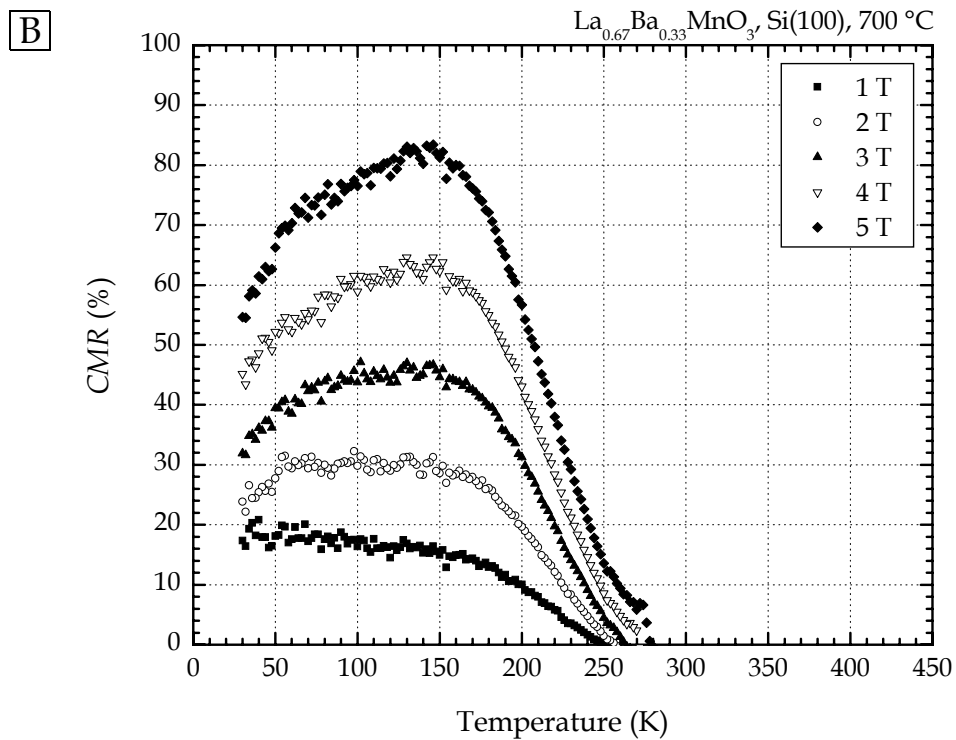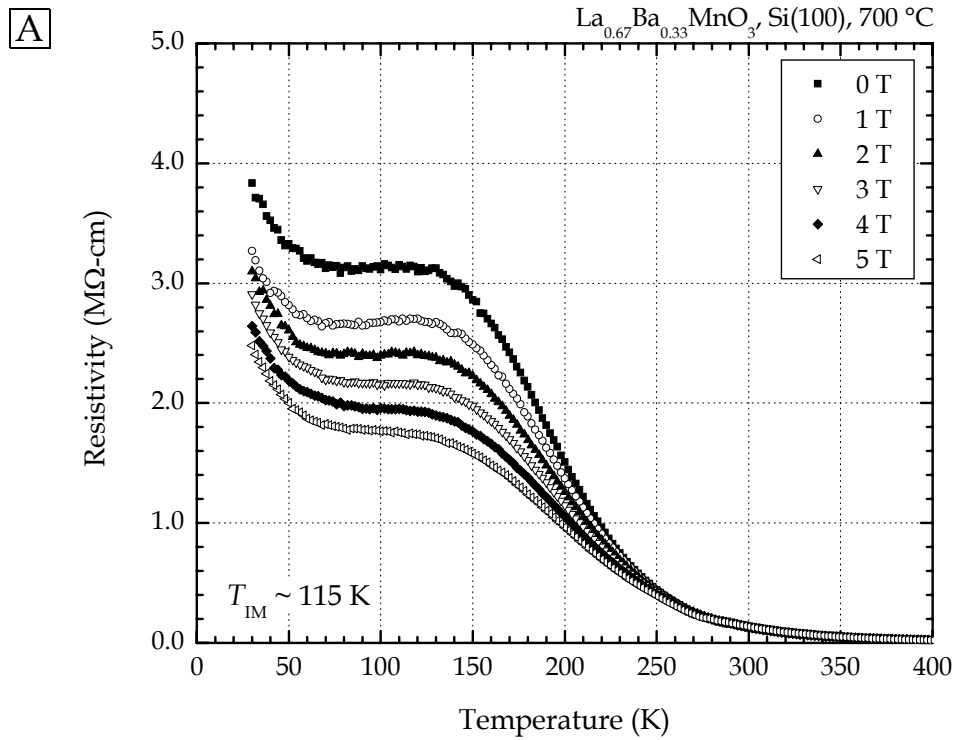
FIGURE 4.27 Magnetotransport of a $La_{0.67}Ba_{0.33}MnO_3$ thin film on Si(100) fired at 700 °C. Resistivity (A) and the *CMR* (B) as a function of temperature and applied field. The T_{IM} value refers to zero field.
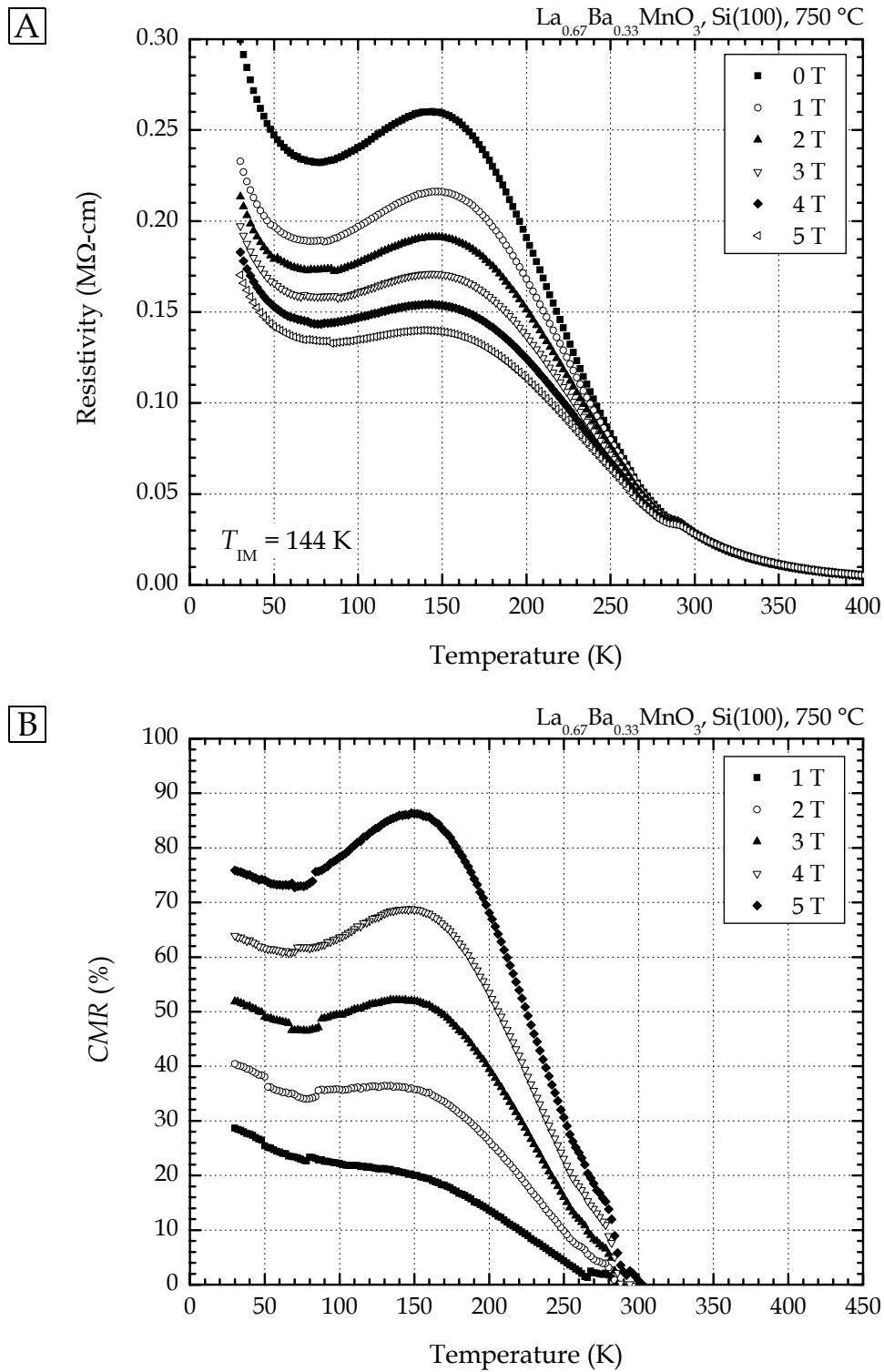
FIGURE 4.28 Magnetotransport of a La$_{0.67}$Ba$_{0.33}$MnO$_3$ thin film on Si(100) fired at 750 °C. Resistivity (A) and the *CMR* (B) as a function of temperature and applied field. The T_{IM} value refers to zero field.
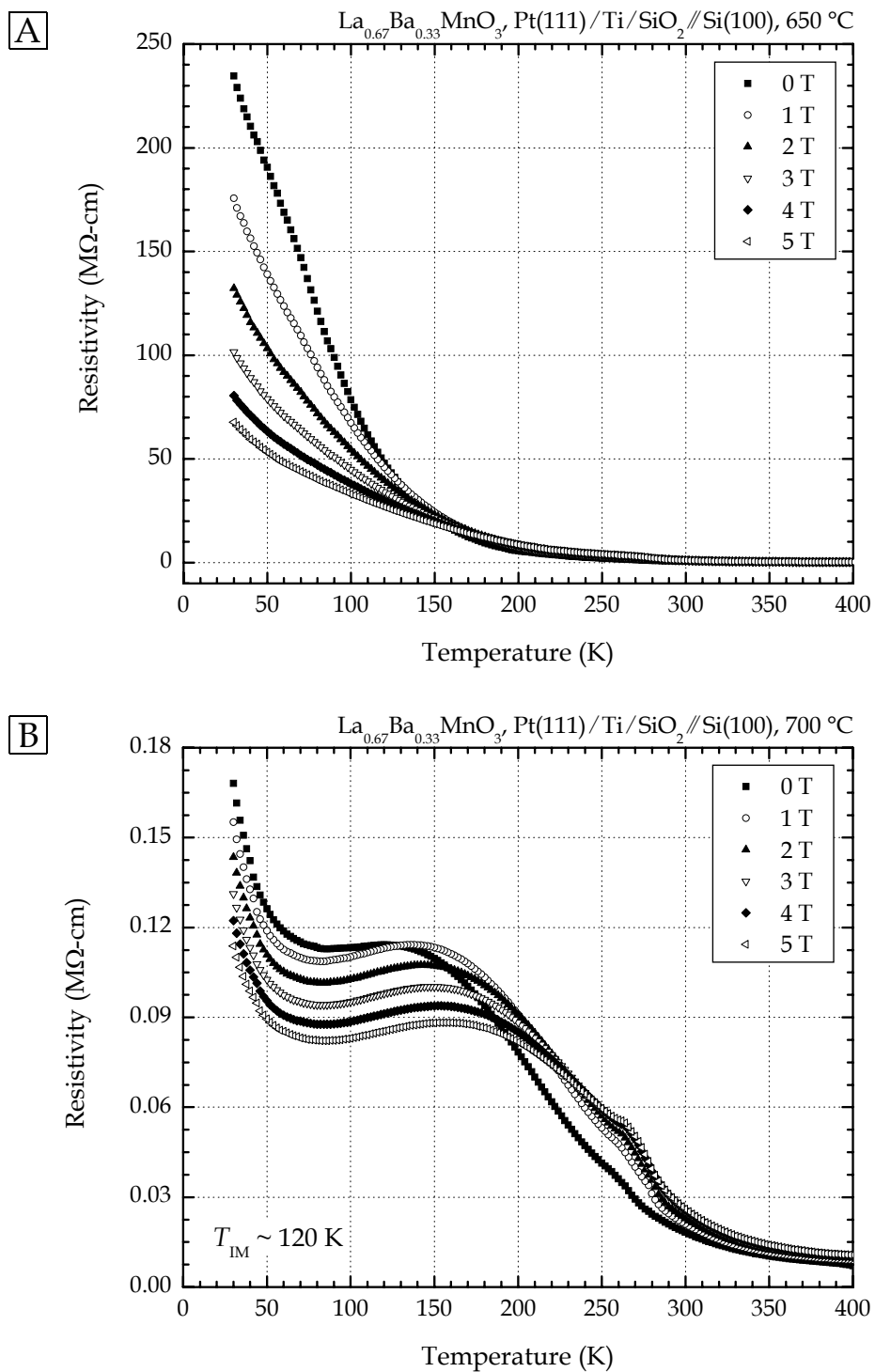
FIGURE 4.29 Magnetotransport of $La_{0.67}Ba_{0.33}MnO_3$ thin films on platinized-Si(100) *(continued on page 210)*. The insulator-metal transition emerges as the firing temperature increases from 650 °C (A) to 700 °C (B). The T_{IM} value refers to zero field.
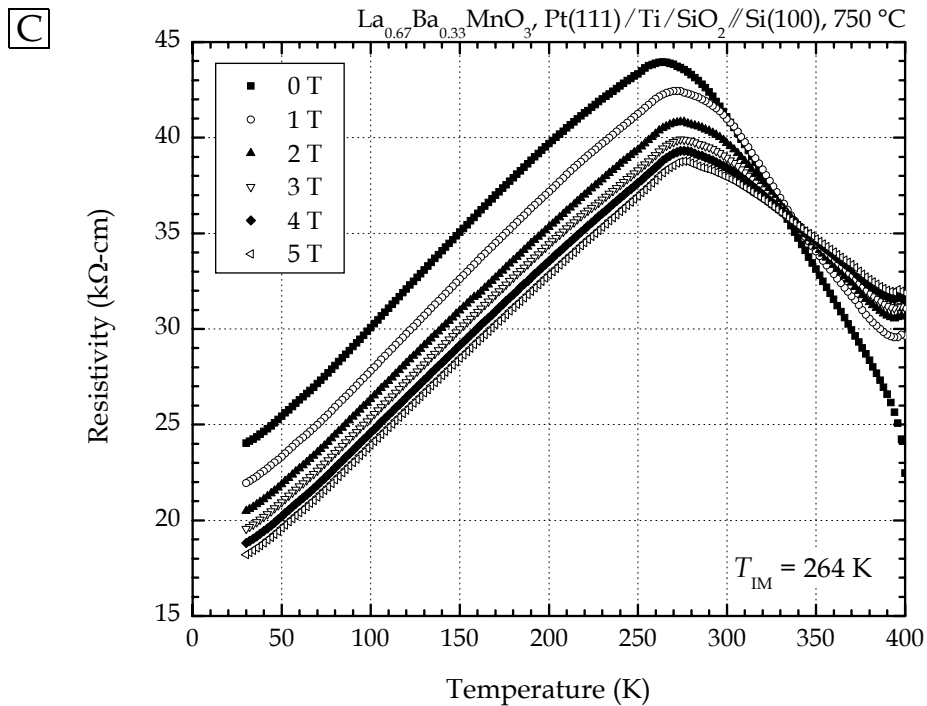
FIGURE 4.29 Magnetotransport of $La_{0.67}Ba_{0.33}MnO_3$ thin films on platinized-Si(100) *(continued from page 209)*. Complete development occurs upon firing at 750 °C (C) as evidenced by distinct metallic and semiconducting regions. The T_{IM} value refers to zero field.
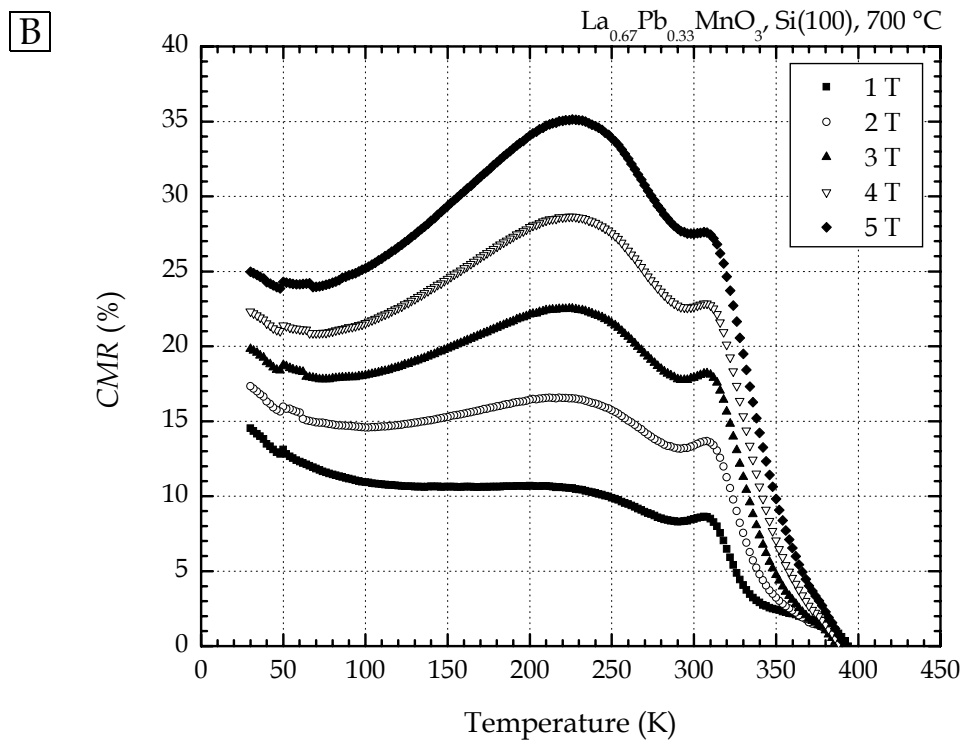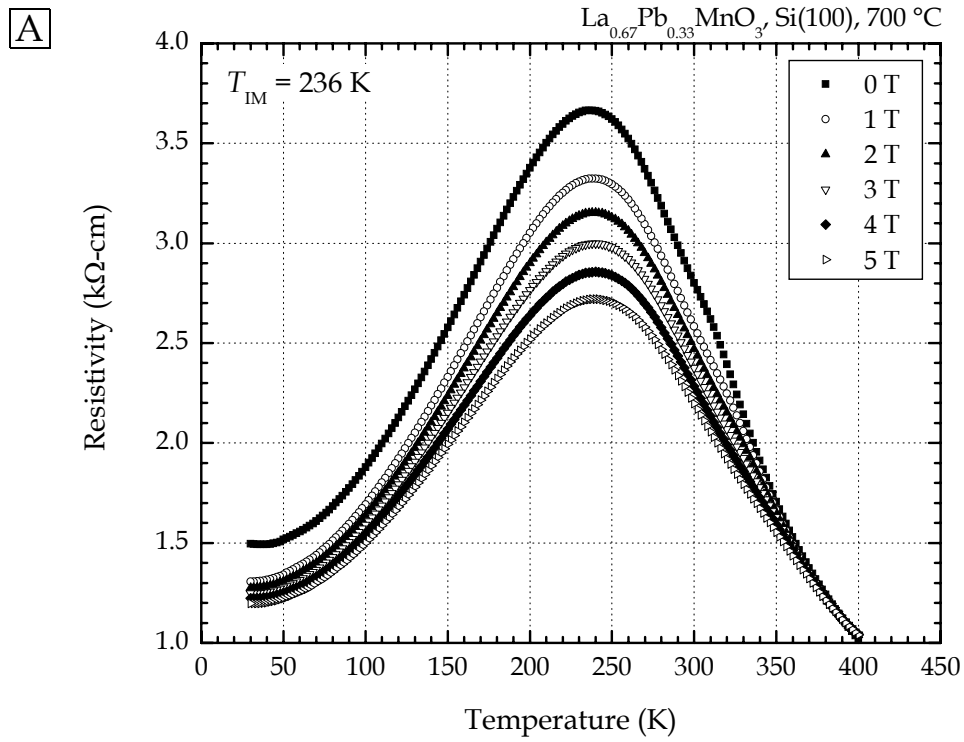
FIGURE 4.30 Magnetotransport of a $La_{0.67}Pb_{0.33}MnO_3$ thin film on Si(100) fired at 700 °C. Resistivity (A) and the *CMR* (B) as a function of temperature and applied field. The T_{IM} value refers to zero field.

211
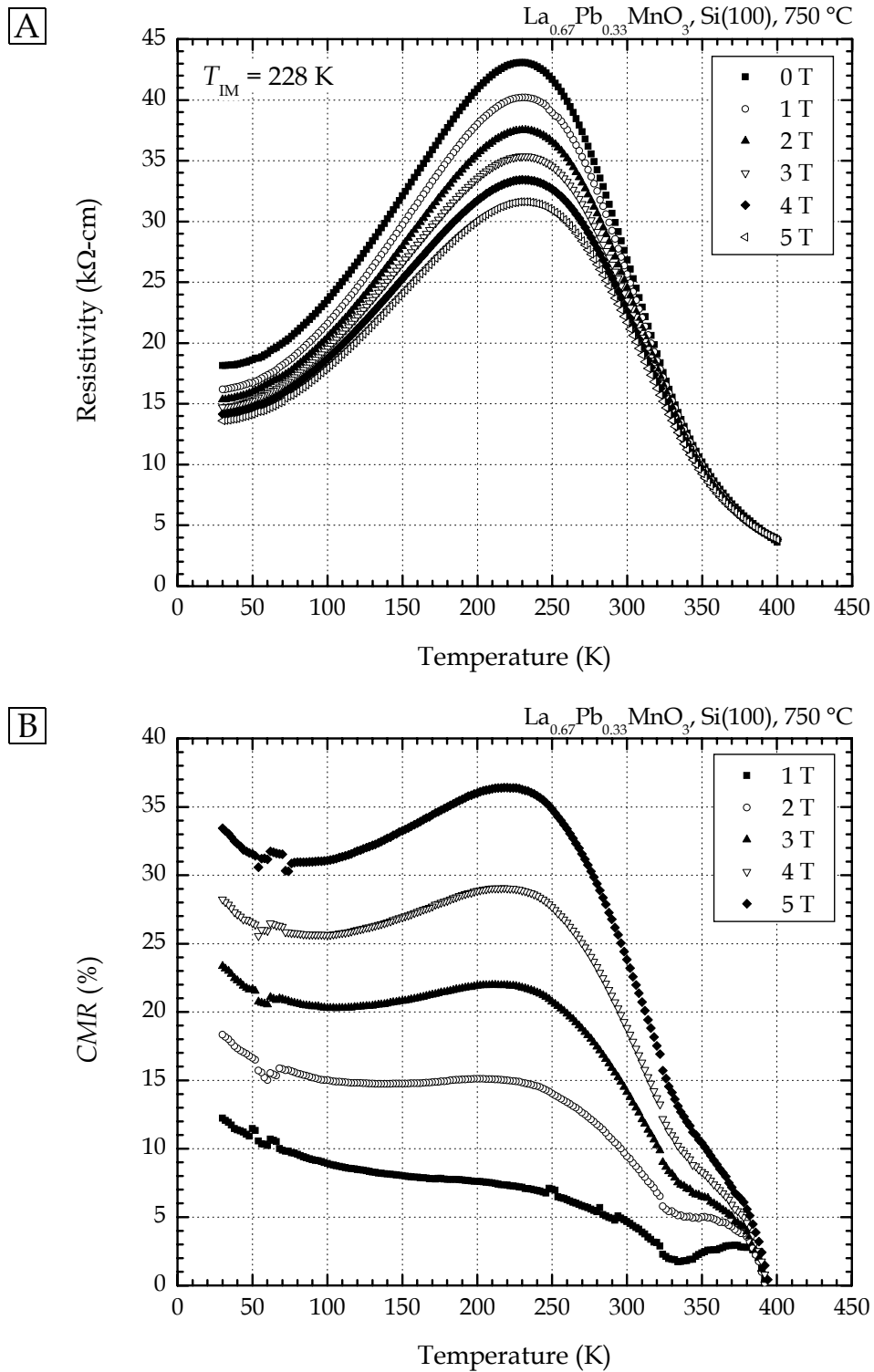
FIGURE 4.31 Magnetotransport of a $La_{0.67}Pb_{0.33}MnO_3$ thin film on Si(100) fired at 750 °C. Resistivity (A) and the *CMR* (B) as a function of temperature and applied field. The T_{IM} value refers to zero field.
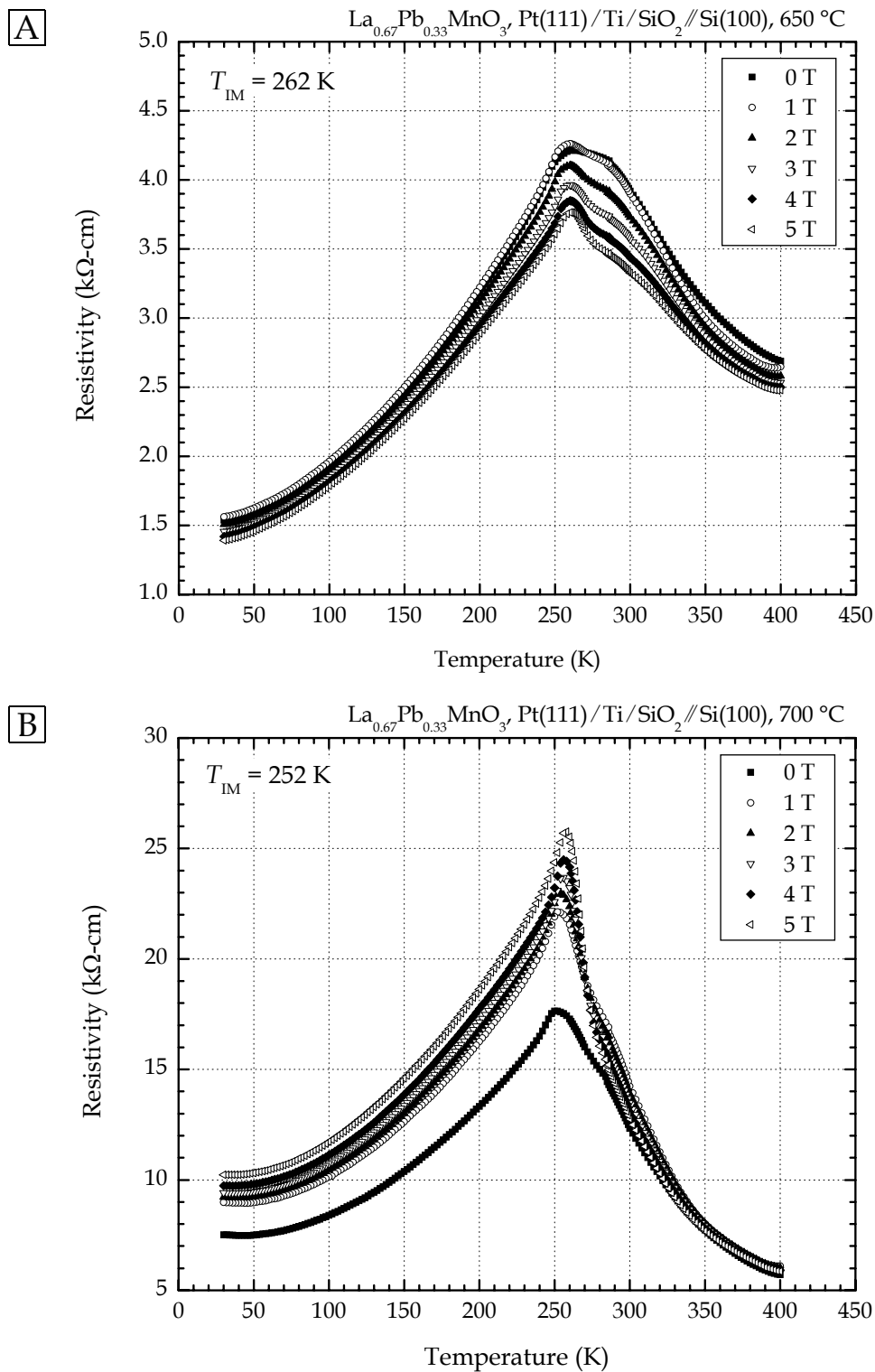
FIGURE 4.32 Magnetotransport of $La_{0.67}Pb_{0.33}MnO_3$ thin films on platinized-Si(100) *(continued on page 214)*. The insulator-metal transition sharpens from 650 °C (A) to 700 °C (B). The T_{IM} values refer to zero field.
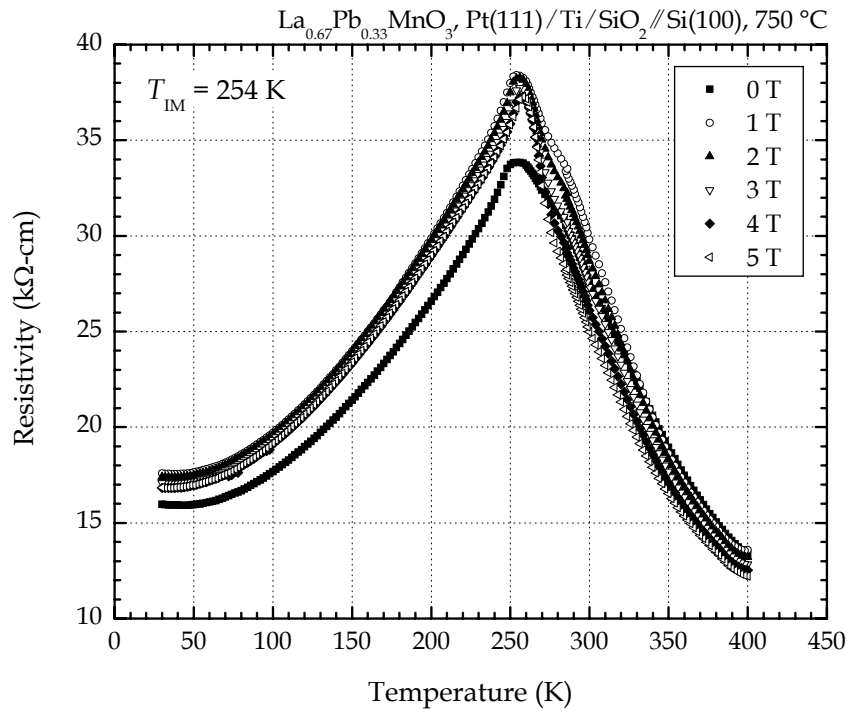
La$_{0.67}$Pb$_{0.33}$MnO$_3$, Pt(111)/Ti/SiO$_2$//Si(100), 750 °C

C

T_{IM} = 254 K

Resistivity (kΩ-cm)

Temperature (K)

■ 0 T
○ 1 T
▲ 2 T
▽ 3 T
◆ 4 T
◁ 5 T

FIGURE 4.32 Magnetotransport of La$_{0.67}$Pb$_{0.33}$MnO$_3$ thin films on platinized-Si(100) *(continued from page 214)*. Firing at 750 °C (C) produces no advantage over the lower processing temperatures. The T_{IM} value refers to zero field.

magnetotransport of the platinized-Si(100) specimens (see Figure 4.32). The T_{IM} values decrease from 262 K to 252 K and 254 K upon increasing heat treatment from, respectively, 650 °C to 700 °C and 750 °C. The relative stability of T_{IM} past 650 °C, however, suggests a fully-formed manganite phase whose electrical properties are now dominated mainly by microstructure (i.e., fine-grain effects). Resistivity magnitudes increase with heat-treatment temperature, strongly suggesting PbO volitilization at the grain surface. Again, T_{IM} values are much higher for platinized-Si(100) than Si(100), suggesting an enhanced $[Mn^{4+}]$ concentration.

A comparison of $La_{0.67}Pb_{0.33}MnO_3$ films crystallized on Si(100) with those on platinized-Si(100) indicates: (1) a reduced symmetry for magnetotransport behavior and (2) an initially positive magnetoresistive response at 1 T. These anomalies, particularly the latter, are unexpected given the excellent properties observed with Si(100). Yet results obtained from other techniques (i.e., SQUID magnetometry, GIXS, etc.) attest to the high quality of the manganite perovskite films, regardless of substrate. So the author believes such anomalies to stem from the inadequacy of the 2-point geometry: the influence of contact resistance remains high possibility. Unfortunately, a definitive root cause was not isolated despite intense efforts by the author.

Weak-field measurements (i.e., for Si(100) substrates only) are provided in Figures 4.33 and 4.34. Like the high-field measurements, resistivities from barium-doped films decrease with increasing heat-treatment temperatures; the converse is found true for $La_{0.67}Pb_{0.33}MnO_3$. All films demonstrate a slight bias towards negative magnetic fields (i.e., ~ 60–80 Oe), due perhaps to an interfacial stress caused by either the Si(100) substrate and/or intermediary reaction layers. The poor insulator-to-metal transition of the $La_{0.67}Ba_{0.33}MnO_3$ thin film fired at 700 °C is apparent by its jittery and discontinous weak-field data: the resistivity was almost too high for the electrical bridge to measure. The 750 °C specimen, however, provides a symmetric, butterfly loop. Past $|H|$ = 300 Oe, changes in resistivity become linear (i.e., $(\Delta\rho/\Delta H)_T$ = –13 Ω-cm/Oe), *producing a response highly-desired for sensor applications*. By comparison, the lead-doped composition at 700 °C exhibits a wider linear range which starts at $|H|$ > 200 Oe (i.e., $(\Delta\rho/\Delta H)_T$ = –0.04 Ω-cm/Oe). The loop does not close completely, being slightly skewed. Heat treatment at 750 °C though, confers a symmetric (and closed) loop with linear tails either side (i.e., $(\Delta\rho/\Delta H)_T$ = –0.44 Ω-cm/Oe).
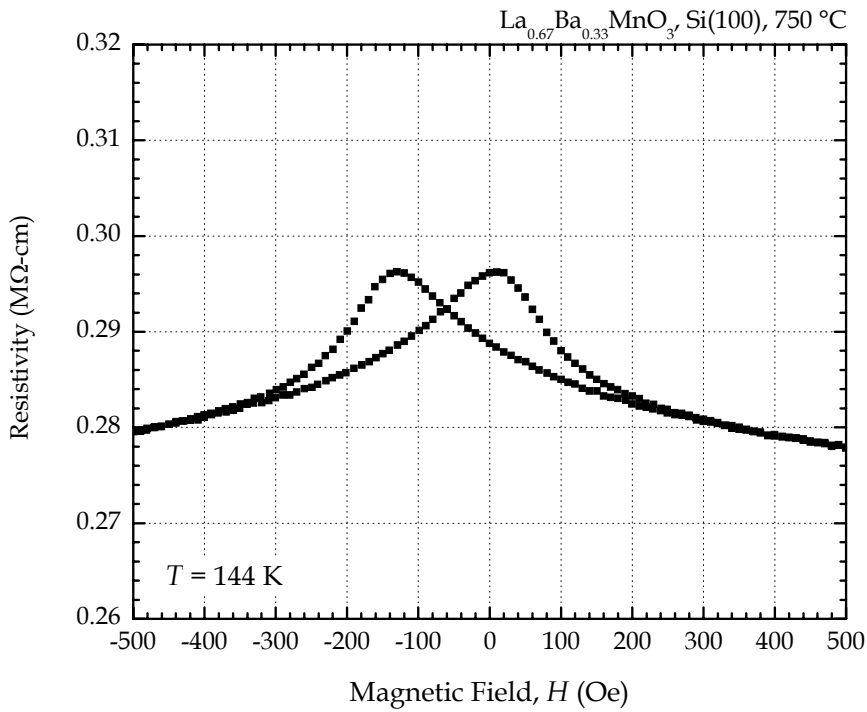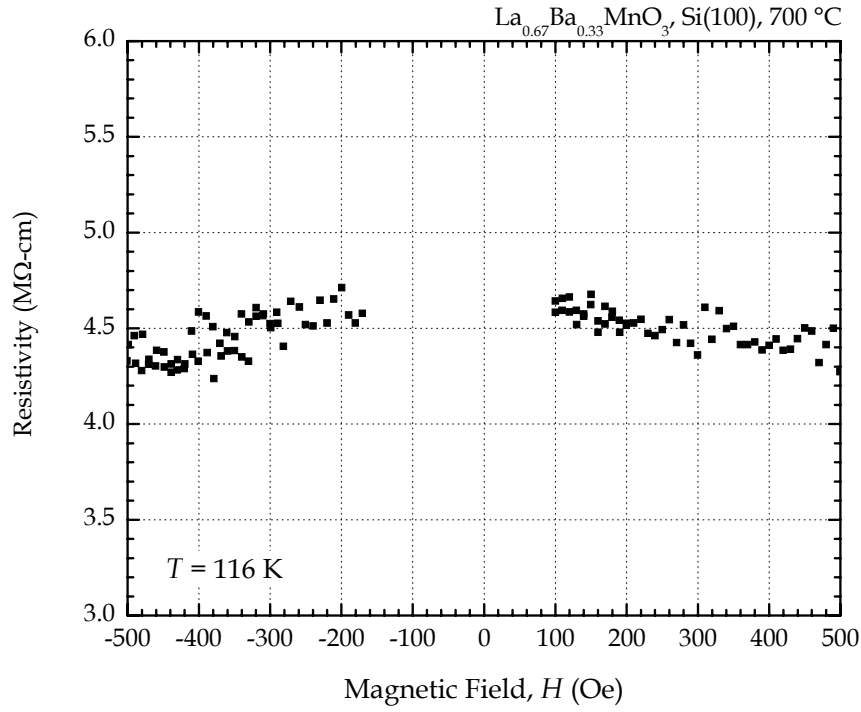
FIGURE 4.33 Weak field magnetotransport of $La_{0.67}Ba_{0.33}MnO_3$ thin films on Si(100). The temperature during measurement was $T = T_{IM}$.

La$_{0.67}$Pb$_{0.33}$MnO$_3$, Si(100), 700 °C

T = 235 K

Resistivity (kΩ-cm)

Magnetic Field, H (Oe)

La$_{0.67}$Pb$_{0.33}$MnO$_3$, Si(100), 750 °C

T = 226 K

Resistivity (kΩ-cm)

Magnetic Field, H (Oe)
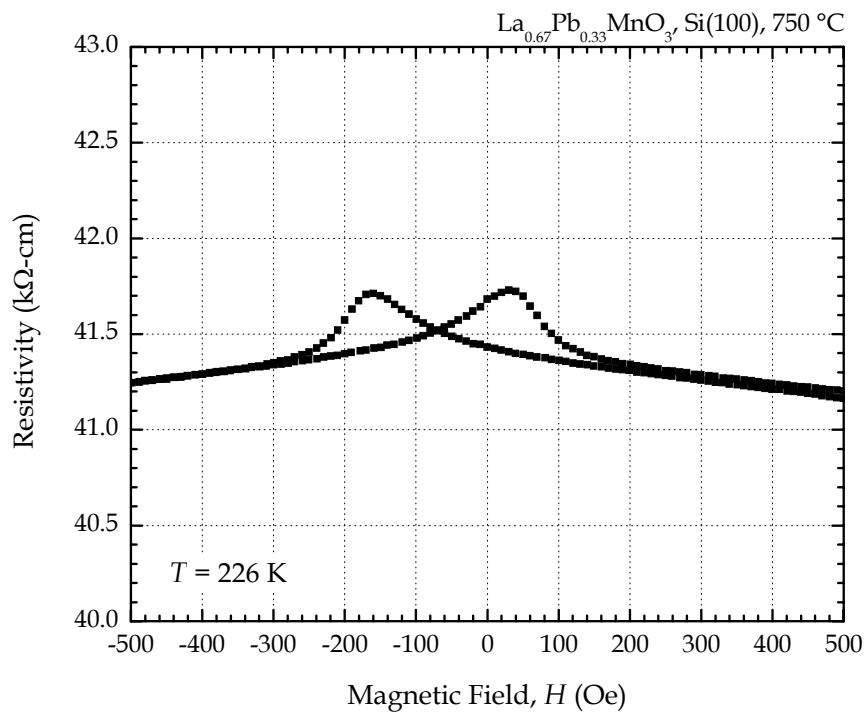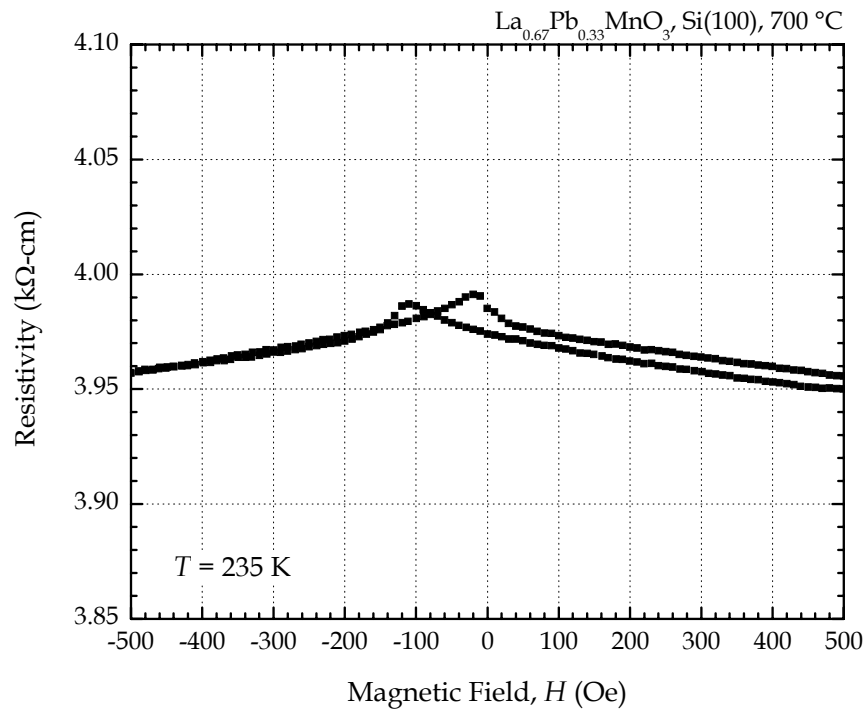
FIGURE 4.34 Weak field magnetotransport of La$_{0.67}$Pb$_{0.33}$MnO$_3$ thin films on Si(100). The temperature during measurement was $T = T_{IM}$.

4.11 SUMMARY

The development of an alkoxy-based, sol-gel processing method for manganite perovskites required the synthesis of a highly-soluble, reactive manganese(II) alkoxide. The infrared spectra of 2-methyl-2-propoxo manganese(II) in 2-methoxyethanol clearly demonstrated a precursor solvated predominately through interactions with the polar $O^{\delta-}-H^{\delta+}$ group of its host solvent. The subsequent preparation of "stock" solutions, free from any products of oxidation, then provided a starting point for conversion into a spinnable sol. The establishment of a polymeric system through mild, partial hydrolysis (i.e., $h = 0.25$) and aging enabled the preparation of dense, pore-free amorphous films by 450 °C (see Section 3.4.3). *Therefore, the design of an all-alkoxide, sol-gel process for doped-lanthanide manganites was successful accomplishing the first objective of this dissertation.*

Strong hydrolysis via post-spinning exposure to humidified air was shown, by thermal analysis, to be a critical step towards the low-temperature crystallization (i.e., < 650 °C) of manganite-perovskite films. Optical and electron micrographs indicated dense, smooth, and defect-free films with no porosity despite the absence of lattice-matched templating. Chemical homogeneity across the film specimens was excellent with no deviation from the desired 2:1:3 stoichiometry. A comparision of the data from thermal analysis, magnetization, and X-ray diffraction yielded a self-consistent conclusion: xerogel coatings prepared from partially-hydrolyzed 0.20 M La-Ba-Mn and La-Pb-Mn sols crystallize below 650 °C into oxide films with perovskite structure. *Thus, compatibility with silicon-based substrates was achieved through low-temperature densification and crystallization, the second objective of this dissertation.*

Crystallization proceeded via rapid nucleation, leaving a microstructure of fine-grain material (i.e., < 50 nm). Such small grains were believed to increase the resistivity (i.e., $> 10^6$ Ω-cm) and lower the insulator-metal transition temperature. Evidence of PbO volitilization in $La_{0.67}Pb_{0.33}MnO_3$ films, however, and subsequent accumulation within the grain boundaries also remained strong. These influences were undesirable because the dopants (and concentrations) were specifically choosen for their room-temperature properties. Optimal magnetoresistive behavior, however, was best demonstrated by $La_{0.67}Pb_{0.33}MnO_3$ films crystallized at 700 °C and 750 °C on Si(100). The corresponding magnetotransport curves were highly symmetrical with distinct maxima. By comparison, films of $La_{0.67}Ba_{0.33}MnO_3$ required platinized-Si(100) substrates and a heat-treatment temperature of 750 °C for optimal magne-

totransport. *Hence, magnetoresistive properties were demonstrated for manganite perovksite films on silicon-based substrates, completing the third and final objective of this dissertation.*

The use of platinized-Si(100) provided an excellent surface for crystallization but a challenging substrate for property measurement. The very-low resistivity of platinum offered a readily-accessible leakage path for electron flow, preventing conventional 4-point (i.e., in-plane) measurements. Difficulties encountered with the alternate 2-point geometry suggest that platinum may be a poor substrate choice unless corrective measures can be implemented.

4.12 REFERENCES

[1] Horvath, B.; Möseler, R.; Horvath, E. G. Manganese(II) Alkoxides. *Zeitschrift für Anorganische und Allgemeine Chemie* **1979**, *449*, 41–51.

[2] Smith, B. *Infrared Spectral Interpretation: A Systematic Approach*; CRC Press: Boca Raton, FL, 1999.

[3] Adams, R. W.; Bishop, E.; Martin, R. L.; Winter, G. Magnetism, Electronic Spectra, and Structure of Transition Metal Alkoxides. *Australian Journal of Chemistry* **1966**, *19* (2), 207–210.

[4] Pohl, A.; Westin, G.; Jansson, K. Preparation of $La_{0.67}Ca_{0.33}MnO_3$ Nanophase Powders and Films from Alkoxide Precursors. *Chemistry of Materials* **2002**, *14* (5), 1981-1988.

[5] Pohl, A.; Westin, G.; Jansson, K. Preparation of $La_{0.75}Sr_{0.25}MnO_3$ Nano-Phase Powders and Films from Alkoxide Precursors. *Journal of Sol-Gel Science and Technology* **2003**, *26* (1–3), 257–260.

[6] Tani, T.; Payne, D. A. Lead Oxide Coatings on Sol-Gel Derived Lead Lanthanum Zirconium Titanate Thin Layers for Enhanced Crystallization into the Perovskite Structure. *Journal of the American Ceramic Society* **1994**, *77* (5), 1242–1248.

[7] Pietambaram, S. V.; Kumar, D.; Singh, R. K.; Lee, C. B. Oxygen Content and Crystallinity Effects in Pulsed Laser Deposited Lanthanum Manganite Thin Films. In *Laser-Solid Interactions for Materials Processing*, Materials Research Society Symposia Proceedings, Vol. 617, San Francisco, CA, Apr 25–27, 2000; Kumar, D., Norton, D. P., Lee, C. B., Ebihara, K., Xi, X. X., Eds.; Materials Research Society: Warrendale, PA, 2001; pp J3.14.1–J3.14.6.

[8] Fors, R.; Khartsev, S.; Grishin, A.; Pohl, A.; Westin, G. Sol-Gel Derived Versus Pulsed Laser Deposited Epitaxial $La_{0.67}Ca_{0.33}MnO_3$ Films: Structure, Transport, and Effect of Post-Annealing. *Thin Solid Films* **2004**, *467* (1–2), 112–116.

[9] Varshneya, A. K. *Fundamentals of Inorganic Glasses*; Academic Press: Boston, 1994.

[10] Sengupta, S. S. Evolution of Local Structure and Stress Development During Thermal Treatment of Sol-Gel Derived PZT-Based Thin Layers. Ph. D. Thesis, University of Illinois, Urbana, IL, Aug 1996

[11] Mahendiran, R.; Mahesh, R.; Raychaudhuri, A. K.; Rao, C. N. R. Resistivity, Giant Magnetoresistance, and Thermopower in $La_{0.7}Sr_{0.3}MnO_3$ Showing a Large Difference in Temperatures Corresponding to the Ferromagnetic Transition and the Insulator-Metal Transition. *Solid State Communications* **1996**, *99* (3), 149–152.

[12] Banerjee, A.; Pal, S.; Bhattacharya, S.; Chaudhuri, B. K. Particle Size and Magnetic Field Dependent Resistivity and Thermoelectric Power of $La_{0.5}Pb_{0.5}MnO_3$ Above and Below Metal-Insulator Transition. *Journal of Applied Physics* **2002**, *91* (8), 5125–5134.

CHAPTER 5

STATEMENT OF CONCLUSIONS

5.1 INTRODUCTION

As originally discussed in Chapter 1, intense current interest in the colossal magnetoresistance of doped-lanthanide manganites reflects attempts to: (1) advance the scientific understanding of magnetotransport phenomena and (2) exploit such behavior for integration into hybrid, silicon-based microelectronics, particularly for sensor applications. The statement of objectives developed for this dissertation thus revolved around the development of a robust, low-temperature sol-gel process for the preparation of general $Ln_{1-x}M_x\text{MnO}_3$ perovskite compositions. The successful demonstration of thin-film deposition and crystallization on Si(100) and platinized-Si(100) substrates, shown extensively throughout Chapter 4, therefore represents a new and significant contribution to the field. Such an achievement is noteworthy in light of: (1) the almost exclusive reliance, in the literature, on vapor-phase techniques and (2) the failure of other reported chemical-solution methods to offer competitive alternatives. Accordingly, this chapter provides the main conclusions for this dissertation as derived from the observations of Chapters 3 and 4.

5.2 CONCLUSIONS

Specific topics and their relation to the research objectives originally outlined in Chapter 1 are summarized below. Five topics are presented in total with brief closing comments from the author given at the end.

(1) *Mn[OC(CH₃)₃]₂ and 2-methoxyethanol produced an effective precursor-solvent system.*
As discussed in Section 2.4, the virtual absence of manganese(II) alkoxides from sol-gel processing stems from the insolubility of preferred, low carbon content derivatives. Deliberate selection of the 2-methyl-2-propoxo ligand conferred an aggregation state between polymeric and crystalline coordination, which upon exposure to the polyfunctional groups of 2-methoxyetha-

nol, enabled immediate dissolution of the solid. Infrared transmission spectroscopy revealed perturbations in the $O^{\delta-}-H^{\delta+}$ bending modes of 2-methoxyethanol which implicate an $Mn^{2+} \leftarrow O^{\delta-}-H^{\delta+}$ interaction as the principal solvation mechanism. Thus, the high solubility of 2-methyl-2-propoxo manganese(II) fulfills a critical need for a hydrolytically-active alkoxide precursor in the sol-gel processing of manganese-containing oxides.

(2) *Establishment of an all-alkoxide sol system enabled crystallization below 650 °C.*
In Section 4.3, the thermal analysis of xerogels indicated crystallization of the manganite perovskite phase at ~ 650 °C and ~ 600 °C for, respectively, La-Ba-Mn (2:1:3) and La-Pb-Mn (2:1:3). This behavior was in good agreement with subsequent onsets measured by GIXS diffraction in $La_{0.67}Ba_{0.33}MnO_3$ and $La_{0.67}Pb_{0.33}MnO_3$ thin films grown on Si(100) and platinized-Si(100). In fact, perovksite structure on the latter substrate was detected at 600 °C! The emergence of stoichiometric manganite perovksite below 650 °C attests to the efficacy of alkoxy ligands in activating hydrolysis and condensation, a critical process for the synthesis of oxo-polymer structure. By comparison, chemical-solution methods derived from surrogate precursors, such as carboxylate or β-diketonates, require temperatures above 850 °C for phase-pure, stoichiometric manganite material.

(3) *Post-spinning hydrolysis was essential for transparent, dense, and defect-free films.*
In Section 3.4.2, a partial hydrolysis of $h = 0.25$ was selected to ensure a polymeric system and maximize spinning longevity. Mild hydrolysis ratios (i.e., $h < 1.0$), however, could not liberate sufficient organic content to prevent the rapid evolution of carbon dioxide during pyrolysis. Such behavior, when left uncorrected, produced phase separation and porosity in the resulting amorphous film. Unfortunately, stronger partial hydrolysis (i.e., $h > 1.0$) quickly induced gelation, rendering the sol unusable for coating processes. Thus, the inclusion of post-spinning hydrolysis via humidified-air proved essential to increase the oxide content of the deposited gel layer. This two-stage procedure then ensured proper hydrolysis, yielding transparent,

dense, and defect-free films. As indicated by optical and scanning electron micrographs, these characteristics were retained through crystallization.

(4) *Magnetotransport properties of $La_{0.67}Pb_{0.33}MnO_3$ emerged before $La_{0.67}Ba_{0.33}MnO_3$.*
A straight-forward comparison, by heat-treatment temperature, of 0–5 T high-field behavior clearly indicates that the lead-doped lanthanum manganite exhibited characteristic magnetotransport curves ~ 50–100 °C lower than the barium analogue (see Figures 4.27 through 4.32). Results from both GIXS diffraction and SQUID magnetometry reveal the earlier crystallization of $La_{0.67}Pb_{0.33}MnO_3$ with a more rapid approach of $[Mn^{4+}]$ to an optimal concentration (i.e., ~ 33%). These observations carry important ramifications for the integration of manganite perovskites into silicon-based microelectronics: of the three dopants which confer room-temperature magnetoresistance (i.e., M = Sr, Ba, and Pb), the constraints of thermally-compatibility favor lead.

(5) *Platinized-Si(100) offers the best surface for crystallization and grain growth.*
In Table 4.2, a review of the cubic lattice parameters, Curie points (T_C), and insulator-metal transitions (T_{IM}) clearly demonstrates that Pt(111) offers a superior surface for low-temperature crystallization and $[Mn^{4+}]$ optimization. Furthermore, AFM measurements reveal larger grain sizes for platinized-Si(100) than for Si(100), suggesting an improvement in growth kinetics on the former substrate. Such observations are not totally unexpected given the small difference in cubic lattice constant between platinum (i.e., 3.923 Å) and the manganite compositions of this dissertation (i.e., ~ 3.90 Å). The well-known catalytic properties of this noble metal also enhance organic decomposition. Unfortunately, the higher-conductivity of platinum enables leakage paths with interfere with the measurement of magnetoresistance. Thus, the author recommends the prior deposition of a very thin (< 50 nm) polycrystalline seed layer of the insulating $SrTiO_3$ (see the last topic of Chapter 6 for further discussion).

As a closing comment, the author wishes to point out that investigations into weak-field response indicated good transport behavior despite the unoptimized nature of the heat-treat-

ment process. For example, when comparing the 14Å-Fe(001)/8Å-Cr(001) superstructure of Chapter 1 with the $La_{0.67}Pb_{0.33}MnO_3$ film crystallized at 750 °C on Si(100) in Chapter 4, sensitivities of, respectively, –1 x 10^{-9} Ω-cm/Oe and –0.44 Ω-cm/Oe are obtained. This result vastly favors the manganite! Unfortunately, transport measurements of the latter were taken at T = 226 K (i.e., at T_{IM}), a temperature unsuitable for practical applications. Optimization of the insulator-metal temperature would therefore be an important priority for any commercial adaptation of the alkoxy, based sol-gel process developed in this dissertation. Property optimizations, however, comprise one of the main themes for future experimental research and will be presented in Chapter 6.

CHAPTER 6

RECOMMENDATIONS FOR FUTURE RESEARCH

6.1 INTRODUCTION

The development of sol-gel processing for doped-lanthanum manganites, as detailed in Chapter 3, depended critically on the optimization of hydrolysis parameters to yield dense, transparent, and defect-free amorphous films by 450 °C. This low-temperature densification resulted specifically from an all-alkoxide solution chemistry devoid of traditional surrogate precursors such as carboxylates or β-diketonates. In particular, the careful design of precursor-solvent interactions enabled the rapid dissolution of a low carbon-content and reactive manganese(II) alkoxide, $Mn[OC(CH_3)_3)]_2$. This accomplishment presents an important new advance in sol-gel processing because, as extensively discussed in Chapter 2, the use of manganese(II) alkoxides for solution chemical deposition remains virtually unknown.

The hydrolytic reduction of organic content also minimized the presence of residual carbonate or oxycarbonate species such that heat-treatments above 600 °C readily induced crystallization of the perovskite phase. As presented by Chapter 4, the emergence of manganite perovskite structure was intimately linked to the simultaneous onset of ferromagnetism and magnetoresistive behavior, both fundamental requisites for the successful achievement of all research objectives originally outlined in Chapter 1. More importantly, the preparation of crystalline $La_{0.67}Ba_{0.33}MnO_3$ and $La_{0.67}Pb_{0.33}MnO_3$ occurred not on refractory, lattice-matched $LaAlO_3(100)$ or $SrTiO_3(100)$ templates, but rather on commercially-relevant, silicon-based substrates. Surfaces of that latter offer poorer epitaxial registry with perovskite manganite phases. Thus, crystallization below 650 °C on such surfaces represents a significant contribution to the field. In contrast, methods based on vapor-phase deposition require processing temperatures above 800 °C, even with lattice-matched templates.

The research documented in this dissertation, however, focused principally on the successful development of an alkoxy-based, sol-gel process for the low-temperature densification and crystallization of magnetoresistive manganite thin films, as summarized in Chapter 5. Results obtained through this investigation clearly reveal opportunities for further

research, specifically regarding the continued optimization of the deposition process, film microstructure, and corresponding electrical properties. Accordingly, this chapter provides recommendations by the author for future experimental work.

6.2 RECOMMENDATIONS

For clarity, the recommendations provided below have been organized into short, concise descriptions and are headed by italicized titles. Seven topics are presented in total with the related recommendations stated in the underlying text.

(1) *Investigation of Mn[OC(CH$_3$)$_3$]$_2$ structure*

In Section 4.2, the dissolution of Mn[OC(CH$_3$)$_3$]$_2$ was demonstrated to result from the coordinating activity of 2-methoxyethanol through its polar O$^{\delta-}$—H$^{\delta+}$ group. This behavior stands in contrast to other coordinating organic solvents (i.e., alcohols, ethers, nitriles, heterocycles, etc.) which failed to disrupt the polymeric aggregation of 2-methyl-2-propoxide manganese(II) (see Section 2.4.4). Furthermore, this composition was isolated as a stable, true alkoxide. The other soluble alkoxide reported for manganite sol-gel processing, a 2-methoxyethoxide prepared by POHL, et al. [1], was reported to spontaneously decompose into an oxoalkoxide *in situ* during synthesis. Thus, further chemical investigation of Mn[OC(CH$_3$)$_3$]$_2$ would be of great interest. The author recommends the crystallization of the solid-state adduct (if possible) with a subsequent characterization of its structure. With this reference information, a better understanding of the solution structure and solvent interactions could be obtained via nuclear magnetic resonance spectroscopy.

(2) *Optimization of hydrolysis*

The viscoelastic behavior of 0.2 M La-Ba-Mn and La-Pb-Mn sols discussed in Section 3.4.2 clearly indicates a high-sensistivity to hydrolytic water: hydrolysis ratios greater than $h = 1.0$ induced rapid gelation. A greater tolerance to water would enhance sol longetivity and perhaps reduce the extent of post-spinning hydrolysis required to ensure dense, transparent, defect-free coatings. As described in Section 2.3.3, the activation of alkoxy-bridging by non-

polar, non-protic media improves resistance to hydrolysis when compared with polar, protic solvents such as alcohols. So the author recommends the re-formulation of "stock" solution synthesis with toluene instead of 2-methoxyethanol. A short reflux would induce solvation via the heterometallic reaction of Equation 2.13. Furthermore, the author noticed that during heat-treatment at 100 °C rapidly evaporating drops of water next to a specimen produced dense, defect-free amorphous coatings — but without slow spinning under humdified air! Thus, the author recommends dessication in strongly-humidified and heated air *devoid of carbon dioxide*. Variables for investigation would include substrate temperature (i.e., not necessarily 100 °C), air temperature, humidity level, and flow-rate.

(3) *Investigation of intermediary pyrolytic compositions*

The thermal analysis given in Section 4.3 clearly indicated the formation of oxycarbonate phases upon pyrolysis. Determination of intermediary compositions, however, would be greatly enhanced by mass spectrometry (TGA-MS) and infrared transmission microscopy (FTIR). The former could identify (and monitor) volatilized organic species and the latter detect carbonate stretching modes (with spatial resolution) in the amorphous and crystallizing thin films. Such investigations would play an important role in isolating decomposition temperatures for intermediate hydroxycarbonate and oxycarbonate phases. Furthermore, the effects of subsequent process optimizations would be more-thoroughly characterized, and hence better understood. For example, the author recommends pyrolysis in purified, flowing oxygen (i.e., no carbon dioxide) to further reduce crystallization temperatures. Conversion into a carbonate-free amorphous oxide film could be directly compared with samples prepared in air.

(4) *Investigation of substrate-film and grain-boundary interfaces.*

In Section 4.7, GIXS revealed two anamolous features, both emerging at 600 °C: (1) an unidentified reaction layer for films crystallized on Si(100) and (2) the possible formation of β-SiO$_2$ (i.e., on either substrate). High-resolution, cross-sectional TEM could probe the film-substrate interface and thereby

reveal local structure and chemical composition. Equally important, the XPS analysis given in Section 4.4 was obtained from multiple 0.3 mm x 0.7 mm rectangular areas sampled from the film surface. Such dimensions clearly cannot resolve non-stoichiometric phases (e.g., PbO) residing within the grain boundaries or verify intra-grain chemical homogeneity. Yet both characteristics influence electrical conduction, and hence, magnetoresistive response. Accordingly, the author recommends the investigation of local grain microstructure via Z-contrast STEM (or phase-contrast TEM) imaging.

(5) *Dependence of $[Mn^{4+}]$ on heat-treatment temperature*

Correlation of the mixed Mn^{3+}/Mn^{4+} valence state with magnetic ordering and magnetotransport in manganite perovskites was extensively developed in Sections 2.2.2 and 2.2.3. Doping levels between $0.2 < x < 0.4$ yield optimal magnetoresistive properties through a critical influence on $[Mn^{4+}]$. The variation of $[Mn^{4+}]$ with heat-treatment temperature thus remains an important metric for characterization. As discussed in Section 3.5.5 though, measurement uncertainties in thin-film dimensions prevented the accurate determination of 0 K saturated moments from high-field magnetization curves. Any subsequent analysis using the method in Appendix A then would only produce unreliable values for $[Mn^{4+}]$. DUPONT, et al. [2], however, have successfully used electron spin resonance (ESR) with $La_{0.67}Ca_{0.33}MnO_3$ thin films to quantify $[Mn^{4+}]$ content. The author therefore recommends the adaptation of ESR to examine $[Mn^{4+}]$ dependence on firing temperature for the sol-gel processing of $La_{0.67}Ba_{0.33}MnO_3$ and $La_{0.67}Pb_{0.33}MnO_3$ coatings.

(6) *Film thickness and thermal processing effects on stress evolution*

In Section 4.9, the influence of interfacial strain on the kinetics of nucleation and grain growth was suggested as a contributing factor to the formation of fine-grain (< 50 nm) microstructures in the manganite films. Furthermore, residual stresses in a crystalline film would assuredly affect $Mn-O-Mn$ bond parameters, critical characteristics governing T_C and T_{IM} as discussed in Section 2.2.2. Accordingly, the author recommends an investigation of stress evolution upon heating amorphous La-Ba-Mn and La-Pb-Mn coatings

to crystallization. Corresponding changes in film stress during cooling (i.e., due to thermal expansion mismatch) would provide the residual values. By comparing against equivalently-processed, polycrystalline (i.e., unclamped) bulk pellets, the role of interfacial strain would be emphasized. Possible mitigating effects from increased film thickness should also be examined, particularly with regard to improving magnetotransport properties.

(7) *Effects of grain size modifications on magnetotransport behavior.*

Correlation of the AFM images presented in Section 4.9 with magnetotransport curves from Section 4.10 suggests that the high resistivities (> 10^6 Ω-cm) exhibited by the manganite films resulted from fine-grains (< 50 nm) with an extensive grain-boundary network. Furthermore, the metal-insulator transition, T_{IM}, was shifted below the Curie point, T_C, preventing an optimal magnetoresistive response at room temperature. Such microstructures stem from the rapid onset of nucleation before grain growth. By refining the sol-gel process to suppress nucleation, increases in grain size can be achieved, possibly improving magnetotransport properties. Modification of alkoxide species, particularly through chelating organic additives (e.g., acid analogues of carboxylate or β-diketonates), has been well-known to influence microstructure [3]. Thus, the author recommends the investigation of solution-chemical alterations on grain size. Perhaps the most direct method to activate kinetics for grain-growth, though, relies on rapid heating to the desired crystallization temperature. For example, HAGBERG, et al. [4] reported that alkoxy-derived LiNbO$_3$ sol-gel films produced larger grain sizes upon direct insertion into a pre-heated furnace (i.e., as opposed to a 10 °C/minute ramp rate). Crystallization of an initial (barrier) coating (i.e., a seed layer) has also been demonstrated to increase grain sizes for subsequent, spin-coated layers [5]. The author therefore also recommends the adaptation of these processing methods to examine their influence on grain size, and hence, magnetotransport behavior.

6.3 REFERENCES

[1] Pohl, I. A. M.; Westin, L. G.; Kritikos, M. Preparation, Structure, and Properties of a New Giant Manganese Oxo-Alkoxide Wheel, $[Mn_{19}O_{12}(OC_2H_4OCH_3)_{14}(HOC_2H_4OCH_3)_{10}] \cdot HOC_2H_4OCH_3$. *Chemistry − A European Journal* **2001**, *7* (16), 3438–3445.

[2] Dupont, F.; de Brion, S.; Chouteau, G.; Leibold, B.; Habermeier, H.-U. High Field Electron Spin Resonance Measurements on $La_{0.67}Ca_{0.33}MnO_3$ Thin Films. *Solid State Communications* **2000**, *113* (9), 499–502.

[3] Brinker, C. J.; Scherer, G. W. *Sol-Gel Science: The Physics and Chemistry of Sol-Gel Processing*; Academic Press: San Diego, CA, 1989.

[4] Hagberg, D. S.; Eichorst, D. J.; Payne, D. A. Electrical and Optical Properties of Alkoxide-Derived Lithium Niobate Thin-Layers. In *Sol-Gel Optics*, Proceedings of the International Society for Optical Engineering, Vol. 1328, San Diego, CA, Jul 11–13, 1990; Mackenzie, J. D., Ulrich, D. R., Eds.; International Society for Optical Engineering: Bellingham, WA, 1990; pp 466–473.

[5] Birnie, D. P., III; Jilavi, M. H.; Krajewski, T.; and Naß, R. The Effect of Barrier Layer Composition and Structure on the Crystallization of PZT Coatings on Silicon. *Journal of Sol-Gel Science and Technology* **1998**, *13* (1–3), 855–859.

Appendix A

Magnetic Characterization

For a doped-lanthanide manganite in the ferromagnetic state, the theoretical saturated magnetization can be calculated by considering the spin-only magnetic moments of individual Mn^{3+} and Mn^{4+} ions.[1] Ignoring any potential nonstoichiometry (i.e., defect states), an ideal formula unit, $(Ln^1_{y_1} Ln^2_{y_2}\dots)^{3+}_{1-x} (M^1_{z_1} M^2_{z_2}\dots)^{2+}_x Mn^{3+}_{1-x} Mn^{4+}_x O^{2-}_3$, implies that $[Mn^{3+}] = 1 - x$ and $[Mn^{4+}] = x$ where $y_1 + y_2 + \dots = 1 - x$ and $z_1 + z_2 + \dots = x$. So the net magnetic moment (per formula unit) then reduces to a weighted average, $\langle m \rangle$, of the individual ionic magnetic moments, $m_{Mn^{3+}}$ and $m_{Mn^{4+}}$

$$\langle m \rangle = (1-x)m_{Mn^{3+}} + (x)m_{Mn^{4+}} = (1-x)(4\mu_B) + (x)(3\mu_B) = (4-x)\mu_B \tag{A.1}$$

where μ_B is the Bohr magneton, 9.2740154 x 10^{-24} A $\cdot$ m^2 (or alternatively, J/T). Extending to the saturated magnetization (per unit mass) yields,

$$M_S = \frac{N_A}{M_r}\langle m \rangle = \frac{N_A}{M_r}(4-x)\mu_B \tag{A.2}$$

where N_A is Avogadro's number, 6.0221367 x 10^{23} mol^{-1} and M_r, the molecular weight of the doped-lanthanide manganite composition in g/mol. Equation A.2 generates values whose units are given in A $\cdot$ m^2/g, but empirical measurements of M_S are often reported in units of emu/g. To reconcile this difference, note the conversion 1 emu/g = 1 A $\cdot$ m^2/kg. Therefore

$$M_S = \frac{N_A}{M_r}(4-x)\mu_B \cdot \left(\frac{1000\text{ g}}{\text{kg}}\right) \tag{A.3}$$

where Equation A.3 now gives M_S in terms of emu/g.

---

[1] Mn^{3+} and Mn^{4+} are randomly distributed when $Ln_{1-x}M_x MnO_3$ ranges between $0.2 < x < 0.4$. This derivation, therefore, does not presume coupled magnetic sublattices (i.e., ferrimagnetic ordering).

APPENDIX B

MANGANESE SITE SYMMETRY

The structural symmetries of $Mn^{3+}O_6$ and $Mn^{4+}O_6$ octahedra play a crucial role in governing the electron transport of doped-lanthanide manganites. Mobility of the e_g electrons, for example, arises specifically from the splitting of manganese 3d energy levels induced by 6-fold oxygen-anion coordination. Accordingly, this appendix builds on the discussion of double exchange originally introduced in Section 2.2.3, moving to a derivation of the manganese octahedral point group, and concluding with crystal field effects on the 3d atomic orbitals. The t_{2g} and e_g lattice orbitals are linked, along with a descent in octahedral symmetry, to structural transitions, and in particular, the Jahn-Teller distortion. This connection provides a starting basis for electron-phonon interactions (i.e., polarons) not accounted for by Zener's double exchange model.

A description of the double exchange model proceeds from the consideration of resonance valence bonds between manganese 3d and oxygen 2p electrons: electrons hop from Mn^{3+} (d^3, $t_{2g}^3 e_g^1$, $S = 2$) to Mn^{4+} (d^4, t_{2g}^3, $S = 3/2$) through the oxygen so that the Mn^{3+} and Mn^{4+} charges change places [1]. The resonance hybrid between these two valence states is illustrated as follows:

$$\psi_1: Mn^{3+} \ O^{2-} \ Mn^{4+} \quad \leftrightarrow \quad \psi_2: Mn^{4+} \ O^{2-} \ Mn^{3+} \tag{B.1}$$
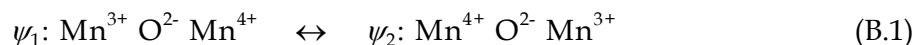
In order for electron transfer to occur, the O^{2-} anion must simultaneously transfer its electron to the Mn^{4+} as the Mn^{3+} transfers its electron to the O^{2-}. The corresponding exchange energy, E, is given explicitly by the integral

$$E = \int \psi_1^*(H - E_0)\psi_2 d\tau \tag{B.2}$$

where H is the Hamiltonian of the system; E_0, the energy associated with the initial states ψ_1 and ψ_2; and the integral extends over the coordinates and spins of all electrons. The integral is non-vanishing only if the spins of the two manganese d shells are parallel. Now a station-

ary state is represented neither by ψ_1 or ψ_2, but rather, by a linear combination of the two (i.e., $\psi_+ = \psi_1 + \psi_2$ and $\psi_- = \psi_1 - \psi_2$). Depending upon the sign of the integral, double exchange raises the energy associated with ψ_+, lowers the energy associated with ψ_-, or vice versa. Thus, the energy of one of these two stationary states (either ψ_+ or ψ_-) is lowered by double exchange which takes place when the 3d spins are parallel. So regardless of the sign of the exchange integral, the energy of the system will be lowered by a parallel alignment of spins. The onset of ferromagnetism below T_C, therefore, favors electron exchange, thereby lowering resistivity and enabling a switch to metallic conduction. The paramagnetic state above T_C, however, contains no magnetic ordering so double exchange does not influence transport in the semiconducting state.

Itinerant electron behavior in doped-lanthanide manganites results from the mobility of electrons occupying the e_g orbitals. A better understanding of this phenomenon can be achieved by expanding the concept of manganese site symmetry introduced in Section 2.2.2. Manganese cations in the perovskite structure are enclosed within an octahedral oxygen "cage", experiencing an electric field reflective of that symmetry. Site symmetry can therefore provide a basis linking the t_{2g} and e_g orbital sets to their energy level splitting. The application of point group symmetry to coordinated metal ions in a crystalline lattice was first explored by BETHE [2] which laid the foundation for crystal field theory (CFT). Consideration of CFT with regard to manganese cations then starts with the identification of all symmetry elements for an ideal octahedral point group, O_h.

Figure B.1 illustrates the seven distinct elements (C_2, C_3, C_4, S_4, S_6, σ_h and σ_d), all of which, intersect the manganese site at the center point of the perovskite unit cell. Operation of any of these symmetry elements on the octahedron results in equivalence; the final state remains indistinguishable from that of the initial. An explanation of the Schönflies notation representing the symmetry elements will clarify this statement. For example, the integer n in C_n, a proper rotation, indicates the angle for which equivalence is maintained (i.e., $360°/n$): a 90° rotation about any C_4 axis would leave the octahedron undifferentiated. Definitions for the remaining elements are then straight-forward. Reflection or mirror planes are given by σ, which in turn, is broken into two classes, horizontal (σ_h) and dihedral (σ_d). The horizontal reflection plane, σ_h, occurs perpendicular to the principal (i.e., highest-order) axis of rotation. So three σ_h planes correspond to each of the three orthogonal C_4 axes. In contrast,

234
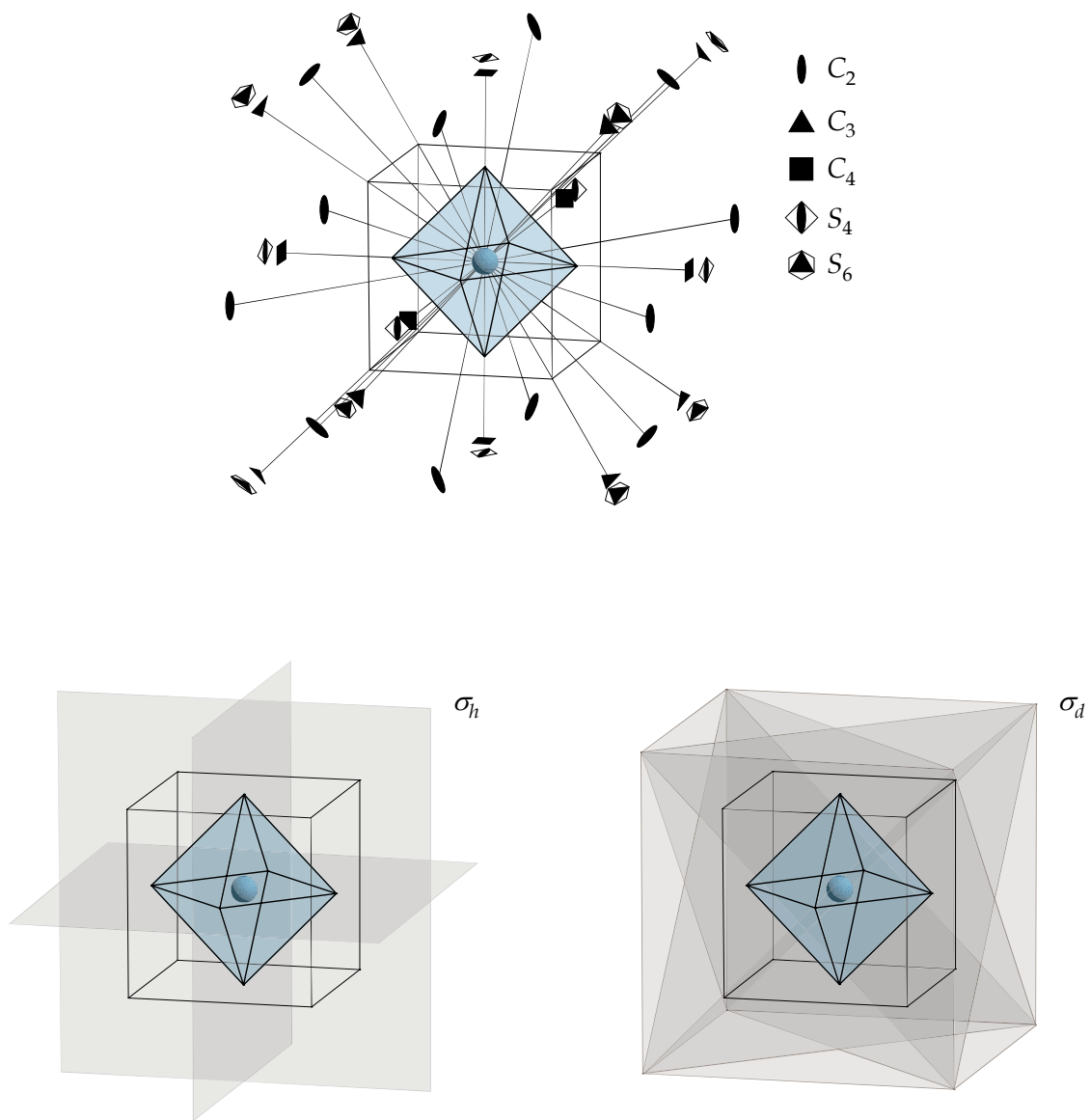
FIGURE B.1 Site symmetry of manganese octahedra in a cubic perovskite unit cell. The inversion element (*i*), present in the manganese position at the site center, has been omitted for clarity.

the dihedral reflection planes, σ_d, contain a principal axis of rotation. So each C_4 axis represents the intersection of two σ_d planes, both perpendicular to a σ_h plane. The symbol, S_n, designates an improper rotation, a compound operation wherein a $360°/n$ rotation is successively followed by reflection through a plane perpendicular to that axis. Two symmetry elements, however, are not shown in Figure B.1: (1) the identity element (E) has been assumed and (2) the inversion element (i), which shifts (x, y, z) into (-x, -y, -z), resides at (i.e., inside) the manganese site. In total, nine symmetry elements comprise the O_h point group.

Associated with the symmetry elements of a point group are the corresponding operations, a result of applying the element itself. For instance, the element C_4 will generate the operations C_4^1, C_4^2, C_4^3, and C_4^4. The superscript denotes the number of times the symmetry element has been applied. So C_4^3 results after three successive 90° rotations about a fourfold axis. Some operations are equivalent to lower symmetry ones and are therefore not unique: C_n^n or $S_n^n = E$, $C_4^2 = C_2$, $S_4^2 = C_2$, $S_6^2 = C_3^1$, $S_6^3 = i$, and $S_6^4 = C_3^2$. The unique symmetry operations generated from a common element together comprise a class. For example, the two C_3^1 and C_3^2 operations associated with each of the four C_3 axes comprise an eight-member C_3 class. Classes associated with a point of symmetry, in turn, form a unique group, hence the term "point group". Table B.1 gives the 10 classes resulting from 48 operations in the O_h point group. Although 10 classes are indicated for O_h, only 9 symmetry elements, in

O_h	E	$8C_3$	$6C_2$	$6C_4$	$3C_2^a$	i	$6S_4$	$8S_6$	$3\sigma_h$	$6\sigma_d$	
A_{1g}	1	1	1	1	1	1	1	1	1	1	$x^2 + y^2 + z^2$
A_{2g}	1	1	-1	-1	1	1	-1	1	1	-1	
E_g	2	-1	0	0	2	2	0	-1	2	0	$(2z^2 - x^2 - y^2, x^2 - y^2)$
T_{1g}	3	0	-1	1	1	3	1	0	-1	-1	(R_x, R_y, R_z)
T_{2g}	3	0	1	-1	-1	3	1	0	-1	-1	(xz, yz, xy)
A_{1u}	1	1	1	1	1	-1	-1	-1	-1	-1	
A_{2u}	1	1	-1	-1	1	-1	1	-1	-1	1	
E_u	2	-1	0	0	2	-2	0	1	-2	0	
T_{1u}	3	0	-1	1	-1	-3	-1	0	1	1	(x, y, z)
T_{2u}	3	0	1	-1	-1	-3	1	0	1	-1	

a Represents C_4^2 and S_4^2.

TABLE B.1 Character table of the octahedral O_h point group.

fact, generate them. This discrepancy can be reconciled by noting that $C_4^2 = S_4^2 = C_2$. Yet the C_2 axis resulting from operations of either the C_4 and S_4 elements is not equivalent to the other C_2 elements. A glance at Figure B.1 shows three $C_4^2 = S_4^2 = C_2$ operations intersecting octahedron vertices whereas the remaining six C_2 operations cross through the equatorial edges. So an additional C_2 class must be present in the character table of O_h.

The first column in Table B.1 lists the Mulliken symbols for the irreducible representations of O_h, which match the number of symmetry classes. Any basis consistent with ideal octahedral symmetry can be broken down into a representation of these symbols. To do so, a member of each symmetry class operates on the basis yielding a character representation. So for example, an s orbital situated at the center of the perovskite cell would have a character representation: 1 1 1 1 1 1 1 1 1 1; each symmetry operation leaves the s orbital unchanged, indicated in all cases by unity. Comparison with Table B.1 links the A_{1g} Mulliken symbol to the s orbital. The atomic s orbital is therefore said to transform as A_{1g} in O_h, or alternatively, belong to the A_{1g} symmetry species in O_h. The last column of Table B.1 provides the binary direct products which correspond to the different symmetry species. Clearly, $x^2 + y^2 + z^2$ can be associated with the spherically symmetric s orbital. Such information also allows for the convenient assignment of manganese 3d orbitals. From Table B.1 then: (1) d_{xy}, d_{xz}, and d_{yz} transform together as T_{2g} in O_h and (2) $d_{x^2-y^2}$ and d_{z^2} transform together as E_g in O_h.[1] The grouping of binary direct products, indicated by parentheses, reflects the degeneracy of the related symmetry species. Integer values under the identity element, E, indicate this degeneracy. So according to Table B.1, any E or T symmetry species is always doubly or triply degenerate, respectively. Therefore, in an octahedral site, the manganese 3d orbitals will form doubly degenerate E_g and triply degenerate T_{2g} sets. Further properties of point groups, their character tables, and applications to site symmetry are given in the reference texts [3–5] and will not presented here.

In an MnO_6 coordination environment, manganese cations experience directional electric fields from six equidistant O^{2-} anions. The O_h point group symmetry of the field splits the quintuply degenerate group of atomic 3d orbitals into triply degenerate t_{2g} and doubly degenerate e_g sets.[2] To determine the relative energy splitting of the symmetry-adapted

---

[1] The notation $2z^2 - x^2 - y^2$ is equivalent to z^2.
[2] Orbitals resulting from crystalline site symmetry employ lowercase Mulliken notation.

sets, the following comparison is useful: an isolated manganese cation (i.e., atomic) belongs to the infinite-order, rotation-inversion point group R_3 which contains all possible operations resulting from symmetry elements intersecting at a common point. This maximum symmetry ensures that the five atomic 3d orbitals are degenerate. If the manganese cation experienced a spherically symmetric field equivalent to six O^{2-} anion charges (i.e., consistent with the R_3 point group), the energy of all five 3d orbitals would increase together and remain degenerate. The descent in symmetry, though, from R_3 to O_h switches the configuration so that the six charges form an octahedron whose vertices (for convenience) lie on the axes of a Cartesian coordinate system. The directional crystalline field splits the fivefold degeneracy, raising the doubly degenerate e_g set but lowering the triply degenerate t_{2g}. The higher relative energy of e_g stems from greater Coulombic repulsions; as shown in Figure B.2, lobes from the $d_{x^2-y^2}$ and d_{z^2} orbitals comprising the e_g set reside on the Cartesian axes, pointing directly at the O^{2-} anions. Lobes from t_{2g}, however, point in between and experience a lower electric field than under R_3 site symmetry. From CFT, the magnitude of this split is represented by $\Delta = 10Dq$. Because an equivalent field is maintained, no net change in energy occurs during the descent from R_3 to O_h point group symmetry. Relative to the hypothetical spherical field then, the energy of the two e_g orbitals increases by $3/5\ \Delta = 6Dq$ and that of the three t_{2g} orbitals decreases by $2/5\ \Delta = 4Dq$. Figure B.3 illustrates the effects of site symmetry on orbital energy for manganese cations in a crystalline field.

Population of the t_{2g} and e_g energy levels follows the Pauli exclusion principle and Hund's rule of maximum multiplicity. Accordingly, all orbitals in a degenerate energy level will: (1) be singly occupied before pairing begins and (2) maximize full spin alignment. Electrons fill the lower t_{2g} energy level first, proceeding then to the e_g level. So for an octahedral coordination, Mn^{3+} and Mn^{4+} cations display, respectively, $t_{2g}^3 e_g^1$ and t_{2g}^3 electronic configurations with all spins in parallel. The d^4 electronic configuration of Mn^{3+}, however, can result in either a high spin (i.e., $t_{2g}^3 e_g^1$) or low spin (i.e., $t_{2g}^4 e_g^0$) state. The actual equilibrium state depends on the energy cost (gain) associated with pairing two electrons of opposite spin in the t_{2g} orbital versus promoting one to the e_g orbital.[3] In doped-lanthanide manganites of

---

[3] In general, determination of the equilibrium spin state results from comparing the relative magnitudes of Δ, the crystal field splitting, and P, the mean pairing energy. If $P < \Delta$, then the low spin state occurs and vice versa for the high spin state. The magnetic interactions of double exchange, however, prevent such a naive description from being extended to doped-lanthanide manganites.

e$_g$

z

y

x

d$_{z^2}$

z

y

x

d$_{x^2-y^2}$

t$_{2g}$

z

y

x

d$_{xy}$

z

y

x

d$_{xz}$

z

y

x

d$_{yz}$
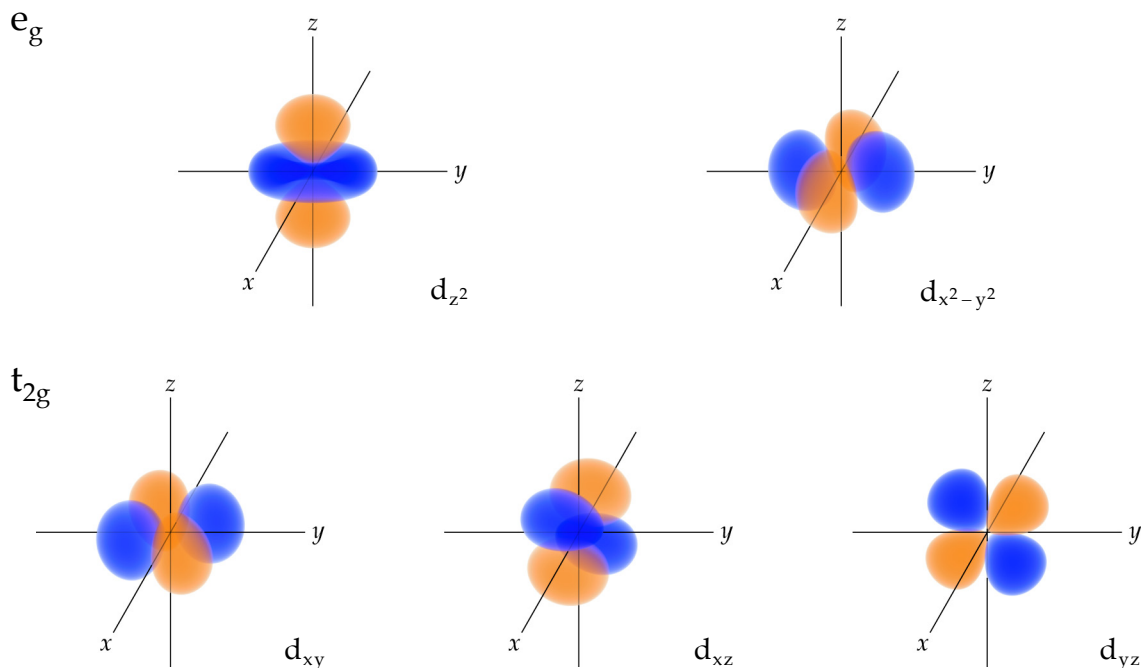
FIGURE B.2 Manganese atomic 3d orbitals grouped according to octahedral site symmetry. Wavefunction amplitudes are distinguished by color (positive for blue, negative for orange).

E

b_{1g} ($d_{x^2-y^2}$)

$\frac{1}{2}\delta_1$

e_g (d_{z^2}, $d_{x^2-y^2}$)

$\frac{1}{2}\delta_1$

a_{1g} (d_{z^2})

$\frac{3}{5}\Delta = 6Dq$

$\Delta = 10Dq$

$\Delta = 10Dq$

(d_{xy}, d_{xz}, d_{yz}, $d_{x^2-y^2}$, d_{z^2})

$\frac{2}{5}\Delta = 4Dq$

b_{2g} (d_{xy})

$\frac{2}{3}\delta_2$

$\frac{1}{3}\delta_2$

t_{2g} (d_{xy}, d_{xz}, d_{yz})

e_g (d_{xz}, d_{yz})

R_3

O_h

D_{4h}
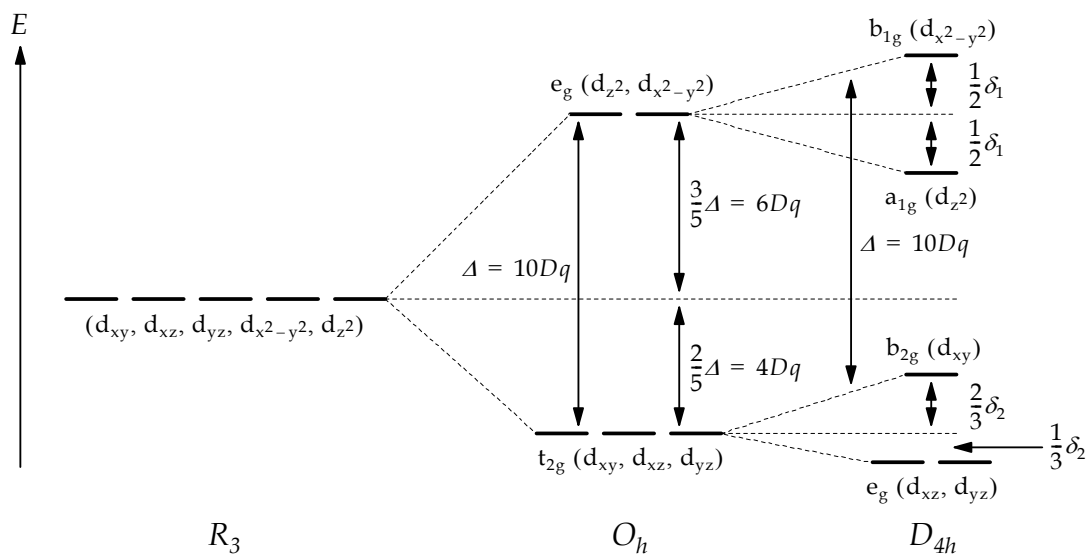
FIGURE B.3 Site symmetry effects on the energy levels of manganese 3d electrons. Stretching of the MnO$_6$ octahedron along its apical axis results in a transition from O_h to D_{4h}.

the compositional range $0.2 < x < 0.4$, the possibility of the low spin state is excluded by empirical determinations of M_S (i.e., when ferromagnetic) and the Curie-Weiss constant (i.e., when paramagnetic) [6]. Regardless of the overall magnetic state (of the material), the manganese cations exhibit the maximum individual spin.

As already discussed in Section 2.2.1, octahedral Mn^{3+} represents a Jahn-Teller ion, which through distortions of its coordination environment, can lower its energy. Indeed, measurements of the $Mn-O$ bond distances in orthorhombic $LaMnO_3$ (i.e., predominately $Mn^{3+}O_6$ octahedra) by Bogush, et al. [7] indicate a preferential stretch along the apical axis. Such a tetragonal distortion corresponds to the loss of C_3 and S_6 symmetry elements as well as a reduction of equatorial C_4 into C_2. This descent in site symmetry, from O_h to its subgroup D_{4h}, causes a split of the t_{2g} and e_g energy levels as indicated in Figure B.3. Correlation of the O_h character table with that of D_{4h} specifies the nature of this transition: (1) two singly degenerate A_{1g} and B_{1g} symmetry species replace the doubly degenerate E_g, and (2) a singly degenerate B_{2g} and doubly degenerate E_g symmetry species replace the triply degenerate T_{2g} species.[4] Accordingly, d_{z^2} transforms as A_{1g} in D_{4h}, $d_{x^2-y^2}$ as B_{1g}, d_{xy} as B_{2g}, and the pair d_{xz} and d_{yz} as E_g. Because of substantial electron density along z, the tetragonal elongation lowers the energy of the d_{z^2}, d_{xz}, and d_{yz} orbitals (i.e., the a_{1g} and e_g sets); the shift of O^{2-} anions away from the manganese site center decreases the Coulombic repulsions. The overall configurational energy, however, is preserved by assuming a matching contraction in the xy plane. This counter-balancing distortion increases the electric field experienced by the $d_{x^2-y^2}$ and d_{xy} orbitals (i.e., the b_{1g} and b_{2g} sets); their energies rise with decreasing O^{2-} anion distance.

The splitting of energy levels in D_{4h} occurs with respect to centers set by the e_g and t_{2g} levels in O_h (i.e., no net change in configurational energy). So b_{1g} and a_{1g} shift, respectively, $+\delta_1/2$ and $-\delta_1/2$ from the e_g level of O_h; b_{2g} and e_g shift, respectively, $+2\delta_2/3$ and $-\delta_2/3$ from the t_{2g} level of O_h. Both δ_1 and δ_2 are small compared to the crystal field splitting, Δ, but the magnitude of δ_1 exceeds that of δ_2 since d_{z^2} and $d_{x^2-y^2}$ point directly at the O^{2-} anions. Note that the equatorial contraction equally affects the energies of the d_{xy} and $d_{x^2-y^2}$ orbitals. Both b_{1g} and b_{2g} rise in parallel with a separation of Δ resulting in

---

[4] For D_{4h} character table, the reader is referred to the reference texts [3–5]. Relationships between point groups and their lower symmetry subgroups are highlighted by correlation diagrams, derived from comparing the character representations of common symmetry classes.

$\delta_1/2 = 2\delta_2/3$. A comparison then of the energy levels given by Figure B.3 illustrates the tendency of $Mn^{3+}O_6$ to form static Jahn-Teller distortions: the $e_g^2 b_{2g}^1 a_{1g}^1$ electronic configuration of D_{4h} is lower in energy than the $t_{2g}^3 e_g^1$ of O_h. For $Mn^{4+}O_6$, no energy benefit results from descending in symmetry to D_{4h} as the $e_g^2 b_{2g}^1$ configuration would remain energetically equivalent to t_{2g}^3. Clearly the occupancy of the split levels, based on the availability of electrons to fill them, can reduce system energy. Such qualitative reasoning, derived from CFT, correlates well with structural observations in doped-lanthanide manganites: raising $[Mn^{4+}]$ shifts the perovskite lattice geometry towards cubic symmetry, the structure observed for optimal magnetoresistive behavior.

The interaction between Mn^{3+} and Mn^{4+} cations, described by Zener's double exchange theory, is contingent on electronic configuration, a product of site symmetry. The increasing presence of $Mn^{4+}O_6$ octahedra mitigates the distortion affiliated with $Mn^{3+}O_6$, decreasing the energy gap between d_{z^2} orbitals on both sites (i.e., the $-\delta_1/2$ splitting between the e_g and a_{1g} levels diminishes so $-\delta_1/2 \to 0$). Because occupation of the d_{z^2} orbital distinguishes the $t_{2g}^3 e_g^1$ state from the t_{2g}^3 state, acceptor-doping with $Mn^{4+}O_6$ then depletes the e_g band of the solid, creating readily-accessible conduction states.[5] The combined process serves to delocalize the e_g electrons through a common influence on the d_{z^2} orbitals, a result crucial to the spin-dependent transport mechanism of double exchange. Among the symmetry-adapted t_{2g} and e_g sets, electrons in the t_{2g} levels are localized due to poor hybridization with the oxygen 2p orbitals. In contrast, the $d_{x^2-y^2}$ and d_{z^2} orbitals of the e_g set point directly into the 2p orbitals of oxygen, overlapping extensively. A strong Hund's interaction between itinerant e_g^1 and localized t_{2g}^3 electrons generates parallel on-site spin-alignment. So magnetic coupling between localized t_{2g}^3 spins on neighboring $Mn^{3+}O_6$ and $Mn^{4+}O_6$ octahedra is mediated via mobile e_g electrons.

Subsequent consideration of Zener's theory of double exchange by ANDERSON and HASEGAWA [9] resulted in the refinement $t_{eff} = b\cos\theta/2$, where b is the transfer integral associated with the resonance hybrid of Equation B.1 and θ is the angle between parallel t_{2g}^3 core spins of neighboring manganese ions. The effective transfer integral then, t_{eff}, is greatest when absolute ferromagnetic alignment occurs (i.e., $\theta = 0$). Any relative spin canting drops

---

[5] Doping in lanthanide manganites shifts the energy of the narrow e_g band such that the Fermi level comes to rest inside, dividing the band into filled and empty states [8].

the magnitude of t_{eff}, lowering the probability of e_g transfer. This theoretical prediction is confirmed, as already discussed in Section 2.2.1, through effects of the actual $Mn-O-Mn$ bond angle: deviations from 180° correspond to increased resistivities and lower Curie temperatures. So the structural impact of $Mn^{4+}O_6$ extends beyond the electronic enhancements presented above; stabilization of an undistorted, cubic symmetry strengthens magnetic interactions between manganese ions resulting in stronger double exchange.

DE GENNES [10] demonstrated that while all the e_g carriers participate in double exchange, only a small fraction of them become involved in the conduction process. For example, X-ray photoelectron spectroscopy (XPS) and ultraviolet photoemission spectroscopy (UPS) of polycrystalline $La_{1-x}Sr_xMnO_3$ indicate a reduced intensity of states at the Fermi level, even in the metallic region (i.e., $0.2 < x < 0.4$) [11]. So the energy gap associated with semiconducting $La_{1-\varepsilon}Mn_{1-\varepsilon}O_3$ (i.e., minor $[Mn^{4+}]$ content) must survive to some extent even if Sr acceptor-doping introduces holes. As a consequence of the interplay between spin order and the small number of mobile charge carriers, the resistivity of doped-lanthanide manganites is readily affected by perturbations of the spin lattice. Near T_C, in the vicinity of the PI to FM transition, T_{IM}, an intermediate spin-disorder state develops, scattering conduction electrons and creating a notable and sharp peak in the resistivity. An applied magnetic field, however, can suppress this spin disorder, causing parallel alignment of the spin lattice, which in turn, enables (or reinforces) the double exchange mechanism. The corresponding suppression of resistivity is therefore proportional to the strength of the magnetic field, forming a basis for *CMR* in doped-lanthanide manganites.

While double exchange highlights the role played by magnetic coupling in spin-dependent transport, the theory and subsequent refinements ignore the possibility electron coupling to lattice vibrations (i.e., polarons). For example, the transport of e_g electrons in an acceptor-doped $Ln_{1-x}M_xMnO_3$ composition (i.e., $0.2 < x < 0.4$) correlates to the mobility of $Mn^{4+}O_6$ holes in a larger $Mn^{3+}O_6$ matrix. Yet the motion of e_g electrons can become dampened if the $t_{2g}^3 e_g^1$ state stabilizes a Jahn-Teller distortion (i.e., the $Mn^{3+}O_6$ octahedra descend in site symmetry to lower configurational energy). So movement of $Mn^{4+}O_6$ holes would require $Mn-O$ bond length changes to $Mn^{3+}O_6$ octahedra along their pathway. Such a traveling deformation field represents a wavestate capable of interacting with lattice phonons.

MILLIS, et al. [12] examined the consequences of double exchange theory in detail: predictions for resistivity are higher by several orders of magnitude than those observed empir-

ically. A strong electron-phonon coupling, resulting from the susceptibility of $Mn^{3+}O_6$ octahedra to form Jahn-Teller distortions, could account for the discrepancy. Specifically, the localization of e_g electrons by slowly fluctuating (i.e., dynamic) Jahn-Teller distortions diminishes substantially at the ferromagnetic onset. In this region, the conduction mechanism switches from thermally-activated hopping to spin-mediated transport. Measurements then of average oxygen root-mean-square displacements near T_C should indicate anomalous behavior. Neutron powder diffraction of $La_{0.65}Ca_{0.35}MnO_3$ by DAI, et al. [13] confirmed small discontinuities in Mn-O bond lengths at the Curie point, providing the first experimental evidence for polaron effects in doped-lanthanide manganites.

In spite of its short-comings though, double exchange still remains at the core of transport theory in manganese perovskites. The focus of current research, however, has advanced to expand Zener's basic considerations of spin-coupling to include complex interactions resulting from structural transitions, orbital degrees of freedom, charge ordering, and electron-phonon coupling (i.e., polarons) [14].

[1] Zener, C. Interaction Between the d-Shells in the Transition Metals. II. Ferromagnetic Compounds of Manganese with Perovskite Structure. *Physical Review* **1951**, *82* (3), 403–405.

[2] Bethe, H. A. Termaufspaltung in Kristallen. *Annalen der Physik* **1929**, *3* (5), 133–208; an English translation, under the title *Splitting of Terms in Crystals*, is available from Books on Demand, a division of University Microfilms, Intl.: Ann Arbor, MI.

[3] Vincent, A. *Molecular Symmetry and Group Theory*, 2nd ed.; John Wiley and Sons: Chichester, U.K., 2001.

[4] Carter, R. L. *Molecular Symmetry and Group Theory*; John Wiley and Sons: New York, 1998.

[5] Cotton, F. A. *Chemical Applications of Group Theory*, 3rd ed.; John Wiley and Sons: New York, 1990.

[6] Liu, J. Z.; Chang, I. C.; Irons, S.; Klavins, P.; Shelton, R. N.; Song, K.; Wasserman, S. R. Giant Magnetoresistance at 300K in Single Crystals of $La_{0.65}(PbCa)_{0.35}MnO_3$. *Applied Physics Letters* **1995**, *66* (23), 3218–3220.

[7] Bogush, A. K.; Pavlov, V. I.; Balyko, L. V. Structural Phase Transitions in the $LaMnO_{3+\lambda}$ System. *Crystal Research and Technology* **1983**, *18* (5), 589–598.

[8] Töpfer, J.; Goodenough, J. B. LaMnO$_{3+\delta}$ Revisited. *Journal of Solid State Chemistry* **1997**, *130* (1), 117–128.

[9] Anderson, P. W.; Hasegawa, H. Considerations on Double Exchange. *Physical Review* **1955**, *100* (1), 675–681.

[10] de Gennes, P.-G. Effects of Double Exchange in Magnetic Crystals. *Physical Review* **1960**, *118* (1), 141–154.

[11] Chainani, A.; Mathew, M.; Sarma, D. D. Electron Spectroscopic Investigation of the Semiconductor-Metal Transition in La$_{1-x}$Sr$_x$MnO$_3$. *Physical Review B* **1993**, *47* (23), 15397–15403.

[12] Millis, A. J.; Littlewood, P. B.; Shraiman, B. I. Double Exchange Alone Does Not Explaing the Resistivity of La$_{1-x}$Sr$_x$MnO$_3$. *Physical Review Letters* **1995**, *74* (25), 5144–5147.

[13] Dai, P.; Zhang, J.; Mook, H. A.; Liou, S.-H.; Dowben, P. A.; Plummer, E. W. Experimental Evidence for the Dynamic Jahn-Teller Effect in La$_{0.65}$Ca$_{0.35}$MnO$_3$. *Physical Review B* **1996**, *54* (6), R3694–R3697.

[14] Salamon, M. B.; Jaime, M. The Physics of Manganites: Structure and Transport. *Reviews of Modern Physics* **2001**, *73* (3), 583–628; see also references therein.

Appendix C

Schlenk Manifold System

Precursors and solutia employed in alkoxy-based sol-gel processing of manganite thin films require strictly anaerobic conditions. Techniques for manipulating such materials were pioneered by Wilhelm Schlenk, resulting in the development of specialized glassware whose internal atmospheres can be evacuated and then flushed with inert gas via an integrated valve [1]. Exposure to vacuum or inert gas, however, is regulated through a glass apparatus comprised of three integral parts: (1) a multi-ported, double-banked manifold, (2) a cryogenic trap connected to a vacuum pump, and (3) an inert-gas delivery system with purification. This appendix describes the design, assembly, and operation of a Schlenk manifold system capable of supplying argon gas with contamination levels less than 20 parts per billion (oxygen and moisture) and a vacuum below 10^{-4} torr. The complete unit is pictured below (Figure C.1), secured to an aluminum-bar scaffold within a safety hood. Detailed pictures (including schematics) of all individual components are provided at the end of this appendix along with an accompanying bill-of-materials.

FIGURE C.1   Fully-assembled Schlenk manifold system.

The glassware comprising this manifold relies exclusively on the Ace-Thred® connector system developed by Ace Glass, Inc. Accordingly, all compression seals utilize FETFE® O-rings, a component standard to the Ace-Thred® joint. Substitution of more chemically resistant Aegis® O-rings, however, occurred at both ends of the tubing segments due their close proximity to aggressive solvents and vapors. Before assembly, individual glass pieces were cleaned and baked according to procedures outlined in Chapter 3, Section 3.2. Seal longevity was enhanced by thoroughly, *but very lightly*, coating FETFE® O-rings with Apiezon N high-vacuum grease. Such treatment, though, is both unnecessary and inconvenient for frequently disassembled joints: O-rings incorporated in the collector flasks and tubing connectors, therefore, remained grease-free.

Design of this Schlenk manifold focused on a flexible arrangement that allows the approach of vacuum or inert-gas sources from either side (see Figure C.6). In addition, horizontal symmetry permits the banks, top or bottom, to contain vacuum or argon gas depending on user preference.[1] Associated with each of the five ports is a pair of greaseless, high-vacuum, tetrafluoroethylene (TFE) valves, one emerging from each of the two banks (see Figure C.9). Their vertical alignment enables the valve state, be it open or shut, to remain clearly visible. The greaseless nature of the TFE stem avoids progressive seal deterioration, a problem common to manifolds constructed from all-glass, but greased, stopcocks.[2] The port itself, centrally located in the valve assembly, is deliberately recessed, thereby protected from accidental "knocks". To allow evacuation of the inert-gas bank (i.e., in case of vapor contamination), a crossover valve was integrated into the bank structure at the rightmost-side.

Threaded glass connectors (female) terminate both the bank and port ends. For all syntheses in this dissertation, the manifold operated with an inert-gas (argon) delivery system coupled to the bottom bank at the left side. The cryogenic trap assembly, on the other hand, attached to the top bank at the right.[3] Mating the argon delivery system to its glass bank required a special Swagelok-adapted, Ace-Thred® fitting (see page 256 for details). But a standard Ace-Thred® bushing sufficed for the cryogenic trap assembly. Slight misalignments between the manifold and trap assembly, however, proved inevitable despite consid-

---

[1] A lone, central top-port serves as a connection for the vacuum gauge. The expected bottom counterpart was deemed unnecessary by the author. So the pictured apparatus presumes a vacuum bank at the top.

[2] Repeated "purge and evacuate" cycles expose stopcocks to solvent vapors during cycling, which in turn, penetrate and dissolve the grease.

[3] The remaining bank ends were left unused and plugged with the appropriate Ace-Thred® fittings.
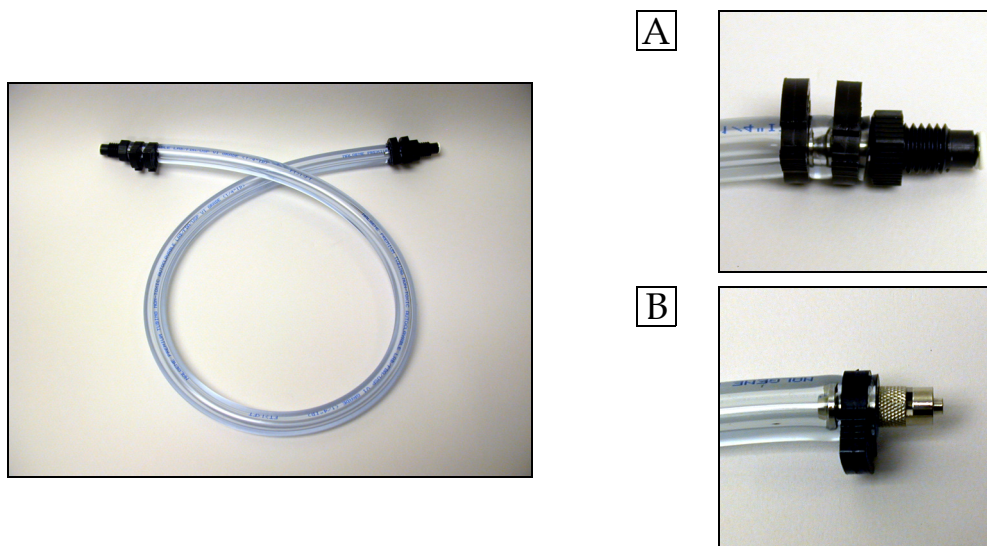
FIGURE C.2 Transparent, flexible vacuum tubing for the Schlenk manifold system . The terminal end varies depending on whether a connection is made to another threaded glass port (A) or a syringe needle via Luer lock (B).

erable efforts to the contrary. So a unique intermediate glass piece with central stainless steel bellows was designed (see Figure C.12). The flexibility of the bellows was able to accommodate misalignment while preserving parallelism. Without this parallelism, compression seals within the Ace-Thred® joints were inadequate, allowing measurable leakage. The S-shape of the piece resulted from an adaptation to the unavoidably short manifold-to-trap distance within the safety hood.

Connection of the Schlenk manifold to reaction glassware occurred through clear, flexible, 33"-long vacuum tubing as depicted above (Figure C.2). Transparent tubing provided a simple, but highly-effective means to monitor condensation of solvent vapors in the interior. Run-off of contaminated liquid back into the reaction vessel would assuredly ruin any ongoing synthesis. To establish a connection, one end of the tubing segment is attached to the manifold port, the other to either: (1) a threaded glass port on the reaction apparatus, or (2) a syringe needle through a standard Luer lock joint. To maximize the manifold's capability, five tubing segments were fabricated with port-to-port ends and two with port-to-Luer ends. Experience demonstrated that gas-tight seals could easily be achieved when disposable, plastic syringe needles were tightly twisted onto the male Luer adapter. The same observation could not be made for all-metal syringe needles, which required Apiezon N high-vacuum
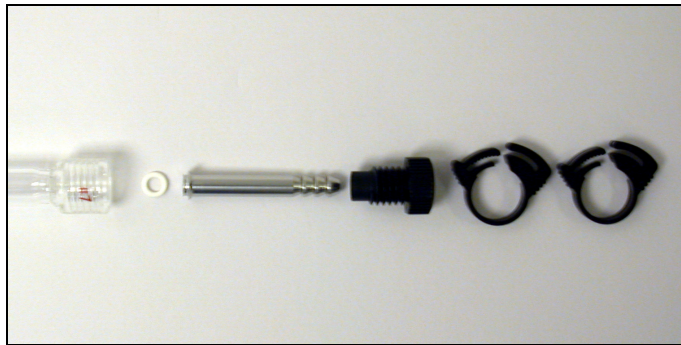
FIGURE C.3 Exploded view of tubing connector joint.

grease. Because of this inconvenience, only disposable, plastic syringe needles were used for syntheses in this dissertation.

Attaching vacuum tubing to threaded glass ports requires a cylindrical tubing connector, as illustrated in Figure C.3. But performance of the standard "Ace-Safe" tubing connector proved unsatisfactory: the geometry of the O-ring seat failed to provide a gas-tight seal. So an improved tubing connector was designed using corrosion-resistant stainless steel 316L (see Figure C.11). In addition, Ace-Thred® fittings of nylon were selected for these new tubing connectors due to greater rigidity.[4] The ribbed ends of the tubing connectors, inserted into the tube interior, formed a friction seal. To ensure a gas-tight fit though, two nylon band clamps were wrapped at each end around the tubing exterior, spaced approximately one centimeter apart along the ribbed end. (Note that the short, ribbed ends of the Luer adapters cannot accommodate two band clamps. The use of one clamp, however, was not observed to detrimentally affect the overall seal.) Whenever not in use, a tubing segment was disconnected from its manifold port, which in turn, was stoppered with an Ace-Thred® plug. This practice prevented two undesirable situations: (1) dangling ends from smashing into the counter top, and (2) dust accumulation in the TFE valve seat. As already stated, the Aegis® O-rings situated in the tubing connectors remained grease-free. If coated, the close proximity of the O-rings to aggressive solvents and vapors would create a contamination hazard for on-going syntheses. Luer-lock joints were also assembled without grease since the disposable, plastic syringe tips, when twisted snugly, formed a leak-free seal.

---

[4] The standard Ace-Thred® fitting material for this Schlenk manifold system is polytetrafluoroethylene (PTFE), selected because of its excellent chemical resistance. Unfortunately, PTFE exhibits creep behavior so frequent assembly and disassembly of tubing compression seals results in rapid degradation of joint performance.
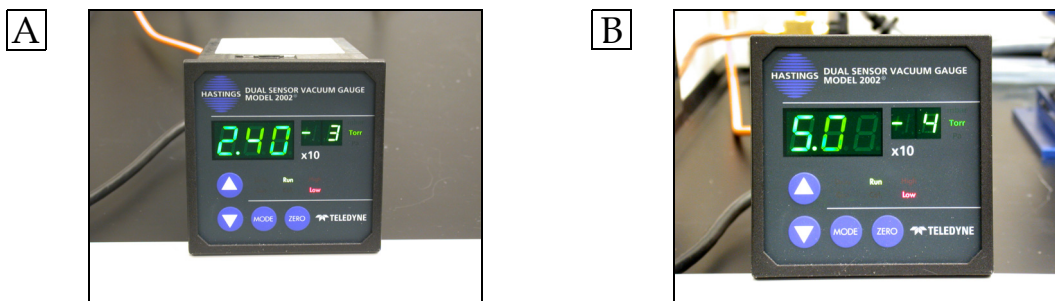
FIGURE C.4 Measurement of manifold vacuum. Cryogenic traps at ambient temperature (A) and submerged in liquid nitrogen (B).[5]

Design of the vacuum system centered around a modular cryogenic trap assembly and a standard rotary-vane mechanical pump. The presence of cryogenic traps improves the ultimate vacuum achievable in the system by condensing and freezing residual gas molecules. Figure C.4 compares the vacuum level attained when the traps are inactive (A) versus that when active (B).[5] An active cryogenic trap provides two benefits: (1) the mechanical pump is protected from aggressive solvent vapors that corrode interior seals and attack the lubricating oil, and (2) the system itself is shielded from volatile material, dissolved in the oil, that might return upstream. To ensure effective evacuation and flush cycles, measurement of the vacuum should occur dynamically, otherwise inadequate seals in the reaction glassware may go unnoticed. To this end, the vacuum bank (top) incorporates a Hastings Instruments model 2002 vacuum gauge, attached through a central, threaded glass port.[6] A special Ace-Thred® adapter with an internal ⅛″ national pipe thread (NPT) through-hole serves as the metal-to-glass coupler, providing an air-tight seal.[7]

The modular design of the cryogenic trap assembly (see Figure C.14) allows establishment of an in-line, multi-trap configuration. For the purposes of this dissertation, the Schlenk manifold system operated with two trap assemblies; the presence of the second trap relieved potential overflows from the first, protecting the otherwise vulnerable mechanical pump. Correct orientation of the assembly, however, requires that the female threaded con-

---

[5] The digital readout does not display values below 5.0×10^{-4} torr even though the vacuum is still improving. The ultimate vacuum level, with cryogenic traps in operation, is suspected to be below 1×10^{-4} torr.

[6] This gauge can read pressure (i.e., vacuum) in the range from 10^3 to 10^{-4} torr.

[7] Threads on the vacuum gauge base (⅛″ NPT male) were *lightly-coated* with Apiezon N high-vacuum grease.

nector (left side in Figure C.14) serve as the inlet. Reversal risks reduced throughput and eventual clogging [2]. To assemble the trap, the mouth of the collection flask should be slid upward along glass collar and secured by twisting *tight* the associated Ace-Thred® bushing.[8] Proper positioning of the collection flask leaves the central glass tube approximately 1–1½″ above the flask interior. A collection flask in the trap assembly can, if full, be isolated by closing both lower valves, removing that cryogenic segment from the vacuum path. As a result, the collection flask is free for replacement with a clean, dry unit. In addition, opening the top bypass valve enables the continued operation of the vacuum bank, despite the partitioning off of the collection flask.[9] In theory, both flasks can be replaced simultaneously. In practice, however, such a procedure was only attempted if the vacuum bank itself could be isolated (i.e., was not in service). Removal of both cryogenic segments from the vacuum path (while in service) guarantees that contaminating vapors will reach the pump oil, a highly-undesirable situation.

In order to generate the required vacuum levels, a 1402 Welch Duoseal® rotary-vane mechanical pump was connected to the cryogenic trap assembly via an L-shaped glass adapter (see Figure C.16) and standard heavy-wall, gum-rubber tubing (1½″ outside diameter, ¾″ inside diameter). Its fast pumping capacity (160 L/min) provided quick evacuation and flush cycles, an important convenience for any synthesis involving air-sensitive manipulations. While elastic, the gum-rubber tubing proved difficult to slide over either glass adapter or pump inlet due to excessive friction. Application of Apiezon N high-vacuum grease to both ends of the tubing interior alleviated this problem; a pair of stainless steel band clamps (four total) ensured a gas-tight seal. The actual physical connection between the glass adapter and pump inlet occurred through a hole in the countertop of the safety hood. Exhaust from the mechanical pump was also routed back through this hole to ensure proper ventilation; gas streams leaving reaction glassware during evacuation often contain toxic chemical vapors, a health hazard for the user.

To enhance longevity, the mechanical pump was left running continuously. But routine maintenance included changing the pump oil when the equilibrium vacuum level (without

---

[8] If the compression seal is not tight, the collection flasks will slide up the collar as the pump evacuates the interior. To prevent this behavior, the O-rings and glass surfaces must be *dry* and *grease-free*. Also, the Ace-Thred® bushings, while tight, should not be over-torqued. Otherwise, the glass may shatter during assembly.

[9] During normal operation all overhead bypass valves remain closed.

cryogenic trap operation) deteriorated to 1 x 10^{-2} torr. Such a reduction in pump perfor-mance indicated unacceptable levels of dissolved solvent molecules out-gassing from the oil. Disconnecting the mechanical pump for maintenance first required that the vacuum system reach atmospheric pressure. This task was easily accomplished by turning off the pump and temporarily opening the crossover valve on the manifold, allowing the vacuum system to flood with argon.[10] The mechanical pump could then be isolated (and subsequently removed) by closing the last lower valve of the cryogenic trap assembly.

Replacement of the pump oil occurred through a two-step process: (1) draining the used, warm oil into an appropriately-sized pan,[11] and (2) introducing fresh oil through the exhaust port of the pump via a small funnel. When necessary, a full-face respirator was worn during draining to prevent exposure to detrimental vapors. To ensure that contaminants were flushed out of the system, the overall process was repeated.[12] HyVac® vacuum pump oil, an ultra-low vapor pressure paraffin oil, proved to be a satisfactory lubricant. All of the used oil was collected and stored in large polypropylene jerry cans, disposed of later according to local environmental health and safety regulations. After oil replacement, the pump was left running for at least 12 hours, allowing the mechanical system to equilibrate thermally. Dur-ing this time frame, the vacuum level improves noticeably and eventually stabilizes.

Proper operation of the cryogenic trap assembly requires *complete evacuation of the vac-uum system by the mechanical pump before submerging the collection flasks in liquid nitrogen*. For example, nitrogen gas liquefies at 77.37 K and freezes at 64.32 K. But oxygen and argon gas liquefy at 90.21 K and 87.48 K, respectively, and freeze at 55.09 K and 83.98 K. So failure to pre-evacuate the vacuum system risks condensing oxygen or solidifying argon within the collection flasks. Any subsequent vaporization upon warming would then pressurize the entire assembly, creating an explosion hazard. The contents of the collection flasks can safely be monitored, however, because of a vertical sequence of viewports along the dewar walls. During operation, these dewars are filled with liquid nitrogen to within 1" of the top, insu-lated by TFE caps (see Figure C.17). The transparency of liquid nitrogen allows a clear view of any condensed material in the collection flasks, alerting the user to potential danger.

---

[10]The cryogenic traps *must not* be submerged in liquid nitrogen during this procedure. The crossover valve should be closed when the Hastings Instruments model 2002 vacuum gauge reaches 760 torr, *and not more*.
[11]The lower viscosity of warm oil enables a more effective and complete drainage.
[12]The mechanical pump was allowed to operate for 15–20 minutes after the first addition. The resulting agita-tion aided the dissolution and removal of any remaining used oil.

The removal and replacement of a full collection flask starts with a simple two-step process: (1) isolation of that cryogenic segment followed by (2) withdrawal of the liquid nitrogen bath. After a short period (i.e., usually 2–3 minutes), the contents of flask will melt and volatilize, partially pressurizing the isolated chamber. This internal pressure, however, remains insufficient to balance external atmospheric pressure, making removal of the flask difficult. To alleviate this situation, argon from the inert-gas bank can be bled into the warming collection flask until the pressure differential is minimal. But before doing so, any reaction apparatus connected to *either the vacuum or inert-gas bank* must be isolated by closing all appropriate manifold valves.[13] Only then should the mechanical pump (still running) be disengaged from the vacuum system by closing the last valve in the vacuum pathway.[14] Accordingly, any active cryogenic segment, if present, is withdrawn from service by closing both lower valves, and if necessary for continuity, opening the top bypass valve. Failure to follow this precaution results in an argon bleed stream that condenses and solidifies in the cryogenic segment. Finally, by temporarily opening the crossover valve on the manifold, argon gas can pressurize the target collection flask, enabling its removal.

A clean, dry glass piece should serve as the replacement collection flask. And if necessary, the remaining FETFE® O-ring should be exchanged with fresh one if overly deformed. (FETFE® and Aegis® O-rings suffering from deformation or reduced elasticity can easily be regenerated by baking in a drying oven at 110 °C for approximately 10 minutes.) After replacement, the mechanical pump is re-engaged with the system, but the isolated cryogenic traps should remain partitioned off until the vacuum level stabilizes. The full pathway can then be returned to service by opening all lower valves and closing the top bypass valves. Finally, the new collection flask is submerged in liquid nitrogen by raising its corresponding dewar. The entire process, while cumbersome in description, can be completed quite efficiently in practice.[15]

---

[13]Flooding the vacuum system with argon creates a brief, but sharp, pressure drop in the inert-gas bank. This decrease in pressure can suck fluids and particulate matter from any connected reaction apparatus directly into the manifold, requiring disassembly and extensive cleaning.

[14]Because of the potential for contaminating leaks, evacuated reaction apparatus should be flooded with argon when isolated from the vacuum bank. Of course, the state or contents of the glassware must be compatible with an inert-gas overpressure.

[15]The author acknowledges a minor oversight in the design of the cryogenic trap assembly. The need to pressurize the collection flask could be avoided entirely by the presence of a high-vacuum venting valve on the "bulb" of the assembly. The author recommends the Chemglass CG-590 Inlet Valve, Chem-Cap®, High Vacuum, pointing towards the user but angled upward at 45°.

Lastly, good operating procedures dictate that the cryogenic trap assembly, when removed from service for long periods (i.e., more than a week), be stored under a slight positive argon pressure. If the mechanical pump is simply turned off, atmospheric gases will diffuse past the O-ring compression seals, driven by the negative pressure differential. Of particular concern is water vapor which chemisorbs onto the interior borosilicate surface. Subsequent evacuation will require some time to restore previous vacuum levels, during which, water molecules slowly but continuously leave the glass surface. To properly shut down the vacuum system then, power to the pump should be turned off and the crossover valve on the manifold opened.[16] Argon flow from the inert-gas bank will pressurize vacuum system reaching two important levels: (1) at 760 torr, the last valve in the vacuum pathway should be closed to isolate the mechanical pump from the vacuum system, and (2) at approximately 850 torr, the crossover valve should be closed. For safety purposes, pressure in the cryogenic assembly should not exceed 850 torr.

The extreme oxygen and moisture sensitivity of manganese(II) silylamide (and subsequent alkoxides) governed the design of this inert gas delivery system. Nitrogen, the most common "inert" source for Schlenk manifold systems, brings two unfortunate disadvantages: (1) many elemental metals react with nitrogen at room temperature, forming stable, protective nitride scales and (2) the density of nitrogen, closely matching that of air, provides a poor diffusive barrier to gaseous contaminants such oxygen and water vapor. In contrast, the chemically-inert nature of argon provides a true non-reactive atmosphere. Its heavier-than-air density allows argon to blanket reaction flask contents should the glassware be momentarily opened. This behavior offers a critical advantage for air-sensitive manipulations. All synthetic procedures detailed in Chapter 3 rely extensively on the removal and exchange of components secured in reaction vessel necks. During the process, an inevitable exposure to air occurs, negated by the presence of outward-flowing argon.[17]

Commercial cylinders of argon gas are readily available in ultra-high purity grade at an economical cost.[18] But to guarantee contamination levels compatible with the synthesis of

---

[16]Once again, the cryogenic traps *must not* be submerged in liquid nitrogen during this procedure.

[17]The reaction apparatus remains continuously under a slight positive argon pressure, maintained by its connection to the inert-gas bank. This precaution ensures only outward flows thereby preventing contamination caused by possible inward-directed air currents.

[18]The total sum of N_2, O_2, CO, CO_2, and hydrocarbon contamination (CH_4 and H_2O) for ultra high purity argon numbers less than 10 parts per million.

manganese(II) silylamide (and corresponding alkoxides), a Matheson model 6427 oxygen and moisture trap was incorporated into the delivery pathway. Its one-piece aluminum canister houses a highly-active, alumina-supported copper oxide catalyst that ensures contamination below 20 parts per billion — provided the combined pressure and flow rate remains below 100 psig and 56.6 slpm.[19] An insertion point for the unit, along with a schematic of the entire inert gas delivery system, is given in Figure C.5 (all numbers correspond to components listed sequentially in the bill-of-materials). To preserve the integrity of the catalyst, the metal plugs at both ends were removed and two instrument ball valves attached via port connectors, *all inside an argon glove box*.[20] Then, with the valves closed, the entire assembly could be returned to atmosphere without saturating (and ruining) the catalytic bed.

Control of inert gas pressure within the delivery system requires a regulator that can: (1) preserve ultra-high purity streams during operation, (2) keep the outlet pressure isolated from a continuously dropping inlet pressure, and (3) adjust and maintain low 3–5 psig pressures. To meet these needs, a Concoa 212 series regulator with, respectively, stainless steel diaphragms, dual-stage construction, and 0–30 psi output served as the pressure control unit. In addition, a Swagelok® QF series quick-connect coupling was mated, on one side, to the regulator's exhaust port, and on the other, to an instrument ball valve. This configuration enabled the convenient exchange of argon cylinders while preventing upstream contamination of the delivery line (see discussion later). To monitor the argon stream during operation, an Omega FMA 1600 series digital mass flow meter with temperature and pressure compensation was placed in the delivery line before the oxygen and moisture trap. Its presence served two purposes: (1) to ensure the gas flow rate never exceeded the limits of the catalytic bed and (2) to monitor the seals of connected and pressurized reaction apparatus.[21]

Leak-free tube joints for the inert gas delivery line relied exclusively on fittings from the Swagelok Company. These components depend on a ferrule-based, metal-to-metal compression seal (i.e., the Swagelok® system), the underlying principle of which is discussed in pro-

---

[19]During service, the inert-gas bank operates at a pressure of 3–5 psig. Exhausting directly to atmosphere never results in a flow rate greater than 3 slpm.

[20]The port alignment given in Figure C.5 for these valves *must be maintained during assembly*.

[21]The importance of this second capability should not be ignored. Often, during the exchange of reaction neck contents, an O-ring will fail to seat properly, creating a leak point invisible to the eye. When pressurized, a small, but steady, positive mass flow appears on the meter. If otherwise unnoticed, any subsequent evacuation would draw air into the apparatus, contaminating the contents.

Inert-gas bank via Ace-Thred® fitting.
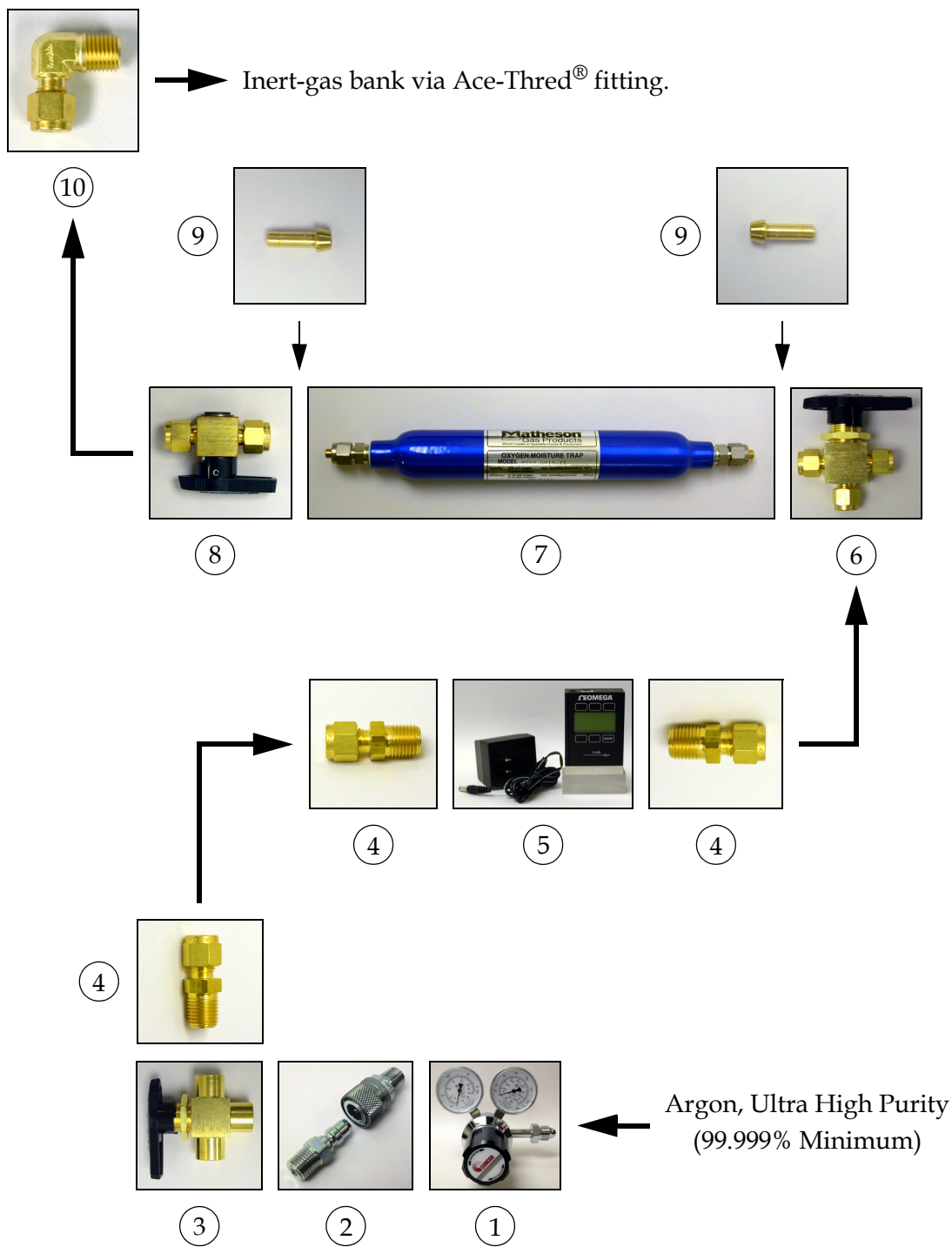
FIGURE C.5 Schematic of the argon delivery system. Numbers   given   on the diagram correspond to components listed sequentially in the bill-of-materials. Thick black lines (long) represent lengths of copper tubing.

Argon, Ultra High Purity
(99.999% Minimum)

motional literature and will not be presented here. However, assembly meticulously followed guidelines given therein with each individual joint being verified by a gap inspection gauge. All metal-to-metal seals, whether Swagelok® or NPT, remained grease-free. Male threads in the NPT joints, though, were wrapped three times with ½″ wide, 0.003″ thick PTFE tape before insertion.[22] This additional step aids the final seal so long as: (1) the first two starting threads at the tip are skipped and (2) the wrap direction spirals toward the base. Standard ¼″ diameter oxygen-free, high-conductivity (OFHC) copper tubing with 0.065″ thick walls comprised the delivery line, connecting the argon source to the inert gas bank. As stated on page 246, a special Swagelok-adapted fitting served to couple the L-shaped, male brass NPT connector to the female glass Ace-Thred® socket on the inert gas bank. This fitting comes fabricated from PTFE, containing interior, precisely-machined female NPT threading. Because of the resulting metal-to-PTFE seal, inclusion of PTFE tape along the threads is uneffective. Instead, the male brass connector was *lightly coated* with Apiezon N high-vacuum grease to ensure leak-free performance.

The entire configuration illustrated in Figure C.5 could be safely assembled in air provided the instrument ball valves protecting the oxygen and moisture trap remained closed.[23] To purge the delivery system after assembly, the first 3-port valve (i.e., attached to the QF series quick-connect coupling) was turned such that flow would be directed into the delivery line. The second 3-port valve (i.e., guarding the entry point to the oxygen and moisture trap) was turned such that flow would exit to atmosphere. Opening the main valve on the argon cylinder flooded the line, displacing air out of the system. At this point the regulator was adjusted for 3–5 psig of operating pressure and the flow allowed to continue for approximately 30 seconds. *With argon still exiting to atmosphere*, the second 3-port valve was then turned to direct flow into the oxygen and moisture trap, pressurizing the canister. As a last step, the crossover valve on the manifold was opened, allowing the mechanical pump to evacuate the inert-gas bank and all space back to the 2-port valve (still closed).[24] When the vacuum stabilized, the crossover valve was closed and the 2-port valve opened, flooding the bank with argon.

---

[22]The CGA-580 connector on the Concoa 212 series regulator also used PTFE tape to ensure a leak-free seal.
[23]Again, the port alignment given in Figure C.5 for all valves *must be maintained during assembly*.
[24]The vacuum system is presumed to be operational although setup of the cryogenic traps is not necessary.

The quality of seals in the inert gas delivery system was verified using the following procedure: (1) the valve on the argon cylinder was closed and (2) the crossover valve on the manifold was opened, evacuating the entire line back to the tank valve. The resulting vacuum level matched that of the isolated vacuum system itself (i.e., 2.4 x 10^{-3} torr with new pump oil). Shutting the crossover valve and then opening the cylinder valve repressurized the delivery system, returning the line and inert gas bank back to service. This procedure was routinely employed to remove solvent vapor contamination from the inert gas bank.[25]

The procedure to exchange argon cylinders is equally straight-forward: the valve on the tank should be closed and the first 3-port valve turned so that space within the Concoa 212 series regulator and QF series quick-connect coupling vents to atmosphere. The argon cylinder (with the regulator still attached) can then be removed from the delivery line. *To avoid bursting the seal, the QF series quick-connect coupling should never be separated while under pressure.* After transferring the regulator to the new argon cylinder, the quick-connect coupling is rejoined, bringing the replacement into service. Opening the tank valve then flushes the regulator-coupling space with argon, displacing air from that segment. When approximately 30 seconds have elapsed, the 3-port valve should be turned *while still purging* so the flow is redirected back into the delivery line. The regulator is then adjusted (if necessary) to ensure the original low-pressure setting still remains.

When use of the inert gas delivery system is not required for long periods (i.e., more than a week), the cylinder valve should be closed and the regulator partially depressurized by momentarily opening the first 3-port valve to atmosphere.[26] This practice lowers the risk of diaphragm failure due to fatigue and prolongs the lifetime of the regulator. In addition, the instrument ball valves attached to the oxygen and moisture trap should be closed. Diffusive leaks past the many elastomeric and TFE compression seals in the manifold can be problematic over extended periods of time. Also, unforeseen or undesired circumstances (i.e., tampering, negligence, forgetting the system state, etc.) may result in contamination of the delivery line or inert gas bank. But if the catalytic bed was isolated, the delivery system can

---

[25]In addition to inert gases, the Matheson model 6427 trap can purify gas streams of many organics including alkanes, alkenes, aliphatic hydrocarbons, low boiling aromatics, carbon dioxide, and carbon monoxide. The catalytic bed will therefore not be deactivated by vapors from solvents used for this dissertation.

[26]The cylinder pressure gauge should indicate the lowest possible value (i.e., the needle rests on its support). But the regulator-coupling space should maintain at the 3–5 psig pressure of the delivery system.

be quickly returned to service by flushing with argon and evacuating.[27] Otherwise, the oxygen and moisture trap may require replacement, a tedious and expensive task.

As a final note, delivery lines for Schlenk manifold systems often contain a mercury (or liquid) bubbler that serves as an emergency one-way pressure relief valve [3]. Typical placement occurs immediately before the inert gas bank. Due to space restrictions in the safety hood though, the configuration of this inert gas delivery system employed an alternative arrangement: an in-line bubbler (see Figure D.2 in Appendix D) was always included with any reaction apparatus. This bubbler contained two pathways: (1) a direct route that allowed argon to reach its destination unabated and (2) a bypass that vented overpressures to atmosphere. A greaseless, high-vacuum TFE metering valve controlled the exhaust rate, and if necessary, could be closed to permit the tubing segment or reaction vessel to be evacuated.[28] Because of toxicity, the use of mercury was eschewed. Instead, 3 mL of 200 centipoise silicon oil was injected into the bubbler reservoir via syringe. Further details on the in-line bubbler can be found in the discussion and figures of Chapter 3.

[1] Tidwell, T. T. Wilhelm Schlenk: The Man Behind the Flask. *Angewandte Chemie International Edition* **2001**, *40* (2), 331–337; see also references therein.

[2] Coyne, G. S. *The Laboratory Companion: A Practical Guide to Materials, Equipment, and Technique;* John Wiley and Sons: New York, 1997; p. 391–393.

[3] Shriver, D. F.; Drezdzon, M. A. *The Manipulation of Air-Sensitive Compounds*, 2nd ed.; John Wiley and Sons: New York, 1986; p. 9–11.

---

[27]The author always flushed and evacuated the delivery system before synthesis to eliminate possible contamination, regardless of the time from service.

[28]Closing the metering valve prevents fluid from being drawn out of the reservoir past the check valve.
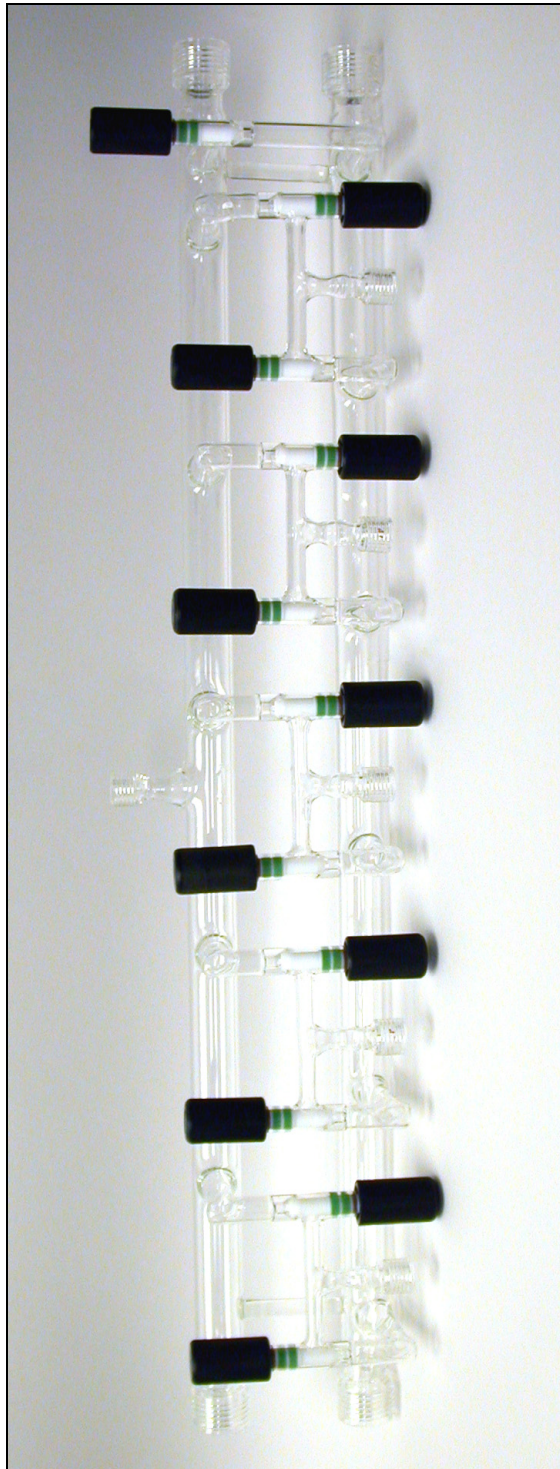
FIGURE C.6 Multi-ported, double-bank manifold.

① Ace Glass 5027-05   Connectors, Threaded, Ace-Thred, Glass, 7 mm Size

② Ace Glass 7644-18   Connectors, Threaded, Ace-Thred, Glass, 18 mm Size

③ Chemglass CGB-601-01   Valve, One Piece Plug, Chem-Cap, One Arm, 0–4 mm Bore

④ Chemglass CG-702-05L   KIMAX Medium Wall Borosilicate Tubing, 1 inch (25.4 mm) O. D.

FIGURE C.7   Schematic of multi-ported, double-bank manifold (front).

Cross Section B-B

Cross Section A-A

FIGURE C.8 Schematic of multi-ported, double-bank manifold (cross section).

261

FIGURE C.9 Front and angled view of manifold valve assembly.
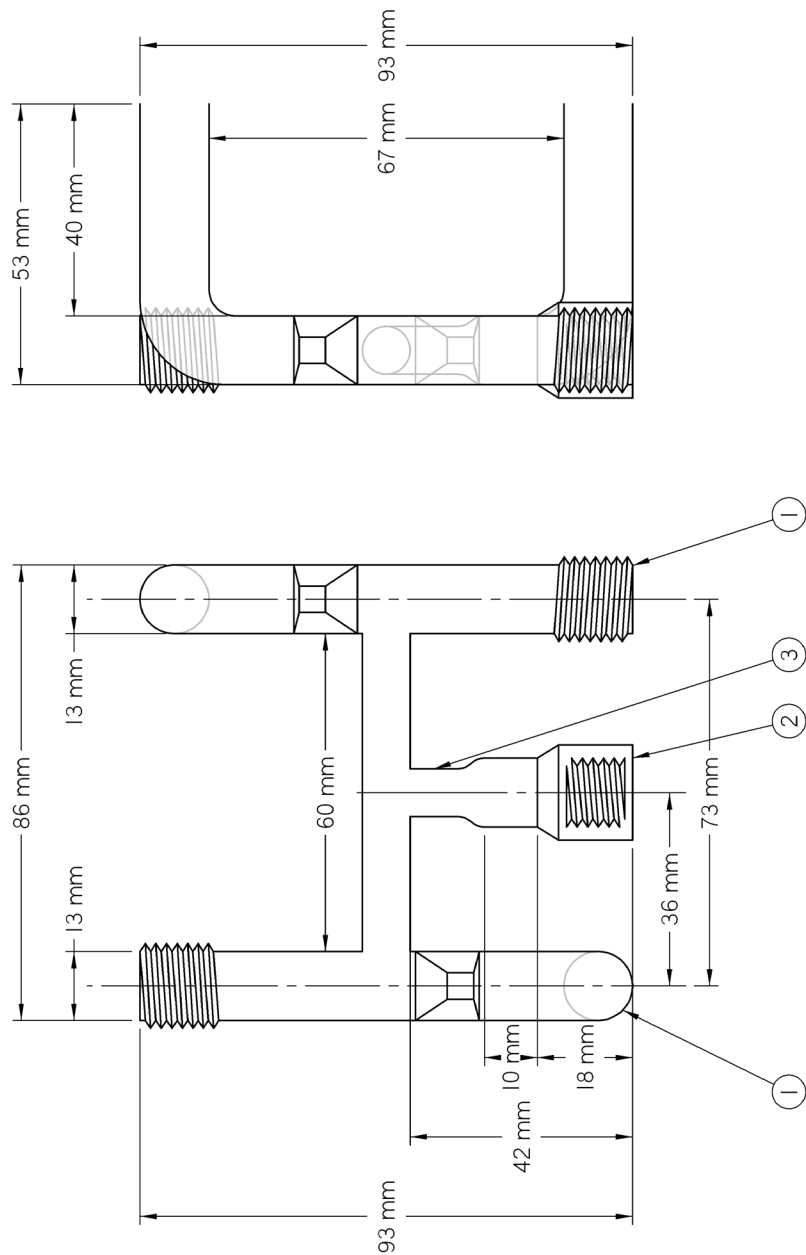
① Chemglass CGB-60I-0I   Valve, One Piece Plug, Chem-Cap, One Arm, 0-4 mm Bore

② Ace Glass 5027-05   Connectors, Threaded, Ace-Thred, Glass, 7 mm Size

③ Chemglass CG-706-03L   KIMAX Special Wall Borosilicate Tubing, 9 mm O. D.

FIGURE C.10   Schematic of manifold valve assembly.

FIGURE C.11 Schematic of stainless steel 316L tubing connector.
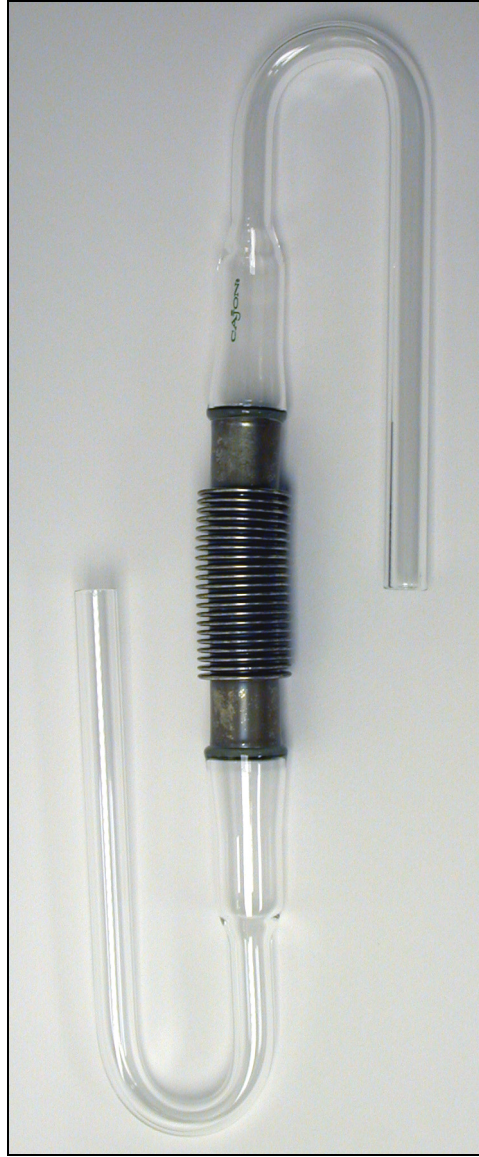
FIGURE C.12 Flexible glass-ended connector.

394 mm

167 mm

63 mm

70 mm
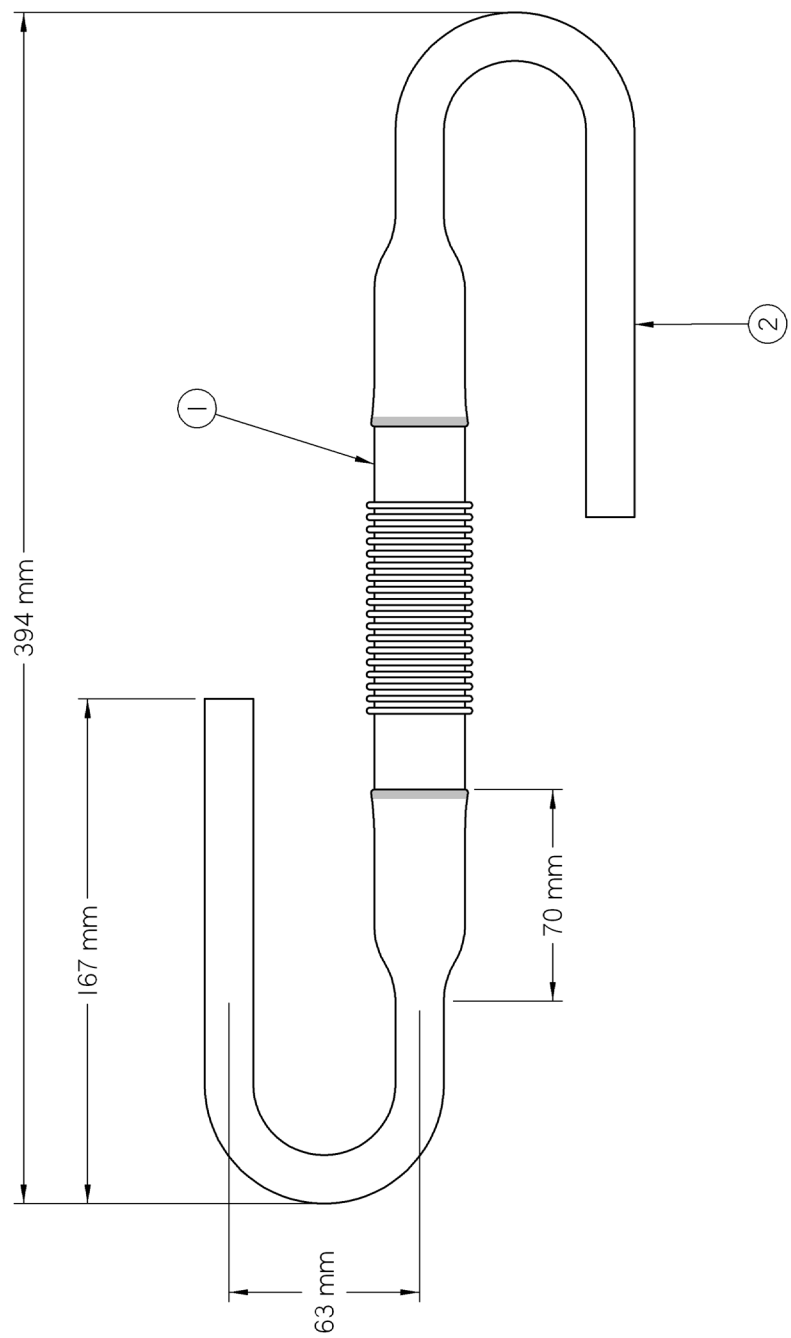
① Swagelok G32I-I6-GXG-3   Flexible Glass-End Tubing, 25 mm Glass O.D.

② Chemglass CG-702-03L   KIMAX Medium Wall Borosilicate Tubing, 5/8 inch (I5.9 mm) O. D.

①
②

FIGURE C.13 Schematic of flexible glass-ended connector.

266
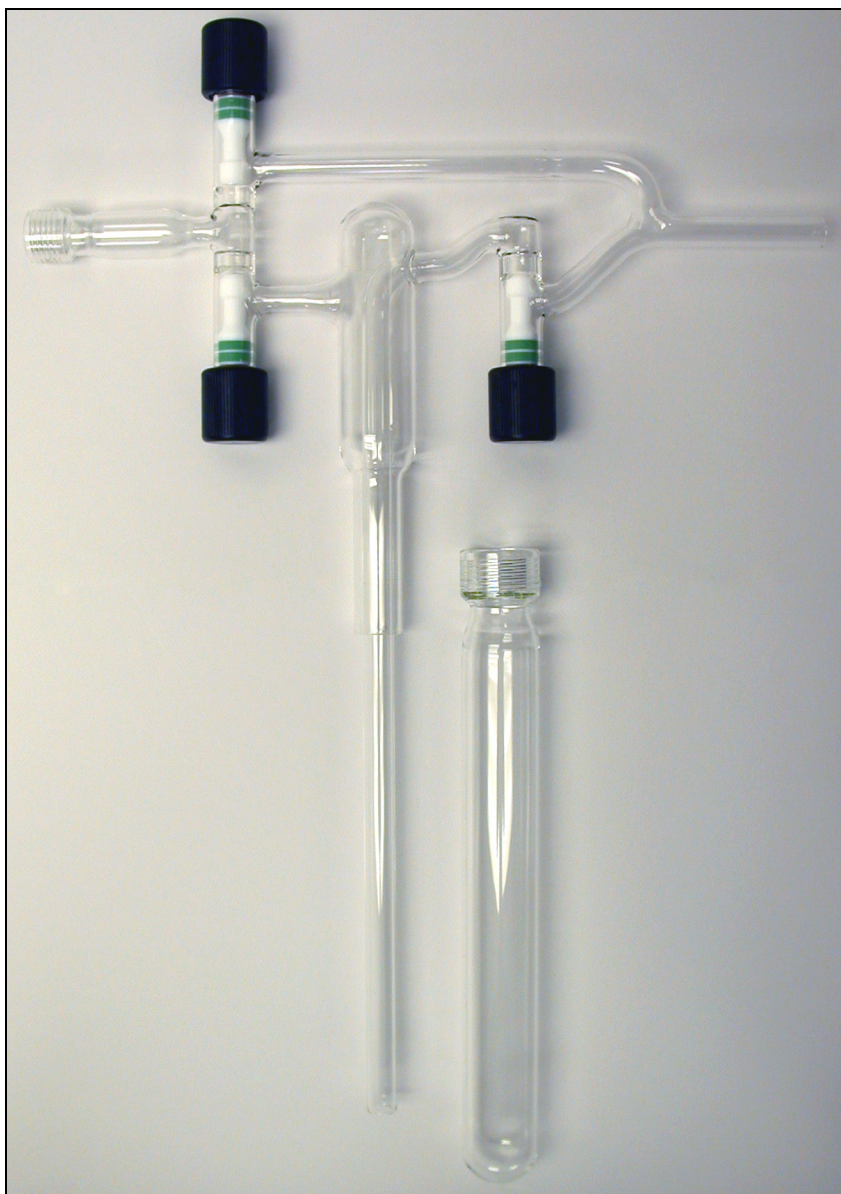
FIGURE C.14 Modular cryogenic trap assembly (shown with collector flask).
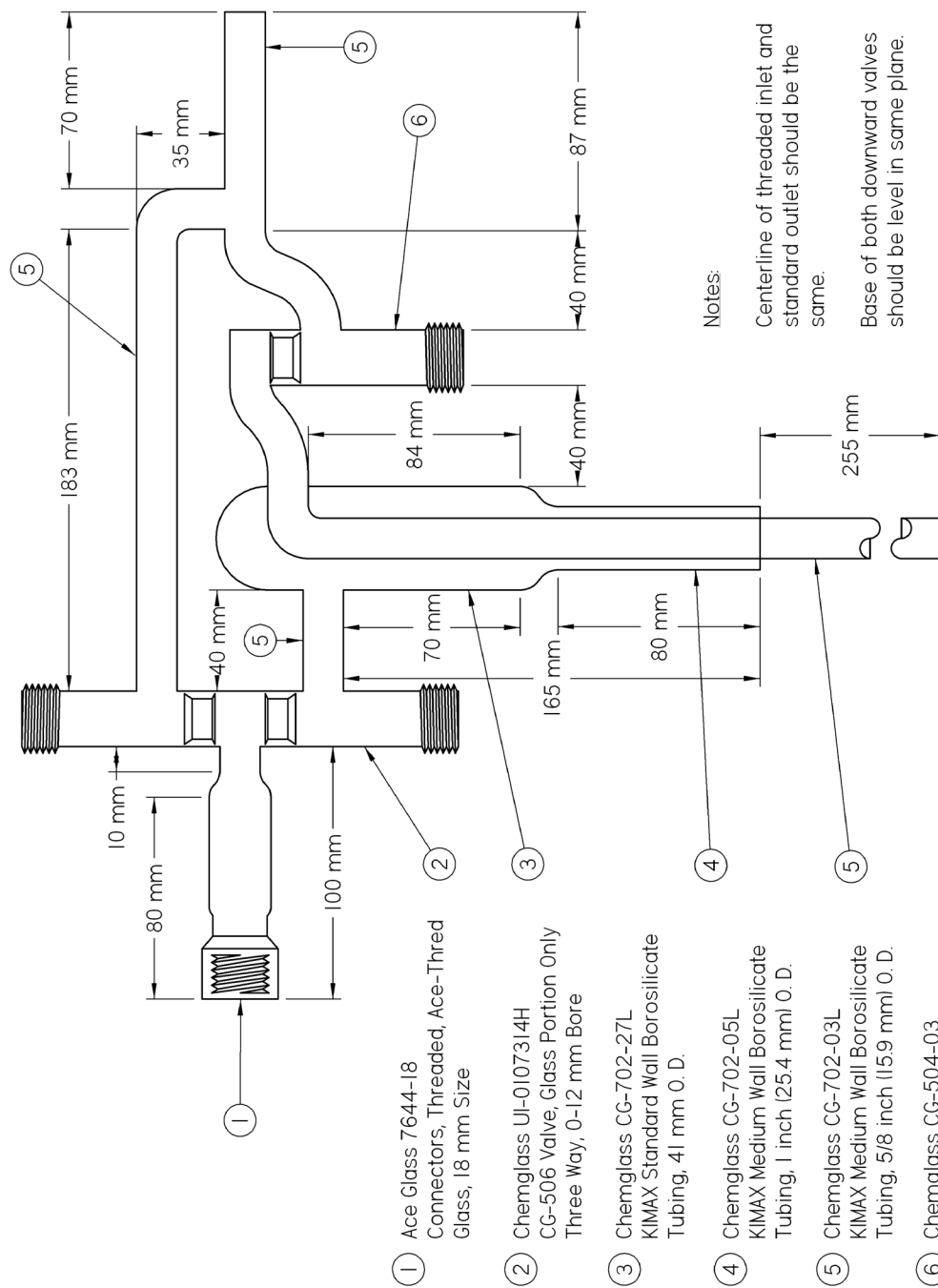
FIGURE C.15 Schematic of modular cryogenic trap assembly.

Notes:

Centerline of threaded inlet and standard outlet should be the same.

Base of both downward valves should be level in same plane.

① Ace Glass 7644-18 Connectors, Threaded, Ace-Thred Glass, 18 mm Size

② Chemglass UI-0107314H CG-506 Valve, Glass Portion Only Three Way, 0-12 mm Bore

③ Chemglass CG-702-27L KIMAX Standard Wall Borosilicate Tubing, 41 mm O. D.

④ Chemglass CG-702-05L KIMAX Medium Wall Borosilicate Tubing, 1 inch (25.4 mm) O. D.

⑤ Chemglass CG-702-03L KIMAX Medium Wall Borosilicate Tubing, 5/8 inch (15.9 mm) O. D.

⑥ Chemglass CG-504-03 Valve, Glass Portion Only, 180 Degree, 0-12 mm Bore

FIGURE C.16 Schematic of the collection flask.

① Ace Glass 7644-20 Connectors, Threaded, Ace-Thred, Glass, 25 mm Size

② Chemglass CG-700-27L KIMAX Standard Wall Borosilicate Tubing, 41 mm O. D.
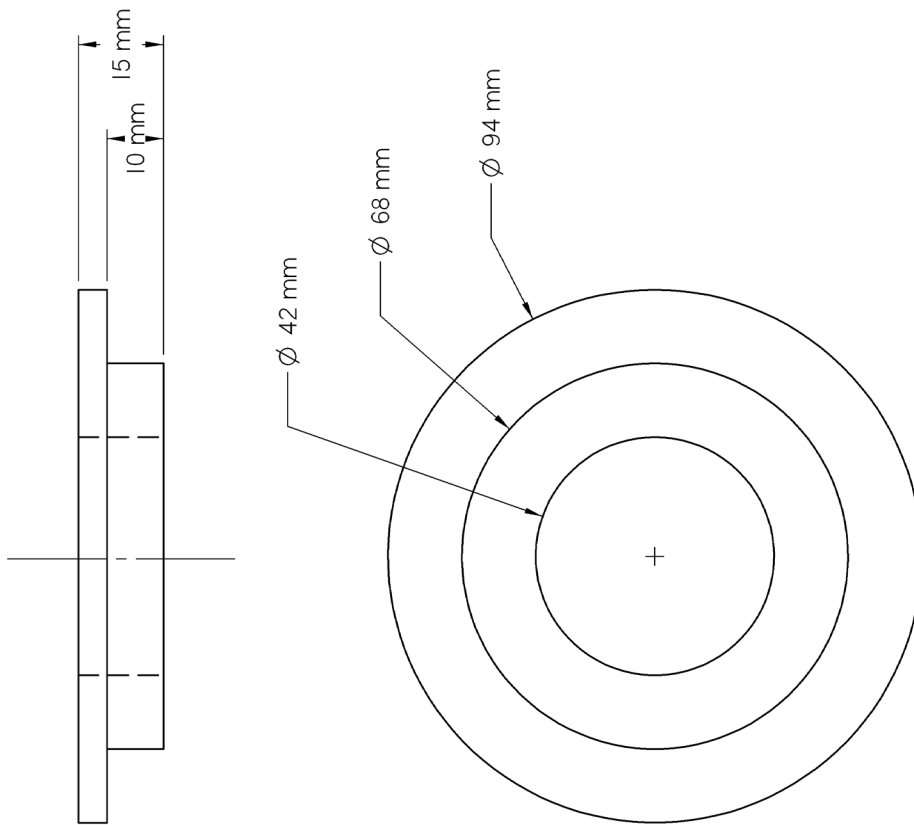
Notes:

Machine from PTFE

Piece should be cut in half

15 mm

10 mm

Ø 42 mm

Ø 68 mm

Ø 94 mm

FIGURE C.17 Insulating caps for liquid-nitrogen dewars.
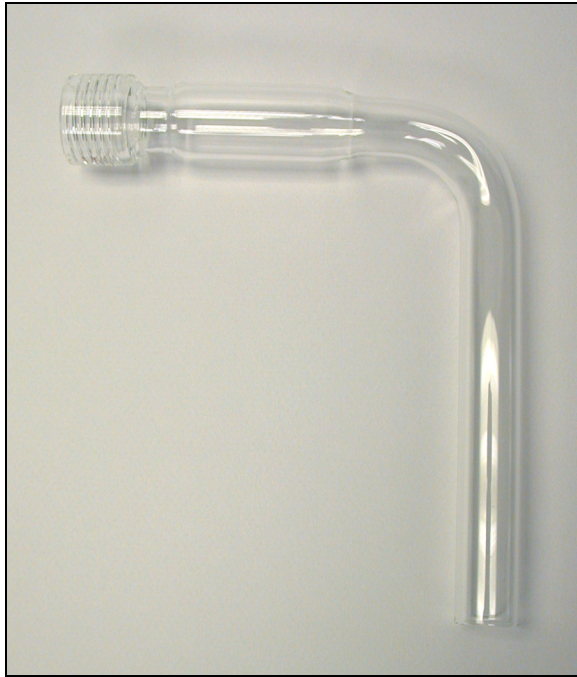
FIGURE C.18 Adapter for vacuum hose connection to pump.

120 mm

10 mm

80 mm

30 mm
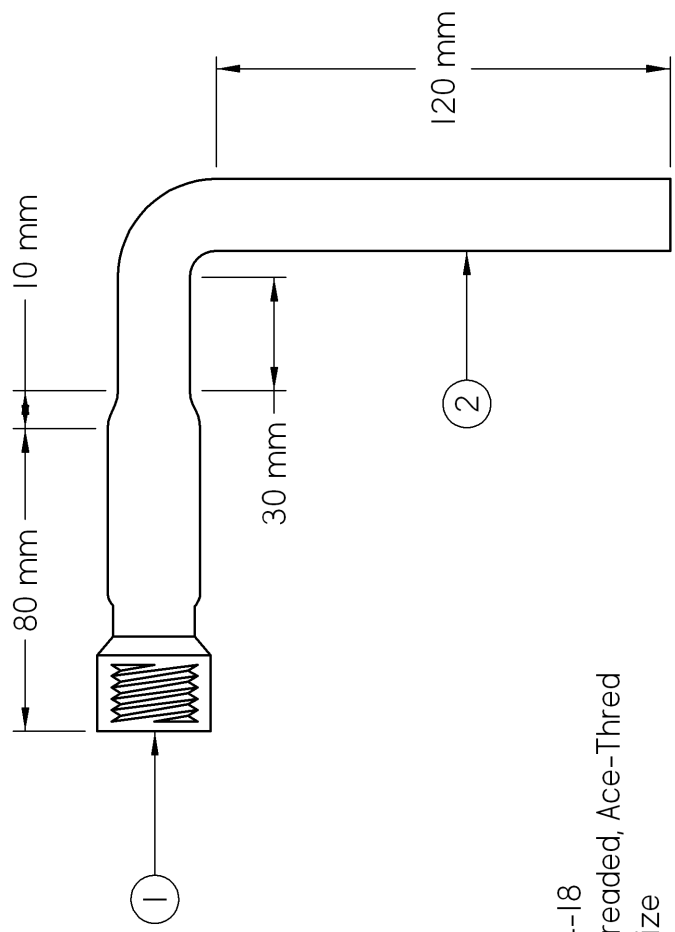
① Ace Glass 7644-18
Connectors, Threaded, Ace–Thred
Glass, 18 mm Size

② Chemglass CG-702-04L
KIMAX Medium Wall Borosilicate
Tubing, 3/4 inch (19.0 mm) O. D.

FIGURE C.19 Schematic of adapter for vacuum hose connection to pump.

Manufacturer	Item Number	Description	Qty.
Glassware			
Chemglass, Inc.	CG-702-05L	KIMAX Medium Wall Borosilicate Tubing O. D.: 1″, 25.4 ± 0.4 mm Wall Thickness: 2.4 ± 0.3 mm Length: 4′	2
Ace Glass, Inc.	7644-18	Connectors, Threaded, Ace-Thred, Glass Size: 18 mm O. D. Tube: 25 mm Wall Thickness: 2.4 ± 0.3 mm O. D. Tube (Thread): 29 mm	1
Chemglass, Inc.	CGB-601-01	Valve, 1-Piece Plug, Chem-Cap, 1-Arm 0–4 mm Bore Barrel O. D.: ½″, 12.7 ± 0.3 mm Barrel Wall Thickness: 1.6 ± 0.2 mm Side Arm O. D.: 9.0 ± 0.3 mm Side Arm Wall Thickness: 1.5 ± 0.2 mm	11
Chemglass, Inc.	CG-706-03L	KIMAX Special Wall Borosilicate Tubing O. D.: 9.0 ± 0.3 mm Wall Thickness: 1.5 ± 0.2 mm Length: 4′	1
Ace Glass, Inc.	5027-05	Connectors, Threaded, Ace-Thred, Glass Size: 7 mm O. D. Tube: 12.5 mm Wall Thickness: 1.6 ± 0.2 mm O. D. Tube (Thread): 18 mm	6
Bushings and Plugs			
Ace Glass, Inc.	5846-49	Plug (Includes FETFE O-Ring) Material: PTFE For Size: 18 mm O-Ring: -113	2

TABLE C.1   Bill-of-materials for multi-ported, double-bank manifold *(continued

Manufacturer	Item Number	Description	Qty.
Bushings and Plugs (Continued)			
Ace Glass, Inc.	7506-29	Bushing (Includes FETFE O-Ring) Material: PTFE For Size: 18 mm I. D.: 17 mm O-Ring: -112	1
Ace Glass, Inc.	5844-969	Adapter, Swagelok (Includes FTFE O-Ring) Material: PTFE For Size: 18 mm ¼″ NPT Thread Size O-Ring: -113	1
Ace Glass, Inc.	5846-44	Plug (Includes FETFE O-Ring) Material: PTFE For Size: 7 mm O-Ring: -009	5
Ace Glass, Inc.	5844-58	Adapter, Swagelok (Includes FTFE O-Ring) Material: PTFE For Size: 7 mm ¼″ NPT Thread Size O-Ring: -009	1
Vacuum Tubing and Connectors			
Sigma-Aldrich	Z25,592-0	Nalgene 180 Vacuum Tubing I. D.: ¼″ O. D.: ⅝″ Wall Thickness: 3/16″ Length: 10′	2
(Machine Shop)	(See Figure C.11)	316L Stainless Steel Connector (No O-Ring) For Size: 7 mm For I. D. Tubing: ¼″ O-Ring Size: -009	12

TABLE C.1 Bill-of-materials for multi-ported, double-bank manifold *(continued from page 273).*

Manufacturer	Item Number	Description	Qty.
Vacuum Tubing and Connectors (Continued)			
Sigma-Aldrich	Z10,116-8	PERFEKTUM Syring Fittings Connector Type: Male Luer Lock to Tube Material: Chrome-plated Brass For I. D. Tubing: ¼"	2
Ace Glass, Inc.	5029-10	Bushing (Includes FETFE O-Ring) Material: Nylon For Size: 7 mm I. D.: 7.5 mm O-Ring: -008	12
Sigma-Aldrich	Z22,420-0	Nylon Tubing Clamps Diameter Range: 17/32–19/32" Quantity: 50 per Package	1
Marco Rubber and Plastic	(Not Applicable)	Aegis White SC1011 O-Ring Size: -009	12

TABLE C.1 Bill-of-materials for multi-ported, double-bank manifold *(continued from page 274)*.

MANUFACTURER	ITEM NUMBER	DESCRIPTION	QTY.
Glassware			
Swagelok	G321-16-GXG-3	Flexible Glass-Ended Tubing Glass O. D.: 25 mm Glass Length: 3.00″ Nominal Produced Flexible Length: 3″ Flexible Length Compressed: 2.50″ Flexible Length Extended: 4.50″ Cuff Length (Metal): 1.00″ Cuff O. D. (Metal): 1″	1
Chemglass, Inc.	CG-702-03L	KIMAX Medium Wall Borosilicate Tubing O. D.: ⅝″, 15.9 ± 0.3 mm Wall Thickness: 1.6 ± 0.2 mm Length: 4′	1

TABLE C.2 Bill-of-materials for flexible glass-ended connector.

MANUFACTURER	ITEM NUMBER	DESCRIPTION	QTY.
Glassware (Includes Material for Two Assemblies)			
Chemglass, Inc.	UI-0107-314H	CG-506 Valve, Glass Portion Only, 3-Way (Includes two CGB-601-12 Plugs) 0–12 mm Bore Barrel O. D.: 22 mm Barrel Wall Thickness: 2.5 mm Side Arm O. D.: ⅝", 15.9 ± 0.3 mm Side Arm Thickness: 1.6 ± 0.2 mm	2
Chemglass, Inc.	CGB-601-12	1-Piece High Vacuum Chem-Cap Plug 0–12 mm Bore	2
Chemglass, Inc.	CG-504-03	Valve, Glass Portion Only, 180° 0–12 mm Bore Barrel O. D.: 22 mm Barrel Wall Thickness: 2.5 mm Side Arm O. D.: ⅝", 15.9 ± 0.3 mm Side Arm Thickness: 1.6 ± 0.2 mm	2
Ace Glass, Inc.	7644-18	Connectors, Threaded, Ace-Thred, Glass Size: 18 mm O. D. Tube: 25 mm Wall Thickness: 2.4 ± 0.3 mm O. D. Tube (Thread): 29 mm	2
Chemglass, Inc.	CG-700-27L	KIMAX Standard Wall Borosilicate Tubing O. D.: 41.0 ± 0.9 mm Wall Thickness: 2.0 ± 0.2 mm Length: 4'	1
Chemglass, Inc.	CG-702-05L	KIMAX Medium Wall Borosilicate Tubing O. D.: 1", 25.4 ± 0.4 mm Wall Thickness: 2.4 ± 0.3 mm Length: 4'	1

TABLE C.3 Bill-of-materials for modular cryogenic trap assembly *(continued on page 278).*

MANUFACTURER	ITEM NUMBER	DESCRIPTION	QTY.
Glassware (Includes Material for Two Assemblies, Continued)			
Chemglass, Inc.	CG-702-03L	KIMAX Medium Wall Borosilicate Tubing O. D.: ⅝″, 15.9 ± 0.3 mm Wall Thickness: 1.6 ± 0.2 mm Length: 4′	1
Bushings and Plugs			
Ace Glass, Inc.	7506-29	Bushing (Includes FETFE O-Ring) Material: PTFE For Size: 18 mm I. D.: 17 mm O-Ring: -112	2

TABLE C.3 Bill-of-materials for modular cryogenic trap assembly *(continued from page 277).*

Manufacturer	Item Number	Description	Qty.
Glassware (Includes Material for Two)			
Ace Glass, Inc.	7644-20	Connectors, Threaded, Ace-Thred, Glass Size: 25 mm O. D. Tube: 32 mm Wall Thickness: 2.4 ± 0.3 mm O. D. Tube (Thread): 41 mm	2
Chemglass, Inc.	CG-700-27L	KIMAX Standard Wall Borosilicate Tubing O. D.: 41.0 ± 0.9 mm Wall Thickness: 2.0 ± 0.2 mm Length: 4′	1
Ace Glass, Inc.	7506-29	Bushing (Includes FETFE O-Ring) Material: PTFE For Size: 25 mm I. D.: 17 mm O-Ring: -220	2
Liquid-Nitrogen Dewars			
(Machine Shop)	(See Figure C.17)	Insulating Caps for Dewars Material: PTFE	1
H. S. Martin, Inc.	611795-2230	Strip-Silvered Dewar Flask (Full Length Base with Viewing Ports) Style 22 I. D.: 68 mm Depth: 300 mm	1

TABLE C.4 Bill-of-materials for collection flasks.

MANUFACTURER	ITEM NUMBER	DESCRIPTION	QTY.
Glassware			
Ace Glass, Inc.	7644-18	Connectors, Threaded, Ace-Thred, Glass Size: 18 mm O. D. Tube: 25 mm Wall Thickness: 2.4 ± 0.3 mm O. D. Tube (Thread): 29 mm	1
Chemglass, Inc.	CG-702-05L	KIMAX Medium Wall Borosilicate Tubing O. D.: 1″, 25.4 ± 0.4 mm Wall Thickness: 2.4 ± 0.3 mm Length: 4′	1
Chemglass, Inc.	CG-702-04L	KIMAX Medium Wall Borosilicate Tubing O. D.: ¾″, 19.0 ± 0.3 mm Wall Thickness: 1.6 ± 0.2 mm Length: 4′	1
Bushings and Plugs			
Ace Glass, Inc.	7506-29	Bushing (Includes FETFE O-Ring) Material: PTFE For Size: 18 mm I. D.: 17 mm O-Ring: -112	1

TABLE C.5 Bill-of-materials for vacuum hose adapter.

Manufacturer	Item Number	Description	Qty.
Components			
Concoa	212 1301-01-580	212 Series Dual Stage Regulator Delivery Pressure: 0–15 psi Inlet Gauge Range: 0–4000 psi Outlet Fittings: ¼″ NPT Female Assembly/Gauge Type: Standard Assembly, psi and kPa Gauges Inlet Connection: CGA-580	1
Swagelok	B-QF4-B-4PM	QF Series Full Flow Quick Connect Coupling - Body Material: Plated Brass Connector: ¼″ NPT Male O-Ring: Buna with Silicone-Based Lubricant	1
Swagelok	B-QF4-S-4PM	QF Series Full Flow Quick Connect Coupling - Stem Material: Plated Brass Connector: ¼″ NPT Male	1
Swagelok	B-43XF4	40 Series Instrument Ball Valve Material: Brass Ports: 3 Connector: ¼″ NPT Female (All Ports)	1
Swagelok	B-400-1-4	Male Connector (Tapered Thread) Material: Brass Connector: ¼″ NPT Female, ¼″ Swagelok	3
Omega Engineering, Inc.	FMA-1609	FMA 1600 Series Mass Flow Meter Connector: ¼″ NPT Female	1

TABLE C.6 Bill-of-materials for inert gas delivery system *(continued on page 282).*

MANUFACTURER	ITEM NUMBER	DESCRIPTION	QTY.
Components (Continued)			
Swagelok	B-43XS4	40 Series Instrument Ball Valve Material: Brass Ports: 3 Connector: ¼″ Swagelok Fitting (All Ports)	1
Swagelok	B-401-PC	Port Connector Material: Brass Connector: For ¼″ Swagelok Fittings	2
Matheson Tri-Gas, Inc.	6427-4S	Model 6427 Series Oxygen and Moisture Trap Connector: ¼″ Swagelok Fitting (All Ports)	1
Swagelok	B-4P4T	P4T Series Plug Valve Material: Brass Connector: ¼″ Swagelok Fitting (All Ports)	1
Swagelok	B-400-2-4	Male Elbow Material: Brass Connector: ¼″ NPT Female, ¼″ Swagelok	1

TABLE C.6 Bill-of-materials for inert gas delivery system *(continued from page 281).*

APPENDIX D

REACTION APPARATUS

The synthesis and subsequent purification of silylamide and alkoxide precursors require sealable reaction apparatus capable of providing leak-free enclosures, whether under vacuum (up to 10^{-4} torr) or inert gas (argon). As discussed in Appendix C, such apparatus, commonly referred to as Schlenkware, incorporates an integrated valve that enables evacuation and flush procedures when connected to a Schlenk manifold system. This appendix provides the pictures, schematics, and bill-of-materials for all reaction apparatus and supporting equipment utilized in Chapter 3. Accordingly, each Schlenkware component depicted herein contains a single greaseless, high-vacuum, tetrafluoroethylene (TFE) valve. In addition, the joints of all reaction apparatus rely exclusively on the Ace-Thred® connector system. The threaded glass port of each Schlenk valve, for example, matches the threaded glass ports on the manifold, thereby providing a universal connection for vacuum tubing.[1] Unlike the Schlenk manifold system, however, compression seals in the reaction apparatus employ only grease-free Aegis® O-rings due to direct interaction with aggressive solvents and vapors.

Information provided in this appendix is organized sequentially into three general (unlabeled) sections: (1) the pictures and associated schematics of the reaction apparatus, (2) the bill-of-materials for the aforementioned glassware, and (3) the bill-of-materials for miscellaneous equipment and supplies. In cases where geometry proved too complex for a two-dimensional schematic, a picture alone serves as the reference. So for example, Figure D.1 provides the photograph for a custom reaction-vessel head. But the matching base, obtained readily from the manufacturer as a standard component, is found only in the bill-of-materials. When not given explicitly by a schematic, all Schlenkware valves follow dimensions given in Figure D.9 for the inlet valve; the taper and its extension, of course, should be ignored. *Particular care must taken during the fusion of Ace-Thred® connectors to glass bodies: the*

---

[1] In contrast, conventional hose joints employ a tapered, ribbed stem which utilizes friction for a leak-free connection. The force for attachment or removal can sometime exceed (unknowingly) the strength the glass component. Fracturing the glassware could cut the user, expose the user to toxic chemicals, or if the contained chemical is pyrophoric (i.e., like *n*-butyl lithium), create an explosion hazard.

length extending below the circumferential O-ring seat should be at least 15 mm, preferably 20 mm. Otherwise during fabrication, heat from the torch can soften and deform the glass O-ring seat. Such a dimensional change, virtually invisible to the eye, results in uneven points-of-contact whose non-uniform pressure creates leak points.[2] Strict adherence to this guideline must be observed when constructing reaction vessels and flasks. Shorter lengths of 10 mm, however, can be accommodated if the working space allows *precise* placement of the flame (e. g., the inlet valve in Figure D.9).

The syntheses presented in Chapter 3 often presume the connection of a bubbler to the main reaction apparatus. This link was routinely achieved using 19"-long vacuum tubing segments assembled in a manner similar to that shown Figures C.2 and C.3 (see discussion in Appendix C). Again, the standard "Ace-Safe" tubing connector was eschewed in favor of an improved stainless steel tubing connector (see Figure C.11). In order to ensure a chemically-resistant, non-contaminating gas-tight joint, only grease-free Aegis® O-rings were employed for the compression seals.

Standard "Ace-Safe" tubing connectors, however, do perform satisfactorily for less critical applications such as in joints enabling the circulation of cooling water. Incorporation of these connectors in tubing segments follows the pattern of Figure C.3 although only a single nylon band clamp is required at each end. The tubing segments (51" long) operate in pairs, one each for transport to and from the reaction apparatus. A silicone O-ring, included by Ace Glass, Inc. with the "Ace-Safe" tubing connector, suffices for the compression seal.

One problem, however, arises when attempting to attach this connector to standard laboratory water sources: faucets in fume hoods typically terminate in tapered, ribbed stems. To overcome the compatibility difference, additional 5"-long tubing segments were secured directly onto the faucets via a nylon band clamp. Special glass adapters were inserted into the remaining end (also secured with a single nylon band clamp).[3] The adapters provide a union joint: one end terminates in a tapered, ribbed stem (i.e., inserted into the tube interior), the other, a threaded port (i.e., accepts the "Ace-Safe" assembly). The 51"-long tubing segments could then be quickly connected (or disconnected) to the port, and hence, the faucet.

---

[2] Asymmetrical pressure along a deformed seat can also unscrew (slowly) a PTFE plug, completely undoing the gas-tight seal.
[3] This glass adapter was fabricated by the simple fusion of a Chemglass, Inc. CG-300-21 Glassblower Hose Connector to an Ace-Glass, Inc., 5027-05, Threaded Ace-Thred® Glass Connector.

FIGURE D.1 Front and top view of reaction vessel head.

FIGURE D.2 In-line bubbler with metering valve.
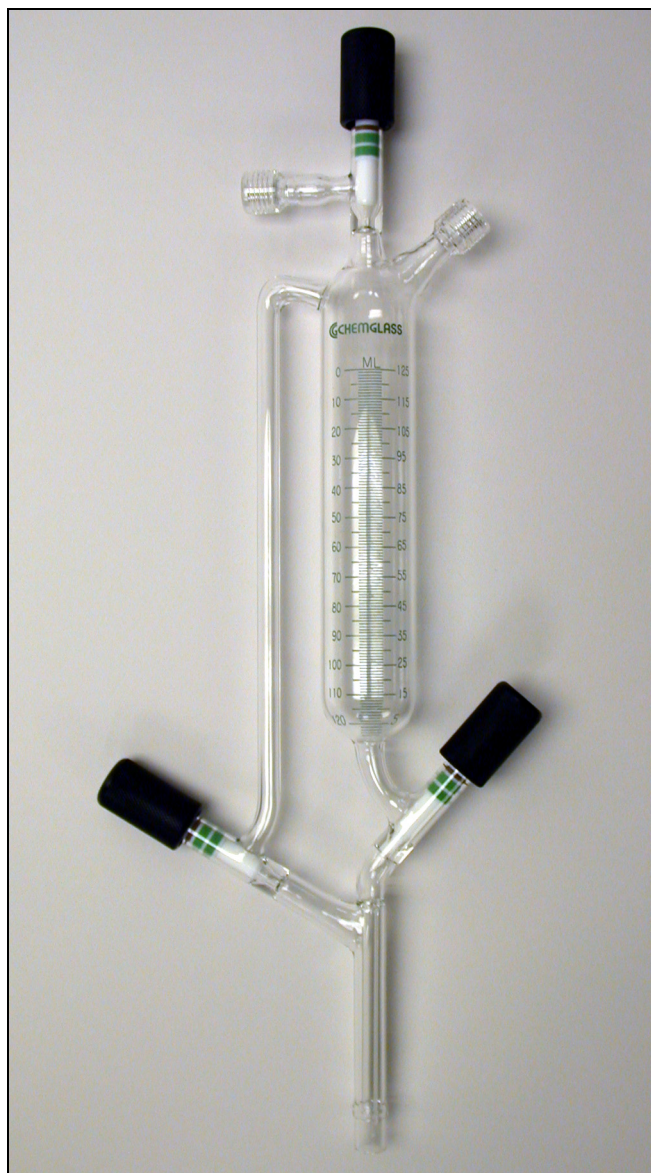
FIGURE D.3 Graduated addition funnel.
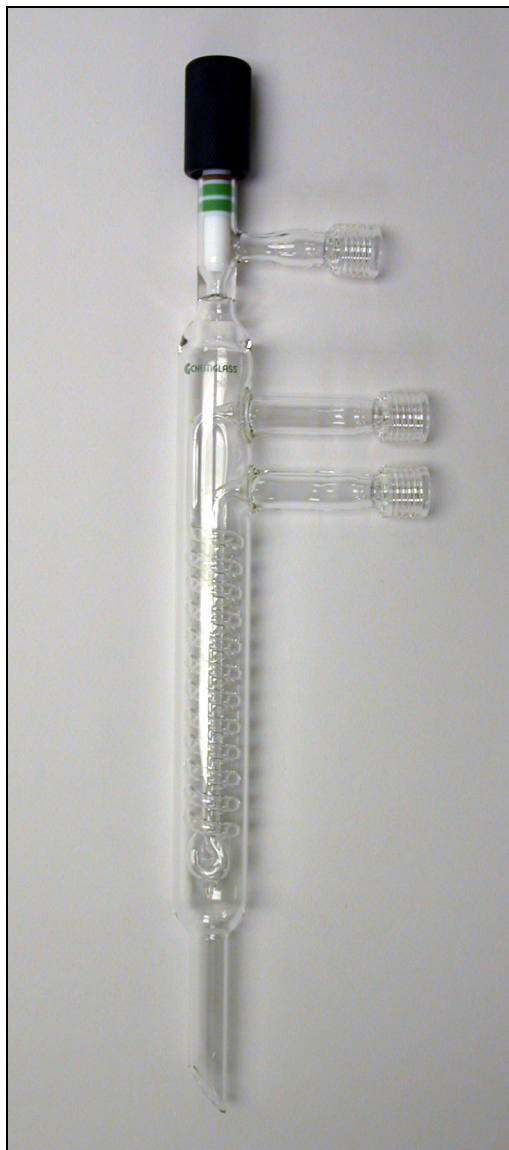
FIGURE D.4 Reflux condenser.
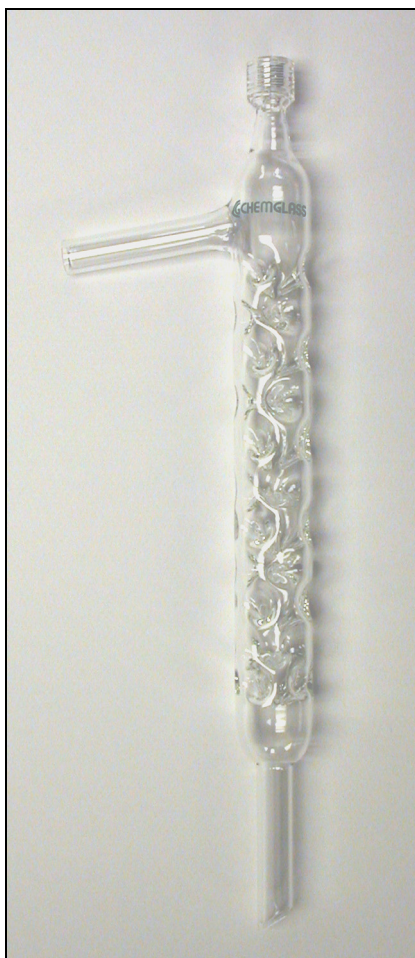
FIGURE D.5   Vigreux distillation column.

FIGURE D.6 Dewar condenser.

FIGURE D.7 Gas-flow metering valve.
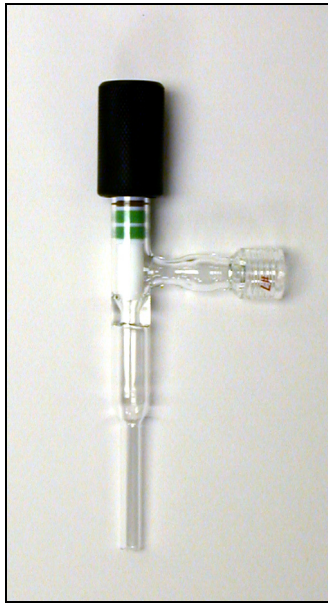
FIGURE D.8 Inlet valve.

① Chemglass CGB-601-01 Valve, One Piece Plug, Chem-Cap, One Arm, 0-4 mm Bore

② Ace Glass 5027-05 Connectors, Threaded, Ace-Thred, Glass, 7 mm Size

③ Chemglass CG-700-06L KIMAX Standard Wall Borosilicate Tubing, 7 mm O. D.
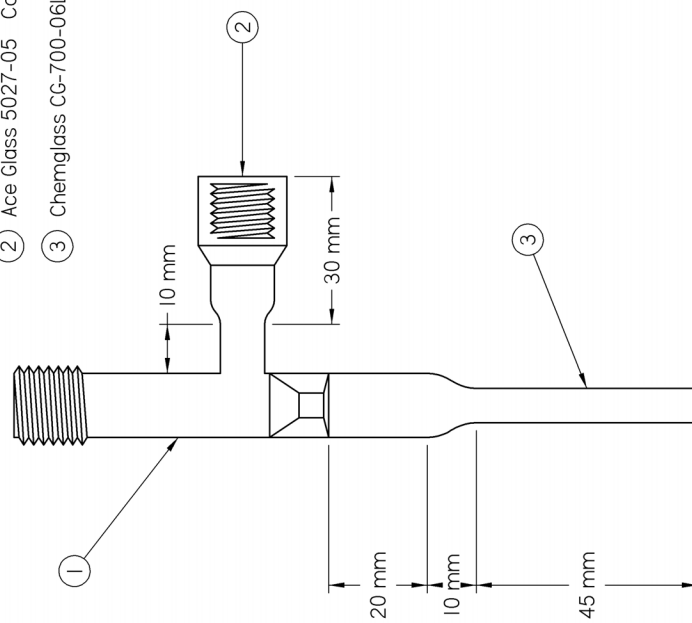
FIGURE D.9 Schematic of inlet valve.

293

FIGURE D.10 Distillation adapter, 75°.

90 mm

75°

90 mm

1 Chemglass CG-700-12L
   KIMAX Standard Wall Borosilicate
   Tubing, 13 mm O.D.
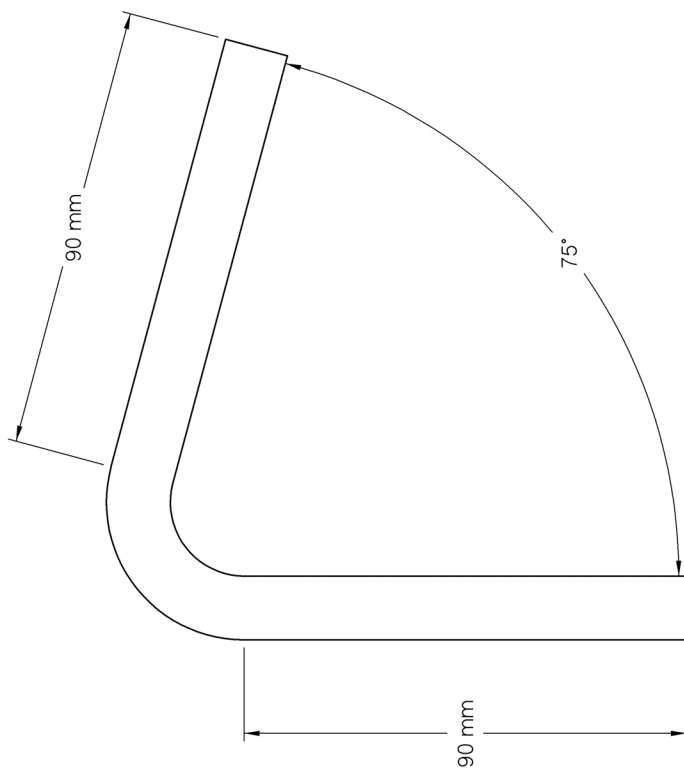
FIGURE D.11 Schematic of distillation adapter, 75°.

FIGURE D.12 Vacuum Caps.

① Ace Glass 7644-15   Connectors, Threaded, Ace-Thred, Glass, 15 mm Size

② Ace Glass 5027-05   Connectors, Threaded, Ace-Thred, Glass, 7 mm Size
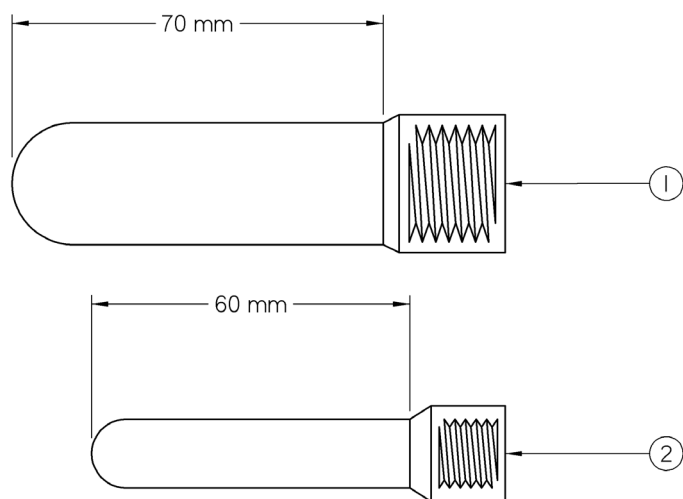
FIGURE D.13 Schematic of vacuum caps.
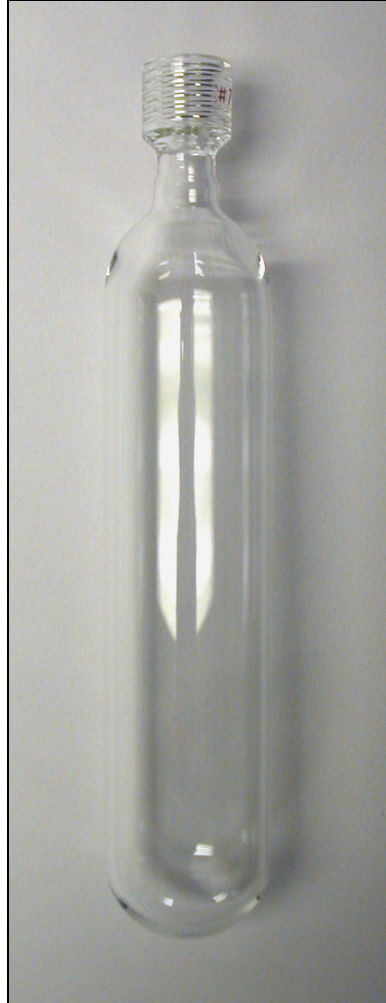
FIGURE D.14   Centrifuge tube.
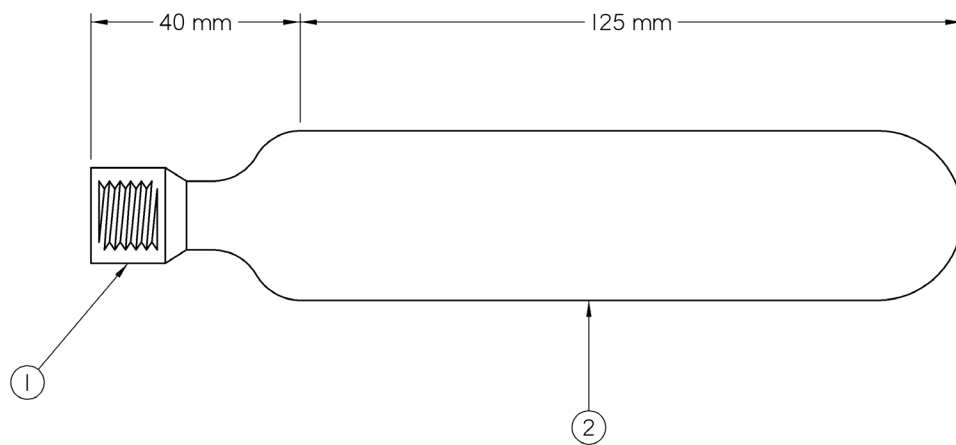
- ① Ace Glass 5027-05 Connectors, Threaded, Ace-Thred, Glass, 7 mm Size
- ② Chemglass CG-700-24L KIMAX Standard Wall Tubing, 32 mm O.D.

FIGURE D.15 Schematic of centrifuge tube.
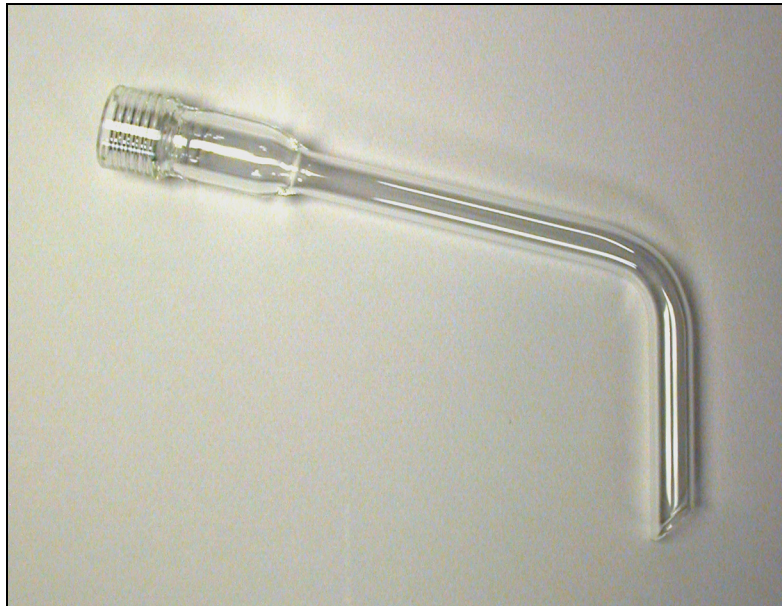
FIGURE D.16 Extension adapter.

165 mm

50 mm

70 mm

75°

45°

① Chemglass CG-700-12L
KIMAX Standard Wall Borosilicate
Tubing, 13 mm O. D.

② Ace Glass 7644-15
Connectors, Threaded, Ace-Thred,
Glass, 15 mm Size
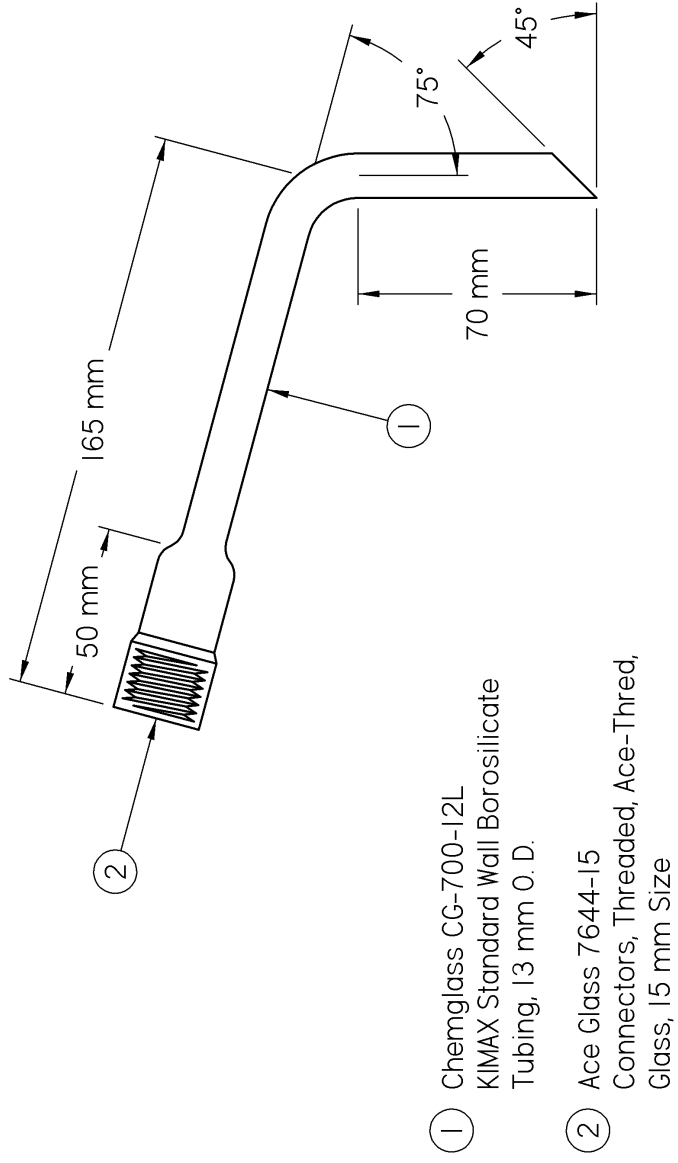
FIGURE D.17 Schematic of extension adapter.
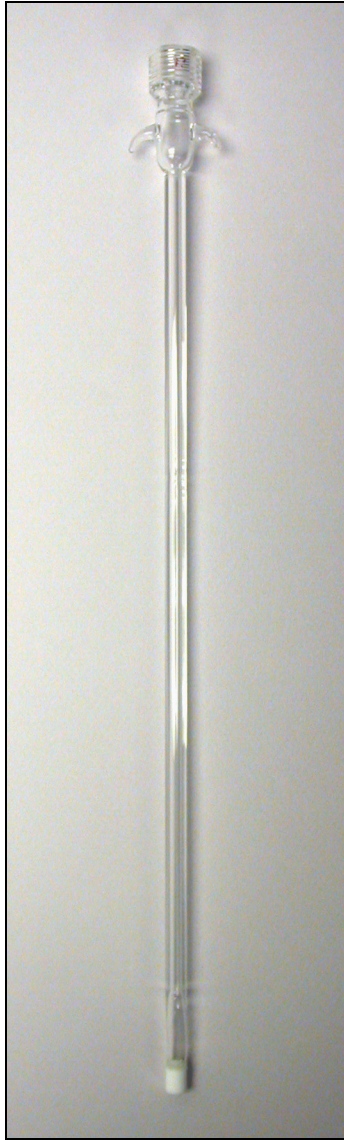
FIGURE D.18 Gas dispersion tube.
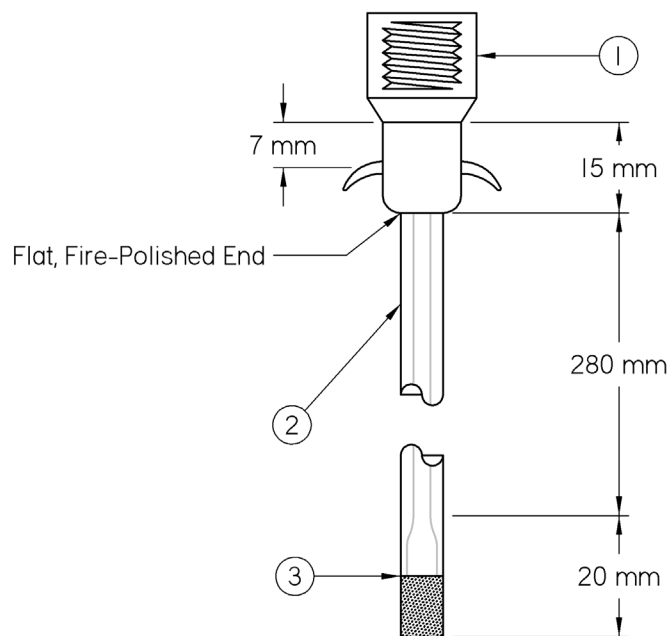
7 mm

15 mm

Flat, Fire-Polished End —

②

280 mm

③

20 mm

① Ace Glass 5027-05   Connectors, Threaded, Ace-Thred, Glass, 7 mm Size

② Chemglass CG-708-04L   KIMAX Borosilicate Capillary Tubing, 7 mm O. D., 2.75 mm Bore

③ Ace Glass 9435-25   Tube, Gas Dispersion, 7 mm O.D., Porosity E

FIGURE D.19 Schematic of gas dispersion tube.
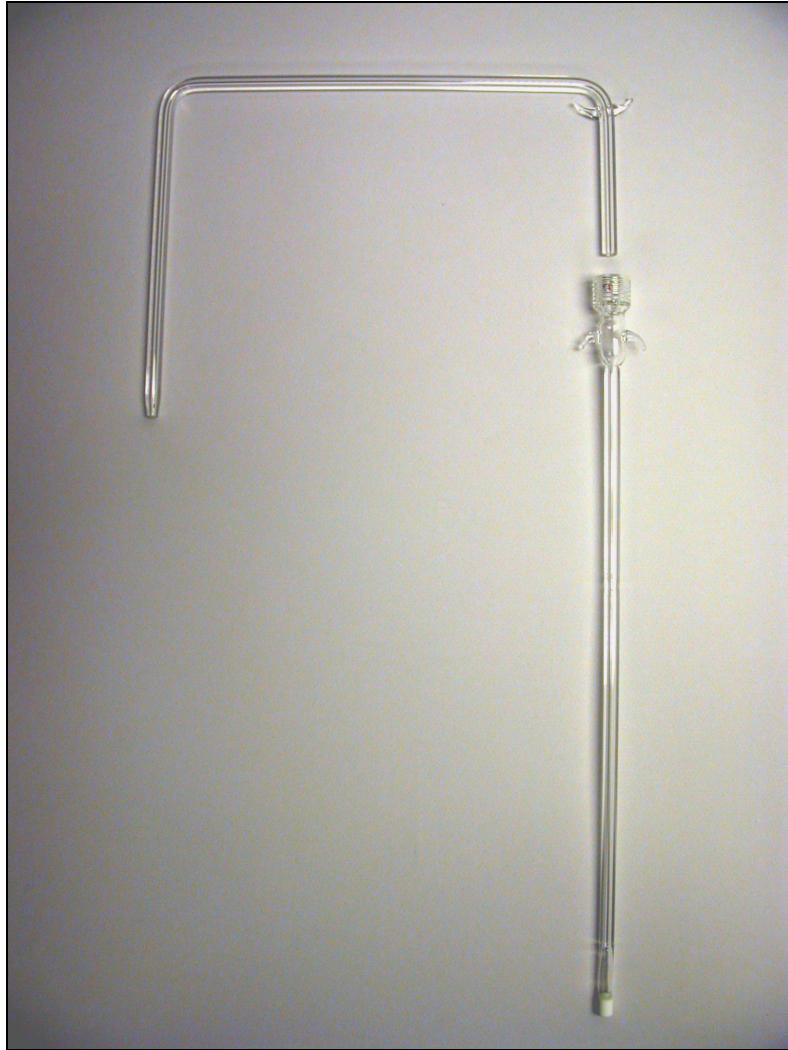
FIGURE D.20 Glass filter cannula.
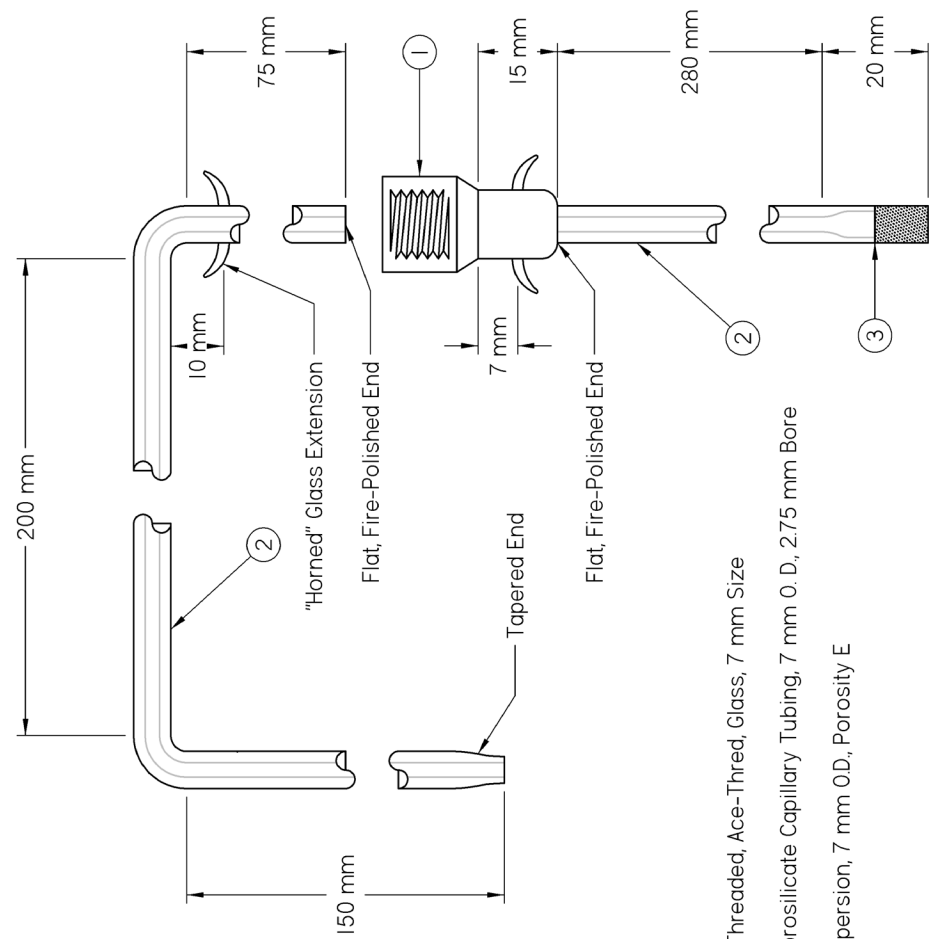
75 mm

200 mm

10 mm

150 mm

"Horned" Glass Extension

Flat, Fire-Polished End

Tapered End

15 mm

280 mm

20 mm

7 mm

Flat, Fire-Polished End

① Ace Glass 5027-05 Connectors, Threaded, Ace-Thred, Glass, 7 mm Size

② Chemglass CG-708-04L KIMAX Borosilicate Capillary Tubing, 7 mm O. D., 2.75 mm Bore

③ Ace Glass 9435-25 Tube, Gas Dispersion, 7 mm O.D., Porosity E

FIGURE D.21 Schematic of glass filter cannula.

FIGURE D.22 Flat-bottom 500-mL, 3-neck flask.

FIGURE D.23   Round-bottom 500-mL, 3-neck flask.

FIGURE D.24 Round-bottom 1000-mL, 3-neck flask.

FIGURE D.25 Front and top view of round-bottom 1000-mL, 4-neck flask.

FIGURE D.26 Sublimation head.
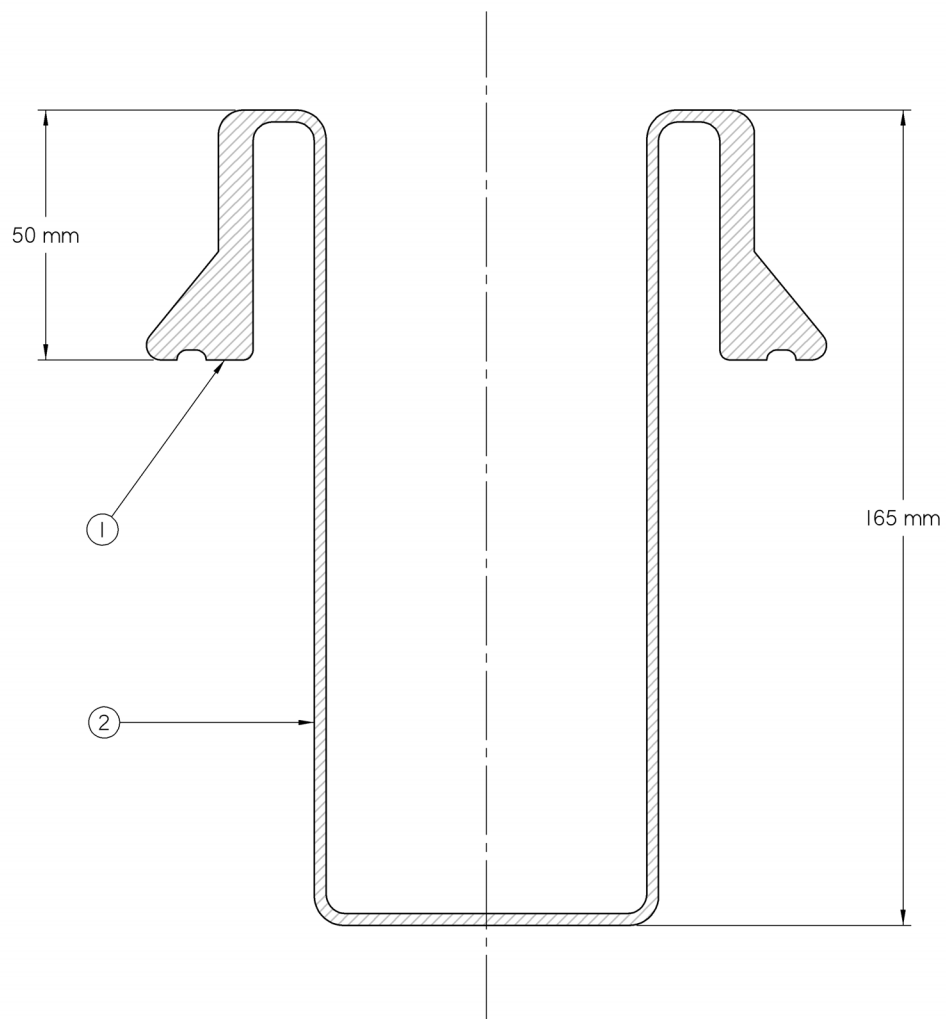
① Ace Glass D115311   Pressure Reaction Flange, 4" I. D., 6" – 7" Schank

② Chemglass CG-700-35L   KIMAX Borosilicate Standard Wall Tubing, 70 mm O. D.

FIGURE D.27 Schematic of sublimation head (cross-section of jar).

45°

20 mm

20 mm

75 mm
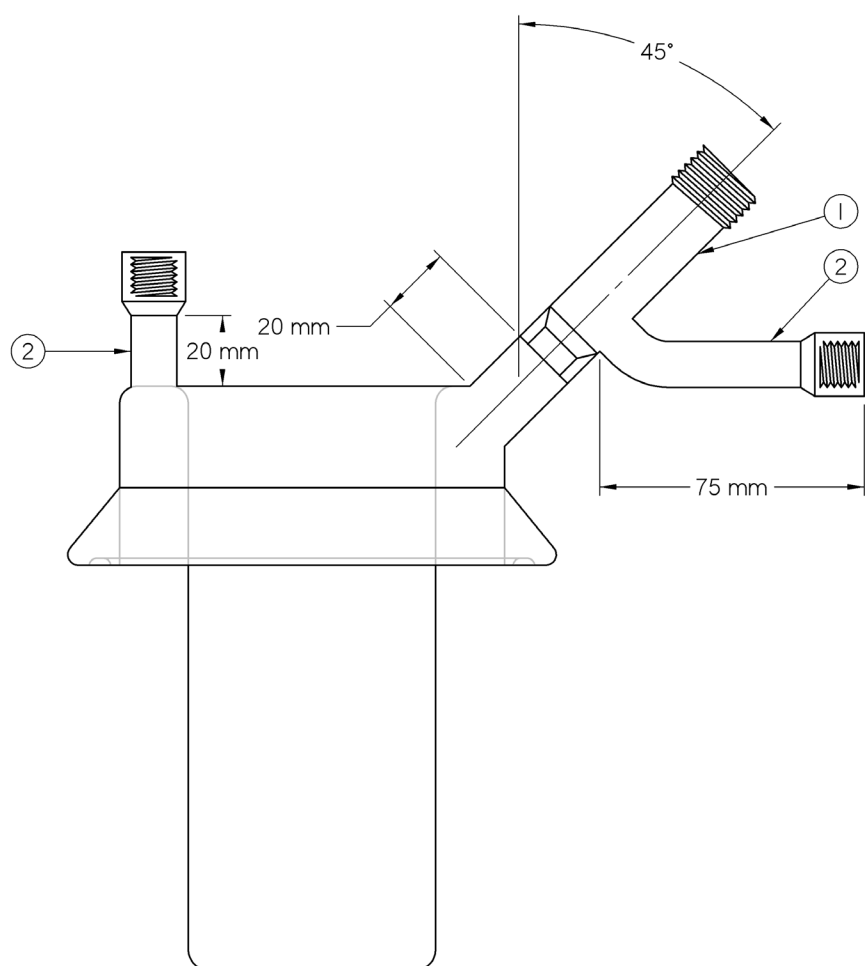
① Chemglass CGB-601-02   Valve, One Piece Plug, Chem-Cap, One Arm, 0-8 mm Bore

② Ace Glass 5027-05   Connectors, Threaded, Ace-Thred, Glass, 7 mm Size

FIGURE D.28 Schematic of sublimation head (port and valve assembly).

FIGURE D.29 Gelation chamber with stackable dishes.
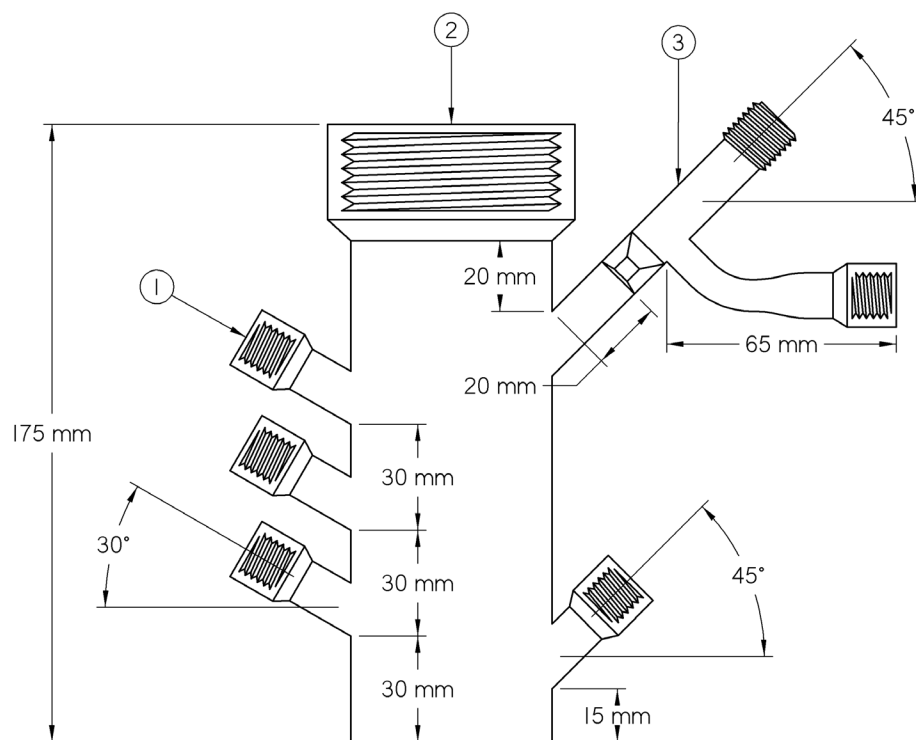
Petri Dish:
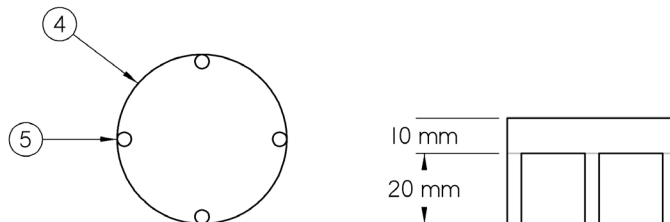
① Ace Glass 5027-05   Connectors, Threaded, Ace-Thred, Glass, 7 mm Size

② Ace Glass 7644-25   Connectors, Threaded, Ace-Thred, Glass, 50 mm Size

③ Chemglass CGB-601-01   Valve, One Piece Plug, Chem-Cap, One Arm, 0-4 mm Bore

④ Chemglass CG-700-29L   KIMAX Standard Wall Borosilicate Tubing, 48 mm O. D.

⑤ Chemglass CG-710-03L   KIMAX Borosilicate Rod, 4 mm O. D.

FIGURE D.30 Schematic of gelation chamber with stackable dishes.

Manufacturer	Item Number	Description	Qty.
Reaction Vessel			
Ace Glass, Inc.	D112029	Modified 6433-35 Head, Pressure Reaction, with Ace-Threds	1
Ace Glass, Inc.	6423-10	Flask, Pressure Reaction, Plain (Includes CAPFE O-Ring) Flange Size: 100 mm (4") Capacity: 1000 mL Depth: 180 mm O-Ring: -348	1
Ace Glass, Inc.	5027-05	Connectors, Threaded, Ace-Thred, Glass Size: 7 mm O. D. Tube: 12.5 mm Wall Thickness: 1.6 ± 0.2 mm O. D. Tube (Thread): 18 mm	3
Ace Glass, Inc.	7644-15	Connectors, Threaded, Ace-Thred, Glass Size: 15 mm O. D. Tube: 23 mm Wall Thickness: 3.2 ± 0.3 mm O. D. Tube (Thread): 26 mm	2
Chemglass, Inc.	CGB-601-01	Valve, 1-Piece Plug, Chem-Cap, 1-Arm 0–4 mm Bore Barrel O. D.: ½", 12.7 ± 0.3 mm Barrel Wall Thickness: 1.6 ± 0.2 mm Side Arm O. D.: 9.0 ± 0.3 mm Side Arm Wall Thickness: 1.5 ± 0.2 mm	1
Ace Glass, Inc.	6517-25	Clamp, "Quick Release" Flange Size: 100 mm (4")	1
Marco Rubber and Plastic	(Not Applicable)	Aegis White SC1011 O-Ring Size: -348	1

TABLE D.1 Bill-of-materials for reaction apparatus *(continued on page 316)*.

Manufacturer	Item Number	Description	Qty.
In-line Bubbler with Metering Valve			
Chemglass, Inc.	UI-0107-310H	Modified CG-4536-01 Bubbler, Pressure Release (Based on CG-562-01 Valve, Chem-Cap, High Vacuum, Metering, 1-Arm)	1
Ace Glass, Inc.	5027-05	Connectors, Threaded, Ace-Thred, Glass Size: 7 mm O. D. Tube: 12.5 mm Wall Thickness: 1.6 ± 0.2 mm O. D. Tube (Thread): 18 mm	2
Graduated Addition Funnel			
Chemglass, Inc.	UI-0212-091MS	Modified CG-1714-02 Funnel, Addition Graduated, Threaded Valve, 125 mL	1
Ace Glass, Inc.	5027-05	Connectors, Threaded, Ace-Thred, Glass Size: 7 mm O. D. Tube: 12.5 mm Wall Thickness: 1.6 ± 0.2 mm O. D. Tube (Thread): 18 mm	2
Reflux Condenser			
Chemglass, Inc.	UI-0212-092MS	Modified CG-1213-01 Condenser, Reflux 200 mm Jacket Length	1
Ace Glass, Inc.	5027-05	Connectors, Threaded, Ace-Thred, Glass Size: 7 mm O. D. Tube: 12.5 mm Wall Thickness: 1.6 ± 0.2 mm O. D. Tube (Thread): 18 mm	3

TABLE D.1 Bill-of-materials for reaction apparatus *(continued from page 315).*

MANUFACTURER	ITEM NUMBER	DESCRIPTION	QTY.
Vigreux Distillation Column			
Chemglass, Inc.	UI-0211-151JS	Modified CG-1231-16 Distilling Column, Vigreux, 150 mm Jacket Length	1
Ace Glass, Inc.	5027-05	Connectors, Threaded, Ace-Thred, Glass Size: 7 mm O. D. Tube: 12.5 mm Wall Thickness: 1.6 ± 0.2 mm O. D. Tube (Thread): 18 mm	1
Dewar Condenser			
Chemglass, Inc.	UI-0211-151JS	Modified CG-1209-A-26 Condenser, Dewar Type, 200 mm Inside Depth, 40 mm I. D.	1
Ace Glass, Inc.	7644-15	Connectors, Threaded, Ace-Thred, Glass Size: 15 mm O. D. Tube: 23 mm Wall Thickness: 3.2 ± 0.3 mm O. D. Tube (Thread): 26 mm	1
Gas-Flow Metering Valve			
Swagelok	SS-2MG2-TFMH	M Series Metering Valve, Straight Stainless Steel ⅛″ NPT Male Ends Teflon™ Stem Packing Vernier Handle	1
Ace Glass, Inc.	5844-58	Adapter, Swagelok (Includes FTFE O-Ring) Material: PTFE For Size: 7 mm ⅛″ NPT Thread Size O-Ring: -009	2

TABLE D.1 Bill-of-materials for reaction apparatus *(continued from page 316)*.

MANUFACTURER	ITEM NUMBER	DESCRIPTION	QTY.
Gas-Flow Metering Valve (Continued)			
Ace Glass, Inc.	5027-05	Connectors, Threaded, Ace-Thred, Glass Size: 7 mm O. D. Tube: 12.5 mm Wall Thickness: 1.6 ± 0.2 mm O. D. Tube (Thread): 18 mm	4
Marco Rubber and Plastic	(Not Applicable)	Aegis White SC1011 O-Ring Size: -009	2
Inlet Valve			
Chemglass, Inc.	CGB-601-01	Valve, 1-Piece Plug, Chem-Cap, 1-Arm 0–4 mm Bore Barrel O. D.: ½″, 12.7 ± 0.3 mm Barrel Wall Thickness: 1.6 ± 0.2 mm Side Arm O. D.: 9.0 ± 0.3 mm Side Arm Wall Thickness: 1.5 ± 0.2 mm	1
Ace Glass, Inc.	5027-05	Connectors, Threaded, Ace-Thred, Glass Size: 7 mm O. D. Tube: 12.5 mm Wall Thickness: 1.6 ± 0.2 mm O. D. Tube (Thread): 18 mm	1
Chemglass, Inc.	CG-700-06L	KIMAX Standard Wall Borosilicate Tubing O. D.: 7.0 ± 0.3 mm Wall Thickness: 1.0 ± 0.1 mm Length: 4′	1
Distillation Adapter, 75°			
Chemglass, Inc.	CG-700-12L	KIMAX Standard Wall Borosilicate Tubing O. D.: 13.0 ± 0.3 mm Wall Thickness: 1.2 ± 0.1 mm Length: 4′	1

TABLE D.1 Bill-of-materials for reaction apparatus *(continued from page 317)*.

MANUFACTURER	ITEM NUMBER	DESCRIPTION	QTY.
Vacuum Caps			
Ace Glass, Inc.	5027-05	Connectors, Threaded, Ace-Thred, Glass Size: 7 mm O. D. Tube: 12.5 mm Wall Thickness: 1.6 ± 0.2 mm O. D. Tube (Thread): 18 mm	1
Ace Glass, Inc.	7644-15	Connectors, Threaded, Ace-Thred, Glass Size: 15 mm O. D. Tube: 23 mm Wall Thickness: 3.2 ± 0.3 mm O. D. Tube (Thread): 26 mm	1
Centrifuge Tube			
Chemglass, Inc.	CG-700-24L	KIMAX Standard Wall Borosilicate Tubing O. D.: 32.0 ± 0.7 mm Wall Thickness: 1.8 ± 0.2 mm Length: 4'	1
Ace Glass, Inc.	5027-05	Connectors, Threaded, Ace-Thred, Glass Size: 7 mm O. D. Tube: 12.5 mm Wall Thickness: 1.6 ± 0.2 mm O. D. Tube (Thread): 18 mm	1
Extension Adapter			
Chemglass, Inc.	CG-700-12L	KIMAX Standard Wall Borosilicate Tubing O. D.: 13.0 ± 0.3 mm Wall Thickness: 1.2 ± 0.1 mm Length: 4'	1

TABLE D.1 Bill-of-materials for reaction apparatus *(continued from page 318)*.

MANUFACTURER	ITEM NUMBER	DESCRIPTION	QTY.
Extension Adapter (Continued)			
Ace Glass, Inc.	7644-15	Connectors, Threaded, Ace-Thred, Glass Size: 15 mm O. D. Tube: 23 mm Wall Thickness: 3.2 ± 0.3 mm O. D. Tube (Thread): 26 mm	1
Gas Dispersion Tube			
Chemglass, Inc.	CG-708-04L	KIMAX Borosilicate Capillary Tubing O. D.: 7.0 ± 0.4 mm Bore: 2.75 ± 0.20 mm Length: 4′	1
Ace Glass, Inc.	5027-05	Connectors, Threaded, Ace-Thred, Glass Size: 7 mm O. D. Tube: 12.5 mm Wall Thickness: 1.6 ± 0.2 mm O. D. Tube (Thread): 18 mm	1
Ace Glass, Inc.	9435-25	Tube, Gas Dispersion Porosity: E O. D. Tube: 7 mm	1
Glass Filter Cannula			
Chemglass, Inc.	CG-708-04L	KIMAX Borosilicate Capillary Tubing O. D.: 7.0 ± 0.4 mm Bore: 2.75 ± 0.20 mm Length: 4′	1
Ace Glass, Inc.	5027-05	Connectors, Threaded, Ace-Thred, Glass Size: 7 mm O. D. Tube: 12.5 mm Wall Thickness: 1.6 ± 0.2 mm O. D. Tube (Thread): 18 mm	1

TABLE D.1 Bill-of-materials for reaction apparatus *(continued from page 319).*

Manufacturer	Item Number	Description	Qty.
Glass Filter Cannula (Continued)			
Ace Glass, Inc.	9435-25	Tube, Gas Dispersion Porosity: E O. D. Tube: 7 mm	1
Ace Glass, Inc.	5029-35	Bushing (Includes FETFE O-Ring) Material: PTFE For Size: 7 mm I. D.: 7.5 mm O-Ring: -008	1
Marco Rubber and Plastic	(Not Applicable)	Aegis White SC1011 O-Ring Size: -008	1
Marco Rubber and Plastic	(Not Applicable)	Aegis White SC1011 O-Ring Size: -005	1
Flat-Bottom 500-mL 3-Neck Flask			
Chemglass, Inc.	CG-619-04	Glass-Blowers Flask Blank, Flat Bottom Size: 500 mL	1
Chemglass, Inc.	CGB-601-01	Valve, 1-Piece Plug, Chem-Cap, 1-Arm 0–4 mm Bore Barrel O. D.: ½″, 12.7 ± 0.3 mm Barrel Wall Thickness: 1.6 ± 0.2 mm Side Arm O. D.: 9.0 ± 0.3 mm Side Arm Wall Thickness: 1.5 ± 0.2 mm	1
Ace Glass, Inc.	5027-05	Connectors, Threaded, Ace-Thred, Glass Size: 7 mm O. D. Tube: 12.5 mm Wall Thickness: 1.6 ± 0.2 mm O. D. Tube (Thread): 18 mm	2
Ace Glass, Inc.	7644-15	Connectors, Threaded, Ace-Thred, Glass Size: 15 mm O. D. Tube: 23 mm Wall Thickness: 3.2 ± 0.3 mm O. D. Tube (Thread): 26 mm	1

TABLE D.1 Bill-of-materials for reaction apparatus *(continued from page 320)*.

MANUFACTURER	ITEM NUMBER	DESCRIPTION	QTY.
Round-Bottom 500-mL 3-Neck Flask			
Chemglass, Inc.	CG-618-09	Glass-Blowers Flask Blank, Round Bottom Size: 500 mL	1
Chemglass, Inc.	CGB-601-01	Valve, 1-Piece Plug, Chem-Cap, 1-Arm 0–4 mm Bore Barrel O. D.: ½″, 12.7 ± 0.3 mm Barrel Wall Thickness: 1.6 ± 0.2 mm Side Arm O. D.: 9.0 ± 0.3 mm Side Arm Wall Thickness: 1.5 ± 0.2 mm	1
Ace Glass, Inc.	5027-05	Connectors, Threaded, Ace-Thred, Glass Size: 7 mm O. D. Tube: 12.5 mm Wall Thickness: 1.6 ± 0.2 mm O. D. Tube (Thread): 18 mm	2
Ace Glass, Inc.	7644-15	Connectors, Threaded, Ace-Thred, Glass Size: 15 mm O. D. Tube: 23 mm Wall Thickness: 3.2 ± 0.3 mm O. D. Tube (Thread): 26 mm	1
Round-Bottom 1000-mL 3-Neck Flask			
Chemglass, Inc.	CG-618-10	Glass-Blowers Flask Blank, Round Bottom Size: 1000 mL	1
Chemglass, Inc.	CGB-601-01	Valve, 1-Piece Plug, Chem-Cap, 1-Arm 0–4 mm Bore Barrel O. D.: ½″, 12.7 ± 0.3 mm Barrel Wall Thickness: 1.6 ± 0.2 mm Side Arm O. D.: 9.0 ± 0.3 mm Side Arm Wall Thickness: 1.5 ± 0.2 mm	1

TABLE D.1 Bill-of-materials for reaction apparatus *(continued from page 321)*.

Manufacturer	Item Number	Description	Qty.
Round-Bottom 1000-mL 3-Neck Flask (Continued)			
Ace Glass, Inc.	5027-05	Connectors, Threaded, Ace-Thred, Glass Size: 7 mm O. D. Tube: 12.5 mm Wall Thickness: 1.6 ± 0.2 mm O. D. Tube (Thread): 18 mm	2
Ace Glass, Inc.	7644-15	Connectors, Threaded, Ace-Thred, Glass Size: 15 mm O. D. Tube: 23 mm Wall Thickness: 3.2 ± 0.3 mm O. D. Tube (Thread): 26 mm	1
Round-Bottom 1000-mL 4-Neck Flask			
Chemglass, Inc.	CG-618-10	Glass-Blowers Flask Blank, Round Bottom Size: 1000 mL	1
Chemglass, Inc.	CGB-601-01	Valve, 1-Piece Plug, Chem-Cap, 1-Arm 0–4 mm Bore Barrel O. D.: ½″, 12.7 ± 0.3 mm Barrel Wall Thickness: 1.6 ± 0.2 mm Side Arm O. D.: 9.0 ± 0.3 mm Side Arm Wall Thickness: 1.5 ± 0.2 mm	1
Ace Glass, Inc.	5027-05	Connectors, Threaded, Ace-Thred, Glass Size: 7 mm O. D. Tube: 12.5 mm Wall Thickness: 1.6 ± 0.2 mm O. D. Tube (Thread): 18 mm	3
Ace Glass, Inc.	7644-15	Connectors, Threaded, Ace-Thred, Glass Size: 15 mm O. D. Tube: 23 mm Wall Thickness: 3.2 ± 0.3 mm O. D. Tube (Thread): 26 mm	1

TABLE D.1 Bill-of-materials for reaction apparatus *(continued from page 322).*

MANUFACTURER	ITEM NUMBER	DESCRIPTION	QTY.
Sublimation Chamber			
Ace Glass, Inc.	D115311	Pressure Reaction Flange, 4" I. D. Flange Surface: Fire-Polished (Not Ground) O-Ring Groove Depth: 0.040 ± 0.015/0.010" O-Ring Drove Diameter: For Size -348 Length (Shank): 6–7" O. D. Shank: 110 mm Wall Thickness: 7 mm	1
Chemglass, Inc.	CG-700-35L	KIMAX Standard Wall Borosilicate Tubing O. D.: 70.0 ± 1.2 mm Wall Thickness: 2.4 ± 0.3 mm Length: 4'	1
Chemglass, Inc.	CGB-601-02	Valve, 1-Piece Plug, Chem-Cap, 1-Arm 0–8 mm Bore Barrel O. D.: ¾", 19.0 ± 0.3 mm Barrel Wall Thickness: 1.6 ± 0.2 mm Side Arm O. D.: 13.0 ± 0.3 mm Side Arm Wall Thickness: 1.2 ± 0.1 mm	1
Ace Glass, Inc.	5027-05	Connectors, Threaded, Ace-Thred, Glass Size: 7 mm O. D. Tube: 12.5 mm Wall Thickness: 1.6 ± 0.2 mm O. D. Tube (Thread): 18 mm	2
Ace Glass, Inc.	6423-10	Flask, Pressure Reaction, Plain (Includes CAPFE O-Ring) Flange Size: 100 mm (4") Capacity: 1000 mL Depth: 180 mm O-Ring: -348	1
Ace Glass, Inc.	6517-25	Clamp, "Quick Release" Flange Size: 100 mm (4")	1
Marco Rubber and Plastic	(Not Applicable)	Aegis White SC1011 O-Ring Size: -348	1

TABLE D.1 Bill-of-materials for reaction apparatus *(continued from page 323).*

MANUFACTURER	ITEM NUMBER	DESCRIPTION	QTY.
Gelation Chamber with Stackable Dishes			
Ace Glass, Inc.	7644-25	Connectors, Threaded, Ace-Thred, Glass Size: 50 mm O. D. Tube: 57 mm Wall Thickness: 3.2 ± 0.3 mm O. D. Tube (Thread): 71 mm	1
Ace Glass, Inc.	5027-05	Connectors, Threaded, Ace-Thred, Glass Size: 7 mm O. D. Tube: 12.5 mm Wall Thickness: 1.6 ± 0.2 mm O. D. Tube (Thread): 18 mm	5
Chemglass, Inc.	CGB-601-01	Valve, 1-Piece Plug, Chem-Cap, 1-Arm 0–4 mm Bore Barrel O. D.: ½″, 12.7 ± 0.3 mm Barrel Wall Thickness: 1.6 ± 0.2 mm Side Arm O. D.: 9.0 ± 0.3 mm Side Arm Wall Thickness: 1.5 ± 0.2 mm	1
Chemglass, Inc.	CG-700-29L	KIMAX Standard Wall Borosilicate Tubing O. D.: 48.0 ± 1.0 mm Wall Thickness: 2.0 ± 0.2 mm Length: 4′	1
Chemglass, Inc.	CG-710-03L	KIMAX Borosilicate Rod O. D.: 4.0 ± 0.4 mm Length: 4′	1
Ace Glass, Inc.	5846-52	Plug (Includes FETFE O-Ring) Material: PTFE For Size: 50 mm O-Ring: -225	1

TABLE D.1 Bill-of-materials for reaction apparatus *(continued from page 324)*.

MANUFACTURER	ITEM NUMBER	DESCRIPTION	QTY.
Bushings and Plugs			
Ace Glass, Inc.	5846-44	Plug (Includes FETFE O-Ring) Material: PTFE For Size: 7 mm O-Ring: -009	a
Ace Glass, Inc.	5029-35	Bushing (Includes FETFE O-Ring) Material: PTFE For Size: 7 mm I. D.: 7.5 mm O-Ring: -008	a
Ace Glass, Inc.	5846-48	Plug (Includes FETFE O-Ring) Material: PTFE For Size: 15 mm O-Ring: -110	a
Ace Glass, Inc.	7506-27	Bushing (Includes FETFE O-Ring) Material: PTFE For Size: 15 mm I. D.: 14 mm O-Ring: -110	a
O-Rings			
Marco Rubber and Plastic	(Not Applicable)	Aegis White SC1011 O-Ring Size: -008	b
Marco Rubber and Plastic	(Not Applicable)	Aegis White SC1011 O-Ring Size: -009	b
Marco Rubber and Plastic	(Not Applicable)	Aegis White SC1011 O-Ring Size: -110	b

TABLE D.2 Bill-of-materials for miscellaneous reaction equipment *(continued on page 327)*.

MANUFACTURER	ITEM NUMBER	DESCRIPTION	QTY.
Septa and Cannula			
Ace Glass, Inc.	12904-06	Silicone Septum O. D.: 11 mm Thickness: 3 mm Quantity: 12 per Package	c
Sigma-Aldrich	Z10,109-5	Double-Tipped Needle Material: Stainless Steel 304 Length: 24″ Gauge: 20	15
Vacuum Tubing and Connectors			
Sigma-Aldrich	Z25,592-0	Nalgene 180 Vacuum Tubing I. D.: ¼″ O. D.: ⅝″ Wall Thickness: 3/16″ Length: 10′	1
(Machine Shop)	(See Figure C.11)	316L Stainless Steel Connector (No O-Ring) For Size: 7 mm For I. D. Tubing: ¼″ O-Ring Size: -009	8
Ace Glass, Inc.	5029-10	Bushing (Includes FETFE O-Ring) Material: Nylon For Size: 7 mm I. D.: 7.5 mm O-Ring: -008	8
Sigma-Aldrich	Z22,420-0	Nylon Tubing Clamps Diameter Range: 17/32–19/32″ Quantity: 50 per Package	1
Marco Rubber and Plastic	(Not Applicable)	Aegis White SC1011 O-Ring Size: -009	8

TABLE D.2 Bill-of-materials for miscellaneous reaction equipment *(continued from page 326).*

MANUFACTURER	ITEM NUMBER	DESCRIPTION	QTY.
Water Tubing and Connectors			
Sigma-Aldrich	Z25,592-0	Nalgene 180 Vacuum Tubing I. D.: ¼" O. D.: ⅝" Wall Thickness: 3/16" Length: 10'	2
Ace Glass, Inc.	5853-06	"Ace-Safe" Connector, Tubing (Includes Nylon Bushing and Silicone O-Ring) Material: Glass-Filled PTFE For Size: 7 mm For I. D. Tubing: ¼" Connector I. D.: ⅛" O-Ring Size: -009	8
Sigma-Aldrich	Z22,420-0	Nylon Tubing Clamps Diameter Range: 17/32–19/32" Quantity: 50 per Package	1
Magnetic Stirring			
Ace Glass, Inc.	13655-29	Stirrer Magnets, Raised Ring, PTFE, Octagonal Length: 1" Diameter: ⅜"	a
Ace Glass, Inc.	13655-33	Stirrer Magnets, Raised Ring, PTFE, Octagonal Length: 1½" Diameter: ⅜"	a
Fisher Scientific, Intl.	14-511-64	Fisherbrand Magnetic Octagonal Bar Length: 1" Diameter: 5/16"	a
Ace Glass, Inc.	13556-501	Stirrer, Homogenizer Drive and Controller	2
Ace Glass, Inc.	8081-30	Flexible Shaft (36"), Complete Kit	2

TABLE D.2 Bill-of-materials for miscellaneous reaction equipment *(continued from page 327).*

MANUFACTURER	ITEM NUMBER	DESCRIPTION	QTY.
Magnetic Stirring (Continued)			
Chemglass, Inc.	CG-2011-20	Stirrer, Magnetic	2
Thermometers			
Fisher Scientific, Intl.	15-041-4D	Fisherbrand Red-Spirit Thermometer, General Purpose Laboratory Range: –20 to 150 °C Sub-Division: 1 °C Immersion: Partial (76 mm) Length: 305	[a]
Fisher Scientific, Intl.	15-077-14	Fisherbrand Traceable Total Range Digital Thermometer Range: –73 to 300 °C Accuracy: ±3 °C from –73 to –1 °C, ±2 °C from 0 to 150 °C, ±3 °C from 151 to 300 °C Thermocouple Probe: Beaded Type-K	1
Cooling			
Chemglass, Inc.	CG-1592-03	Flask, Dewar, Low Form, Cylindrical Capacity: 850 mL (Fits 500-mL Flasks) Depth: 75 mm Diameter: 130 mm	2
Heating			
Glas-Col	104A-PL120	PowerTrol Electrical Rating: 10 A at 120 V (1200 W)	4
Chemglass, Inc.	UI-0108-221D	Modified CG-10009-12 Mantle, Cylindrical Vessel, Bottom Drain Opening	2
Chemglass, Inc.	CG-10000-07	Mantle, Hemispherical, Glas-Col Capacity: 500 mL (Fits 500-mL Flasks)	2

TABLE D.2 Bill-of-materials for miscellaneous reaction equipment *(continued from page 328).*

Manufacturer	Item Number	Description	Qty.
Heating (Continued)			
Glas-Col	100A O1063	Mantle, Spherical Capacity: 500 mL (Fits 500-mL Flasks)	2
Chemglass, Inc.	CG-10000-08	Mantle, Hemispherical, Glas-Col Capacity: 1000 mL (Fits 1000-mL Flasks)	2
Glas-Col	100A O1083	Mantle, Spherical Capacity: 1000 mL (Fits 1000-mL Flasks)	2
Glas-Col	103B CC3	400 °C Cal-Cord Heating Cord Length: 3'	2
Glas-Col	103B CC4	400 °C Cal-Cord Heating Cord Length: 4'	2
Chemglass, Inc.	CG-10010-04	Mantle, Extension Support, Glas-Col Capacity: 500-mL Hemispherical Mantle	2
Chemglass, Inc.	CG-10010-05	Mantle, Extension Support, Glas-Col Capacity: 1000-mL Hemispherical Mantle	2

[a] Purchased as needed to supplement reaction apparatus.
[b] Purchased in one-to-one correspondence with matching bushings and plugs.
[c] Consumable item purchased routinely.

TABLE D.2 Bill-of-materials for miscellaneous reaction equipment *(continued from page 329).*

APPENDIX E

EQUIPMENT LISTS FOR SYNTHESES

In order to complete the silylamide and alkoxide syntheses presented in this dissertation, the Schlenkware described in Appendix D must be chemically cleaned, baked dry, and then assembled in an argon glove box. The resulting apparatus formed by these modular components represent functional units specialized for different stages of the reaction. This appendix provides detailed component lists, segmented by synthesis stage, that correlate to the various pictures given in Chapter 3. Certain equipment items (i.e., heating mantles, stirring shafts, etc.) are not included since any preparative effort required for their use is trivial. While not explicitly stated in the tables that follow, each synthesis presumes the availability (and attachment) of an in-line bubbler to vent any excess pressure inside the apparatus.

ITEM	QTY.
Reflux of Solvent	
Round-Bottom 1000-mL 4-Neck Flask	1
Ace-Thred Bushing, 15 mm, PTFE	1
Aegis O-Ring, Size: -110	1
Reflux Condenser	1
Thermometer, Red-Spirit	1
Ace-Thred Bushing, 7 mm, PTFE	2
Aegis O-Ring, Size: -008	1
Silicone Septa	1
1" Magnetic Octagonal Stir Bar, PTFE	1
Ace-Thred Plug, 7 mm, PTFE (Leave in Drying Oven Until Needed)	2
Aegis O-Ring, Size: -009 (Leave in Drying Oven Until Needed)	2
Ace-Thred Plug, 15 mm, PTFE (Leave in Drying Oven Until Needed)	1
Aegis O-Ring, Size: -110 (Leave in Drying Oven Until Needed)	1
Sparging with Argon	
Gas Dispersion Tube (Leave Assembled in Drying Oven Until Needed)	1
Ace-Thred Plug, 7 mm, PTFE (Leave Assembled in Drying Oven Until Needed)	1
Aegis O-Ring, Size: -009 (Leave Assembled in Drying Oven Until Needed)	1
Ace-Thred Bushing, 7 mm, PTFE (Leave Assembled in Drying Oven Until Needed)	1
Aegis O-Ring, Size: -008 (Leave Assembled in Drying Oven Until Needed)	1
Vacuum Cap, 15 mm (Leave Assembled in Drying Oven Until Needed)	1

TABLE E.1 Equipment list for solvent purification.

ITEM	QTY.
Weighing/Transfer Flask for 1,1,1,3,3,3-Hexamethyldisilazane	
Flat-Bottom 500-mL 3-Neck Flask	1
Ace-Thred Plug, 15 mm, PTFE	1
Aegis O-Ring, Size: -110	1
Ace-Thred Bushing, 7 mm, PTFE	1
Silicone Septa	1
Reaction of 1,1,1,3,3,3-Hexamethyldisilazane with n-Butyl Lithium	
Reaction Vessel Head	1
Reaction Vessel Flask, 1000-mL	1
Aegis O-Ring, Size: -348	1
"Quick Release" Clamp	1
1½" Magnetic Raised-Ring Octagonal Stir Bar, PTFE	1
Ace-Thred Plug, 15 mm, PTFE (Place in Drying Oven After Removal)	2
Aegis O-Ring, Size: -110 (Place in Drying Oven After Removal)	2
Ace-Thred Bushing, 7 mm, PTFE	2
Silicone Septa	2
Thermometer, Red-Spirit	1
Ace-Thred Bushing, 7 mm, PTFE	1
Aegis O-Ring, Size: -008	1
Reflux Condenser	1
Graduated Addition Funnel, 125 mL	1
Ace-Thred Bushing, 15 mm, PTFE	2
Aegis O-Ring, Size: -110	2
Vacuum Cap, 15 mm	2
Ace-Thred Plug, 7 mm, PTFE	2
Aegis O-Ring, Size: -009	2
Removal of Solvent under Reduced Pressure	
Round-Bottom 1000-mL 3-Neck Flask	1
Ace-Thred Plug, 7 mm, PTFE	1
Aegis O-Ring, Size: -009	1
Dewar Condenser	1

TABLE E.2 Equipment list for lithium silylamide synthesis *(continued on page 334).*

ITEM	QTY.
Removal of Solvent under Reduced Pressure (Continued)	
Ace-Thred Bushing, 15 mm, PTFE	3
Aegis O-Ring, Size: -110	3
Distillation Adapter, 75°	1
Vacuum Cap, 15 mm	1
Spare Items	
Ace-Thred Bushing, 7 mm, PTFE (Leave in Drying Oven Until Needed)	2
Silicone Septa (Leave in Drying Oven Until Needed)	4

TABLE E.2 Equipment list for lithium silylamide synthesis *(continued from page 333).*

ITEM	QTY.
Weighing/Transfer Flask for Pentane	
Flat-Bottom 500-mL 3-Neck Flask	1
Ace-Thred Plug, 15 mm, PTFE	1
Aegis O-Ring, Size: -110	1
Ace-Thred Bushing, 7 mm, PTFE	1
Silicone Septa	1
Weighing/Transfer Flask for Tetrahydrofuran	
Flat-Bottom 500-mL 3-Neck Flask	1
Ace-Thred Plug, 15 mm, PTFE	1
Aegis O-Ring, Size: -110	1
Ace-Thred Bushing, 7 mm, PTFE	1
Silicone Septa (Leave One in Drying Oven Until Needed)	2
Dissolution of LiN[Si(CH$_3$)]$_2$	
Flat-Bottom 500-mL 3-Neck Flask	1
Ace-Thred Plug, 15 mm, PTFE	1
Aegis O-Ring, Size: -110	1
Ace-Thred Bushing, 7 mm, PTFE	1
Silicone Septa (Leave One in Drying Oven Until Needed)	2
1″ Magnetic Octagonal Stir Bar, PTFE	1
Reflux and Reaction of MnCl$_2$ in Tetrahydrofuran	
Round-Bottom 1000-mL 4-Neck Flask	1
Reflux Condenser	1
Ace-Thred Bushing, 15 mm, PTFE	1
Aegis O-Ring, Size: -110	1
Thermometer, Red-Spirit	1
Ace-Thred Bushing, 7 mm, PTFE	2
Aegis O-Ring, Size: -008	1
Silicone Septa	1
1″ Magnetic Octagonal Stir Bar, PTFE	1
Ace-Thred Plug, 7 mm, PTFE (Leave in Drying Oven Until Needed)	2

TABLE E.3 Equipment list for manganese(II) silylamide synthesis *(continued on page 336)*.

ITEM	QTY.
Reflux and Reaction of MnCl$_2$ in Tetrahrydofuran (Continued)	
Aegis O-Ring, Size: -009 (Leave in Drying Oven Until Needed)	2
Silicone Septa (Leave in Drying Oven Until Needed)	1
Ace-Thred Plug, 15 mm, PTFE (Leave in Drying Oven Until Needed)	1
Aegis O-Ring, Size: -110 (Leave in Drying Oven Until Needed)	1
Removal of Solvent under Reduced Pressure	
Round-Bottom 500-mL 3-Neck Flask	1
Ace-Thred Plug, 7 mm, PTFE	1
Aegis O-Ring, Size: -009	1
Dewar Condenser	1
Ace-Thred Bushing, 15 mm, PTFE	3
Aegis O-Ring, Size: -110	3
Distillation Adapter, 75°	1
Vacuum Cap, 15 mm	1
Ace-Thred Bushing, 7 mm, PTFE (Leave in Drying Oven Until Needed)	1
Silicone Septa (Leave in Drying Oven Until Needed)	1
Filtration of LiCl	
Round-Bottom 1000-mL 3-Neck Flask	1
Ace-Thred Plug, 15 mm, PTFE	1
Aegis O-Ring, Size: -110	1
1" Magnetic Octagonal Stir Bar, PTFE	1
Glass Filter Cannula	1
Aegis O-Ring, Size: -005	1
Ace-Thred Bushing, 7 mm, PTFE	3
Aegis O-Ring, Size: -008	3
Vacuum Cap, 7 mm	1
Ace-Thred Plug, 7 mm, PTFE (Leave in Drying Oven Until Needed)	1
Aegis O-Ring, Size: -009 (Leave in Drying Oven Until Needed)	1
Distillation and Thermolysis of Mn{N[Si(CH$_3$)]$_2$}$_2$ · xC$_4$H$_8$O	
Round-Bottom 500-mL 3-Neck Flask	1
Ace-Thred Plug, 7 mm, PTFE	2

TABLE E.3 Equipment list for manganese(II) silylamide synthesis *(continued from page 335).*

ITEM	QTY.
Distillation and Thermolysis of Mn{N[Si(CH₃)]₂}₂ · xC₄H₈O (Continued)	
Aegis O-Ring, Size: -009	2
1" Magnetic Octagonal Stir Bar, PTFE	1
Ace-Thred Bushing, 15 mm, PTFE	3
Aegis O-Ring, Size: -110	3
Extension Adapter	1
Vigreux Distillation Column	1
Vacuum Cap, 15 mm	1
Ace-Thred Plug, 15 mm, PTFE (Leave in Drying Oven Until Needed)	1
Aegis O-Ring, Size: -110 (Leave in Drying Oven Until Needed)	1
Inlet Valve (Leave Assembled in Argon Glove Box Until Needed)	1
Ace-Thred Bushing, 7 mm, PTFE, (Leave Assembled in Argon Glove Box Until Needed)	1
Aegis O-Ring, Size: -008 (Leave Assembled in Argon Glove Box Until Needed)	1
Vacuum Cap, 7 mm (Leave Assembled in Argon Glove Box Until Needed)	1
Crystallization of Purified Mn{N[Si(CH₃)]₂}₂	
Reaction Vessel Head	1
Reaction Vessel Flask, 1000-mL	1
Aegis O-Ring, Size: -348	1
"Quick Release" Clamp	1
1" Magnetic Octagonal Stir Bar, PTFE	1
Ace-Thred Plug, 15 mm, PTFE	2
Aegis O-Ring, Size: -110	2
Ace-Thred Plug, 7 mm, PTFE	1
Aegis O-Ring, Size: -009	1
Ace-Thred Bushing, 7 mm, PTFE	1
Silicone Septa	1
Ace-Thred Plug, 7 mm, PTFE, (Leave in Drying Oven Until Needed)	1
Aegis O-Ring, Size: -009, (Leave in Drying Oven Until Needed)	1
Spare Items	
Ace-Thred Bushing, 7 mm, PTFE (Leave in Drying Oven Until Needed)	3
Silicone Septa (Leave in Drying Oven Until Needed)	6

The table headers use italic formatting where shown. Section titles with formulas: *Distillation and Thermolysis of* $Mn\{N[Si(CH_3)]_2\}_2 \cdot xC_4H_8O$ *(Continued)* and *Crystallization of Purified* $Mn\{N[Si(CH_3)]_2\}_2$

TABLE E.3 Equipment list for manganese(II) silylamide synthesis *(continued from page 336).*

Item	Qty.
Weighing/Transfer Flask for Pentane	
Flat-Bottom 500-mL 3-Neck Flask	1
Ace-Thred Plug, 15 mm, PTFE	1
Aegis O-Ring, Size: -110	1
Ace-Thred Bushing, 7 mm, PTFE	1
Silicone Septa (Leave One in Drying Oven Until Needed)	2
Weighing/Transfer Flask for Tetrahydrofuran	
Flat-Bottom 500-mL 3-Neck Flask	1
Ace-Thred Plug, 15 mm, PTFE	1
Aegis O-Ring, Size: -110	1
Ace-Thred Bushing, 7 mm, PTFE	1
Silicone Septa (Leave One in Drying Oven Until Needed)	2
Dissolution of $LiN[Si(CH_3)]_2$	
Flat-Bottom 500-mL 3-Neck Flask	1
Ace-Thred Plug, 15 mm, PTFE	1
Aegis O-Ring, Size: -110	1
Ace-Thred Bushing, 7 mm, PTFE	1
Silicone Septa (Leave One in Drying Oven Until Needed)	2
1" Magnetic Octagonal Stir Bar, PTFE	1
Reaction of $PbCl_2$ in Tetrahydrofuran	
Round-Bottom 500-mL 3-Neck Flask	1
Ace-Thred Plug, 15 mm, PTFE	1
Aegis O-Ring, Size: -110	1
Ace-Thred Bushing, 7 mm, PTFE	1
Silicone Septa	1
1" Magnetic Octagonal Stir Bar, PTFE	1
Ace-Thred Plug, 7 mm, PTFE (Leave in Drying Oven Until Needed)	1
Aegis O-Ring, Size: -009 (Leave in Drying Oven Until Needed)	1

TABLE E.4 Equipment list for lead(II) silylamide synthesis *(contin-
ued on page 339)*.

Item	Qty.
Removal of Solvent under Reduced Pressure	
Round-Bottom 500-mL 3-Neck Flask	1
Ace-Thred Plug, 7 mm, PTFE	1
Aegis O-Ring, Size: -009	1
Dewar Condenser	1
Ace-Thred Bushing, 15 mm, PTFE	3
Aegis O-Ring, Size: -110	3
Vigreux Column	1
Ace-Thred Bushing, 7 mm, PTFE (Leave One in Drying Oven Until Needed)	2
Silicone Septa (Leave two in Drying Oven Until Needed)	3
Vacuum Cap, 15 mm	1
Ace-Thred Plug, 7 mm, PTFE (Leave in Drying Oven Until Needed)	1
Aegis O-Ring, Size: -009 (Leave in Drying Oven Until Needed)	1
Filtration of LiCl	
Round-Bottom 500-mL 3-Neck Flask	1
Ace-Thred Plug, 15 mm, PTFE	1
Aegis O-Ring, Size: -110	1
1" Magnetic Octagonal Stir Bar, PTFE	1
Glass Filter Cannula	1
Aegis O-Ring, Size: -005	1
Ace-Thred Bushing, 7 mm, PTFE	3
Aegis O-Ring, Size: -008	3
Vacuum Cap, 7 mm	1
Ace-Thred Plug, 7 mm, PTFE (Leave in Drying Oven Until Needed)	1
Aegis O-Ring, Size: -009 (Leave in Drying Oven Until Needed)	1
Reduced Pressure Distillation of $Pb\{N[Si(CH_3)]_2\}_2$	
Reaction Vessel Head	1
Reaction Vessel Flask, 1000-mL	1
Aegis O-Ring, Size: -348	1
"Quick Release" Clamp	1
1" Magnetic Octagonal Stir Bar, PTFE	1
Ace-Thred Plug, 15 mm, PTFE	2

TABLE E.4 Equipment list for lead(II) silylamide synthesis *(continued from page 338).*

ITEM	QTY.
Reduced Pressure Distillation of Pb{N[Si(CH$_3$)]$_2$}$_2$ (Continued)	
Aegis O-Ring, Size: -110	2
Ace-Thred Plug, 7 mm, PTFE	2
Aegis O-Ring, Size: -009	2
Extension Adapter	1
Ace-Thred Bushing, 15 mm, PTFE	1
Aegis O-Ring, Size: -110	1
Removal of Pentane after Cleaning of Reaction Flask Interior	
Distillation Adapter, 75°	1
Ace-Thred Bushing, 15 mm, PTFE	1
Aegis O-Ring, Size: -110	1
Vacuum Cap, 15 mm	1
Spare Items	
Ace-Thred Plug, 15 mm, PTFE (Leave in Drying Oven Until Needed)	2
Aegis O-Ring, Size: -110 (Leave in Drying Oven Until Needed)	2
Ace-Thred Bushing, 7 mm, PTFE (Leave in Drying Oven Until Needed)	3
Silicone Septa (Leave in Drying Oven Until Needed)	6

TABLE E.4 Equipment list for lead(II) silylamide synthesis *(continued from page 339).*

ITEM	QTY.
Weighing/Transfer Flask for Pentane	
Flat-Bottom 500-mL 3-Neck Flask	1
Ace-Thred Plug, 15 mm, PTFE	1
Aegis O-Ring, Size: -110	1
Ace-Thred Bushing, 7 mm, PTFE	1
Silicone Septa	1
Weighing/Transfer Flask for 2-Methyl-2-Propanol	
Flat-Bottom 500-mL 3-Neck Flask	1
Ace-Thred Plug, 15 mm, PTFE	1
Aegis O-Ring, Size: -110	1
Ace-Thred Bushing, 7 mm, PTFE	1
Silicone Septa	1
Reaction of Dissolved Silylamide with Alcohol	
Reaction Vessel Head	1
Reaction Vessel Flask, 1000-mL	1
Aegis O-Ring, Size: -348	1
"Quick Release" Clamp	1
1½" Magnetic Raised-Ring Octagonal Stir Bar, PTFE	1
Ace-Thred Plug, 15 mm, PTFE	2
Aegis O-Ring, Size: -110	2
Ace-Thred Plug, 7 mm, PTFE	1
Aegis O-Ring, Size: -009	1
Ace-Thred Bushing, 7 mm, PTFE	1
Silicone Septa	1
Ace-Thred Plug, 7 mm, PTFE (Leave in Drying Oven Until Needed)	1
Aegis O-Ring, Size: -009 (Leave in Drying Oven Until Needed)	1
Removal of Solvent under Reduced Pressure	
Round-Bottom 500-mL 3-Neck Flask	1
Ace-Thred Plug, 7 mm, PTFE	1
Aegis O-Ring, Size: -009	1

TABLE E.5 Equipment list for conversion of silylamide to alkoxide *(continued on page 342)*.

ITEM	QTY.
Removal of Solvent under Reduced Pressure (Continued)	
Dewar Condenser	1
Ace-Thred Bushing, 15 mm, PTFE	3
Aegis O-Ring, Size: -110	3
Distillation Adapter, 75°	1
Vacuum Cap, 15 mm	1
Spare Items	
Ace-Thred Bushing, 7 mm, PTFE (Leave in Drying Oven Until Needed)	3
Silicone Septa (Leave in Drying Oven Until Needed)	6

TABLE E.5 Equipment list for conversion of silylamide to alkoxide *(continued from page 341).*

ITEM	QTY.
Weighing/Transfer Flask for Benzene	
Flat-Bottom 500-mL 3-Neck Flask	1
Ace-Thred Plug, 15 mm, PTFE	1
Aegis O-Ring, Size: -110	1
Ace-Thred Bushing, 7 mm, PTFE	1
Silicone Septa	1
Weighing/Transfer Flask for 2-Methyl-2-Propanol	
Flat-Bottom 500-mL 3-Neck Flask	1
Ace-Thred Plug, 15 mm, PTFE	1
Aegis O-Ring, Size: -110	1
Ace-Thred Bushing, 7 mm, PTFE	1
Silicone Septa (Leave One in Drying Oven Until Needed)	2
Reaction of Barium Granules with Alcohol	
Reaction Vessel Head	1
Reaction Vessel Flask, 1000-mL	1
Aegis O-Ring, Size: -348	1
"Quick Release" Clamp	1
1½" Magnetic Raised-Ring Octagonal Stir Bar, PTFE	1
Ace-Thred Plug, 15 mm, PTFE	2
Aegis O-Ring, Size: -110	2
Ace-Thred Plug, 7 mm, PTFE	1
Aegis O-Ring, Size: -009	1
Ace-Thred Bushing, 7 mm, PTFE	1
Silicone Septa	1
Ace-Thred Plug, 7 mm, PTFE (Leave in Drying Oven Until Needed)	1
Aegis O-Ring, Size: -009 (Leave in Drying Oven Until Needed)	1
Removal of Solvent under Reduced Pressure	
Round-Bottom 500-mL 3-Neck Flask	1
Ace-Thred Plug, 7 mm, PTFE	1
Aegis O-Ring, Size: -009	1

TABLE E.6 Equipment list for synthesis of 2-methyl-2-propoxo barium

ITEM	QTY.
Removal of Solvent under Reduced Pressure (Continued)	
Dewar Condenser	1
Ace-Thred Bushing, 15 mm, PTFE	3
Aegis O-Ring, Size: -110	3
Distillation Adapter, 75°	1
Vacuum Cap, 15 mm	1
Spare Items	
Ace-Thred Bushing, 7 mm, PTFE (Leave in Drying Oven Until Needed)	3
Silicone Septa (Leave in Drying Oven Until Needed)	6

TABLE E.6 Equipment list for synthesis of 2-methyl-2-propoxo barium *(continued from page 343).*

APPENDIX F

SYNTHESIS OF LANTHANUM SILYLAMIDE

The author's first attempts to synthesize lanthanum silylamide were adapted from BRA-
DLEY, et al. [1], and thus, relied on $LiN[Si(CH_3)_3]_2$ as the starting reagent. But despite pro-
longed reflux (i.e., both before and after exposure of the suspended chloride to lithium
silylamide) no meaningful lanthanum content was detected in the resulting white sublimate.
On the contrary, chemical analysis indicated good agreement with theoretical values for
$LiN[Si(CH_3)_3]_2$. Furthermore, subsequent efforts to synthesize 2-methyl-2-propoxo lantha-
num by alkoxy metathesis (i.e., see EVANS, et al. [2]) left only the reagent compounds and not
the expected products. Clearly, the suspended $LaCl_3$ was behaving as inert matter, a result
of poor solvent coordination (i.e., from THF in both cases). The author ultimately traced this
problem to the morphology provided by the commercial source: the corresponding small,
spherical (i.e., 2–3 mm diameter) pellets were very dense, and even after extensive grinding,
failed to confer adequate surface area for solvation.

A proper methodology dictates the dehydration of $LaCl_3 \cdot 7H_2O$ (i.e., heating in flowing
HCl gas). This process would transform the chloride into a highly-susceptible, broken crys-
talline state (see Section 2.4.4). Unfortunately, due to time constraints, the author was unable
incorporate such a remedy. This appendix presents a typical synthesis using (instead) potas-
sium silylamide (i.e., as recommended by ANWANDER [2]). The full optimizations discussed
in Section 2.4.5, however, were discovered much later and therefore were not included. All
preparative procedures and air-sensitive techniques for this reaction follow the guidelines
given by Chapter 3. An equipment list for the *optimized* synthesis method concludes this
appendix but presumes a suitable commercial (or readily-available) $LaCl_3$ source.

To a round-bottom 1000-mL, 3-necked flask was added 39.567 g (0.1613 mol) of Alfa
Aesar 35702, lanthanum(III) chloride, ultra dry, 99.9% (REO), packed under argon. This
reagent, however, came from the manufacturer as spherical pellets and therefore required
grinding into a fine powder. A milky, white suspension was created by adding 158.75 g (179
mL) of THF via cannulation (see Figure F.1).[1] Separately, 96.40 g (0.4832 mol) of Aldrich
32,467-1, potassium bis(trimethylsilyl)amide, 95% was dissolved via the addition of 371.62 g

(418 mL) of THF. The silylamide solution was transferred into the chloride suspension and stirred at room temperature overnight (i.e., ~ 12 hours).[2] The ethereal solvent was then stripped under reduced pressure to leave a light-tan solid.[3]

To enable separation, this residue was exposed to 306.54 g (490 mL) of pentane (see Figure F.2). Aggressive stirring with gentle heating activated the extraction process. Aliquots of the resulting mostly-clear, golden solution were transferred into centrifuge tubes, which in turn, were loaded into a Damon/IEC Division HN-SII centrifuge and spun at 1000 rpm for 10–15 minutes. The resulting supernatant was cannulated into a cylindrical reaction kettle. After stripping the pentane, the kettle was moved into a glove box and the dried, off-white solid ground in a mortar and pestle, creating a fine powder.

This powder was subsequently placed into a sublimation chamber (see Figure F.2). A glass wool plug was inserted within the glass stem of the exit valve to prevent contamination of the vacuum manifold. The apparatus was placed *under vacuum first* and then *slowly heated* to 100 °C. Residual organic volatiles (i.e., THF and pentane) were driven out during ramp-up, after which, the vacuum stabilized (i.e., ~ 1×10^{-1} torr). Dry-ice pellets and 2-propanol were added to the cold finger between 80–90 °C causing the internal pressure to drop (i.e., ~ 1×10^{-2} torr). Above 95 °C, faint transparent crystallites could be seen forming on the internal base of the cold finger. Their volume, however, was barely discernable and could not be easily photographed. As already mentioned in the introduction, such a negligible yield stemmed from the use of $LaCl_3$ reagent with an unsuitable starting morphology.

[1] Bradley, D. C.; Ghotra, J. S.; Hart, F. A. Low Co-ordination Numbers in Lanthanide and Actinide Compounds. Part I. The Preparation and Characterization of Tris{bis(trimethylsilyl)-amido}lanthanides. *Journal of the Chemical Society, Dalton Transactions* **1973**, (10), 1021–1023.

[2] Evans, W. J.; Sollberger, M. S.; Hanusa, T. P. Synthesis and Structure of the Polymetallic Yttrium Alkoxide Complex $Y_3(\mu_3\text{-OCMe}_3)(\mu_3\text{-Cl})(\mu\text{-OCMe}_3)(\text{OCMe}_3)_4(\text{THF})_2$ and Related Complexes: $Ln_3(\mu_3\text{-OR})(\mu_3\text{-X})(\mu\text{-OR})_3$ Building Blocks in Yttrium and Lanthanide Alkoxide Chemistry. *Journal of the American Chemical Society* **1988**, *110* (6), 1841–1850.

[3] Anwander, R. Lanthanide Amides. *Topics in Current Chemistry* **1996**, *179*, 33–112.

---

[1] Ideally, reflux should be conducted at this point to enhance the coordination of THF to the suspended chloride.
[2] In the refined method, the combined system must be refluxed for 4–6 hours.
[3] For the optimized method, thermolysis at 150 °C must be conducted immediately thereafter.
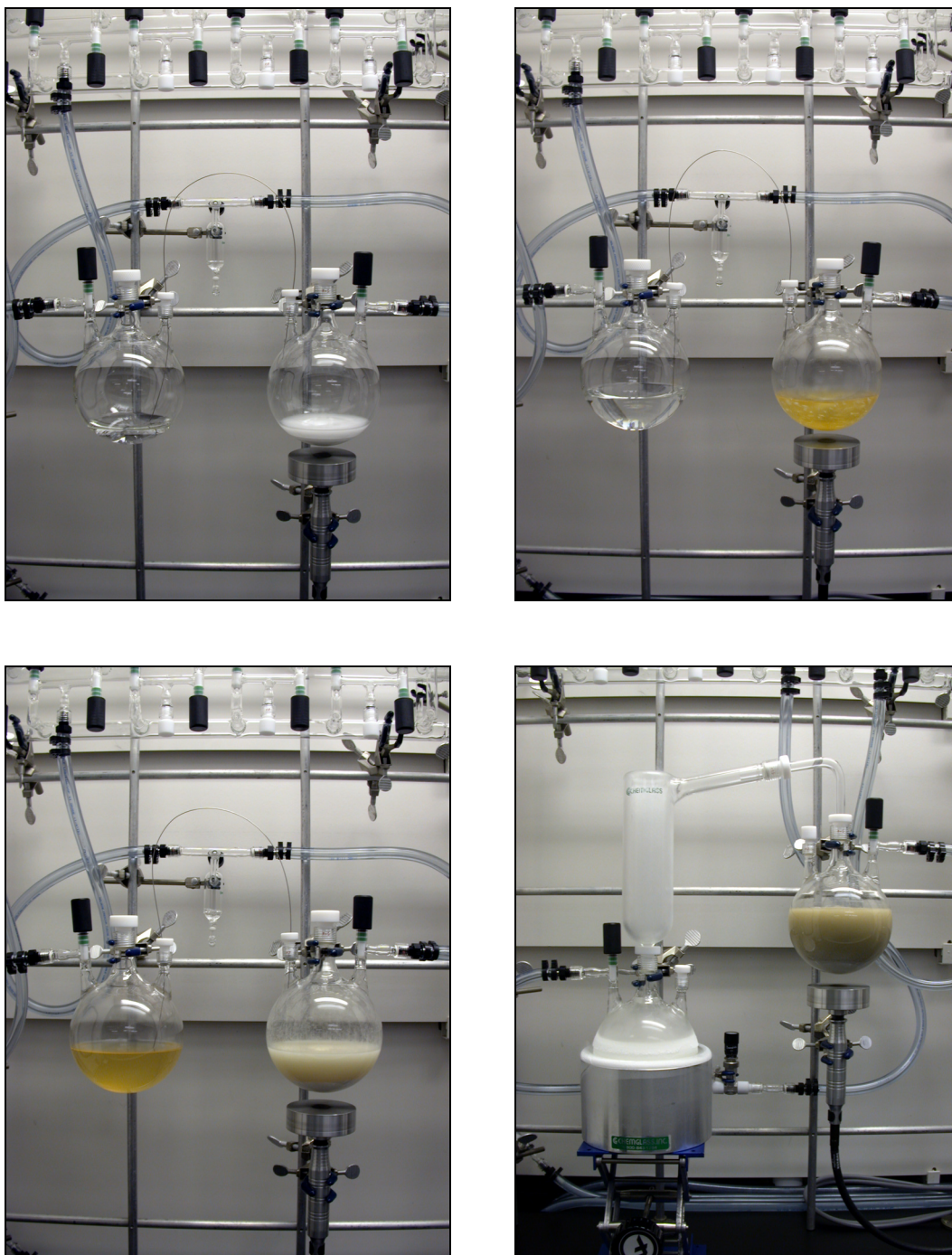
FIGURE F.1 The synthesis of lanthanum silylamide. The top row depicts the addition of THF to anhydrous lanthanum chloride (left) and potassium silylamide (right). Cannulation (bottom row) of the silylamide solution into the chloride suspension (left) is eventually followed by solvent removal (right).

FIGURE F.2 Separation of lanthanum silylamide from potassium chloride. The cannulation of pentane (left) onto the residue allows extraction via centrifuge (right). Transfer of the resulting supernatant into a container suitable for solids removal allows the necessary solvent strip (bottom row).
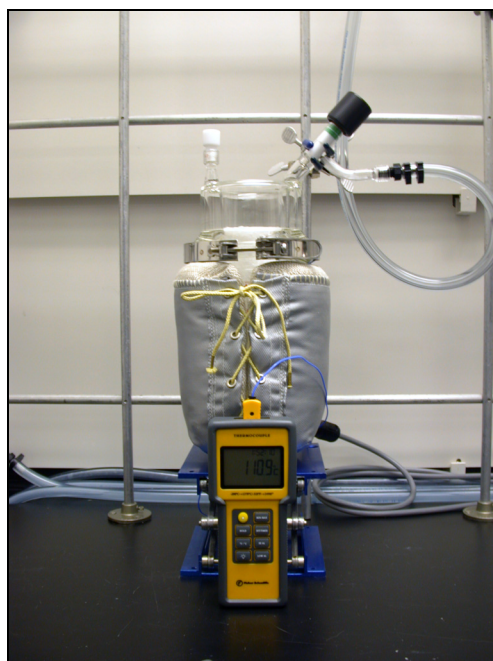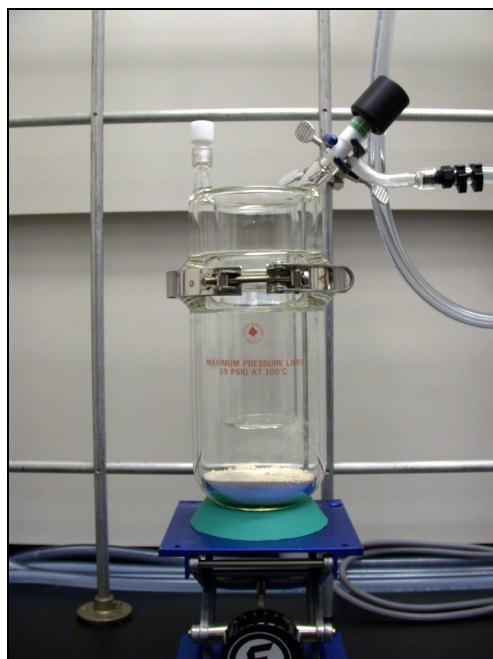
FIGURE F.3 Sublimation of lanthanum silylamide. The interior cold finger is filled with a 2-propanol/dry ice bath. A glass wool plug resides within the side valve stem, shielding the vacuum manifold from contaminants.

ITEM	QTY.
Weighing/Transfer Flask for Pentane	
Flat-Bottom 500-mL 3-Neck Flask	1
Ace-Thred Plug, 15 mm, PTFE	1
Aegis O-Ring, Size: -110	1
Ace-Thred Bushing, 7 mm, PTFE	1
Silicone Septa	1
Weighing/Transfer Flask for Tetrahydrofuran	
Flat-Bottom 500-mL 3-Neck Flask	1
Ace-Thred Plug, 15 mm, PTFE	1
Aegis O-Ring, Size: -110	1
Ace-Thred Bushing, 7 mm, PTFE	1
Silicone Septa (Leave One in Drying Oven Until Needed)	2
Dissolution of $KN[Si(CH_3)]_2$	
Flat-Bottom 500-mL 3-Neck Flask	1
Ace-Thred Plug, 15 mm, PTFE	1
Aegis O-Ring, Size: -110	1
Ace-Thred Bushing, 7 mm, PTFE	1
Silicone Septa (Leave One in Drying Oven Until Needed)	2
1" Magnetic Octagonal Stir Bar, PTFE	1
Reaction of $LaCl_3$ in Tetrahydrofuran	
Round-Bottom 1000-mL 3-Neck Flask	1
Ace-Thred Plug, 15 mm, PTFE	1
Aegis O-Ring, Size: -110	1
Ace-Thred Bushing, 7 mm, PTFE	1
Silicone Septa	1
1" Magnetic Octagonal Stir Bar, PTFE	1
Ace-Thred Plug, 7 mm, PTFE (Leave in Drying Oven Until Needed)	1
Aegis O-Ring, Size: -009 (Leave in Drying Oven Until Needed)	1

TABLE F.1 Equipment list for lanthanum silylamide synthesis *(continued on page 351).*

ITEM	QTY.
Removal of Solvent under Reduced Pressure	
Round-Bottom 1000-mL 3-Neck Flask	1
Ace-Thred Plug, 7 mm, PTFE	1
Aegis O-Ring, Size: -009	1
Dewar Condenser	1
Ace-Thred Bushing, 15 mm, PTFE	3
Aegis O-Ring, Size: -110	3
Distillation Adapter, 75°	1
Vacuum Cap, 15 mm	1
Ace-Thred Bushing, 7 mm, PTFE (Leave in Drying Oven Until Needed)	1
Silicone Septa (Leave in Drying Oven Until Needed)	1
Thermolysis of Li-La Silylamide-Chloride Residue	
Inlet Valve	1
Ace-Thred Bushing, 7 mm, PTFE	1
Aegis O-Ring, Size: -008	1
Vacuum Cap, 7 mm	1
Removal of LiCl by Centrifuge	
Centrifuge Tube	10
Ace-Thred Bushing, 7 mm, PTFE	10
Silicone Septa (Leave in Drying Oven Until Needed)	10
Collection of Dissolved La{N[Si(CH$_3$)]$_2$}$_3$	
Reaction Vessel Head	1
Reaction Vessel Flask, 1000-mL	1
Aegis O-Ring, Size: -348	1
"Quick Release" Clamp	1
1" Magnetic Octagonal Stir Bar, PTFE	1
Ace-Thred Plug, 15 mm, PTFE	2
Aegis O-Ring, Size: -110	2
Ace-Thred Plug, 7 mm, PTFE	1
Aegis O-Ring, Size: -009	1
Ace-Thred Bushing, 7 mm, PTFE	1

TABLE F.1 Equipment list for lanthanum silylamide synthesis *(continued from page 350)*.

ITEM	QTY.
Silicone Septa (Leave One in Drying Oven Until Needed)	2
Ace-Thred Plug, 7 mm, PTFE, (Leave in Drying Oven Until Needed)	1
Aegis O-Ring, Size: -009, (Leave in Drying Oven Until Needed)	1

Sublimation of La{N[Si(CH$_3$)]$_2$}$_3$

Sublimation Head	1
Reaction Vessel Flask, 1000-mL	1
Aegis O-Ring, Size: -348	1
"Quick Release" Clamp	1
Ace-Thred Plug, 7 mm, PTFE	1
Aegis O-Ring, Size: -009	1

Spare Items

Ace-Thred Bushing, 7 mm, PTFE (Leave in Drying Oven Until Needed)	3
Silicone Septa (Leave in Drying Oven Until Needed)	6

TABLE F.1 Equipment list for lanthanum silylamide synthesis *(continued from page 351).*

AUTHOR'S BIOGRAPHY

Brent Allen Clothier was born in Fort Rucker, Alabama in 1970. In 1989, he enrolled in the Plan II/Engineering honors program at the University of Texas at Austin, completing both a B.S. in Mechanical Engineering (1994) and a B.A. in Plan II Liberal Arts (1995, in absentia). His Plan II senior thesis, conducted under the supervision of Professor Arumugam Manthiram, investigated the influence of firing temperature on the structure and properties of $YBa_2Cu_3O_{6+x}$ ceramics synthesized by aqueous solution processing. After graduation he joined Motorola, Inc. as a process engineer in the manufacture of surface mount electronics.

In 1995, he entered the University of Illinois at Urbana-Champaign, beginning work in the Department of Materials Science and Engineering under the direction of Professor David A. Payne. Initial research focused on characterizing the electrical and magnetic properties of bulk single crystal doped-lanthanide manganites, the results of which were published in 1999. During this investigation, though, he received an IMAPS Educational Foundation Grant (1998) to develop sol-gel processing methods to deposit thin films of commercially-promising manganite compositions. This dissertation reflects the culmination of research originally fostered by that award. Brent is a member of the American Ceramics Society (ACerS), the Materials Research Society (MRS), the International Microelectronics and Packaging Society (IMAPS), and the National Society of Professional Engineers (NSPE).